



FEUP FACULDADE DE ENGENHARIA
UNIVERSIDADE DO PORTO

***RELIABILITY ANALYSIS APPLIED TO THE
OPTIMIZATION OF DYNAMIC SCOUR
PROTECTIONS FOR OFFSHORE WINDFARM
FOUNDATIONS***

TIAGO JOÃO FAZERES MARQUES FERRADOSA

Doctoral Program in Civil Engineering

Supervisor: Professor Doctor Francisco de Almeida Taveira Pinto

Co-Supervisor: Professor Doctor Luciana Paiva das Neves

Co-Supervisor: Engineer Doctor Maria Teresa Leal Gonsalves Veloso dos Reis

PORTO, 24TH MAY 2018

DOCTORAMENTO EM ENGENHARIA CIVIL 2017/2018

DEPARTAMENTO DE ENGENHARIA CIVIL

Tel. + 351-22-508 1901

Fax +351-22-508 1446

Email: prodec@fe.up.pt

Edited by

FACULDADE DE ENGENHARIA DA UNIVERSIDADE DO PORTO

Rua Dr. Roberto Frias s/n

4200-465 PORTO

Portugal

Tel. + 351-22-508 1400

Fax +351-22-508 1440

Email: feup@fe.up.pt

Website: <http://www.fe.up.pt>

Partial reproductions of this document are authorized provided that the author's name is mentioned and that reference is made to Doctoral Program in Civil Engineering 2017/2018, Department of Civil Engineering, Faculty of Engineering, University of Porto.

The opinions and information provided in this work correspond to the author's view alone.

**RELIABILITY ANALYSIS APPLIED TO THE OPTIMIZATION OF DYNAMIC SCOUR PROTECTIONS FOR
OFFSHORE WIND FOUNDATIONS**

TIAGO JOÃO FAZERES MARQUES FERRADOSA

DOCTORAL PROGRAM IN CIVIL ENGINEERING

MAY 24, 2018

ABSTRACT

Scour protection is an important and expensive component of fixed bottom foundations for offshore wind turbines. Depending on the hydrodynamic conditions, they might be indispensable to avoid the structural collapse of the foundation due to scour phenomena. The optimisation of scour protections is a key step towards the improvement of cost-benefit ratios related to the construction of offshore windfarms. The design of scour protections is typically deterministic, which often results in overestimated mean diameters of the armour layer. Moreover, the design methodologies currently applied do not provide a measure of safety associated to the proposed design. Therefore, at the state-of-the-art, when optimising a scour protection, the reliability of the proposed solution remains unknown. Firstly, because no reliability analysis is commonly performed and, secondly because the optimisation by means of dynamic stability is yet to be fully understood. The possibility of implementing dynamic scour protections, instead of the traditional statically stable ones, is of great importance to minimise the investments required for an offshore fixed foundation. However, an underlying question remains: *is a dynamic scour protection as reliable as statically stable one?*

The present research aims at answering this question while, simultaneously, contributing to optimise the design of dynamic scour protections. In order to reach this objective, a physical model study was performed concerning the analysis of the damage number in scour protections. The physical models considered a monopile foundation subjected to storm conditions, typical from the North Sea. The present thesis, the physical models and the reliability analysis specifically focus on monopile foundations, considering the met-ocean data available for the offshore windfarm Horns Rev 3 (Denmark). The reliability analysis considered the Monte-Carlo simulation method, which is used to obtain the probability of failure of both static and dynamic scour protections. The failure mode studied in this work concerns the erosion of the top layer, which was defined by means of the threshold of motion and the acceptable number.

The results obtained from the physical modelling study contributed to validate the limits of the acceptable damage number, for dynamic scour protections. The configurations studied for the scour protection show that under the same hydrodynamic conditions, the design based on the damage number consistently leads to reduced, i.e. optimised, mean stone diameters of the armour layer, whereas the design based on the threshold of motion leads to larger diameters. The reliability analysis concluded that it is possible to perform a probabilistic and reliability-based design that defines the safety level associated to different mean stone diameters, between the statically stable and the dynamically stable design. The present research contributes with a reliability assessment methodology that enables the designer to optimize a static scour protection towards a dynamically stable one with a similar probability of failure, i.e. measure of safety.

KEYWORDS:

Dynamic Scour Protection; Reliability; Physical Modelling; Damage Number; Probability of Failure

RESUMO

Uma proteção contra erosões localizadas é um componente importante e oneroso, utilizado em fundações fixas de turbinas eólicas *offshore*. Dependendo das condições hidrodinâmicas, estas proteções podem ser indispensáveis para acautelar o colapso estrutural da fundação, causado pelos fenómenos de erosões localizadas. A otimização destas proteções é um passo crucial para a melhoria dos rácios custo-benefício relacionados com a construção de parques eólicos *offshore*. O dimensionamento deste tipo de proteções é tipicamente determinístico, o que resulta, frequentemente, no sobredimensionamento dos blocos utilizados no manto resistente da proteção. Acresce-se ainda o facto de as metodologias, correntemente aplicadas, não fornecerem uma medida de fiabilidade associada ao dimensionamento proposto. De acordo com o estado da arte, a fiabilidade de uma proteção otimizada é ainda uma variável desconhecida. Primeiramente, porque a análise de fiabilidade não é comumente aplicada e, em segundo lugar, porque a otimização baseada na estabilidade dinâmica se encontra ainda por compreender, na sua totalidade.

A possibilidade de utilizar proteções dinâmicas, em vez das tradicionais proteções estáticas, é de suma importância para minimizar o investimento financeiro associado às fundações fixas *offshore*. No entanto, a questão subjacente é: *será que uma proteção dinâmica é tão segura como uma proteção estática?* A presente investigação pretende responder a esta questão, contribuindo simultaneamente para a otimização do dimensionamento de proteções dinâmicas. Para cumprir com este objetivo, efetuou-se a análise do parâmetro de danos em proteções contra erosões localizadas através de um estudo experimental, com recurso à modelação física. A presente tese, os modelos físicos e a análise de fiabilidade focam-se especificamente numa fundação do tipo monopilar sujeita a condições de tempestade, típicas do Mar do Norte. Levou-se a cabo um estudo de fiabilidade utilizando dados meta-oceânicos do parque eólico *offshore* Horns Rev 3 (Dinamarca). O estudo de fiabilidade baseou-se no método de simulação de Monte-Carlo, para a obtenção da probabilidade de falha associado a proteções estáticas e dinâmicas. O modo de falha estudado diz respeito à erosão do manto resistente, sendo que este foi definido com base nas condições de início de movimento e no parâmetro de danos aceitável.

Os resultados obtidos da modelação física validaram os limites aceitáveis para o parâmetro de danos. As configurações estudadas, sob as mesmas condições hidrodinâmicas, mostraram que o dimensionamento baseado no parâmetro de danos conduziu, sistematicamente, a diâmetros médios dos blocos que se encontram otimizados, isto é menores, do que aqueles que foram obtidos pelo dimensionamento baseado nas condições de início de movimento. A análise de fiabilidade permitiu concluir que é possível efetuar um dimensionamento probabilístico, que define o nível de segurança associado a diferentes diâmetros médios dos blocos, entre o dimensionamento estático e dinâmico. A presente investigação fornece uma metodologia de avaliação da segurança da proteção, permitindo a otimização de uma proteção estática que caminha para uma estabilidade dinâmica com uma probabilidade de falha, isto é uma medida de segurança, semelhante.

PALAVRAS CHAVE:

Proteção Dinâmica; Fiabilidade; Modelação Física; Parâmetro de Danos; Probabilidade de Falha.

*To Joana, Francisco,
Daniel and Dulce*

*“I bargained with Life for a penny,
And Life would pay no more,
However I begged at evening
When I counted my scanty store;*

*For Life is a just employer,
He gives you what you ask,
But once you have set the wages,
Why, you must bear the task.*

*I worked for a menial’s hire,
Only to learn, dismayed,
That any wage I had asked of Life,
Life would have paid.”*

*My Wage
Jessie B. Rittenhouse (1869 – 1948)*

ACKNOWLEDGEMENTS

More than a scientific challenge the PhD is an endurance test, full of learning experiences that come with a full measure of sacrifice. However, the present research is a result of numerous contributions, without them this work would not be possible. Therefore, the author sincerely acknowledges each and every person or institution that has somehow contributed to the development of the this research.

The author acknowledges his Supervisor, Professor Doctor Francisco Taveira Pinto, for the exceptional support throughout this work and for granting to the author the professional and academic opportunities of a lifetime (FEUP), for being a mentor more than a Supervisor. The author acknowledges the Co-supervisor, Professor Luciana das Neves (FEUP/IMDC) for the help throughout MARINET project. A particular acknowledgement is made to Co-supervisor, Doctor Maria Teresa Reis (LNEC), for the motivation and the detailed scientific guidance of this thesis.

The author sincerely acknowledges to Professor Doctor Richard Simons (UCL) for his incommensurable kindness and support during these years. Professor Doctor Richard Simons was the main responsible for introducing the author to wonders of research in maritime engineering. No words can express the importance of the author's time spent at University College London under his supervision.

A word of gratitude to the author's friends and colleagues at FEUP, Guillerme, Vanessa, Bruno, Eliamin and Ricardo, which helped the author to overcome the difficulties of the academic world. The author also recognizes Bruno's contribution to the some of the computational scripts of this work.

An acknowledgement is also made to Professor Doctor Xavier Romão (FEUP and Doctor Erik Vanem (DNVGL) for the important contributions concerning reliability analysis and statistical modelling. The author expresses his gratitude to Professor Doctor Rodrigo Maia (FEUP), for his unparalleled human dimension and kindness since the first day of the author's career. Deep gratitude to Doctor Richard Whitehouse (HRW), Doctor John Harris (HRW) and Doctor Leen De Vos for the enlightening discussions on scour research. The author kindly acknowledges all the partners of the project MARINET proposal 61, which have contributed with an important part of the results analysed in this research. A recognition is given to Doctor José Correia (FEUP) for his efforts in helping the author to reach new and ambitious personal and professional goals. The author thanks to all the members of the Board of Studies of INFRARISK Doctoral Program, for believing that he would be capable of performing the present research and for granting him his PhD scholarship.

The upmost acknowledgement to Professor Doctor Miguel Castro for his true friendship, for his priceless advices and for being present in each and every single defining moment of the author's professional and personal path.

Finally, the present work was a result of the support of an amazing family! The author acknowledges his brother Daniel for his support throughout the last 28 years, his mother, Dulce, for the unlimited affection and encouragement. A recognition is given to the author's grandparents, to Maria do Carmo

and all his family members, who kept him going through the tough years of this research. The deepest acknowledgement his made to his father, Francisco, not only for his support and advices throughout the PhD years, but mostly for being the first to believe that this endeavour was a real possibility.

Finally and foremost, the author acknowledges his wife Joana, for her patience and kindness for her companionship in the lonely hours spent writing this thesis, analysing data and for motivating me throughout all the moments of doubt and disbelief. She is the main reason why this work has started and she is the main reason why this work has come to a good end.

This research and T. Fazeres-Ferradosa are funded by the Portuguese Foundation for Science and Technology (FCT), under the Ph.D. scholarship PD/BD/113454/2015 – Doctoral Program INFRARISK.

FCT Fundação para a Ciência e a Tecnologia
MINISTÉRIO DA CIÊNCIA, TECNOLOGIA E ENSINO SUPERIOR



NOMENCLATURE

Symbols

| | |
|---|--|
| A | [m] – Amplitude of the orbital motion at the bed or wave stroke |
| A, A ₁ , A ₂ | [-] – Constant |
| A _{sub} | [m ²] – Area of the sub-area of the scour protection, $\pi D_p^2/4$ |
| A* | [m ²] – Projected area of the grain on the horizontal plane |
| a | [m] – Wave amplitude, H/2 |
| a0 | [-] – Coefficient for hydrodynamic conditions |
| a1 | [-] – Regression fitting coefficient |
| a2 | [-] – Regression fitting coefficient |
| a3 | [-] – Regression fitting coefficient |
| a4 | [-] – Coefficient for hydrodynamic conditions |
| B, B ₁ | [-] – Constants |
| B _{ij} | [m.s] – Bin of size i×j |
| b ₀ | [-] – Regression fitting coefficient |
| C | [-] – Confidence level |
| C(u,v) | [-] – Copula function |
| C, C ₁ , C ₂ , C ₃ | [-] – Constants |
| Ch | [m ^{1/2} /s] – Chézy coefficient |
| C _{ij} | [-] – i th copula with parameters j of an extra-parametrized copula |
| C _n | [-] – Empirical copula |
| C _s | [-] – Stability coefficient |
| C _v | [-] – Velocity distribution coefficient |
| C _μ | [-] – Confidence interval of μ |
| C _σ | [-] – Confidence interval of σ |
| c' | [-] – Concordant pair |
| c | [-] – Copula density |
| c _p | [-] – Control limit of the Chi-plot |
| D | [-] – Failure domain |
| D* | [-] – Dimensionless grain size |
| D ₅₀ | [m] – Mean stone diameter of the scour protection |
| D ₅₀ * | [-] – Equivalent reduced mean stone diameter as an optimization of D ₅₀ . |
| D _k | [-] – Debye function applied to the copula parameter |
| D _n | [m] – Nominal diameter |
| D _p | [m] – Pile diameter |
| D _r | [m] – Minimum stone diameter |
| D _s | [m] – Diameter of a sphere |
| D _{sx} | [m] – Characteristic size of an equivalent for which x% is finer by weight |
| D _x | [m] – Stones size for which x% is finer by weight |
| d | [m] – Water depth |
| d ₅₀ | [m] – Mean diameter of the sediments |
| d' | [-] – Discordant pair |
| d _s | [m] – Diameter of the sediment grain |

| | |
|----------------|---|
| d_x | [m] – Sediments size for which x% is finer by weight |
| E | [-] – Expected value of a variable |
| e | [-] – Nepper's number |
| F | [-] – Cumulative distribution function |
| F1_00j | [-] – Scour test number j of series F1 |
| F_D | [N] – Horizontal drag force |
| F_i, G_i | [-] – Empirical cumulative distribution functions |
| F_L | [N] – Vertical lift force |
| F_{np} | [-] – p th empirical cumulative distribution function |
| Fr | [-] – Froude number |
| F_s | [N] – Frictional force between grains |
| f | [-] – Probability density function |
| f_0 | [1/s] – First natural frequency |
| f_c | [-] – Current friction coefficient |
| f_i | [1/s] – Wave frequency. $1/T_i$ |
| f_n | [1/s] – Natural frequency |
| $f_{nyquist}$ | [1/s] – Nyquist frequency |
| f_p | [1/s] – Peak frequency |
| f_s | [1/s] – Sampling frequency |
| f_w | [-] – Wave friction factor |
| G | [-] – Standardized limit state function |
| g | [-] – Limit state function |
| g | [m/s ²] – Gravitational acceleration |
| $\tilde{g}(X)$ | [-] – Analytical approximated function of the limit state function |
| H | [m] – Wave height |
| H_0 | [-] – Dimensionless wave height parameter, $H_s/(\Delta D_{50})$ |
| $H_{1/n}$ | [m] – Mean wave height of the highest 1/n wave heights |
| H_b | [m] – Wave breaking height |
| H_d | [m] – Design wave height |
| H_i | [-] – Empirical joint cumulative distribution function |
| H_i | [s] – Wave height of an individual wave in an irregular wave train |
| H_m | [m] – Mean wave height |
| H_{m0} | [m] – Spectral wave height, calculated through the spectral density |
| $H_{m0,N}$ | [m] – Spectral wave height from the 0 th order moment of a wave train with N waves |
| H_{max} | [m] – Maximum wave height in a wave train |
| H_{rms} | [m] – Root-mean-square wave height |
| H_s | [m] – Significant wave height |
| H_{si} | [m] – i th significant wave height |
| H_{smax} | [m] – Maximum significant wave height |
| H_{tot} | [N] – Total maximum transversal load at the monopile's interface with the soil |
| I | [-] – Indicator function |
| J_1 | [-] – Distribution function of the indicator function |
| K_0 | [-] – Dependence curve between random variables |
| KC | [-] – Keulegan Carpenter number |
| K_d | [-] – Flow depth factor |
| K_{gr} | [-] – Correction factor for a group of piers |
| K_1 | [-] – Side slope correction factor |

| | |
|--------------------|---|
| KS | [-] – Kolmogorov-Smirnov distance |
| K_s | [-] – Pier shape factor |
| k_s | [m] – Bottom roughness $2.5d_{50}$ |
| K_{si} | [-] – Pier size factor |
| K_{sl} | [-] – Slope factor |
| K_T | [-] – Turbulence factor |
| K_w | [-] – Correction factor for sediment dimension |
| K_α | [-] – Pier alignment factor |
| K_σ | [-] – Grain size distribution factor |
| k | [-] – Number of parameters in a copula-based models |
| k | [-] – Von Karman constant |
| k | [-] – Wave number, $2\pi/L$ |
| k_i | [-] – Negative second partial derivative at the standardized design point y^* |
| L | [m] – Wave length |
| L_{ext} | [m] – Radial extent of the scour protection |
| $\log(\mu)$ | [-] – Mean parameter of the log normal distribution |
| $\log(\sigma)$ | [-] – Standard deviation parameter of the lognormal distribution |
| L_s | [m] – Extension of the scour protection |
| M | [-] – Safety margin |
| m | [kg] – Mass |
| m_n | [-] – n^{th} order moment |
| M_{tot} | [N.m] – Total maximum momentum at the bed |
| N | [waves] – Number of waves |
| N_{charac} | [waves] – Characteristic number of waves |
| n | [-] – Sample size or number of simulations |
| n_a | [m] – Armour layer thickness |
| n_f | [m] – Filter layer thickness |
| P_f | [-] – Probability of failure |
| P_{f0} | [-] – Annual probability of failure |
| P_r | [-] – Probability of reliability, $1-P_f$ |
| R | [-] – Resistance |
| R^2 | [-] – Squared correlation coefficient |
| Re | [-] – Reynolds number |
| Re^* | [-] – Grain Reynolds number |
| Re_A | [-] – Wave stroke Reynolds number |
| Re_p | [-] – Pile Reynolds number |
| Ri_{Sj} | [-] – Sub-area, Sector j of Ring i |
| R_p | [-] – Parameter of the Rayleigh distribution |
| r_x | [-] – Rank of x |
| r_y | [-] – Rank of y |
| S | [-] – Structural response given by response surface methods |
| S | [-] – Load |
| S | [m] – Scour depth |
| $S(f)$ | [m^2/s] – Spectral density |
| S_{3D} | [-] – Dimensionless damage number |
| S_{3D}/n_a | [-] – Damage number per number of layers in the scour protection |
| $S_{3Dacceptable}$ | [-] – Acceptable damage number |
| $S_{3Dmeasured}$ | [-] – Measured damage number |

| | |
|-----------------------------|---|
| $S_{3DN_{\text{measured}}}$ | [-] – Damage number after N waves |
| $S_{3D_{\text{predicted}}}$ | [-] – Predicted damage number |
| $S_{3D_{\text{sub}}}$ | [-] – Damage number of the sub-area |
| S_b | [-] – Dimensionless damage number of a breakwater |
| S_c | [m] – Current-induced scour depth |
| S_e | [m] – Equilibrium scour depth |
| S_f | [-] – Safety factor |
| $S_U(f)$ | [m ² /s] – Power spectrum of the bottom velocity |
| s | [-] – Crámer-von Mises distance |
| s | [-] – Specific density, ρ_s/ρ_w |
| si_{0j} | [-] – MARINET scour test number j of series i |
| $stab$ | [-] – Stability parameter, $\theta_{\text{max}}/\theta_{\text{cr}}$ |
| T | [-] – Time scale of the scour process |
| T | [s] – Wave period |
| $T(f)$ | [s] – Wave period as function of the frequency |
| T_0 | [s] – Measurement duration of a wave record |
| T_{CW} | [s] – Time scale in clear-water regime |
| T_i | [s] – Wave period of an individual wave in an irregular wave train |
| T_{LB} | [s] – Time scale in live-bed regime |
| $T_{m-1,0}$ | [s] – Energy wave period |
| $T_{mi,j}$ | [s] – Wave period obtained from the i th order moment and the j th order moment |
| T_p | [s] – Wave peak period |
| $T_{p\text{max}}$ | [s] – Maximum peak period |
| T_{wi} | [s] – Wave period of the i th wave |
| T_r | [years] – Return period |
| T_z | [s] – Mean up- or down-crossing wave period |
| t | [s] – Time |
| t_0 | [m] – Pile penetration depth |
| t_e | [s] – Time scale of the equilibrium scour depth |
| t_{sp} | [m] – Scour protection thickness |
| t_v | [-] – Student t- distribution |
| t_w | [m] – Wall thickness of the monopile foundation |
| U | [m/s] – Velocity |
| U_b | [m/s] – Current velocity at 0.1d counting from the bottom |
| U_c | [m/s] – Depth-averaged current velocity |
| U_{combined} | [m/s] – Current velocity in combined wave and current flow |
| U_{cr} | [m] – Critical velocity |
| U_{cw} | [-] – Velocity ratio, $U_c/(U_c+U_m)$ |
| U_{cwN} | [m/s] – Velocity ratio after N waves |
| U_m | [m/s] – Maximum wave orbital velocity |
| $U_{m10\%}$ | [m/s] – Orbital velocity amplitude exceeded by 10% of the waves |
| U_r | [-] – Ursell number |
| U_w | [m/s] – Horizontal wave orbital velocity |
| u | [-] – Uniform transformed variable of x, $F^{-1}(x)$ |
| u | [m/s] – Amplitude of the horizontal velocity |
| u^* | [m/s] – Friction velocity |
| u_{cr}^* | [m/s] – Critical friction velocity |
| V_d | [m ³] – Volume of empty spaces between particles |

| | |
|------------------|---|
| V_e | [-] – Eroded volume |
| V_s | [m ³] – Volume of a solid rock |
| v | [-] – Uniform transformed variable of y , $F^{-1}(y)$ |
| W | [m] – Scour hole extent |
| W | [N] – Submerged weight of a grain particle |
| w | [rad/s] – Angular frequency |
| W_{50} | [N] – Mean weight of the stones of the armour layer |
| $W_{i:n}$ | [-] – Expectation of the i^{th} order statistic in a random sample of size n from K_0 to H_i |
| W_p | [m] – Scour hole extent in the orthogonal direction of W |
| WS | [-] – Wasserstein distance |
| w_{ij} | [-] – Weights attributed to the errors of a copula-based model |
| w_s | [m/s] – Settling or fall velocity |
| X | [-] – Vector of basic random variables |
| x | [m] – Horizontal distance |
| x_{eff} | [m] – Effective length of the horseshoe vortex in streamwise direction |
| x_i | [-] – Random variable |
| x_i^* | [-] – Coordinate of the design point |
| x_{ij} | [-] – Number of points from an empirical dataset that fall into B_{ij} |
| X_m | [-] – Mean point composed of the mean values of the vector X |
| X_{rel} | [m] – Relative length of the horseshoe vortex in streamwise direction |
| y | [m] – Vertical distance |
| y_i | [-] – Random variable in the standardized space |
| y_i^* | [-] – Coordinate of the design point in the standardized space |
| y_{ij} | [-] – Number of points from a simulated dataset that fall into B_{ij} |
| z | [m] – Vertical distance, $z=0$ at the water level |
| z_0 | [m] – Roughness length |

Greek Symbols

| | |
|------------------------|---|
| α | [-] – Amplification factor |
| α | [-] – Scale parameter |
| α | [-] – Spectral constant |
| α | [-] – Parameter of an extra-parametrized copula |
| α | [-] – Integral precision |
| α_{down} | [°] – Downstream slope of the scour hole |
| α_i^* | [-] – Coefficient of the Hasofer-Lind method |
| α_{up} | [°] – Upstream slope of the scour hole |
| β | [-] – Reliability index |
| β | [-] – Shape parameter |
| β | [-] – Spectral constant |
| β | [-] – Parameter of an extra-parametrized copula |
| γ | [-] – Location parameter |
| γ | [-] – Peak enhancement factor |
| δ | [m] – Boundary layer thickness |
| Δ | [-] – Relative density of sediment $(\rho_s - \rho_w)/\rho_w$ |
| Δf | [1/s] – Frequency band |
| ΔH | [m] – Eroded height |
| ΔS_{3D} | [-] – Variation of the damage number |
| ε | [-] – Error of J_1 |
| ε | [-] – Stability correcting factor |

| | |
|-----------------|---|
| ε | [-] – Tawn type 2 copula parameter |
| θ | [-] – Copula parameter |
| θ | [-] – Shields parameter |
| θ_{cr} | [-] – Critical Shields parameter |
| θ_{max} | [-] – Maximum Shields parameter |
| λ | [-] – Regression constant for sensitivity analysis |
| λ_i | [-] – Measure of distance of the pair X_i, Y_i from the centre of the dataset |
| λ_L | [-] – Lower tail coefficient |
| λ_U | [-] – Upper tail coefficient |
| μ | [-] – Mean |
| μ_x' | [-] – Parameter mean of the equivalent normal distribution of x |
| $\mu_{Y X}$ | [-] – Mean of Y conditioned on X |
| ν | [m ² /s] – Kinematic viscosity of water |
| ξ | [-] – Tawn type 2 copula parameter |
| ρ_d | [kg/m ³] – Bulk density |
| ρ_s | [kg/m ³] – Sediment or stones mass density |
| ρ_{spear} | [-] – Spearman's rho |
| ρ_w | [kg/m ³] – Water mass density |
| σ | [-] – Standard deviation |
| σ_U | [-] – Uniformity parameter |
| σ_V | [-] – Orbital velocity spectrum |
| σ_x | [-] – Parameter standard deviation of the equivalent normal distribution of x |
| $\sigma_{Y X}$ | [-] – Standard deviation of Y conditioned on X |
| τ | [N/m ²] – Amplified bed shear stress |
| τ_{∞} | [N/m ²] – Undisturbed bed shear stress |
| τ_b | [N/m ²] – Bed shear stress |
| $\tau_{b,c}$ | [N/m ²] – Undisturbed current-induced bed shear stress |
| $\tau_{b,w}$ | [N/m ²] – Undisturbed wave-induced bed shear stress |
| τ_c | [N/m ²] – Current-induced bed shear stress |
| τ_{cr} | [N/m ²] – Critical bed shear stress |
| τ_{cw} | [N/m ²] – Wave- and current-induced bed shear stress |
| τ_K | [-] – Kendall's tau |
| τ_m | [N/m ²] – Mean combined bed shear stress, current- and wave-induced. |
| τ_{max} | [N/m ²] – Maximum combined bed shear stress, current- and wave-induced. |
| τ_w | [N/m ²] – Wave-induced bed shear stress |
| ν | [-] – Number of degrees of freedom |
| ν | [-] – Rate parameter of the exponential distribution |
| φ | [-] – Generator function of a copula |
| ϕ | [-] – Standardized normal distribution |
| ϕ | [°] – Angle between the propagating direction of waves and currents |
| ϕ_i | [°] – Internal friction angle of the soil |
| Φ | [-] – Standardized normal distribution of a uniform transformed variable |
| χ_j | [-] – Chi statistic of the pair X_i, Y_i |
| Ψ | [rad] – Phase shift |
| Ψ_{cr} | [-] – Stability factor |
| Ω | [-] – Pearson coefficient |

ABBREVIATIONS

ACF – Auto-Correlation Function
ADV – Acoustic Doppler Velocimeter
AF – Amplification Factor
AIC – Akaike Information Criteria
AMH – Ali-Mikhail-Haq
BIC – Bayesian Information Criteria
BKDE – Bi-variate Kernel density estimation method
CAPEX – Capital Expenditures
CDF – Cumulative distribution function
DK – Denmark
DMI – Danish Meteorological Institute
ECDF – Empirical cumulative distribution function
EEW – Erndtebrücker Eisenwerk Hermann Klein Co. and GmbH
EU – European Union
EWEA – European Wind Energy Association
FEUP – Faculty of Engineering of University of Porto
FGM – Farlie-Gumbel-Morgenstern
FLS – Fatigue limit state
FORM – First-Order Reliability Method
GBF – Gravity Based Foundations
GEV – Generalized Extreme Value distribution
GP – Generalized Pareto distribution
HR – Hüssler-Reiss
HRW – HR Wallingford
IMDC – International Marine and Dredging Consultants
JONSWAP – Joint North Sea Wave Project
LCoE – Levelized Cost of Energy
LSF – Limit state function
MARINET – Marine Renewables Infrastructure Network
MVFORM – Advanced First-Order Second-Method
MVFOSM – Mean Value First-Order Second-Moment
MLE – Maximum Likelihood Estimation
O&M – Operance and Maintenance
OPEX – Operance Capital Expenditures
OPTI-PILE – Optimisation of Monopile foundations for offshore wind turbines in deep water and North Sea conditions
PDF – Probability density function
PM – Pierson-Moskowitz
PT – Portugal
ROM – Recomendaciones para Obras Marítimas

SLS – Service limit state
SORM – Second-Order Reliability Method
SWL – Still-water level
TRL – Technology Readiness Level
UK – United Kingdom
ULS – Ultimate limit state
USA – United States of America
WG – Wave gauge
WRSME – Weighted-root-mean-square error

TABLE OF CONTENTS

| | |
|--|---------------|
| TABLE OF CONTENTS..... | xxi |
| LIST OF FIGURES | xxvii |
| LIST OF TABLES | xxxiii |
| 1 Introduction..... | 1 |
| 1.1 <i>Introductory note</i> | <i>1</i> |
| 1.2 <i>Brief overview of the European offshore wind sector</i> | <i>1</i> |
| 1.3 <i>Key trends and the need to optimise the foundations</i> | <i>2</i> |
| 1.4 <i>Thesis scope and objectives</i> | <i>8</i> |
| 1.5 <i>Thesis outline</i> | <i>9</i> |
| 2 Fundamentals of Scour | 13 |
| 2.1 <i>Introduction to scour in offshore wind turbines</i> | <i>13</i> |
| 2.2 <i>Bed shear stress and boundary layers.....</i> | <i>13</i> |
| 2.2.1 <i>Waves and current</i> | <i>13</i> |
| 2.2.2 <i>Combined waves and current.....</i> | <i>18</i> |
| 2.3 <i>Amplified bed shear stress and amplification factor.....</i> | <i>19</i> |
| 2.4 <i>Threshold of motion</i> | <i>20</i> |
| 2.5 <i>Hydrodynamic flow around a monopile foundation</i> | <i>22</i> |
| 2.5.1 <i>Downflow in front of the pile</i> | <i>23</i> |
| 2.5.2 <i>Horseshoe vortex.....</i> | <i>23</i> |
| 2.5.3 <i>Lee-wake vortices</i> | <i>24</i> |
| 2.5.4 <i>Contraction of the streamlines</i> | <i>24</i> |
| 2.6 <i>Global and local Scour.....</i> | <i>24</i> |
| 2.7 <i>Equilibrium scour depth and time-scaling of scour</i> | <i>25</i> |
| 2.8 <i>Clear-water scour versus live-bed scour.....</i> | <i>26</i> |
| 2.9 <i>Scour depth around a monopile foundation</i> | <i>27</i> |
| 2.9.1 <i>Scour prediction in a steady current</i> | <i>27</i> |
| 2.9.2 <i>Scour prediction in waves.....</i> | <i>28</i> |
| 2.9.3 <i>Scour prediction in combined waves and current.....</i> | <i>29</i> |
| 2.10 <i>Scour extent</i> | <i>32</i> |
| 2.11 <i>Conclusions.....</i> | <i>32</i> |
| 3 Scour Protection Design | 35 |
| 3.1 <i>Introduction to scour protection</i> | <i>35</i> |

| | | |
|----------|---|-----------|
| 3.2 | <i>The need of scour protections for the design of offshore wind turbines</i> | 36 |
| 3.3 | <i>Failure modes of a scour protection</i> | 40 |
| 3.4 | <i>Design parameters of scour protections</i> | 41 |
| 3.5 | <i>Environmental parameters</i> | 42 |
| 3.5.1 | Water depth | 43 |
| 3.5.2 | Wave characteristics | 43 |
| 3.5.2.1 | Non-linear waves | 45 |
| 3.5.2.2 | Irregular waves | 47 |
| 3.5.2.3 | Design wave height and period | 51 |
| 3.5.3 | Number of waves | 52 |
| 3.5.4 | Flow characteristics | 53 |
| 3.5.5 | Sediment characteristics | 53 |
| 3.6 | <i>Structural parameters</i> | 54 |
| 3.6.1 | Density of the rock material | 55 |
| 3.6.2 | Stone size and weight | 55 |
| 3.6.3 | Stone grading and shape | 56 |
| 3.7 | <i>Design criteria for scour protections around monopile foundations</i> | 57 |
| 3.7.1 | Required minimum stone size | 57 |
| 3.7.1.1 | Static versus dynamic scour protections | 57 |
| 3.7.1.2 | Statically stable stone size | 58 |
| 3.7.1.3 | Optimised statically stable stone size | 61 |
| 3.7.1.4 | Dynamically stable stone size | 71 |
| 3.7.1.5 | Optimised dynamically stable stone size | 72 |
| 3.7.2 | Radial extent and thickness of the scour protection | 80 |
| 3.8 | <i>Notes on the deterministic optimised design</i> | 84 |
| 3.9 | <i>Notes on scale effects, physical modelling and monitoring of scour protections</i> | 85 |
| 3.10 | <i>Conclusions</i> | 90 |
| 4 | Experimental Study on Dynamic Scour Protections | 93 |
| 4.1 | <i>Introduction and background of the experimental research</i> | 93 |
| 4.2 | <i>Experimental research program within the MARINET proposal 61</i> | 93 |
| 4.2.1 | Introduction | 93 |
| 4.2.2 | Prototype conditions | 95 |
| 4.2.3 | Facilities, scour protection test setup and model conditions | 96 |
| 4.2.3.1 | Hydrodynamic model conditions | 102 |
| 4.2.3.2 | Scour protection model | 104 |
| 4.2.3.3 | Measurements and equipment | 106 |
| 4.2.3.4 | Range of test conditions | 107 |
| 4.2.3.5 | Scour protection tests and configurations | 110 |
| 4.2.4 | Methodology of analysis | 111 |
| 4.2.5 | Discussion of scale and model effects of the MARINET proposal 61 | 115 |
| 4.2.6 | Analysis and discussion of results from MARINET proposal 61 | 117 |

| | | |
|---------|---|-----|
| 4.2.6.1 | Measured conditions | 117 |
| 4.2.6.2 | Test repeatability | 119 |
| 4.2.6.3 | Overall measured damage numbers..... | 124 |
| 4.2.6.4 | Damage location | 146 |
| 4.2.6.5 | Acceptable damage of a scour protection | 152 |
| 4.3 | <i>Experimental research programme at FEUP</i> | 161 |
| 4.3.1 | Prototype conditions | 162 |
| 4.3.2 | Facilities at the laboratory, scour protection test setup and model conditions..... | 163 |
| 4.3.2.1 | Model hydrodynamic conditions | 167 |
| 4.3.2.2 | Scour protection model | 168 |
| 4.3.2.3 | Measurements and equipment | 169 |
| 4.3.2.4 | Note on the range of test conditions..... | 170 |
| 4.3.2.5 | Scour protection tests and configurations..... | 171 |
| 4.3.3 | Methodology of analysis..... | 171 |
| 4.3.4 | Discussion of scale and model effects of the experimental work at FEUP | 172 |
| 4.3.5 | Analysis and discussion of results from the experimental work at FEUP | 174 |
| 4.3.5.1 | Measured conditions | 174 |
| 4.3.5.2 | Test repeatability | 176 |
| 4.3.5.3 | Overall measured damage numbers..... | 177 |
| 4.3.5.4 | Measured damage numbers and type of stability | 179 |
| 4.3.5.5 | Comparison with the stability parameter from OPTI-PILE..... | 181 |
| 4.3.5.6 | Predicted damage numbers..... | 182 |
| 4.4 | <i>Conclusions</i> | 184 |

5 Fundamentals of Reliability Analysis and Statistical Modelling189

| | | |
|---------|---|-----|
| 5.1 | <i>Introduction</i> | 189 |
| 5.2 | <i>Background and introduction to reliability analysis</i> | 190 |
| 5.3 | <i>Probabilistic reliability measure and reliability problems</i> | 191 |
| 5.3.1 | Probabilistic measure of reliability | 191 |
| 5.3.2 | Fundamental reliability problem | 193 |
| 5.3.3 | Probability of failure for normally distributed variables alone..... | 195 |
| 5.3.4 | General case of a reliability problem..... | 196 |
| 5.4 | <i>Methods of reliability analysis</i> | 197 |
| 5.4.1 | Approximate methods | 199 |
| 5.4.1.1 | Mean-Value First-Order Second-Moment (MVFOSM) method..... | 199 |
| 5.4.1.2 | Advanced First-Order Second-Moment (MVFORM) method | 201 |
| 5.4.1.3 | Second-order methods | 203 |
| 5.4.2 | Direct integration methods | 205 |
| 5.4.2.1 | Standardised integral region..... | 205 |
| 5.4.2.2 | Joint probability density function | 205 |
| 5.4.2.3 | Multivariate integration..... | 206 |
| 5.4.3 | Simulation methods..... | 206 |
| 5.4.3.1 | Monte Carlo Simulation method | 207 |

| | | |
|----------|---|------------|
| 5.4.3.2 | Required sample size | 209 |
| 5.4.3.3 | Response surface methods | 211 |
| 5.5 | <i>Notes on the choice of reliability methods for scour protection design</i> | 214 |
| 5.6 | <i>Limit state functions and the need to model correlated variables and statistical model framework</i> | 215 |
| 5.7 | <i>Goodness-of-fit of the Marginal Distributions</i> | 217 |
| 5.8 | <i>Correlated variables and measures of dependence</i> | 220 |
| 5.8.1 | Measures of dependence | 220 |
| 5.8.2 | Assessing dependence with graphical tools | 220 |
| 5.9 | <i>Introduction and review of joint models applied to correlated wave heights and wave periods</i> | 223 |
| 5.10 | <i>Copula-based models</i> | 226 |
| 5.10.1 | Introduction to copulas | 226 |
| 5.10.2 | Basic copula families | 227 |
| 5.10.2.1 | Empirical and Independent copulas..... | 227 |
| 5.10.2.2 | Elliptical copulas..... | 227 |
| 5.10.2.3 | Archimedean copulas..... | 228 |
| 5.10.3 | Extra-parametrization of copulas | 229 |
| 5.10.3.1 | Extra-parametrization with an independent copula | 229 |
| 5.10.3.2 | Extra-parametrization with a pairwise copula | 230 |
| 5.10.4 | AIC and BIC criterion | 230 |
| 5.11 | <i>Conditional modelling approach</i> | 230 |
| 5.12 | <i>Kernel density estimation method</i> | 231 |
| 5.13 | <i>Conclusions</i> | 232 |
| 6 | Reliability Analysis of Dynamic Scour Protections..... | 235 |
| 6.1 | <i>Introduction</i> | 235 |
| 6.2 | <i>Reliability assessment of dynamic scour protections at Horns Rev 3 with copula models</i> | 236 |
| 6.2.1 | Failure criterion of dynamic scour protections..... | 236 |
| 6.2.2 | Reliability assessment of dynamic scour protections | 237 |
| 6.2.3 | Horns Rev 3 offshore windfarm | 238 |
| 6.2.4 | Statistical model and Marginal distributions | 240 |
| 6.2.4.1 | Significant wave heights and peak period..... | 241 |
| 6.2.4.2 | Current velocity..... | 243 |
| 6.2.4.3 | Water depth..... | 243 |
| 6.2.4.4 | Nominal mean stone diameter of the armour layer | 244 |
| 6.2.5 | Joint models for significant wave heights and peak periods | 245 |
| 6.2.5.1 | Measures of dependence | 245 |
| 6.2.5.2 | Assessing dependence with graphical tools..... | 246 |
| 6.2.5.3 | Independent copula and Bivariate Kernel density estimation method (BKDE) | 248 |
| 6.2.5.4 | Copula-based models..... | 250 |
| 6.2.5.5 | AIC and BIC criteria | 254 |
| 6.2.6 | Probability of failure of dynamic scour protections | 255 |
| 6.2.6.1 | Validation and comparison of results | 255 |
| 6.2.6.2 | Application to Horns Rev 3..... | 259 |

| | | |
|----------|---|------------|
| 6.2.7 | Tail dependence analysis | 262 |
| 6.2.8 | Influence of Kendall's τ (τ_K) | 263 |
| 6.2.9 | Sensitivity analysis | 264 |
| 6.2.9.1 | Sensitivity to the mean stone diameter (D_{50}) | 264 |
| 6.2.9.2 | Sensitivity to current velocity (U_c) | 265 |
| 6.2.9.3 | Sensitivity to the acceptable damage number ($S_{3Dacceptable}$) | 266 |
| 6.2.9.4 | Sensitivity to the water depth (d) | 268 |
| 6.2.10 | Final remarks on the reliability of dynamic scour protections with copulas | 268 |
| 6.3 | <i>Asymmetric copula-based distribution models for met-ocean data</i> | 269 |
| 6.3.1 | Wave data | 270 |
| 6.3.2 | Wave data pre-processing | 271 |
| 6.3.3 | Marginal distributions | 276 |
| 6.3.4 | Copula-based models for the significant wave height and up-crossing mean period | 278 |
| 6.3.4.1 | Empirical copula | 278 |
| 6.3.4.2 | Symmetric copula-based models | 279 |
| 6.3.4.3 | Extra-parametrization with an independent copula | 281 |
| 6.3.4.4 | Extra-parametrization with a pairwise copula | 285 |
| 6.3.4.5 | Extra-parametrization with a Gumbel copula | 287 |
| 6.3.5 | Tail dependence analysis | 289 |
| 6.3.6 | WRMSE analysis | 292 |
| 6.3.6.1 | Extra-parametrized copulas (independent and pairwise copula) | 292 |
| 6.3.6.2 | Extra-parametrized copulas with a Gumbel copula | 295 |
| 6.3.7 | Discussion and applications to wind engineering | 296 |
| 6.3.8 | Final remarks on asymmetric copula-based distribution models for met-ocean data | 298 |
| 6.4 | <i>Conclusions</i> | 298 |
| 7 | Safety of Static and Dynamic Scour Protections | 301 |
| 7.1 | <i>Introduction</i> | 301 |
| 7.2 | <i>Revisiting the deterministic design and failure of scour protections</i> | 302 |
| 7.2.1 | Static scour protections | 302 |
| 7.2.2 | Dynamic scour protections | 303 |
| 7.2.3 | Notes on the design methodologies | 303 |
| 7.3 | <i>Reliability analysis and probabilistic design of scour protection</i> | 304 |
| 7.4 | <i>Design Results</i> | 309 |
| 7.4.1 | Deterministic design results | 309 |
| 7.4.2 | Probabilistic design of scour protections | 313 |
| 7.5 | <i>Conclusions</i> | 318 |
| 8 | Conclusions and Future Developments | 321 |
| 8.1 | <i>Conclusions</i> | 321 |

| | | |
|-----------|------------------------------|------------|
| 8.2 | <i>Future research</i> | 324 |
| 9 | Bibliography | 327 |
| 10 | APPENDIX 1 | 349 |
| 11 | APPENDIX 2 | 357 |

LIST OF FIGURES

Chapter 1

| | |
|--|---|
| Figure 1.1 – Estimated LCoE from 2015-2030 [15]. | 3 |
| Figure 1.2 – Projects’ average water depth and distance to shore in 2014 [20]. | 4 |
| Figure 1.3 – Projects’ average water depth and distance to shore in 2016 [5]. | 5 |

Chapter 2

| | |
|--|----|
| Figure 2.1 – Wave-induced shear stress for different formulations of the wave friction factor, as function of the stone mean diameter D_{50} ($H_s=6.5$ m, $T_p=11.2$ s; $\rho_s=2650\text{kg/m}^3$; $d=18$ m) [44]. | 17 |
| Figure 2.2 – Forces acting on the sediment grain. | 20 |
| Figure 2.3 – Shields curve adapted by [52] for the threshold of sediment motion for waves and/or currents [1]. | 21 |
| Figure 2.4 – Flow patten around a slender pile due to the flow-structure interaction [66]. | 22 |
| Figure 2.5 – Characteristic equilibrium scour hole pattern for a vertical cylinder in a steady current [49]. | 23 |
| Figure 2.6 – Global and local scour at a jacket foundation [49]. | 25 |
| Figure 2.7 – Time development of the scour depth. | 26 |
| Figure 2.8 – Scour depth evolution and time-scale comparison between live-bed and clear-water scour [11]. | 27 |
| Figure 2.9 – Dimensionless equilibrium scour depth in combined waves and current [61]. | 30 |
| Figure 2.10 – Equilibrium scour depth as a function of KC and U_{cw} , [95]. | 31 |
| Figure 2.11 – Typical scheme of a scour hole. | 32 |

Chapter 3

| | |
|--|----|
| Figure 3.1 – Sensitivity to scour of the natural frequency of the support structure of a 6 MW turbine [104]. | 36 |
| Figure 3.2 – Frequency spectrum of dynamic loads and design choices for the natural frequency (adapted from [18]). | 37 |
| Figure 3.3 – Structural measures to account for scour phenomena effects, without using a scour protection (taken fom [1] and originally [97]). | 39 |
| Figure 3.4 – Example of a scour protection presented at [107]. | 39 |
| Figure 3.5 – Scheme of a riprap scour protection around a cylinder monopile. | 40 |
| Figure 3.6 – Failure modes of a riprap scour protection (adapted from [1]). | 41 |
| Figure 3.7 – Parameters of scour protection design (Adapted from [1]). | 42 |
| Figure 3.8 – Example of the effect of the water depth in the orbital bottom velocity, H is the significant wave height. | 43 |
| Figure 3.9 – Definition of the wave characteristics – linear wave theory [1]. | 44 |
| Figure 3.10 – Validity regions for different wave theories [114]. | 45 |
| Figure 3.11 – Example of Fenton’s Fourier series: water surface elevation and horizontal bottom velocity [1]. | 46 |
| Figure 3.12 – Representation of an irregular wave train. | 47 |
| Figure 3.13 – Representation of the energy spectral density [1]. | 49 |
| Figure 3.14 – JONSWAP spectra comparison (and PM spectra for $\gamma=1$) [122]. | 51 |
| Figure 3.15 – Log-probability plot of a wide and a narrow grain size distribution [1]. | 54 |
| Figure 3.16 – Static and dynamic design of scour protections from the OPTI-PILE project [100]. | 61 |
| Figure 3.17 – Damage categories as a function of the stability parameter [100]. | 63 |
| Figure 3.18 – Damage categories as a function of the stability parameter [145]. | 64 |
| Figure 3.19 – Wave friction factor (f_w) as a function of wave stroke to bed roughness ratio [147]. | 65 |
| Figure 3.20 – Scour tests setup used in [1] and [30]. | 66 |
| Figure 3.21 – Top view of scour protection without the pile before loading [30]. | 67 |

| | |
|--|----|
| Figure 3.22 – Wave-induced bed shear stress as a function of the wave period for different formulations of the wave friction factor [30]. | 68 |
| Figure 3.23 – Iterative process required to design a statically stable scour protection according to [1, 30], (adapted from [1]). | 70 |
| Figure 3.24 – Example of a static design approach. Graphical solution with the shear stress as a function of the mean stone size [30]. | 71 |
| Figure 3.25 – Visual damage level versus the stability parameter [32]. | 73 |
| Figure 3.26 – Division of the scour protection into subareas according to [32]. | 74 |
| Figure 3.27 – Comparison between the measured damage number and the visual damage level from [32]. | 75 |
| Figure 3.28 – Original comparison between $S_{3Dmeasured}/N^{b0}$ and $S_{3Dpredicted}/N^{b0}$ [32]. | 77 |
| Figure 3.29 – Visual damage levels versus the predicted damage number [32]. | 77 |
| Figure 3.30 – Soil triangle that provides the lateral bearing capacity of the pile [1]. | 81 |
| Figure 3.31 – Influence of the armour layer thickness on the damage number of the protection according to [1]. | 83 |
| Figure 3.32 – Physical model of a damaged scour protection around a monopile from [169]. | 88 |
| Figure 3.33 – Top view and side profiles of the scour monitoring results reported in [173], profiles taken for different angles of the scour protection. | 89 |
| Figure 3.34 – Photographic record of sand and gravel exposure at the monopile wall in Arklow Bank [13]. | 90 |

Chapter 4

| | |
|---|-----|
| Figure 4.1 - Location of the Acoustic Doppler Velocimeters (ADV) and the wave gauges (WG) for current and wave monitoring. | 97 |
| Figure 4.2 – Representation of the wave-current flume used at Aalborg University. | 98 |
| Figure 4.3 – Front view of the pump outlet box plus current distribution box and metal panels (“throat”) to isolate the pipe outlets from the flow. | 98 |
| Figure 4.4 – Sand gravel placed on the upward slope to reduce turbulence and smooth the boundary layer. | 99 |
| Figure 4.5 – Downstream view of the bypass section, wave gauge and ADV, without the monopile present. | 99 |
| Figure 4.6 – Scour protection system with monopile installed with the holding system after a waves and steady current loading. | 100 |
| Figure 4.7 – Hydrodynamic conditions at the model with depth-averaged current velocity measured at 40% of the water depth from the bottom. | 103 |
| Figure 4.8 – Testing in the wave-current flume with the protected monopile present [102]. | 104 |
| Figure 4.9 - Concentric configuration of the coloured rings around the monopile base, without the monopile. | 105 |
| Figure 4.10 – Granular filter layer being placed beneath the amour layer stones. | 105 |
| Figure 4.11 – Top-view of the scour protection and radial extent of the scour protection model. | 105 |
| Figure 4.12 – Example of an eroded scour protection and respective digital terrain model. Flow direction from bottom to top. | 106 |
| Figure 4.13 – Illustration of visual damage levels of tested scour protections [175]. Flow direction from bottom to top. | 112 |
| Figure 4.14 – Division of the scour protection into sub-areas (adapted from [175]). | 113 |
| Figure 4.15 – Colour code used to analyse the dynamic behaviour of the scour protections [175]. | 114 |
| Figure 4.16 – Type of stability versus $S_{3Dmeasured}$. Comparison between the present research and the datasets from [32] and [148]. | 126 |
| Figure 4.17 - Type of stability versus $S_{3Dmeasured}$. Comparison between the present research and the datasets from [32] and [148]. Zoom in the interval $S_{3Dmeasured}=[0;4]$. | 127 |

| | |
|--|-----|
| Figure 4.18 – Visual comparison of damage after 5000 waves in test s3_008 ($S_{3D\text{measured}5000}=1.01$; $H_{m0}=0.143$ m; $T_p=1.52$ s; $U_c=0.222$ m/s), on the left, and test s3_009 ($S_{3D\text{measured}5000}=0.71$; $H_{m0}=0.136$ m; $T_p=1.54$ s; $U_c=0.182$ m/s), on the right. Flow direction from bottom to top. | 130 |
| Figure 4.19 – Influence of the wave height on the measured damage number. | 130 |
| Figure 4.20 – Influence of the peak period in the damage number of the scour protection [1]. | 131 |
| Figure 4.21 – Influence of the orbital bottom velocity on the measured damage number after 3000 waves for tests s1_005 and s3_011, s1_006 and s2_003. | 132 |
| Figure 4.22 – Influence of flow velocity on the measured damage number. | 134 |
| Figure 4.23 – Influence of U_{cw} on S_{3D5000} [-] for comparable scour protections ($D_{50}=4.135$ mm) in different series. | 137 |
| Figure 4.24 – Comparison of profile evolution for a dynamically stable test (left) and failure (right) for 1000, 3000 and 5000 waves [26]. | 138 |
| Figure 4.25 - Damage increase $\Delta S_{3D}/na$, for statically stable (top), dynamically stable (middle) and failure (bottom) tests [26]. | 139 |
| Figure 4. 26 – Measured damage number after each wave train for statically stable, dynamically stable and failure tests taken from series s2 ($d=0.36$ m). | 140 |
| Figure 4.27 – Influence of the stone size on the measured damage number after 5000 waves. | 142 |
| Figure 4.28 – General scour pattern after 5000 waves [183]. | 146 |
| Figure 4.29 – Examples of Digital Terrain Models – Left: Statically stable scour protection (s2_001). Middle: Dynamically stable scour protection (s2_004). Right: Failure at the scour protection (and developed V-shape). Flow direction from bottom to top [26]. | 147 |
| Figure 4.30 – Smoothed average 2D cross profiles after 5000 waves [26]. | 148 |
| Figure 4.31 – General deposition pattern [183]. | 149 |
| Figure 4.32 – Evolution of the V-shape form registered during s1_005: left – after 1000 waves, middle – after 3000 waves, right – after 5000 waves. Flow direction from the bottom to the top. | 150 |
| Figure 4.33 – Left: test s1_001 statically stable with less deposition at the downstream side. Right: test s1_002 with downstream deposition at the white ring. Flow direction from the bottom to the top. | 150 |
| Figure 4.34 – General edge accretion and scour pattern for the MARINET tests. | 151 |
| Figure 4.35 – Comparison between the measured and the predicted values of S_{3D} (after 3000 waves) [151]. . | 153 |
| Figure 4.36 – Comparison between measured and predicted values of S_{3D} for test series s1 ($d=0.24$ m) [151]. | 154 |
| Figure 4.37 – Comparison between measured and predicted values of S_{3D} for test series s2 ($d=0.36$ m) [151]. | 155 |
| Figure 4.38 - Comparison between measured and predicted values of S_{3D} for test series s3 ($d=0.50$ m) [151]. | 155 |
| Figure 4.39 – Zoom in the interval of $S_{3D}= [0;3]$, [151]. | 156 |
| Figure 4.40 – Influence of the water depth on measurements and predictions of S_{3D} [151]. | 157 |
| Figure 4.41 – Test classification and measured S_{3D} with the limits for static and dynamic stability [151]. | 158 |
| Figure 4.42 – Test classification versus stability parameter (blue left line – $stab=0.416$, red right line – $stab=0.460$), [151]. | 159 |
| Figure 4.43 – Ratio of the damage number divided by the number of rock layers used in the protection versus the stability parameter, [151]. | 160 |
| Figure 4.44 – Scheme of the overall wave tank at FEUP (adapted from [157]). | 163 |
| Figure 4.45 – Wave tank view from the downstream side, at the absorbing beach, towards the multi-element wave paddles. | 163 |
| Figure 4.46 – Downstream view of the wave flume (wave tank corridor) with the model of the monopile placed at the center [157]. | 164 |
| Figure 4.47 – Velocity profiles obtained after the pumps installation, without the monopile present and at the monopile section ($d=0.24$ m). | 165 |
| Figure 4.48 – Upstream view (left) and downstream view (right) of the approaching slopes and the sediment box, before the sand bed installation. | 166 |

| | |
|---|-----|
| Figure 4.49 – Monopile base and transition piece at 40 cm height. | 166 |
| Figure 4.50 – Scheme of the setup used for test series F1. | 167 |
| Figure 4.51 – Model of the monopile foundation: during testing without protection (left), before testing with protection (center), during testing with protection (right). | 167 |
| Figure 4.52 – Monopile and scour protection models after a test. | 169 |
| Figure 4.53 – 2D bed profiler mounted on the longitudinal rail (left) and ruled cross-sectional rail used to guide the profiler in the measurement grid. | 170 |
| Figure 4.54 – Variation of $S_{3Dmeasured}$ with increasing armour layer thickness. | 179 |
| Figure 4.55 – Type of stability versus the evolution of $S_{3Dmeasured}$. Vertical lines $S_{3Dmeasured}=0.25$ and $S_{3Dmeasured}=1$ | 180 |
| Figure 4.56 – Measured damage number ($S_{3Dmeasured}$) versus stability parameter (stab) per wave train. | 182 |
| Figure 4.57 – Comparison between measured and predicted damage numbers for test series F1 (includes 1000, 3000 and 5000 wave trains). | 183 |
| Figure 4.58 – Comparison between predicted and measured damage numbers for series F1, [32] and [148]. . | 184 |

Chapter 5

| | |
|---|-----|
| Figure 5.1 – General reliability problem (adapted from [194]). | 192 |
| Figure 5.2 - Graphic representation of the failure domain and the associated probability of failure, [216]. | 194 |
| Figure 5.3 – Representation of the probability of failure as a solution for Eqs. (5.8) and (5.10). | 195 |
| Figure 5.4 – Graphic representation of the probability density function for the Normal distributed safety margin M and the reliability index β [191]. | 196 |
| Figure 5.5 – Geometric representation of the limit state function ($M=g(x)=0$) and the reliability index (β) in the standardized space of loads (S) and resistances (R). | 201 |
| Figure 5.6 – FORM and SORM approximations to the limit state surface at the design point [227]. | 204 |
| Figure 5.7 - Scheme of random generation of the random basic variables (Adapted from [216]). | 208 |
| Figure 5.8 – Importance sampling in the most likely point of failure Y , in the normal reduced space of variables (adapted from [194]). | 211 |
| Figure 5.9 – Experimental design for a two variable problem with X_m as the mean point, [217]. | 213 |
| Figure 5.10 – Generic example of an experimental design for three variables, [217]. | 213 |
| Figure 5.11 – Scheme of the Kolmogorov-Smirnov distance and the Wasserstein distance between two distributions. | 218 |
| Figure 5.12 – Comparison between the fit of a Normal and a Rayleigh distribution to the empirical distribution of x | 219 |
| Figure 5.13 – Example of a Chi-plot for X and Y (independent variables). | 222 |
| Figure 5.14 – Example of Kendall plots for situation A - Independent X and Y ; situation B - Perfect positive dependence of X and Y ; situation C - Perfect negative dependence of X and Y | 223 |

Chapter 6

| | |
|--|-----|
| Figure 6.1 – Flow chart of the reliability analysis of scour protections and statistical framework. | 235 |
| Figure 6.2 – Location of Horns Rev 3 at the Danish Sector of the North Sea [287]. | 239 |
| Figure 6.3 – Scatter diagram and histograms of the 124 months dataset ($H_s; T_p$) [223]. | 241 |
| Figure 6.4 – Water depth at Horns Rev 3 [286]. | 244 |
| Figure 6.5 – Chi-plots ($\lambda_i; \chi_i$) for 1, 6 and 12 months randomly selected from the 124 months dataset. | 247 |
| Figure 6.6 – Kendall plots for 1, 6, 12 and 31 months randomly selected from the 124 months dataset. | 247 |
| Figure 6.7 – Random sample of 10 000 pairs of H_s and T_p from the independent copula over the 124 months of hindcast data. | 249 |
| Figure 6.8 – Random sample of 10 000 pairs of H_s and T_p from the independent copula over the 124 months of hindcast data. | 249 |

| | |
|---|-----|
| Figure 6.9 – Random sample of 10 000 pairs of H_s and T_p from the Gaussian copula over the 124 months of hindcast data. | 250 |
| Figure 6.10 – Random sample of 10 000 pairs of H_s and T_p from the t-copula over the 124 months of hindcast data. | 251 |
| Figure 6.11 – Random sample of 10 000 pairs of H_s and T_p from the Clayton copula over the 124 months of hindcast data. | 252 |
| Figure 6.12 – Random sample of 10 000 pairs of H_s and T_p from the Frank copula over the 124 months of hindcast data. | 252 |
| Figure 6.13 – Random sample of 10 000 pairs of H_s and T_p from the Gumbel copula over the 124 months of hindcast data. | 253 |
| Figure 6.14 – Random sample of 10 000 pairs of H_s and T_p from the Tawn type 2 copula over the 124 months of hindcast data. | 254 |
| Figure 6.15 – Situation A for low probabilities of failure ($H_{smax}=4$ m; $T_{pmax}=22s$). | 257 |
| Figure 6.16 – Situation B for high probabilities of failure ($H_{smax}=6$ m; $T_{pmax}=22s$). | 257 |
| Figure 6.17 – Situation C for intermediate probabilities of failure ($H_{smax}=6$ m; $T_{pmax}=22s$). | 258 |
| Figure 6.18 – Probability of failure versus τ_K per dataset for the Frank, the Tawn type 2, the t-copula and the BKDE, $n=300\ 000$ | 264 |
| Figure 6.19 – Probabilities' sensitivity to the mean stone diameter of the armour layer modelled with triangular distribution with lower and upper limits of $\mu_{D50} \pm 0.1m$, e.g. for $\mu_{D50}=0.4$ m $D_{50}=[0.3;0.5]$ m. | 265 |
| Figure 6.20 – Probabilities' sensitivity to the currents mean velocity ($\sigma_{uc}=0.2$ m/s). | 266 |
| Figure 6.21 – Probabilities' sensitivity to different limits of acceptable damage number. | 267 |
| Figure 6.22 – Probabilities' sensitivity to the water depth. | 268 |
| Figure 6.23 - Autocorrelation function for the maximum value selected for different time intervals. | 272 |
| Figure 6.24 – Subsamples obtained from choosing the maximum H_s and the coexisting T_z for intervals of 2 days. | 272 |
| Figure 6.25 - Autocorrelation functions for the original hindcast data (left) and the pre-processed data (right). Values presented for H_s | 274 |
| Figure 6.26 – Comparison of H_s and T_z before and after the subsampling and the pre-processing. | 275 |
| Figure 6.27 – Empirical copulas of the pre-processed data in the (u,v)-space. | 279 |
| Figure 6.28 – Symmetric copulas without extra-parametrization with the lowest Crámer-von Mises distances, (u,v)-space per dataset. | 280 |
| Figure 6.29 – Asymmetric copulas, with extra-parametrization with an independent copula, with the lowest Crámer-von Mises distance, (u,v)-space per dataset. | 284 |
| Figure 6.30 – Generated series (+) of 1887 pairs of ($H_s;T_z$) over the subsampled data (o) based on the best copulas extra-parametrized with and independent copula. | 284 |
| Figure 6.31 - Autocorrelation function for H_s in the generated series of 1887 pairs of ($H_s;T_z$) based on the best copulas extra-parametrized with an independent copula. | 284 |
| Figure 6.32 – Asymmetric copulas, with extra-parametrization with a pairwise copula, with the lowest Crámer-von Mises distance, (u,v)-space per dataset. | 286 |
| Figure 6.33 – Generated series (+) of 1887 pairs of ($H_s;T_z$) over the original hindcast data (o) based on the best copulas extra-parametrized with a pairwise copula. | 287 |
| Figure 6.34 – Autocorrelation function for H_s in the generated series of 1887 pairs of ($H_s;T_z$) based on the best copulas extra-parametrized with a pairwise copula. | 287 |
| Figure 6.35 – Asymmetric copulas, with extra-parametrization with a Gumbel copula, with the lowest Crámer-von Mises distance, (u,v)-space per dataset. | 289 |
| Figure 6.36 – Generated series (+) of 1887 pairs of ($H_s;T_z$) over the original hindcast data (o) based on the best copulas extra-parametrized with a Gumbel copula. | 289 |

Chapter 7

| | |
|---|-----|
| Figure 7.1 – Reliability analysis and procedure to associate each mean stone diameter to a certain safety level. | 306 |
| Figure 7.2 – Hindcast data concerning the significant wave height and peak period at Horns Rev 3 and random generated sample with $n=50\ 000$ pairs of $(H_s; T_p)$ | 308 |
| Figure 7.3 – Probability of failure for each design methodology versus number of simulated values of H_s , T_p and U_c | 311 |
| Figure 7.4 – Safety comparison between static design criteria ($n=300\ 000$). AF – amplification factor. | 313 |
| Figure 7.5 – Influence of the amplification factor in the probability of failure for methodology [52] ($n=300\ 000$). | 314 |
| Figure 7.6 – Comparison of the critical bed shear stress calculated by the methods in [30] and [52]..... | 315 |
| Figure 7.7 – Influence of U_m in the probability of failure for the methodology in [52], compared with the application of the methodology in [30] ($n=300\ 000$). | 316 |
| Figure 7.8 – Probabilities of failure as a function of the mean stone diameter. Comparison between static [30] and dynamic design [32]. | 318 |

APPENDIX 2

| | |
|--|-----|
| Figure A2.1 – Comparison of the S_{3Dsub} after 5000 waves for tests s1_003 and s1_006. | 357 |
| Figure A2.2 – Comparison of the S_{3Dsub} after 5000 waves for tests s2_004 and s2_006. | 357 |
| Figure A2.3 – Comparison of the S_{3Dsub} after 3000 waves for tests F1_001 and F1_002. | 358 |

LIST OF TABLES

Chapter 1

| | |
|---|---|
| Table 1.1 – Examples of pile diameter and water depth in offshore windfarms. | 6 |
|---|---|

Chapter 3

| | |
|--|----|
| Table 3.1 – Mean diameter and weight of the armour layer stones at different offshore windfarms [2]. | 56 |
| Table 3.2 – Test conditions used in the OPTI-PILE project [30]. | 62 |
| Table 3.3 – Damage categories for different rock grading [100]. | 63 |
| Table 3.4 – Range of model test conditions used by [1, 30, 32]. | 66 |
| Table 3.5 – Comparison of the optimised static design approach proposed by [30] and the traditional static design approaches proposed by [52] and [57]. | 71 |
| Table 3.6 – Required stone size, i.e. mean stone diameter D_{50} (m), for a dynamic scour protection considering $H_s=6.5$ m, $T_p=11.2$ s and $D_{85}/D_{15}=2.5$, $U_c=1.5$ m/s, $d=20$ m. Optimised dynamic approach with Eq. (3.57). | 79 |
| Table 3.7 – Recommended radial extent of scour protection. | 80 |
| Table 3.8 – Scour protections’ thicknesses for the armour and the filter layer [2]. | 82 |

Chapter 4

| | |
|--|-----|
| Table 4.1 – Prototype hydrodynamic conditions and monopile diameter. | 95 |
| Table 4.2 – Prototype characteristics of the armour layer stones, granular filter and sediments. | 96 |
| Table 4.3 – Prototype and model hydrodynamic conditions. | 102 |
| Table 4.4 – Characteristics of the scour protection rock material (values at model and prototype). | 106 |
| Table 4.5 – Comparison of different sources target test conditions for dynamic scour protections. | 108 |
| Table 4.6 – Scour protection tests and configurations, with overall hydrodynamic conditions. | 111 |
| Table 4.7 – Measured hydrodynamic conditions for scour protection tests. | 118 |
| Table 4.8 – Visual damage comparison between tests s1_003 and s1_006. Flow direction from bottom to top. | 119 |
| Table 4.9 – Damage number (S_{3Dsub}) per sub-area, i.e. ring and sector for test s1_003, after each wave train. | 120 |
| Table 4.10 – Damage number (S_{3Dsub}) per sub-area, i.e. ring and sector for test s1_006, after each wave train. | 121 |
| Table 4.11 – Measured damage ($S_{3Dmeasured}$) for s1_003 and s1_006 ($D_{50}=4.135$ mm; $3D_{50}$ thickness; $d=0.24$ m). | 121 |
| Table 4.12 - Visual damage comparison between tests s2_004 and s2_006. Flow direction from bottom to top. | 122 |
| Table 4.13 – Damage number (S_{3Dsub}) per sub-area, i.e. ring and sector for test s2_004, after each wave train. | 122 |
| Table 4.14 – Damage number (S_{3Dsub}) per sub-area, i.e. ring and sector for test s2_006, after each wave train. | 123 |
| Table 4.15 – Measured damage ($S_{3Dmeasured}$) for s2_004 and s2_006 ($D_{50}=4.135$ mm; $4D_{50}$ thickness; $d=0.50$ m). | 123 |
| Table 4.16 – Measured damage numbers ($S_{3Dmeasured}$) after 1000, 3000, 5000 and 7000 waves representative overall value of the scour protection, positive values representing erosion. | 125 |
| Table 4.17 – Visual comparison of damage between for different water depths ($D_{50}=2.686$ mm; $n_a=8D_{50}$) [175]. Flow direction from bottom to top. | 128 |
| Table 4.18 – Influence of the water depth in the measured damage number ($D_{50}=2.686$ mm; $n_a=8D_{50}$). | 128 |
| Table 4.19 – Influence of the water depth in the measured damage number ($D_{50}=4.135$ mm; $n_a=2D_{50}$). | 129 |
| Table 4.20 – Wave-current dominance on the flow regime per test, by means of velocity ratio (U_{cw}). | 135 |
| Table 4.21 – Velocity ratios and damage numbers for comparable scour protections in test series s1 and s3. | 136 |

| | |
|---|-----|
| Table 4.22 - Velocity ratios and damage numbers for comparable scour protections in series s2 | 136 |
| Table 4.23 – Classification of tests results: failure (red), statically stable (blue) and dynamically stable (green) tests [26] | 141 |
| Table 4.24 – S_{3Dsub} in the upstream sectors of ring R6 for scour protections with different number of stone layers (n_a). Negative values – erosion, Positive values – accretion. | 152 |
| Table 4.25 – Hydrodynamic prototype target conditions at FEUP. | 162 |
| Table 4.26 – Prototype characteristics of the armour layer stones and granular filter for series F1. | 162 |
| Table 4.27 – Target prototype and model hydrodynamic conditions. | 168 |
| Table 4.28 – Model and prototype values used for the armour layer in series F1. | 169 |
| Table 4.29 – Range of target test conditions at FEUP. | 171 |
| Table 4.30 – Scour protection tests and configuration with overall hydrodynamic conditions at FEUP. | 172 |
| Table 4.31 – Measured hydrodynamic conditions of series F1. | 175 |
| Table 4.32 – Damage number (S_{3Dsub}) per sub-area, i.e. ring and sector for test F1_001, after each wave train. | 176 |
| Table 4.33 - Damage number (S_{3Dsub}) per sub-area, i.e. ring and sector for test F1_002, after each wave train. | 177 |
| Table 4.34 - Measured damage numbers ($S_{3Dmeasured}$) after 1000, 3000 and 5000 waves representative overall value of the scour protection, positive values representing erosion. | 178 |
| Table 4.35 – Stability parameter (stab) per test and per wave train..... | 181 |
| Table 4.36 – Predicted damage numbers for test series F1. | 183 |

Chapter 5

| | |
|---|-----|
| Table 5.1 – Classification of reliability methods [221] | 198 |
| Table 5.2 – Relation between measures of dependence and the tail dependence coefficients for Archimedean copulas [270]..... | 229 |

Chapter 6

| | |
|--|-----|
| Table 6.1 – Descriptive statistics of the significant wave height and peak period at Horns Rev 3 offshore wind farm..... | 239 |
| Table 6.2 – Summary of the hindcast data characteristics and validation. | 240 |
| Table 6.3 – Summary of the statistical analysis and correlations..... | 240 |
| Table 6.4 – Chronological division of the hindcast data into datasets of 62 and 31 months. | 241 |
| Table 6.5 – Parameters of the tested distributions for the 124 months data set of H_s and T_p | 242 |
| Table 6.6 – Kolmogorov-Smirnov and Wasserstein distances for the tested distributions. | 242 |
| Table 6.7 – Measure of dependence, τ_k , per dataset. | 245 |
| Table 6.8 – Copula parameters and AIC and BIC criteria used to select the best model for each dataset. | 255 |
| Table 6.9 – Simulation conditions for situation A, B and C..... | 256 |
| Table 6.10 – Probabilities of failure for the Tawn type 2 and the Independent copula for situations A, B and C. | 258 |
| Table 6.11 – Reference values used to calculate the probabilities of failure for a dynamic scour protection at Horns Rev 3 offshore windfarm. | 259 |
| Table 6.12 – Probabilities of failure for the scour protection considered in the case study ($D_{50}=0.4$ m). | 259 |
| Table 6.13 – Annual probability of failure (P_{f0}) for marine structures [220]. | 261 |
| Table 6.14 – Theoretical and non-parametric estimation tail dependence coefficients for the 124 months dataset. | 263 |
| Table 6.15 – Descriptive statistics for the combined sea state, the wind-sea and swell components (hindcast data of 124 months – $n = 90\ 553$). | 270 |

| | |
|--|-----|
| Table 6.16 – Shapiro-Wilk test for normality of the log(Hs) and log(Tz) applied to each subsample. Confidence interval of 90%. Rejection of null hypothesis H_0 for $p < 0.1$ | 273 |
| Table 6.17 – Measure of dependence (τ_k) for the original data, the subsamples and the pre-processed data. | 276 |
| Table 6.18 – Kolmogorov-Smirnov (KS) and Wasserstein (WS) distances between theoretical marginal distribution and the empirical cumulative distribution function of the Pre-processed data. | 277 |
| Table 6.19 – Parameters and 95% Confidence interval of the lognormal distribution fitted to the pre-processed data. C is the respective 95% confidence interval. | 277 |
| Table 6.20 – Descriptive statistics of the pre-processed data. | 278 |
| Table 6.21 – Estimated symmetric copulas, without extra-parametrization and their Crámer-von Mises distances (lowest in italics). | 281 |
| Table 6.22 – Estimated asymmetric copulas, with extra-parametrization with an independent copula and their Crámer-von Mises distances (lowest in italics). | 283 |
| Table 6.23 – Estimated asymmetric copulas, with pairwise extra-parametrization, and their Crámer-von Mises distances (lowest s in italics). | 286 |
| Table 6.24 – Estimated asymmetric copulas, with extra-parametrization with a Gumbel copula and their Crámer-von Mises distances. | 288 |
| Table 6.25 – Non-parametric estimation of the tail dependence at the 5% and the 95% quantiles for extra-parametrized copulas (closest values to empirical estimation in italics- bold). | 291 |
| Table 6.26 – WRMSE for the extra-parametrization with Independent and Pairwise copulas. Lowest WRMSE in bold italics. | 294 |
| Table 6.27 – WRMSE for the extra-parametrization with a Gumbel copula (lowest WRMSE in bold italics). | 295 |

Chapter 7

| | |
|--|-----|
| Table 7.1 – Deterministic design of the scour protection at Horns Rev 3. | 310 |
| Table 7.2 – Stabilized probability of failure calculated with the Conditional model approach (124 months). ... | 312 |

APPENDIX 1

| | |
|---|-----|
| Table A1.1 - Measured damage numbers for test F1_001. | 349 |
| Table A1.2 - Measured damage numbers for test F1_002. | 349 |
| Table A1.3 – Measured damage numbers for test F1_003. | 350 |
| Table A1.4 – Measured damage numbers for test F1_004. | 351 |
| Table A1.5 – Measured damage numbers for test F1_004*. | 352 |
| Table A1.6 – Measured damage numbers for test F1_005. | 352 |
| Table A1.7 – Measured damage numbers for test F1_006. | 353 |
| Table A1.8 – Measured damage numbers for test F1_008. | 354 |
| Table A1.9 – Measured damage numbers for test F1_008. | 355 |

CHAPTER 1

Introduction

1.1 Introductory note

The present thesis is mainly focused on the scour phenomenon and the scour protection research. Both terms are frequently mentioned throughout this Introduction. They are explained with further detail in the following chapters. However, for a better understanding of this Introduction, the following simplified definitions are provided:

- Scour – the erosion of the sea-bed in the structure foundation’s vicinity. When a structure is placed into a flow, scour occurs as a result of the soil-fluid-structure interaction resulting in a generalized lowering of the sea-bed. Scour may cause the foundation’s structural collapse.
- Scour protection – the scour mitigation system applied to prevent the generalized loss of sediments in the structures’ vicinity. Several types of protections might be used. This research concerns rip-rap protections, which are further described in future chapters.

Scour research is one of the oldest and vastest fields of Hydraulic Engineering. For the sake of clarity, it would be impossible to include in this thesis all the subjects related to this research field. Nevertheless, an effort was made to include the most important ones, in order to contribute for a better understanding of the main findings of this thesis.

1.2 Brief overview of the European offshore wind sector

Offshore wind energy has reached a mature state within the European renewable energy sector [1]. Ever since the first offshore windfarm “Vindeby” placed in Denmark, in 1991, the development of offshore renewable energy has increased considerably over the following 25 years [2]. This development was accompanied by increasing efforts towards a sustainable exploitation of energy resources. Those efforts also related to a more conscious perception of a sustainable future, not only in ecological terms, but also regarding the associated socio-economic issues. In the last three decades, this perception became evident, for instance, in the commitment of several countries to reduce the greenhouse gases and to use clean energy, within the Kyoto Protocol [2, 3]. Offshore wind energy presents itself as one of the major sources of clean energy. During the last two years, the discussion on the future of the Offshore Wind Sector gained a new dimension with the decision of the United States of America (U.S.A.) Government of abandoning the Paris Agreement [4]. However, the sector’s growth and its goals ambition are undeniable.

According to the statistics provided by the European Wind Energy Association [5], Europe is in the lead regarding the number of installed offshore windfarms. Moreover, the predictions for 2030 indicate that the capacity installed will range between 49 to 99 GW in offshore wind turbines, which

corresponds to about 6.5 to 14.9% of the electricity demand met by offshore wind energy in the European Union (EU) [6]. These values represent a minimum increase of 4 times the current installed capacity in Europe, to be achieved in 10-12 years only.

By the end of 2016 and at the beginning of 2017, the total installed capacity reached 12 631 MW, with 338 new grid-connected offshore wind turbines installed across Europe, which had 81 offshore windfarms fully operating, representing only a small fraction of the offshore wind energy potential available [5]. Furthermore, at that time, the capital investment in the offshore wind sector reached €18.2 bn, with 80% of the investment held by the United Kingdom (UK), Germany, Denmark, Belgium and Norway [5]. After the first half of 2017, an additional amount of 6.1 GW of new wind energy capacity was installed in Europe, with 18 new offshore wind projects led by Germany, UK, Belgium and Finland [7]. The interest and capital exposure to the offshore wind sector reached the most powerful economies in Europe, and caught the attention of other several other countries, namely the ones that were still trying to emerge from the 2008-2011 global crisis, e.g. Portugal, Greece and Ireland [8].

During the last 28 years, the growth in the cumulative installed capacity was considerably high [9]. During the last 2 years 24.2 GW were consented for new projects of offshore windfarms [5]. This growth is also sustained by the so-called 20-20-20 targets defined for the European Union. These targets include a 20% reduction in greenhouse gas emissions compared to 1990, 20% of primary energy from renewables, and a 20% reduction in primary energy demand through energy efficiency by 2020. Offshore wind energy plays a significant role in meeting these goals [10]. The growth presented by the European market also contributed to the increasing efforts around the World to move forward in the offshore wind energy sector. The offshore wind resources in countries as India, U.S.A., China, Korea and Japan led to a significant increase in the number of planned and consented offshore windfarms. A fairly recent and comprehensive review of the offshore wind market of these countries is provided in [11] and was developed during the course of this research. As it will be seen through this work, the present research is particularly interesting for the majority of the offshore wind foundations used in the European market, which justifies the emphasis given to the European sector.

The registered growth leads to one main idea: *The path towards wind energy development and efficiency has become an indubitable reality in nowadays Society*. As such, this path brought new prospects to the engineering world, which are definitely challenging from the intellectual and the socio-economic points of view. All of them represent true opportunities for several fields of engineering to rise up to their full potential by providing novel and creative solutions for problems that come with the natural evolution of this industry.

This research is mainly focused on the optimisation of scour protections for offshore foundations, which is, perhaps, one of the most important research areas in the offshore wind sector, due to its cost, complexity and multi-disciplinary nature. Scour protections are a common element in fixed-bottom foundations, widely used in the aforementioned market (see [12] and [13]). The following section provides an insight to the main reasons that led to the need for the optimisation of this element. Particular focus is given to the monopile foundation, which corresponds to the case study of this research.

1.3 Key trends and the need to optimise the foundations

The path towards the competitive edge of offshore wind may come in several forms, e.g. more powerful wind turbines or the access to locations with better wind resources. However, the common denominator of them all is the need to drop the cost of energy production, more specifically the so-

called Levelized Cost of Energy (LCoE), which measures the lifetime cost divided by energy production. The LCoE is a key measure of investment in an offshore windfarm, as it represents the present value of the total cost of building, operating and maintaining a power plant over an assumed lifetime [14].

By 2015 the LCoE of offshore wind turbines ranged from 130 to 170 €/MWh [16]. In 2017 this value ranged from 120 to 150 €/MWh. However the target ambition is to reduce this range by 2030 from about 90 €/MWh, as shown in Figure 1.1, to 60 €/MWh [15, 17]. The foundation costs of an offshore wind turbine typically may range from 20 to 35% of the overall investment [18]. An important part of those costs is related to the scour protection, which affects both the initial capital expenditures (CAPEX) and the operation capital expenditures (OPEX) [14].

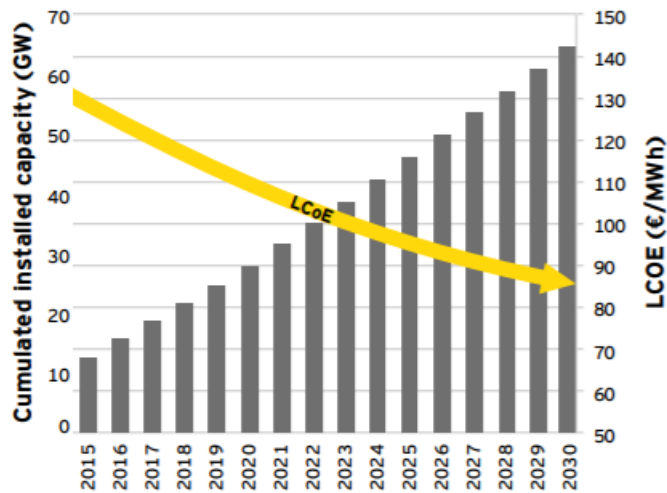


Figure 1.1 – Estimated LCoE from 2015-2030 [15].

In terms of offshore structures used for wind energy exploitation, the monopile remains the most common type of foundation [19], with 88% of the European market share [5]. A total of 438 monopile foundations were installed in 2017, which compares to 67 Jacket substructures in Europe. Note that all of them are fixed-bottom foundations, which are the ones for which scour phenomena are most severe [11]. Besides the importance of the foundation in the costs related to the total investment, some key trends adopted by the market increased the need to optimise the foundation.

One of those trends is the increasing water depth and distance to shore adopted for the new offshore windfarms, aiming at better locations for high efficiency. The market assessment conducted by [20] showed that this was a clear trend world-wide (Figure 1.2), while the report concerning 2016 activities in Europe showed that the range of water depth and distance to shore was taken even further (Figure 1.3). With further distance to shore there is an increase in the water depth. This tendency makes the market more prone to invest in offshore floating foundations, which are fixed by means of mooring lines. However, the market evolution also aimed at new concepts for fixed-bottom foundations, e.g. the XL monopiles [20] or innovative Gravity Based Foundations (GBF) as the one proposed in the DEMOGRAV13 project, planned for the Portuguese coast. This tendency led to a generalized increase in the diameters used for fixed-bottom foundations, which is directly related to an increase in the scour phenomena and the design of scour protections, thus aggravating the need for scour protections and the foundation's optimisation. Typical monopile foundations were being used for water depths between 0 to 30 m [1, 21] Presently, XL monopiles are designed to comply with water depths up to 50 m [20].

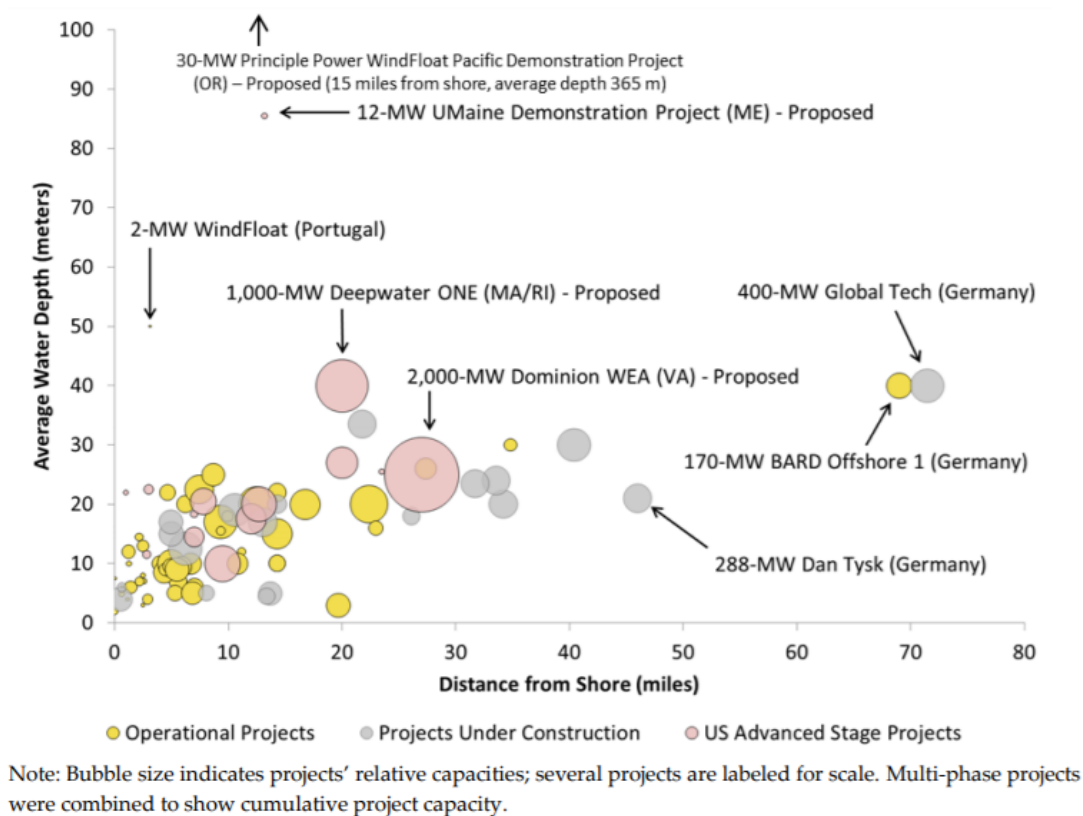


Figure 1.2 – Projects' average water depth and distance to shore in 2014 [20].

Larger diameters of the foundation increase the costs of the scour protection, because its extent, thickness and the dimension of the armour material are related to the foundation's size. Moreover, with the increasing dimensions of the foundation, the number of wind turbines deployed to sea also increased [22]. Manufacturers such as Siemens, Vestas, BARD or Alstom, among others, aimed at larger and more innovative turbine models to address the specific conditions and the challenges of offshore environment. New and ambitious targets were defined for the superstructure of a typical offshore wind turbine, e.g. novel blade's design, increasing reliability, larger hub heights, rotor's diameter and blade's length, as well as higher installed capacity [20]. Nowadays, offshore turbine technology comprises multi-megawatt machines, which contribute to a new generation of offshore windfarms that require larger foundations with higher bearing load capacity.

The average rated capacity presented significant progresses from 1991 to 2013. The average capacity of wind turbines was 3.9 MW by the end of 2013, and 4 MW in 2014. During the last three years the average capacity increased to about 4.8 MW and the grid-connected turbines ranged from 3 to 8 MW [5, 22]. However, new models of 5 MW and 6.15 MW became more common, leading to increased rated capacity. These models were deployed in large scale, for example, at the Thornton Bank Phase II, project in Belgium. The increasing dimensions related to more ambitious turbines were also reflected in the need for larger foundations and once again to an increasing need to reduce their influence in the CAPEX and OPEX parcels of the LCoE. Furthermore, the number of wind turbines per offshore windfarm is also increasing. Hence, any optimisation in the foundation design has a considerable effect in the total cost of the windfarm. Any savings in one foundation are multiplied by the number of the foundations installed. This represents a major competitive edge in large windfarms with dozens of wind turbines, e.g. London Array with 175 turbines or Horns Rev 1, Horns Rev 2 and Horns Rev 3 (under-development) with a total of 220 turbines.

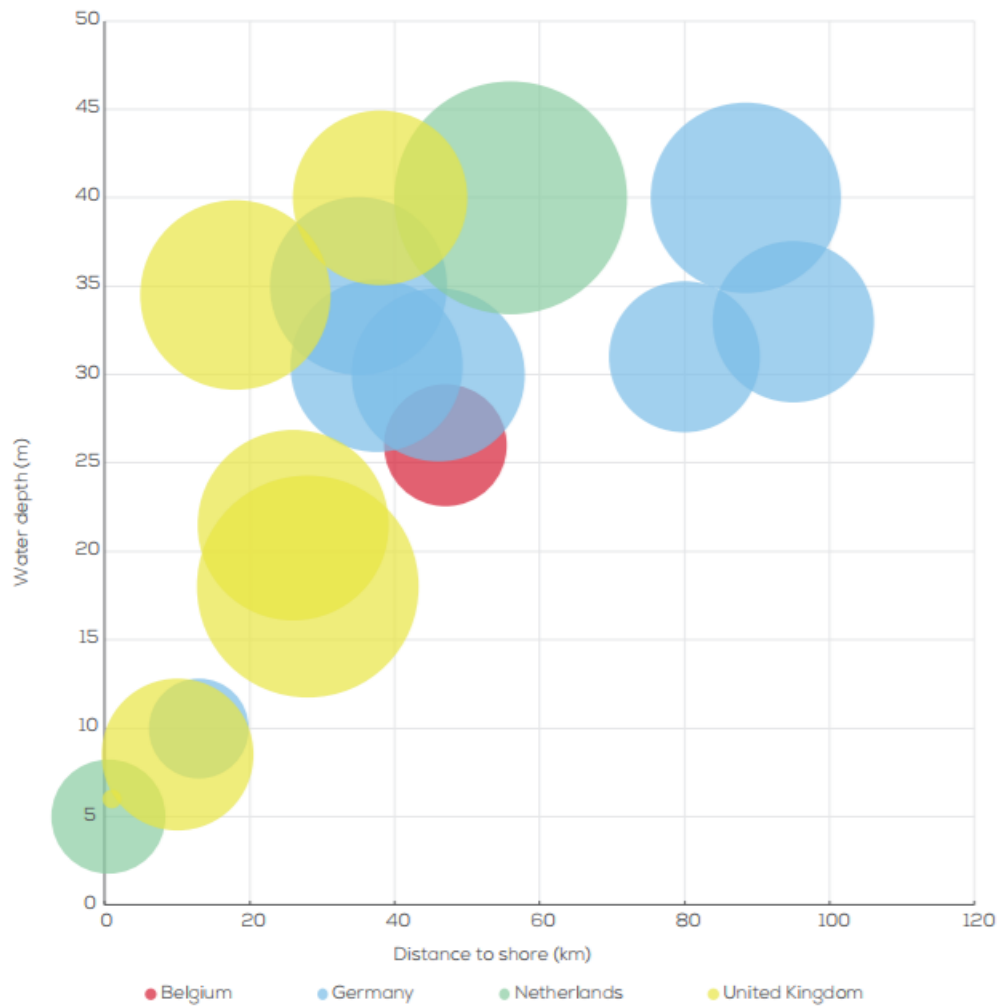


Figure 1.3 – Projects' average water depth and distance to shore in 2016 [5].

The recent years have shown several innovations in the design and installation of the substructures, in order to accompany the challenges of the market's evolution and to reduce the costs per energy unit produced [20]. Nevertheless, the evolution in the substructures used for offshore windfarms is limited by the installation site and its endogenous factors. The uncertainties in the design of these foundations are related to factors such as: the properties of the soil and its interaction with the structure, the water depth, the sea state, the scour phenomena, among others [23].

The opportunity for new and innovative solutions is considerable, since there are several unique combinations of needs to be fulfilled in each project. Depending on the implantation conditions, namely the water depth, different types of foundations can be adopted, e.g. floating foundations, tripods, monopiles or jacket foundations. A detailed review on the trends and technology improvements concerning these types of foundations is presented in [11]. The present case addresses the main trends and challenges concerning the monopile foundations, which are the main focus of this research.

In order to reach the market's demands, the recent concept of XL monopile has been introduced. Frequently, monopile diameters range from 3 to 7 m. In July 2013, EEW Special Pipe Construction has presented the fabrication equipment capable of rolling 10 m diameter piles [20]. Danish civil-engineering firm MT Højgaard has analysed a monopile foundation for water depths of up to 35 m.

This analysis concluded that, when comparing monopile and jacket foundation concepts suitable for a generic 6 MW turbine, in terms of cost, risk and the time taken for design, manufacture, installation and maintenance, XL monopiles compared favourably. It is estimated that XL monopiles have the potential to be developed for water depths up to 50 m [20].

Similarly to the evolution of other components of offshore windfarms, the XL monopiles are subjected to the ability of the supply chain to support the trends of increasing dimensions and weights, namely regarding vessels, lifting equipment capacity and installation constraints. Both for XL monopiles and typical ones, the market shows a clear trend for large diameters. As mentioned before, this leads to an aggravated need to account for scour phenomena and optimise the scour protections. Recently, [24] performed a study regarding local scour around large-diameter monopiles in a combined waves and current environment, recognizing that, in recent decades, piles with diameters up to 6 m became more common. The tendency for increased diameters can be seen in Table 1.1, which extends the survey presented in [1] and [11].

Table 1.1 – Examples of pile diameter and water depth in offshore windfarms.

| Offshore Windfarms | Year of Installation | Type of Foundation | Pile Diameter (m) | Water Depth (m) |
|--------------------|----------------------|------------------------------------|-------------------|-----------------|
| Vindeby | 1991 | Gravity based | - | 2.5 - 5 |
| Lely | 1994 | Monopile | 3.2 - 3.7 | 4 - 5 |
| Tun Knob | 1995 | Gravity based | - | 3 - 5 |
| Dronten | 1996 | Monopile | ? | 1 - 2 |
| N7 | 1997 | Monopile | 6 | 7 |
| Bockstigen | 1998 | Monopile | 2.25 | 5.5 -6.5 |
| Blyth Offshore | 2000 | Monopile | 3.5 | 6 - 11 |
| Utgrunden | 2000 | Monopile | 3 | 7 - 10 |
| Middelgrunden | 2001 | Gravity based | - | 5 - 10 |
| Yttre Stengrund | 2001 | Monopile | 3 - 3.5 | 8 |
| Scarweather Sands | 2002 | Monopile | 2.2 | 11.7 |
| Horns Rev 1 | 2002 | Monopile | 4 | 6 - 14 |
| Frederikshaven | 2003 | 1 Bucket foundation 3 Monopiles | ? | 4 |
| Samsø | 2003 | Monopile | 4.2 | 11 - 18 |
| North Hoyle | 2003 | Monopile | 4 | 12 - 20 |
| Arklow Bank | 2004 | Monopile | 5 | 2 - 6 |
| Nysted | 2004 | Gravity based | - | 6 - 10 |
| Arklow Bank | 2004 | Monopile | 5.1 | 5 |
| Scroby Sands | 2004 | Monopile | 4.2 | 21 (max) |

Table 1.1 (cont.) – Examples of pile diameter and water depth in offshore windfarms.

| Offshore Windfarms | Year of Installation | Type of Foundation | Pile Diameter (m) | Water Depth (m) |
|------------------------|----------------------|--------------------|----------------------|-----------------|
| Ems-Emden | 2004 | Like land based | - | 2 (max) |
| Kentish Flats | 2005 | Monopile | 4 | 5 |
| Thornton Bank | 2006 | GBF | 6.5 - 17 | 10 - 24 |
| Breitling | 2006 | Like land based | - | 2 |
| Barrow | 2006 | Monopile | 4.75 | 15-20 |
| Lynn & Inner Dowsing | 2007 | Monopile | 4.74 | 6 - 13 |
| Beatrice (Moray Firth) | 2007 | Lattice towers | - | 45 |
| Egmond aan Zee | 2007 | Monopile | 4.6 | 19 - 22 |
| Burbo | 2007 | Monopile | 4.7 | 1 - 8 |
| Lillgrund | 2007 | Gravity based | - | 4 - 8 |
| Q7 | 2008 | Monopile | 4 | 20 - 24 |
| Rhyl Flats | 2009 | Monopile | 4.7 | 6.5 - 12.5 |
| Horns Rev 2 | 2009 | Monopile | 4 | 9 - 17 |
| Thanet Substation | 2010 | 4 Skirt piles | 1.83 (4 skirt piles) | 22 |
| Gunfleets Sands | 2010 | Monopile | 5 | 0 - 13 |
| Robbin Rigg | 2010 | Monopile | 4.3 | 4 - 13 |
| Sheringham Shoal | 2012 | Monopile | 4.3 - 5.7 | 14 - 23 |
| Greater Gabbard | 2013 | Monopile | 6.3 | 4 - 37 |
| London Array Phase 1 | 2013 | Monopile | 4.7 - 5.7 | 0 - 25 |
| Teesside | 2014 | Monopile | 4.6 | 8 - 22 |
| West of Duddon Sands | 2014 | Monopile | 5 - 6 | 17 - 21 |
| Humber Gateway | 2015 | Monopile | 4.2 | 10 - 18 |
| Dudgeon East | 2017 | Monopile | 7 - 7.4 | 18 - 25 |
| Horns Rev 3 | 2018 | Monopile | 6.5 | 10 - 21 |

The increasing diameters and the possibility of extending the fixed-bottom foundations to new locations sustains the monopile foundations as the most common foundation for offshore wind turbines. Therefore, the potential for evolution and optimization of this substructure remains with good perspectives, namely regarding scour protections, where recent research is being developed, aiming for better performances and more attractive cost/benefit ratios [25, 26].

Finally, another important trend in offshore wind industry is the lifetime extension of the windfarms. According to [16], a 5 years lifetime extension enables a cost reduction per kWh of 6%. The lifetime extension aims at lowering the LCoE by increasing the potential number of hours for wind energy production, associated to a predefined CAPEX [14]. At present, the design lifetime of an offshore windfarm is expected to be 20–25 years. However, new projects seek to extend this limit. For example, the foundations used at Nysted offshore windfarm were designed for a 50 years lifetime. Lifetime extension also opens the possibility of partial or full repowering of operating offshore windfarms [27, 28]. However, there are scarce data on the individual duration of the components,

namely the foundations and the scour protection [29]. A clear industry gap exists on both how to have a precise estimation of the remaining useful life of the foundation and how to precisely assess the implications of such lifetime periods in terms of design, operation and repowering activities. Scour phenomena are considered one of the major uncertainty sources in design, operation and extension of lifetime of an offshore wind turbine [23]. Therefore, the market's goal to extend the lifetime of the offshore windfarms also requires new insights and deeper knowledge on the optimisation of the foundation and its protection. Furthermore, this aspect can be framed in broader goals such as the influence of extreme events in the foundation's behaviour, for example related to Climate Change scenarios.

1.4 Thesis scope and objectives

As described before, the aforementioned trends of the offshore wind sector closely relate to the need of optimising the foundation and its associated scour protection. In this sense, the present research is encompassed in the sector's generalised effort to improve the design and construction of offshore windfarms, towards the competitive edge of offshore renewable energy. Scour phenomena and their inherent uncertainties are a crucial aspect in offshore foundations design. Besides scour importance to the structural stability of the foundation, it often leads to an excessive amount of material and financial resources employed in the construction and maintenance operations. Often, due to uncertainty, scour protections are overdesigned [30], hence leading to excessive costs, particularly in terms of the CAPEX. A possible way to account for uncertainty is to adopt a detailed risk and reliability based analysis, which is able to provide a measure of the reliability of the protection. Such procedure aims at an optimization of the scour protection dimensions associated to a probability of failure [12].

Marine scour research is recently betting on two major ways of reducing the design uncertainty and to optimise scour protections. The first one by conducting physical and numerical modelling of new concepts of the filter and armour layers, e.g. [30], [26], [31]. This thesis mainly addresses the concept of dynamic scour protections [32]. The second one focuses on the methodology used to design the protection [12]. The majority of these studies propose empirical approaches to scour evolution and protection criteria [2, 33, 34, 35]. Empirical and semi-empirical design do not directly account for long-term modelling of the environmental variables that lead to scour and response variables that reflect the performance of the foundation and its protection. Risk-based methodologies imply the calculation of failure probabilities, which provide a measure of risk instead of the typical safety factor concept. Risk and reliability techniques have been mainly developed as structural design methodologies, typically applied in structural components, such as piles, beams and other elements of buildings' design, e.g. [36].

Some works have extended the probabilistic approaches to scour phenomena in fluvial conditions, e.g. [37, 38, 39, 40, 41]. However, the lack of methodologies for risk-based design of scour protections in offshore environments is evident. Risk-based design moves towards the optimisation of the protection accounting for the uncertainty of design, installation and exploitation of the offshore wind foundation. An extensive work was performed in Recomendaciones para Obras Marítimas (ROM) series 0.0 [42] to implement the probability of failure concept in the design of maritime and coastal structures. Nevertheless, the application of such concept to offshore scour protections is yet to be developed and standardized. Recent works have been presented in this matter by [11, 43, 44]. This thesis also intends to contribute to the optimisation of scour protections, mainly by adopting reliability techniques in order to assess their safety.

The scope of the present thesis relies on the introduction of innovative concepts: i) the dynamic scour protections, and ii) new design methodologies, as the reliability techniques, which still represent literature gaps in scour research. These two paths towards optimisation have an interesting potential to improve the cost/benefit ratios of offshore wind foundations. Furthermore, reliability techniques also account for the uncertainty in the phenomena, which contributes to scour risk mitigation. Moreover, the improvements made in these matters may also be applicable to other fields of marine renewable energy, namely concerning the foundations used for recently developed wave energy converters, e.g. [45, 46], or the development of offshore hybrid-platforms, e.g. [47], among several other fields related to the large energy potential of marine and offshore environment [48].

Within the referred scope, the present thesis aims at the optimisation of scour protections by accomplishing two major objectives:

- Provide a contribution to the novel concept of Dynamic Scour Protections, by means of a physical model study;
- Propose a Reliability Assessment Methodology for Scour Protections, by developing a statistical framework to perform the safety analysis of scour protections.

The physical models included in this research as well as the case study are mainly inspired in North Sea conditions. This is mainly due to the fact that the monopile foundations at intermediate and shallow waters, say water depths below 30 m, are very common in the North Sea Basin. Moreover, Northern European countries, e.g. Denmark, Belgium, Germany and Norway (also the UK in the North Atlantic) represent the major stakeholders in the offshore wind industry. Therefore, being responsible for the majority of the market's share in terms of the development of offshore wind foundations. The case study used for the present thesis concerns to the Horns Rev 3 offshore windfarm, which is still under development, thus, this is a case which might be open for discussion in terms of the possible solutions for the protection.

The main subject of this thesis concerns the optimisation of the mean stone diameter that can be used in the armour layer of the protection placed at the foundation. The present research focuses on the optimisation of this design parameter by associating it to a measure of safety. However, the design of scour protections includes several other parameters, namely, the armour thickness and extent, which were not optimised in this work. Regarding dynamic scour protections, the present thesis aims at contributing for a deeper knowledge on the feasibility of such solutions, which provide an alternative to static scour protections that use larger armour material. The reliability analysis intends to analyse the safety of the semi-empirical solutions proposed by the physical models. One is interested in understanding if a dynamic scour protection provides a similar safety level as a traditional static scour protection.

Finally, the contributions given to improve the feasibility of dynamic scour protections, and to accurately assess the reliability of their application, aim to be a step towards the competitive edge of offshore renewable energy.

1.5 Thesis outline

The present thesis is divided in 8 chapters, which aim to start from a global perspective of the wind energy sector and then progressively narrowing the scope of the work towards the optimisation of offshore scour protections. In a non-formal way, this thesis might be divided into two parts. The first one concerns Chapters 2, 3 and 4, which are dedicated to the concept of dynamic scour protections for offshore wind turbines. This first part includes the experimental work, which is mainly focused on the

damage number of these protections. The second part of this thesis is dedicated to the reliability analysis of dynamic scour protections and includes Chapters 5, 6 and 7. The following paragraphs describe the scope of each chapter, aiming at a general perception of the rational adopted for the research:

Chapter 1 starts with a description of the present situation in the offshore wind sector. An explanation is provided concerning the motivation and the objectives of the research hereby developed, with a particular focus on the need to optimise scour protections. This chapter also provides a brief introduction on the scientific contents addressed in each chapter.

Chapter 2 provides the basic notions regarding scour phenomena around marine foundations. Although this thesis is focused on scour protections, it would be impossible to address this research topic without including the basic concepts that lead to scour occurrence. Therefore, this chapter addresses fundamental notions required to implement the scour protection design addressed in further chapters. Moreover, Chapter 2 elaborates on the important limitations of the methodologies commonly used to account for scour severity and the horizontal bed shear stresses acting at the base of offshore fixed foundations.

Chapter 3 narrows the scope of the present thesis to the design of scour protections. The aim of this chapter is to provide a detailed notion regarding their design, in marine environment. Furthermore, this chapter elaborates on the key design variables, which are further addressed in the reliability analysis performed at the second part of the thesis. Chapter 3 also provides a detailed explanation regarding the background of dynamic scour protections and discusses the earlier studies performed on this optimised concept, which is then studied in Chapter 4. Finally, the literature gaps concerning dynamic protections are identified and discussed, so that experimental research of the next chapter contributes to cover the existent lack of knowledge.

Chapter 4 aims at accomplish with the first objective of the thesis (section 1.4). This chapter provides the experimental research concerning dynamic scour protections, for which two physical models were developed. The first physical model study was developed as a part of the project “MARINET proposal 61 - Optimising the design of dynamic scour protection around offshore foundations” in Aalborg University, whereas the second one was performed at Porto University. This chapter addresses the stability of dynamic scour protections under different hydrodynamic conditions, including a detailed analysis of the damage number of these protections and the potential effects of the armour layer thickness. The results obtained in this chapter also aimed at a validation of the damage number formula, which is used to implement the reliability analysis of scour protections. Chapter 4 provides crucial insights on the failure of dynamic protections by means of the erosion of the armour layer. This information is then used in Chapters 5, 6, and 7 to propose and analyse the limit state functions that will be used to assess the reliability of scour protections.

Chapter 5 introduces the reliability fundamental notions and techniques that can be used in order to develop a reliability assessment methodology for dynamic scour protections. The suitability of several reliability techniques for the present research is discussed. Moreover, the fundamentals regarding the correlation between random variables are provided and its importance for the reliability assessment of scour protections is discussed. The joint statistical models used to deal with correlated variables are presented, to ensure a proper simulation of the limit state functions in Chapters 6 and 7. Chapter 5 includes the discussion on the limit state functions used for the reliability analysis.

Chapter 6 introduces the met-ocean data available for the present reliability study, which concerns to Horns Rev 3 offshore windfarm. Chapters 6 and 7 are dedicated to the second main objective this thesis (section 1.4). In Chapter 6, the reliability of dynamic scour protections is assessed

by means of copula-based models applied to the significant wave height and peak or up-crossing mean wave periods. This chapter elaborates on how to obtain the probability of failure for a scour protection inspired in the case study Horns Rev 3. The importance of this chapter relies on the fact that it shows how to provide a measure of safety associated to a specific design criterion of the protection. Noting that the copula-based models accuracy can be improved, this chapter also proposes new extra-parametrized copulas that might be useful for future research performed on the reliability of scour protections.

Chapter 7 uses the conditional modelling approach (recommended from offshore wind engineering standards) to compare the reliability and safety of both dynamic and static scour protections. Using the same met-ocean data of the previous chapter, it is shown how the designer can evaluate if a certain dynamic scour protection is as reliable as the traditional statically stable one. Going one step further, this chapter aims to contribute to the current design practices by establishing the relationship between the probability of failure and the mean stone size of the case study scour protection. Through this relationship, it is described how to perform the probabilistic design of the protection, towards an optimised (reduced) mean stone diameter for a pre-defined safety level, i.e. probability of failure.

Chapter 8 reviews and summarises the conclusions obtained from the present research and highlights the future research topics that should be addressed to improve and generalise the findings of this work.

Fundamentals of Scour

2.1 Introduction to scour in offshore wind turbines

Offshore wind turbines are typically founded on movable sea-beds, i.e. composed either by cohesive or non-cohesive sediments. When into the sea the interaction between the structure and the fluid tends to increase the bed shear stress, which tends to cause sediment transport and to drag the sediments away from the structures' vicinity [49].

Sediment transport is the physical phenomenon that lies in the basis of scour around marine structures, in general, and offshore wind foundations in particular. The sediment transport might be induced by the action of waves, currents and tides, which induce the erosion of the movable sea-bed, due to the bed shear stress. The particular erosion phenomenon caused by the flow around a structure is typically called scour, as already mentioned.

This chapter provides a brief overview of the basic concepts related to scour research, which were found to be indispensable to comprehend the developed practical research. The present research builds its experimental work and reliability assessment of scour protections on the previous work [1, 30, 32]. An effort was made to formulate the nomenclature and the explanations as coherent as possible with the ones presented in these references. However, it was intentionally avoided unnecessary subjects or theoretical formulations that might be consulted in those works and that are not of crucial relevance to the practical chapters of this thesis. Through the course of this thesis, a more extensive review of the basic concepts of the scour phenomenon was developed and presented in [11]. Often, for detailed explanations on basic fundamentals and concepts of scour research the reader is referred to other literature. This was intentionally done for the sake of clarity and to maintain the focus on future chapters related to scour protections, risk and reliability analysis.

2.2 Bed shear stress and boundary layers

2.2.1 Waves and current

The bed shear stress, τ_b (N/m²) is the frictional force per unit of the sand-bed area responsible for the sediment motion. It is often expressed as the friction velocity u^* (m/s) and it is typically calculated according to Eq. (2.1).

$$\tau_b = \rho_w (u^*)^2 \quad (2.1)$$

This concept is commonly referred to in its dimensionless form and expressed by the dimensionless Shields parameter (θ), discussed below, which is obtained from the ratio of load on the grain to gravitational force that resists movement [50]. It is obtained from Eq. (2.2), which depends on the gravitational acceleration (g), the water density and the density of the sediment grains. Often this expression is simplified to include the so-called specific density (s), which is the ratio of densities of the water and the grains. The variable d_s is the diameter of the sediment grain.

$$\theta = \frac{\tau_b}{g(\rho_s - \rho_w)d_s} = \frac{(u^*)^2}{g(s-1)d_s} \quad (2.2)$$

The part of the flow responsible for the sediment transport is often defined as the boundary layer flow [51]. According to [1] the bottom boundary layer (δ) can be defined as the layer inside which the flow is considerably influenced by the sand-bed. For detailed definitions on the boundary layer thickness the reader is referred to [30] or [52]. The most common definition is the distance from the boundary surface to the point where the local velocity is equal to 0.995 times the depth-averaged flow velocity (U_c) [1].

Typically, waves have much smaller boundary layer thicknesses than a steady current. For smaller bed boundary layers, the shear stress tends to be larger, for the same U_c . Since the flow ability to transport sediments depends on the bed shear stress, waves tend to dominate over currents in what concerns sediment entrainment. However, as pointed by [1], the oscillatory nature of the wave orbital velocity makes the current as the dominant factor in transporting the entrained sediments [53].

The present research is mainly concentrated in the bed shear stress induced by waves and a steady current, as they are the main variables considered in the optimised design of scour protections proposed by [1] and [30]. However, details on other complex flow regimes, e.g. tidal current effects, can be found in [49]. Moreover, details on the type of flow in terms of its turbulence are compiled in [54] or [55]. For now, the reader should keep in mind that the present research and theories involved are mainly related to the turbulent flow regime for combined waves and current, which is found in the offshore marine environment.

For cases with a current alone, the bottom shear stress ($\tau_{b,c}$) is dependent on the bottom roughness, the friction near the sand bed and the depth average current velocity (U_c). It is commonly calculated according to Eq. (2.3).

$$\tau_{b,c} = \frac{1}{2} \rho_w f_c U_c^2 \quad (2.3)$$

in which f_c stands for the so-called dimensionless friction factor (or coefficient) of the bed. There are several formulations to obtain f_c , e.g. see [1] and [54]. However, for practical purposes, the current friction factor employed in this thesis is provided by [56], more specifically the one for hydraulically rough flows presented in Eq. (2.4).

$$f_c = \frac{2g}{Ch^2} = \frac{2g}{\left[\frac{\sqrt{g}}{k} \ln \left(\frac{d}{z_0 e} \right) \right]^2} = \begin{cases} \frac{0.06}{\left[\log \left(\frac{12d}{3.3 \frac{v}{u^*}} \right) \right]^2}; & \frac{u^* k_s}{v} \leq 5 \quad \text{smooth flow} \\ \frac{0.06}{\left[\log \left(\frac{12d}{k_s} \right) \right]^2}; & \frac{u^* k_s}{v} \geq 70 \quad \text{rough flow} \end{cases} \quad (2.4)$$

In Eq. (2.4) Ch is the Chézy coefficient ($m^{1/2}/s$), k is the Von Karman constant, equal to 0.4, e is the Nepper's number, v is the water kinematic viscosity and z_0 is the roughness length. According to the formulation presented by [56] (as cited in [1]), in the hydraulically smooth flow, the bed roughness is so small, that roughness elements stay within the viscous sublayer and do not affect the distribution of the flow's velocity. On the other hand, for hydraulically rough flows, there is no viscous sublayer and the flow velocity does not depend on the viscosity. Between both regimes there is the transitional one, for which the velocity is affected both by the viscosity and the bed roughness. In the present research the bed roughness can be considered quite large, since it deals with the flow above the scour protection, which consists on rock material with large dimensions. Therefore, the f_c calculation has to be performed for the hydraulically rough flows only. Furthermore, in Eq. (2.4), d stands for the water depth and the bottom roughness (k_s) is obtained for the case with no ripples, i.e. $k_s = 2.5d_{50}$, where d_{50} concerns the sediment mean diameter (referred to D_{50} - in the case of the rock material used in the scour protection). The bottom roughness is obtained with Eq. (2.5), which is further simplified into Eqs. (2.6) and (2.7) for rough and smooth flows, respectively.

$$z_0 = \frac{k_s}{30} + \frac{v}{9u^*} \quad (2.5)$$

$$z_0 = \frac{k_s}{30}; \quad \frac{k_s u^*}{v} \geq 70 \quad (2.6)$$

$$z_0 = \frac{v}{9u^*}; \quad \frac{k_s u^*}{v} \leq 5 \quad (2.7)$$

In the case of a steady current along the boundary layer thickness was found to be very accurately approximated by a logarithmic profile [1] as in Eq. (2.8). This equation provides the flow velocity at a specific depth (z). Moreover, if Eq. (2.6) and Eq. (2.8) are combined, it is possible to conclude that the average flow velocity (U_c) is obtained at 40% of the water depth counting from the sand bed ($0.368d \approx 0.4d$). This is the common reference also used to measure the mean current velocity in experimental work, as recommended by the practical guidance given in [49].

$$U(z) = \frac{u^*}{k} \ln \left(\frac{z}{z_0} \right) \quad (2.8)$$

In the presence of sand ripples, at the bottom the bed shear stress increases. This is not considered in the present work, in order to agree with the implementation of the design methodologies presented by [30] and [32], addressed in Chapters 3 and 4. For this matter the reader is referred to [1]. For the

bed shear stress induced by waves an extensive review is provided in [52]. The wave-induced shear stress ($\tau_{b,w}$) is obtained according to Eq. (2.9), where f_w is the wave friction factor and U_m is the wave orbital velocity. Note that this shear stress is oscillatory and has an amplitude $\tau_{b,w}$.

$$\tau_{b,w} = \frac{1}{2} \rho_w f_w U_m^2 \quad (2.9)$$

Waves in shallow-enough water depths (say $d/L < 0.5$) generate an oscillatory horizontal velocity at the sea-bed. The amplitude of this horizontal velocity just above the bed (U_m) can be obtained from the linear wave theory with Eq. (2.10). For dynamic scour protections design this value is obtained from the wave spectrum as it will be explained later. H and T are the wave height and the wave period, respectively, while L is the wave length.

$$U_m = \frac{\pi H}{T} \cdot \frac{1}{\sinh\left(\frac{2\pi d}{L}\right)} \quad (2.10)$$

The wave friction factor also has several formulations, e.g. [52, 57, 58]. According to [30] the estimate of f_w considerably influences the values obtained for the wave induced bed shear stress. Since the present research is developed as an improvement of the work performed by [1], the same formulations are followed. Particular attention is given to the one presented in [52], since it was adopted for the majority of the work performed on the reliability assessment of scour protections. Furthermore, since the scour protection can be considered a rough bed compared with the sediment sea-bed, the formulations concerning smooth beds are not presented. Also, the sand bed is, in general, considered rough if the waves are large enough to cause the particles transport. According to [57] a theoretical solution for the wave friction factor over a rough bed can be obtained with a momentum-based method. This leads to Eq. (2.11) for the friction factor and to Eq. (2.12) for the wave boundary layer thickness (δ).

$$f_w = \begin{cases} 0.04 \left(\frac{A}{k_s}\right)^{-0.25}, & \frac{A}{k_s} > 50 \\ 0.4 \left(\frac{A}{k_s}\right)^{-0.75}, & \frac{A}{k_s} < 50 \end{cases} \quad (2.11)$$

$$\frac{\delta}{k_s} = 0.09 \left(\frac{A}{k_s}\right)^{0.82} \quad (2.12)$$

where A is the amplitude of the wave orbital motion at the bed and is obtained with Eq. (2.13), which depends on the calculation of U_m and the wave period, T .

$$A = \frac{U_m T}{2\pi} \quad (2.13)$$

When the ratio of amplitude of the wave orbital motion to k_s assumes small values, an adjustment is recommended by the formulation given in [58], i.e. Eqs. (2.14) and (2.15).

$$f_w = 0.32 \left(\frac{A}{k_s} \right)^{-0.8}, \quad 0.2 < \frac{A}{k_s} < 10 \quad (2.14)$$

$$\frac{\delta}{k_s} = 0.08 \left[\left(\frac{A}{k_s} \right)^{0.82} + 1 \right], \quad 0.5 < \frac{A}{k_s} < 5000 \quad (2.15)$$

The wave friction factor on a rough bed may also be obtained by Eq. (2.16), which corresponds to the formulation yielded by [53].

$$f_w = \exp \left[5.5 \left(\frac{k_s}{A} \right)^{0.2} - 6.3 \right] \quad (2.16)$$

The expression in Eq. (2.17) corresponds to the wave friction factor given by [52], which was implemented as in [55]. The expression is also valid for a rough bed and all values of A/k_s with the bed roughness length calculated as $z_0 = d_{50}/12$.

$$f_w = 1.39 \left(\frac{A}{z_0} \right)^{-0.52} \quad (2.17)$$

As it will be discussed in the practical chapters 4, 6 and 7, for statically stable scour protections, the point is to analyse when the combined waves and current induce a bed shear stress sufficiently large to overcome the threshold of motion. In this sense, an accurate evaluation of the wave induced bed shear stress is crucial. Figure 2.1 illustrates the influence of the aforementioned formulations in the values of $\tau_{b,w}$, which is also designated by t_w in Figure 2.1.

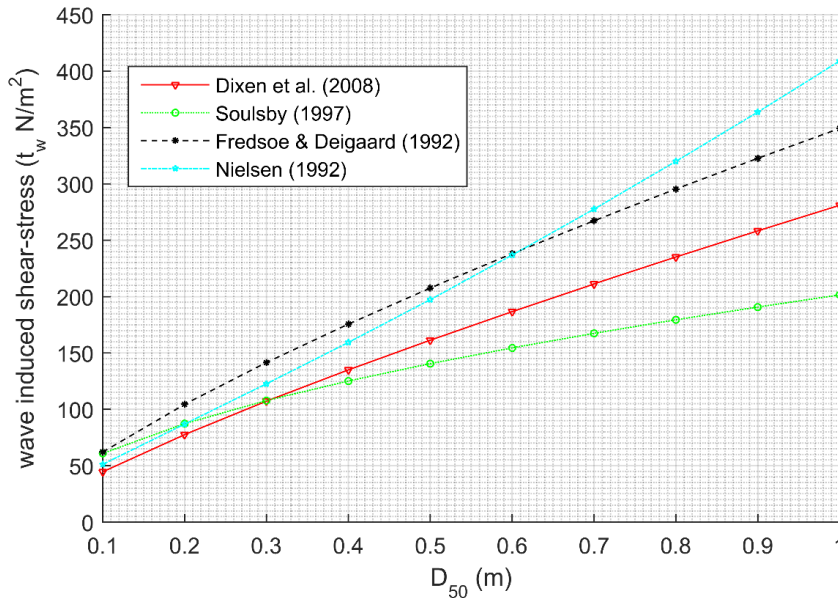


Figure 2.1 – Wave-induced shear stress for different formulations of the wave friction factor, as function of the stone mean diameter D_{50} ($H_s=6.5$ m, $T_p=11.2$ s; $\rho_s=2650$ kg/m³; $d=18$ m) [44].

The values are calculated for several mean stone diameters (D_{50}) used in the armour layer. The differences are more noticeable for an increasing diameter. However, for common values of D_{50} reported in the literature, which typically range from 0.15 to 0.60 m (see [13] and [59]), the differences may indeed be considerable. Figure 2.1 highlights the importance of the wave friction factor, particularly for larger grain sizes. As it was noted in [44], this aspect does influence the reliability assessment of the protection. Since it directly affects the output of the wave-induced bed shear stress that contributes to the failure of the scour protection.

2.2.2 Combined waves and current

Common offshore conditions often combine the effect of waves and current acting simultaneously on the scour protection and the wind turbine foundation. As noted in several works of the literature, e.g. [54, 24] or [60] their combined effect is not a result of the linear combination of both components. This is also valid in bed shear stress calculations, for which the combined effect is not equal to $\tau_{b,c}$ plus $\tau_{b,w}$.

Moreover, the coexistence of waves and current also leads to changes in the wave field, namely, in the wave height and period, as well as in the velocity field. Often for the sake of simplicity this tends to be ignored [1]. In the present research this is not assumed as the main focus, mainly because other uncertainties, as the ones related to the variability of the environmental loads, the design methodologies or the multivariate models used to simulate the sea state, are considered to be larger compared to this aspect. In order to obtain the boundary layer thicknesses and the combined shear stress, the present research uses two theories, which were introduced in detail in [52] and [57]. In a similar way to the wave friction factor, the theoretical formulations used to compute the combined bed shear stress may considerably differ in their results. This also affects the analysis performed when dealing with scour protection design and their reliability assessment.

For cases where waves coexist with a weak parallel current, [57] suggest that the boundary layer thickness is determined by the wave motion only. This enables the use the Eq. (2.18) to obtain the mean combined shear stress (τ_m). In this case the wave friction factor (f_w) is calculated according to Eq. (2.11) and the boundary layer thickness is provided by Eq. (2.12). The combined maximum bed shear stress is given in Eq. (2.21).

$$\tau_m = \frac{2}{\pi} \rho_w f_w U_m U_\delta \quad (2.18)$$

$$U_\delta = C - \sqrt{C^2 - U_c^2} \quad (2.19)$$

$$C = U_c + \frac{1}{\pi} f_w U_m \left(6.2 + \frac{1}{k} \ln \left(\frac{d}{30\delta} \right) \right) \quad (2.20)$$

$$\tau_{\max} = \frac{2}{\pi} \rho_w f_w (U_m + U_\delta) \cdot |U_m + U_\delta| \quad (2.21)$$

According to [1], the alternative proposed by [52] was developed experimentally and proved to give almost as good fits as the ones provided by the best theoretical models [1]. In [55] it is recommended that the combined mean bed shear stress, from Eq. (2.22), is necessary for sediment

diffusion, while the maximum bed shear stress, Eq. (2.23), is necessary to determine the threshold of motion, which is also a requirement for scour protection design.

$$\tau_m = \tau_c \left[1 + 1.2 \left(\frac{\tau_w}{\tau_c + \tau_w} \right)^{3.2} \right] \quad (2.22)$$

$$\tau_{\max} = \left[(\tau_m + \tau_w \cos \phi)^2 + (\tau_w \sin \phi)^2 \right]^{1/2} \quad (2.23)$$

2.3 Amplified bed shear stress and amplification factor

The presence of a monopile foundation in the flow leads to an increase in the bed shear stress [49], due to the increasing turbulence. The increased values of the bed shear stress will be larger compared to the natural flow situation (undisturbed). In order to express the structure's presence, the amplification factor (α) is often used, which is defined as the ratio between the amplified bed shear stress (τ) and the undisturbed bed shear stress (τ_∞), as shown in Eq. (2.24).

$$\alpha = \frac{\tau}{\tau_\infty} \quad (2.24)$$

Although several studies have been performed on the amplification factor, it is hard to find consensual information on the values to be adopted for separated or combined waves and current [51, 61, 62]. Since the concept is assessed with experimental work and the ratio between the bed shear stresses may be influenced by several factors besides the structure itself, different values are reported. In a similar way to the theoretical formulations regarding the induced shear stress, the amplification factor also influences the reliability assessment of a scour protection. This occurs because the assessment of the acting bed shear stress on the protection is typically done by computing the undisturbed values, which are then multiplied by α . A possible way to avoid this is to use design methodologies, which are not directly relying on the estimation of the amplification factor. This is the case of the design optimisation for static scour protections proposed by [1] and summarized in [30] (see section 3.7.1.3).

Ultimately, the amplification factor is very much dependent on the type of flow and the foundation's geometry. According to [1], typical values of α for waves in a slender pile range from 2.2-2.5, although [61] also uses 3, while for a steady current the amplification factor is considered to be 4, e.g. [49, 33]. For further details on this subject the reader is referred to [11], which also provides some values for other geometries and practical cases.

It is relevant to mention that, for the different situations, the amplification factor seems to show variations in its behaviour, although there are some facts that can be briefly reported based on the common findings in the literature. Firstly, the increase of the flow velocity tends to increase the bed shear stress, which leads to larger values for α . These values are also generally higher near the structure, where the flow gets more disturbed.

Also, α decreases with the distance from the structure, with the amplification factor distribution directly linked to the pattern of the scour process, which is more intense in the regions with larger amplification factors. In the marine environment there is a time variation in the position of α , depending on the angle between the wave and the current flow. Typically, the amplification factor is obtained by means of physical model study. Therefore, the value to be used is of empirical nature. The influence of the amplification factor in the reliability of scour protections is addressed in section 7.4.2.

2.4 Threshold of motion

The threshold of motion is defined by [63] as the moment in time for which the forces produced by the flow in the particle are large enough to overcome the stabilizing gravity force. Thus, leading to the motion of the sediment grains. Although several factors may induce the threshold of motion, the present thesis is mainly focused on the horizontal bed shear stresses, as they are the key parameter considered for the design of static scour protections, further introduced in Chapter 3. The threshold of motion of sand particles is a complex research topic, which is only summarized at the present section. Further details on this topic for offshore environment can be found in [52].

For a particle in the sand-bed, the horizontal drag force (F_D) and the vertical lift force (F_L) are the ones contributing to the motion occurrence. The drag force is dependent on the particle's shape and the particle's Reynolds number (Re^*). If A^* is the projected area of the grain on the horizontal plane, then the bottom bed shear stress is obtained by Eq. (2.25).

$$\tau_b = \frac{F_D}{A^*} \quad (2.25)$$

The forces contributing for the particle to remain in place are the submerged weight (W) and the frictional forces (F_s) between the particle and the surrounding grains. Those forces are represented in Figure 2.2.

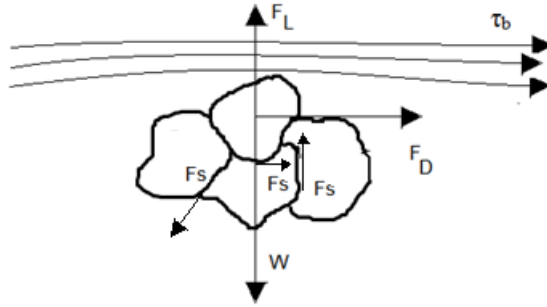


Figure 2.2 – Forces acting on the sediment grain.

To know the acting forces on the particle is not enough to identify when a grain will be entrained. It is also necessary to know the duration of the forces, because the forces should act long enough to entrain the particle. Moreover, the application point of the forces and the correlation between the drag and lift forces affect the threshold of motion.

The bed shear stress for which the threshold of motion occurs is commonly referred to as the critical bed shear stress. In [50] the critical shear stress was extensively studied for a uniform flow and the concept of the critical Shields parameter (θ_{cr}) was introduced. The critical Shields parameter is directly related to the critical bed shear stress and it defines the minimum shear stress that leads to the grain's motion at each moment and in each part of the bed. This critical Shields parameter is obtained from Eq. (2.26), for $\Delta = (\rho_s - \rho_w) / \rho_w$. If the critical Shields parameter is exceeded then the generalised movement of the grains occurs. When referring to the movement of the armour stones in the protection, then d_s can be changed by D_{50} .

$$\theta_{cr} = \frac{\tau_{cr}}{g(\rho_s - \rho_w)d_s} = \frac{(u_{cr}^*)^2}{g\Delta d_s} \quad (2.26)$$

In order to analyse if the grain protrudes into the turbulent boundary layer or stays in the viscous sub-layer, [50] presented the Shields curve. This curve relates the Shields parameter with the grain Reynolds number (Re^*) defined as $Re^* = u^*d_s/\nu$. For large enough dimensions of the grains, the curve indicates that the critical Shields parameter reaches a constant value of 0.056. [49] states that no scour occurs for values of the undisturbed bed shear stress, which are smaller than 25% of the critical value for the shear stress. However, some particles may start to move before the generalised movement occurs. This was noted by [33] who suggested a broad belt instead of a Shields curve, distinguishing the type of movement between the occurrence at some locations of the bed and the generalised sediment movement. Therefore, [30] suggests that for scour protection design a slightly lower value should be used, in this case 0.035. A main disadvantage of the Shields curve is the fact that plotting θ_{cr} as a function of Re^* leads to an implicit function that has the bed shear stress on both sides. A solution for this is to transform the original Shields curve into the one proposed by [52], which plots the Shields parameter as a function of the dimensionless grain size, D^* , Eq. (2.27). The previously mentioned curve is presented in Figure 2.3, which also includes an alternative calculation for the critical Shields parameter (see [52] for further details).

$$D^* = \left(\frac{g(s-1)}{v^2} \right)^{1/3} d_s \quad (2.27)$$

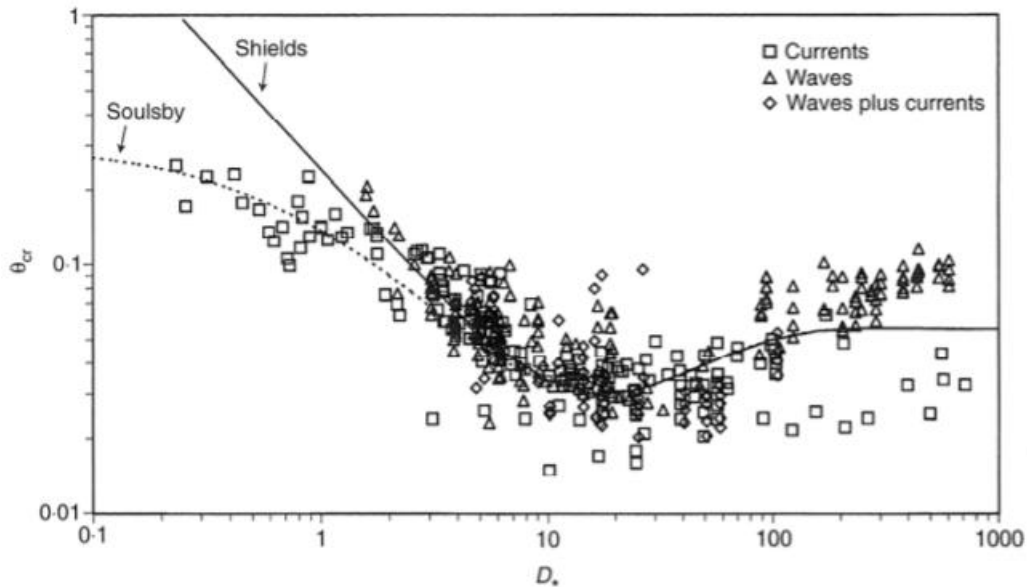


Figure 2.3 – Shields curve adapted by [52] for the threshold of sediment motion for waves and/or currents [1].

The present research was developed for scour protections located at a horizontal bed. This is valid for the physical models of dynamic scour protections and the reliability assessment. Such fact is based on the assumption that for the extent of the protection the bed can be considered horizontal. However, these formulations slightly change for relevant slopes, since the component of weight, which is obliquously projected on the slope direction, is also contributing to increase the drag force. For details on how to adapt the critical bed shear stress for non-horizontal bed slopes the reader is referred to [1].

2.5 Hydrodynamic flow around a monopile foundation

The previous sections referred mainly to the basic concepts related to the particle movements, which when generalised lead to scour phenomena. Before detailing the fundamentals of scour, it is important to understand the basic scour mechanisms derived from the soil-fluid-structure interaction. Therefore, a comprehension is required on the main changes exerted in the fluid by the physical boundaries provided by the foundation and the soil.

A monopile foundation deployed at an offshore windfarm can be seen as a slender pile embedded in a flow. The influence of the vertical slender pile in the flow pattern of a steady current has been extensively studied in the literature, e.g. [64, 65, 66, 51, 67]. Regarding the flow pattern around a vertical pile in a wave field, comprehensive works can be found in [51] and [52, 68, 69]. Nevertheless, for combined waves and current the number of works available in the literature is limited. However, research on this specific subject has been increasing due to its importance for the offshore structures field, e.g. [70, 71, 72]. The major influences on the flow pattern near a slender pile placed at sea are identified by [61] and [63], as follows (see Figure 2.4):

- A downflow is formed in front of the pile;
- A horseshoe vortex is originated on the upstream side of the pile;
- A vortex flow pattern is formed at the lee-side of the pile (also with vortex shedding);
- The streamlines are contracted at the side edges of the pile.

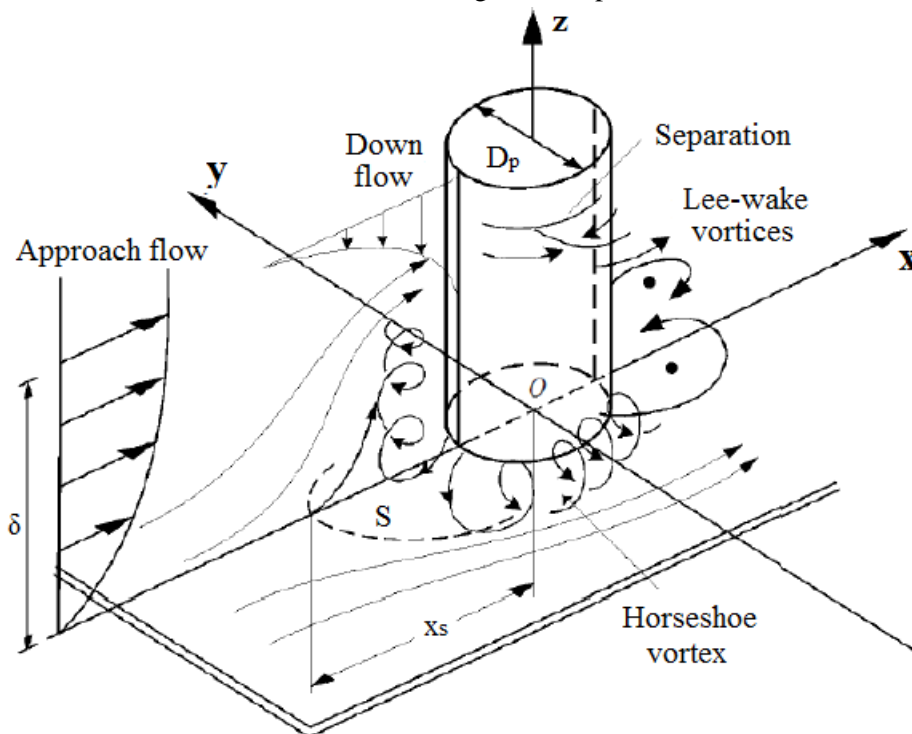


Figure 2.4 – Flow patter around a slender pile due to the flow-structure interaction [66].

The aforementioned changes in flow pattern tend to increase the shear stress, as discussed previously in the introduction of the amplification factor (section 2.3). They also cause an increase in the turbulence levels. As noted in [1], much more is known about the influence on the bed shear stress than the one that occurs in the turbulence. Nevertheless, [61] stated that turbulence does play a major role as a scour mechanism, particularly in obstructed fields. For offshore scour protections at monopile

foundations the static stability of the stones is very much dependent on the bed shear stress, thus the turbulence aspect will not be as deeply focused as the bed shear stress acting on the protection.

2.5.1 Downflow in front of the pile

According to [63] (as cited in [1]), the downflow is originated as the flow comes to rest at the front of the pile. The velocity decreases from the surface downwards and the stagnation pressure ($\rho_w U^2/2$) also decreases from the surface down, which creates a down pressure gradient.

2.5.2 Horseshoe vortex

The bed shear stress near the bottom layers of the flow present lower values of flow velocity and, due to this fact, the bed boundary layer is formed. If the velocities are higher in the upper fluid layers, because of the absence of the friction against the bed, the flow pressure towards the pile is also larger in these layers than in the bottom ones. This will cause the flow near the upstream face of the pile to go downwards. However, because of the physical barrier represented by the bed the boundary layer will inevitably separate and roll up, creating a vortex with a shape of a horseshoe. This vortex goes downstream of the pile, as it can be seen in Figure 2.4, where the separation is represented by the dashed line [61].

The presence of this vortex generates an increase of the bed shear stress compared to the values of the undisturbed flow, which leads to scour on the upstream side of the pile. According to [49] the horseshoe vortex is the major scour mechanism around the base of the vertical pile, and it is also responsible for the scouring pattern shown in Figure 2.5.

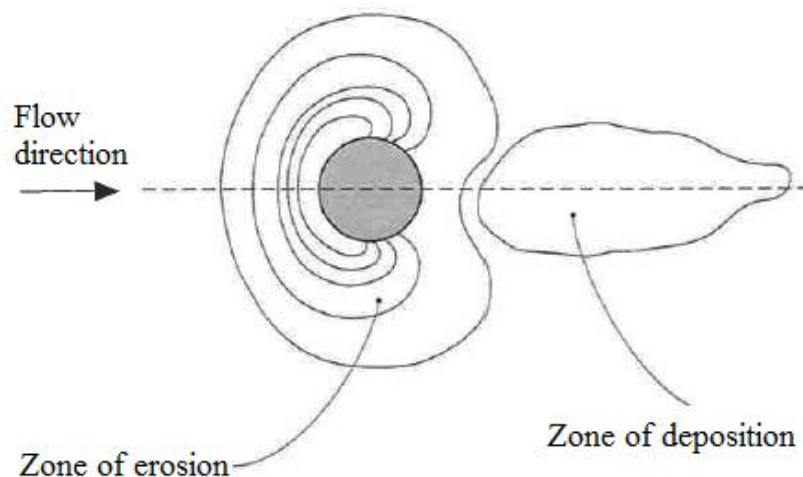


Figure 2.5 – Characteristic equilibrium scour hole pattern for a vertical cylinder in a steady current [49].

The contribution of the horseshoe vortex to the scour process and the pattern of the scour pit was studied by several authors, e.g. [73, 74], who studied its turbulence structures or vortex formation under oscillatory flow [75]. For further detailed information regarding the horseshoe vortex (including its dependence on the boundary layer thickness and on the Reynolds number of the pile diameter (Re_p) or grains Reynolds number (Re^*) or pile geometry and height), the reader is referred to [49]. Moreover, in [51] and [61] details may be found on the horseshoe vortex in a wave environment, for which the influence of the Keulegan-Carpenter number (KC) is deeply studied. The KC number is commonly defined as $KC = U_m T / D_p$, where D_p stands for the pile diameter.

2.5.3 Lee-wake vortices

The lee-wake vortices are formed on the downstream side of the pile and are also a scour mechanism. The presence of the pile in the flow causes its separation, which is revealed by the rotation in the boundary layer over the surface of the pile leading to the formation of this type of vortices. This phenomenon can be interpreted as the roll up of the shear layers arising from the edges of the pile.

The existence of these vortices creates fluctuations in the flow velocity, which increases the turbulence levels on the downstream face of the foundation. The lee-wake vortices contribute to the increase of the bed-shear stress, thus, leading to scouring on the downstream side of the pile. The particles lifted by the vortices tend to be dragged away from the structure, until the deposition occurs due to the effect of the amplified bed shear stress being no longer enough to generate the sediment transport. This deposition zone is also identified in Figure 2.5.

According to [61], in a steady current environment the lee-wake flow mainly depends on the pile Reynolds number (Re_p) and the pile geometry. More information regarding this matter can be found in [2], including the influence of Re_p and the roughness of the pile's surface, the effect of the cross-section shape, the vortex shedding frequency and other aspects of lee-wake vortices.

In oscillatory flows, the KC number plays an important role in lee-wake vortices. Several studies have shown that, in this type of flow, the lee-wake side of the pile is primarily ruled by KC [61]. Details regarding the lee-wake vortices, including the influence of KC, in oscillatory flows, the reader is referred to [51].

2.5.4 Contraction of the streamlines

As mentioned previously, the separation of the flow near the side of the pile can also lead to scour. This phenomenon of separation is a result of the increasing water velocity due to the bending of the flow around the cylinder, which causes the streamlines to contract. When the flow hits the upstream side of the pile, it drastically slows down to experience a new acceleration towards the downstream face. This process, that includes the acceleration and sub-consequently the increase of flow velocity, results in an increase of the bed shear stress, which promotes scour. According to [51], the increase of the bed shear stress near the side edges of the pile, linked to the contraction of the streamlines, is larger in a steady current environment than in the waves.

2.6 Global and local Scour

The scour process is commonly divided into two types of scour, according to their position and influence on the bed lowering: the global and the local scour. If the structure is an offshore platform it will probably include a set of piles.

The scour developed around the vicinity of each pile is manifested by steep-sided pits around the bottom of the single piles. Those pits correspond to the so-called local scour. There is also a tendency for a wide depression to be formed under the structure surrounding all of the supporting piles; this depression usually presents a saucer-shape [61]. Both types of scour are represented for a jacket type structure in Figure 2.6.

The local scour process is a result of the particular hydrodynamic processes, such as the increasing bed shear stress and the horseshoe or lee-wake vortices. On the other side the global scour can be a result of a combination of general flow effects, namely the ones produced by individual structural elements and the contraction of the flow, geomorphologic changes, human activities, meander

formation and migration, bank erosion or changes in river's flow [65]. It is also important to note that there are important overall sea-bed movements caused by natural processes, as the erosion and deposition of sediments, which can contribute to the lowering bed process, increasing scour signs.

Although being very site specific, global scour is important for the design of the foundation and the scour protection [76]. Nevertheless, the present thesis focuses only on local scour at the monopile foundation, which is the most common type of scour found in this type of substructures [1].

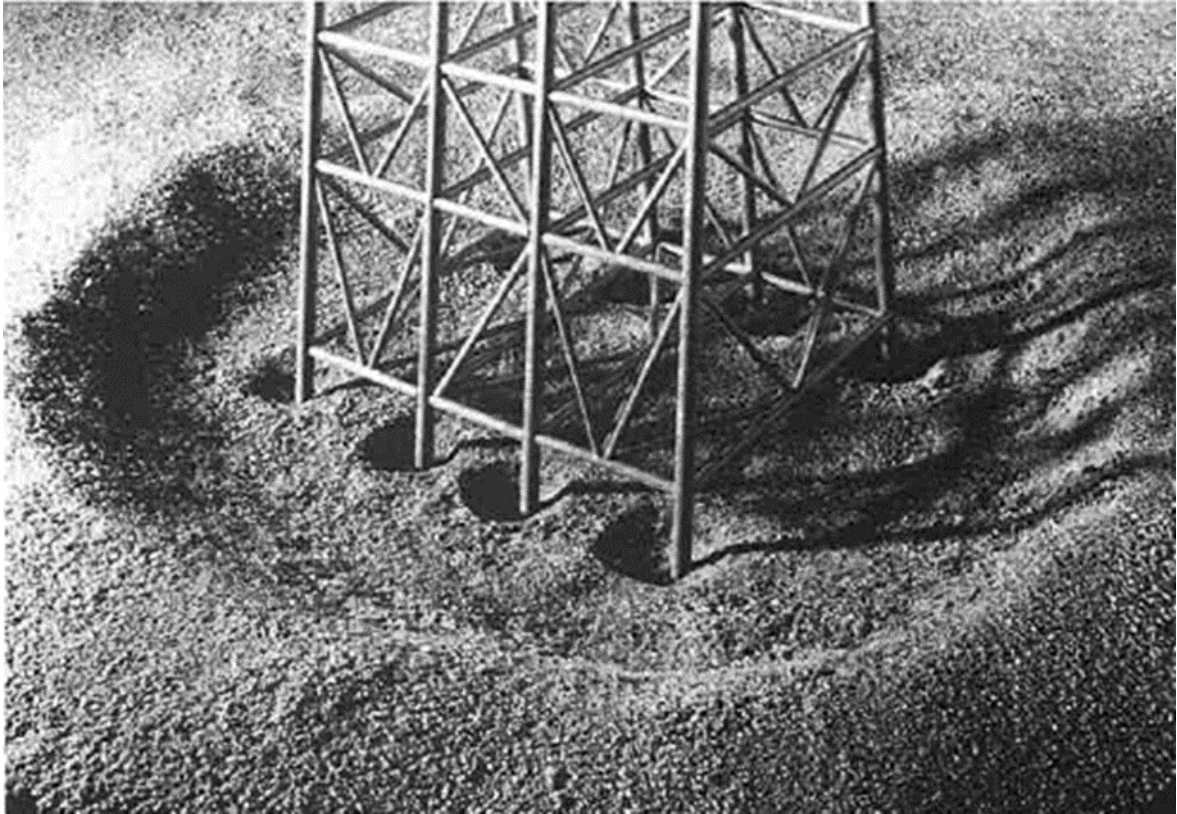


Figure 2.6 – Global and local scour at a jacket foundation [49].

2.7 Equilibrium scour depth and time-scaling of scour

The scour phenomenon tends to be an asymptotic process towards an equilibrium stage. When designing the foundation, it is important to know the equilibrium scour depth, i.e. the depth for which scour stops to develop and that, theoretically, corresponds to the maximum eroded depth. Thus, the scour depth (S) that leads to the worst conditions in terms of the structural stability of the foundation.

However, since the scour depth takes some time to reach the equilibrium phase, it is also crucial to have a perception of the time that the scour hole takes to develop. If the time development is known, than it is possible to predict if the equilibrium scour depth will be reached during a storm (in cohesive soils) or to assess the time-window for the installation of the scour protection [76]. The typical asymptotic behaviour of the scour depth as a function of time is shown in Figure 2.7.

Due to its importance for the design of the foundation, several works have been performed to account for time development of the scour hole. Two of the most well-known methods are given in Eqs. (2.28) and (2.29), from [77] and [78], respectively. S_e is the equilibrium scour depth and T is the

time scale of the scour process. T is defined in [49] as the time necessary to develop a scour depth of 63% of the equilibrium value.

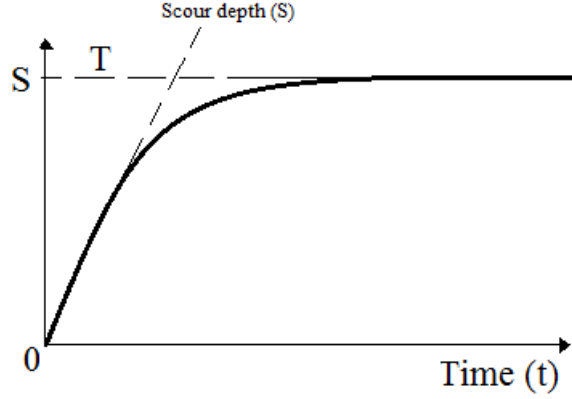


Figure 2.7 – Time development of the scour depth.

$$S(t) = S_e (1 - \exp(-t/T)) \quad (2.28)$$

$$\frac{S(t)}{S_e} = \exp \left[-0.03 \left| \frac{U_{cr}}{U} \ln \left(\frac{t}{t_e} \right) \right|^{1.6} \right] \quad (2.29)$$

In Eq. (2.29) U is the average current velocity, U_{cr} is the critical velocity and t_e is the time needed to reach the equilibrium scour depth. The value of t_e can be estimated by Eq. (2.30), which depends on the water depth (d) and the pile diameter (D_p).

$$t_e \text{ (days)} = \begin{cases} 48.26 \frac{D_p}{U} \left(\frac{U}{U_{cr}} - 0.4 \right) & , \frac{d}{D_p} > 6 \\ 48.26 \frac{D_p}{U} \left(\frac{U}{U_{cr}} - 0.4 \right) \left(\frac{d}{D_p} \right)^{0.25} & , \frac{d}{D_p} \leq 6 \end{cases} \quad (2.30)$$

2.8 Clear-water scour versus live-bed scour

Regarding the flow's regime, scour is classified into two different categories: the clear-water scour and the live-bed scour. In the clear-water scour, the sediment motion takes place only near the vicinity of the structure, i.e. the bed shear stress is lower than the critical shear stress or, in terms of the Shields parameter, $\theta < \theta_{cr}$. However, in the structure vicinity, scour occurs due to the amplified bed shear stress. On the other hand, when the Shields parameter for the undisturbed conditions (θ) has values above the critical one (θ_{cr}), the regime is usually called the live-bed regime. In this regime the sediment transport prevails over the entire sand bed, even away from the structure vicinity, because $\theta > \theta_{cr}$ over each location of the sand bed.

The clear-water scour depends strongly on the Shields parameter, since for small values of θ the induced sediment transport is small. The bed shear stress is too small to induce the generalized sediment motion. Once scour is initiated, the scour depth increases with θ until it reaches a maximum for $\theta = \theta_{cr}$ in the undisturbed conditions. After that, the live-bed scour occurs, which varies only slightly

with the Shields parameter, since changes in θ result in a changed sediment transport, both inside and outside the scour hole. According to [61, 63], the equilibrium clear-water scour develops slower than the live-bed scour. However, it has about a 10% larger maximum equilibrium depth [63] (Figure 2.8). In the live-bed scour, the sediments dragged downstream of the pile are compensated by the ones that are coming from the undisturbed zone upstream, which contributes for a faster time-scale in the live-bed regime (T_{LB}), i.e. a sooner equilibrium, compared with the time-scale of the clear-water scour (T_{CW}).

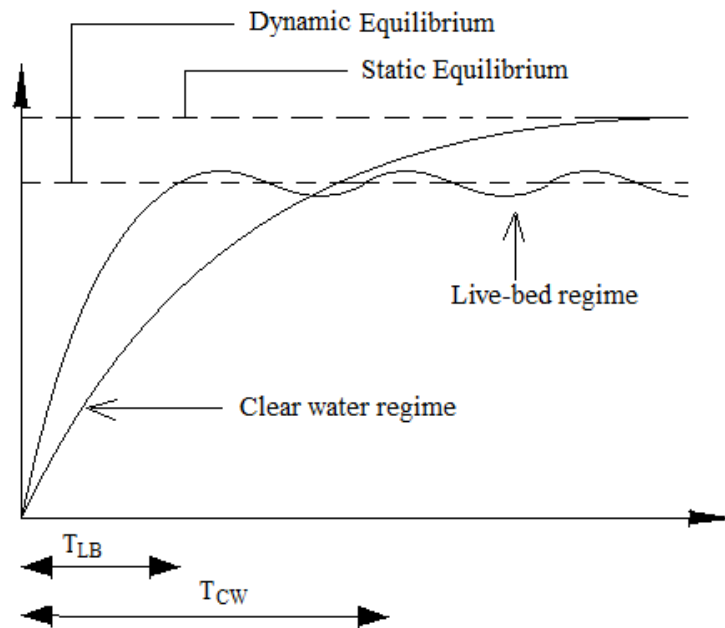


Figure 2.8 – Scour depth evolution and time-scale comparison between live-bed and clear-water scour [11].

2.9 Scour depth around a monopile foundation

The maximum scour depth is one of the most important parameters to design a foundation resistant to scour. The majority of the formulations used to determine the expected maximum scour depth during the structure lifetime is of a semi-empirical nature, that is derived from experimental data [12]. However, as stated by [1], laboratory studies and field measurements, e.g. [13] or [79, 80], as well as measurements in prototype scour holes [81, 82, 83], show a reasonable agreement between empirically predicted scour depths and prototype scour depths. Scour depth prediction is commonly different for cohesive and non-cohesive sediments. The present research concerns the latter, which is the most common type of soil in the marine environment. For details on scour depth prediction in cohesive soils the reader is referred to [84].

2.9.1 Scour prediction in a steady current

The majority of the studies regarding scour depth prediction concern to the steady current environment, most of them related to scour at bridge piers and abutments [83]. A comprehensive review on scour prediction in steady current is provided in [85]. The following paragraphs summarize some of the most important and widely used ones. According to [63] the clear-water and live-bed equilibrium scour depths (S_e) are obtained from Eq. (2.31) and Eq. (2.32) respectively.

$$\frac{S_e}{D_p} = 2.3K_s K_\sigma K_\alpha K_{si} K_d \quad (2.31)$$

$$\frac{S_e}{D_p} = 2.3K_s K_\alpha K_{si} K_d \quad (2.32)$$

where, K_s is the shape factor (1 for cylindrical monopile), K_σ is a factor depending on the grain size distribution. K_α is a pier alignment factor (1 for a cylindrical monopile), K_{si} is a pier size factor (1 for the relevant values of D_p/d_{50} in marine environment) and K_d is a flow depth factor (1 for $d/D_p > 3$). In [1] the calculations of K_σ and K_d for $d/D_p \leq 3$ are presented.

In [75], Eq. (2.33) is used for live-bed scour, with σ_s equal to 0.7. This equation is also used in [49], which also uses Eq. (2.34) for clear-water scour.

$$\frac{S_e}{D_p} = 1.3 + \sigma_s \quad (2.33)$$

$$\frac{S_e}{D_p} = 1.3 \left[2 \sqrt{\frac{\theta}{\theta_{cr}}} - 1 \right] \quad (2.34)$$

The physical model studies performed by [86] led to Eq. (2.35), based on the depth-averaged velocity (U_c) and the critical velocity (U_{cr}). This equation leads to a maximum value of S_e/D_p of 2.64.

$$\frac{S_e}{D_p} = 3.77 \frac{U_c}{U_{cr}} - 1.13 \quad \text{for} \quad 0.3 \leq \frac{U_c}{U_{cr}} \leq 1 \quad (2.35)$$

In [33], Eqs. (2.36) and (2.37) are proposed for the clear-water ($0.5 < U_c/U_{cr} < 1$) and the live-bed scour, respectively. This formulation considers that scour does not occur for U_c/U_{cr} below 0.5. K_i is a correction factor calculated as $K_i = K_s K_\alpha K_\sigma K_{gr}$, which are obtained as discussed for Eqs. (2.31) and (2.32), while K_{gr} accounts for the case of scour in a group of piles (i.e., 1 for a cylindrical monopile).

$$\frac{S_e}{D_p} = 2K_i \left(2 \frac{U_c}{U_{cr}} - 1 \right) \tanh \left(\frac{d}{D_p} \right) \quad (2.36)$$

$$\frac{S_e}{D_p} = 1.5K_i \tanh \left(\frac{d}{D_p} \right) \quad (2.37)$$

More complex equations are provided for example by [87, 88, 89] and summarized in [83]. However, for a detailed review of scour prediction in monopiles in steady currents the reference [2] is suggested.

2.9.2 Scour prediction in waves

Wave-induced scour significantly differs from steady current scour, mainly due to the diffraction effects [1]. These effects are considered to be important if the monopile diameter to wave length ratio (D_p/L) is larger than 0.2, or $KC > 1$ [51] which is the case for offshore wind turbines in storm

conditions. Since the KC number plays a major role in scour occurring in the wave's environment, the majority of the predicting equations take this parameter into consideration. In [90] the empirical formula given in Eq. (2.38) is suggested.

$$\frac{S_e}{D_p} = KC - 6 \quad (2.38)$$

According to [75] for KC smaller than 6 the scour is practically non-existent, the empirical Eq. (2.39) is used, where $A=1.3$, $B=0.03$ and $C=6$ for vertical cylindrical piles.

$$\frac{S_e}{D_p} = A \left[1 - \exp(-B[KC - C]) \right], \quad KC \geq 6 \quad (2.39)$$

This formula is valid for the live-bed regime. Moreover, for large values of KC, the scour depth tends to the equivalent scour depth caused by a steady current. According to [91], for irregular waves, the same formula can be used, as long as the KC number is obtained with the orbital bottom velocity (U_m), obtained from the orbital velocity spectrum (σ_v), i.e. $U_m = 2^{0.5} \sigma_v$, and the peak wave period, T_p . Note that σ_U stands for the root-mean-square value of the orbital velocity U_m at the bed (see [1] for further details).

2.9.3 Scour prediction in combined waves and current

The combined effect of waves and current presents a more complex problem, since the scour depth does not simply correspond to a linear sum of their separated components. Scour in combined waves and current has been the matter of relatively more recent studies. A review of this subject can be seen in [92].

According to [1], it is generally recognised that scour depths for combined waves and current are lower than in a steady current environment. However, in [91], it is noted that for small KC numbers, even a slight current superimposed on the waves may lead to a considerable increase in the scour depth. Moreover, in [93], it was noted that this difference is also affected by the water depth. Often, the literature uses the dimensionless parameter velocity ratio, U_{cw} , to define the waves or current dominance in the scour process for a combined environment, i.e. Eq. (2.40).

$$U_{cw} = \frac{U_c}{U_c + U_m} \quad (2.40)$$

If U_{cw} presents small values, the lee-wake vortices are the dominant scour mechanism and the scour depth tends to the wave alone current case (2.39). Conversely, as U_{cw} increases, the horseshoe vortex becomes the predominant scour mechanism and the scour depth tends to Eq. (2.33). In [61] the direction between wave and current (following or opposing direction) does not play a significant role in the scour depth. However, other works report that this is not the case, namely in scour-induced damage on the protection, e.g. [30]. The dimensionless scour depth (S/D_p) as a function of the KC number and the U_{cw} for an equilibrium situation is presented in Figure 2.9.

In [61], Eq. (2.41) is suggested to obtain the scour depth in a combined environment for $KC > 4$. S_c (m) is the scour depth for a steady current alone, where parameters A and B are obtained from Eq. (2.42) and Eq. (2.43), respectively.

$$\frac{S}{D_p} = \frac{S_c}{D_p} \left[1 - e^{-A(KC-B)} \right] \quad (2.41)$$

$$A = 0.03 + \frac{3}{4} (U_{cw})^{2.6} \quad (2.42)$$

$$B = 6e^{-4.7U_{cw}} \quad (2.43)$$

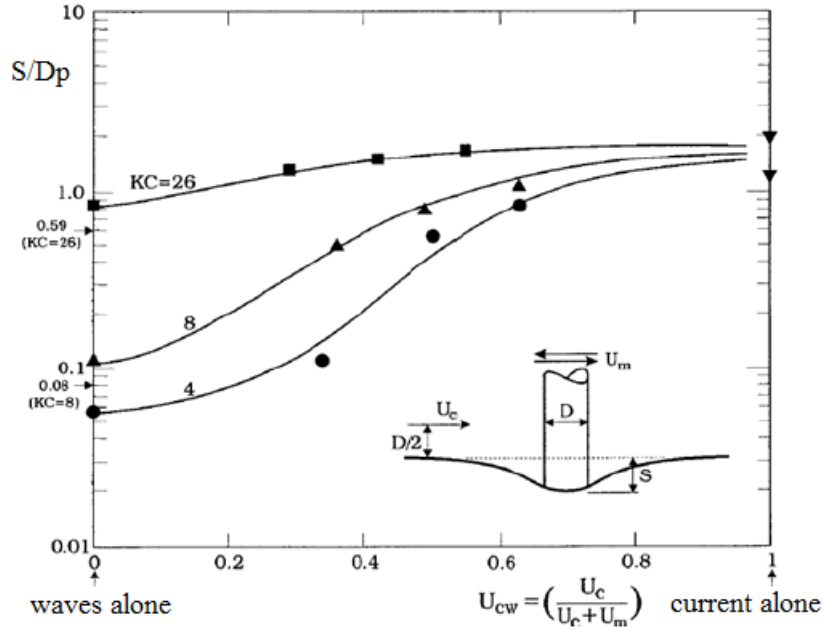


Figure 2.9 – Dimensionless equilibrium scour depth in combined waves and current [61].

The research presented by [94] proposed Eq. (2.44), which was developed for the live-bed scour and as an improvement of the proposed by [61]. According to this formulation, for moderated wave conditions, the scour depth tends towards the current alone value. Eqs. (2.44), (2.45) and (2.46) were developed for KC numbers between 1 and 10.

$$\frac{S}{D_p} = 1.3 \left[1 - e^{-A_1(KC-B_1)} \cdot (1-U_{cw})^{C_1} \right] \quad (2.44)$$

$$A_1 = 0.03 + \frac{3}{2} U_{cw}^4 \quad (2.45)$$

$$B_1 = 6e^{-5U_{cw}} \quad (2.46)$$

Eq. (2.47) can also be used and was developed by [95] to obtain the equilibrium scour depth (S_e), where K_w is a correction factor for the sediment dimension, Eq. (2.48), and K_s is a shape correction factor, Eq. (2.49). In this case d stands for the water depth and d_p stands for the submerged pile height. The values obtained from the experimental results from [95] show that for U_{cw} larger than 0.7 the largest values of the equilibrium scour depth are obtained.

$$\frac{S_e}{D_p} = 1.5 \tanh\left(\frac{d}{D_p}\right) K_w K_s \quad (2.47)$$

$$K_w = 1 - e^{-A_2} \quad (2.48)$$

$$K_d = \left(\frac{d_p}{d}\right)^{0.67} \quad (2.49)$$

$$A_2 = 0.03 + \frac{3}{2} (U_{cw})^4 \quad (2.50)$$

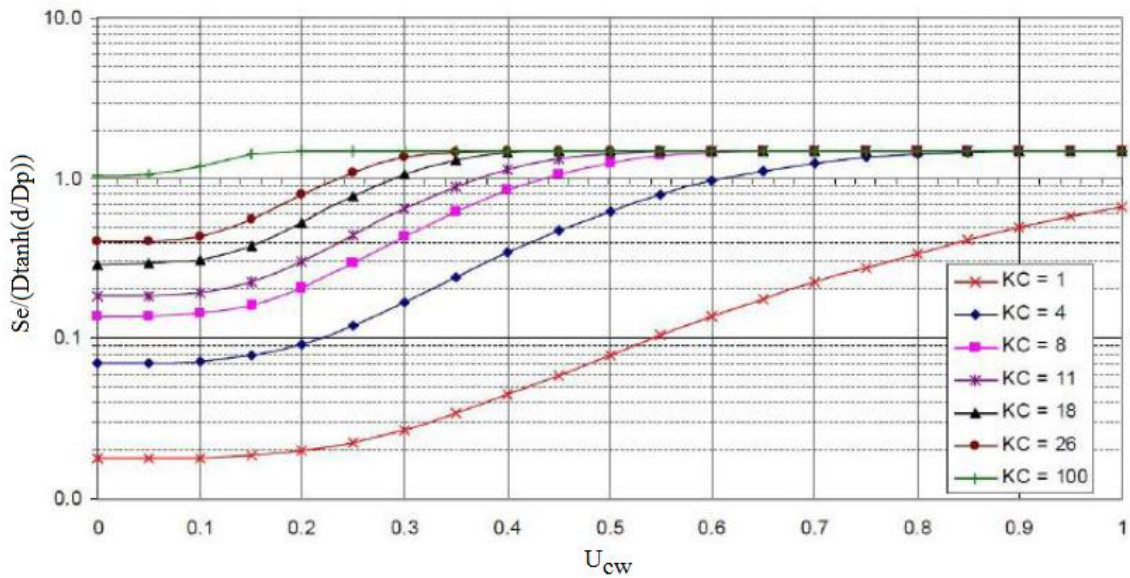


Figure 2.10 – Equilibrium scour depth as a function of KC and U_{cw} , [95].

More recently in [96], Eq. (2.51) was proposed to obtain the maximum dimensionless scour depth to pile diameter ratio (S/D_p). The dimensional analysis showed that the key parameters for scour prediction under waves and current combined were the ratio between the flow velocity (U) evaluated at the bottom and the critical flow velocity (U_{cr}) and the KC number. The previously mentioned equation extended the range of KC, which was varied in physical models between 6 and 10^5 , while U/U_{cr} was tested between 0.6 and 4.5. Moreover, this formulation showed that the soils' characteristics also played an important role in scour prediction for waves with a superimposed current, which had not been recognized in [61] and [95].

$$\left(\frac{S}{D_p}\right)_{\max} = 2.5 \left(1 - 0.5 \frac{U}{U_{cr}}\right) X_{rel} \quad (2.51)$$

$$X_{rel} = \frac{x_{eff}}{1 + x_{eff}} \quad (2.52)$$

$$x_{eff} = 0.03\pi \left(1 - 0.35 \frac{U_{cr}}{U} \right) (KC - 6) \quad (2.53)$$

2.10 Scour extent

The shape of the scour hole is typically simplified by a truncated asymmetrical cone. A scheme is presented in Figure 2.11. The dimensions of the scour hole can be obtained with the upstream and downstream slopes, α_{up} and α_{down} respectively, and the scour extent (W) according to Eq. (2.54) [1].

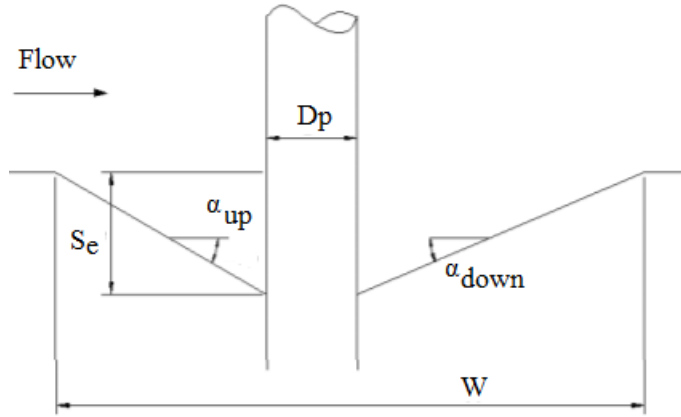


Figure 2.11 – Typical scheme of a scour hole.

$$W = D_p + S_e \left[\cot(\alpha_{up}) + \cot(\alpha_{down}) \right] \quad (2.54)$$

In a steady current situation the upstream slope is approximately equal to the internal friction angle of the sediments ϕ_i [33]. The downstream angle tends to be less steep than the upstream one, and according to [33], it is approximately equal to half of the upstream slope, while [62] it is considered equal to 25° .

The extent side slope of the hole (W_p), i.e. in the perpendicular direction of the flow, is similar to Figure 2.11 with both slopes equal to $\alpha_{up} = \phi_i$. For cylindrical piles the scour hole is theoretically symmetric on the cross-section to the flow. This leads to Eq. (2.55).

$$W_p = D_p + 2S_e \left[\cot(\phi_i) \right] \quad (2.55)$$

The aforementioned equations concern non-cohesive soils. For cohesive ones, the scour hole tends to be steeper due to the attraction forces between particles.

2.11 Conclusions

In this chapter, the very basic fundamentals of the scour phenomenon were presented. The evaluation of the bed shear stress in typical offshore environments was addressed and it was concluded that this parameter is the basis of the scour phenomenon, which is the hazard that primarily justifies the development of the present thesis. A review of the empirical theories used to calculate the bed shear stress was provided, due to its importance for scour protection design methodologies, analysed in Chapter 3. Moreover, it was seen that the existing literature widely recognises the differences between

current- and wave-induced bed shear stress. Throughout this brief review, it was noted that the uncertainty related to these methodologies is present in several aspects, namely the wave friction coefficient, the amplification factor, the Shields parameter or the definition of the threshold of motion. These uncertainties contribute to a somehow non-consensual design of the scour protection, which will depend on the methodologies used to account for the combined bed shear stress. It was also concluded that some of these uncertainties may lead to differences in the reliability assessment of scour protections.

The main conclusions to retain from this chapter are:

- Scour phenomena leads to the structural instability of the scour protection and it is one of the vastest subjects of hydraulic and civil engineering research;
- Scour is caused by the current- or wave-induced bed shear stress. In offshore wind turbines both of them tend to be present;
- Typically, the wave-induced bed shear stress is larger than the current-induced one;
- The combined effect of waves and current is not equal to the linear sum of the effects caused by each component, which is valid both for the scour depth and the bed shear stress;
- The stability of non-cohesive soils, as the sand bed or the rock material applied to the top layer of the protection, can be defined according to the critical shear stress, which sets the threshold of motion;
- Despite the threshold of motion definition, in current situations, the soil particles or the armour units in the protection do not start to move all at the same time. This is due to the variability in the granulometric characteristics of the particles;
- The scour phenomenon occurs due to the action of scour mechanisms, e.g. horseshoe vortex, lee-wake vortices and the contraction of the stream lines. Depending on the type of flow the importance of each mechanism in the severity of the scour phenomenon may vary;
- The amplification factor of the bed shear stress varies considerably, sometimes reaching values of 7-11. Typically, these values are lower for waves alone than for a steady current alone;
- The maximum scour depth is the most important parameter to describe the scour hole. The methodologies reported in the literature have a semi-empirical nature. These formulas indicate that the maximum scour depth varies between 1 and 2.6 times the pile diameter.

The complexity of scour phenomena and the variety of empirical considerations associated to its prediction directly influence the design of the protection. Therefore, these influences are expected to contribute for different results in the reliability analysis of scour protections, which are designed according to different methodologies despite the similar environmental conditions. Chapter 3 addresses the most known methodologies of scour protection design, based on the fundamentals previously presented in Chapter 2.

Scour Protection Design

3.1 Introduction to scour protection

When designing an offshore wind turbine, the expected maximum scour depth must be accounted for. Then the design of the foundation can be performed according to the need of bearing higher momentum and axial loads, or a scour protection can be applied around the foundation.

The literature has reported several methodologies concerning scour protection design, most of them developed for a steady current environment, e.g. [33, 86, 97, 98]. Reviews of countermeasures for steady current-induced scour can also be seen in [85] and [99]. The studies regarding scour protections at combined waves and current were only developed later [1]. However, during the last 10 to 15 years, novel approaches have been presented, e.g. [1, 2, 30, 76, 100]. More recently, research projects have also been performed on the optimisation of scour protections, e.g. [32, 101]. Novel design concepts, as the dynamically stable and the wide-graded scour protections, were introduced and developed in the state-of-the-art, namely, in [26, 32, 102] and [103].

In offshore windfarms, scour protections are commonly designed based on the threshold of motion criterion, followed by a physical model study [1]. Since the present thesis concerns the optimisation of scour protections, as explained in Chapter 1, a particular focus will be given to the concept of dynamic stability. Moreover, the design methodologies reported in the literature are of a semi-empirical nature and are typically applied in a deterministic perspective, as it will be seen throughout this chapter. Although the use of a wave spectrum corresponds to a probabilistic short-term analysis of the sea-state characteristics, it does not represent a long-term probabilistic analysis. Hence, even when using spectral analysis, these methodologies do not account for the long-term evolution of the design wave height. The probabilistic design approaches are described in further chapters. However, for a proper understanding of probabilistic design and reliability assessment, the present chapter is dedicated to the study of the traditional design of scour protections. Furthermore, a review of physical model studies of scour protections is presented, as a basis for the further contributions given by this thesis to the dynamic stability concept.

The aim of this chapter is:

- To provide a background on traditional scour protection design;
- To discuss the design parameters, the resistance properties and the loads acting on scour protections applied to offshore windfarms;
- To discuss the studies that led to the development of dynamic scour protections;
- To discuss the main differences of designing a statically or a dynamically stable scour protection.

This chapter gives particular focus to the methodologies in [1, 30] and [32], which represent the basis of the experimental study developed in this thesis. Moreover, after this chapter, the reader should be able to understand scour protection as a system, whose properties can be divided into resistance properties and acting loads. The present chapter is also focused on the mean diameter of the armour stones used in the protection, since this variable will be the object of optimization during the reliability analysis. Throughout the chapter, an important distinction is made between statically stable scour protections and dynamically stable ones. This aspect will be detailed in further sections. At the present stage, the reader should bear in mind that the former scour protections correspond to the traditional design, for which no movement of the top layer stones is allowed. Conversely, a dynamic scour protection is designed to allow for a certain degree of movement of the armour units, without causing failure of the protection, i.e. the exposure of the filter layer or the sand bed beneath.

3.2 The need of scour protections for the design of offshore wind turbines

Offshore wind turbines with monopile foundations are commonly seen as a very slender structure. This is valid when the designer is focused on the hydrodynamic loads acting on the structure, but also when the designer focuses on the dynamic behaviour of the wind turbine. One of the most important design aspects of offshore wind turbines is the natural frequency of the structure (f_n). The natural frequency is influenced by the free spanning of the substructure [104]. If scour occurs, the structure is more prone to suffer from fatigue problems [105], since the increasing free spanning of the monopile also increases the natural frequency, eventually leading to resonance. This effect is particularly evident in monopile foundations, due to their slenderness. Figure 3.1 shows the relative natural frequency as a function of the scour depth, for an offshore wind turbine of 6 MW. It shows that scour contributes to a considerable decrease of f_n . Moreover, the second natural frequency is also affected. The frequency must be controlled at a design stage to avoid excessive displacements at the top of the structure [21].

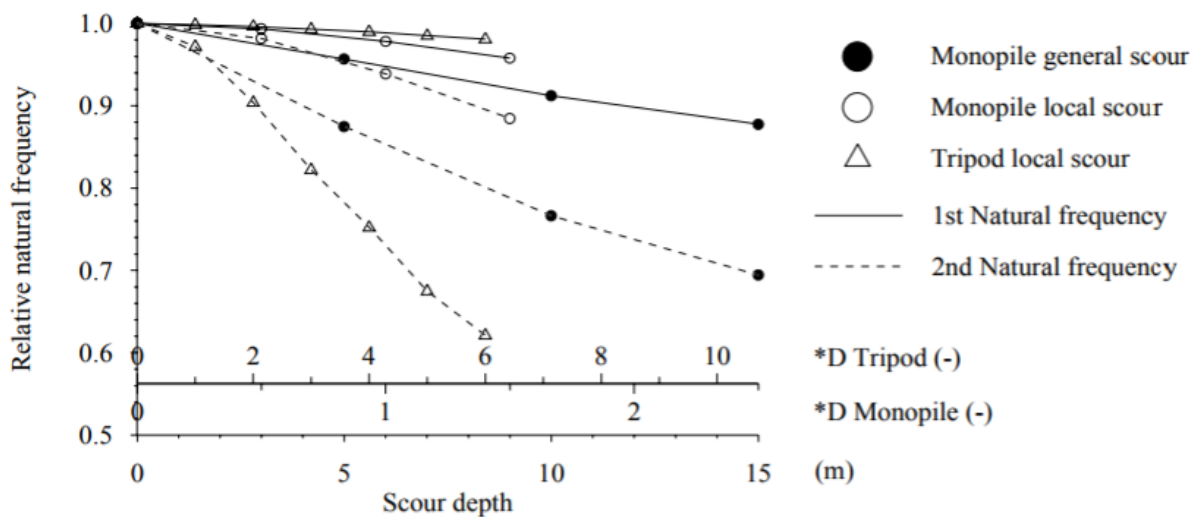


Figure 3.1 – Sensitivity to scour of the natural frequency of the support structure of a 6 MW turbine [104].

When designing an offshore wind turbine the load caused by the vibration at the hub level has a frequency equal to the rotational frequency of the rotor, often referred to 1P loading. However, since the industrial wind turbines may be variable speed machines, 1P corresponds to a frequency band, associated to the lowest and highest rotations per minute, rather than a single frequency alone [18]. Furthermore, the blades of the wind turbine passing in front of the tower cause a shadowing effect and produce a loss of wind load on the tower. This leads to a dynamic load with a frequency that is either

equal to three times (3P) or to two times (2P) the rotational frequency of the turbine. Therefore, the designer has to select a system frequency that lies outside these frequencies to avoid resonance and fatigue-induced damage. Regarding the first natural frequency (f_0), the wind turbine is typically designed for three possible situations, according to [18]:

- Soft-soft design – where f_0 is placed below the 1P frequency range, which is a very flexible structure and difficult to design for a bottom fixed structure;
- Soft-stiff design – where f_0 lies between the 1P and 3P frequency ranges, which is the most common in current offshore development;
- Stiff-stiff design – where f_0 has a higher natural frequency than the upper limit of the 3P band, which implies a very stiff support structure.

The industry standards [21] and [106] indicate that the first natural frequency should not be within the 10% of the 1P and 3P ranges, as shown in Figure 3.2. This leads to a design for which the natural frequency needs to be fitted into a very narrow band. Moreover, in some cases the 1P and 3P ranges may even coincide, leaving no gap for a soft-stiff design [18].

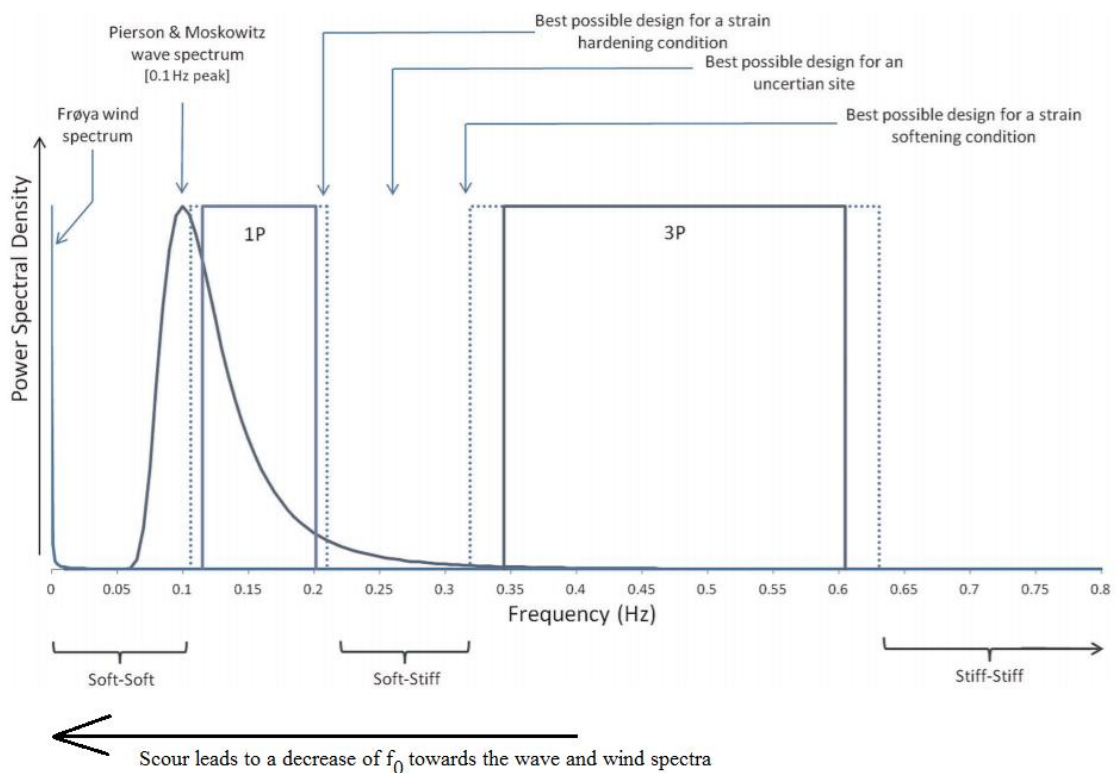


Figure 3.2 – Frequency spectrum of dynamic loads and design choices for the natural frequency (adapted from [18]).

The design of the offshore wind turbine is only conservative, from a dynamic point of view, if an accurate prediction of the first natural frequency is obtained. The aim can be a very stiff solution, placing the natural frequency above the 3P range. However, this leads to massive support structures, which are not economically viable. Therefore, the offshore wind turbines are commonly designed for a soft-stiff design. The first modal frequency of these structures typically lies in the range of 75 to 120% of the excitation frequencies [18, 104]. As a result, dynamic amplifications of the responses are expected. In soft-stiff design, any change in the natural frequency may lead to an increase of the vibration amplitudes, eventually leading to fatigue damage. Scour occurrence is one of the cases that

may contribute to enhance this problem. Therefore, to avoid the use of large supporting structures, scour protections are applied to the foundation, preventing the increase of the monopile free spanning due to the sand bed generalized loss of material.

Still the design of the scour protection ought to be simultaneously effective and efficient. Effective, means that the protection correctly fulfils its purpose, which is to avoid the erosion around the monopile, enabling a proper dynamic behaviour of the structure. On the other hand, efficient means that this purpose is achieved for the lowest cost possible [1]. The most used type of scour protection consists in loose rocks, often called riprap. The main advantage of riprap scour protections is the low cost associated to rock material and its wide availability. Conversely, one of the main disadvantages lies in the non-uniformity of the rocks, which may present a wide grade possibly more prone to damage in riprap layer. The studies presented by [31] and [103] suggest that wide graded scour protections might be a feasible alternative to the traditional protection (armour layer with rocks placed over a filter layer). However, the material employed in current practice may sometimes present an excessive amount of smaller stones, which do not offer the required size and weight to resist the hydrodynamic environment. Nevertheless, it is also important to note that the smaller stones gathered on the top surface of the armour layer tend to be “washed out” at the first moments after the installation of the protection. Still, the designer needs to account for this material loss, which can increase the required volume to build the protection, thus increasing its cost.

During the design of the offshore wind turbine, it is necessary to calculate the loads acting on the structure and the maximum expected scour depth. Then, the following structural measures may be used, which do not require the actual placement of a scour protection system but allow for scour development (see Figure 3.3):

- Increase the bearing capacity of the pile, by driving it deeper into the ground, reducing the percentage of free spanning length of the monopile compared with the total length (Figure 3.3a);
- Increase the pile diameter and the wall thickness to increase the moment bearing capacity (Figure 3.3b);
- Increase the pile stiffness, by also increasing the wall thickness, to account for the increased eigenfrequency of the structure due to scour (Figure 3.3c);
- Solve the free spanning of the cables, eventually considering supporting the cables with piles, as detailed in [107] (Figure 3.3d).

Additionally, according to [1], it is also possible to take other scour reducing measures, namely, the use of a horizontal deflector/collar [64]. Also, in a fluvial environment, sacrificial piles or vertical vanes are often employed. However, these are not suitable for a marine environment, because they are developed for unidirectional flows [33]. An alternative to the aforementioned solutions is the use of a riprap scour protection. Economic studies comparing the previously mentioned measures and the use of scour protections have been performed [107, 108] and [109], concluding that scour protections tend to be less costly than structural measures. However, and as mentioned in Chapter 1, scour protections still represent a considerable cost of an offshore wind turbine, which emphasizes the need for their optimization. For instance, in [107], a riprap scour protection with a thickness of 1.5 m, an extent of 25 m outside the pile with a diameter of 3.5 m, has an estimated cost of €350 000 per turbine, which is a considerable investment if an offshore windfarm is designed to have 100 turbines or more (see Figure 3.4).

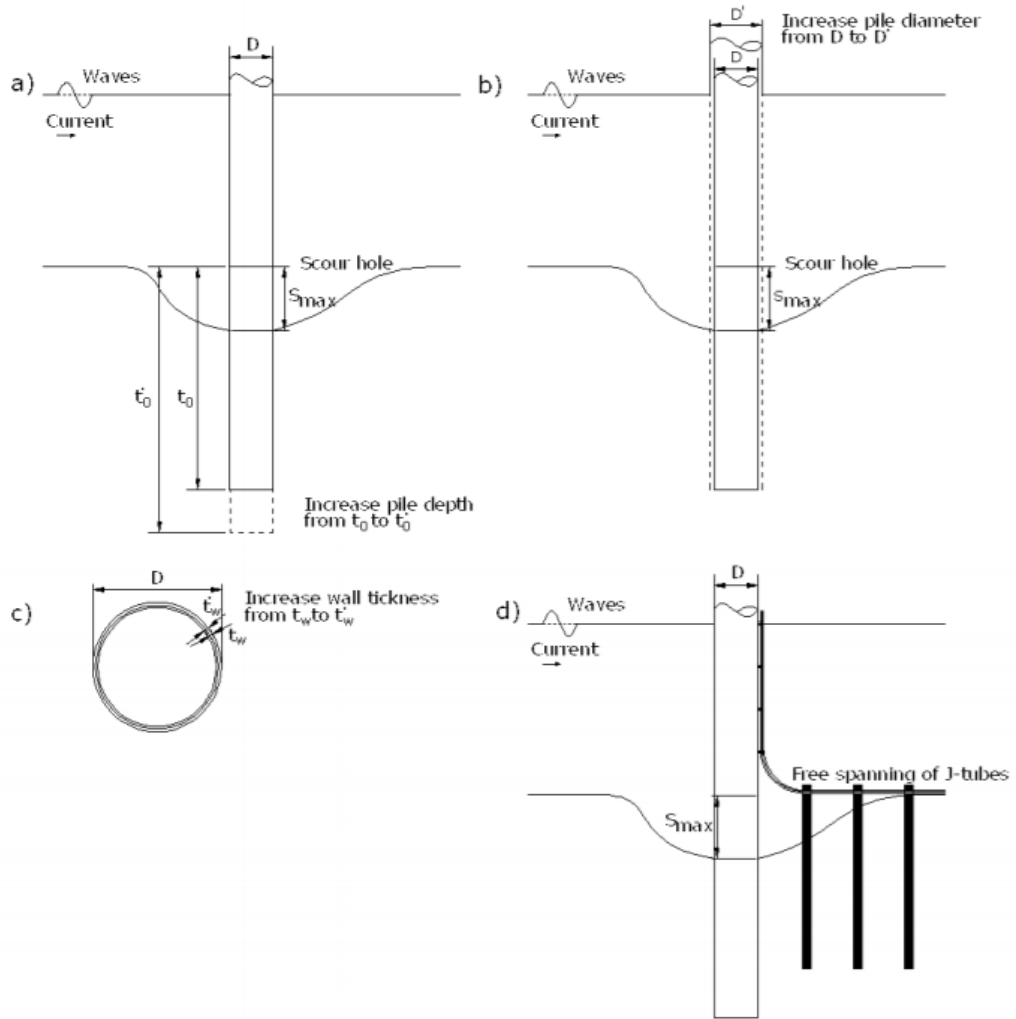


Figure 3.3 – Structural measures to account for scour phenomena effects, without using a scour protection (taken from [1] and originally [97]).

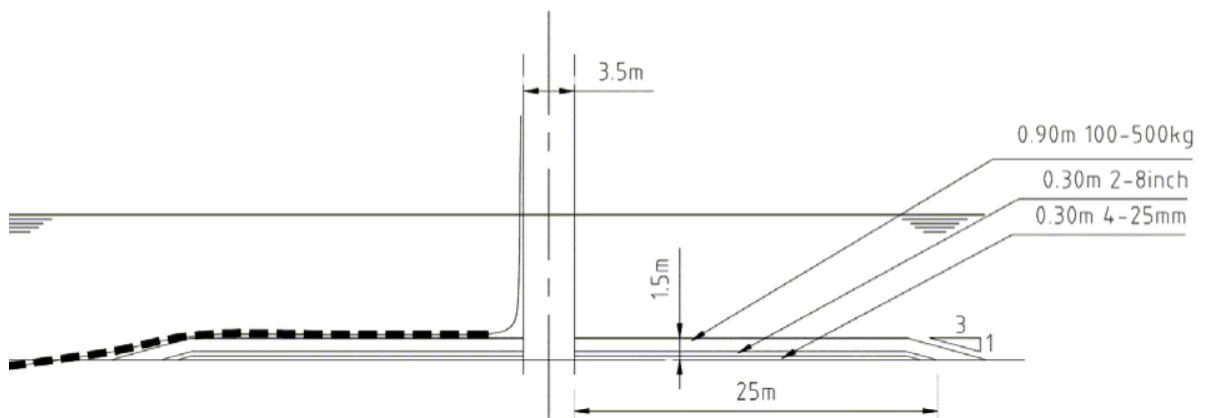


Figure 3.4 – Example of a scour protection presented at [107].

3.3 Failure modes of a scour protection

Several types of protection systems can be employed in offshore wind foundations, e.g. stone or concrete pitching, soil-cement bagging or grouted fabric mattress, with the positioning of a horizontal collar/deflector. Other solutions, based on geotextile containers, are also used [2, 110]. For details on these scour countermeasures the reader is referred to [33]. Nevertheless, and as stated before, this research is focused on riprap scour protections. This section addresses their typical failure modes.

A riprap scour protection commonly consists in a two-layered structure. The top layer, also designated as the armour layer, is made out of loose stones, i.e. rock material. The bottom layer usually consists of a filter layer, which might be composed by a geotextile filter or granular sand material. A scheme is presented in Figure 3.5.

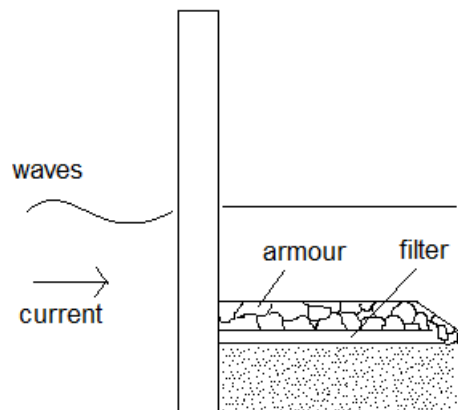


Figure 3.5 – Scheme of a riprap scour protection around a cylinder monopile.

The design of a scour protection generally implies the definition of four key elements [104]. Firstly, the grading of the rock material must be chosen to ensure that the top layer is stable under waves and current conditions. Secondly, the definition of the thickness of the armour layer is carried out. Then, the grading and thickness of the filter layer must be specified to avoid the washing out of soil or intermediate rock layers. Finally, the protection's extent must also be determined to ensure that the soil is stabilized in the vicinity of the foundation.

Each of those four elements can be associated to different scour protection failure modes, as defined by [33] and discussed by e.g. [1] and [61] (Figure 3.6):

- Erosion of the top layer – enough scour occurs in the armour layer, exposing the filter layer or even leading to scour in the soil near the structure;
- Loss of subsoil through the scour protection – which leads to the sinking of the top layer;
- Edge scour – the abrupt change in bottom roughness between the sand-bed and the riprap generates scour at the edge of the protection, thus leading to an undersized protection in the horizontal dimensions;
- Flow slide – the scour hole at the edge of the protection is too steep and leads to flow slide phenomenon that can damage the edge of the protection.

Other mechanisms, as the soil liquefaction, are also reported in the literature as possible failure modes of the protection. For details on liquefaction references [11] and [61] are recommended. Liquefaction tends to cause the sinking of the scour protection, which was studied in detail by [111], who concluded that the design of the filter layer plays a major role in the sinking-induced failure. The loss of subsoil through the protection is very much related to the sinking of the protection and its occurrence is commonly caused by a non-efficient design of the filter layer.

The edge scour and the associated flow slide phenomenon are studied with further detail by [34], who concluded that the large diameters of the armour stones increase the difference of roughness between the protection and the sand bed, leading to an enhanced scour phenomenon. In this sense, the optimization proposed in this thesis, which reduces the diameter of the stones, also contributes to improve the scour protection design, accounting for these failure modes. Nevertheless, the present research is focused on the first failure mode, i.e. the erosion of the top layer. This failure mode depends on the dimensions of the rock material employed in the armour layer. Usually, the rock material is defined by the mean stone diameter, D_{50} , which corresponds to the side of the sieve with square openings through which 50% of stones pass (by weight). In fact, the stone size and the weight play a major role in preventing the displacement of the stones, as seen in Chapter 2. The relationship between stone size and weight is usually defined as the equivalent volume cube (with side D_n , also known as the nominal diameter [1]). Several ways of defining D_n can be found in [112]. To obtain the mean nominal diameter of the stones, the relationship $D_{n50}/D_{50}=0.84$ was applied, as proposed in [112]. Typically, when considering the first failure mode, the value of D_{50} , or D_{n50} , must be found, which ensures the stability of the armour layer.

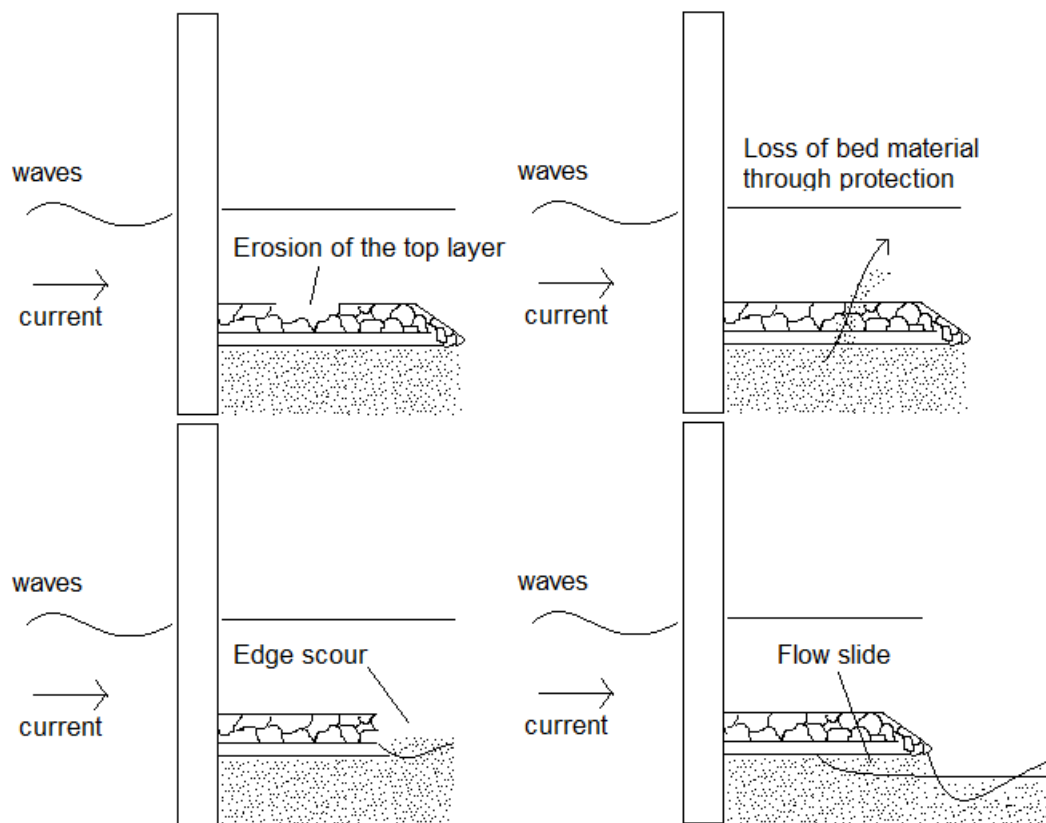


Figure 3.6 – Failure modes of a riprap scour protection (adapted from [1]).

3.4 Design parameters of scour protections

There are several parameters that determine the design of a scour protection. They are often divided into structural parameters, which can be related to the resistance of the scour protection, and the acting loads, or the environmental parameters that solely relate to the loads.

In order to adopt a reliability terminology, the term resistance is used, which in the literature, e.g. [2], is commonly designated as the strength of the protection. The resistance is defined by the critical

shear stress, which is calculated according to Eq. (2.26). However, the value of d_s in Eq. (2.26) corresponds to the mean diameter of the stones used in the armour layer of the protection, i.e. D_{50} . Also, the critical shields parameter is the one that corresponds to D_{50} .

The loads acting on the scour protection are the bed shear stress, which for the present research is both wave- and current-induced, and the turbulence level. As stated in Chapter 2, the knowledge concerning the turbulence level on scour protections is limited compared with the one already acquired for the bed shear stress [61]. Therefore, the scour protection design is frequently based on the bed shear stress calculations, namely those performed with Eqs. (2.18), (2.21), (2.22) and (2.23). In this research, the formulas proposed by [1] and [30] will be added to the analysis.

An effective design of scour protections is a result of a balance between the environmental and the structural parameters. As mentioned before, the environmental parameters solely relate to the loads acting on the protection, whereas the structural parameters may also be related to the loads besides the resistance, e.g. the D_{50} is a direct input in the critical shear stress but it also influences the wave friction factor, as shown in the previous chapter (Figure 2.1), which influences the acting bed shear stress.

The design methodologies studied in this chapter consider the design parameters as deterministic variables, in terms of their long-term behaviour. The following paragraphs address some of the variables that will be used to perform the reliability assessment of the scour protection used in the case study. Figure 3.7 shows a simple diagram of the design parameters of a scour protection, as in [1].

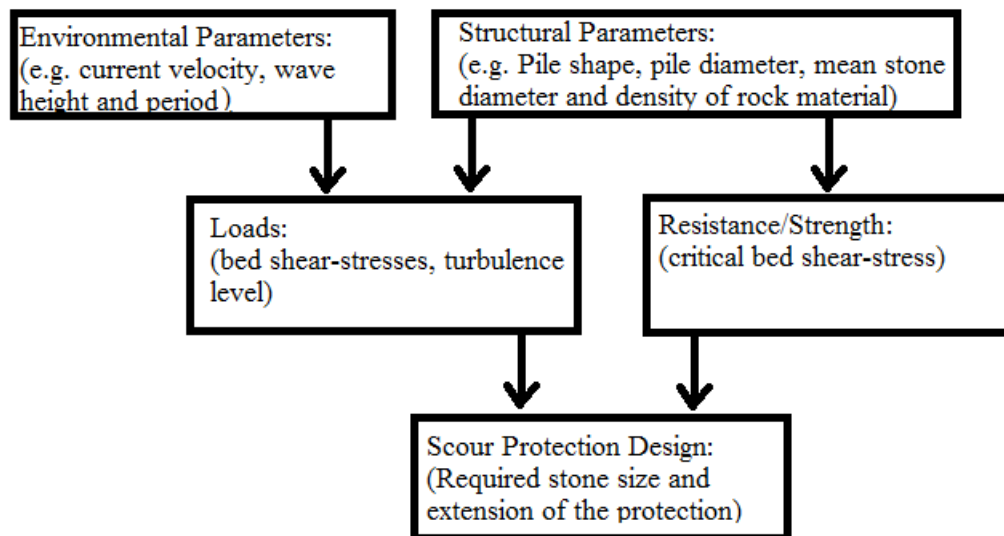


Figure 3.7 – Parameters of scour protection design (Adapted from [1]).

3.5 Environmental parameters

The environmental parameters typically considered in scour protection design are:

- The water depth – it influences the current- and wave-induced bed shear stresses;
- The wave characteristics, i.e. the wave height (H) and period (T) – they determine the wave-induced bed shear stress, by means of the orbital bottom velocity (U_m);
- The current velocity (U_c) – it determines the current-induced shear stress;
- The sediment properties.

3.5.1 Water depth

The effects of the water depth (d) on the loads are mainly reflected on the current and the orbital bottom velocity. For the same wave height (H) and wave period (T), increasing the water depth leads to smaller bottom velocities. Figure 3.8 provides an example of U_m as a function of d , for a significant wave height of 4 m and a peak period (T_p) of 8.8 s, assuming a JONSWAP spectrum with a peak enhancement factor of 3.3. Figure 3.8 considers the calculation of U_m according to [113]. However, a decreasing water depth limits the maximum non-breaking wave height possible at the location, thus limiting larger orbital bottom velocities associated to large wave heights. On the other hand, smaller water depths lead to larger current velocities, for a constant rate velocity. Due to this combined effect, it is not possible to know, *a priori*, which water depth leads to the highest load on the scour protection [1].

Moreover, it is important to note that offshore wind turbines are commonly installed at locations, which are not under the effect of breaking waves, in order to avoid their destructive power not only on the foundation piece, but also on the protection itself. Therefore, design methodologies for scour protections in offshore environment are commonly developed for non-breaking waves. This is also the case considered under the present research. However, it should be noted that the reduction of the water depth may induce to wave breaking, which may lead to the collapse of the protection, albeit not presenting the largest wave height possible.

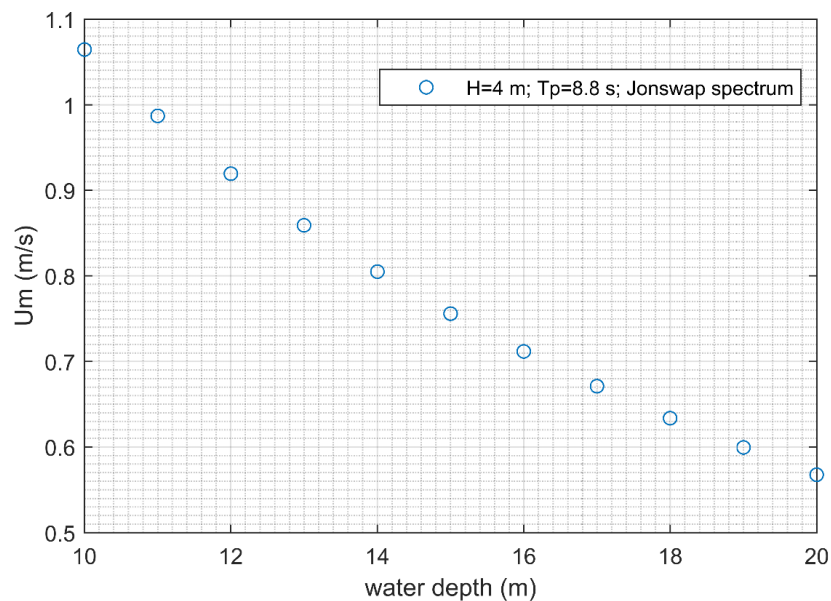


Figure 3.8 – Example of the effect of the water depth in the orbital bottom velocity, H is the significant wave height.

3.5.2 Wave characteristics

In order to design the scour protection, the sea-state characteristics have to be defined and they represent a very important part of the environmental conditions at an offshore location. The sea state acting on the scour protection is mainly defined by a characteristic wave height (H) and a characteristic wave period (T). An extensive review of these parameters is provided in [114].

The wave height can be defined as the vertical distance between the highest point of the water surface elevation (crest) and the lowest point (trough). For linear or small-amplitude waves, the

distance between the wave crest and the still-water level (SWL) and the distance between the trough and the SWL are, each, equal to the wave amplitude (a), thus $a=H/2$ (m) for linear waves, as shown in Figure 3.9. The wave period is defined as the time interval between the passage of two successive wave crests or troughs at a given point. The wave length (L) is the horizontal distance between two identical points (in the same phase) on successive waves. The linear wave theory, or the Airy theory, originally introduced by [115], is one of the most used theories to describe the wave characteristics. This fact is due to its straightforward application and reasonable approximation of the wave characteristics for a wide range of wave parameters. Moreover, this approximation is still useful, even for some situations for which the requirements of the linear theory are not valid.

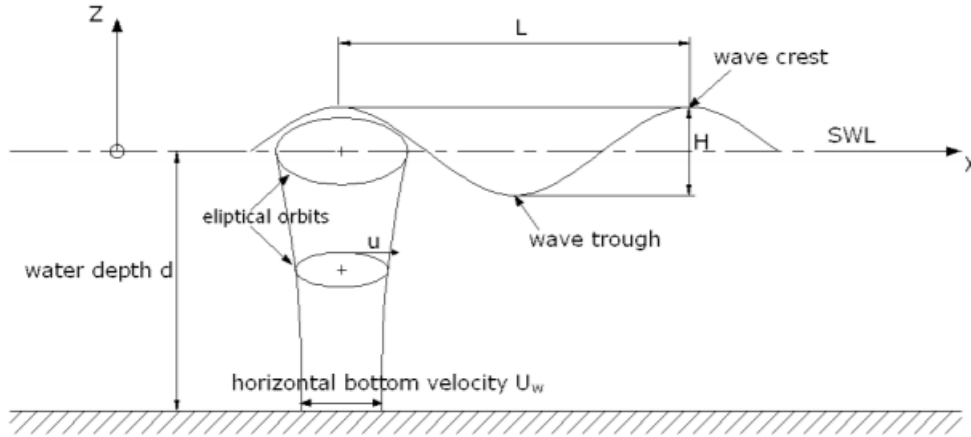


Figure 3.9 – Definition of the wave characteristics – linear wave theory [1].

According to the linear wave theory, the water surface elevation (η) at a given point x is represented by a cosine profile [114] as in Eq. (3.1), where $k=2\pi/L$ is the wave number, w is the angular frequency, with $w=2\pi/T$, and Ψ is the phase shift.

$$\eta(x,t)=\frac{H}{2}\cos(k \cdot x-w \cdot t-\Psi) \quad (3.1)$$

The wave length is obtained from the dispersion relationship, as in Eq. (3.2), where g represents the gravitational acceleration ($g=9.81 \text{ m/s}^2$).

$$L=\frac{gT^2}{2\pi}\tanh\left(\frac{2\pi d}{L}\right) \quad (3.2)$$

The motion of a water particle in a finite water depth has an elliptical orbit, while the velocity is determined by a horizontal component and a vertical component. Towards the bottom, the orbits are more flattened and only the horizontal velocity component remains [114]. At any depth (z), the amplitude of the horizontal velocity (u) is obtained as in Eq. (3.3). If $z=-d$, the amplitude of the bottom horizontal velocity (U_m) is obtained by Eq. (3.4). Substituting Eq. (3.2) into Eq. (3.4), U_m is calculated from the linear wave theory as in Eq. (3.5).

$$u = \frac{H}{2} \cdot \frac{gT}{L} \cdot \frac{\cosh\left(\frac{2\pi(z+d)}{L}\right)}{\cosh\left(\frac{2\pi d}{L}\right)} \quad (3.3)$$

$$U_m = u(z=-d) = \frac{H}{2} \cdot \frac{gT}{L} \cdot \frac{1}{\cosh\left(\frac{2\pi d}{L}\right)} \quad (3.4)$$

$$U_m = \frac{\pi H}{T} \cdot \frac{1}{\sinh\left(\frac{2\pi d}{L}\right)} \quad (3.5)$$

3.5.2.1 Non-linear waves

In the case of non-linear waves, i.e. when the wave amplitude is no longer small compared with the water depth, the relation $a=H/2$ is not valid. Typically, the troughs become less deep and wider, whereas the crests become steeper and higher, thus meaning that deviations occur from the cosine profile assumed by the linear wave theory. If the water depth decreases significantly or the wave steepness increases, then higher-order theories must be used. They are often called finite-amplitude wave theories, Figure 3.10.

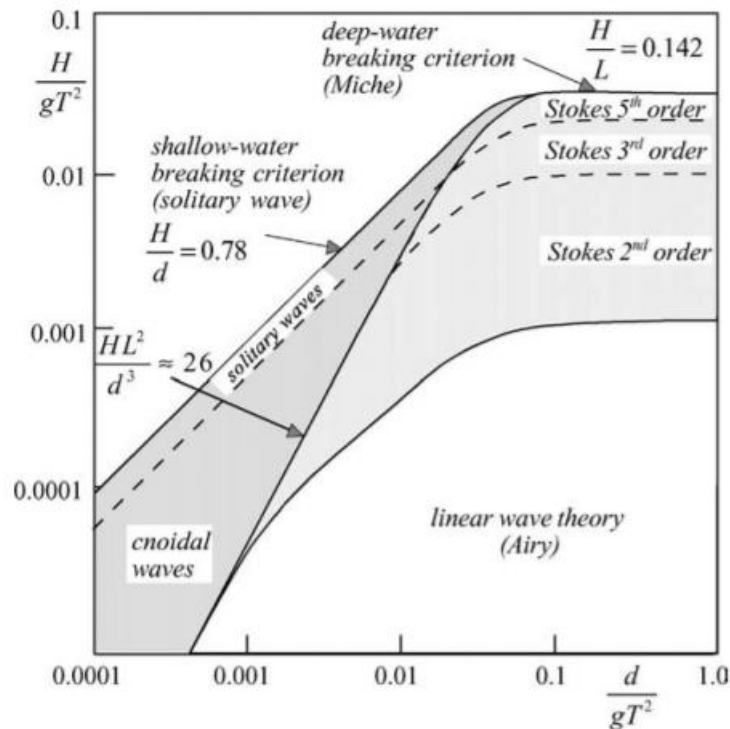


Figure 3.10 – Validity regions for different wave theories [114].

For larger wave heights and not too small water depths, the Stokes higher-order theories are often applicable. A complete theoretical description of the wave surface is obtained by summing many successive approximations, where each additional term in the series is a correction to preceding terms

[1]. In Stokes higher-order theories, the first and second order terms for elevation and horizontal velocity, at a z level below the SWL, are given by Eqs. (3.6) and (3.7), respectively.

$$\eta = \frac{H}{2} \cos(kx - \omega t) + k \frac{H^2 \cosh(kd)}{16 [\sinh(kd)]^3} \cdot (2 \cosh(2kd)) \cos(2(kx - \omega t)) \quad (3.6)$$

$$u = \frac{H}{2} \cdot \frac{gk}{w} \cdot \frac{\cosh(k(z+d))}{\cosh(kd)} \cdot \cosh(kx - \omega t) + \frac{3kH^3 w}{16} \cdot \frac{\cosh(2k(z+d))}{[\sinh(kd)]^4} \cdot \cos(2(kx - \omega t)) \quad (3.7)$$

Another possibility is to use the so-called Fenton's Fourier series theory, originally introduced by [116]. According to [1], this theory provides better approximations than the previous similar theories for all water depths, while being independent from water depth. Moreover, in [1], an example of the Fenton's Fourier series is provided for $d=10$ m, $H=5$ m and $T=10$ s as a function of x/L (see Figure 3.11). Through this example, it is noted that the trough velocity is smaller than that of the wave crest. However, the velocity in the trough persists much longer than in the crest. During a wave period (T), the horizontal velocity is higher than 1 m/s during 2.24 s, while it is lower than -1 m/s during 4.72 s. As noted by [1], this influences the bed shear stress, because the horseshoe vortex is developed only when the velocity persists long enough. Note that the life span of the horseshoe vortex depends on the KC number, i.e. the life span increases with the KC number.

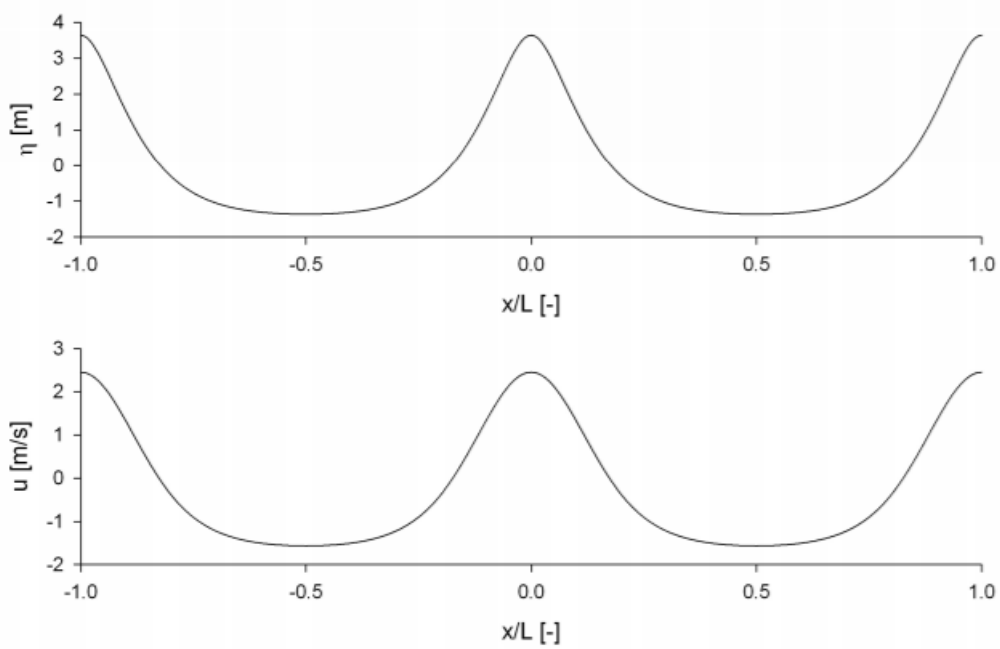


Figure 3.11 – Example of Fenton's Fourier series: water surface elevation and horizontal bottom velocity [1].

Another important aspect regarding the wave characteristics lies on the height physical limitation imposed by the water depth and its wave length. In deep water, waves break when they are too steep. Therefore, the breaking wave height is a function of the wave length only. The relationship proposed by [117] is commonly considered in the literature, as in Eq. (3.8).

$$\frac{H_b}{L} = 0.142 \quad (3.8)$$

For transitional and shallow waters, the beaker index (H_b/d) is considered in order to define the breaking wave height (H_b), because the breaking wave height is a function of the water depth (d). In this case, waves break when their heights are too high compared to the water depth. A detailed discussion of the breaker index can be found in [114] and [118]. Typically, a theoretical first estimate for regular waves is given by [119] as in Eq. (3.9). Another possibility is to use the formulation given by Eq. (3.10) [120].

$$\frac{H_b}{d} = 0.78 \quad (3.9)$$

$$\frac{H_b}{d} = \frac{0.0141063\left(\frac{L}{d}\right) + 0.0095721\left(\frac{L}{d}\right)^2 + 0.0077829\left(\frac{L}{d}\right)^3}{1 + 0.078834\left(\frac{L}{d}\right) + 0.0317567\left(\frac{L}{d}\right)^2 + 0.0093407\left(\frac{L}{d}\right)^3} \quad (3.10)$$

The present work will make use of Eq. (3.9), which provides good approximations to Eq. (3.10) for oscillatory waves, as proved in [119] through physical model studies. However, it should be noted that the present research only concerns scour protections placed at a sea-bed with a horizontal slope. The slope of the sea-bed may considerably influence the ratio presented by Eq. (3.9). Therefore, in similar studies with non-horizontal bed, it is advised to adjust this value.

3.5.2.2 Irregular waves

In a real situation, the sea surface is composed of waves with different heights and periods, which may propagate in different directions. Therefore, the measurements of the sea surface on a single point during the time interval, T_0 , produce an irregular wave train, as shown in Figure 3.12.

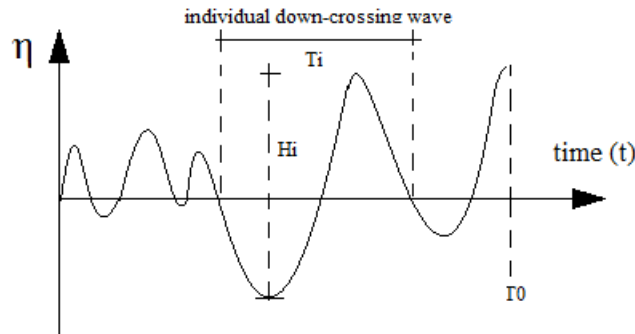


Figure 3.12 – Representation of an irregular wave train.

In order to analyse irregular waves, two methods may be used: the spectral method, which is based on the Fourier transform of the wave train and the wave-by-wave (wave train) analysis, which is based on the time-history of the sea surface at one point. The wave-by-wave analysis does not consider the different incident directions of the waves at the measurement point. Conversely, the spectral analysis is linear, which may distort the representation of non-linear waves [1].

The wav-by-wave analysis is performed according to the zero down-crossing or the zero up-crossing methods, which are used to identify the individual waves present on the irregular wave train. Statistically, both methods provide similar values of the wave height and wave period. The present research applies the down-crossing method, for the sake of coherence with the research developed in

[30] and [32]. In this method a wave is identified by two consecutive zero crossings on a downward direction of the water surface elevation (Figure 3.12), with each individual wave presenting its wave height (H_i) and its wave period (T_i).

The wave height is determined as the vertical distance between the lowest point of the water surface elevation and the consecutive highest point, between the two zero down-crossings. The wave period is the time interval between the two zero down-crossings. The wave-by-wave analysis aims at describing the irregular sea state by characteristic values of the wave height (H) and the wave period (T). The characteristic value of the wave height can be defined in several manners [114], e.g. the mean wave height (H_m) or the root-mean-square wave height (H_{rms}). For design purposes, the most commonly used value is the average of the highest one-third of all waves in the wave train. This value is known as the significant wave height, denoted by $H_{1/3}$ or H_s . Similarly, $H_{1/n}$ can also be used, which concerns the mean value of the highest $1/n$ of all waves in the considered time interval. In marine structures design, $H_{1/10}$ and $H_{1/100}$ are typically used. The maximum wave height registered in the wave train is denoted H_{max} . Regarding the wave period, the mean (down or up) zero-crossing period (T_z) is commonly used, which is the mean of all the registered wave up-crossing or down-crossing periods.

For a sufficiently large number of waves in a time series and if the individual components are independent, the probability that a wave height, characterized by H_{rms} , exceeds a given H_d value, follows a Rayleigh distribution, as shown in Eq. (3.11) [114]. This distribution is valid for deep-water waves, whereas it tends to overestimate the larger wave heights for waves in limited water depth situations.

$$P(H \geq H_d) = e^{-\frac{H_d}{H_{rms}}} = e^{-\sqrt{\frac{1}{N} \sum_{i=1}^N (H_i)^2} \frac{H_d}{H_{rms}}} \quad (3.11)$$

Assuming a Rayleigh distribution, it is possible to relate the H_{rms} with other characteristic wave heights, as shown in Eq. (3.12) [1]

$$\begin{aligned} H_m &= 0.886 H_{rms} \\ H_s &= 1.416 H_{rms} \\ H_{1/10} &= 1.80 H_{rms} \\ H_{1/100} &= 2.359 H_{rms} \\ H_{max} &= 2.63 H_{rms} \end{aligned} \quad (3.12)$$

Note that that the Rayleigh distribution is only applicable for short-term statistics, say a storm or a short-duration record. The long-term predictions of the wave height may follow other statistical distributions, which are studied in Chapter 6 (see also section 6.3). The long-term behaviour is of great importance in reliability analysis of scour protections, since the safety of the scour protection is analysed for long-duration records (see also section 3.8)

In the spectral approach, the irregular waves are considered a superposition of a number of regular waves, each one characterized by H_i and T_i . If x is assumed to be zero at the measurement location, then the elevation of the surface is given as in Eq. (3.13).

$$\eta(t) = \sum_i \frac{H_i}{2} \cos(w_i t + \psi_i) \quad (3.13)$$

Often, the water surface elevation is represented in the frequency domain, instead of the time domain expressed in Eq. (3.13). This implies the definition of an amplitude spectrum and a phase spectrum using a Fourier transformation. Typically, only the amplitude spectrum is used and for each frequency $f_i=1/T_i$, the wave amplitude (a) or the wave energy (proportional to a^2) is plotted [1]. The energy spectral density or the variance spectral density, $S(f)$, is then represented by Eq. (3.14). The value of $\Delta f=1/T_0$ defines the so-called frequency band and depends on the duration of the measurement, T_0 (Figure 3.12).

$$S(f)=\frac{\frac{1}{2}a^2}{\Delta f} \quad (3.14)$$

The Fourier transformation yields a double and symmetrical spectrum around the Nyquist frequency (f_{nyquist}), which is equal to half of the sampling frequency, i.e. $f_{\text{nyquist}}=f_s/2$. Therefore, only the first half of the spectrum is used. This means that the irregular waves must not have frequencies above f_{nyquist} to avoid aliasing [1]. Only the left part of the Fourier transformation represents the actual energy of the wave field. An example of the energy spectral density of an irregular wave train is show in Figure 3.13.

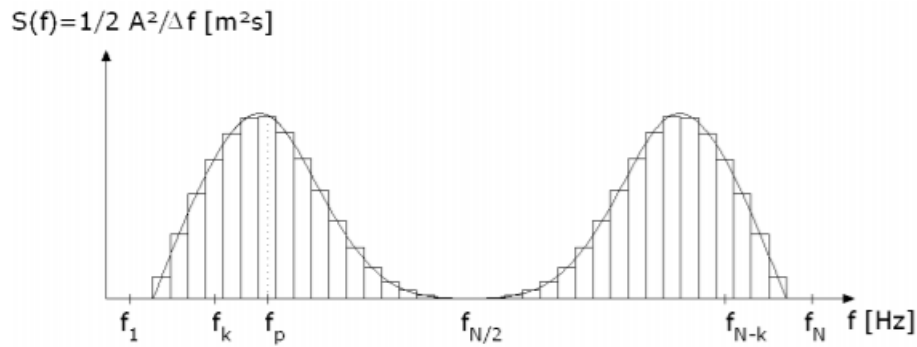


Figure 3.13 – Representation of the energy spectral density [1].

When using the spectral analysis, the moments of the spectrum are often used in order to obtain the characteristic wave heights and periods. In case of the energy of the irregular wave train, Eq. (3.15) is used, where m_0 is the zero-order moment.

$$m_0 = \int_0^{+\infty} S(f)df \quad (3.15)$$

The significant wave height (H_{m0}) obtained from the spectrum is given by Eq. (3.16).

$$H_{m0} = 4.004 \sqrt{\int_0^{+\infty} S(f)df} = 4.004 \sqrt{m_0} \quad (3.16)$$

The value of H_{m0} is very often used as a substitute of H_s . Although not very different, departures between H_s and H_{m0} occur for small water depths or for very steep waves [119]. The mostly used characteristic wave period is the peak period (T_p), obtained from the peak frequency of the spectrum (see Figure 3.13), i.e. $T_p=1/f_p$. However, because T_p depends on the choice of the frequency band width (Δf), other characteristic periods are also used and derived from the spectral moments, as shown in Eq. (3.17). The period $T_{m-1,0}$ is the energy wave period and it is of great importance for the damage

number (S_{3D}) of dynamic scour protections [32], introduced afterwards. Similarly, the wave period $T_{m2,0}$ is often used as the mean up-crossing wave period obtained from the time-domain analysis.

$$\begin{aligned} T_{m-1,0} &= T_c = \frac{m_{-1}}{m_0} \\ T_{m2,0} &= \frac{m_2}{m_0} \\ T_{m0,1} &= \frac{m_0}{m_1} \end{aligned} \quad (3.17)$$

The n^{th} moment of the spectral density m_n is defined as in Eq. (3.18).

$$m_n = \int_0^{+\infty} f^n S(f) df \quad (3.18)$$

Several theoretical spectra can be used to define the wave spectrum, based on the wind speed. The mostly used ones are the Pierson-Moskowitz (PM) and the JONSWAP spectrums. Both can be parametrized by means of H_{m0} and T_p . Also, the JONSWAP spectrum depends on the peak enhancement factor (γ), which for North Sea conditions is commonly assumed as 3.3 (mean value). Moreover, both spectra coincide for $\gamma=1$. The JONSWAP spectrum extends the PM spectrum to include fetch limited seas, describing developing sea states. These spectra describe wind sea conditions that often occur for the most severe sea states. For practical purposes, the present research uses the JONSWAP spectrum, because it was specifically developed for North Sea conditions, as the ones present at the Horns Rev 3 offshore windfarm. Figure 3.14 shows a comparison between the JONSWAP spectrum and the PM spectrum, for different peak enhancement factors. These spectra are calculated as in Eqs. (3.19) and (3.20). For further details on spectral analysis of ocean waves the reader is referred to [121].

$$S_{PM}(f) = \frac{5}{16} H_s^2 f_p^4 f^{-5} \exp \left[\frac{-5}{4} \left(\frac{f_p}{f} \right)^4 \right] \quad (3.19)$$

$$S_{JON}(f) = \alpha \frac{5}{16} H_s^2 f_p^4 f^{-5} \gamma^\beta \exp \left[\frac{-5}{4} \left(\frac{f_p}{f} \right)^4 \right] \quad (3.20)$$

with α and β obtained from Eqs. (3.21) and (3.22), respectively, [121].

$$\alpha = \frac{0.0624}{0.23 + 0.0336 \left(\frac{0.185}{1.9 + \gamma} \right)} \quad (3.21)$$

$$\beta = \exp \left[- \frac{(f - f_p)^2}{2\sigma^2 f_p^2} \right] \quad (3.22)$$

$$\sigma = \begin{cases} 0.07 & \text{for } f \leq f_p \\ 0.09 & \text{for } f > f_p \end{cases} \quad (3.23)$$

As mentioned before, the present research has used the JONSWAP spectrum with $\gamma=3.3$, which enables the application of Eq. (3.24) to relate the peak period and the remaining n^{th} moment spectral periods [122].

$$\begin{aligned} T_p &= 1.286T_{m0,2} \\ T_p &= 1.1986T_{m0,1} \\ T_p &= 1.107T_{m-1,0} \end{aligned} \quad (3.24)$$

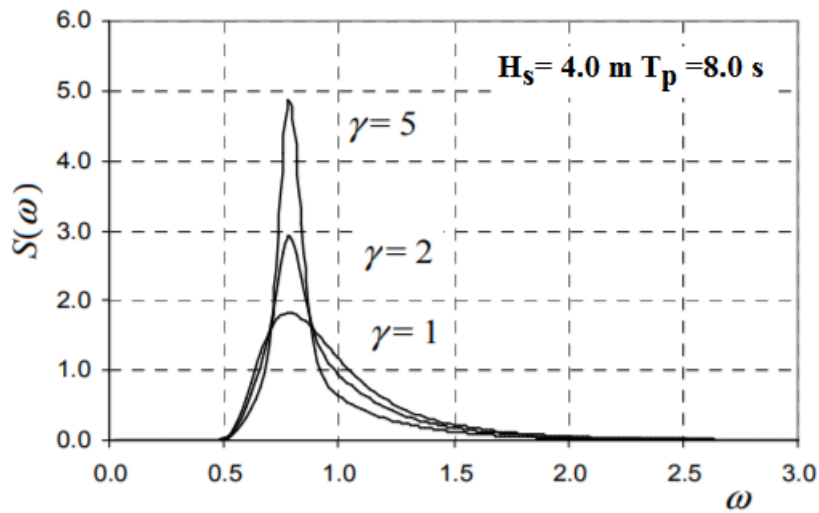


Figure 3.14 – JONSWAP spectra comparison (and PM spectra for $\gamma=1$) [122].

3.5.2.3 Design wave height and period

In general, for marine structures design, the wave height is considered as the dominant variable [123], whereas the concurrent wave period is then conditioned to the design wave height. Typically, the design wave height is described in terms of a return period (T_r) and the encounter probability. However, it is common to consider return periods that exceed by far the duration of existent wave height records at a specific offshore location. This is also the case for traditional scour protection design, which is performed for wave heights associated to a $T_r=50$ years [30] and sometimes 100 years [1]. Moreover, monopile foundations are designed for a lifetime of 20 years [21]. Therefore, it is commonly required to extrapolate the design wave height from the wave probability distribution, evaluated from the available measurements at the location. In the present research, advanced joint-models for the long-term description of wave heights and periods are presented in Chapter 5 and applied in the reliability analysis performed in Chapters 6 and 7, namely based on copulas theory, e.g. [123, 124, 125], or the conditional model approach, e.g. [122] or [126].

If the design wave height (H_d) is selected, then, according to [127], the exceeding probability of H_d is obtained from Eq. (3.25), where $P(H > H_d)_{H_{si}}$ is the exceeding probability of H_d in a storm with the significant wave height H_{si} obtained for example with the Rayleigh distribution.

$$P(H \geq H_d) = \sum_i P(H > H_d)_{H_{si}} \cdot P(H_{si}) \quad (3.25)$$

The wave period is also important in terms of the loads acting on the protection. Typically, the value of the wave period is determined conditioned on the value of H . One of the most used relationships between the wave period and H_s , for cases where only the significant wave height is known, is provided in [52], which gives an estimate for the up-crossing mean period (T_z) as in Eq. (3.26). However, it is important to note that such relationship is site specific and care must be taken when using them outside the region for which they are intended.

$$T_z = 11 \sqrt{\frac{H_s}{g}} \quad (3.26)$$

3.5.3 Number of waves

According to [1], the development of damage on a scour protection subjected to regular waves is faster than the one occurring under irregular waves. In regular waves, the same wave and the same bed-shear stress is acting on the protection each time, whereas for irregular waves, the shear stress varies each time a wave passes over the protection and the equilibrium state takes longer to be reached. Therefore, the number of waves (N) considered in a storm has a considerable influence on the stability tests.

Physical model studies concerning rubble-mound breakwaters concluded that 3000 waves are sufficient to obtain a profile close to the equilibrium profile [128]. Moreover, it is also noted that when comparing regular with irregular wave tests the characteristic wave height and period must be obtained for the irregular sea state. Often the significant wave height and the peak period are used. In a spectral analysis, H_s is commonly substituted by H_{m0} .

For statically stable scour protections the number of waves is not directly considered in the design formulas, as it will be shown in further chapters. However, this is not the case when calculating the damage number of the protection, as shown in [32]. The physical model scour tests concerning dynamic scour protections and presented in [1] and [32] indicate that the damage rate is considerably larger until $N=3000$ waves than afterwards, when the rate of damage tends to decrease. However, it is noted that a larger number of waves should be used in order to reach the equilibrium profile. In those studies, the damage was still developing for $N=5000$ waves. The physical model study conducted during the present research, reported in [26] and [102] as well, also concluded that $N=3000$ waves might not be a sufficient number to obtain the equilibrium profile and that a dynamic equilibrium profile was obtained after 5000 waves [26]. However, it also showed that after $N=3000$ waves, there was a significant decrease in the damage progression rate. In these studies, some tests were performed for $N=7000$ waves and it was observed that for a dynamic equilibrium of the scour protection, existent scour holes were backfilled, while new scour holes appeared to be backfilled again as time progressed. In [103], long-duration scour tests were performed for $N=9000$ waves, and it was concluded that damage progression was still occurring for scour protections made of coarse wide-graded grain material. Nevertheless, this study reports a rather reduced number of tests and no generalization of this conclusion is possible.

For further reliability assessment, based on the methodology provided in [32], $N=3000$ waves is assumed because this was the number used in order to develop the formula proposed for the damage number of scour protections. Moreover, as it will be shown in further chapters, the present research concluded that failure of the tested dynamic scour protections tends to occur between 3000 and 5000

waves. Therefore, the reliability assessment was performed for 3000 waves, since it makes no sense to evaluate the failure at 5000 waves provided that the protection has already failed for 3000 waves.

3.5.4 Flow characteristics

The sea currents are essentially driven by tides and ocean circulations, or eventually due to the outflow of a river, which is not the case for Horns Rev 3 windfarm described in section 6.2.3 (also see section 6.2.4.2). Also, in shallow water, a steady current can be caused by breaking waves. The current velocity at the foundation of the protection varies slower than the loads caused by the wave or the wind climate. Commonly used standards and recommended practice consider that the current velocity might be regarded as constant for design purposes, with the magnitude and the direction of the current a function of the water depth. The current profile is dependent on the boundary layer, as explained in the previous chapter.

The current velocity ultimately influences the combined waves and current shear stress acting on the scour protection. The flow characteristics used in the present research are the depth-averaged flow velocity (U_c), the current direction and the velocity profile with the water depth. The long-term influence of the current velocity in the wave field, as well as their correlation, are discussed in detail in [129] and [130]. Both works, concluded that neglecting the long-term correlation between current and wave characteristics leads to an overestimation of the ultimate limit state (ULS) loads considered to design an offshore structure (see [106] for details on the ULS). The present research does not consider this correlation, as it will be explained in further chapters. However, further research should be performed to assess the effect of this assumption on the reliability assessment of the scour protection. Often in offshore structures design, the value of U_c associated to a 10-year return period is combined with the 50-year or 100-year wave height [131].

3.5.5 Sediment characteristics

As mentioned in the previous chapter, this thesis is focused on non-cohesive sediments. The sediment characteristics of the seabed where the protection is to be placed have a considerable influence in the filter layer design and also on the extension of the scour protection. Note that the latter depends on the slope of the scour hole, which is dependent on the sediment's angle of repose (ϕ), as seen in Eq. (2.55). For non-cohesive sands, the repose angle lies between 30° and 40° [132].

Moreover, the sediment properties also influence the extent of the scour at the edge of the protection and the settling velocity, which is a direct input for the damage number calculation used for dynamic scour protections.

Typically, non-cohesive grain diameters vary from 0.062 mm to 2 mm. For practical purposes, the grain size is often characterized by the mean diameter, which is denoted by d_{50} for the sand-bed sediments and by D_{50} for the armour stones of the protection.

The mean diameter corresponds to the sieve size (with square openings) through which 50% of the material (in weight) passes. The grain size distribution is commonly represented by a log-linear distribution plot, as shown in Figure 3.15. The standard deviation of the grading (σ_U) is often defined as d_{85}/d_{15} , i.e. the ratio of diameter for which 85% of the material is finer by weight (d_{85}) to diameter for which 15% of the material is also finer by weight (d_{15}).

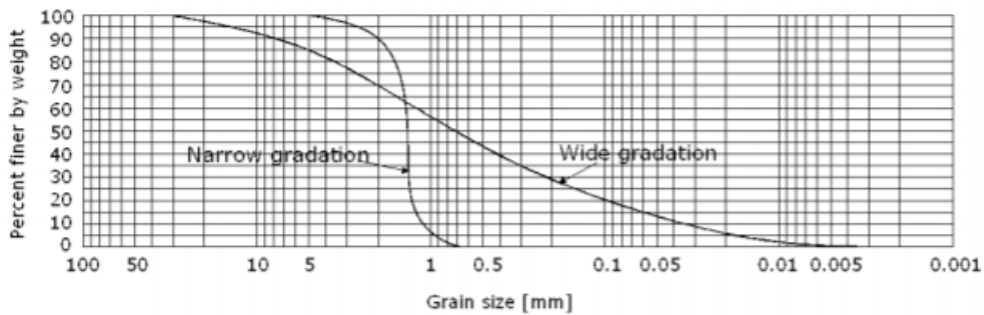


Figure 3.15 – Log-probability plot of a wide and a narrow grain size distribution [1].

Regarding the settling velocity, the present research is interested in the settling velocity concerning the mean stone diameter of the rock material, since this is the value required in the methodology [32] to design dynamic scour protections. Therefore, despite of the several formulas existent in the literature, which account for different grain shapes and sizes, this research only uses the formula proposed for non-spherical particles with diameters larger than 1000 μm introduced by [133], also used in the calculation of the damage number reported in [32]. The settling velocity is therefore calculated according to Eq. (3.27), where for the scour protection, d_s is considered as D_{50} , $s = \rho_s / \rho_w$ and $g = 9.81 \text{ m/s}^2$. An extensive review of this matter is provided by [134].

$$w_s = 1.1 \left[(s-1) g d_s \right]^{1/2} \quad (3.27)$$

The consideration made regarding the sediment characteristics are valid for both the diameters of the sand bed and the scour protection. However, only the sediments of the sand bed correspond to an environmental parameter; the values used for the scour protection, e.g. D_{50} or D_{85} , are considered as structural parameters.

3.6 Structural parameters

This section is mainly focused on the structural parameters that are related to the characteristics of the scour protection. The pile diameter and shape are also considered as structural parameters, in this case related to the structure characteristics. Both of them influence the scour phenomenon, as seen in Chapter 2. Furthermore, they have a direct impact on the resistance and on the load bearing capacity of the foundation [131]. Nevertheless, in order to avoid the influence of the pile shape and to account for different incident directions, typical for offshore locations, the majority of the offshore wind turbines are founded in circular shaped monopiles. This is also the case of the Horns Rev 3 offshore windfarm, introduced in section 6.2.3.

Moreover, the design of dynamic scour protections according to [30] and [32] do not directly account for the monopile diameter in the design of the protection (see sections 3.7.1.3 and 3.7.1.5). Therefore, this thesis does not pursue detailed explanations on the structural parameters of the foundation itself, which can be found in [61]. Even though such parameters are expected to influence the failure mode of the scour protection, at this stage, the interest resides in the definition of the parameters that directly determine the design of the protection, namely, the ones that influence bed shear stress and the damage number at the armour layer. Note, however that the shape and diameter of the foundation has an effect on the amplification factor, commonly assessed by means of physical model studies. Notes on the potential influence of the pile diameter are provided in Chapter 4.

3.6.1 Density of the rock material

The mass density of the rock material (ρ_s) used in the scour protection has a major influence in the stability of the armour layer. This occurs because ρ_s determines the stabilizing gravitational force of the armour stones, as seen in section 2.4, dedicated to the threshold of motion for non-cohesive particles. The mass density corresponds to the ratio of mass (m) per unit volume (V_s) of a solid rock, i.e. $\rho_s = m/V_s$ (kg/m^3). The density of the rock material applied in riprap scour protections typically ranges from 2600 kg/m^3 (e.g. granite) to 3100 kg/m^3 (e.g. basalt) [1, 135]. However, artificial blocks with higher density, thus more stable for the volume considered, can also be used instead of the common rock material.

If instead of using the solid volume the volume including the empty spaces between particles (V_d) is used, the bulk density is obtained as $\rho_d = m/V_d$ (kg/m^3). The bulk density is more difficult to determine than the mass density, because it implies assumptions regarding the empty spaces in the sample of rock material. It depends on the compaction of the protection, which in practical situations is hard to assess during the installation process. Nevertheless, as stated in [1], the bulk density is needed to estimate the required weight of the stones to obtain the volume of the scour protection. Note that this volume also depends on the protection's thickness and extension. Details concerning the porosity of riprap material and its bulk density may be found in [135].

3.6.2 Stone size and weight

As referred in section 2.4, the stone weight is the major stabilising force that contributes to avoid the stones' displacement at the armour layer of the protection. Since the riprap material is composed of a varying grading and the stone shape is often irregular, the nominal diameter of the stone (D_n) is commonly used, i.e. the side of the cube with an equivalent volume to the stone considered. The diameter of a sphere (D_s) may also be adopted, again with an equivalent volume to the stone [112]. In the present work, the value of D_n is used for the sake of coherence with the work presented in [26, 30, 32] and [102]. The values of D_n and D_s are obtained from Eqs. (3.28) and (3.29), respectively.

$$D_n = \left(\frac{W}{\rho_s} \right)^{1/3} \quad (3.28)$$

$$D_s = 1.24 \left(\frac{W}{\rho_s} \right)^{1/3} \quad (3.29)$$

In the absence of further information, in this work, the nominal diameter is always referred to the mean value, i.e. the one obtained from the mean stone diameter D_{50} or from the mean weight W_{50} , using Eq. (3.30), as in [112].

$$D_{n50} = \left(\frac{W_{50}}{\rho_s} \right)^{1/3} = 0.84 D_{50} \quad (3.30)$$

The individual stone size affects both the resistance, i.e. the critical shear stress, and the acting bed shear stress, due to its influence on the bed roughness and on the friction coefficients (f_c , f_w). Moreover, it has an impact in particular scour phenomena, as the edge scour previously mentioned. Therefore, the optimum design value of D_{50} , or D_{n50} , must be large enough to ensure the stability of the

armour layer, but not so large that leads to failure caused by the increasing roughness of the protection.

3.6.3 Stone grading and shape

Typically, the stones used for riprap material in offshore scour protections vary in size, from small gravel to large blocks. The stone weight distribution is frequently presented in a percentage lighter by weight cumulative curve, where W_{50} represents the block weight for which 50% of the material in the sample is lighter. In a similar way to granulometric curves, the steepness of the weight curve indicates the grading width. In [112], the ratio D_{85}/D_{15} is used to distinguish the stones grading as follows:

- Narrow grading: $D_{85}/D_{15} \leq 1.5$;
- Wide grading: $1.5 < D_{85}/D_{15} \leq 2.5$;
- Very wide or quarry run grading: $2.5 < D_{85}/D_{15} \leq 5$.

When the value of D_{50} is determined for a scour protection design, the rock material applied in the armour layer must follow the standard rock grading that complies with the preferred choice. Moreover, these curves also state the upper and lower limits of the stone weight, which must be respected. In [112], standard grading curves are provided with further detail for different weight categories, e.g. for weights ranging between 2-80kg, 2-300kg or 80-300 kg. Some examples of the mean stone diameter and the mean stone weight applied in armour layer of several offshore windfarms are available in Table 3.1. A comprehensive review of grading control on quarried rock frequently employed in these cases is provided by [136].

Table 3.1 – Mean diameter and weight of the armour layer stones at different offshore windfarms [2].

| Windfarm | D_{50} [m] | W_{50} [kg] |
|----------------|--------------|---------------|
| North Hoyle | 0.300 | 72 |
| Egmond aan Zee | 0.400 | 170 |
| Thornton Bank | 0.350 | 114 |
| Horns Rev 1 | 0.400 | 170 |
| Scroby Sands | 0.150 | 9 |
| Arklow Bank | 0.425 | 205 |

The stone grading used in the scour protection has shown to have a considerable influence in the stability of scour protections under combined waves and current [103, 137]. Possible reasons for the wide grading positive effect on the stability of the protection are pointed out in [30], which states that, for wide graded scour protections, smaller stones find better shelter between large stones, thus being less likely to be dragged away for lower bed shear stresses. When computing the critical bed shear stress, [30] proposes the use of the stone diameter $D_{67.5}$ to account for this effect. This is discussed with further detail later, in the reliability assessment of scour protections.

The stone shape also contributes to the stability of the protection, due to the entrainment of the stone. According to [112], the largest dimension of the stone should not exceed three times the shortest dimension. The number of stones that do not comply with this requirement should also not exceed 5% of the total stones used in the armour layer. Therefore, when the rock material is selected, some losses may occur due to shape rejection, which are typically 15% of the total rock material [1]. This thesis

does not go into details on the stone classification, which is available, for example, in [112] and [135]. Nevertheless, the reader should keep in mind that scour protections are often built with the available material, which might vary depending on the nearest location. Angular or blocky stones are preferred to rounded ones, because the former provide a better entrainment than the latter. Quarry-produced stones are commonly angular. However, stones extracted from glacial deposits or alluvial zones are usually rounded [1].

3.7 Design criteria for scour protections around monopile foundations

In order to properly design the scour protection, one must define the grading and thickness of both the armour layer and the filter layer and the extension of the armour layer as seen in section 3.3. The present thesis is mainly focused on the optimisation of the mean diameter of the stones of the armour layer. In the following paragraphs, a review is performed on the design criteria regarding the stone size and thickness of the scour protection, the radial extension is also addressed. However, since the practical part of the present thesis did not focus on the filter layer design this subject will not be pursued here, for this matter the reader is referred to [1] or [97]. A particular focus is given to the methodologies developed in [32] and [101], due to their important contributions to the design of dynamic scour protections.

3.7.1 Required minimum stone size

3.7.1.1 Static versus dynamic scour protections

A major aspect of scour protection design is the definition of the mean diameter of the stones (D_{50}) of the armour layer placed above the filter [107]. Scour protections are typically designed in a deterministic way, mainly based on empirical methodologies that account for the combined wave- and current-induced bed shear stress.

In static scour protections, the armour stones are not allowed to move. This means that the mean diameter of the stones is defined so that, for a specific weight of the rock material, the wave- and current-induced shear stress in the foundation's vicinity is not enough to overcome the critical shear stress of the stones [30]. Since the critical shear stress defines the threshold of motion, i.e. the minimum shear stress necessary to drag the stones from their initial position, then the failure of a static scour protection is considered to occur when there is movement of the stones used in the armour layer.

Alternatively, dynamic scour protections allow for a certain degree of movement of the armour stones, without exceeding a maximum exposed area of the filter layer defined by [32] and [100] as $4D_{50}^2$. Allowing for some movement of the stones enables the reduction of the mean diameter, because there is no need to ensure that the acting shear stress is not equal or larger than the critical one. Dynamic scour protections were extensively studied in [1], which introduced a design criterion based on the dimensionless damage number (S_{3D}). The damage number provides a measure of the damage expected to occur in the protection for design hydrodynamic conditions and the mean diameter used.

The majority of the methodologies available to determine the minimum stone size of the armour layer are based on the threshold of motion criteria, which is not directly applicable to dynamic scour protections. Section 3.7.1.2 and 3.7.1.3 elaborate on the methodologies to obtain a statically stable mean diameter, whereas section 3.7.1.4 and 3.7.1.5 focus on how to obtain the dynamically stable mean diameter.

3.7.1.2 Statically stable stone size

In order to obtain the minimum stone size for static stability, the majority of the proposed methodologies, e.g. [33, 52], compare the amplified bed shear stress near the pile with the critical shear stress provided by the Shields criterion [50]. The amplified bed shear stress is often calculated for an amplification factor (α) of 4, e.g. [33, 63] or [138]. Then, the required stone size, e.g. the design value of D_{50} or, alternatively, D_{n50} , is the minimum value that complies with Eq. (3.31) if using the critical shear stress (τ_{cr}), or with Eq. (3.32) if using the critical velocity (U_{cr}).

$$\tau_{cr} > 4\tau_{\infty} \quad (3.31)$$

$$U_{cr} > 2U_c \quad (3.32)$$

For sufficiently coarse material, the critical shear stress is obtained considering the critical Shields parameter (θ_{cr}) equal to 0.055, which is the asymptotic value of the Shields curve for an increasing particle size. According to [52], this is valid for mean diameters larger than 10 mm, which correspond to the dimensionless grain diameter (see Eq. (2.27)) larger than 200. In [63], Eq. (3.33) is used to obtain the minimum stone diameter (D_r) of the armour layer. However, it has been developed for a current alone situation. This equation assumes θ_{cr} equal to 0.040. The water depth is represented by d , U_{cr} is the critical velocity at the bottom and $\Delta = (\rho_s - \rho_w) / \rho_w$. Moreover, [63] notes that the characteristic representative size of the riprap should be equal to D_{67} in weight.

$$U_{cr} = 4.8 \sqrt{\Delta} D_r^{\frac{1}{3}} d^{\frac{1}{6}} \quad (3.33)$$

The methodology proposed by [97], again developed for current alone, suggests that the mean or the largest value is chosen from the three empirical formulas developed by [139, 140] and [141]. These correspond to Eqs. (3.34), (3.35) and (3.36), respectively [2]:

$$D_{n50} = 4.11 \frac{U_b^2}{2g(s-1)} \quad (3.34)$$

$$D_{n50} = \frac{\varepsilon}{s-1} \cdot \frac{0.035 K_T K_d U_c^2}{2 \Psi_{cr} g K_{sl}} \quad (3.35)$$

$$D_{s30} = S_f C_s C_v d \left(\sqrt{\frac{1}{s-1}} \cdot \frac{U_c}{\sqrt{K_l g d}} \right)^{2.5} \quad (3.36)$$

where D_{n50} (m) is the nominal mean diameter of the stones, d (m) is the water depth, g is the gravitational acceleration (9.81 m/s^2), U_b (m/s) is the current velocity at $0.1d$ counting from the bottom, U_c (m/s) is the depth-averaged flow velocity, ε is the stability correcting factor (0.75 for continuous protection and 1 to 1.5 for edges and transitions), Ψ_{cr} is the stability factor (0.035 for riprap protections), K_T is the turbulence factor (1 to 2 for high turbulence situations), K_d is the depth factor (equal to $(D_{n50}/d)^{0.2}$ for turbulent flows), K_{sl} is the slope factor (1 for horizontal bottoms), D_{s30} is the characteristic size of an equivalent sphere of which 30% is finer by weight, C_s is a stability coefficient (0.3 for angular rocks and 0.375 for rounded rocks), C_v is the velocity distribution coefficient (1 for straight channels and 1.25 downstream of a hydraulic structure), s is the relative density, i.e. ρ_s/ρ_w , and

K_1 is a side slope correction factor (1 for a horizontal slope). Still referring to current alone conditions and based on the failure of riprap protections at bridge piers, [86] suggested Eq. (3.37), which depends on a function of the ratio of pile diameter, D_p , to D_{50} , and of the ratio of water depth to pile diameter, calculated according to Eqs. (3.38) and (3.39).

$$\frac{U_c}{U_{cr}} = \frac{0.3}{K\left(\frac{D_p}{D_{50}}\right) \cdot K\left(\frac{d}{D_p}\right)} \quad (3.37)$$

$$K\left(\frac{D_p}{D_{50}}\right) = \begin{cases} 0.398 \ln\left(\frac{D_p}{D_{50}}\right) - 0.034 \left[\ln\left(\frac{D_p}{D_{50}}\right) \right]^2, & 1 \leq \frac{D_p}{D_{50}} < 50 \\ 1, & \frac{D_p}{D_{50}} \geq 50 \end{cases} \quad (3.38)$$

$$K\left(\frac{d}{D_p}\right) = \begin{cases} 0.783 \left(\frac{d}{D_p}\right)^{0.322} - 0.106, & 0 \leq \frac{d}{D_p} < 3 \\ 1, & \frac{d}{D_p} \geq 3 \end{cases} \quad (3.39)$$

Eq. (3.37) yields a minimum value of U_c/U_{cr} equal to 0.3. The methodology suggested by [86] proposes an iterative calculation for which the first estimate of the mean stone diameter is the one provided by $U_c/U_{cr}=0.3$. Eq. (3.37) and Eq. (3.40) are applied to iteratively obtain the required stone size D_{50} .

$$D_{50} > \frac{U_c^3}{5.956 \sqrt{d} \left(\left(\frac{U_c}{U_{cr}} \right) \sqrt{g(s-1)} \right)^3} \quad (3.40)$$

The previous formulas were mainly developed for scour protections for fluvial environments, concerning the problem of scour at bridge piers. Their application remains until the present days. A recent review of this matter is provided in [142]. In order to account for current effects and wave effects, [52] presented Eqs. (3.41) and (3.42), which are also applied in [49]. Note, however, that this methodology does not account for the combined effect of current and waves. Eq. (3.41) is applicable to a current alone, whereas Eq. (3.42) is applicable to waves. The variables in these equations are defined as in the aforementioned equations and T stands for the wave period.

$$D_{n50} = \frac{0.25 U_c^{2.8}}{d^{0.4} [g(s-1)]^{1.4}} \quad (3.41)$$

$$D_{n50} = \frac{97.9U_w^{3.08}}{T^{1.08} [g(s-1)]^{2.08}} \quad (3.42)$$

According to [49], the main difficulty of addressing combined waves and current and the required size of the stones for the armour layer lies in the calculation of the combined acting bed shear stress for a material that is not known *a priori*. Therefore, in [49], it is suggested that an initial estimate of D_{n50} is obtained from Eqs. (3.41) and (3.42) and then, an iterative approach must be adopted based on the calculation of the combined and the critical bed shear stress, as calculated in Eqs. (2.23) and (2.26).

Literature reviews, namely the ones presented in [2] and [30], show that the minimum required stone size for a scour protection under combined waves and current has not been extensively addressed yet. More recent works are found in [13, 76, 143]. However, none of them leads to a straightforward formula that can be used to determine the minimum D_{n50} . Present scour protection design often uses one of the methodologies presented in this section, which is further validated by means of physical model studies, e.g. [34, 100, 144].

Alternative methodologies to obtain the minimum value of D_{50} or D_{n50} for combined waves and current were further introduced in [1, 30], using a new calculation of the combined bed shear stress acting on the protection, or in [2, 59], based on the dimensionless wave height parameter (H_0). Although the methodology presented in [2, 59] is focused on providing an estimation of the scour protection extension based on H_0 , this parameter may provide an estimation of the minimum D_{n50} . H_0 is calculated according to [128], i.e. $H_0=(H_s)/(\Delta D_{50})$. In [2, 59], the authors analyse a series of offshore windfarms, e.g. Horns Rev 1, Scroby Sands, Arklow Bank, amongst others, and propose a classification of the scour protections based on H_0 , which for the studied cases ranged from 6 to 15. In [1, 30], a novel static design approach is proposed, with an innovative empirical formula to calculate the wave- and current-induced bed shear stress, Eq. (3.48). Despite being based on the threshold of motion criterion, the proposed design led to optimised minimum values of the mean stone diameter, for a typical North Sea scour protection [30].

As noted before, the majority of these formulas are based on the threshold of motion criteria, which yields some disadvantages:

- There are several methodologies to calculate the combined wave- and current-induced bed shear stress, as seen in Chapter 2.
- The hydraulic roughness of the sand bed is smaller than that of the protection, which may lead to other failure mechanisms, e.g. edge scour (see section 3.3), which are not accounted for by the aforementioned formulas.
- As referred in Chapter 2 and seen in Eq. (3.31), the amplification factor also influences the design of the stone size and the values reported in the literature present a wide range. While several authors use $\alpha=4$ for a steady current, others assume that this value should be lower for waves, e.g. [138] uses $\alpha=2.25$ for waves with a $KC<6$, (whereas [61] states that no scour occurs for $KC<6$) and even higher values are reported in other works, e.g. [64] reports $\alpha=3$ to 11 for a steady current with a horseshoe vortex combined with streamlines' contraction.
- These methodologies tend to provide conservative values of the required mean stone diameter, as discussed in [30] and [32], since no movement is allowed for the stones in the armour layer.

3.7.1.3 Optimised statically stable stone size

The first main project dedicated to the optimisation of the design of scour protections was the so-called “Optimisation of Monopile foundations for offshore wind turbines in deep water and North Sea conditions” (OPTI-PILE) [101]. This project (2002-2004) was coordinated by E-Connection Project BV (The Netherlands), which led the consortium with the partners Vestas – Wind Systems (Denmark) and Germanischer Lloyd Windenergie (Germany). The full details of this research are reported in [100, 101] and [145]. The OPTI-PILE project was part of the engineering of the 120 MW offshore windfarm Q7-WP, located 23 km off the Dutch coast at Ijmuiden, with water depths ranging from 20 to 25 m [30]. The improvement of scour protection design under combined waves and current was one of the main goals of the project. Therefore, a physical model study was performed on a geometric scale of 1/47.25 (Froude similitude) in order to study the scour depth at unprotected monopiles and the damage of different scour protection designs.

The OPTI-PILE project is considered to be the first one to introduce, at least in a systematic way, the differences between the static design and the dynamic design of scour protections. Static scour protections were designed according to the threshold of motion criterion, as previously explained. However, for the dynamic scour protections, a scour hole was allowed to develop before being backfilled with scour protection material, in a similar way to the design described for Scroby Sands windfarm, detailed in [76] and [146]. The static and dynamic scour protections tested in the OPTI-PILE project had configurations that are represented in Figure 3.16.

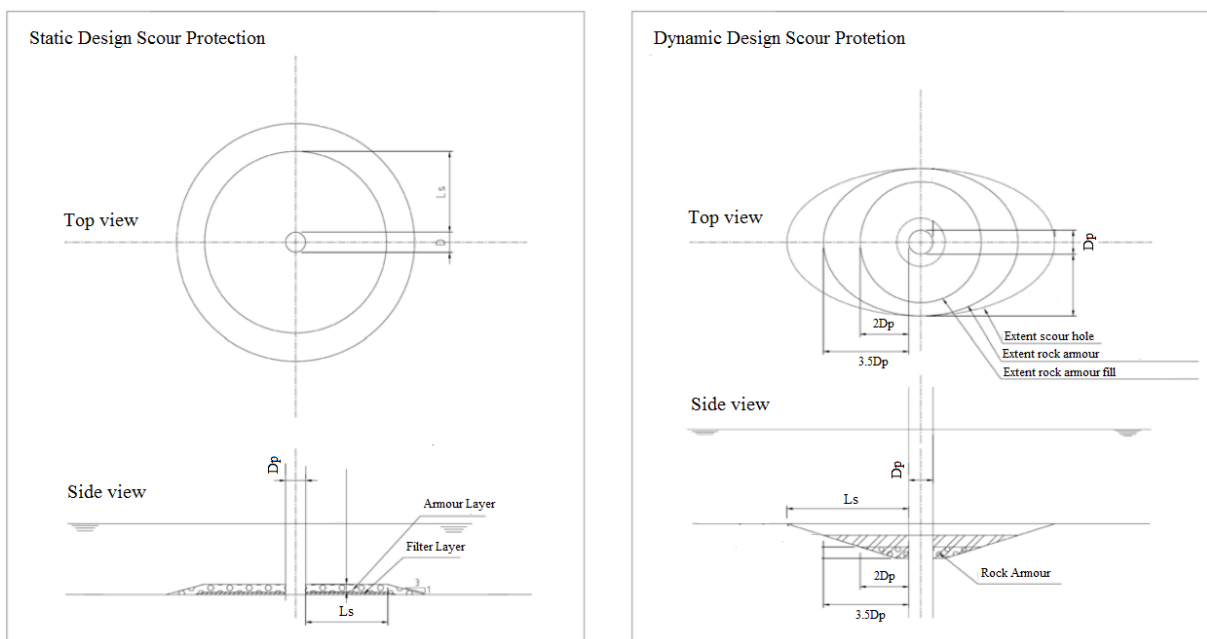


Figure 3.16 – Static and dynamic design of scour protections from the OPTI-PILE project [100].

As it is possible to see, the dynamic scour protections were designed to have the armour layer slightly below or at the level of the sea-bed, thus minimizing the acting bed shear stress at the top layer. The aim of this design was to enable for a lower mean stone diameter of the protection for which some movement was allowed. As it will be seen later, the approaches, adopted in [1, 11, 26, 32, 102] and in this research, design the dynamic scour protection above the sea-bed level, which is the most common configuration adopted in the more recent physical model studies. This is justified due to the fact that placing the scour protection above the level of the surrounding sea-bed is a more economical solution than dredging and levelling the scour protection with the bed [108]. Furthermore,

[30] notes that the increase of the wave load due to the higher location of the top layer is very limited. Dynamic scour protections are detailed in the section 3.7.1.4. However, this note is important to understand some of the comments regarding the stability parameter (stab) from the OPTI-PILE project to differentiate static and dynamic stabilities. The OPTI-PILE test conditions are in Table 3.2.

Table 3.2 – Test conditions used in the OPTI-PILE project [30].

| Variable | Symbol | Units | Range of values | |
|--|----------------|-------|----------------------------|--------------------------------|
| | | | Prototype scale | Model scale |
| Significant wave height | H_s | [m] | 6.5-8.5 | 0.138-0.180 |
| Mean wave period | T_z | [s] | 8.9-9.6 | 1.3-1.4 |
| Current velocity in combined wave and current | $U_{combined}$ | [m/s] | 1.01-1.15 | 0.147-0.170 |
| Current velocity in current alone | U_c | [m/s] | 2.01-2.06 | 0.2905-3.03 |
| Water depth | d | [m] | 24 | 0.508 |
| Extension of the Protection | L_s | [m] | 15; 25; 35 | 0.32-0.53-0.74 |
| Pile diameter | D_p | [m] | 4.2 | 0.89 |
| Mean stone diameter (Static protection) | D_{50} | [m] | 0.607; 0.396; 0.222 | 0.0115; 0.0075; 0.0042 |
| Armour layer thickness (Static Protection) | [-] | [-] | $3D_{n50}$ | $3D_{n50}$ |
| Filter layer thickness (Static protection) | [-] | [m] | 0.5 | 0.01 |
| Mean stone diameter (Dynamic protection) | D_{50} | [m] | 0.591; 0.396; 0.220; 0.121 | 0.0112; 0.0075; 0.0042; 0.0023 |
| In-fill height of dynamic protection | [-] | [-] | 1/3; 2/3; fully filled | 1/3; 2/3; fully filled |

During the tests a touch-sensitive bed profiler was used to measure radial bed profiles, after one hour tests in the model. The profile results showed that without scour protection, the scour depth reached a maximum of $1.75D_p$. Both static and dynamic scour protections prevented the erosion around the monopile foundation, with the mean stone size being significantly lower in dynamic scour protections than in static ones [30]. Moreover, the stability parameter (stab) was defined according to Eq. (3.43).

$$stab = \frac{\theta_{max}}{\theta_{cr}} \quad (3.43)$$

The scour tests were classified into three damage categories, according to the stability of the scour protection [100]:

- No movement of rocks (static stability);
- Some movement of rocks, but not sufficient to cause failure (dynamic stability);
- Failure.

In the OPTI-PILE project, the static scour protections were considered to fail when the exposed area of the filter layer exceeded the minimum value of $4D_{50}^2$. The dynamic scour protection were designed without filter by applying a wide-graded rock material. Therefore, it was assumed that the failure of dynamic scour protections occurred when the volume of rock that disappeared was equal to the volume of rock required to cause failure in the static protection. The rock material grading and the result obtained regarding the type of stability, i.e. the damage category, is provided in Table 3.3. The table shows that the dynamic stability was obtained for smaller gradings (5-40 kg and 10-200kg) than the ones used to obtain static stability (200-500 kg).

Table 3.3 – Damage categories for different rock grading [100].

| Grading class of the rock material | Static protection | Dynamic protection |
|------------------------------------|------------------------------|------------------------------|
| 200-500 kg wave height | No movement | - |
| 50-60 kg | - | No movement |
| 10-200 kg | Some movement but no failure | Some movement but no failure |
| 5-40 kg | Failure | Some movement but no failure |
| 2-8'' | - | Failure |

The stability parameter defined in Eq. (3.43) was calculated for tested protections and it was concluded that the following limits could be used to establish the transition between the damage categories. It was concluded that the transition between “no movement” and “some movement but no failure” corresponded to $stab=0.416$, whereas $stab=0.460$ corresponded to the transition between “some movement but no failure” and “failure”. These limits were also observed to be valid in the physical model study performed by [145], which was based on the site conditions at Arklow Bank offshore windfarm (geometric scale of 1/36). The original results from [100] and the ones from [145] are shown in Figure 3.17 and Figure 3.18, respectively.

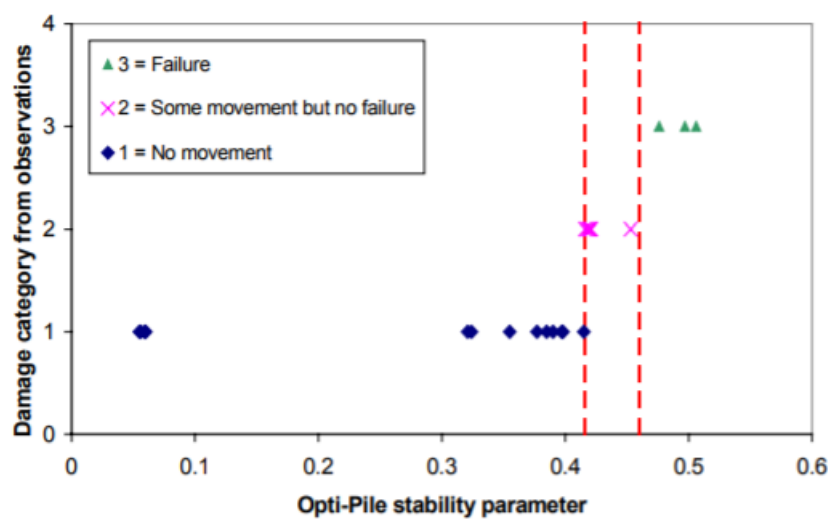


Figure 3.17 – Damage categories as a function of the stability parameter [100].

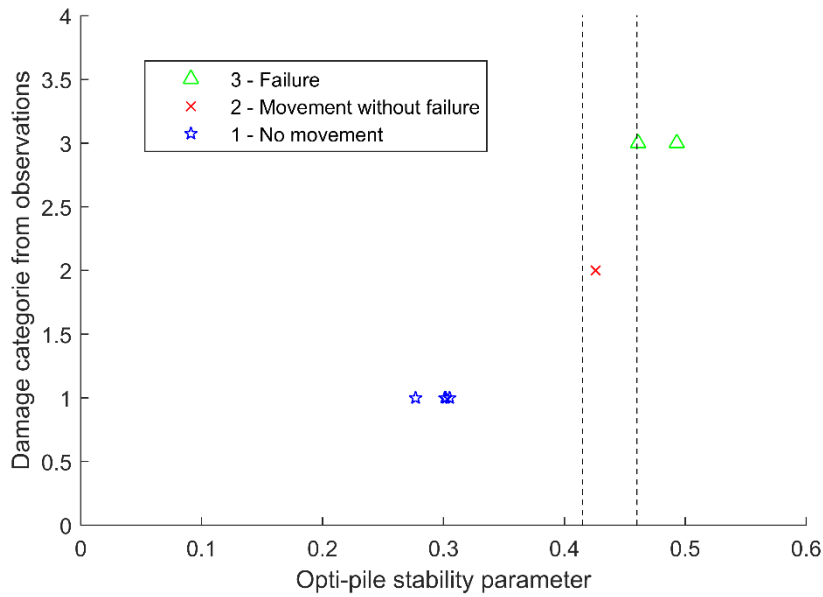


Figure 3.18 – Damage categories as a function of the stability parameter [145].

Besides the established limits for the stability parameter, Figure 3.17 and Figure 3.18 emphasize the somehow rather short number of tests performed. The research developed in [30] and in the present thesis showed, later on, that these limits would not hold for an extended range of test conditions, namely, regarding the mean diameter of the stones and the hydrodynamic conditions, e.g. current velocity, wave height and period. In [145], it is also concluded that the stab parameter was not closely related to the actual maximum damage of the protection and would need to be recalibrated for the specific circumstances at Arklow Bank offshore windfarm (physical model geometric scale of 1/36).

The OPTI-PILE project uses a critical Shields parameter (θ_{cr}) of 0.056, while the maximum Shields parameter (θ_{max}) is obtained for Eq. (3.44).

$$\theta_{max} = \frac{\tau_{max}}{\rho_w g (s-1) D_{50}} \quad (3.44)$$

As concluded in section 3.7.1.2, [100] also points out that the formulation used to obtain the wave friction factor (f_w), required to obtain the maximum combined bed shear stress (τ_{max}), significantly affected θ_{max} , thus influencing the output of the stab parameter. Moreover, as stated in [30], the f_w applied in [100] has a weak dependence on the value of D_{50} , which means that the boundaries of stability could be less clear.

Recently, [147] proposed a combination of existing expressions to obtain f_w to cover relative bed roughness from sand over gravel to coarse armour rock, as shown in Figure 3.19, which compares f_w with wave stroke to bed roughness ratio (A/k_s), with $A=U_m T_p/(2\pi)$. However, the studies reported in the literature did not extensively address the influence of the wave friction factor in the maximum Shields parameter or the stab parameter.

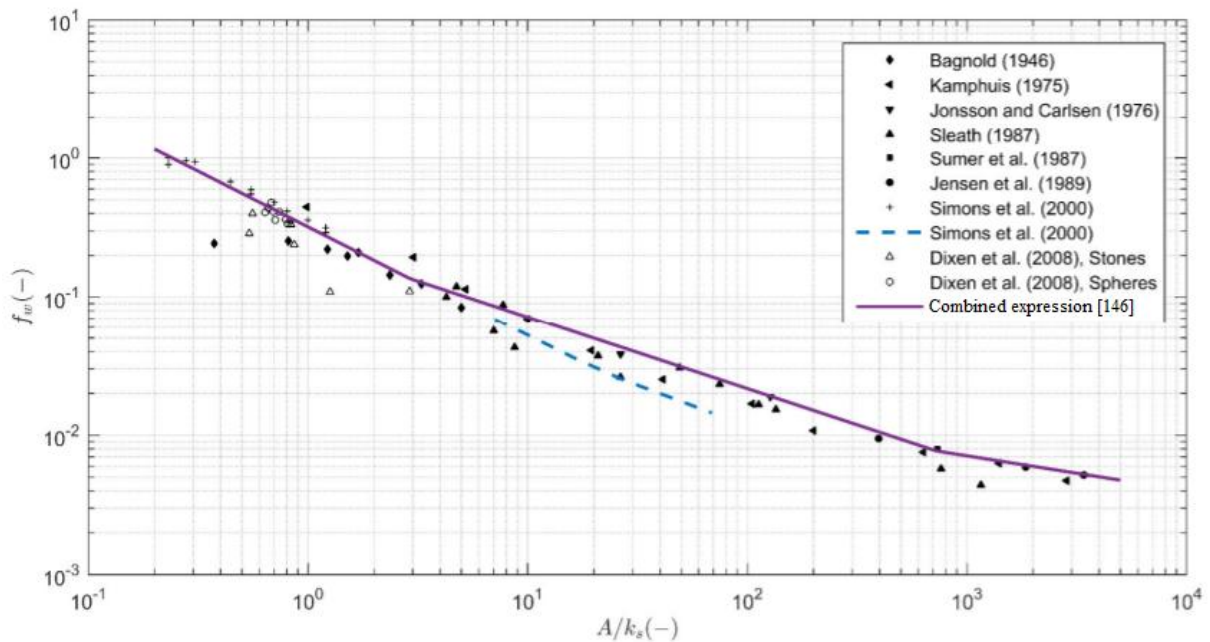


Figure 3.19 – Wave friction factor (f_w) as a function of wave stroke to bed roughness ratio [147].

Despite the impossibility of generalization of the limits proposed for the stability parameter, the overall conclusion of the OPTI-PILE project was that dynamic scour protections could be built with smaller stone sizes, i.e. optimised minimum D_{50} , compared to the diameters used in static scour protections. However, the specific optimisation of a statically stable stone size is not clearly stated in [100] or [145].

Still in the pursuit of an optimised design of scour protections, the research performed by [1] and further revisited in [30] contributed with a novel methodology for statically stable scour protections. Moreover, important contributions were given to the design of dynamic protections, which will be addressed in sections 3.7.1.4 and 3.7.1.5. In fact, a somehow elegant aspect of the research conducted in [1] consists in the double contribution to an optimised statically stable stone size, analysed in the following paragraphs and an optimised dynamically stable stone size (section 3.7.1.4).

The main improvements given by [1] and [30] regarding the design of statically stable scour protections (for the minimum stone size) are summarized as follows:

- A linear relationship is proposed between the current-induced shear stress, the wave shear stress and the combined wave- and current-induced shear stress;
- The proposed relationship does not require assumptions on the amplification factor and it was specifically developed for monopile foundations;
- The critical shear stress is derived for $\theta_{cr}=0.035$, which compares to $\theta_{cr}=0.056$, used in in the OPTI-PILE project [100, 101] or to $\theta_{cr}=0.040$ used in earlier [63]. A comparison was established with the limits for stability parameter (stab) introduced in OPTI-PILE;
- The critical shear stress is derived for the characteristic diameter $D_{67.5}$, which compares with the typical D_{50} ;
- The statically stable diameters obtained according to [1, 30] led to lower values of D_{50} , compared with former methodologies, namely the one presented in [52].

In [30], 40 scour tests are reported, for varying wave heights, wave periods and depth-averaged current velocity. These tests were performed in a wave and current flume, at a geometric scale of 1/50

(Froude similitude), as shown in Figure 3.20. The model test conditions are also summarized in Table 3.4.

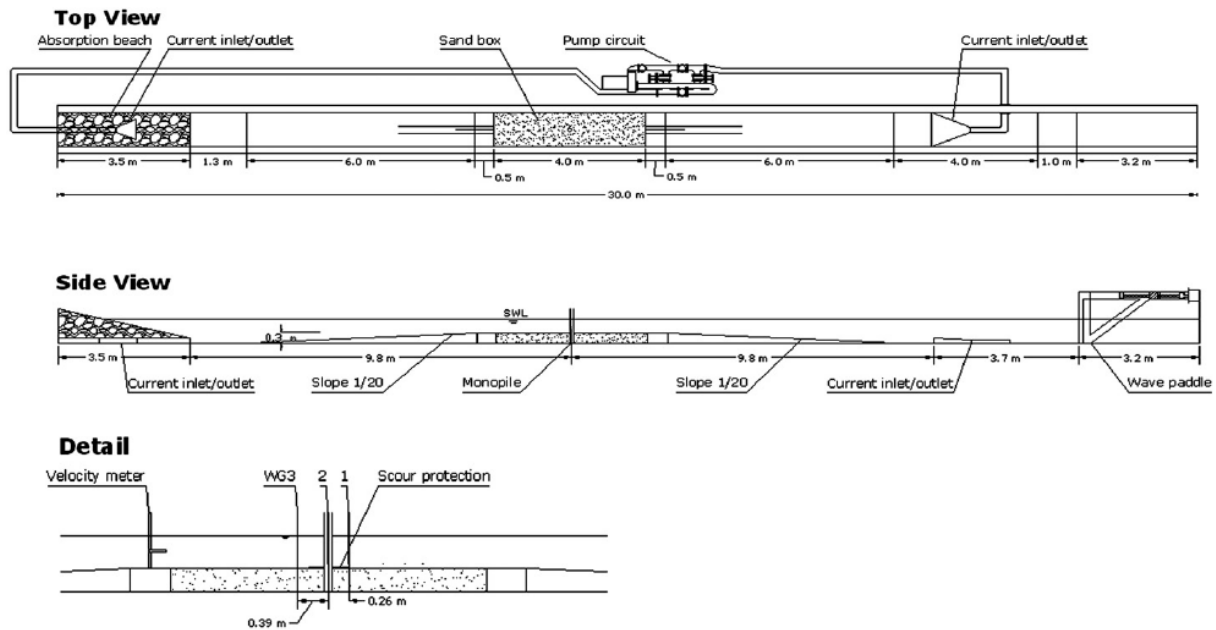


Figure 3.20 – Scour tests setup used in [1] and [30].

Table 3.4 – Range of model test conditions used by [1, 30, 32].

| Variable | Symbol | Unit | Range of values |
|-------------------------|----------|----------------------|---------------------|
| Significant Wave Height | H_{m0} | [m] | 0.05-0.168 |
| Peak Period | T_p | [s] | 1.13-1.7 |
| Current velocity | U_c | [m/s] | 0-0.30 |
| Currents Direction | ϕ | [-] | Following; Opposing |
| Water Depth | d | [m] | 0.2-0.4 |
| Pile Diameter | D_p | [m] | 0.1 |
| Mean Stone Diameter | D_{50} | [mm] | 4.1-8.5 |
| Mass density | ρ_s | [kg/m ³] | 2650-3200 |
| Armour thickness | n_a | [m] | 0.0086-0.0179 |

The physical model described in [1] and [30] used a pile diameter of 0.1 m. A scour protection made of stones was placed around the monopile foundation. The armour layer was placed on top of a geotextile filter layer and the stones were painted in different colours to allow visual observation of the amount and direction of displacements. The coloured stones were placed in 4 concentric rings, each one with a width equal to the pile radius [1]. A similar physical model is also used and detailed in following chapters of the present research. The total extension of the scour protection was equivalent

to 5 times the pile diameter. At the edge of the outer ring, 10% of extra material was added beside the geotextile layer to ensure that no decreasing height was experienced in the outer ring. The tests reported in [1] and [30] used a thickness of the scour protection layer equal to $2.5D_{n50}$. The configuration of this scour protection without the pile is shown in Figure 3.21.

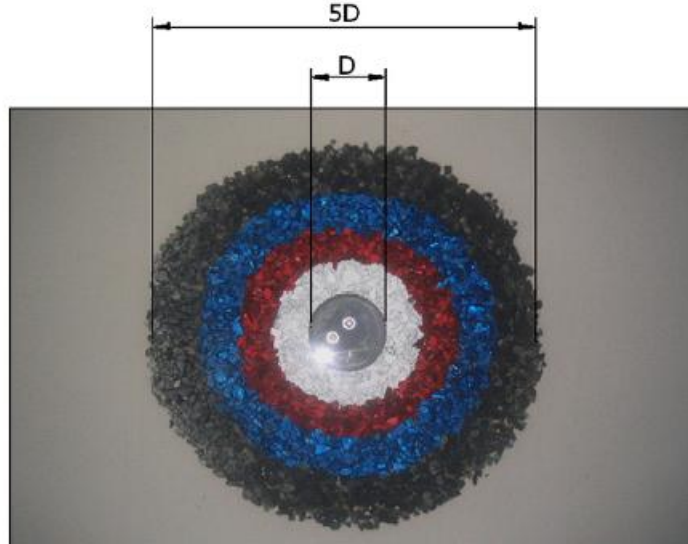


Figure 3.21 – Top view of scour protection without the pile before loading [30].

Typically, scour protections are built with a granular filter layer instead of a geotextile. In [1] and [30] the use of the geotextile filter layer is justified because the focus of the research was on the armour layer and the use of geotextile instead of granular material contributed to a simpler and faster setup. However, in the present research a granular filter layer is used to ensure more realistic conditions of the physical model, i.e. more similar to prototype situations for which the protection may fail because the granular filter and the sand-bed might be washed out through the armour layer. Note that the protection shown in Figure 3.21 was placed above the seabed level as stated before. This may contribute to the occurrence of the edge scour phenomenon, which was not addressed by [30]. The linear relationship between the wave- (τ_w) and current-induced shear stress (τ_c) and their combined value (τ_{cw}) was developed for regular waves and a steady current. Then an adaptation of the formula was proposed to account for the irregular sea state [30]. The linear relationship obtained was then presented in the general form as Eq. (3.45), where C_1 , C_2 and C_3 are the regression constants [30].

$$\tau_{cw} = C_1 + C_2 \tau_c + C_3 \tau_w \quad (3.45)$$

The wave height used for analysis purposes was the maximum wave height at the pile location. The averaged current velocity was measured at $0.4d$ above the bed and behind the pile, as recommended in [49]. The hydrodynamic conditions of these tests ranged between the wave dominated regime, i.e. $\tau_c/(\tau_c + \tau_w) = 0$, and the wave-current interaction regime with a maximum $\tau_c/(\tau_c + \tau_w) = 0.78$. Current alone conditions, i.e. $\tau_c/(\tau_c + \tau_w) = 1$, were not tested. Note that wave and current dominance can also be assessed according to Eq. (2.40). Angular rocks with $\rho_s = 2650 \text{ kg/m}^3$ were used in the model's armour layer, with D_{50} equal to 4.1, 6.0 and 8.5 mm, which corresponded to the prototype grading classes of 2-80, 2-300 and 80-300 kg, respectively [30]. The tested range of mean stone diameters was not very large. Therefore, [1] and [30] recommended the static design approach to be limited to the tested values presented in the mentioned research. This limitation was also perceived

by [26, 102] and [148], who tested the design approaches proposed by [1, 30] and [32] for new hydrodynamic conditions and mean diameters of the armour stones. The authors concluded that the approaches tended to be conservative outside the original range presented in Table 3.4. This conservative behaviour is important for reliability analysis performed outside the original prototype conditions foreseen by these design approaches. The reason for this is the fact that this conservative behaviour avoids overestimations of the protection’s reliability. In order to calculate the loading bed shear stress, the static design approach uses the linear wave theory to obtain the orbital bottom velocity (U_m), as in Eq. (2.10), which is equivalent to Eq. (3.46).

$$U_m = \frac{gHT}{2L} \cdot \frac{1}{\cosh\left(\frac{2\pi d}{L}\right)} \quad (3.46)$$

As seen in section 3.7.1.2, several studies propose a minimum stone size as a function of the wave or current velocity (U), which is found to be dependent on U^2 or U^3 , e.g. [86] or [97]. The study performed by [30] reported that a direct relationship between D_{50} and U could not be found for the scour tests performed. Therefore, the author proposed a regression analysis, which led to the previously mentioned linear relationship between the wave- and current-induced shear stress and their combined value. According to [1] and [30], the best results for the regression were obtained when using the current friction factor (f_c) calculated according to [56] and the wave friction factor (f_w) according to [58]. However, one should note that the calculation of f_w according to [58] is limited to the wave stroke to bed roughness ratio between 0.2 and 10, as introduced in Eq. (2.14). Therefore, when dealing with wave data outside this range, the formulations proposed by [52] or [57] might have to be considered. The reliability analysis performed in further chapters mainly uses the wave friction factor calculated according to [52] and its improvement to account for non-linear effects introduced in [54]. The design approach presented by [1] and [30] does not recommend the use of the formulation introduced by [53]. This is justified due to the fact that the wave friction factor obtained as in [53] tended to provide unreasonably large values of the wave-induced bed shear stress for small values of the wave period, as shown in Figure 3.22.

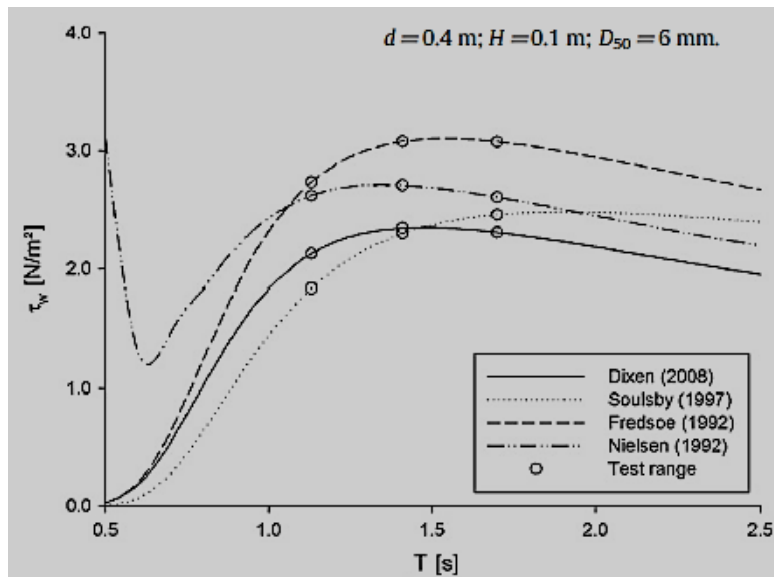


Figure 3.22 – Wave-induced bed shear stress as a function of the wave period for different formulations of the wave friction factor [30].

The tests performed in the aforementioned research led to the linear relationship provided in Eq. (3.47), which assumes a bed roughness equal to 2.5 times the mean stone diameter of the protection layer, i.e. $k_s=2.5D_{50}$. This equation yielded a squared correlation coefficient (R^2) equal to 0.90 for the tests presented in [30].

$$\tau_{cw} = 1.659 + 3.569\tau_c + 0.765\tau_w \quad (3.47)$$

Since Eq. (3.47) was obtained for a length scale of 1/50, i.e. it is a dimensional dependent equation with the bed shear stress expressed in N/m^2 , it must be converted to full scale (1/1), which leads to Eq. (3.48).

$$\tau_{cw} = 83 + 3.569\tau_c + 0.765\tau_w \quad (3.48)$$

Note that the wave- and current-induced bed shear stress (τ_{cw}) presented in Eqs. (3.47) and (3.48) can be seen as the load acting on the top layer of the scour protection. This is important for reliability purposes as it helps to separate the loads and resistance parcels related to the protection system. The scour test results from [1] and [30] showed that stones in a scour protection with a smaller grading tend to move faster than those with a wide grading. Therefore, the static design approach suggests that the critical bed shear stress is calculated with the characteristic diameter $D_{67.5}$, instead of D_{50} applied in the previously mentioned approaches, e.g. [52]. Moreover, the tests performed to develop the static design approach considered $\theta_{cr}=0.035$, because the smallest stone diameter (D_{50}) corresponded to a dimensionless grain size (D^*) larger than 100 [52]. The calculation of the critical bed shear stress is performed according to Eq. (3.49).

$$\tau_{cr} = \theta_{cr} g (\rho_s - \rho_w) D_{67.5} \quad (3.49)$$

The characteristic diameter $D_{67.5}$ assumes a linear variation of the stone size in the grading curve with a semilog diagram. Therefore, one may estimate $D_{67.5}$ according to Eq. (3.50), which is simplified into Eq. (3.51), where $\sigma_U = D_{85}/D_{15}$ as in [112]. In the research developed by [1], σ_U lies between 1.39 and 4.0. As a result, this fact should also be taken into consideration when using this approach for wider gradings, e.g. $\sigma_U > 5$ as studied in [31, 137].

$$\log\left(\frac{D_{67.5}}{D_{50}}\right) = \frac{67.5-50}{85-15} \log\left(\frac{D_{85}}{D_{15}}\right) \quad (3.50)$$

$$D_{67.5} = D_{50} \cdot (\sigma_U)^{0.25} \quad (3.51)$$

Although Eq. (3.49) does not consider the difference between regular and irregular waves, this is not the case for Eqs. (3.47) and (3.48), which were developed based on regular wave tests. Therefore, it is important to understand which characteristic loading value should be used in order to account for irregular waves. In [1], it is noted that the loading is mainly determined by the orbital bottom velocity (U_m), which is used to compute τ_w as in Eq. (2.9). If U_m is larger than the protection, stones are more likely to move [30]. To account for the presence of irregular waves, one could calculate the orbital bottom velocity directly from the wave spectrum, which is the method adopted for the dynamic design approach presented in [32]. However, the static design approach presented in [30] proposes an adjustment for irregular waves, which corresponds to the calculation of the orbital bottom velocity (U_m) with Eq. (3.46) using the characteristic value $H_{1/10}$ and the peak wave period (T_p). Note that $H_{1/10}$ is the average of the highest 10% of the waves, which for Rayleigh distributed waves is related to the

significant wave height as $H_{1/10}=1.27H_s$. The characteristic values $H_{1/10}$ and T_p are also used to determine the wave stoke (A) to bed roughness ratio (k_s), as seen in Eq. (3.52).

$$\frac{A}{k_s} = \frac{U_{m10\%} T_p}{2.5 D_{50}} \quad (3.52)$$

The adjustment proposed in Eq. (3.52), thus affecting Eqs. (2.9) and (3.46), is also followed in the present research when applying the static design approach. This is performed for the sake of comparison when analysing the results of the present research. However, as recommended in [32], the dynamic approach directly calculates U_m from the wave spectrum, as showed in the section 3.7.1.4.

It is now possible to calculate the acting load on the scour protection, i.e. using Eq. (3.48), and the resistance associated to the minimum stone size applied to the top layer, Eq. (3.49). An iterative process is required to obtain the minimum stone size for static stability. This process is summarized in Figure 3.23.

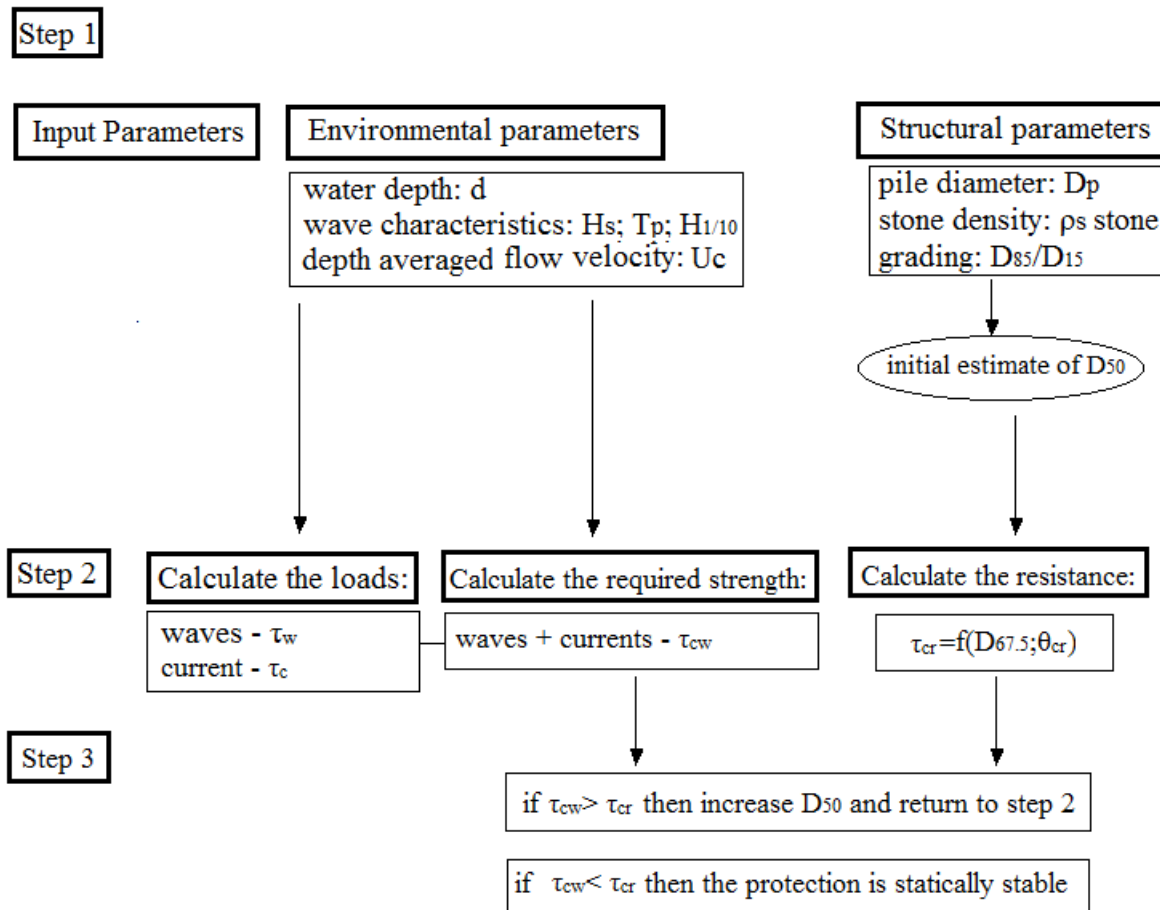


Figure 3.23 – Iterative process required to design a statically stable scour protection according to [1, 30], (adapted from [1]).

The correspondent graphical solution is obtained in plotting the acting combined shear stress and the critical bed shear stress as a function of D_{50} (also see Figure 3.24). In [30], the static design approach is compared with the traditional ones implemented by [52] and [57]. The design example is performed for typical North Sea conditions, for a significant wave height (H_s) of 6.5 m, a peak wave period (T_p)

of 11.2 s, a depth-averaged velocity (U_c) of 1.5 m/s and a uniformity parameter (σ_U) of the protection stones of 2.5. The minimum required stone size for static stability, i.e. no movement of the top stones allowed, is given in Table 3.5, while the graphical solution is given in Figure 3.24. It can be seen that the optimisation presented by [30] leads to smaller values of D_{50} and does not imply the assumption of a specific amplification factor.

Table 3.5 – Comparison of the optimised static design approach proposed by [30] and the traditional static design approaches proposed by [52] and [57].

| α | Traditional approach [57] with Eq. (2.18) | Traditional approach [52] with Eq. (2.23) | Optimised static approach [30] with Eq. (3.48) |
|----------|--|--|---|
| | D_{50} [m] | D_{50} [m] | D_{50} [m] |
| 2 | 0.68 | 0.66 | |
| 3 | 1.30 | 1.51 | 0.496 |
| 4 | 1.97 | 2.75 | |

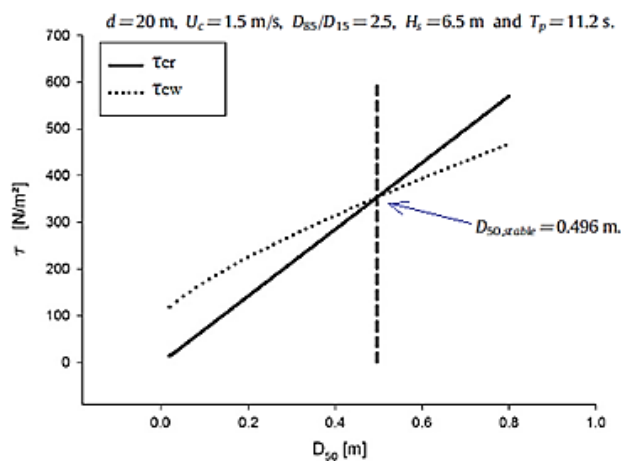


Figure 3.24 – Example of a static design approach. Graphical solution with the shear stress as a function of the mean stone size [30].

3.7.1.4 Dynamically stable stone size

So far, this thesis has revised several methods used to define the minimum stone size for a statically stable scour protection. As introduced in the previous section, a dynamic scour protection may, alternatively, be applied. The idea behind this approach is that smaller diameters of the stones can be used in the armour layer, because movement (without failure) is allowed. However, allowing for movement means that the threshold of motion may no longer be a suitable criterion to define the failure of the scour protection. Nevertheless, the physical model study conducted in the OPTI-PILE project led to the conclusion that the stability parameter, obtained from Eq. (3.43), could be used to obtain dynamically stable protections. In section 3.7.1.3, it was seen that the boundary between “static stability” and “some movement but no failure” (dynamic stability) was set for $stab=0.460$. Despite, the possibility of relating the stability parameter with the dynamic stability of the protection, it is important to note that this parameter remains closely related to the threshold of motion criterion. As it

will be discussed in section 3.7.1.5, this is not the case when using the damage number introduced in [32].

Another important aspect is that, unlike the representation shown in Figure 3.17 and Figure 3.18, the results obtained from the OPTI-PILE project showed that the boundaries of the stab parameter were in fact gradational, not sharp, so that cases with values of the stability parameter close to a boundary could in practice fall into an adjacent damage category. This poses a difficulty for design situations, e.g. the transition between “some movement but no failure” and “failure” might be blurry, thus heading to a mean stone diameter that might lead to failure of the protection.

The development of the stability parameter was based in the data available from Q7 offshore windfarm [101]. Hence, in order to extend its applicability to other offshore windfarms, a calibration of this parameter is required as mentioned in [100, 145] and [149]. Moreover, in the original OPTI-PILE work [101], it is noted that for conditions outside the tested range, the stability parameter only provided an indicator of response, which needs to be calibrated by means of physical model studies adapted for the specific location where the new protection is going to be placed. One of these limitations is the armour layer thickness, limited to $2.5D_{n50}$.

Despite the results reported in [100, 145] and [149], the literature review conducted in the present research was not able to find any clear guidance on the actual application of the OPTI-PILE tool to perform the mentioned works. This is due to the fact that the project was bounded by confidential policies. Nevertheless, [100] provides the key coefficients that were calibrated for the OPTI-PILE tool, when addressing the stability parameter and the stone size of the scour protections at Horns Rev 1 and Scroby Sands offshore windfarms, and the scour depth at an unprotected monopile at the N7 sector of the North Sea. The calibrated coefficients included the ratio of maximum scour depth to pile diameter [100], the angle of the side slope of the unprotected scour pit, the limits of the stability parameter (from Figure 3.17) and the angle of the slope of the falling rock apron with degraded seabed. The work presented by [100] found that for Horns Rev 1, a smaller stone size could have been applied, whereas the authors expected some damage to the Scroby Sands scour protection, which was however designed as a non-maintenance free scour protection.

The overall application of the stability parameter, as response indicator that allows for the design of dynamic and static scour protections, with the configurations shown in Figure 3.16, led to the conclusion that significantly smaller stone sizes could be used in dynamic scour protections, compared with the ones required for static stability (discussed in section 3.7.1.2).

3.7.1.5 Optimised dynamically stable stone size

Although the stability parameter set the first steps to implement a dynamically stable design, it was still very much based on the threshold of motion criterion. Therefore, in addition to the limitations previously discussed, this approach still presented some of the problems related with the approximations used to evaluate the bed shear stress under combined waves and current or the values considered for θ_{cr} and α , which directly influence the assessment of the damage level. Furthermore, according to [150], the stability parameter is not dependent on the applied volume of rock, although applying a larger volume can still be a viable alternative. In this case, a larger deformation will occur during severe conditions but this will not be problematic as long as the deformation is restricted to the armour layer of the protection.

Aiming at improving the limitations of the stability parameter, a novel dynamic design approach was developed also in [1] and [32]. Using a set of 85 scour tests, with a physical model equal to the

one presented in section 3.7.1.3 and a range of test conditions as shown in Table 3.4, the concept of the non-dimensional damage number (S_{3D}) of the scour protection was introduced.

The scour tests reported in [32] considered irregular wave conditions, unlike the set used to develop the static design approach, as it will be discussed in the present section. The set of tests used to develop the dynamic design approach considered an armour layer thickness of $2.5D_{50}$, with the exception of 2 of them, which were performed with an armour layer thickness of $3D_{50}$.

The results obtained from the physical model study presented in [32] showed that the stability parameter failed to accurately predict the damage levels of the new test series. In [32], this parameter tended to underestimate the damage in the protection, particularly for large current velocities ($U_c > 0.2 \text{ m/s}$, scale 1/50), for large peak wave periods ($T_p = 1.7 \text{ s}$, scale 1/50) combined with small stone sizes, and for waves in opposing currents. Underestimations were also found for high density stones and small wave heights. The same study showed that overestimations occurred for the large stone sizes, depending on the peak period. Also, [150] notes that the formula proposed by [32] attributes considerably more weight to the wave period and the orbital bottom velocity than the previously introduced stability parameter. The difference of sensitivity to the wave period between the stability parameter and the damage number was particularly evident for large KC numbers [150].

Noting the gradational transition between the damage categories to define the damage level, in the OPTI-PILE project, the research presented in [1, 32] defined the following four categories (i.e. visual damage levels):

- Damage level 1: no movement of stones (except for initial stabilisation);
- Damage level 2: very limited movement of stones;
- Damage level 3: significant movement of stones, without failure of the protection;
- Damage level 4: failure of the protection.

Moreover, the damage level of each scour test performed in [32] was then plotted against the OPTI-PILE stab parameter (Figure 3.25). These results show that the stability parameter fails to accurately predict the damage levels of the new test series. Although some trend is observed, there is a spreading around the limits provided by $0.416 < \text{stab} < 0.460$.

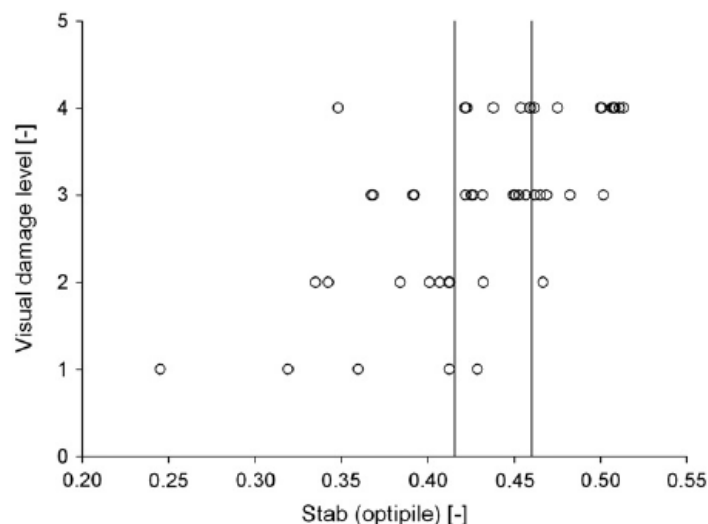


Figure 3.25 – Visual damage level versus the stability parameter [32].

According to [32] and as referred in section 3.7.1.3, the static scour protections were considered to fail when the exposed area of the filter layer exceeded the minimum value of $4D_{50}^2$. This was also

applied by [32] for the dynamic scour protections. The present research also employs the referred criterion. However, it is crucial to note that when designing single-layer scour protections this may not be a suitable criterion. For example, sometimes, in very wide graded scour protections, no filter material is applied, because only one layer of wide graded rock material is used. This single layer is expected to act simultaneously as a filter and as an armour layer. In those cases, as reported in [100], one should refer to the eroded volume of rocks (see section 3.7.1.3). In order to obtain the measured damage number ($S_{3D\text{measured}}$) of the scour protection, which would be then used to develop the empirical formula proposed by [32], the scour protections were subjected to irregular wave trains superimposed on a steady current flow. An initial wave train of 1000 waves was followed by two wave trains of 2000 waves each. If the failure of the protection occurred after 3000 waves, the second wave train of 2000 waves was not applied. The irregular wave trains were generated by means of a JONSWAP spectrum with a peak enhancement factor (γ) equal to 3.3. The characteristic weighted wave height used for analysis after 3000 waves was then obtained as in Eq. (3.53).

$$H_{m0} = \frac{1}{3} (H_{m0,1000} + 2H_{m0,2000}) \quad (3.53)$$

where $H_{m0,1000}$ and $H_{m0,2000}$ correspond to the spectral wave height obtained from the zero-order moment of the JONSWAP spectrum for the first 1000 waves and the second wave train of 2000 waves, respectively. In [32], H_{m0} simplistically referred to the significant wave height. Note that, as discussed in Chapter 2, these concepts are not exactly the same. A similar method is then used if 5000 waves are applied to the scour protection, as stated in Eq. (3.54).

$$H_{m0} = \frac{1}{5} (H_{m0,1000} + 2H_{m0,2000} + 2H_{m0,2000}) \quad (3.54)$$

After each wave train, 3D bed profiles were used to measure the erosion and the accretion occurring on the scour protection area. For details on the laser profiler used and the measurements' accuracy the reader is referred to [32]. The configuration, i.e. extent, of the scour protection used in [32] is the same as the one employed in [30], which is shown in Figure 3.21. In order to obtain the measured damage number, the scour protection was divided into sub-areas, each one with an area equal to the cross-section of the monopile (Figure 3.26), i.e. $A_{\text{sub}} = \pi D_p^2 / 4$.

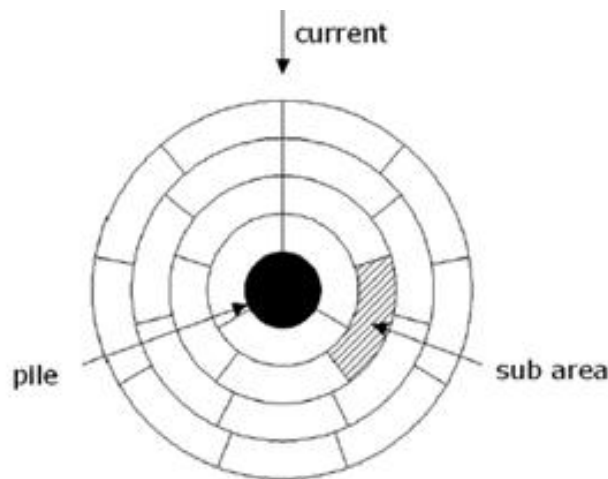


Figure 3.26 – Division of the scour protection into subareas according to [32].

The damage parameter in each sub-area ($S_{3D\text{sub}}$) was obtained as in Eq. (3.55), where V_e is the eroded volume, measured with the 3D laser profiler, and D_p is the pile diameter. Then, the overall

representative $S_{3D\text{measured}}$ of the scour protection corresponded to the maximum damage number measured for all the sub-areas, as in Eq. (3.56).

$$S_{3D\text{sub}} = \frac{V_e}{D_{n50} \pi \frac{D_p^2}{4}} \quad (3.55)$$

$$S_{3D\text{measured}} = \max_{i=1\text{to}\#\text{sub-areas}} (S_{3D\text{sub},i}) \quad (3.56)$$

Eq. (3.55) divides the eroded volume by the area of each sub-area, which corresponds, in fact, to the scour depth at the protection. Then, this depth is divided by the nominal mean stone diameter (D_{n50}). This implies that, if $S_{3D\text{sub}}=1$, the height of the scour protection has decreased in this sub-area over a distance equal to D_{n50} . An important aspect regarding Eq. (3.56) is that only the maximum damage is considered as representative of the protection, which ignores the cumulative effects of the damage occurring in the several sub-areas of the protection. Although the literature does not report any studies regarding these cumulative effects between sub-areas, further research should be performed to clarify this aspect. Note that it can be intuitively thought that a scour protection with one sub-area with $S_{3D\text{sub}}=1$ and the remaining sub-areas with very small $S_{3D\text{sub}}$, e.g. <0.25 , is not the same as having a scour protection with one sub-area with $S_{3D\text{sub}}=1$ and the remaining areas with damage numbers smaller but much closer to 1, say 0.80.

The measured damage number obtained for the set of tests from [32] is plotted against the visual damage levels previously defined in Figure 3.27, showing a much clear trend and less gradational transition between the damage levels than the one obtained from Figure 3.25 for the stability parameter.

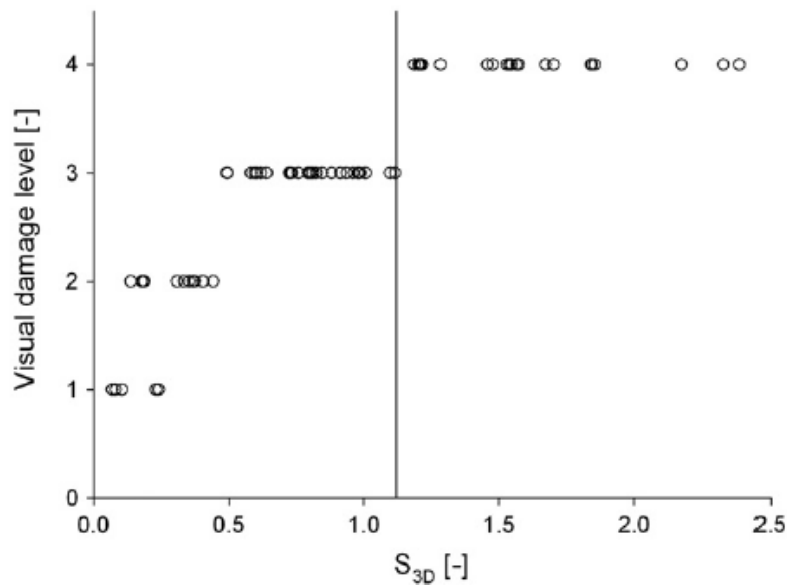


Figure 3.27 – Comparison between the measured damage number and the visual damage level from [32].

There is more evident superimposition for the first two levels, i.e. “no movement” and “very limited movement” of the stones. However, [32] states that this is due to the fact that the 3D profiler tended to slightly overestimate small damage numbers, for which no movement could not be visually seen. Figure 3.27 includes the limit $S_{3D\text{measured}}=1.1$, which corresponded to the maximum measured

damage number before failure of the protection occurred. As it will be seen, the predicted formula used to estimate the damage number, shows that this region also presents a superimposition of both dynamic scour protections and failure occurrences.

Aiming at a novel design methodology for dynamic scour protections, the research performed by [1] and [32] suggested a new predictive formula to estimate the damage parameter. Moreover, the formula considered a direct relationship with the nominal mean stone diameter, thus being suitable for design purposes, i.e. to obtain the minimum stone size required for dynamic stability. As it will be discussed in Chapter 4, this formula was later on applied in [26, 102] and [151], which successfully obtained dynamically stable scour protections according to this parameter. The non-dimensional damage number, $S_{3D\text{predicted}}$, is obtained as in Eq. (3.57).

$$\frac{S_{3D\text{predicted}}}{N^{b_0}} = a_0 \frac{U_m^3 T_{m-1,0}^2}{\sqrt{gd} (s-1)^{\frac{3}{2}} D_{n50}^2} + a_1 \left(a_2 + a_3 \frac{\left(\frac{U_c}{w_s}\right)^2 (U_c + a_4 U_m)^2 \sqrt{d}}{g D_{n50}^{\frac{3}{2}}} \right) \quad (3.57)$$

where N is the number of waves, w_s is the fall velocity, d is the water depth, U_m is the bottom orbital velocity calculated from the wave spectrum, U_c is the depth-averaged current velocity and $T_{m-1,0}$ is the energy spectral wave period, calculated from the spectrum's moments m_{-1} and m_0 or simplified by the relationship $T_p = 1.107 T_{m-1,0}$ for a JONSWAP spectrum with a peak enhancement factor of $\gamma = 3.3$.

The orbital bottom velocity (U_m) is obtained from the orbital velocity spectrum (σ_v) with Eq. (3.58), Eq. (3.59) and Eq. (3.60), where $S_U(f)$ is the power spectrum of the bottom velocity, $S(f)$ is the amplitude spectrum, $T(f)$ is the wave period as function of the frequency (f) and L is the wave length, also a function of the frequency.

$$U_m = \sqrt{2} \sigma_v \quad (3.58)$$

$$\sigma_v = \int_0^{\infty} S_U(f) df \quad (3.59)$$

$$S_U(f) = \left[\frac{2\pi}{T(f) \sinh\left(\frac{2\pi d}{L(f)}\right)} \right]^2 S(f) \quad (3.60)$$

The parameters b_0 , a_0 , a_2 and a_3 in Eq. (3.57) were determined through regression and are equal to 0.243, 0.00076, -0.022 and 0.0079 , respectively. The parameters a_1 and a_4 depend on the hydrodynamic conditions and are obtained using Eqs. (3.61) and (3.62), where U_r is the Ursell number defined as in Eq. (3.63) [119].

$$a_1 = \begin{cases} 0 & \text{for } \frac{U_c}{\sqrt{g D_{n50}}} < 0.92 \text{ and collinear waves and currents} \\ 1 & \frac{U_c}{\sqrt{g D_{n50}}} \geq 0.92 \text{ or opposing waves and currents} \end{cases} \quad (3.61)$$

$$a_4 = \begin{cases} 1 & \text{for collinear waves and currents} \\ \frac{U_r}{6.4} & \text{for opposing waves and currents} \end{cases} \quad (3.62)$$

$$U_r = \frac{L^2 H_{m0}}{d} \quad (3.63)$$

The comparison between the measured damage number, from Eq. (3.56), and the predicted damage number, from Eq. (3.57), both divided by the common factor N^{b_0} , is provided in Figure 3.28, which indicates a reasonable agreement for the test conditions in the original physical model.

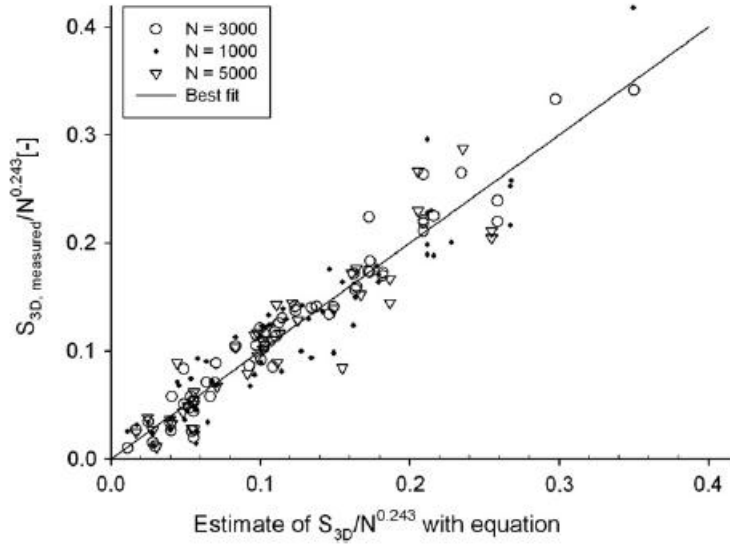


Figure 3.28 – Original comparison between $S_{3D, measured}/N^{b_0}$ and $S_{3D, predicted}/N^{b_0}$ [32].

Furthermore the analysis performed in [1] and [32] compared the predicted damage number with the visual damage level, in a similar way to the procedure shown in Figure 3.17 and Figure 3.25. These results are shown in Figure 3.29.

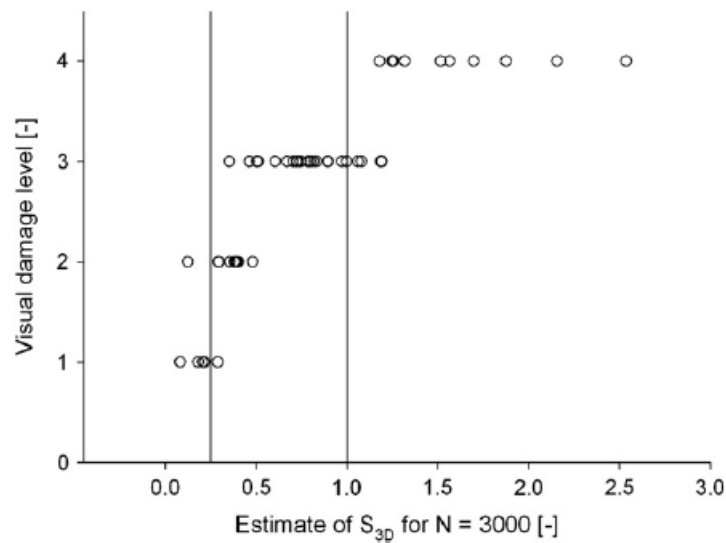


Figure 3.29 – Visual damage levels versus the predicted damage number [32].

Figure 3.29 shows that despite the less gradational transition between damage levels, compared with the original results from the stability parameter, the damage number also presented some superimposition in the transition regions between static stability, dynamic stability and failure of the scour protection. The limits used for further reliability assessment of scour protections are discussed in the following chapters. Nevertheless, Figure 3.27 and Figure 3.29 show that dynamic stability was still reached after $S_{3D}=1$. Dynamic profiles were roughly obtained for a predicted damage ranging from about 0.25 to 1.25, while statically stable profiles of the scour protection were obtained for $S_{3D} \leq 0.25$. The authors recognise that the limits for the acceptable damage of the scour protection may not be immediately clear. However, taking into consideration the tested range used to develop the predictive formula, [32] states that a conservative acceptable damage ($S_{3D\text{acceptable}}$) to obtain dynamically stable scour protections lies in $S_{3D\text{acceptable}}=1$. Also, it is stated that higher damage numbers than 1 might be acceptable if the designer ensures that there is no further damage progression over time. In practical situations, since it might not be possible to ensure that damage progression will not occur, it is recommended not to use values above 1.

The dynamic design approach based on the formula proposed by [32] represents a contribution to the design of dynamic scour protections. On one hand, it provides optimised values for the minimum stone size required, even compared with the static design approach [30], which was already an optimisation of the methodologies previously introduced in section 3.7.1.2. On the other hand, it avoids the calculation of the combined wave- and current-induced bed shear stress and the inherent disadvantages already discussed.

Still some aspects are left uncovered by the proposed formulation that culminated in Eq. (3.57). Firstly, the dynamic design approach solely considers waves in an unidirectional following or opposing current, which is a limitation compared with other formulations that include the angle between current and waves, e.g. the mean and maximum combined bed shear stress calculated according to [52] and [57]. Another aspect is the mentioned difficulty of defining clear limits for the transition between “some movement but no failure” and “failure”. Moreover, it is not clear how to define the reference number of waves used to determine the damage number. Such definition not only relates to the peak wave period used in the physical model but also to the duration of the design storm, which is inherent to the local where the scour protection is going to be placed. The maximum number of waves (N) adopted by [32] is 5000, which may not ensure the equilibrium profile of the protection. In fact, [150] notes that due to the “formula’s shape” (see Eq. (3.57)), deformation never reaches an equilibrium, while other many scour-related formulations predict development towards an equilibrium, as long as the armour layer is not fully eroded. To account for this fact, [150] suggests a modified predictive formula, as shown in Eq. (3.64), which depends on N_{charac} , which is the characteristic number of waves, i.e. the number of waves associated to a specific design storm. The formulation introduced by [150] leads to a stabilization of the damage number for N between 2500-3000 waves. The research performed in the present thesis and presented in [26] concluded that from 1000 to 5000 waves, the damage progression rate decreases after 3000 waves. However, it was not possible to conclude that the equilibrium of the scour protection’s profile was undoubtedly reached.

$$\frac{S_{3D\text{predicted}}}{N^{b_0}} = \left(\frac{S_{3D\text{predicted}}}{b_1 \left[1 - \exp\left(-\frac{N}{N_{\text{charac}}}\right) \right]} \right) \quad (3.64)$$

It can also be noted that the dynamic design approach (Eq. (3.57)) does not consider the pile diameter, which was not varied in the scour tests performed. Hence, this may lead to a reduced

performance of the predictive formula for different pile diameter to water depth ratios (D_p/d). The present research also aimed at a contribution to improve the range of test conditions that led to Eq. (3.57), but the pile diameter remained the same. Finally, it is also possible to see that the damage number formula does not include the KC number, which was identified in Chapter 2 as a dominant factor of the scour phenomenon under waves. The effect of the KC number is indirectly accounted for by including the orbital bottom velocity and the energy spectral period in Eq. (3.57). Despite the disadvantages of the dynamic design approach, the applications reported in [26, 102] and [151] added to the original set of tests presented in [1] and [32] showed that this approach consistently led to smaller mean diameters of the stones used in the armour layer, considering a maximum acceptable damage number of 1, while providing satisfactory results in the physical model configurations inspired in typical North Sea conditions.

A similar example to the one provided for the static design approach (Table 3.5) is presented in Table 3.6. A significant wave height (H_s) of 6.5 m, a peak wave period (T_p) of 11.2 s, a uniformity parameter ($\sigma_{U=D_{85}/D_{15}}$) of the protection stones of 2.5, an averaged depth velocity (U_c) of 1.5 m/s and a water depth (d) of 20 m are used for this example as well. It is possible to see that the formula provides considerably smaller mean diameters than the ones from Table 3.5. This becomes particularly evident for an acceptable damage level of 1 (dynamic stability).

Table 3.6 – Required stone size, i.e. mean stone diameter D_{50} (m), for a dynamic scour protection considering $H_s=6.5$ m, $T_p=11.2$ s and $D_{85}/D_{15}=2.5$, $U_c=1.5$ m/s, $d=20$ m. Optimised dynamic approach with Eq. (3.57).

| $S_{3D_{\text{acceptable}}}$ | Following waves and current | Opposing waves and current |
|------------------------------|-----------------------------|----------------------------|
| 0.2 | 0.44 | 0.46 |
| 0.5 | 0.32 | 0.36 |
| 1 | 0.27 | 0.28 |

It is also interesting to note that for a smaller value of the acceptable damage, i.e. $S_{3D_{\text{acceptable}}}=0.5$, D_{50} drops from 0.496 m (static design approach - Table 3.5) to 0.36 m (dynamic design approach – waves in an opposing current, Table 3.6), which is a considerable size reduction. If one recalls that $S_{3D_{\text{acceptable}}}=0.25$ was associated to the transition between movement and no movement, then one would expect that for $S_{3D_{\text{acceptable}}}=0.20$, the value of D_{50} would be close to the one provided by the static design approach, i.e. $D_{50}=0.496$ m. Table 3.6 shows that this is not the case, as the minimum mean stone size is $D_{50}=0.44$ m for waves in a following current or 0.46 m for waves in an opposing current.

Moreover, the mean stone diameter associated to a $S_{3D_{\text{acceptable}}}=0.25$ is $D_{50}=0.53$ m (using Eq. (3.57)) for waves in an opposing current, which does not exactly match the 0.496 m (although being close). Despite the fact that the difference is not so large, roughly 4 cm, it must be noted that when designing a statically stable scour protection, the approach discussed in section 3.7.1.3 should be used, rather than the dynamic one discussed here. This slight inconsistency is related to the fact that the dynamic design approach is based on the assumption that movement is allowed, while the equivalent damage number for absolutely no movement, i.e. below the threshold of motion, is theoretically given by $S_{3D_{\text{acceptable}}}=0$. Moreover, the overestimation of the damage number provided by the 3D profiler used in original research also contributes for the difference between the statically stable outputs of both methodologies. Note that, according to [1], the S_{3D} given by the 3D profiler for statically stable scour protections was limited to 0.25, which is an overestimation of the damage since one knows that no movement should have occurred.

Generally, the dynamic design approach also concluded that waves in opposing currents tended to cause more damage to the protection than waves in following currents [1]. However, this seems to become more evident for sufficiently large values of U_c .

3.7.2 Radial extent and thickness of the scour protection

In addition to the minimum required stone size, the full design of a typical scour protection also includes the definition of the radial extent (L_{ext}) and the thickness (t_{sp}) of the scour protection. This section briefly addresses them both. However, the reader should note that the radial extent is not the main focus of the present research, while the thickness of the protection is studied in the physical modelling activities of Chapter 4, but still with less detail than the minimum required stone size, which is the aim of the reliability analysis presented in Chapters 6 and 7.

There are several methodologies that can be used to determine the radial extent of the protection. The underlying idea of the radial extent is to ensure that the protection has a sufficiently large horizontal dimension to prevent significant scour in the region where the bed shear stress is considerably amplified due to the presence of the monopile foundation. Moreover, the radial extent (and the thickness) is also important when accounting for damage propagation, namely the one related to the edge scour phenomenon. According to [2] and [59], the majority of the methodologies suggest that the extent is provided as a function of the pile diameter. In [152], it is stated that the typical extent of a scour protection is 3-4 times the pile diameter. Table 3.7 summarizes some of the recommendations given in the literature, which were developed for fluvial environments and non-cohesive sediments.

Table 3.7 – Recommended radial extent of scour protection.

| Reference | L_{ext} |
|-----------|-------------------|
| [33] | $2.5D_p - 4D_p$ |
| [63] | $3D_p - 4D_p$ |
| [64] | $2.5D_p$ |
| [65] | $3D_p - 4D_p$ |
| [97] | $2D_p$ |
| [153] | $2.5D_p - 4.5D_p$ |

Other formulations suggested that the extent of the scour protection should be calculated as a function of the friction angle of the sand-bed sediments. This is the case of the formulas proposed by [100] and [154], which are only applicable for non-cohesive sediments. The formula suggested by [154] considers the friction angle (ϕ_i°), the maximum scour depth (S_e) at the unprotected monopile and the safety factor (S_f), as shown in Eq. (3.65). Note that for $S_f=1$, a friction angle of 30° and a scour depth of $1.5D_p$, this equation leads to a radial extent of $2.6D_p$. Also note that the value of L_{ext} does not include the extra material needed to cover the edges of the filter layer, if existent, which is typically applied as an extra slope of 1/3 or 2/3.

$$L_{ext} = S_f S_e \cot(\phi_i^\circ) \quad (3.65)$$

The formula proposed by [100], specifically developed for the marine environment, is presented as Eq. (3.66), which uses the maximum scour depth (S_{max}) and the actual angle of the scour hole ϕ_s° .

$$L_{ext} = S_{max} \cot(\phi_s^\circ) \quad (3.66)$$

Another possibility is to follow the recommendation provided in [21], which corresponds to Eq. (3.67), which depends on the equilibrium scour depth (S_e), the friction angle of the sediments (ϕ_i°) and the pile diameter D_p .

$$L_{ext} = \frac{D_p}{2} + S_e \cot(\phi_i^\circ) \quad (3.67)$$

An alternative based on the load bearing capacity of the monopile is suggested in [1]. This formulation considers the soil's part for which the lateral load capacity is defined (Figure 3.30). This part of the soil corresponds to a triangle and is defined as a function of the buried length of the pile (t_0) and the sediments' friction angle (ϕ – in Figure 3.30) in radians [1]. According to this formulation, the minimum radial extent to ensure the required lateral bearing capacity of the monopile is given by Eq. (3.68), which does not depend on the scour depth, as in Eqs. (3.65), Eq. (3.66) and Eq. (3.67).

$$L_{ext} = t_0 \tan\left(\frac{\pi}{4} + \frac{\phi}{2}\right) \quad (3.68)$$

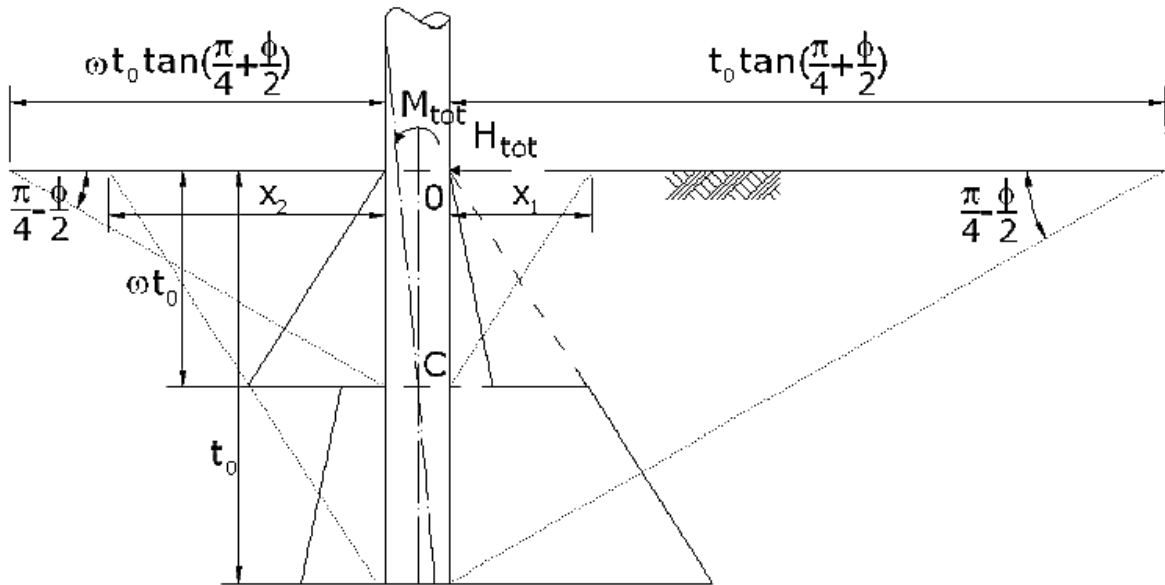


Figure 3.30 – Soil triangle that provides the lateral bearing capacity of the pile [1].

Despite the fact that this formulation indirectly considers the effect of the environmental variables, e.g. the wave height and wave period, by means of the total momentum (M_{tot}) and the total transversal load (H_{tot}) on the monopile's interface with the soil, it is noted by [2] that the environmental variables are consistently ignored in the discussed formulations used to obtain the radial extent of the protection.

An extensive comparison between the aforementioned methodologies is reported in [2], e.g. for Horns Rev 1, North Hoyle, Kentish Flats, Princess Amalia (Q7) and Robbin Rigg offshore windfarms. This study concluded that the methodology proposed by [1] provided considerably larger values compared with the formulations proposed by [21, 100] and [154]. In order to include the effect of the

environmental variables in the design of the radial extent, [2] and [32] concluded that the formula introduced by [155], i.e. Eq. (3.69), originally developed for berms of vertical breakwaters, could also be used, provided that the resultant of L_{ext} was between $L/4$ and $L/2$, with L being the wave length at the pile location, calculated with the peak wave period (T_p), and H the wave height.

$$L_{\text{ext}} = \frac{L}{2\pi} \arccos \left[\frac{-\pi H}{L} \coth(L) \tanh \left(\frac{2\pi H}{L} \right) \right] \quad (3.69)$$

The thickness of the scour protection (t_{sp}) is determined by the dimension of the rock material used in the protection, i.e. the stones of the armour layer and the granular material of the filter layer. Therefore, the thickness of each layer is not the same, with the filter layer being the one that presents a smaller thickness [2]. Note, however, that one may also use a single layer, as already mentioned, for which a wide grading is used to ensure that the single layer acts, simultaneously, as filter and armour. The use of a single wide graded layer is not focused in the present research. Therefore, the recommendations for the protection's thickness discussed here may not be suitable for that particular case. The majority of the recommendations provided for the protection's thickness were developed for scour protections under a steady current, e.g. [63] or [65].

Common applications, as the one given by [63], consider that the minimum thickness should be at least two times larger than the mean stone diameter applied in the armour layer of the scour protection. The same is recommended by [49] when designing scour protections for marine environment. In [152], it is noted that the minimum thickness commonly employed in scour protections around monopile foundations ranges from 1 to 1.5 m. Table 3.8 provides some examples regarding the protection's thickness. The armour layer thickness is denoted as n_a and the thickness of the filter layer as n_f . Similarly, D_{50} concerns the mean stone diameter of the armour layer, while d_{50} is used for the filter material. Table 3.8 shows that the combined thickness (filter plus armour) is at least 2 times D_{50} . However, it is also noted that for several cases, the thickness is unknown, which might be due to the confidential policies of the offshore wind industry. Nevertheless, this lack of information contributes to a considerable difficulty when trying to compare different windfarms with different features.

Table 3.8 – Scour protections' thicknesses for the armour and the filter layer [2].

| Windfarm | D_{50} [m] | d_{50} [m] | n_a [m] | n_f [m] |
|----------------|--------------|--------------|-----------|-----------|
| North Hoyle | 0.3 | - | - | - |
| Egmond aan Zee | 0.4 | 0.05 | 1.4 | - |
| Thornton Bank | 0.35 | - | 0.7 | - |
| Horns Rev 1 | 0.4 | 0.2 | 1 | 0.5 |
| Scroby Sands | 0.15 | - | - | - |
| Arklow bank | 0.425 | - | - | - |

In [86], the influence of the thickness of the rip-rap layer on the failure of the scour protection is investigated and it was found that an increased velocity could be withstood with increasing layer thickness. The author used rather small stone sizes and the increase in resistance was mainly caused by the fact that for sufficiently thick layers, a redistribution of the scour protection material could re-fill the possible gaps at the armour layer. The research performed by [1] compared tests in similar conditions but with different armour thicknesses (tests 37 and 38 had $n_a=2.5D_{n50}$ and tests 39 and 40

had $n_a=3D_{n50}$ – see Figure 3.31). It was concluded that the influence of the thickness of the armour layer in the damage number was very limited for small damage numbers. The author pointed out that this results from the fact that the stones are not moving in the protection for small S_{3D} , thus the bed material will not be displaced independently from the thickness. On the other side, for large damage numbers and when the protection has failed, the damage reduced for a thicker scour protection, possibly due to the redistribution of the scour protection material. The influence of the scour protection's thickness is assessed in the experimental work developed within the scope of the present thesis, namely in section 4.3.5.

Another important aspect related to the protection's thickness is its influence on the edge scour phenomenon, due to the sudden difference of the roughness between the sand bed and the armour layer. The roughness affects the bed boundary layer, which may cause failure at the edge of the protection [111]. Also, an increase of the scour protection leads to a decrease of the water depth, which enhances the scour process on the top layer. As discussed previously, this effect may not be so significant if the water depth is large enough compared to the thickness of the protection. Moreover, an increase of the thickness of the scour protection may also affect the stiffness of the foundation, because the stiffness of the armour layer is not the same as the one presented by the sediments at the sand bed. Therefore, the thickness may also affect the natural frequency of the monopile. Although several works have been performed regarding the scour effects on the monopile's eigenfrequency, e.g. [104, 105] or [156], there is a lack of studies concerning the effect of the scour protection in the dynamic structural behaviour of the foundation. The preliminary results from the physical model study performed by [157] suggested that the configuration of the protection affects the natural frequency of the structure. In this sense, using a dynamic scour protection may also contribute to a lower influence on the vibration of the structure than the one caused by a static scour protection. Recognising this possible effect, recently, HR Wallingford and the Oxford University started a project entitled "Effects of Scour and Scour Protection on Offshore Wind Monopiles", performed under the Renewable Energy Marine Structures (REMS) consortium [158, 159]. The results from this project are yet to be known.

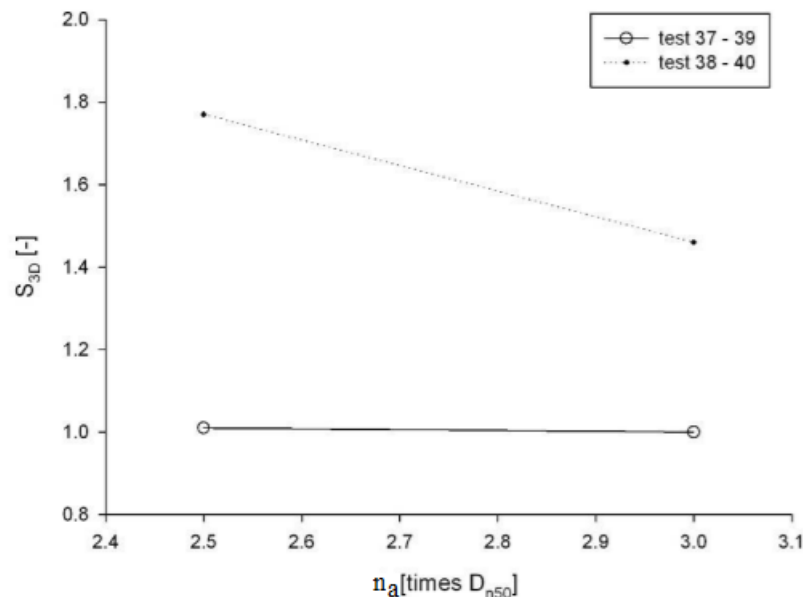


Figure 3.31 – Influence of the armour layer thickness on the damage number of the protection according to [1].

3.8 Notes on the deterministic optimised design

Besides the experimental contribution of the present research to the development of dynamic scour protections, this work intends to provide innovative guidance on how to perform the reliability assessment of scour protections, including their probabilistic design. The probabilistic aspects of the reliability analysis are addressed in following chapters. However, a brief note is hereby given concerning the deterministic aspects of the design methodologies presented throughout Chapter 3.

During the previous sections, namely the ones related to the mean stone diameter required for dynamic and static stabilities, there were several random variables included in the presented deterministic design methodologies. This occurred for both the traditional approaches, e.g. [52] and [57], and the optimised ones, e.g. [30] and [32]. When calculating the bed shear stress for static protections or the damage number for dynamic ones, it is crucial to define the values of the design wave height (H_d) and the associated wave period (T), which are used to determine the orbital bottom velocity (U_m). Moreover, the design depth-averaged current velocity (U_c) should also be addressed, among several other variables. The deterministic design of scour protections often uses the wave height associated to a specific return period (T_r), typically 50 years [30]. In the methodology used for static scour protections, the authors calculate U_m for $H_{1/10}$. On the other hand, [32] uses the orbital bottom velocity calculated from the wave JONSAWP spectrum, with a peak enhancement factor of 3.3, defined by H_s and T_p . These characteristic values are representative of short-term characteristics or associated to a return period that intends to reflect an extreme value over a long-term period, considering that the short-term characteristics remain the same over time.

Furthermore, the wave spectrum corresponds to a short-term analysis of the sea-state characteristics, thus not being representative of the actual long-term probabilistic behaviour of the sea state. Hence, even when using spectral analysis, these methodologies do not account for the long-term evolution of the design wave height. Moreover, they do not include the long-term dependence between the wave heights and the peak period (or any other wave period for that matter). Also, the correlation between waves and a current environment is not taken into account. The present research did not focus on the waves and current correlation. However, recent works have been performed concerning this subject. For example, in [130], a conditional model is proposed to perform the joint model of waves and currents and it is concluded that the joint behaviour of these variables produces differences in hydrodynamic load estimation. In [129], it is concluded that offshore standards tend to overestimate the ultimate limit state loads, because they do not account for long-term correlation between waves and currents. These works indicate that this long-term correlation should indeed be addressed, and this is here recognised as an important aspect of further research.

The deterministic methodologies presented so far are also not able to consider the combined variability of the environmental factors and the structural parameters of the protection, e.g. the D_{50} , the uniformity parameter of the sediments, the density of the rock material or the protection's thickness. However, in a probabilistic design, the simulation procedure enables the combination of different values of these random variables. Therefore, a probabilistic design allows for the analysis of the occurrence of failure in multiple loading and resistance scenarios combined with different characteristics of the protection. Therefore, design methodologies presented so far are defined as deterministic ones in the sense that they do not account for long-term behaviour and multivariable correlations, which are crucial aspects of the probabilistic design, risk and reliability analysis. The methodologies previously introduced tend to provide different results and configurations of the scour protection for the same hydrodynamic, structural and geotechnical conditions. The answer to which configuration can be considered the best one in terms of the costs (efficiency) and safety (effectiveness) remains unknown. The present research is mainly focused on the adaptation of some of

these methodologies towards a novel probabilistic approach that not only provides the optimised design, but also gives a measure of safety (reliability) of the scour protection.

3.9 Notes on scale effects, physical modelling and monitoring of scour protections

The research performed on the configuration and optimisation of scour protections can be divided into four main types, i.e. research based on physical models, research based on numerical models, research based on hybrid modelling activities (composite modelling), which combine both the physical and numerical models and, finally, research based on monitoring and field measurements. The present research is dedicated to the first type of modelling activities, which is also the focus of the present section. Extensive reviews on this and the other types of modelling are provided in [2, 13] or in [160, 161, 162].

The main advantage of the physical over the numerical modelling is the fact that no simplifying assumptions are needed concerning the governing physical processes [1]. Moreover, they also represent a less costly alternative to the field measurements, added to the fact that laboratory and physical modelling measurements can be performed in a controlled environment that enables the separation of loading conditions and influencing effects to be studied [1]. Although the ideal situation would be to combine the physical and the numerical modelling with field measurements, in the absence of that possibility, the small-scale physical models remain the most reliable tool for designing and testing most types of coastal and offshore structures [163]. According to [49], the physical modelling is indispensable for the design process of scour protection of offshore monopile foundations, due to the complex flow regime that results from the combined effect of waves and current.

Conversely, the use of reduced scales in the model, compared with the real dimensions of the prototype structure, may lead to discrepancies between the model and the prototype behaviours. Several studies are now being performed in considerably large scales, e.g. [164] performs a physical model study at the Fast Flow Facilities (HR Wallingford) using a Froude similitude and geometric scales of 1/16.67 and 1/8.33, which are scales considerably larger than the ones typically reported, i.e. 1/50 and 1/100, e.g. [102]. Nevertheless, scale effects remain a shortcoming of the physical modelling, with their full extent far from being completely understood. The discrepancies between the laboratory and the field measurements are mainly caused by model and scale effects [1]. For example, on model effects, there is the generation of long waves, side wall effects, bottom topography, wave reflection and sediment supply. On scale effects, there is the influence of the Reynolds number on the vortex shedding, the sediment scaling, the morphological features (e.g. unscaled ripples), the pile roughness and the bed boundary layer. According to [165], the distinction between scale and model effects is often difficult. According to [1], it is commonly believed that scale effects have more influence on the results than model effects, thus more attention is often given to scales effects. It is important to note that these influences should be accounted when planning and preparing the physical modelling activities.

The correct scaling of waves and currents in laboratory studies must preserve the Froude (Fr) and the Reynolds (Re) numbers, respectively defined by Eqs. (3.70) and (3.71), where U is the flow velocity and ν is the kinematic viscosity.

$$Fr = \frac{U}{\sqrt{gd}} \quad (3.70)$$

$$Re = \frac{U \cdot D_p}{\nu} \quad (3.71)$$

The accurate preservation of the the geometric length scale, implies a correct Froude scaling, which may lead to a Reynolds number which is not preserved between the model and the prototype. Typical scour protection models aim at an accurate scaling of the hydrodynamic conditions, which implies that the Froude similitude is adopted, i.e. the Froude number in the prototype must be equal to the one in the model. If one intends to study viscous effects, then the Reynolds number must be correctly scaled. The non-scaled Reynolds number often loses its importance in the majority of the scour protection models under combined waves and current, because the flow regime tends to be turbulent, for which viscous effects can be disregarded if $Re \geq 1 \times 10^4$ [163]. However, effects will always be present, when dealing with certain aspects of the protection's behaviour. For example, the flow and the pressure gradient in the filter layer of the protection are affected when the Reynolds similitude is disregarded. Such variables may contribute for the protection's failure and, even though it might be difficult to quantify these effects, it should be recognised that they exist, thus contributing for the uncertainty of the results obtained with models based on Froude similitude.

In [166], a comprehensive review of scale effects in the physical modelling of offshore and coastal structures is provided. The authors note that the Froude similitude will adequately scale the wave height and period, provided that viscous effects can be ignored. The non-linearity of the waves is commonly described by the Ursell number (U_r), which is also required for a direct application of the methodology presented in [32]. Therefore, it is also important to preserve this number in the model. The Ursell number is calculated according to the previously mentioned Eq. (3.63). Since the Ursell number is dependent on the wave height, the wave length and the water depth, all of them geometrically scaled with the Froude similarity, then the Ursell number remains the same in the model, meaning that non-linearity is also preserved by the Froude scaling.

The vortex formation around the pile is particularly important, as it influences the amplification of the bed shear stress. The vortex shedding may depend on the pile Reynolds number for a steady current, while for waves it depends on the KC number [61]. The KC number depends on the orbital bottom velocity, the wave period and the pile diameter, which scale geometrically, thus the KC number is also preserved with Froude scaling. Conversely, for a flow around a pile, [166] state that the Reynolds number is important for values up to 2×10^5 .

Moreover, it is also noted that the vortex shedding is dependent on the pile roughness that is not scaled correctly. Therefore, it is important to ensure that the combined waves and current regime is in the turbulent domain, preferably with $Re > 2 \times 10^5$. Nevertheless, some authors consider that for wave scour modelling, the KC number should preferably be respected, while the Reynolds number and the pile roughness might be considered of secondary importance, e.g. [77] or [163]. Scale effects due to the inaccurate scaling of Re are reported to be limited in the scour research presented by [77] for $10^3 < Re < 10^5$.

The bed boundary layers will be similar in the model and the prototype for a turbulent regime [166]. According to [145], the turbulent boundary layer is obtained when the rough flow wave friction factor and the smooth flow wave friction factor are equal. This equality is represented in Eq. (3.72) if it considers the formulation developed by [52], for which $z_0 = k_s/30$ and Re_A is the Reynolds number with respect to the wave stroke, i.e. $Re_A = U_m A / \nu$.

$$1.39 \left(\frac{A}{z_0} \right)^{-0.52} = 0.0521 (R_{eA})^{-0.187} \quad (3.72)$$

Noting that the bed roughness k_s is considered as $2.5D_{50}$, it is possible to re-arrange Eq. (3.72) to obtain the lower limit for the stone diameter D_{50} , which is given by Eq. (3.73).

$$D_{50} = \left[\frac{0.0521 \left(\frac{U_m^2 T}{2\Pi v} \right)^{-0.187} \left(\frac{6U_m T}{\Pi} \right)^{0.52}}{1.39} \right]^{1/0.52} \quad (3.73)$$

In a similar way, if the formulation proposed by [57] is considered, the turbulent boundary layer is obtained either for Eq. (3.74) or (3.75).

$$0.04 \left(\frac{A}{k_s} \right)^{-0.25} = 0.035 (R_{eA})^{-0.16}, \text{ for } (A/k_s) > 50 \quad (3.74)$$

$$0.4 \left(\frac{A}{k_s} \right)^{-0.75} = 0.035 (R_{eA})^{-0.16}, \text{ for } (A/k_s) \leq 50 \quad (3.75)$$

Again, considering a bed roughness of $k_s = 2.5D_{50}$, the following lower limits are obtained for the mean stone diameter, i.e. Eqs. (3.76) and (3.77) [1].

$$D_{50} = \left[\frac{0.035 \left(\frac{U_m^2 T}{2\Pi v} \right)^{-0.16} \left(\frac{6U_m T}{\Pi} \right)^{0.25}}{0.04} \right]^4 \quad (3.76)$$

$$D_{50} = \left[\frac{0.035 \left(\frac{U_m^2 T}{2\Pi v} \right)^{-0.16} \left(\frac{6U_m T}{\Pi} \right)^{0.75}}{0.4} \right]^{4/3} \quad (3.77)$$

One of the most important aspects regarding scale effects lies in the scaling of the bed roughness, specifically when attempting to scale the sand-bed sediments. It is possible to geometrically scale the bed roughness, which is commonly determined by the dimensions of the bed material (d_{50}), as noted in [1]. However, while for the stones of the scour protection this does not pose any practical problems, it does lead to difficulties in the sediments. This occurs because the sand-bed sediments usually present considerably small dimensions, which if geometrically scaled become even smaller. As the diameter decreases, the sediments may acquire cohesive properties, which for example would correspond to a foundation soil similar to clays. This poses a problem, since the non-cohesive properties of the soil should be kept, which is the most common in offshore monopiles. Another aspect is the fact that when ripples are formed, the bed roughness is determined by the ripples' height, as shown in [30]. Therefore, the ripples are also not scaled and may represent a contribution to the sediment transport that may not correspond to prototype conditions.

Regarding the sediment transport, [166] notes that the Shields parameters must also be preserved. When dealing with live-bed scour, the models tend to be more accurately reproduced, because the scour depth is less dependent on the Shields parameter for the live-bed scour than in the clear-water

scour. The sediment transport is mainly determined by the falling velocity (w_s), which according to [1], should also be scaled according to the Froude similitude.

Several other aspects could be discussed regarding scale effects. The present section summarized the most important ones. Regarding the physical model studies of scour protections, the Froude scaling is the one followed by the majority of the studies. For the aforementioned reasons and the nature of the scour phenomenon, the present research is also based in the same hydraulic similitude.

As seen throughout Chapter 3, several physical models studies have been performed concerning scour protections around monopile foundations. An extensive and recent review is presented in [167]. The majority of the physical models concerning scour protections consider a steady current flow, typically found in bridge piers, e.g. [33, 65, 86] or, more recently, [168]. However, in a similar way to the lack of studies regarding the wave and current-induced scour, there is also a small number of studies related to the physical modelling of scour protections in offshore environments, i.e. under waves and current. Noting this literature gap, the present thesis also aimed to contribute with physical model results obtained from this research, presented in [26, 102] and [151]. Those studies are addressed in following chapters. Moreover, the absence of scour protection studies under combined waves and current becomes even more evident for dynamically stable protections. On one hand, the concept is fairly recent and despite the first studies having started with the OPTI-PILE project, i.e. [100, 101] and [149], only after the study performed by [1] and [32] the dynamic scour protections started to be more systematically addressed in the literature, namely, in the aforementioned studies and e.g. in [43] and [148]. The knowledge acquired for dynamic scour protections is not yet comparable to the one gathered for statically stable ones. For this reason, the majority of the scour protections implemented in the prototype are statically stable, e.g. Horns Rev 1 or Arklow Bank [13]. Exceptions are the Princess Amalia and the Scroby Sands offshore windfarms, in which the actual design and application of dynamically stable protections were implemented [2].

In [169], a physical model, with a Froude similitude at a geometric scale of 1/50, was used to study scour protections for monopile foundations and gravity-based foundations, as shown in Figure 3.32. The tests considered different prototype mean diameters of the stones (D_{50} =93 mm, 258 mm, 365 mm and 585 mm). However, the study did not perform any test concerning dynamic scour protections.



Figure 3.32 – Physical model of a damaged scour protection around a monopile from [169].

In [170], the performance of the scour protection at the Egmond ann Zee was studied by means of a physical model, later compared with field measurements. However, the authors did not give any details on the rock material dimensions or the scale used to perform the tests.

The research presented by [171] used a physical model to study gravity-based foundations at Thornton Bank offshore windfarm. The study was performed at a Froude scale of 1/52, enabling the improvement of the protection’s configuration, for which the authors stated that costs could be reduced.

Regarding dynamic scour protections as a complement to the studies performed in the OPTI-PILE project [101] and in [1], an extended validation of the damage number formula, i.e. Eq. (3.57), was reported in [148] and also in [172], also using a Froude scale of 1/50.

Despite the similar scales employed in the aforementioned studies, this review found that scour protection research, based on physical models of offshore foundations, often fails to cover a broad range of the protection’s configuration, namely, regarding crucial variables such as the stone size used in the model, the thickness of the protection or even its radial extent. These gaps are added to the already mentioned lack of studies regarding dynamic stability. Therefore, it is common to see that design proposals for scour protections are very much related to technicalities and specifications of the prototype used as a case study. As a result, the design of a scour protection often implies the application of several methodologies, which are then compared and validated in the laboratory before being implemented at full scale.

Once the scour protection is implemented, or even if it has not been applied, it is common to monitor the scour at the foundation. Firstly, to understand if scour is reaching any alarming level from the structural point of view; and secondly, in case the protection has been applied, to see if it has failed, thus meaning that backfilling interventions might be required. Notwithstanding the confidential policies typical of the offshore wind industry, some monitoring campaigns have been reported, e.g. [13, 150] and others. In [173], monitoring results at Egmond ann Zee’s protection are reported and an example is shown in Figure 3.33. The monitoring activities stated that the edge scour phenomenon has occurred at some of the foundations, which contributed to a decrease of the radial extent of the protections even during “normal” hydrodynamic conditions, thus expecting an increase of damage for storm events.

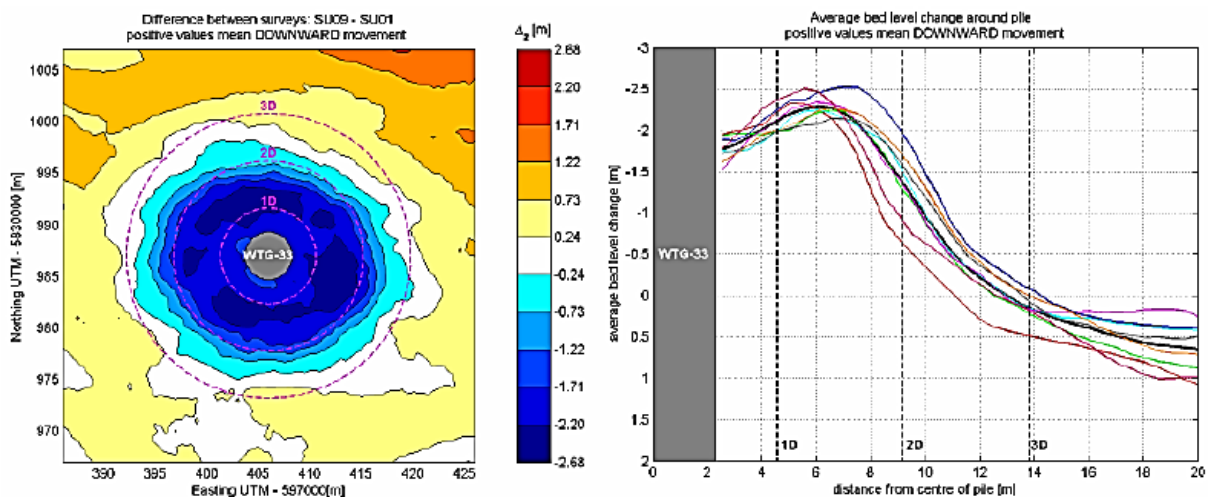


Figure 3.33 – Top view and side profiles of the scour monitoring results reported in [173], profiles taken for different angles of the scour protection.

The review of monitoring results presented in [13] includes the analysis of the scour protections placed at Horns Rev 1, Scroby Sands and Arklow Bank. For Horns Rev 1, [13] found that some loss of filter material had occurred, as well as the lowering/sinking of the armour layer. The sinking depth reached $0.35D_p$, i.e. close to 1.5 m [13]. In Scroby Sands, it is reported that the protection had clearly

contributed to avoid the increase of scour depths. However, it was noted that secondary scour occurred in the seabed around the rock dump. Nevertheless, no failure occurrence due to the flow slide mechanism was reported. Regarding Arklow Bank offshore windfarm, [13] shows that diver surveys indicated an exposure of sand or gravel at the protection, thus meaning that voids in armour layer were existent (Figure 3.34). Even though the protection was supposed to be statically stable, the absence of marine fouling on the wall of the monopile indicated that the bed level was likely to have fallen or it was a sign of sediment mobility with gravel abrasion on the monopile, keeping it clear [13].



Figure 3.34 – Photographic record of sand and gravel exposure at the monopile wall in Arklow Bank [13].

As mentioned, the access to real scour data is often difficult to obtain, not only due to the costs of the monitoring campaigns but also due to the confidential policies of the sector. Therefore, if the failure of a scour protection occurs, the event often remains unknown to the general public. Nevertheless, as demonstrated from the previous monitoring campaigns and also as reported in [174], failure does occur. This fact emphasizes the importance of the present work, both in terms of its contribution to the physical model studies, but also regarding the efforts developed to establish a procedure to assess the reliability and safety of scour protections.

3.10 Conclusions

The present chapter addressed the design of scour protections, being dedicated to the analysis of the environmental and structural parameters that determine the configuration of the protection. A presentation was performed on the failure modes of a scour protection. A review was performed on the methodologies used to define the minimum required stone diameter, the armour layer thickness and the radial extent of the scour protection. A particular focus was given to the minimum stone diameter definition, which is crucial to account for the failure mode caused by the erosion of the top layer. The filter layer design was not approached, because it lies outside the main scope of the present research. This thesis mainly concerns the erosion of the top layer, which is much dependent on the stone diameter that might be defined according to the type of stability.

Regarding the type of stability, a scour protection might be designed to be statically or dynamically stable. The following conclusions arose from this chapter:

- The design parameters of a scour protection might be divided into environmental parameters, which describe the water motion near the bed (e.g. the current velocity, the wave height and

period or the sediment characteristics) and the structural parameters, which are responsible for the structure's stability, including the foundation and the protection (i.e. the pile diameter, the density, size and grading of the stones).

- The design parameters mainly determine the loads acting on the scour protection and the system's resistance. However, some parameters may influence both of these components. For example, the mean diameter of the stones in the top layer influences both the loads and the resistance components, e.g. by means of the bed roughness and the critical Shields parameter, respectively.
- The majority of the design methodologies are developed for a steady current environment. A lower number of methodologies are available to design scour protections under waves, whilst the design under combined waves and current is even less documented in the literature.
- The available methodologies mainly concern the design of statically stable scour protections. For both static and dynamic scour protections, these methodologies have a remarkable semi-empirical nature focused on a deterministic perspective. The long-term and correlated behaviour of design variables is neglected.
- The methodologies used for static stability are deeply based on the threshold of motion criterion. The ones oriented for dynamic stability aim at the definition of new parameters, which account for movement without failure, e.g. the stability parameter and the damage number.
- The results obtained in the physical model studies performed in the OPTI-PILE project [101] and in [1, 30, 32] led to different design methodologies aiming at an optimised stone diameter of the scour protection. The analysed results enabled the following important remarks:
 - Dynamic scour protections lead to a reduced size of D_{50} , which may reduce the overall costs;
 - In static stability, the transitions between damage categories ("some movement but no failure" and "failure") are gradational; therefore, both the stability parameter and the damage number present a gradational behaviour, which makes it difficult to define a sharp limit for each damage category and leads to the need of further validation of the referred methodologies and, sometimes, a case-to-case calibration, which is the case of the stability parameter;
 - Static stability can be obtained for $stab=0.416$, whilst dynamic stability is achieved between 0.416 and 0.460. Similarly, static scour protections can be obtained for $S_{3D}=0.25$ and dynamic scour protections for $S_{3D}=1$.
- Scour protection design is still very much based on physical model studies, due to the complexity of the scour phenomenon and the soil-fluid-structure interaction.
- Existing studies are often bound by confidential policies of the offshore wind sector; therefore, it is often difficult to have access to detailed information regarding the results and conclusions obtained.
- Scale and model effects often represent a source of uncertainty in physical model studies. Froude similitude is the most used one for the scour protection tests reported in the literature.
- It is often difficult to obtain datasets that cover a wide range of testing conditions, namely, regarding the tested stone diameters and the hydrodynamic conditions.
- Not many results from monitoring campaigns are available in the literature concerning damage and long-term behaviour of scour protections. Still, the scour protection is a common requirement in several offshore windfarms, which may experience failure.

Troughout this chapter, it was noted that dynamic scour protections have not been systematically introduced at full scale offshore windfarms. Its implementation in commercial projects is almost negligible in comparison to statically stable scour protections. Therefore, this somehow novel concept

still requires additional research to help building the stakeholders confidence in the feasibility of this type of solution. In this sense, Chapter 4 is a contribution to this matter by means of experimental research activities, as the first major objective outlined in section 1.4.

Experimental Study on Dynamic Scour Protections

4.1 Introduction and background of the experimental research

The experimental study performed within the scope of this thesis was carried out to investigate the damage development around a protected monopile foundation in a combined waves and current climate. This test programme and respective analysis are divided into two parts. The first one concerns the physical model study performed at Aalborg University (DK), within the MARINET proposal number 61, “Optimising the design of dynamic scour protection around offshore foundations” [175]. This experimental research aimed at validating and extending the range of application of the dynamic scour protection design proposed in [1] and [32] (discussed in section 3.7.1.5). These scour tests were mainly dedicated to the analysis of the mean stone diameter required for dynamic stability. The second part of the experimental research concerns the physical model study performed at University of Porto (PT), dedicated to the analysis of the damage number under waves alone (APPENDIX 1). The considerations and some of the main findings related to the present research are also reported in [26, 102] and in [151].

4.2 Experimental research program within the MARINET proposal 61

4.2.1 Introduction

The proposed experimental programme focused on the following research questions:

- Is there a dynamically stable scour protection for a given combination of waves and current loading and a stone size smaller than the one for a static scour protection system for these design conditions?
- How thick should this armour layer be to allow for reshaping but to maintain full coverage of the filter layer?

Tests were carried out with a constant depth-averaged current velocity (target velocity 0.18 m/s) with following superimposed irregular waves (JONSWAP target spectrum, with a peak enhancement factor $\gamma=3.3$). A total of 23 irregular wave tests were performed, organized in three test series with varying water depth. In each test, 3D profiles and cross-sections of the scour protection were taken after 1000, 3000 and 5000 waves. The tests are based on a similar setup to the ones presented in [1] and [148]. The tests aimed to answer the following research questions, added to the previously stated ones:

- Where is failure initiated? Is it always at the same place or is it dependent on the storm conditions?

- How does the profile evolve once the filter is exposed over a certain area?
- Where did the stones move to? Do they stay inside the original area of the scour protection or do they disappear? Do the stones accumulate in a specific area or is it the influence of the waves/current important for the profile response?
- Does the profile still change a lot between 3000 and 5000 waves or is it already more or less stable?

The present chapter aims to analyse the obtained data, in order to validate the concept of dynamic scour protection. Once this new concept is experimentally assessed and proves to be feasible, it will be possible to analyse it in terms of its reliability and to measure the risks involved in its collapse.

The scour tests and experimental work hereby presented are a result of the present doctoral study and a collaboration of the Faculty of Engineering of the University of Porto (FEUP) with HR Wallingford (HRW - UK), International Marine Dredging Consultants (IMDC - Be), Ghent University (Be) and University of Aalborg (DK). The reliability and risk analysis of a scour protection imply a proper definition of the design methodology, which determines the characteristics of the scour protection. Therefore, this experimental work provides a validation of the design methodology, which is further used to obtain the ultimate limit state (ULS) function. This function is required for the computation of the reliability measure of the system and the inherent risk assessment (see Chapter 5 and section 5.6).

The design of the dynamic scour protection is not only determined by the environmental conditions, i.e. the waves and current climate. In order to obtain a feasible dynamic scour protection in commercial and industrial terms, one must also attend to the following aspects:

- The maximum stone size, which can typically be placed with the currently available equipment (fall-pipe vessels);
- The function of the protection layer: prevent scouring of the seabed around the offshore foundation;
- The use of a smaller stone size that allows the implementation of a (more) closed filter layer and consequent cost savings.

Since velocities are only amplified within a limited area around the monopile, one should expect a reshaped scour protection: a local depression in the scour protection near the pile, but a thicker circular layer all around, which prevents further loss of stones from nearby the pile.

As seen in Chapter 3, most of the former research projects are focused on the design of statically stable scour protections. Therefore, the damage allowance on the armour layer of a scour protection is still a gap in the literature, which requires further clarification. Taking this into consideration, the present research aimed at a physical model study that could be directly comparable with the research performed by [1, 32] and [148].

Scour affects several types of fixed bottom foundations, as the jacket and gravity based foundations and others. However, these experiments were carried out with a monopile foundation. This choice is justified by the need to use a foundation of a simple type, for which the geometry effects are well known, enabling the reduction of the number of additional effects on the damage development that arises from secondary variables, as the foundation geometry. Secondly, because this choice enables one to start by studying the typical static design, which can be reasonably predicted, before moving on to the damage analysis of dynamic configurations, which is not so vastly discussed in the literature.

The use of a cylindrical monopile also allowed a straight comparison of the present results with the ones presented by [1, 32] and [148]. Besides that, considering the available facilities at Aalborg University and FEUP’s laboratory, a better scale could be used for this type of sub-structures compared to larger ones, as gravity based or jacket foundations. It can also be noted that, as seen in section 1.3, monopile structures are the most widely used in offshore wind engineering.

4.2.2 Prototype conditions

The present test programme considered environmental variables representative of typical North Sea conditions and loads, as defined in [175]. The values were also adopted due to the need of increasing the range of test conditions reported in [1] and [32]. Several monopiles included in offshore wind turbine structures are exposed to North Sea conditions and are subjected to major scouring problems, as seen in some of the monitoring cases described in section 3.9.

Table 4.1 summarizes the conditions (water depth, d ; depth-averaged current velocity, U_c ; significant wave height, H_s ; peak wave period, T_p) for three series of tests defined for a monopile diameter $D_p=5$ m. Note that the classification of shallower, intermediate and deeper water depth, does not refer to the classification according to the ratio of wave height to wave length (H/L), i.e. wave steepness, nor to the breaker index (H/d), which are used for validation of different wave theories (see Figure 3.10).

Table 4.1 – Prototype hydrodynamic conditions and monopile diameter.

| Test Series | d [m] | U_c [m/s] | H_s [m] | T_p [s] | D_p [m] | Water depth |
|----------------------|---------|-------------|-----------|-----------|-----------|---|
| 1 st (s1) | 12 | 1.3 | 4.5 | 10.7 | 5 | Shallower water, without breaking waves |
| 2 nd (s2) | 18 | 1.6 | 7.5 | 11.3 | 5 | Intermediate water depth |
| 3 rd (s3) | 25 | 1.3 | 8.0 | 11.0 | 5 | Deeper water depth |

The shallow water series was adapted in order to avoid breaking waves at the vicinity of the monopile. The intermediate and deep water depths presented no problem and the waves were not depth limited. Between tests, different characteristics were considered for the protection system, namely, the mean stone diameter and the thickness of the armour layer (top layer):

- Stone size of the armour layer – expressed in terms of its mean diameter D_{50} ;
- Armour layer thickness – expressed as a multiple of D_{50} , e.g. $3D_{50}$, $4D_{50}$.

The armour layer was installed over a granular filter for a better representation of reality. Note that this is a considerable difference compared with the tests performed in [1] and [32], which used a geotextile filter. Nevertheless, the granular material is the most common type of filter layer used in practical situations. Moreover, this enables one to understand if damage allowance contributes for the sinking of the scour protection [111]. The choice of the diameter of the stones was made according to its possible installation with fall-pipe vessels, which is a common constructive technique used in such situations [26]. Furthermore, the rock material considered for the armour layer is also comparable with the ones applied in well-known cases (see Table 3.1 and [2]). The prototype characteristics of the armour stone, the granular filter and the seabed sediments are provided in Table 4.2.

For each grading considered, the first configuration used in the scour tests was the one corresponding to the reproduction of a statically stable design, in order to compare the values of scour depth and extent with the ones obtained in [1] and [148]. At this point, a validation of the setup was performed in order to guarantee that dynamic configurations could be tested further on. All tests were performed with an unidirectional current and were conducted with series of waves representative of a storm duration in the North Sea. Profiles of the seabed and the armour layer of the protection were taken after 1000, 3000 and 5000 waves. Note that this procedure was also applied in [1, 30] and [32], as discussed in Chapter 3, sections 3.7.1.3 and 3.7.1.5.

Table 4.2 – Prototype characteristics of the armour layer stones, granular filter and sediments.

| Material | D_{50,prototype} [m] | D_{n50,prototype} [m] | ρ_s [kg/m³] | Prototype grading | Installation |
|-----------------|---|--|---|--------------------------|---|
| Armour 1 | 0.375 | 0.315 | 2650 | 50-150mm | Slightly too big for fall pipe installation |
| Armour 2 | 0.301 | 0.253 | 2564 | 80-200mm | Can be installed with a fall pipe |
| Armour 3 | 0.207 | 0.174 | 2597 | 10-60kg | Can be installed with a fall-pipe vessel |
| Armour 4 | 0.134 | 0.113 | 2564 | 40-200kg | Can be installed with a fall-pipe vessel |
| Filter | 0.05 | 0.042 | 2632 | - | Can be installed with a fall-pipe vessel |
| Sand | 0.009 | 0.008 | 2564 | - | Not applicable |

4.2.3 Facilities, scour protection test setup and model conditions

These scour tests were performed at the Fluids Laboratory of Aalborg University. All tests were performed in a wave-current flume with a length of 21.4 m, and a cross-section 1.2 m wide and 1.5 m deep. The physical model was built at a 1/50 scale, following the Froude similitude. The flume had an upward slope in the approaching section of 1/90, followed by a flat sand bed at the monopile section (35 cm of minimum thickness) and a downward slope at the rear end. At this end of the flume, a bypass system was installed in order to separate the 4 pumps used for current generation and the pipe system from the central area, where the monopile was installed. The flow pipes, connected to the pumps, were elevated above the flume's surface and extended to the section behind the wave paddle. A scheme of the setup used to monitor the current and wave distribution is provided in Figure 4.1. The scheme of the general setup is provided in Figure 4.2.

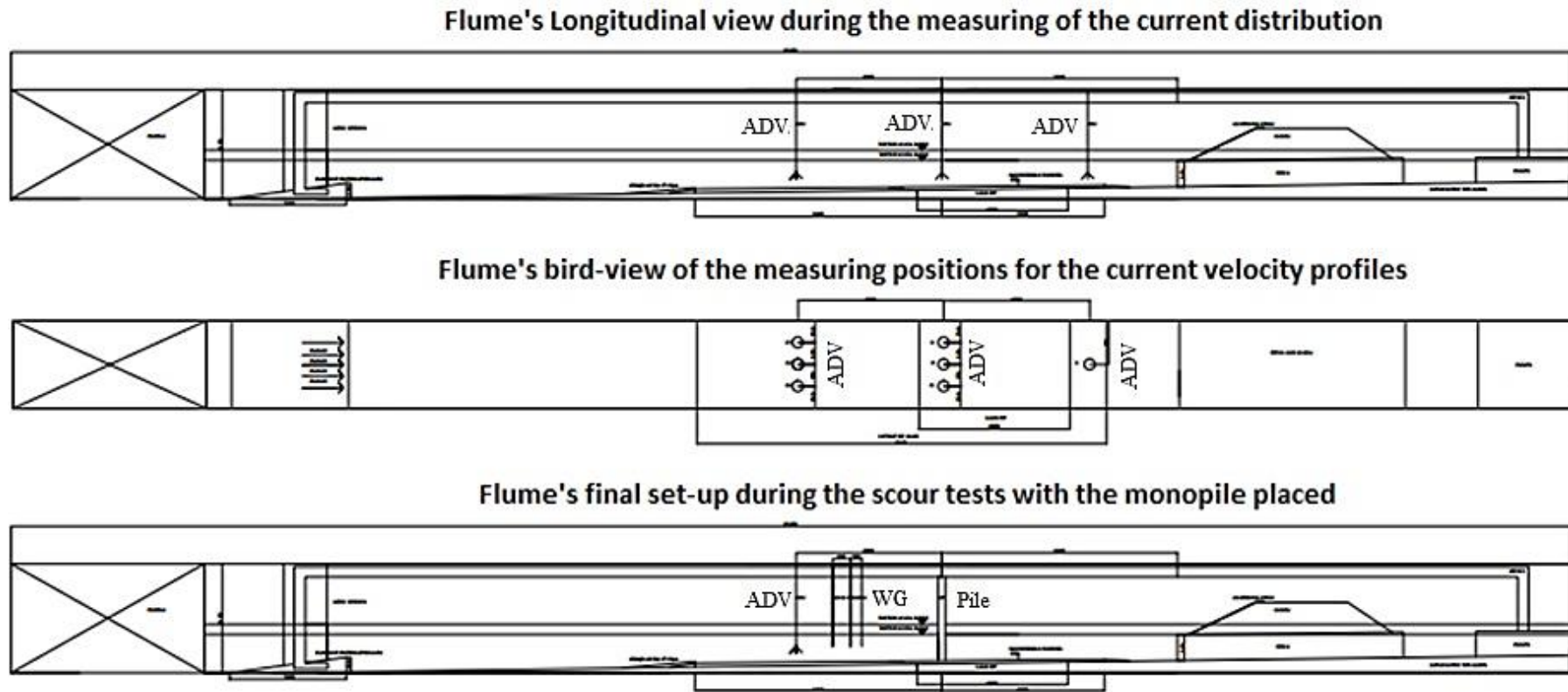


Figure 4.1 - Location of the Acoustic Doppler Velocimeters (ADV) and the wave gauges (WG) for current and wave monitoring.

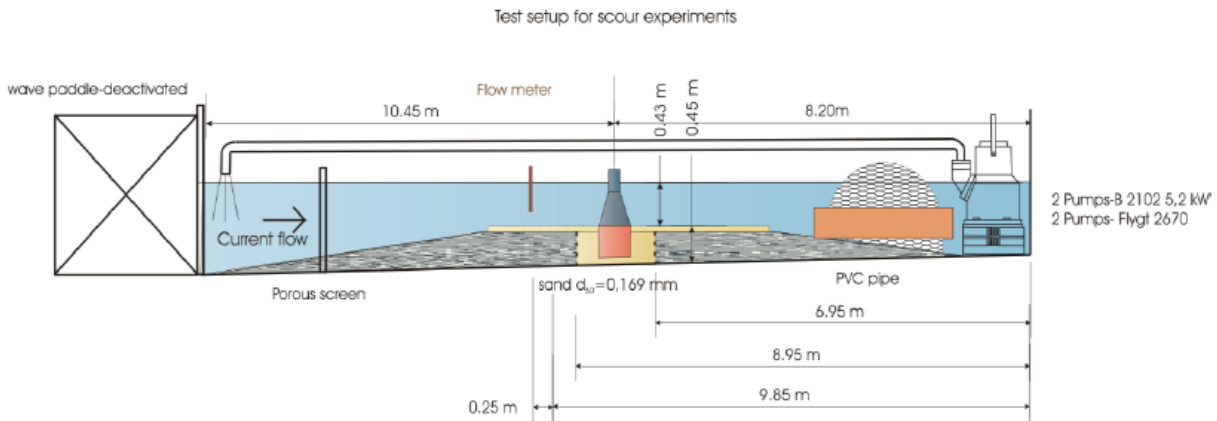


Figure 4.2 – Representation of the wave-current flume used at Aalborg University.

Since the current turbulence had to be controlled, pipes were also connected to an outlet box (Figure 4.3) to ensure a steady current at the monopile section.



Figure 4.3 – Front view of the pump outlet box plus current distribution box and metal panels (“throat”) to isolate the pipe outlets from the flow.

The turbulence was also reduced by the upward slope, which was covered with some gravel in order to increase the friction factors and smooth the bed boundary layer (Figure 4.4). Regarding the model setup, a movable sand bed was placed around the monopile foundation. The sandbox had a minimum depth of 35 cm and a length of approximately 4.0 m. For the foundation soil, uniform fine sand was used with a mean diameter of 0.170 mm.

The tests were performed in live-bed regime in order to include the effects of edge scour. The monopile, which had a diameter of 5.0 m in the prototype, had a 10 cm diameter in the model. The downstream view of the flume, with the Acoustic Doppler Velocimeter (ADV) and wave gauges, can be seen in Figure 4.5, without the monopile present. Figure 4.5 also includes the bypass section, with PVC pipes used to separate the pump system from the monitored flow section where the tests were performed.



Figure 4.4 – Sand gravel placed on the upward slope to reduce turbulence and smooth the boundary layer.



Figure 4.5 – Downstream view of the bypass section, wave gauge and ADV, without the monopile present.

The monopile was installed in the central sandpit, coupled with a holding system, which is shown in Figure 4.6. The holding system was used in order to avoid pile oscillation due to the momentum generated by combined current and waves. Although the monopile oscillations may interfere with the scour depth development, the scaling procedure did not account for the mass and stiffness scaling of the structure. Therefore, it was not possible to ensure that the existing oscillations corresponded to the expected prototype vibration frequencies. The holding system eliminates this effect, which ensures that the damage at the scour protection is a direct result of the amplified bed shear stress and the turbulence structures that result from modelled flow conditions. Note, however, that holding systems

are not recommended if one aims at a proper study of the natural frequency of the monopile under the scour phenomenon, as studied in [105].

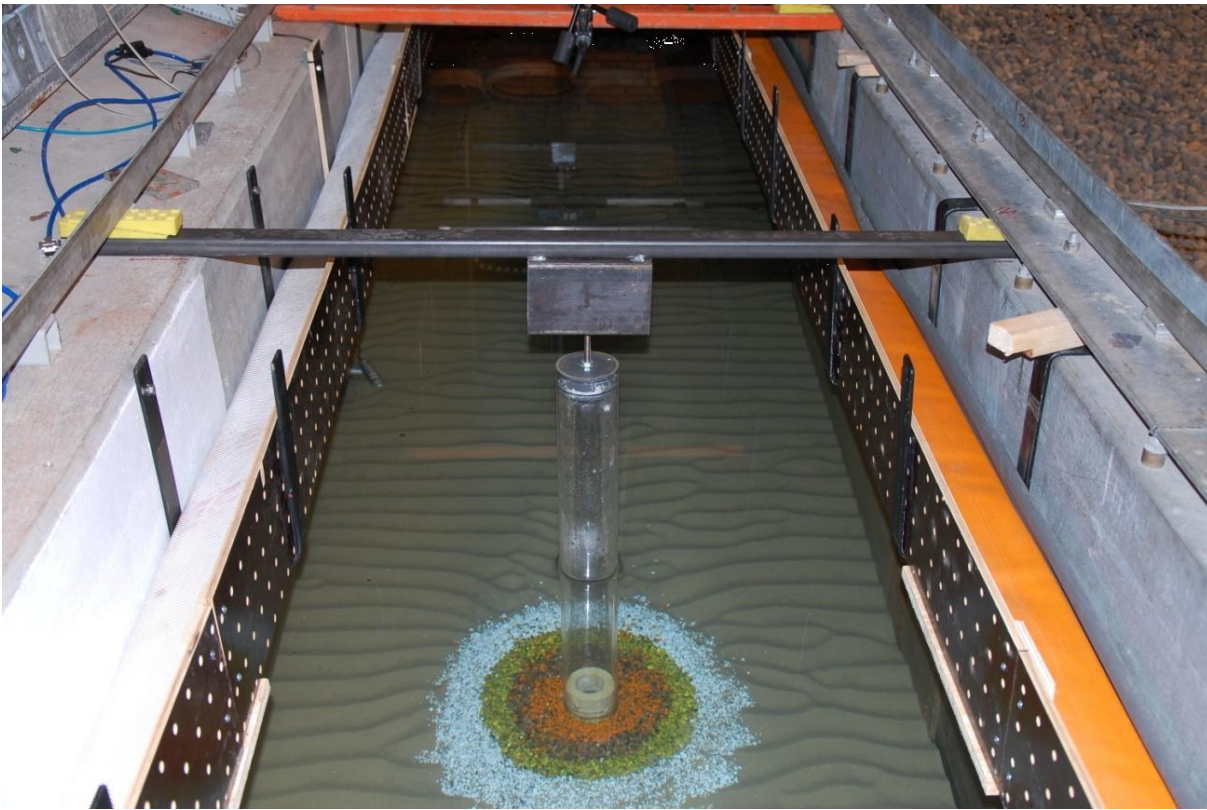


Figure 4.6 – Scour protection system with monopile installed with the holding system after a waves and steady current loading.

Figure 4.6 also shows the scour protection system, which already presents some deformations caused by the wave train with a current superimposed during the test. The current combined with waves tended to generate the rippled pattern in the sand bed, which were monitored with a 3D laser profiler, to ensure that no abnormal values were obtained. Note that live-bed regime may, eventually, lead to non-scaled ripples, which affect the accuracy of the scour and accretion results occurring on top of the scour protection. This effect occurs because non-scaled ripples have a direct influence on the boundary layer and generated turbulence.

In order to avoid unscaled initial ripples, the sand bed was flattened, as typically applied in experimental scour works, e.g. [83]. Moreover, during tests in live-bed regime, as in this case, ripples will always be formed when waves are present. It is of course important to recognise that in laboratory tests with quartz sand the ripples may be large compared with the scale model installation, eventually producing an unrealistic bed friction regime. However, as noted in [49], the effect of ripples on the scour development, and inherent boundary layer, is often found to be negligible. According to [49], this is because the enhanced bed shear stress and turbulence levels adjacent to the monopile structure cause the ripples to be locally washed out, whilst elsewhere, ripples can be treated as a periodic “noise” around the mean bed elevation. A possibility to reduce the ripples’ effects would be to use coarser material at the sand bed, although this does also affect the bed roughness at the model. In this case, the sand-bed material has a mean diameter that is very small, i.e. $d_s=0.170$ mm is much smaller than the pile diameter. According to the mentioned research and [63], if $d_s < D_p/25$, the influence of the sediment grading and of the formed ripples may be considered negligible. However, it is also

important to note that, for large sand-bed sediments (which is not the case of the present research), the ripples' effects must be taken into account. Furthermore, [1, 30] and [32] note that the bed roughness is considered as $k_s=2.5D_{50}$ (bed roughness without ripples) and although the original research states that this must be adapted to consider the ripples' height (if ripples are present and provided that they cannot be neglected), the original work solely considers the aforementioned bed roughness, i.e. $2.5D_{50}$. This is also considered in the present work, since the laboratory tests performed are an extension of the ones considered in [1, 30] and [32] and the sediment diameter is lower than $D_p/25$. This is an interesting aspect to be addressed, but due to its complexity, the possible effects on the bed boundary layer and turbulence levels should be the aim of further research.

The present test programme consisted of two phases: a phase in which the flume is prepared and the equipment is calibrated; and a phase in which the scour protection tests are performed. During calibration, the wave heights and periods were registered and compared to the input provided to the wave generator. For this, at least one wave gauge was required, although a minimum of 3 wave gauges were distributed along the wave flume, to evaluate the possible distortions of the wave field.

The goal of the experimental measurements was to determine the position of the protection elements in time, and gather data on the behaviour of the current around the monopile foundation. In order to achieve the first goal, the movements of the sand bed were measured by means of a laser profiler, which scanned the area around the monopile foundation and generated a 3D rendering of this zone. This is described with further detail in the following sections. The profiler images gave a thorough overview of the bed evolution, yet they did not provide insight into the behaviour of the different elements of the scour protection. The best way to facilitate this was by taking photographs of the bed before and after the experiment. Photographic records taken during the tests, i.e. after each wave train, are useful to determine the visual damage level of the scour protection. However, taking photographs during the experiment proved to be difficult, as the flume was not transparent and the influence of waves and optical breaking suggested against taking photographs from a top-down perspective. Waves and optical breaking also make it difficult, if not impossible, to register the time evolution of the bed by making videos. Therefore, an underwater camera was also used, to follow the dynamic behaviour of the scour protection during the model tests from one fixed angle. From these movies, pictures and short films could be extracted at the desired instants in time.

Gathering data on the general flow conditions during the experiment was essential. Wave conditions were known *a priori* (and perfect replication of these conditions in the flume was ensured during calibration), while the mean flow velocity was registered by using an ADV in a zone that was undisturbed by the monopile foundation (i.e. far enough upstream of the foundation, as recommended in [163]).

An ADV measures the three velocity components in one point, so by positioning it at a distance from the bed that is 40% of the water depth, the mean velocity of the current can be determined [49]. Although its influence on the flow field near the monopile foundation was negligible when positioned far enough upstream of it, it is still advisable not fully align the ADV with the foundation, but rather position it to the side of the flume. Naturally, enough distance between the flume walls and the ADV must remain to avoid the wall effects on the measurements.

The following equipment was used during the scour protection tests:

- 3 wave gauges;
- Laser profiler;
- Photo camera (to take overhead pictures);
- Submersible camera;

- Video camera;
- 3 ADV for calibration and 1 ADV during the tests.

The monopile was placed 3.39 m behind the beginning of the sand bed. The ADV was placed 2 m in front of the monopile. The wave gauges were placed in front of the location of the monopile. The regular video camera and the submersible video camera were placed 1 m behind the monopile and were continuously filming the scour protection during testing.

The model of the monopile was a clear perspex cylinder with 0.10 m of external diameter (D_p), replicating a 5 m diameter in the prototype, as mentioned before. Using this diameter avoided the blockage effect by keeping the ratio of D_p to flume's width below 1/6, as recommended in [49] and [163]. The flume was equipped with an absorbing beach at the downstream side of the monopile, in order to minimize wave reflections and disturbances caused by the pumping installation [102] (see also section 4.2.3.1).

4.2.3.1 Hydrodynamic model conditions

The scour tests were performed with fresh water temperatures between 9°C and 13°C. Water density $\rho_w=1000 \text{ kg/m}^3$ was used, thus the mean diameter of stones at the scour protection was scaled to account for the difference between the fresh water density and the sea water density ($\rho_w=1025 \text{ kg/m}^3$).

The tests were conducted with combined uni-directional irregular waves and current. Due to the non-reversible configuration of the wave flume, it was not possible to test waves in an opposing current, which represents a shortcoming of the present test programme, since the approach presented by [1] and [32] covers both combinations. Table 4.3 provides the hydrodynamic conditions at the prototype and the model scales. Depending on the water depth, the test series are designated as s1, s2 and s3 for the 1st, the 2nd and the 3rd test series from Table 4.2, respectively.

Table 4.3 – Prototype and model hydrodynamic conditions.

| Target prototype values | | | | | | |
|--|-------|-------------|--------------|-----------|-----------|--------------|
| Test series | d [m] | U_c [m/s] | H_{m0} [m] | T_p [s] | D_p [m] | d/ D_p [-] |
| s1 | 12 | 1.3 | 4.5 | 10.7 | 5 | 2.4 |
| s2 | 18 | 1.6 | 7.5 | 11.3 | 5 | 3.6 |
| s3 | 25 | 1.3 | 8.0 | 11.0 | 5 | 5.0 |
| Target model values (1/50 scale – Froude similitude) | | | | | | |
| Test series | d [m] | U_c [m/s] | H_{m0} [m] | T_p [s] | D_p [m] | d/ D_p [-] |
| s1 | 0.24 | 0.18 | 0.09 | 1.51 | 0.1 | 2.4 |
| s2 | 0.36 | 0.23 | 0.15 | 1.60 | 0.1 | 3.6 |
| s3 | 0.50 | 0.18 | 0.16 | 1.56 | 0.1 | 5.0 |

The currents were calibrated without the monopile present, at a height of 0.4d above the sand bed, as previously mentioned and shown in Figure 4.7. In this figure, the depth-averaged current velocity is

defined as U_c , and n_f and n_a correspond to the thicknesses of the filter layer and the armour layer, respectively. Before the wave generation, the currents were run for about 10 min to achieve steady flow conditions.

The wave trains were generated according to the JONSWAP spectrum, with a peak enhancement factor $\gamma=3.3$. The spectral significant wave heights (H_{m0}) were defined at the monopile location with the steady current, but without the monopile present. The wave reflection was limited to 18% according to the 3-point wave reflection analysis described by [176]. The scour tests had a duration between 1000 and 5000 waves (with one test performed for 7000 waves to analyse the effect of long storm durations).

The damage numbers analysed in this work correspond mainly to those obtained after 3000 waves. This option was made to avoid conversion bias between the 5000 waves in the MARINET tests to the reference values of 3000 waves used in the majority of the tests presented by [32] and [148]. Moreover, test s3_001 was excluded due to the lack of information collected regarding the damage level classification, a key aspect for the present analysis.

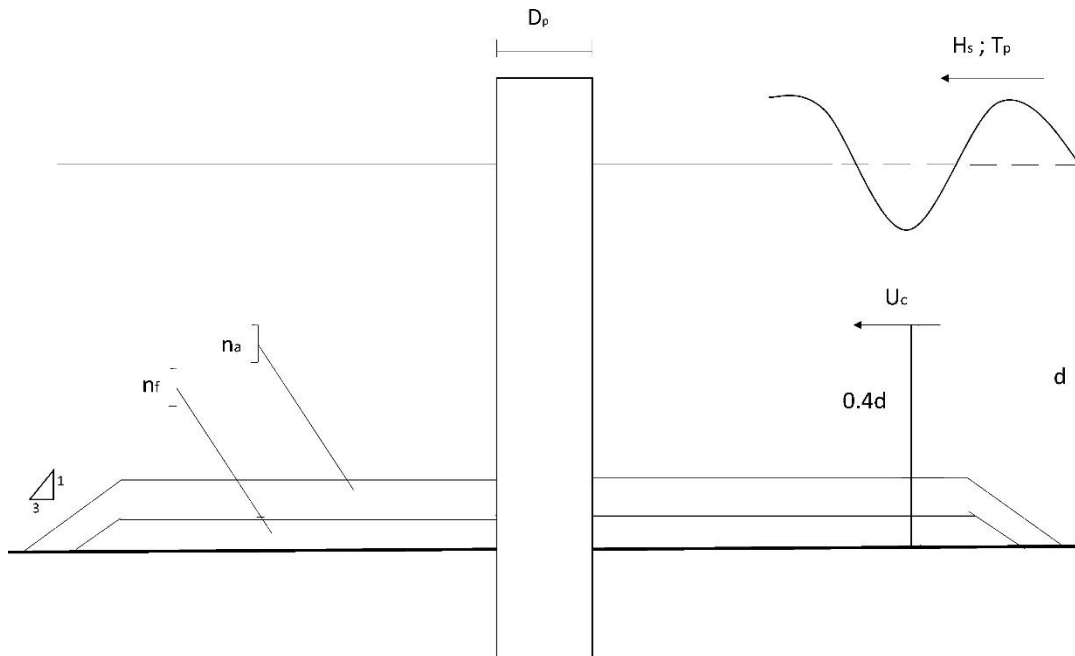


Figure 4.7 – Hydrodynamic conditions at the model with depth-averaged current velocity measured at 40% of the water depth from the bottom.

The tests were performed with the following sequence: step 1) run 1000 waves; step 2) collect the Digital Terrain Model (EPro Software [177] and laser profiler), to measure the damage level after 1000 waves (S_{3D1000}) and take photographic records; step 3) run 2000 waves; step 4) repeat step 2 to obtain S_{3D3000} ; step 5) run 2000 waves; step 6) repeat step 2 to obtain S_{3D5000} . Note that for a peak period $T_p=1.52$ s, 1000, 3000 and 5000 waves correspond to storm durations of 2h57min, 8h57min and 14h50min, respectively, in prototype values [26]. Figure 4.8 shows a test in a wave-current flume, with the protected perspex model of the monopile under waves and current.



Figure 4.8 – Testing in the wave-current flume with the protected monopile present [102].

4.2.3.2 Scour protection model

The model of the scour protection was also geometrically scaled, unlike the sand-bed sediments. The present research concerned a typical scour protection, which is made out of a filter layer and an armour layer, as shown in Figure 4.7. In a similar way to the tests presented in [1, 30] and in [32], no single-layer scour protections were used, i.e. protections for which the same rock material acts as both the armour and the filter layers.

The armour layer was placed in four concentric rings (width equal to the pile radius) with different colours. In this way, it was possible to visually observe where the stones moved to during the test. For each test, the same colour code was used: the orange stones were placed in the ring closest to the monopile; the uncoloured stones were placed in the second ring; the yellow stones were placed in the third ring; and the white stones were placed in the outer ring. The last ring (white ring) was extended under a slope of 1/3, in order to prevent/minimize edge scour, whilst covering the edge of the filter layer. Figure 4.9 shows the scour protection and its concentric coloured rings, without the monopile present.

The scour protection had radial extent, w_a , equal to 5 times the pile diameter, i.e. $5D_p$, plus the extra material needed to obtain the 1/3 edge slopes. The granular filter layer was placed on top of the sand bed, as shown in Figure 4.10. This layer consisted of small stone material with a mean diameter of 0.991 mm (roughly 0.05 m in the prototype) and had a thickness of 10 mm (0.5 m in the prototype). Several thicknesses of the armour layer were tested, ranging between $2D_{50}$ and $8D_{50}$. Note that this range improves the one reported in [32], which only tested $2.5D_{n50}$ and $3D_{n50}$. The model characteristics of the scour protection are presented in

Table 4.4 and the top view of the scour protection and its radial extent are provided in Figure 4.11.

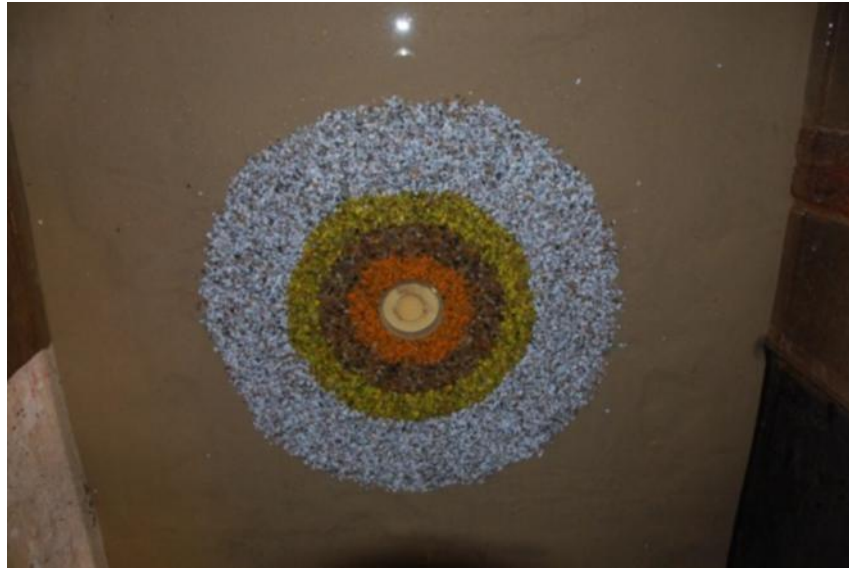


Figure 4.9 - Concentric configuration of the coloured rings around the monopile base, without the monopile.



Figure 4.10 – Granular filter layer being placed beneath the armour layer stones.

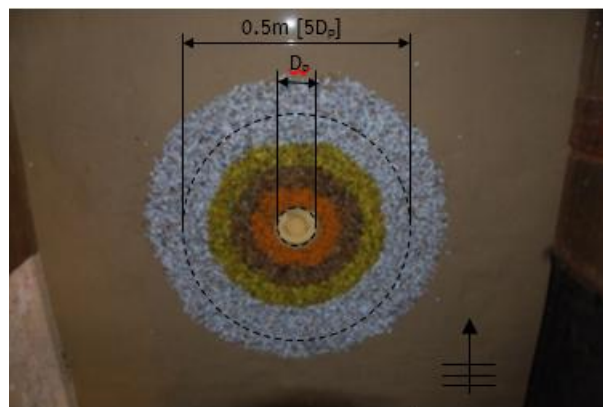


Figure 4.11 – Top-view of the scour protection and radial extent of the scour protection model.

Table 4.4 – Characteristics of the scour protection rock material (values at model and prototype).

| Material | $D_{50,model}$ [mm] | $D_{n50,model}$ [mm] | $D_{50,prototype}$ [m] | $D_{n50,prototype}$ [m] | ρ_s [kg/m ³] |
|----------|------------------------|-------------------------|---------------------------|----------------------------|----------------------------------|
| Armour 1 | 7.500 | 6.300 | 0.375 | 0.315 | 2650 |
| Armour 2 | 6.015 | 5.053 | 0.301 | 0.253 | 2564 |
| Armour 3 | 4.135 | 3.473 | 0.207 | 0.174 | 2597 |
| Armour 4 | 2.686 | 2.260 | 0.134 | 0.113 | 2564 |
| Filter | 0.991 | 0.832 | 0.050 | 0.042 | 2632 |

4.2.3.3 Measurements and equipment

Velocity profiles of the current flow were measured with a Nortek Vectrinoplus, 2 m upstream of the pile, with an Acoustic Doppler Velocimeter (ADV), at a height of 0.4d above the sand bed. The device had an accuracy of $\pm 1\%$, i.e. ± 1 mm/s. The waves were measured 1.5 m upstream of the monopile, with 3 wave gauges, with an error of ± 0.4 mm. The sampling frequency for the ADV and the wave gauges was set to 40 Hz (selected as the optimum combination between both devices). Wavelab software [177] was used for data acquisition. The damage number was measured by means of the EPro Software [177], which was used to remotely control the 3D laser profiler. The profiles, i.e. the digital terrain models (DTM), enabled the erosion volume (V_e) to be measured in order to obtain the values of the damage number, as in Eq. (3.55). The laser profiler is a non-contact device, able to take measurements under water, hence avoiding the need to empty the wave flume between wave trains. This equipment and its use are fully described in [178]. The measurement grid used for the 3D profiles was set to 5 mm by 5 mm, which corresponded to a resolution of 250 mm at prototype scale. The centre of the monopile was used to set the XY reference of the profiles. The measurement accuracy was 2 mm, which was considered acceptable, since this is lower than the smallest rock size used (

Table 4.4 – Armour 4). Figure 4.12 shows an example of the DTM taken with the profiler and the corresponding photograph of the eroded protection.

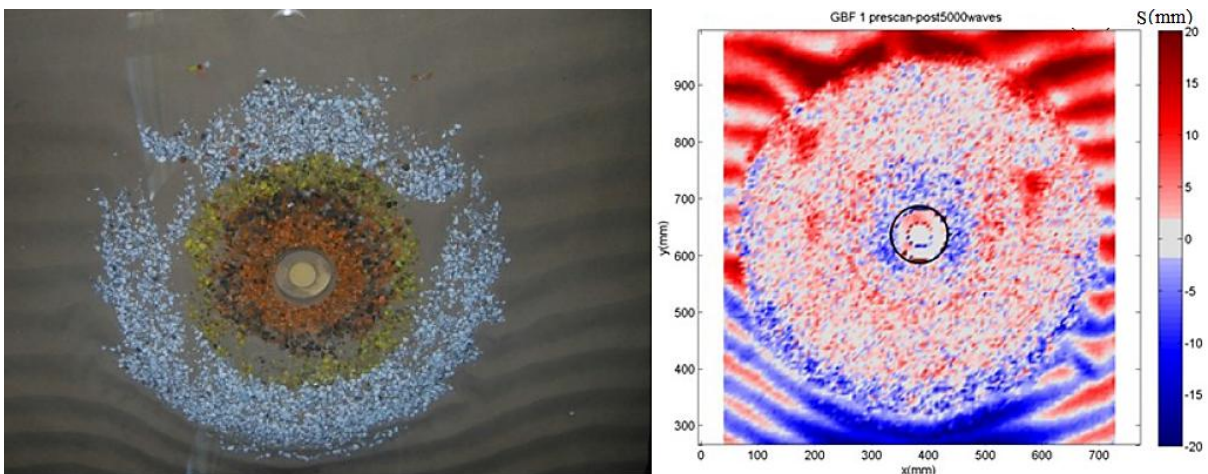


Figure 4.12 – Example of an eroded scour protection and respective digital terrain model. Flow direction from bottom to top.

The colour scale is set to give blue values for scour and red values for accretion (deposition). Visual scour assessment showed good agreement with the difference plots between the pre- and post-test profiles, both for scour holes and sand accumulation on top of the scour protection. The scouring was also evaluated through visual observation, from inspection of overhead pictures taken before, between and after each test.

4.2.3.4 Range of test conditions

As noted previously, the present research, also published in [151], is based on the MARINET data, which were also further analysed in [26] and [102]. The MARINET data extend the range of test conditions of the dynamic approach provided in [32]. A similar extended validation was also provided by [148]. These conditions are summarized in Table 4.5.

Despite the extended validation performed with the present research, some shortcomings exist in this set of scour tests. Firstly, due to the laboratory facilities at the University of Aalborg, it was not possible to test scour under waves in an opposing current. This is an important aspect, since so far, it is not clearly reported in the literature which case leads to the largest scour induced-damage. However, despite not concerning damage on protections, the works by [24] and [179], focused on scour depth evolution, presented physical model results that suggest that waves in an opposing current lead to smaller scour depths than uni-directional combined flows. In [179] the suspended sediment flux and bedload transport decreased as the angle between waves and current increased.

The literature shows a lack of results for scour protection damage in this matter. Nevertheless, it is possible to note that for waves in a following current, the predictive formula proposed by [32], i.e. Eq. (3.57), only considers the second term when $a_1=1$, i.e. for waves in an opposing current in Eq. (3.61). Also, coefficient a_4 typically achieves larger values for waves in an opposing current than for waves in a following current.

Note that the Ursell number directly depends on a squared power of the wave length (L^2). Therefore, the value of a_4 will be larger than the unitary value obtained for waves in a following current. Hence, Eq. (3.57) provides larger damage numbers for waves in an opposing current, provided that the values of U_c are sufficiently large. This behaviour somehow contradicts the notions introduced by [24] and [179].

This behaviour somehow contradicts the notions introduced by [24] and [179]. [148] also noted that waves in an opposing current lead to larger damage numbers of the protection. However, no specific reason was pointed out as the cause of such remark. Further research should address this aspect with more detail. The present research is not suitable to draw significant conclusions on this matter. Moreover, as already mentioned, the formula only addresses $\phi=0^\circ$ or $\phi=180^\circ$; other angles of attack are not covered, but this is seen as a limitation of the approach itself, rather than a limitation of the tested conditions. Although not investigated in this work, a possible reason for larger damage numbers for waves in an opposing current compared with the uni-directional combined flow might be the larger turbulence levels.

The same scale is used for all tests, thus a direct comparison can be made regarding the range of model conditions tested. In terms of the significant wave height and the peak period, the present research does not address a different range of test conditions. Regarding the water depth, this study introduced two new values, $d=0.24$ m and $d=0.36$ m. These new cases are added to $d=0.5$ m, which was also used in this research and introduced in [148] too. The influence of the water depth on the accuracy of the predictive formula is analysed in further sections. Nevertheless, in a similar way to the flow direction,

the water depth also has an influence on the scour severity. However, such influence is yet to be fully understood. A key aspect regarding this influencing factor is related with the ratio of water depth to pile diameter.

Table 4.5 – Comparison of different sources target test conditions for dynamic scour protections.

| Variable | Symbol | Units | [32] | [148] | Present research and [26, 102, 151] | Overall |
|----------------------------------|---|----------------------|------------------------|------------------------|-------------------------------------|------------------------|
| Significant | | | | | | |
| Wave Height | H_{m0} | [m] | 0.05-0.168 | 0.06-0.16 | 0.08-0.144 | 0.05-0.168 |
| Peak Period | T_p | [s] | 1.13-1.7 | 1.42-2.12 | 1.52-1.55 | 1.13-2.12 |
| Current Velocity | U_c | [m/s] | 0-0.30 | 0-0.31 | 0.150-0.226 | 0-0.31 |
| Current Direction | ϕ | [-] | Following; Opposing | Following; Opposing | Following | Following; Opposing |
| Water Depth | d | [m] | 0.2-0.4 | 0.2-0.5 | 0.24-0.5 | 0.2-0.5 |
| Pile Diameter | D_p | [m] | 0.1 | 0.05-0.125 | 0.1 | 0.05-0.125 |
| Mean Stone Diameter | D_{50} | [mm] | 4.1-8.5 | 4.1-11.9 | 2.7-7.5 | 2.7-11.9 |
| Mass density | ρ_s | [Kg/m ³] | 2650-3200 | 2650 | 2564-2650 | 2564-3200 |
| Armour Thickness | n_a | [m] | 0.0086-0.0179 | 0.0086-0.025 | 0.007-0.0252 | 0.007-0.0252 |
| Keulegan-Carpenter Number | KC | [-] | 3.4-6.3 | 0.8-3.6 | 3.4-7.6 | 0.8-7.6 |
| Pile Reynolds Number | Re_p | [-] | 15000-43000 | 6900-23500 | 11220-16780 | 6900-43000 |
| Scale | Geometric scale of 1/50 (Froude similitude) | | | | | |

Considering an unprotected slender monopile foundation under a steady current, when the water depth (d) is too large compared to the pile diameter (D_p), i.e. $d \gg D_p$, the scour depth becomes less dependent on d and starts to increase with increasing pile diameters. In this situation, it can be stated that the horseshoe vortex mechanism and the oncoming flow pressure are mainly associated to the pile diameter [83]. If d is much smaller than D_p , i.e. $d \ll D_p$, the opposite situation occurs: the scour depth increases with increasing water depths and it becomes less dependent on the pile diameter [83]. In the

third case, the scour depth is strongly dependent on both parameters. For lower values of the water depth, the horseshoe vortex might be affected by the surface roller, which has a different rolling direction than the one from the horseshoe vortex. If this happens, the horseshoe vortex loses erosion power and the scour depth decreases.

Taking into account that the bottom friction velocity is obtained as $u^*=(gdi)^{0.5}$, if d increases, the friction velocity increases, which means that the bed shear stress will present larger values, leading to larger scour depths. Since i stands for the slope of the sand bed, for flat horizontal sand beds, this formula is not directly applicable.

Moreover, with combined waves and current, the water depth influence on the horseshoe vortex and other scour mechanisms may become less clear, because the wave orbital bottom velocity also influences the downcoming flow and the scour mechanisms. Still, according to [49], it is generally agreed that for $d/D_p > 3$ the effects of the water depth on the scour depth are negligible. Also, despite the fact that the scour depth is often reduced for $d/D_p < 3$, the comprehensive review presented by [49] states that this reduction factor is not of practical significance for most piled structures in the marine environment, as typically $d \gg D_p$.

Furthermore, in terms of the scour phenomenon, it is commonly considered that for $d/D_p \geq 5$, a deep water situation is faced. The present range of test conditions provides an interesting dataset for shallower water depths $d/D_p = 2.4$ (series s1, $d/D_p < 3$), intermediate water depths $d/D_p = 3.6$ (series s2, d/D_p between 3 and 5), and deeper water depths $d/D_p = 5$ (series s3). In this sense, it is expected that the influence of the water depth is less evident for series s3 and more evident for series s1.

Based on the MARINET data, it was further concluded that the damage number of the scour protection increased for decreasing water depths, as mentioned in [11] and [175]. Despite this observation, the accuracy of the predictive formula under different water depths was not systematically addressed yet. This aspect is analysed in further sections. It can also be noted that in comparison with the physical model studies presented by [32] and [148], the present study adds a set of scour protection tests concerning $3 < d/D_p < 5$, which was not presented before.

Regarding the pile diameter, the present setup does not provide any new input. The predictive formula proposed for the damage number, i.e. Eq. (3.67), does not depend on the pile diameter, at least in a direct manner. This is important, as typical scour predictive formulae, e.g. [63] or [75], suggest that scour severity increases for increasing pile diameters. As noted previously, this dependence becomes more evident for increasing water depths. Nevertheless, the research performed by [148] led to the conclusion that the damage number is affected by the pile diameter.

However, the authors also noted that the damage development is not directly related to the pile diameter but to the Keulegan-Carpenter (KC) number and the pile Reynolds number (Re_p). Despite the reduced number of tests performed in [148], only 5, the results suggested that for small pile diameters, the KC number determined the damage development, whilst for large pile diameters, the Re_p number was the dominant parameter. This aspect is not addressed with the present range of test conditions.

In scour and scour protection tests, the mean stone diameter is often a result of the available material for the physical model, even though there might be a need for a correct scaling of the stones. Despite this fact, Table 4.5 shows that a minimum $D_{50} = 2.7$ mm in the model is added to the test conditions. Since dynamic scour protections lead to reductions of the stone diameter, testing small diameters is of great importance to analyse the extent of possible reductions without compromising the armour layer stability.

The stability of the scour protection is a result of a balance between the mean stone diameter and the armour thickness (n_a). The present set of tests also adds a new minimum value of $n_a=7$ mm in the model (0.35 m in the prototype). Such thickness is already very small compared to the ones found in practical cases, which are around 1 m, as shown in Table 3.8 (see also [59]). As discussed in section 3.7.2, the results obtained in [1] indicate that the influence of the armour thickness is limited for small damage numbers. However, for situations near failure, i.e. increasing damage numbers and large mobility of the stones, the armour thickness plays an important role in avoiding the exposure of the filter layer (when some of the stones are already displaced).

As it can be confirmed from the findings of [102] and [151], the armour layer thicknesses tested in the present setup range between 2 and 8 times the value of D_{50} . It should also be kept in mind that, for the same armour thickness, the damage number varies depending on the stone size and, possibly, on the uniformity parameter of the stones, as discussed in [32] and [103]. At the present state-of-the-art, it is important to note that the influence of the armour thickness is an aspect yet to be fully understood.

Finally, as mentioned before, the present setup uses a granular filter, which will also enable a more realistic discussion of the failure occurrence, as it corresponds to a more realistic representation of common prototype conditions compared with the use of a geotextile filter layer. The filter layer thickness applied in the MARINET tests is the same for all tested configurations, i.e. about 1 cm in the model (0.5 m in prototype conditions). However, it should also be noted that these

4.2.3.5 Scour protection tests and configurations

When referring to any test performed under the MARINET setup, the adopted designation corresponds to the number of the test series (s), as in Table 4.3, and the concurrent test number. For instance, test s2_005 refers to test number 5 from series 2 (performed with $d=0.36$ m).

As defined in the test programme presented in [26] (see also [175]), Table 4.6 depicts the configuration of the scour protection and the hydrodynamic conditions in each test, for which H_{m0} is obtained according to Eq. (3.54). Test s3_004 was the only test performed for 7000 waves and the spectral significant wave height was calculated in a similar manner.

The rationale for the test series with the reproduction of a statically stable design in a combined waves and current climate is based on the test results of [1, 32] and [148]. Such tests are comparable to those performed by the previous authors. The tests for the dynamically stable design result from smart choices on the rock size and armour layer thickness made during the test programme with the objective of getting the most out of it.

Basically, depending on the failure mechanisms observed in a previous test, one of the following three things would change in the next test, thus trying to optimise the previous configuration:

- (i) thicker armour layer if the filter became exposed;
- (ii) wider scour protection if failure started at the edges of the scour protection and;
- (iii) smaller stone size if no failure occurred at all.

During test s3_001, the paddle was stopped abruptly, generating a big wave. Some minutes before that, there was a breaking wave at the monopile. For both reasons, there are no measurements available for this test series and therefore it has been excluded from the present analysis.

Table 4.6 – Scour protection tests and configurations, with overall hydrodynamic conditions.

| Test-series | D_{50} [mm] | n_a [mm] | n_a [times D_{50}] | H_{m0} [m] | T_p [s] | d [m] | N [-] | U_c [m/s] | |
|-------------|------------------|---------------|-------------------------------|--------------|-----------|---------|---------|-------------|-------|
| s1 | 001 | 7.500 | 30.0 | 4 | 0.092 | 1.53 | 0.24 | 5000 | 0.161 |
| | 002 | 6.015 | 12.0 | 2 | 0.097 | 1.53 | 0.24 | 5000 | 0.147 |
| | 003 | 4.135 | 12.4 | 3 | 0.092 | 1.53 | 0.24 | 5000 | 0.178 |
| | 004 | 4.135 | 8.3 | 2 | 0.089 | 1.53 | 0.24 | 5000 | 0.185 |
| | 005 | 2.686 | 21.5 | 8 | 0.089 | 1.53 | 0.24 | 5000 | 0.182 |
| | 006 | 4.135 | 12.4 | 3 | 0.086 | 1.52 | 0.24 | 5000 | 0.186 |
| s2 | 001 | 7.500 | 15.0 | 2 | 0.140 | 1.52 | 0.36 | 5000 | 0.175 |
| | 002 | 6.015 | 12.0 | 2 | 0.129 | 1.52 | 0.36 | 5000 | 0.174 |
| | 003 | 4.135 | 12.4 | 3 | 0.129 | 1.52 | 0.36 | 5000 | 0.175 |
| | 004 | 4.135 | 16.5 | 4 | 0.130 | 1.52 | 0.36 | 5000 | 0.175 |
| | 005 | 2.686 | 21.5 | 8 | 0.134 | 1.52 | 0.36 | 5000 | 0.172 |
| | 006 | 4.135 | 16.5 | 4 | 0.111 | 1.52 | 0.36 | 5000 | 0.193 |
| s3 | 001 | 6.015 | 12.0 | 2 | 0.134 | 1.51 | 0.50 | 5000 | 0.190 |
| | 002 | 4.135 | 12.0 | 2 | 0.140 | 1.51 | 0.50 | 5000 | 0.226 |
| | 003 | 4.135 | 16.5 | 4 | 0.141 | 1.52 | 0.50 | 5000 | 0.220 |
| | 004 | 4.135 | 12.4 | 3 | 0.140 | 1.50 | 0.50 | 7000 | 0.221 |
| | 005 | 2.686 | 21.5 | 8 | 0.145 | 1.51 | 0.50 | 5000 | 0.211 |
| | 006 | 2.686 | 10.7 | 4 | 0.141 | 1.52 | 0.50 | 5000 | 0.220 |
| | 007 | 2.686 | 16.1 | 6 | 0.142 | 1.41 | 0.50 | 3000 | 0.219 |
| | 008 | 4.135 | 12.4 | 3 | 0.143 | 1.53 | 0.50 | 5000 | 0.222 |
| | 009 | 4.135 | 12.4 | 3 | 0.136 | 1.54 | 0.50 | 5000 | 0.181 |
| | 010 | 4.135 | 12.0 | 2 | 0.113 | 1.54 | 0.50 | 5000 | 0.181 |
| | 011 | 2.686 | 21.5 | 8 | 0.114 | 1.54 | 0.50 | 5000 | 0.179 |

4.2.4 Methodology of analysis

The methodology of analysis applied to the aforementioned data is similar to the one presented in [1] and [32], which is introduced in section 3.7.1.5. Here the procedure adopted to measure and predict the damage number of the scour protections from Table 4.6 is provided.

As performed during the OPTI-PILE project and in [1] and [32], the scour protection tests were visually analysed and classified according to 4 visual damage levels:

- **Damage level 1:** no movement of stones (except for initial stabilisation);
- **Damage level 2:** very limited movement of stones;
- **Damage level 3:** significant movement of stones, without failure of the protection;
- **Damage level 4:** failure of the protection.

These levels are illustrated in the photographic records in Figure 4.13. It is expected that the damage levels identified can be associated to both the predicted and the measured damage numbers. As discussed before [32, 151] and confirmed in the present study, this association might not be immediately clear. In dynamic scour protection systems, the failure criterion is often defined as a maximum exposed area of the filter layer [43]. In this study, it was considered that failure occurred when the area of exposed filter layer exceeded $4(D_{50})^2$, which corresponds to the removal of four stones in the armour layer.

Note that this is valid for scour protections with at least two layers. One may opt, for example, to use a single layer, for which the failure criterion must be adapted, because the single layer acts both as filter and as armour. In static scour protections, the design is purely based on the shear stress that defines the initiation of motion, whereas in dynamic protections, the performance can be specified in terms of the acceptable damage. This damage allows for dynamic reshaping of the scour protection whilst still providing a specified reduction in foundation scour depth and volume [102].

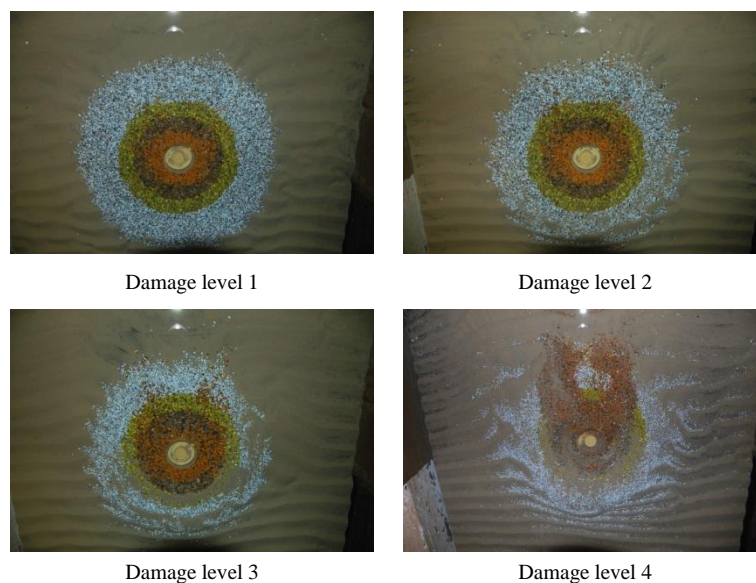


Figure 4.13 – Illustration of visual damage levels of tested scour protections [175]. Flow direction from bottom to top.

As mentioned before (section 4.2.3.3), a 3D laser profiler was used to obtain measured damage numbers ($S_{3D\text{measured}}$). For the analysis of the profiler measurements, only the area which is covered by the scour protection (ring with outer diameter of $5D_p$, inner diameter of D_p and a 1:3 slope) is considered. The scour protection is divided into sub-areas to quantify the damage [175].

The coloured rings of the model (Figure 4.11) are divided into different sub-areas. This division is done as shown in Figure 4.14, which is slightly different from the one employed in [1, 32] and [148], shown in Figure 3.26. The division made in Figure 4.14 enables the reference to each sub-area according to its ring number (R_i) and the radial sector (S_i), thus facilitating the comparison between

different profiles, i.e. different DTM. In this sense, the nomenclature R3S5 refers to the sub-area from ring number 3 and sector 5.

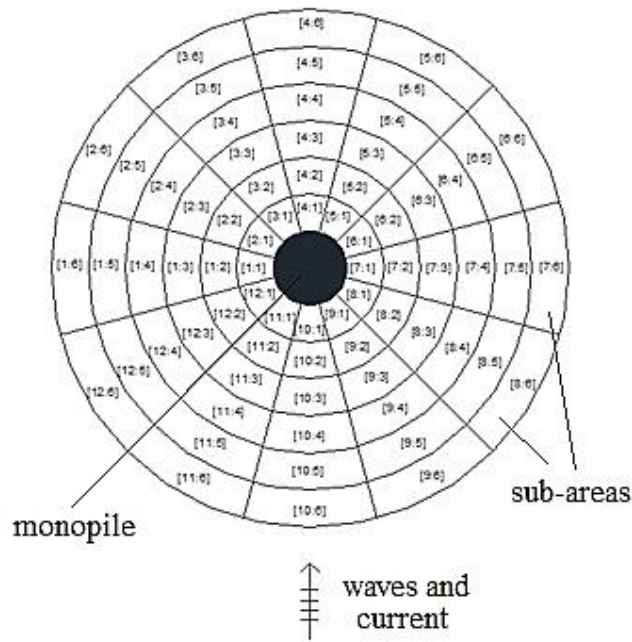


Figure 4.14 – Division of the scour protection into sub-areas (adapted from [175]).

The concept of damage was initially introduced by [128], which presented a two-dimensional damage number for breakwaters (S_b), which according to [128] cited in [1], it is obtained as in Eq. (4.1), where A_e is the eroded cross-sectional area of the profile.

$$S_b = \frac{A_e}{D_{n50}^2} \quad (4.1)$$

This implies that the damage S_b is equal to the number of squares, with side D_{n50} , that fit into A_e .

As in the present research the applied stones are small, another definition is used for the quantitative analysis of damage. The three-dimensional damage number S_{3D} is defined per sub-area as the ratio of eroded volume (V_e) to surface of the sub-area (A_{sub}) times the nominal stone diameter (D_{n50}) [175], Eq. (4.2).

$$S_{3D} = \frac{V_e}{D_{n50}^3} \quad (4.2)$$

with V_e the eroded volume, S_{3D} equals the number of cubes with side D_{n50} that fit into V_e . As the applied stones are small, another definition is used for the quantitative analysis of the damage. The three dimensional damage number S_{3Dsub} is defined per sub-area as the ratio of eroded volume V_e to the surface of the sub-area times the nominal stone diameter [175]:

$$S_{3Dsub} = \frac{V_e}{D_{n50} A_{sub}} = \frac{\Delta H A_{sub}}{D_{n50} A_{sub}} = \frac{\Delta H}{D_{n50}} \quad (4.3)$$

The damage S_{3Dsub} represents the average height that has disappeared over the considered sub-area, expressed as a function of D_{n50} . It is calculated for each sub-area (Figure 4.14) according to Eq. (4.3)

and the measured damage number $S_{3D\text{measured}}$ is defined as the highest damage obtained by considering all the sub-areas, as in Eq. (4.4), repeated from Eq. (3.56):

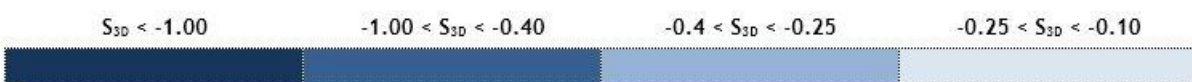
$$S_{3D\text{measured}} = \max_{i=1\text{to}\#\text{sub-areas}} (S_{3D\text{sub},i}) \quad (4.4)$$

An important aspect of the present methodology of analysis lies in the definition of the sub-areas used to measure the average eroded height at the scour protection (ΔH), which is different from the one used in the previous studies. In [1, 32] the sub-areas are equal to the pile’s cross-sectional area, whereas in the Marinet setup the sub-areas vary depending on the ring and sector on which the sub-area is located. Note that the areas of the outer rings in Figure 4.14 are larger than the ones near the pile, but the number of sectors remains the same. Since the eroded height is being evaluated in different sub-areas, differences might be expected when comparing the present results with the ones obtained in [1, 32]. Moreover, when the eroded height is being averaged per sub-area and the Eq. (4.4) is used as a representative measure of the protection’s damage, it becomes difficult to understand if several adjacent sub-areas are displaying considerably large values of S_{3D} close to each other. Note that if a protection has several local maxima in adjacent sectors or at the sectors’ intersection (e.g. say $S_{3D} > 1$) it might be more prone to have a filter exposure than, for example, a protection that presents two sub-areas with large values of S_{3D} but that are distant from each other.

This shortcoming of the aforementioned measurement procedure may contribute to the existence of scour protections, which under the same measured damage number can be classified as a failure or as dynamically stable configuration. Albeit not studied in this dissertation, it should be recognised that further research is required to quantify the influence of this aspect in the results obtained and the comparisons between these data and other datasets. In the present thesis it is important to note that the aforementioned procedure was used to analyse the S_{3D} per sub-area. However, an exception occurs for the overall damage numbers provided in Table 4.16 (in section 4.2.6.3), which results from the data provided to the present research by Ghent University under the MARINET proposal 61, which considers equal sub-areas as in [1, 32].

In the present study, when analysing the damage number of each sub-area and the corresponding erosion or accretion of sediments, it has been assumed that the negative values of S_{3D} correspond to erosion, whilst positive values correspond to sediment accretion (Figure 4.15). However, one should not confuse this referential with the one adopted in further analysis concerning the overall damage number of the protection, for which only positive values are used, which represent erosion, namely, when discussing the limits of dynamic stability and the comparison with the stability parameter from the OPTI-PILE project. This choice was made for the sake of simplicity when analysing the overall $S_{3D\text{measured}}$ of the scour protection.

Erosion:



Accretion:



Figure 4.15 – Colour code used to analyse the dynamic behaviour of the scour protections [175].

Finally, the methodology of analysis of the present thesis is mainly based on comparisons between the measured ($S_{3D\text{measured}}$) and the predicted ($S_{3D\text{predicted}}$) damage numbers. This is performed since a deep knowledge on the accuracy of the predictive formula is required before introducing the reliability analysis of dynamic scour protections, which is presented in following chapters. As introduced in section 3.7.1.5, the value of $S_{3D\text{predicted}}$ is obtained according to Eq. (3.57).

4.2.5 Discussion of scale and model effects of the MARINET proposal 61

As introduced in section 3.9, some model and scale effects are inherent to the physical models used for scour research. It is not always possible to mitigate them completely and sometimes it is very difficult to assess the extent of their influence on the results in the absence of a 1/1 representation between the model and the prototype. In this section the potential effects of the model and the research programme are discussed and identified.

Firstly, when superimposing the waves and the steady current, a model effect may arise from the onset of current, which tends to generate a current-induced wave. To minimize the possible effects of at current-induced wave, the steady current was slowly started. Each pump was started at a different time until the four pumps were on, thus leading to the current target velocity (0.18 m/s at 0.4d). When shutting down the pumps, the inverse procedure was applied to avoid the abrupt stoppage of the flow. When generating waves in a laboratory flume a standing wave might be present, due to the existence of bounded long waves and eventual differences in the absorption characteristics of the absorbing beach. Regarding the side wall effects, [1] states that they can be disregarded when the waves are being measured at the monopile location, which was also performed in the present tests. However, due to the location of the pile in the center of the flume, possible blockage effects may occur if the pile diameter is large enough. Blockage effects may lead to an unreal constriction of the flow, increasing local velocities at the bottom, thus unrealistically increasing the amplified bed shear stress. This may lead to overestimation of the scour-induced damage at the protection. To avoid blockage effects, [49] and [166] recommend that the ratio of pile diameter to flume's width is kept below 1/6, i.e. 0.167. The present model was built with a ratio of 0.1/1.2, i.e. 0.083. This ratio compares with 1/10 used in [1, 32] and [148]. Also, the "throats" used to cover the pipes at the outlet box section (Figure 4.3) presented a slightly higher ratio of 1/6. Despite being near the limit suggested by [49] and [166], this influence is registered considerably upstream of the monopile section. However, the wave gauges monitored the waves at the monopile section and no abnormal values were identified in the tests (for the wave height across the flume's length and width).

A gentle upward approach slope of 1/90 was used, as discussed in section 4.2.3. This value compares to the slope of 1/20 used in [1] and [32]. These changes in the bathymetry of the setup influence the wave height. However, as the wave characteristics are monitored at the location of the monopile, this does not influence the outcome of the research. Nevertheless, the 1/90 slope was used to make a gentle transition between the upstream section of the flume and the sediment box with a flat sand bed. The waves reflection is also a common problem when dealing with wave generation at a laboratory model. In the present case, the incident wave height is monitored and the consequent analysis takes into consideration the actual value at the monopile section, despite the possible departures from the target hydrodynamic values discussed in sections 4.2.2 and 4.2.3.1. As mentioned previously (see section 4.2.3.1), wave reflection was limited to 18% according to the 3-point wave reflection analysis described by [176]. This compares to a 15% wave reflection reported in [1] and [32]. For the present setup, the mentioned reflection can be considered negligible [163].

In this model, no artificial sediment feeding was present during the tests. The sandbox was made large enough to avoid influences of the deficit on sediment supply. The sediment in suspension was also transported by the pumps and some sediment rested at the upward slope. However, during the tests, it was not possible to assess the amount of sediment supply eventually provided by the pumps. Still, no major scour holes were encountered at the interface of the upward slope and the bedding of the sediment box. When placing the stones in the armour layer, it was not possible to accurately place them with the flume filled with water, which would correspond to the most realistic situation at prototype scale. Therefore, the scour protection model was built with saturated sand, but with the flume drained until the sand-bed level. A model effect that arises from this procedure, typically adopted in scour tests (e.g. [49] and [157]), is that some protection stones might be uplifted and dragged downstream when the flume is being filled. Therefore, in order to avoid the overestimation of the damage caused by the stones displaced prior to the actual scour test, the initial profiles were taken with the 3D laser profiler after the flume being filled. These initial displacements were not considered for damage quantification. This problem was also reported in [1] and [32], which have applied the same procedure as the one adopted in the present research. Future research on this aspect should be performed, eventually, by placing the scour protection filter and rock material with geometrically modelled pipes that could represent the fall-pipe vessel installation. Then the damage obtained could be compared with the one for the same scour protection placed with a drained flume. The research presented in this programme did not address this potential model effect. Also note that for an even more realistic representation, the scour protection should be placed under modelled normal sea-state conditions, since in the prototype one tries to predict these conditions to define the installation time/weather window.

The scale effects on the bed boundary layer can also be present. It needs to be ensured that a rough boundary layer is obtained in all circumstances, i.e. in each test. One has used Eq. (3.73), as in [52], and Eqs. (3.76) and (3.77), as in [57], to estimate the minimum mean stone diameter (D_{50}) that ensures the rough boundary layer for the target conditions presented in Table 4.3. It has been concluded that Eq. (3.73) leads to a minimum value of 0.042 mm, whilst Eqs. (3.76) and (3.77) lead to a minimum diameter of 1.2 mm. Since all tested stones are above these values, the requirement is fulfilled for all tests. Nevertheless, since scour protection stones are geometrically scaled, the bed boundary layer on top of the protection would not be expected to be considerably affected (see section 4.2.3). This is not the case for the sediments of the sand bed, for which the scaling procedure is not performed to avoid unreal cohesive properties of the scaled material. Another aspect to be mentioned regarding the sand-bed sediments, is the ripples' formation. This was already discussed in section 4.2.3, and based on the considerations made and the guidance given by [49], the present setup enables the minimization of the unscaled ripples' effects, thus the bed roughness k_s is used as $2.5D_{50}$ throughout this research.

The influence of the pile Reynolds number can be reflected mainly on the vortex shedding and the viscous effects. In section 3.9, it was seen that the influence on the vortex shedding can be disregarded if $Re_p > 2.5 \times 10^5$. Table 4.5 shows that this physical model study was performed for a Re_p ranging from 1.1×10^4 to 1.7×10^4 . Therefore, a different flow-shedding regime exists in the model and in the prototype situation. This problem is also common to the studies performed by [32] and [148]. In the model, a laminar boundary layer exists, whilst the one from the prototype is a turbulent one. [75] identified this problem as well, but without presenting further information on the consequences for the scour protection [1]. Still, the research conducted by [75] concluded that for small KC numbers, there is a small effect of Re_p on the vortex shedding regime. This is assumed in [32], which presents a maximum value of $KC=6.3$, which compares to a maximum of 7.6 used in this research. Therefore, the results of the present research may be considered comparable with the aforementioned research, as both of them present small KC numbers, according to [75]. Moreover, the limit $Re \geq 1 \times 10^4$ proposed by

[163] in order to disregard viscous effects is fulfilled. Note, however, that the differences in Reynolds number, between the prototype and the model, is also expected to affect the pressure gradients at the filter layer, which contributes to an influence of the scale effects in the final results. The present research is more focused on the behaviour of the armour layer for which the flow-shedding regime is indeed important. Nevertheless, the effects that arise from the behaviour of the filter layer and the pore pressure inside the protection remain to be quantified. Further research on the inherent scale effects is required, since this lies outside the focus of the present research. Finally, regarding the pile roughness, the perspex monopile foundation has a smoother surface than the one expected in prototype foundations. Furthermore, fouling occurrence is common in offshore environments, which considerably increases the pile roughness near the water level. This has not been taken into account, but influences on the vortex shedding regime arising from fouling should be expected at the prototype. As a guidance for the future research of scale effects in scour protection tests, it is important to mention that the literature shows a reduced number of studies with large scale physical models, as close as possible to 1 to 1 geometric scale. Using new physical models at larger scales than the commonly used 1 to 100 or 1 to 50, will contribute to a clarification of this aspect in the results obtained.

4.2.6 Analysis and discussion of results from MARINET proposal 61

The present section provides and discusses the results obtained from the experimental programme developed under the MARINET proposal 61. Since this research was included in a wider research programme, which concerns the joint work with other institutions and researchers (see [175]), whenever analysis of results under the responsibility of others is performed, the referred work is cited. However, note that the discussion of those results is an original part of the research hereby presented.

4.2.6.1 Measured conditions

Table 4.7 provides the measured conditions after each irregular wave train according to Eq. (3.24). Test s3_007 was only performed until 3000 waves because failure of the protection occurred. As mentioned before, test s3_001 was not analysed in terms of the damage number since there was an abrupt stoppage of the paddle and a breaking wave occurred prior to that event. Test s3_004 was performed up to 7000 waves to analyse if the dynamic scour protection developed for 5000 waves remained stable at the end of a new wave train of 2000 waves.

Experimental Study on Dynamic Scour Protections

Table 4.7 – Measured hydrodynamic conditions for scour protection tests.

| Series | Test | | | | | 1000 waves | | | | | 3000 waves | | | | | 5000 waves | | | | | 7000 waves | | | | |
|----------|------------|------|-----------------|-----------------------|----------------------------------|------------|-----------------|----------------|--------------------|----------------|------------|-----------------|----------------|--------------------|----------------|------------|-----------------|----------------|--------------------|----------------|------------|-----------------|----------------|--------------------|----------------|
| | | d | D ₅₀ | na | D ₈₅ /D ₁₅ | N | H _{m0} | T _p | T _{m-1,0} | U _c | N | H _{m0} | T _p | T _{m-1,0} | U _c | N | H _{m0} | T _p | T _{m-1,0} | U _c | N | H _{m0} | T _p | T _{m-1,0} | U _c |
| | | [m] | [mm] | times D ₅₀ | [-] | [-] | [m] | [s] | [s] | [m/s] | [-] | [m] | [s] | [s] | [m/s] | [-] | [m] | [s] | [s] | [m/s] | [-] | [m] | [s] | [s] | [m/s] |
| series 1 | s1_001 | 0.24 | 7.5 | 4 | - | 1000 | 0.091 | 1.46 | 1.33 | 0.155 | 3000 | 0.092 | 1.52 | 1.33 | 0.159 | 5000 | 0.092 | 1.53 | 1.33 | 0.161 | - | - | - | - | - |
| | s1_002 | 0.24 | 6.015 | 2 | 5.17 | 1000 | 0.094 | 1.46 | 1.33 | 0.154 | 3000 | 0.095 | 1.52 | 1.35 | 0.151 | 5000 | 0.097 | 1.53 | 1.35 | 0.147 | - | - | - | - | - |
| | s1_003 | 0.24 | 4.135 | 3 | 1.45 | 1000 | 0.090 | 1.46 | 1.34 | 0.175 | 3000 | 0.091 | 1.52 | 1.34 | 0.18 | 5000 | 0.092 | 1.53 | 1.34 | 0.180 | - | - | - | - | - |
| | s1_004 | 0.24 | 4.135 | 2 | 1.45 | 1000 | 0.089 | 1.46 | 1.33 | 0.182 | 3000 | 0.089 | 1.52 | 1.34 | 0.185 | 5000 | 0.089 | 1.53 | 1.34 | 0.186 | - | - | - | - | - |
| | s1_005 | 0.24 | 2.686 | 8 | 1.51 | 1000 | 0.088 | 1.46 | 1.34 | 0.173 | 3000 | 0.089 | 1.52 | 1.34 | 0.179 | 5000 | 0.089 | 1.53 | 1.34 | 0.182 | - | - | - | - | - |
| | s1_006 | 0.24 | 4.135 | 3 | 1.45 | 1000 | 0.085 | 1.46 | 1.34 | 0.179 | 3000 | 0.086 | 1.52 | 1.34 | 0.185 | 5000 | 0.086 | 1.52 | 1.36 | 0.186 | - | - | - | - | - |
| series 2 | s2_001 | 0.36 | 7.5 | 2 | - | 1000 | 0.149 | 1.60 | 1.44 | 0.174 | 3000 | 0.142 | 1.54 | 1.45 | 0.175 | 5000 | 0.140 | 1.52 | 1.45 | 0.175 | - | - | - | - | - |
| | s2_002 | 0.36 | 6.015 | 2 | 5.17 | 1000 | 0.122 | 1.60 | 1.44 | 0.173 | 3000 | 0.128 | 1.54 | 1.44 | 0.175 | 5000 | 0.129 | 1.52 | 1.44 | 0.174 | - | - | - | - | - |
| | s2_003 | 0.36 | 4.135 | 3 | 1.45 | 1000 | 0.136 | 1.60 | 1.43 | 0.177 | 3000 | 0.129 | 1.54 | 1.44 | 0.176 | 5000 | 0.129 | 1.52 | 1.44 | 0.175 | - | - | - | - | - |
| | s2_004 | 0.36 | 4.135 | 4 | 1.45 | 1000 | 0.139 | 1.60 | 1.44 | 0.176 | 3000 | 0.132 | 1.54 | 1.44 | 0.175 | 5000 | 0.130 | 1.52 | 1.44 | 0.175 | - | - | - | - | - |
| | s2_005 | 0.36 | 2.686 | 8 | 1.51 | 1000 | 0.140 | 1.60 | 1.44 | 0.175 | 3000 | 0.135 | 1.54 | 1.44 | 0.172 | 5000 | 0.134 | 1.52 | 1.44 | 0.172 | - | - | - | - | - |
| | s2_006 | 0.36 | 4.135 | 4 | 1.45 | 1000 | 0.118 | 1.60 | 1.45 | 0.185 | 3000 | 0.112 | 1.54 | 1.45 | 0.192 | 5000 | 0.111 | 1.52 | 1.45 | 0.193 | - | - | - | - | - |
| series 3 | s3_001 | 0.5 | 6.015 | 2 | 5.17 | 1000 | 0.119 | 1.60 | 1.43 | 0.181 | 3000 | 0.131 | 1.52 | 1.42 | 0.19 | 5000 | 0.134 | 1.51 | 1.41 | 0.19 | - | - | - | - | - |
| | s3_002tris | 0.5 | 4.135 | 2 | 1.45 | 1000 | 0.146 | 1.60 | 1.42 | 0.223 | 3000 | 0.142 | 1.52 | 1.41 | 0.226 | 5000 | 0.140 | 1.51 | 1.41 | 0.226 | - | - | - | - | - |
| | s3_003 | 0.5 | 4.135 | 4 | 1.45 | 1000 | 0.142 | 1.60 | 1.43 | 0.215 | 3000 | 0.140 | 1.54 | 1.41 | 0.219 | 5000 | 0.141 | 1.52 | 1.41 | 0.220 | - | - | - | - | - |
| | s3_004 | 0.5 | 4.135 | 3 | 1.45 | 1000 | 0.140 | 1.60 | 1.42 | 0.218 | 3000 | 0.137 | 1.52 | 1.41 | 0.221 | 5000 | 0.139 | 1.51 | 1.41 | 0.220 | 7000 | 0.14 | 1.50 | 1.41 | 0.221 |
| | s3_005 | 0.5 | 2.686 | 8 | 1.51 | 1000 | 0.148 | 1.60 | 1.42 | 0.21 | 3000 | 0.144 | 1.52 | 1.42 | 0.21 | 5000 | 0.145 | 1.51 | 1.41 | 0.211 | - | - | - | - | - |
| | s3_006 | 0.5 | 2.686 | 4 | 1.51 | 1000 | 0.145 | 1.60 | 1.43 | 0.217 | 3000 | 0.141 | 1.54 | 1.41 | 0.219 | 5000 | 0.141 | 1.52 | 1.41 | 0.220 | - | - | - | - | - |
| | s3_007 | 0.5 | 2.686 | 6 | 1.51 | 1000 | 0.144 | 1.60 | 1.42 | 0.216 | 3000 | 0.142 | 1.52 | 1.41 | 0.219 | - | - | - | - | - | - | - | - | - | - |
| | s3_008 | 0.5 | 4.135 | 3 | 1.45 | 1000 | 0.147 | 1.60 | 1.43 | 0.221 | 3000 | 0.143 | 1.54 | 1.41 | 0.224 | 5000 | 0.143 | 1.52 | 1.41 | 0.222 | - | - | - | - | - |
| | s3_009 | 0.5 | 4.135 | 3 | 1.45 | 1000 | 0.137 | 1.60 | 1.50 | 0.183 | 3000 | 0.136 | 1.55 | 1.49 | 0.182 | 5000 | 0.136 | 1.54 | 1.49 | 0.181 | - | - | - | - | - |
| | s3_010 | 0.5 | 4.135 | 2 | 1.45 | 1000 | 0.114 | 1.60 | 1.50 | 0.178 | 3000 | 0.113 | 1.55 | 1.50 | 0.18 | 5000 | 0.113 | 1.54 | 1.50 | 0.181 | - | - | - | - | - |
| | s3_011 | 0.5 | 2.686 | 8 | 1.51 | 1000 | 0.117 | 1.60 | 1.51 | 0.182 | 3000 | 0.114 | 1.55 | 1.50 | 0.18 | 5000 | 0.114 | 1.54 | 1.50 | 0.179 | - | - | - | - | - |

4.2.6.2 Test repeatability

During the assessment of the test results, the repeatability conditions were analysed in [175]. The reproducibility of both the loading conditions (waves and currents) and the damage is essential in order to validate the predictive formula of the damage number. The test repeatability was analysed between test s1_003 and s1_006, and also between s2_004 and s2_006.

The visual damage after 1000, 3000 and 5000 waves is presented in Table 4.8 for the first two tests. The resulting damage number per sub-area is presented numerically in Table 4.9 and Table 4.10, and for the entire scour protection in Table 4.11. Both s1_003 and s1_006 protections were identified as being dynamically stable, thus agreeing in the final damage classification, as visually observed from Table 4.8. Despite the visually good agreement, the aforementioned tables lead to the conclusion that the location and intensity of damage number between both tests may vary. Moreover, it was confirmed that, after 5000 waves, the values of S_{3Dsub} present considerable differences with very low R^2 as noted in Figure A2.1 (APPENDIX 2). The almost non-existent linear correlation might be a result of the differences noted between the wave height and the depth-averaged current velocity of both tests. This aspect was not noted in the analysis performed in [175]. Despite the similar classification, regarding the type of stability, some caution is advisable when comparing these tests with the damage number per sub-area of new datasets.

Table 4.8 – Visual damage comparison between tests s1_003 and s1_006. Flow direction from bottom to top.







| Test | Overhead pictures | | |
|--------|---|--|---|
| | 1000 waves | 3000 waves | 5000 waves |
| S1_003 |  |  |  |
| S1_006 |  |  |  |

Table 4.9 and Table 4.10 indicate that, after the first 1000 waves, test s1_003 presents slightly less edge scour at the outer rings (R5 and R6) than s1_006. This situation becomes less evident between 1000 and 3000 waves, as both profiles present similar damage numbers. Between 3000 and 5000 waves, both scour protections also showed similar damage numbers, but in this case the edge scour at R6 becomes more severe in s1_003 than in s1_006. Despite the location differences and the intensity variations, the most critical sub-areas seem to be consistent between both tests. The critical sub-areas, i.e. the ones that eroded the most, are the edge ring R6 (sometimes R5) between sectors S6 and S12, and also the inner rings R1 and R2, between sectors S3 and S5. The analysis shows that overall damage occurred on the upstream side of the scour protection at the outer rings (edge scour) and on the downstream side right behind the pile, in the inner rings. It is also clear that both tests presented the ability to recover from damage occurrence, since between 3000 and 5000 waves some S_{3Dsub} are

smaller than the ones registered between 1000 and 3000 waves. This reshaping capacity seems to be less effective in the outer ring R6.

Table 4.9 – Damage number (S_{3Dsub}) per sub-area, i.e. ring and sector for test s1_003, after each wave train.

| {0;1000} waves | S1 | S2 | S3 | S4 | S5 | S6 | S7 | S8 | S9 | S10 | S11 | S12 |
|-------------------|-------|-------|-------|-------|-------|-------|-------|-------|-------|-------|-------|-------|
| R1 | 0.15 | 0.94 | 0.55 | -0.71 | -0.35 | 0.61 | -0.31 | -0.78 | -0.11 | -0.15 | -0.08 | -0.25 |
| R2 | 0.06 | 0.07 | -0.14 | -0.46 | -1.03 | 1.26 | 0.76 | -0.11 | -0.03 | -0.22 | -0.23 | -0.14 |
| R3 | 0.04 | -0.14 | 0.02 | -0.04 | 0.08 | 0.15 | 0.20 | -0.15 | -0.04 | 0.03 | 0.00 | -0.09 |
| R4 | 0.08 | -0.02 | -0.03 | 0.06 | 0.07 | -0.01 | 0.09 | 0.02 | 0.12 | 0.09 | 0.10 | 0.15 |
| R5 | 0.11 | 0.11 | -0.04 | 0.07 | 0.12 | 0.62 | 0.64 | 0.30 | 0.28 | 0.24 | 0.27 | -0.03 |
| R6 | 0.70 | 1.70 | 0.57 | 1.97 | 0.32 | 1.29 | 1.94 | 0.16 | -0.14 | -0.27 | -0.86 | -0.36 |
| {1000;3000} waves | S1 | S2 | S3 | S4 | S5 | S6 | S7 | S8 | S9 | S10 | S11 | S12 |
| R1 | -0.34 | 0.07 | -0.21 | -0.33 | 0.26 | -0.38 | -0.24 | -0.12 | -0.26 | -0.14 | -0.13 | -0.23 |
| R2 | 0.07 | 0.39 | -0.25 | -0.56 | 0.00 | -0.08 | 0.13 | 0.01 | 0.00 | -0.04 | 0.04 | 0.04 |
| R3 | -0.14 | 0.00 | 0.03 | 0.01 | -0.05 | 0.00 | -0.10 | 0.03 | 0.01 | -0.05 | 0.01 | 0.03 |
| R4 | -0.08 | 0.00 | -0.05 | -0.09 | -0.08 | 0.11 | -0.01 | 0.09 | 0.06 | 0.13 | 0.00 | 0.08 |
| R5 | -0.15 | 0.10 | 0.08 | 0.02 | 0.18 | 0.89 | -0.54 | -0.21 | -0.09 | -0.12 | -0.23 | -0.18 |
| R6 | -0.53 | 0.22 | 0.40 | -0.02 | 0.59 | 1.24 | -2.23 | -1.55 | -1.68 | -0.88 | -1.12 | -1.14 |
| {3000;5000} waves | S1 | S2 | S3 | S4 | S5 | S6 | S7 | S8 | S9 | S10 | S11 | S12 |
| R1 | -0.05 | -0.41 | -0.19 | -0.44 | -0.91 | -0.47 | -0.20 | -0.35 | -0.22 | -0.15 | -0.28 | -0.25 |
| R2 | -0.16 | -0.01 | -0.08 | -0.64 | -0.28 | 0.07 | 0.19 | -0.04 | 0.01 | 0.23 | 0.22 | -0.14 |
| R3 | 0.02 | -0.10 | -0.23 | -0.16 | -0.08 | 0.08 | 0.06 | 0.10 | 0.04 | 0.20 | 0.14 | -0.09 |
| R4 | 0.03 | 0.00 | -0.07 | -0.11 | -0.12 | -0.22 | -0.08 | -0.07 | -0.14 | -0.16 | -0.12 | 0.15 |
| R5 | -0.20 | 0.24 | 0.07 | -0.25 | -0.29 | -1.13 | -0.40 | -0.29 | -0.36 | -0.18 | -0.23 | -0.03 |
| R6 | -0.56 | 0.19 | 0.26 | -1.34 | -0.19 | -1.85 | -0.77 | -1.21 | -0.81 | -0.39 | -0.77 | -0.36 |

Table 4.11 shows that departures occur between the overall $S_{3Dmeasured}$ of each wave train. However, these values correspond to the maximum S_{3Dsub} of the protection, regardless of the damage location. Therefore, despite the differences noted through the analysis presented in APPENDIX 2, Table 4.11 shows damage numbers, which seem to be reproducible in terms of the overall classification, particularly, if one notes that there was an agreement between the visual damage of each scour protection, despite the differences between U_c and H_{m0} reported in Table 4.7.

Regarding test s2_004 and s2_006 a similar comparison can be made. In both tests, the scour protections were also identified as dynamically stable. The visual damage presented in Table 4.12 seems slightly different between both tests. For the first 1000 wave train, more deposition seems to occur in s2_006 than in s2_004. This could be caused by the depth-averaged current velocity, which is slightly larger in s2_006 ($U_{c1000}=0.185$ m/s) than in s2_004 ($U_{c1000}=0.176$ m/s), in spite of the smaller significant wave height after 1000 waves ($H_{m0,1000}$), which is 0.118 m in s2_006 and 0.139 m in s2_004.

These differences, i.e. smaller H_{m0} but larger U_c in s2_006 than in s2_004, remain throughout the rest of the test, for 3000 waves and 5000 waves, thus justifying the difference in the visual damage presented in Table 4.12. These differences are also noted in Figure A2.2 (APPENDIX 2).

Table 4.10 – Damage number (S_{3Dsub}) per sub-area, i.e. ring and sector for test s1_006, after each wave train.

| {0;1000} waves | S1 | S2 | S3 | S4 | S5 | S6 | S7 | S8 | S9 | S10 | S11 | S12 |
|--------------------------|-----------|-----------|-----------|-----------|-----------|-----------|-----------|-----------|-----------|------------|------------|------------|
| R1 | -0.55 | 0.23 | -0.41 | -0.89 | -0.33 | 0.25 | -0.39 | -0.93 | -0.23 | -0.14 | -0.14 | -0.41 |
| R2 | 0.60 | 1.06 | -0.91 | -0.35 | -0.79 | 0.55 | 0.22 | 0.09 | -0.09 | -0.05 | 0.05 | 0.21 |
| R3 | 0.04 | 0.02 | 0.24 | 0.19 | 0.35 | 0.18 | 0.06 | -0.03 | 0.05 | 0.05 | 0.04 | -0.05 |
| R4 | 0.06 | 0.07 | 0.20 | 0.00 | 0.11 | 0.11 | -0.01 | -0.01 | 0.05 | 0.02 | -0.04 | -0.05 |
| R5 | 0.10 | 0.33 | 0.08 | 0.02 | 0.01 | 0.22 | 0.16 | 0.01 | 0.14 | 0.00 | -0.09 | -0.01 |
| R6 | 0.39 | 1.21 | 0.32 | 1.17 | 0.04 | 0.28 | -0.08 | -0.63 | -0.73 | -0.99 | -1.35 | -0.55 |
| {1000;3000} waves | S1 | S2 | S3 | S4 | S5 | S6 | S7 | S8 | S9 | S10 | S11 | S12 |
| R1 | -0.09 | -0.16 | 0.58 | -0.61 | -0.28 | -0.40 | -0.21 | 0.08 | 0.02 | 0.05 | 0.00 | -0.21 |
| R2 | -0.03 | 0.12 | 0.00 | -0.99 | -0.41 | 0.48 | 0.13 | 0.02 | -0.01 | -0.02 | 0.12 | 0.06 |
| R3 | 0.08 | 0.11 | -0.37 | 0.03 | 0.08 | 0.06 | -0.05 | 0.05 | 0.08 | 0.13 | 0.07 | 0.07 |
| R4 | 0.03 | 0.06 | 0.16 | 0.03 | 0.09 | 0.02 | 0.02 | 0.14 | 0.09 | 0.12 | 0.08 | 0.09 |
| R5 | -0.18 | -0.04 | 0.17 | 0.10 | 0.02 | -0.04 | -0.15 | -0.04 | -0.09 | -0.02 | -0.30 | -0.08 |
| R6 | -2.00 | -1.22 | 0.10 | -0.06 | -0.36 | -1.26 | -1.46 | -1.06 | -1.43 | -0.86 | -1.44 | -1.34 |
| {3000;5000} waves | S1 | S2 | S3 | S4 | S5 | S6 | S7 | S8 | S9 | S10 | S11 | S12 |
| R1 | 0.01 | -0.09 | -0.29 | 0.10 | 0.19 | 0.27 | 0.29 | -0.22 | -0.18 | 0.05 | 0.03 | -0.41 |
| R2 | 0.04 | 0.12 | 0.25 | -0.09 | -0.12 | 0.25 | -0.21 | 0.03 | 0.13 | 0.20 | -0.03 | 0.21 |
| R3 | 0.12 | 0.17 | 0.05 | 0.03 | 0.15 | 0.09 | 0.23 | 0.21 | 0.20 | 0.25 | 0.19 | -0.05 |
| R4 | 0.13 | 0.09 | 0.08 | 0.06 | 0.08 | 0.08 | 0.24 | 0.11 | 0.18 | 0.06 | 0.15 | -0.05 |
| R5 | -0.09 | 0.11 | 0.07 | 0.05 | 0.12 | 0.03 | 0.14 | 0.01 | -0.02 | -0.01 | -0.06 | -0.01 |
| R6 | -0.44 | 0.32 | -0.75 | -0.74 | -0.43 | 0.92 | -0.14 | -0.26 | -0.23 | -0.47 | -0.38 | -0.55 |

Table 4.11 – Measured damage ($S_{3Dmeasured}$) for s1_003 and s1_006 ($D_{50}=4.135$ mm; 3D50 thickness; $d=0.24$ m).

| Test | $S_{3Dmeasured}$ [-] | | |
|---------------|--|---------------------------|---------------------------|
| | {0; 1000} waves | {1000; 3000} waves | {3000; 5000} waves |
| S1_003 | -1.03 | -2.23 | -1.85 |
| S1_006 | -1.35 | -2.00 | -0.75 |

Table 4.13 and Table 4.14 show that the damage numbers per sub-area, S_{3Dsub} , are not in perfect agreement. However, between 0 and 1000 waves and also between 3000 and 5000 waves, the overall damage number of the protection are rather close to each other, as shown in Table 4.15. The same table shows that agreement is not so satisfactory between 1000 and 3000 waves. Similarly to the previous tests, s2_004 and s2_006 also evidence a reshaping ability, which is more noticeable between 3000 and 5000 waves. This is an important aspect as one is looking for dynamic stability, which implies the ability to recover from previous scour-induced damage.

As it will be analysed in further sections, [26] points out that the rate of damage development diminishes between 3000 and 5000 waves. Although this conclusion is valid for the present dataset, further research should be performed before a proper generalisation is made, because as mentioned before, research performed for long-duration tests was not able to unequivocally prove that the equilibrium profile is reached for 5000 waves, e.g. [31, 32] or [103].

Table 4.12 - Visual damage comparison between tests s2_004 and s2_006. Flow direction from bottom to top.

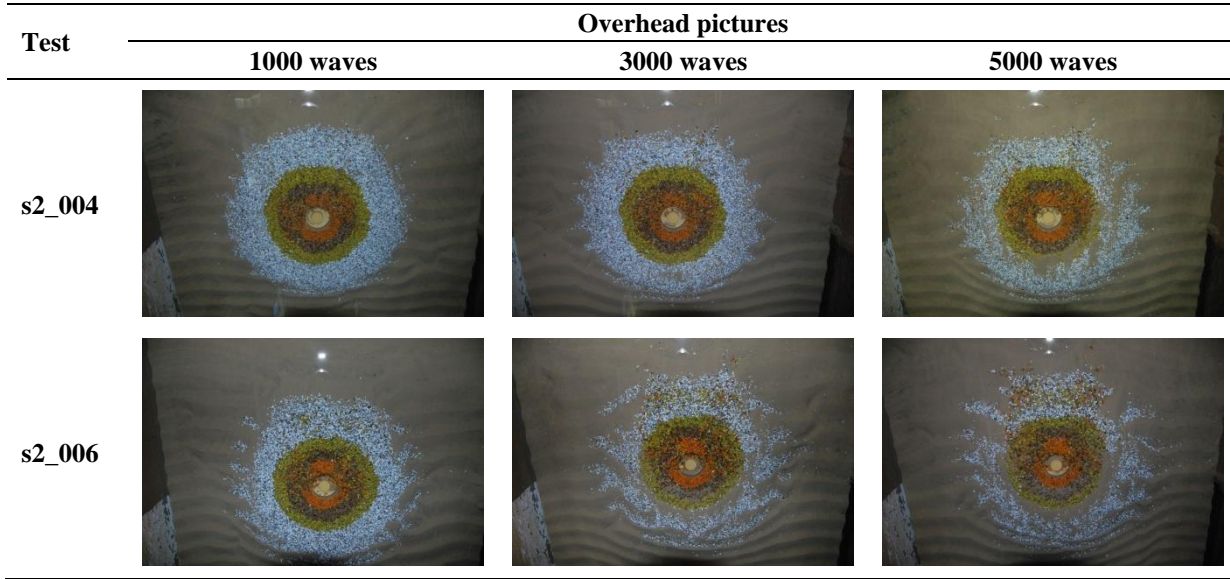


Table 4.13 – Damage number (S_{3Dsub}) per sub-area, i.e. ring and sector for test s2_004, after each wave train.

| {0;1000} waves | S1 | S2 | S3 | S4 | S5 | S6 | S7 | S8 | S9 | S10 | S11 | S12 |
|-------------------|-------|-------|-------|-------|-------|-------|-------|-------|-------|-------|-------|-------|
| R1 | 0.30 | 0.90 | -0.90 | -1.28 | -0.09 | 1.22 | -0.76 | -0.96 | -0.68 | -0.33 | -0.35 | -0.59 |
| R2 | 0.36 | 0.80 | -1.81 | -1.05 | -1.32 | 1.08 | 0.71 | 0.06 | -0.15 | -0.12 | -0.12 | 0.26 |
| R3 | -0.04 | 0.12 | 0.08 | 0.16 | -0.18 | -0.06 | -0.03 | -0.10 | -0.08 | -0.16 | -0.03 | -0.03 |
| R4 | 0.00 | -0.06 | 0.08 | -0.08 | -0.02 | -0.07 | -0.02 | -0.08 | 0.01 | 0.00 | -0.05 | -0.12 |
| R5 | -0.09 | -0.20 | -0.10 | -0.10 | -0.26 | -0.09 | -0.03 | -0.03 | -0.05 | 0.07 | -0.14 | -0.23 |
| R6 | 0.23 | 0.60 | 0.46 | 1.09 | 0.32 | 0.89 | 0.45 | 0.21 | -0.69 | -0.37 | -0.95 | -0.84 |
| {1000;3000} waves | S1 | S2 | S3 | S4 | S5 | S6 | S7 | S8 | S9 | S10 | S11 | S12 |
| R1 | -0.97 | -0.73 | -0.12 | -0.73 | -0.36 | -0.63 | 0.06 | -0.27 | -0.08 | -0.05 | -0.29 | -0.51 |
| R2 | 0.10 | -0.01 | 0.15 | -0.58 | -0.71 | -0.11 | -0.18 | -0.12 | -0.21 | -0.20 | -0.12 | -0.29 |
| R3 | -0.20 | -0.16 | -0.33 | -0.18 | -0.54 | -0.02 | -0.15 | -0.14 | -0.11 | -0.03 | -0.11 | -0.24 |
| R4 | -0.23 | -0.24 | -0.12 | -0.15 | -0.13 | -0.17 | -0.16 | -0.07 | -0.08 | 0.17 | -0.10 | -0.12 |
| R5 | -0.16 | -0.10 | -0.12 | 0.03 | -0.01 | -0.09 | -0.06 | -0.18 | -0.17 | -0.27 | -0.36 | -0.31 |
| R6 | 0.18 | -0.43 | -0.01 | 1.70 | 0.48 | 0.35 | 0.76 | -0.54 | -0.40 | -1.00 | -0.93 | 0.06 |
| {3000;5000} waves | S1 | S2 | S3 | S4 | S5 | S6 | S7 | S8 | S9 | S10 | S11 | S12 |
| R1 | 0.03 | -0.06 | -0.30 | 0.04 | -0.55 | -0.23 | -0.19 | -0.45 | 0.01 | -0.03 | 0.18 | -0.59 |
| R2 | 0.42 | 0.40 | -0.33 | -0.46 | -0.18 | 0.25 | 0.37 | 0.11 | 0.36 | 0.33 | 0.12 | 0.26 |
| R3 | 0.17 | 0.09 | 0.04 | 0.15 | -0.06 | 0.43 | 0.46 | 0.40 | 0.44 | 0.79 | 0.38 | -0.03 |
| R4 | 0.25 | 0.26 | 0.18 | 0.13 | 0.14 | 0.25 | 0.47 | 0.46 | 0.22 | 0.06 | 0.22 | -0.12 |
| R5 | 0.14 | 0.30 | 0.05 | 0.08 | -0.05 | 0.54 | 0.13 | 0.08 | 0.09 | 0.00 | -0.23 | -0.23 |
| R6 | 0.52 | 1.51 | 0.49 | 0.58 | -0.09 | -0.14 | -0.99 | -0.35 | -0.35 | -0.10 | -0.17 | -0.84 |

Table 4.13 and Table 4.14 also show that the most critical areas, i.e. the ones that experience more scour occurrence in adjacent sub-areas, are similar to the ones from tests s1_003 and s1_006. The critical areas are the ones presented in R6, in front of the pile, at the edge of the protection, and the ones immediately behind the pile, on the downstream side (R1 and R2, sectors S3 to S5).

Nevertheless, after 5000 waves, both s2_004 and s2_006 presented less edge scour in R6 than the previous two tests, which were performed with a lower water depth.

The visual difference shown in Table 4.12 and the similar measured damage numbers from Table 4.15 also point to the fact that the transition between damage levels does not exactly correspond to a sharp limit, which was already noted for the stability parameter in the OPTI-PILE project and in the research presented in [1] and [32]. Nevertheless, it is important to note that the differences between the S_{3Dsub} of each test are not negligible, even if the overall measured damage number is similar. Therefore, it should be stressed that the conclusions obtained from the present results should be cautiously interpreted and validated in future research, particularly before a generalization of these outcomes is performed based on this dataset.

Table 4.14 – Damage number (S_{3Dsub}) per sub-area, i.e. ring and sector for test s2_006, after each wave train.

| {0;1000} waves | S1 | S2 | S3 | S4 | S5 | S6 | S7 | S8 | S9 | S10 | S11 | S12 |
|--------------------------|-----------|-----------|-----------|-----------|-----------|-----------|-----------|-----------|-----------|------------|------------|------------|
| R1 | 0.40 | 1.41 | -1.04 | -1.46 | -0.37 | 0.85 | 0.22 | -0.40 | -0.36 | -0.06 | -0.26 | -0.18 |
| R2 | 0.40 | 1.51 | -1.54 | -1.83 | -1.58 | 1.25 | 0.84 | -0.01 | -0.03 | -0.08 | -0.05 | 0.10 |
| R3 | 0.07 | 0.05 | -0.61 | -0.12 | -1.23 | 0.04 | 0.05 | -0.01 | 0.00 | 0.02 | 0.03 | 0.04 |
| R4 | 0.05 | -0.03 | 0.02 | 0.13 | 0.17 | -0.07 | -0.01 | -0.05 | -0.06 | -0.05 | -0.19 | 0.00 |
| R5 | 0.23 | 0.69 | 0.39 | 0.27 | 0.44 | 0.49 | 0.54 | 0.40 | 0.12 | 0.27 | 0.23 | -0.07 |
| R6 | -0.35 | 0.63 | 0.84 | 1.67 | 0.55 | -0.08 | 0.14 | -0.01 | 0.12 | -0.52 | -0.67 | -1.03 |
| {1000;3000} waves | S1 | S2 | S3 | S4 | S5 | S6 | S7 | S8 | S9 | S10 | S11 | S12 |
| R1 | -0.92 | -1.21 | -0.02 | -0.74 | -1.16 | -0.33 | -0.54 | -0.39 | -0.16 | -0.07 | -0.19 | -0.85 |
| R2 | 0.68 | -0.48 | -1.12 | -1.30 | -1.63 | -0.93 | 0.11 | 0.20 | 0.02 | 0.07 | 0.04 | -0.04 |
| R3 | 0.45 | 0.46 | -1.30 | -0.80 | -1.02 | 0.24 | 1.14 | 0.85 | 0.74 | 0.87 | 0.81 | 0.31 |
| R4 | 0.37 | 0.55 | 0.18 | 0.40 | 0.12 | 0.19 | 0.26 | 0.24 | 0.12 | 0.25 | 0.16 | 0.14 |
| R5 | -0.11 | 0.38 | 1.51 | 0.35 | 1.60 | 0.33 | -0.82 | 0.11 | 0.25 | -0.06 | -0.11 | 0.06 |
| R6 | -0.24 | -0.61 | -0.10 | -0.73 | 0.20 | -0.09 | -2.27 | -1.59 | -1.93 | -1.15 | -1.52 | 0.16 |
| {3000;5000} waves | S1 | S2 | S3 | S4 | S5 | S6 | S7 | S8 | S9 | S10 | S11 | S12 |
| R1 | 0.14 | 0.17 | 0.60 | 0.14 | 0.30 | -0.17 | 0.12 | -0.18 | 0.08 | -0.15 | 0.07 | -0.18 |
| R2 | -0.22 | 0.22 | 0.71 | 0.01 | 0.88 | 0.35 | -0.08 | -0.13 | -0.07 | -0.04 | -0.05 | 0.10 |
| R3 | -0.44 | -0.26 | 0.24 | 0.14 | 0.21 | -0.15 | -0.89 | -0.38 | -0.36 | -0.42 | -0.36 | 0.04 |
| R4 | -0.10 | -0.45 | -0.10 | -0.22 | -0.09 | -0.17 | -0.06 | -0.03 | -0.11 | -0.18 | 0.02 | 0.00 |
| R5 | 0.16 | -0.03 | -0.49 | -0.27 | -1.09 | -0.19 | 0.25 | -0.06 | 0.10 | -0.02 | 0.33 | -0.07 |
| R6 | -0.19 | 0.47 | -0.19 | 0.48 | -0.81 | -0.46 | 0.72 | 0.59 | 0.70 | 0.60 | 0.72 | -1.03 |

Table 4.15 – Measured damage ($S_{3Dmeasured}$) for s2_004 and s2_006 ($D_{50}=4.135mm$; $4D_{50}$ thickness; $d=0.50m$).

| Test | $S_{3Dmeasured}$ [-] | | |
|---------------|--|---------------------------|---------------------------|
| | {0; 1000} waves | {1000; 3000} waves | {3000; 5000} waves |
| s2_004 | -1.81 | -1.00 | -0.99 |
| s2_006 | -1.83 | -2.27 | -1.09 |

4.2.6.3 Overall measured damage numbers

Table 4.16 provides the measured damage number of the scour protection calculated between the initial 3D profile and the 3D profile after the accumulated wave trains superimposed on a steady current. In this case, for the sake of simplicity, positive values of the damage number represent erosion (unlike in the previous section). Table 4.16 also provides the type of stability, i.e. the classification of the scour protection in terms of “no movement”, “some movement but no failure” and “failure”, which correspond to statically stable, dynamically stable and failure of the scour protection, respectively.

It may be noted that these values are not directly comparable with the ones measured in [1] and [32]. This is caused by the fact that these tests are performed under different hydrodynamic conditions, even for the cases for which the scour protection has the same thickness and similar mean stone diameter. In [175], it is stated that test s3_001 was performed to replicate test number 46 presented in [32]. However, as explained before, test s3_001 was not considered suitable to be included in the analysis. During this research, this test was not repeated due to lack of time. The detailed comparison between the present research and the results obtained in [1] and [32] is provided in following sections.

The range of test conditions leads to measured damage numbers roughly between 0 and 4, whilst [32] reports measured values between 0 and 2.5. The exceptions of the present dataset are tests s1_005 and s2_005, which presented a measured damage number equal to 12.70 and 7.54, respectively. Both of these tests were considered as “failure”, i.e. the exposed area of the filter layer has exceeded $4(D_{n50})^2$.

The scour protections of the MARINET dataset were divided into statically stable ($y=1$), dynamically stable ($y=2$) and failure ($y=3$), depending on the visual damage level. Note that the dynamic stability encompasses visual damages 2 and 3, previously defined as “very limited movement” and “significant movement without failure”. The dataset available in [32] and [148] was also classified according the stability of the scour protection. Figure 4.16 provides the type of stability as a function of the measured damage number ($S_{3D\text{measured}}$). It is possible to conclude that the present dataset is dealing with a wider range of measured damage numbers. Moreover, the measured limits of the damage number, for which dynamic scour protections are obtained, are considerably broader than the ones concerning the research developed in [32] and [148]. In fact, dynamic scour protections were obtained for measured damage numbers that clearly overcome the failure cases shown in former researches. Although the limits of the acceptable damage number for dynamic stability are analysed in following sections, at this point, one should bear in mind that the present dataset seems to cover the range of $S_{3D\text{measured}}$ shown in the two previous researches. Nevertheless, it is also important not to forget the limitations of the tested range of conditions discussed in section 4.2.3.4 and the potential differences caused by the scale and model effects discussed in section 4.2.5.

Regarding the static stability, not many tests are reported in the analysed datasets. However, the agreement seems fairly reasonable as well. [1] and [32] concluded that static stability was obtained for a measured damage number of 0.25 and neither the MARINET data nor the results from [148] seem to be further way from this limit, which is also discussed when addressing the accuracy of the predictive formula, Eq. (3.57). It can be noted that this limit is slightly exceeded in the zoom performed in Figure 4.17. The failure occurrences from tests s1_005 and s2_005 present very large damage numbers, which makes a good perception of the results obtained near the original range difficult. Therefore, a zoom in the interval of $S_{3D\text{measured}}$ between 0 and 4 is presented in Figure 4.17. The zoom performed shows that the dynamic stability of the MARINET data was obtained for numbers that considerably exceed the other datasets. However, there is a considerable overlap with the failure occurrence in other scour protections. A possible reason for this may be related to the extended range of scour protection

thicknesses tested within the MARINET proposal 61, which is also analysed in following sections. It is expected that a thicker armour layer is able to support a larger damage number whilst still remaining stable.

Table 4.16 – Measured damage numbers ($S_{3D_{measured}}$) after 1000, 3000, 5000 and 7000 waves representative overall value of the scour protection, positive values representing erosion.

| Series | Test | $S_{3D_{measured}}$ [-] | | | | Type of Stability |
|----------|--------|-------------------------|-------|-------|------|-------------------|
| | | 1000 | 3000 | 5000 | 7000 | |
| | | [-] | [-] | [-] | - | |
| series 1 | s1_001 | 0.31 | 0.29 | 0.37 | - | Static |
| | s1_002 | 0.27 | 0.30 | 0.23 | - | Static |
| | s1_003 | 0.78 | 1.13 | 1.56 | - | Dynamic |
| | s1_004 | 2.05 | 2.03 | 2.27 | - | Failure |
| | s1_005 | 4.47 | 10.63 | 12.70 | - | Failure |
| | s1_006 | 0.95 | 1.50 | 1.79 | - | Dynamic |
| series 2 | s2_001 | 0.31 | 0.41 | 0.36 | - | Static |
| | s2_002 | 0.39 | 0.40 | 0.44 | - | Dynamic |
| | s2_003 | 1.55 | 1.77 | 1.56 | - | Failure |
| | s2_004 | 1.58 | 1.98 | 2.47 | - | Dynamic |
| | s2_005 | 3.31 | 6.63 | 7.54 | - | Failure |
| | s2_006 | 2.01 | 2.82 | 3.19 | - | Dynamic |
| series 3 | s3_001 | - | - | - | - | - |
| | s3_002 | 1.01 | 1.70 | 1.96 | - | Failure |
| | s3_003 | 0.48 | 1.23 | 1.62 | - | Dynamic |
| | s3_004 | 2.28 | 2.29 | 2.40 | 2.33 | Dynamic |
| | s3_005 | 2.75 | 3.53 | 3.70 | - | Dynamic |
| | s3_006 | 2.99 | 3.18 | 3.99 | - | Failure |
| | s3_007 | 2.89 | 3.68 | - | - | Failure |
| | s3_008 | 0.48 | 0.95 | 1.01 | - | Dynamic |
| | s3_009 | 0.42 | 0.75 | 0.71 | - | Dynamic |
| | s3_010 | 0.91 | 1.35 | 2.00 | - | Failure |
| | s3_011 | 1.79 | 2.38 | 3.07 | - | Dynamic |

For scour protections classified with failure occurrence (Table 4.16), the $S_{3D\text{measured}}$ increased over time, i.e. with the cumulative loading conditions (waves and current). The reported $S_{3D\text{measured}}$ increases from 0 to 1000 waves, from 1000 to 3000 and, finally, from 3000 to 5000 waves. This behaviour seems indicative of progressive damage, which accumulates between wave trains. The only exception occurs for test s2_003, for which the measured damage number after 5000 waves ($S_{3D5000\text{measured}}=1.56$) decreases from the measured damage number after 3000 waves ($S_{3D3000\text{measured}}=1.77$). Nevertheless, this test had already failed after 1000 waves ($S_{3D1000\text{measured}}=1.55$). Dynamic scour protections are intended to resist to damage progression. Ideally, it would be expected that such protection could reduce or at least maintain the damage number obtained in the previous wave train, e.g. as in tests s3_004 and s3_009. As it is observed from Table 4.16, the decrease of the overall measured damage number between 3000 and 5000 or 7000 waves only occurred, for dynamically stable tests, in the third series ($d=0.5$ m). Such observation may point to the fact that, for smaller water depths, it might be difficult to find a dynamically stable configuration. This fact was also pointed out in [1], but further research is needed to clarify this aspect. In some of the dynamic scour protections, e.g. test s2_002 and s3_008, the damage number remains quite similar. However, this is not the case, for example, in tests s2_004 or s3_003. This raises an important question, which is: what would happen if some of these tests were carried out with longer durations? For the present analysis, these tests are considered dynamically stable, since the classification was based on the visual damage number. Nevertheless, this observation emphasizes the fact that future research should address the effect of longer time series, which is yet poorly covered in the literature.

The measured damage numbers presented in this section are a result of the varying hydrodynamic conditions and scour protection characteristics. Some of these influences are addressed in the following sections, before dealing with the accuracy of the damage predictive formula, further used in reliability and risk analysis.

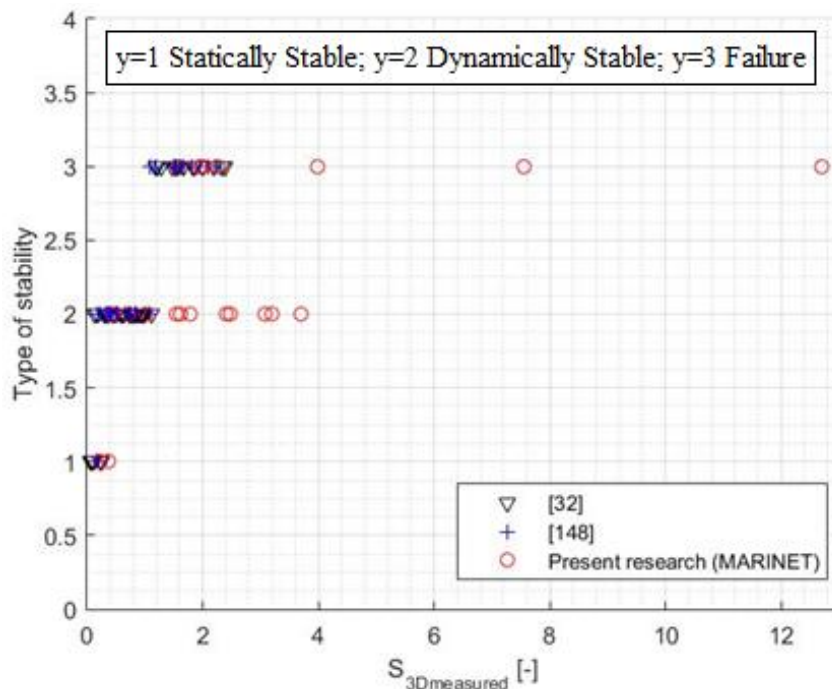


Figure 4.16 – Type of stability versus $S_{3D\text{measured}}$. Comparison between the present research and the datasets from [32] and [148].

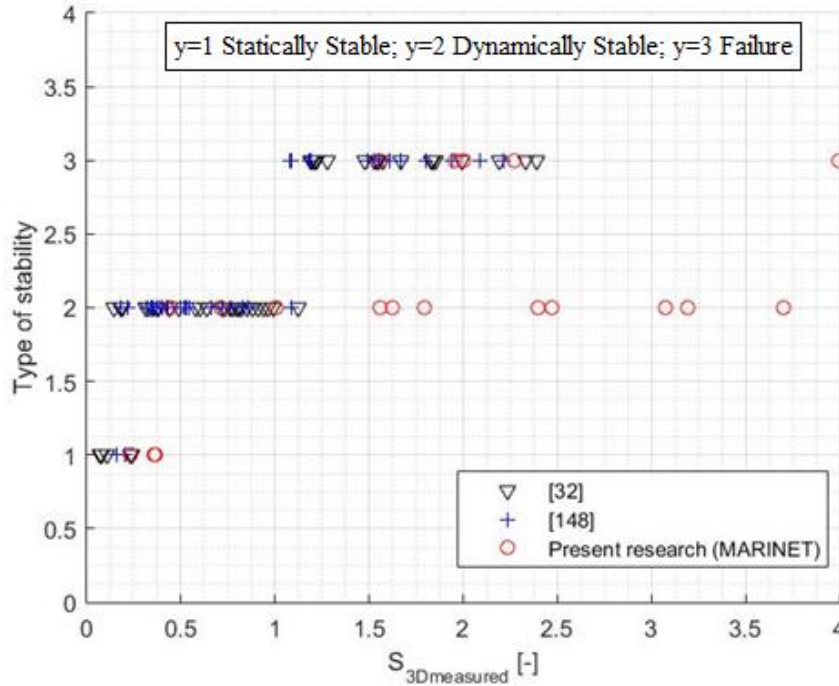


Figure 4.17 - Type of stability versus $S_{3Dmeasured}$. Comparison between the present research and the datasets from [32] and [148]. Zoom in the interval $S_{3Dmeasured}=[0;4]$.

4.2.6.3.1 Influence of the water depth

The influence of the water depth was one of the aspects that was not extensively studied in [1] and [32]. Most of the scour protection tests were performed with $d=0.40$ m, whilst a reduced number was performed with $d=0.20$ m. As discussed in section 4.2.3.4, it is recognised that scour severity tends to increase for smaller water depths, provided that the remaining variables are constant, e.g. [61]. Still, the influence of the water depth on scour protection damage is not thoroughly studied in the literature. According to [1], this influence has a significant impact on the damage development of the scour protection. The damage increase with decreasing water-depths is attributed to several causes. First of all, the orbital velocity is a function of the water depth, so that when given a certain wave height and period, the orbital velocity at the bottom will be smaller for larger water depths. The converse of this implies that the orbital velocity near the bottom increases for smaller water depths. Secondly, the bed shear stress caused by the flow velocity increases for decreasing water depths. In the present case study, tests s1_005, s2_005 and s3_005 were first used to assess the influence of the water depth on the measured damage numbers. Recalling Table 4.7, test s1_005 has a smaller significant wave height than test s2_005, which has a wave height that is smaller than s3_005. This is valid for all wave trains. Also, the differences in the energy spectral wave period ($T_{m-1,0}$) are not very significant, with a maximum difference of 5.7% found between test s1_005 and s2_005. The depth-averaged current velocity (U_c) is clearly larger for s3_005 and it is reasonably similar between s1_005 and s2_005. Taking this into consideration, one would be led to think that the measured damage number is larger in test s3_005, followed by s2_005 and then by s1_005. This does not occur, due to the influence of the water depth.

Table 4.17 shows that damage increases for decreasing water depths, unlike initially expected when solely considering the effects of U_c , H_{m0} and $T_{m-1,0}$. Moreover, in this table, test s3_011 is also presented and it has slightly less severe hydrodynamic conditions than the remaining tests. The differences between series 1 and 2 are even larger for s3_011 than for s3_005. This occurs, not only

because the water depth increases, but also because the significant wave height and the depth-averaged current velocity are smaller in s3_011 than in s3_005. The conclusion that arises from Table 4.17 is also confirmed when looking at the overall measured damage numbers in Table 4.18.

Table 4.17 – Visual comparison of damage between for different water depths ($D_{50}=2.686$ mm; $n_a=8D_{50}$) [175].
Flow direction from bottom to top.

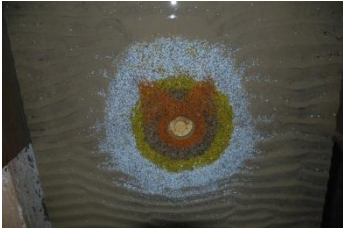

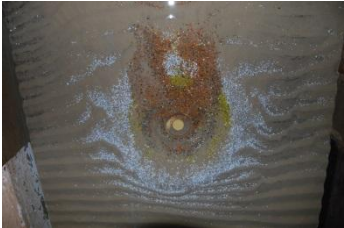



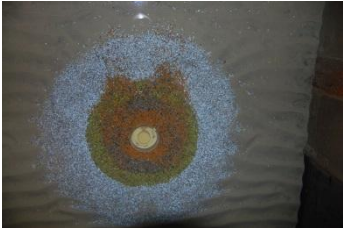
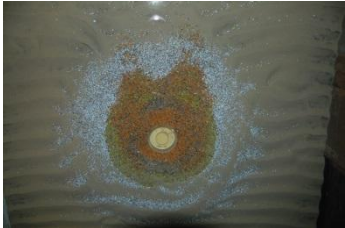

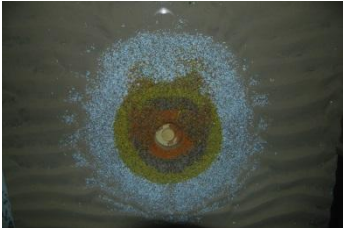
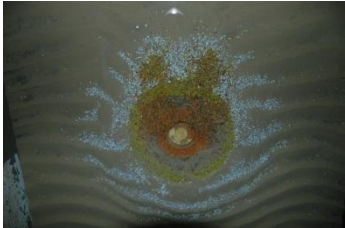
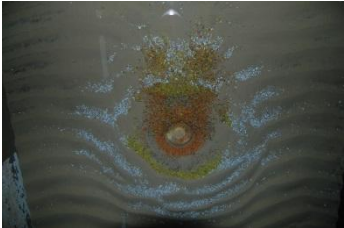
| Test-series | Overhead pictures | | |
|-------------|---|---|---|
| | 1000 waves | 3000 waves | 5000 waves |
| s1_005 |  |  |  |
| s2_005 |  |  |  |
| s3_005 |  |  |  |
| s3_011 |  |  |  |

Table 4.18 – Influence of the water depth in the measured damage number ($D_{50}=2.686$ mm; $n_a=8D_{50}$).

| Test | d [m] | $S_{3Dmeasured}$ [-] | | |
|--------|-------|----------------------|------------|------------|
| | | 1000 waves | 3000 waves | 5000 waves |
| s1_005 | 0.24 | 4.47 | 10.63 | 12.7 |
| s2_005 | 0.36 | 3.31 | 6.63 | 7.54 |
| s3_005 | 0.50 | 2.75 | 3.53 | 3.7 |
| s3_011 | 0.50 | 1.79 | 2.38 | 3.07 |

A similar analysis can be performed for tests s1_004, s2_003 and s3_002 concerning a larger mean stone diameter but smaller armour layer thickness. In this case, the damage number also decreases

with increasing water depth, with the exception occurring from test s2_003 to s3_002 (at 5000 waves). However, this might be influenced by the fact that test s3_002 presented a larger U_c than test s2_003. These values are presented in Table 4.19. The increasing damage number for decreasing water depths was also noted by [148], which indicated that this was also observed for tests with waves in an opposing current, which are not covered in this dataset. Based on these results and on the short range of water depths used to develop Eq. (3.57), it is expected that the accuracy of the predictive formula might be dependent on the water depth (as confirmed in section 4.2.6.5).

Table 4.19 – Influence of the water depth in the measured damage number ($D_{50}=4.135$ mm; $n_a=2D_{50}$).

| Test | d [m] | S _{3D} measured [-] | | |
|---------------|-------|------------------------------|------------|------------|
| | | 1000 waves | 3000 waves | 5000 waves |
| S1_004 | 0.24 | 2.05 | 2.03 | 2.27 |
| s2_003 | 0.36 | 1.55 | 1.77 | 1.56 |
| s3_002 | 0.50 | 1.01 | 1.7 | 1.96 |

4.2.6.3.2 Influence of the wave height

Due to the tested range of the MARINET data, which covered very limited conditions in terms of the target significant wave height, it becomes difficult to assess the influence of the significant wave height while the remaining variables are kept constant. Note, that the significant wave height does not vary considerably within the same test series. The wave heights from series s1 are smaller than in the other series. However, a comparison between tests from different series will include the influence of the wave height as well as the influence of the water depth. Hence, it is difficult to analyse which part of the damage variation is caused by the significant wave height itself or by the other variables that may slightly vary. One also encounters this problem in [1, 32] and [148], which is mainly caused by the fact that the target conditions are not perfectly matched, due to multiple factors, such as the inherent uncertainty in the laboratory environment or the uncertainty in the measurement equipment.

Nevertheless, this section tries to analyse a set of tests with similar conditions or tests that enable one to perceive the combined influence of the wave height with other influencing factors. The present analysis is focused on perceiving if the significant wave height is influencing the damage number in a comparable way to the one identified in the previous datasets.

Considering tests s3_008 and s3_009 (same D_{50} and n_a), the significant wave height experiences a small variation, with the one from the first test being larger than the second for all wave trains. The depth-averaged current velocity is also slightly larger in test s3_008 than in test s3_009. Test s3_009 presents a smaller damage number than test s3_008, as shown in Table 4.16. This is also evident in the visual record presented in Figure 4.18. This effect is also added to the effect of U_c . Although in Figure 4.18 the deposition on top of test s3_009 does not enable the clearest visual assessment, it is possible to note the displacement of the stones in the yellow ring that occurs in s3_008 but does not occur in s3_009.

In order to avoid the eventual bias caused by the differences in the depth-averaged current velocity, tests with the same value of U_c may also be considered. However, for the present dataset, this implies that scour protections that may have different thicknesses of the armour layer are analysed. In this case, a possible analysis can be performed between tests s1_004 and s1_006 or between tests s2_003 and s2_004. This comparison is performed in Figure 4.19, where the damage number is divided by the number of layers (n_a), where each layer has a thickness of D_{50} , i.e the comparison is

performed with $S_{3D}/(n_a)$. This transformation enables the comparison between the measured damage numbers for scour protections with the same D_{50} but with different thicknesses. This procedure was also implemented in [26] and [102].

Figure 4.19 shows that the damage number tends to increase with increasing significant wave height. However, the short range of values of H_{m0} within the same test series becomes evident, thus further analysis recommended for a wider range than the one presented here. Although the results from Figure 4.19 are in agreement with the ones reported in [1, 32] and [148], the short range of tested values of H_{m0} is a common denominator of all these datasets. Figure 4.19 represents H_{m0} in millimeters to make the differences more perceivable. It includes another example, s3_005 and s3_011, for which the significant wave height increases simultaneously with the current velocity, thus increasing the damage number of the scour protection. It can also be noted in Figure 4.19, that the effect of H_{m0} is less perceived in the comparison between s3_005 and s3_011, which present the same armour thickness. Looking at the remaining comparisons, it is possible to see that the changes in the armour layer thickness is also affecting the present results.

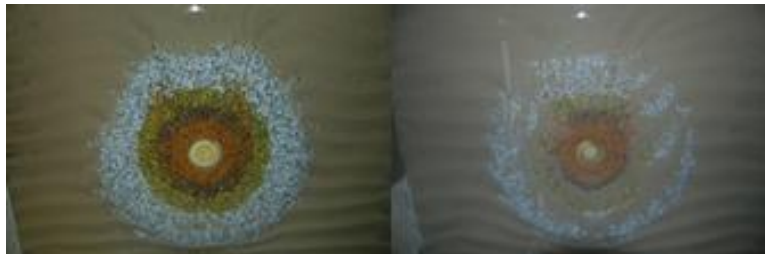


Figure 4.18 – Visual comparison of damage after 5000 waves in test s3_008 ($S_{3Dmeasured5000}=1.01$; $H_{m0}=0.143$ m; $T_p=1.52$ s; $U_c=0.222$ m/s), on the left, and test s3_009 ($S_{3Dmeasured5000}=0.71$; $H_{m0}=0.136$ m; $T_p=1.54$ s; $U_c=0.182$ m/s), on the right. Flow direction from bottom to top.

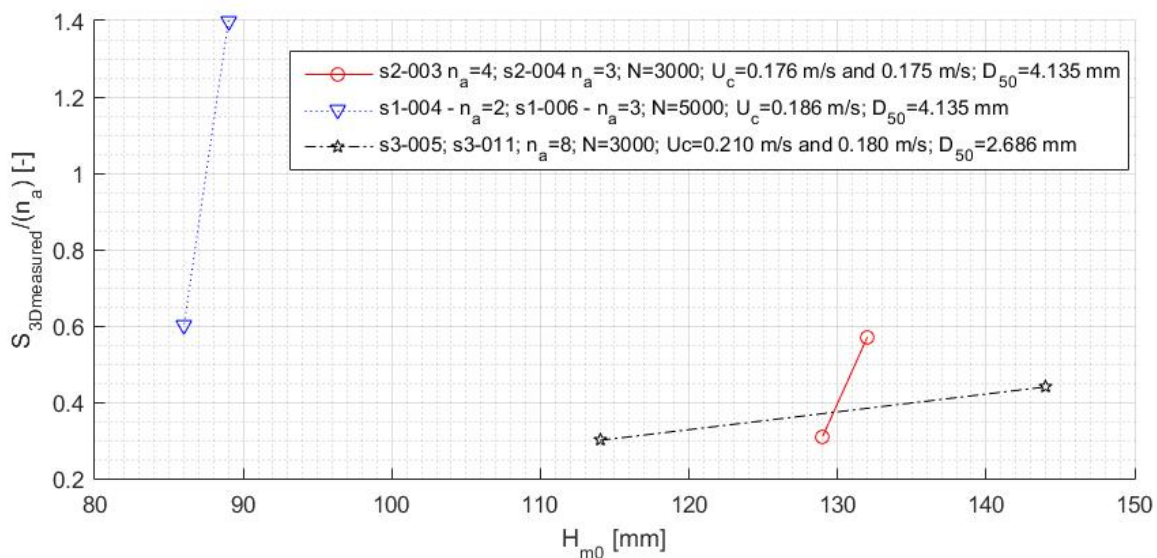


Figure 4.19 – Influence of the wave height on the measured damage number.

4.2.6.3.3 Influence of the wave period

The research programme did not aim at an extensive analysis of the influence on the damage number of the peak wave period nor the energy spectral wave period. Therefore, as it is possible to see in Table 4.7, both of these periods do not cover a sufficient range for a proper analysis of their influence.

Nevertheless, it is important to state that the main findings that resulted from the research presented in [1] and [32] led to the conclusion that the damage number of the scour protection increases for increasing wave periods (both T_p and $T_{m-1,0}$), provided that the significant wave height remains the same. As no analysis was performed regarding the MARINET data, one points out to Figure 4.20, which refers to the tests performed in [1]. According to [1], this effect is related to the fact that the motion of the stones is not only dependent on the shear stress acting on the protection, but also on the duration (time interval) to which the stones are subjected to that same stress. In this sense, the longer the stones are exposed to the high values of the shear stress (i.e. the longer the periods) the larger the damage is expected to be.

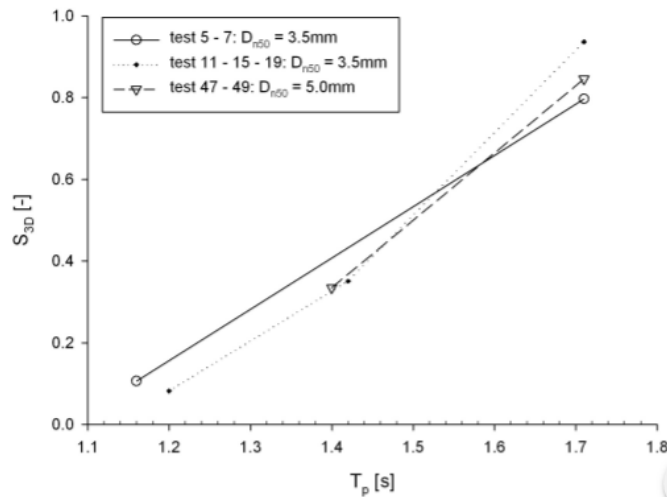


Figure 4.20 – Influence of the peak period in the damage number of the scour protection [1].

4.2.6.3.4 Influence of the wave-induced bottom velocity

Taking into consideration Eqs. (3.46) and (3.58), and as noted in [1], the influence of the water depth, the wave height and the wave period can be translated into an influence on the orbital bottom velocity (U_m). For the present analysis, the orbital bottom velocity is calculated by means of spectral analysis, according to Eq. (3.58), considering a JONSWAP spectrum with a peak enhancement factor $\gamma=3.3$, as described in [113].

The influence of the wave-induced bottom velocity (U_m) can be assessed, for example, with tests s1_005 and s3_011 after 3000 waves, both of them with $n_a=8D_{50}$ and $D_{50}=2.686$ mm. Both tests have almost the same value of U_c , while H_{m0} varies from 0.089 m to 0.114 m, respectively. In this case, the peak period changes from 1.52 (s1_005) to 1.55 s (s3_011). However, the water depth is not the same and the reduced water depth in series s1 has larger impact on U_m than the increased peak period between both tests. For test s1_005, $U_m=0.159$ m/s and $S_{3D3000}=10.63$, which compares to test s3_011, with $U_m=0.114$ m/s and $S_{3D3000}=2.38$. These tests show an increase in the measured damage number for increasing bottom velocities. For this case, the water depth has a large residual influence on damage even when the peak period only has a very small change. This observation had already been noticed in [1]. Nevertheless, and as observed in section 4.2.6.3.3, the peak period is not considerably varied in this dataset, thus not enabling a full analysis of the influence of U_m related to large variations of T_p .

Another example is found for tests s1_006 and s2_003 after 3000 waves. Both tests vary in water depth, peak period and significant wave height. $U_m=0.155$ m/s and 0.172 m/s, respectively. In this case, for test s2_003, $U_c=0.176$ m/s, which is smaller than $U_c=0.185$ m/s from test s1_006. Despite the

smaller depth-averaged current velocity, the damage is larger in s2_003 than in s1_006 because of a larger orbital bottom velocity. The damage number after 3000 waves for tests s1_006 and s2_003 was equal to 1.5 and 1.77, respectively. These two comparisons are shown in Figure 4.21.

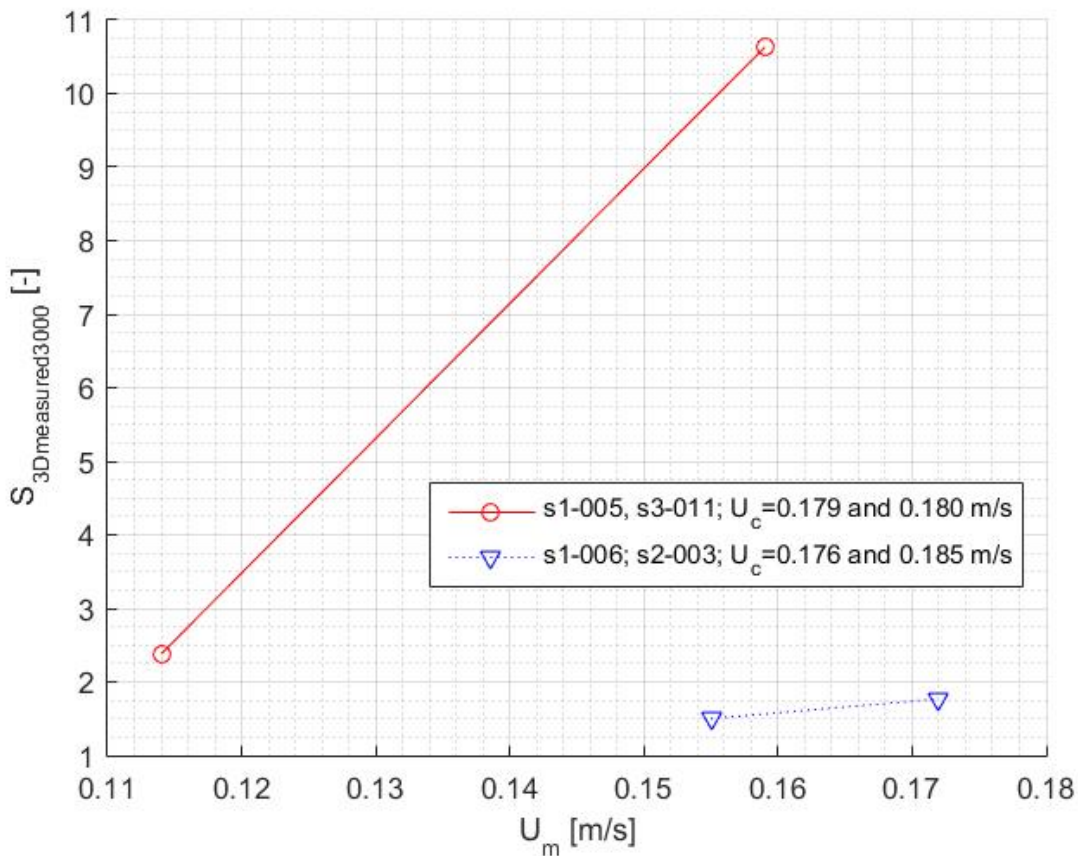


Figure 4.21 – Influence of the orbital bottom velocity on the measured damage number after 3000 waves for tests s1_005 and s3_011, s1_006 and s2_003.

4.2.6.3.5 Influence of the flow velocity

As seen in section 2.9.1 and throughout Chapter 3, the flow velocity plays an important role in both scour and damage development. In the present case, the flow velocity is analysed by means of the depth-averaged current velocity measured at a distance of $0.4d$ from the bed level. The influence of the average flow velocity on the damage number depends both on the magnitude of the velocity and on the stone size applied to the scour protection.

Regarding the stone sizes used in [1, 32] and [148], former research on the damage number of scour protections has concluded that the flow velocity has a more pronounced influence when the smallest stone size ($D_{50}=4.2$ mm) is used in the armour layer. When adopting larger diameters, i.e. 6.1 mm and 8.45 mm, this influence is less pronounced but it is still present. In light of these results, it is expected that for $D_{50}=2.686$ mm or 4.135 mm, the influence of the flow velocity is more noticeable than the one for the armour layers tested with $D_{50}=6.02$ mm and 7.5 mm.

Tests s3_004 and s3_009 are both performed with the same stone size (4.135 mm) and protection thickness ($3D_{50}$). After 3000 waves, both tests present a very similar significant wave height, i.e. 0.137 m in test s3_004 and 0.136 m in test s3_008. However, the depth-averaged current velocity is equal to 0.221 m/s and 0.182 m/s, respectively. When considering the damage number developed after 3000 waves (Table 4.16), test s3_004, with $U_c=0.221$ m/s, has a damage number of 2.29 (or

$S_{3D3000}/(n_a)=0.75$), which is larger than the value of 0.75 (or $S_{3D3000}/(n_a)=0.25$) presented for test s3_009 with $U_c=0.182$ m/s. So, the damage number considerably increased due to the magnitude of the flow velocity.

Considering tests with the smallest diameter ($D_{50}=2.868$ mm), one may look again at tests s3_005 and s3_011, for which the depth-averaged velocity varies with a cumulative effect added to the significant wave height. As reported in Table 4.16 (see also Table 4.17), test s3_005 presents larger damage numbers than test s3_11, since both the wave height and the current velocity are systematically larger in the first test than in the second, for all wave trains. For example, after 3000 waves, for s3_005, $S_{3D3000}=3.53$, whilst for test s3_011, $S_{3D3000}=2.38$, i.e. $S_{3D3000}/(n_a)=0.44$ and 0.30, respectively.

Regarding the large diameters, the MARINET dataset is not very suitable for a systematic assessment of the influence of the flow velocity, because for the stone diameters of 6.02 mm and 7.5 mm, no tests were repeated within the same series, thus meaning that the water depth changed. The reason for this is the fact that these scour protection tests were mainly designed to empirically obtain dynamic configurations of the protection. Therefore, since most of these protections were identified as being statically stable or dynamically stable (but with small stones movement), the following tests were performed either for a smaller diameter or a smaller thickness, compared with the previous test. Moreover, as noted in [1], the flow velocity has more influence on the S_{3D} values for small diameters, thus justifying the attention given to tests with $D_{50}=2.686$ mm or 4.135 mm. When aiming at optimized scour protections, the intention is to use smaller diameters than in statically stable ones [151] (also discussed in sections 3.7.1.4 and 3.7.1.5), which also justifies the lack of tests performed for the largest diameters.

Nevertheless, and despite the variation in the water depth, it addresses the following comparisons: s1_002 and s2_002 ($D_{50}=6.02$ mm; $n_a=2D_{50}$) and s1_001 and s1_002 ($D_{50}=7.5$ mm; $n_a=4D_{50}$ and $2D_{50}$, respectively). Test s1_002 has a smaller current and smaller wave height and period than the ones presented in s2_002. Moreover, the flow velocity is also smaller in s1_002 than in s2_002, $U_c=0.151$ m/s and 0.175 m/s, respectively (after 3000 waves). Table 4.16 shows that the damage number is smaller in s1_002 than in s2_002 for all wave trains. However, despite the combined effect of all these variables, it is perceivable that the damage number does not differ considerably, i.e. $S_{3D3000}=0.30$ in s1_002 ($S_{3D3000}/(n_a)=0.15$) and $S_{3D3000}=0.40$ in s2_002 ($S_{3D3000}/(n_a)=0.20$). However, this may occur due to three possible situations:

- despite the smaller H_{m0} , T_p and U_c , test s1_002 has a smaller water depth ($d=0.24$ m), which contributes to approximate the damage number to the one obtained in test s2_002 ($d=0.36$ m);
- the large stone diameter used is less influenced by the hydrodynamic conditions (including the influence of U_c) than the small diameters tested in s3_005, s3_011, s3_004 and s3_009, which is also in agreement with the findings reported in [1, 32] and [148];
- test s1_002 was identified as statically stable, thus no movement occurrence was registered, which contributes to a very low dependence on the tested hydrodynamic conditions, which are not able to generate significant differences in the damage number. Test s2_002 was dynamically stable, but the damage numbers reported are near the statically stable limit (S_{3D}) defined by [32]. Although these limits are discussed in following sections, this scour protection, albeit being dynamic, is near static stability (damage level 2, i.e. movement occurs but not so significant as in damage level 3, where significant movement occurs without failure), thus damage development is also small, despite the larger U_c than in s2_002.

Regarding tests s1_001 and s2_001, the armour thickness is different, as shown in Table 4.6. Both scour protections are identified as statically stable, thus the tested hydrodynamic conditions were not able to cause significant movement. Again, for 3000 waves, the depth-averaged current velocity is smaller in s1_001 than in s2_001, as well as the significant wave height and the water depth. For test s1_001, $S_{3D3000}=0.29$, whilst for test s2_001 $S_{3D3000}=0.41$. In this case, for s1_001, the damage number per meter of the armour layer, $S_{3D3000}/(n_a)=0.07$, and for test s2_001, $S_{3D3000}/(n_a)=0.20$.

These comparisons are graphically represented in Figure 4.22, where it is possible to see that the damage number increases for increasing depth-averaged current velocities. As discussed before, the effects of the flow direction are not considered in the present analysis, because only waves in following steady currents were tested. In the aforementioned studies, it was found that, for waves in an opposing current, the damage number also increases for an increasing flow velocity [1, 32].

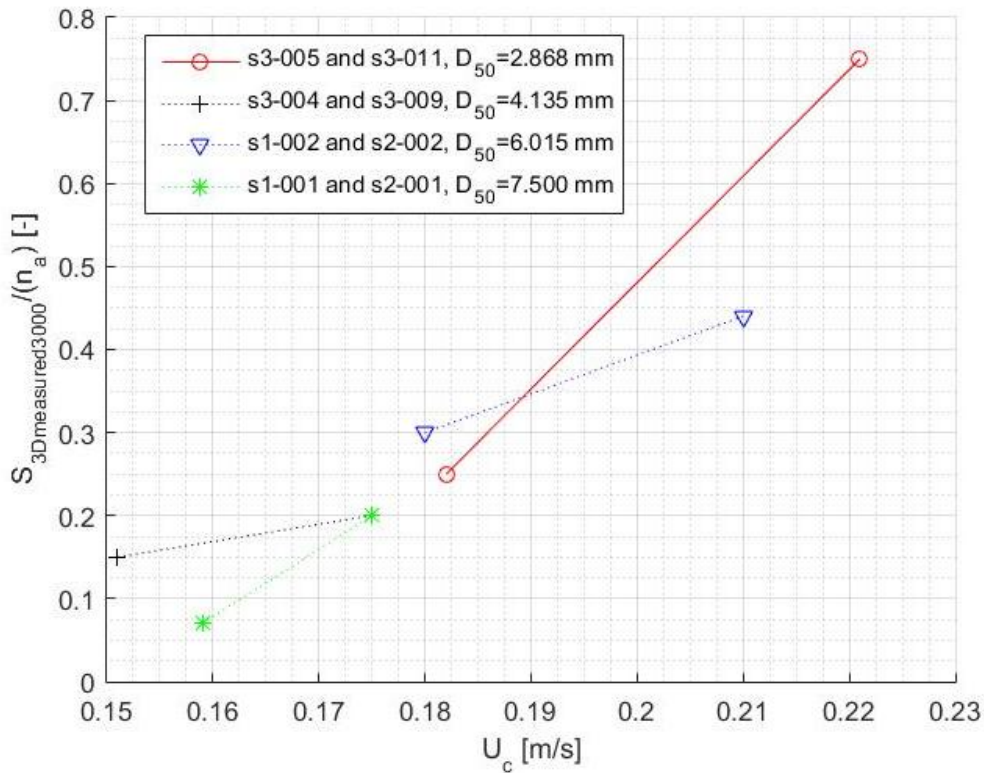


Figure 4.22 – Influence of flow velocity on the measured damage number.

4.2.6.3.6 Notes on the wave-current interaction

The range of test conditions targeted a flow regime that was expected to be equally dominated by waves and current. Therefore, the wave or current dominance on the flow regime was not varied considerably. As mentioned in section 3.7.1.3, the wave or current dominance over the flow regime can be assessed by means of the bed shear-stress ratio $\tau_c/(\tau_c + \tau_w)$ or, alternatively, by means of the velocity ratio (U_{cw}) calculated from Eq. (4.5) [91].

$$U_{cw} = \frac{U_c}{U_c + U_m} \quad (4.5)$$

If $U_{cw}=1$ then the flow is dominated by the steady current alone (no waves present); if it tends to 0 then the flow regime tends to be more dominated by the waves' presence (until the flow is composed

by waves alone). For $U_{cw}=0.5$, the regime is equally dominated by the waves and the current. These values are provided in Table 4.20, which shows that U_{cw} ranges between 0.458 m/s (slightly dominated by waves) and 0.623 m/s (steady current dominated).

Table 4.20 – Wave-current dominance on the flow regime per test, by means of velocity ratio (U_{cw}).

| Test | D_{50} | na | U_{cw} [-] | | |
|------------|----------|-------------------|--------------|------------|------------|
| | [mm] | [times D_{50}] | 1000 waves | 3000 waves | 5000 waves |
| s1_001 | 7.50 | 4 | 0.491 | 0.492 | 0.494 |
| s1_002 | 6.02 | 2 | 0.481 | 0.468 | 0.458 |
| s1_003 | 4.14 | 3 | 0.525 | 0.524 | 0.521 |
| s1_004 | 4.14 | 2 | 0.538 | 0.538 | 0.539 |
| s1_005 | 2.69 | 8 | 0.528 | 0.530 | 0.531 |
| s1_006 | 4.14 | 3 | 0.544 | 0.545 | 0.548 |
| s2_001 | 7.50 | 2 | 0.461 | 0.481 | 0.485 |
| s2_002 | 6.02 | 2 | 0.511 | 0.508 | 0.505 |
| s2_003 | 4.14 | 3 | 0.488 | 0.505 | 0.507 |
| s2_004 | 4.14 | 4 | 0.481 | 0.500 | 0.504 |
| s2_005 | 2.69 | 8 | 0.479 | 0.489 | 0.492 |
| s2_006 | 4.14 | 4 | 0.535 | 0.563 | 0.568 |
| s3_001 | 6.02 | 2 | 0.597 | 0.597 | 0.593 |
| s3_002tris | 4.14 | 2 | 0.598 | 0.618 | 0.623 |
| s3_003 | 4.14 | 4 | 0.596 | 0.613 | 0.614 |
| s3_004 | 4.14 | 3 | 0.602 | 0.622 | 0.620 |
| s3_005 | 2.69 | 8 | 0.580 | 0.598 | 0.600 |
| s3_006 | 2.69 | 4 | 0.592 | 0.610 | 0.614 |
| s3_007 | 2.69 | 6 | 0.594 | 0.611 | - |
| s3_008 | 4.14 | 3 | 0.594 | 0.613 | 0.612 |
| s3_009 | 4.14 | 3 | 0.565 | 0.572 | 0.573 |
| s3_010 | 4.14 | 2 | 0.604 | 0.615 | 0.617 |
| s3_011 | 2.69 | 8 | 0.603 | 0.612 | 0.611 |

Several works performed on the scour phenomenon, e.g. [91] or [180], reported that scour depths increase for increasing U_{cw} , i.e. for a steady current predomination. Moreover, the current dominance over the flow regime becomes more evident for $U_{cw}>0.7$ [180]. In this research, no cases were tested above this limit. As seen in the previous environmental parameters, several of the influences on the scour depth are somehow comparable to the ones obtained for the damage number in scour protections. Therefore, it is expected that the damage number increases for increasing values of U_{cw} , even though not many works are available relating the relationship between S_{3D} and U_{cw} . It should also be noted that previous research directly related to this test programme, i.e. [1, 30, 32] and [148], did

not elaborate on this relationship, which is valuable when attempting to perceive the nature of damage development under a wave-current regime.

When analysing comparable scour protections, the tests presented in Table 4.21 are addressed, which are ordered by their value of U_{cw} within each wave train. It must be recognised that Table 4.21 covers a rather short range of values of U_{cw} (see also Table 4.22). Series s2 is not included in Table 4.21 because only one test was performed with $D_{50}=4.14$ mm and a thickness of the armour layer of $3D_{50}$.

However, it is possible to note that within the same series, i.e. the same water depth, the damage number increases for increasing velocity ratios, as previously expected. As a corollary, it can be noted that, for the tests in Table 4.21, damage increases when the wave-current regime is dominated by the current component. Hence, it seems that the maximum damage occurs for a steady current alone, which is somehow comparable to the assumption made by the formulation introduced by [61], for which the maximum scour depth, according to Eqs. (2.41) and (2.44), is reached when a current is acting without waves.

However, the generalization of this conclusion requires further research. In test series s2, one compared test s2_004 with test s2_006, which also presented an increase in the measured damage number with increasing U_{cw} . However, these scour protections have an armour layer thickness of $4D_{50}$ instead of $3D_{50}$. These values are shown in Table 4.22. The results from Table 4.21 and Table 4.22 after 5000 waves are represented in Figure 4.23.

Table 4.21 – Velocity ratios and damage numbers for comparable scour protections in test series s1 and s3.

| Test | D_{50} | d | n_a | U_{cw1000} | U_{cw3000} | U_{cw5000} | S_{3D1000} | S_{3D3000} | S_{3D5000} |
|--------|----------|------|-------------------|--------------|--------------|--------------|--------------|--------------|--------------|
| | [mm] | [m] | [times D_{50}] | [m/s] | [m/s] | [m/s] | [-] | [-] | [-] |
| s1_003 | 4.14 | 0.24 | 3 | 0.525 | 0.524 | 0.521 | 0.78 | 1.13 | 1.56 |
| s1_006 | 4.14 | 0.24 | 3 | 0.544 | 0.545 | 0.548 | 0.95 | 1.5 | 1.79 |
| s3_009 | 4.14 | 0.50 | 3 | 0.565 | 0.572 | 0.573 | 0.42 | 0.75 | 0.71 |
| s3_008 | 4.14 | 0.50 | 3 | 0.594 | 0.613 | 0.612 | 0.48 | 0.95 | 1.01 |
| s3_004 | 4.14 | 0.50 | 3 | 0.602 | 0.622 | 0.620 | 2.28 | 2.29 | 2.40 |

Table 4.22 - Velocity ratios and damage numbers for comparable scour protections in series s2

| Test | D_{50} | d | n_a | U_{cw1000} | U_{cw3000} | U_{cw5000} | S_{3D1000} | S_{3D3000} | S_{3D5000} |
|--------|----------|------|-------------------|--------------|--------------|--------------|--------------|--------------|--------------|
| | [mm] | [m] | [times D_{50}] | [m/s] | [m/s] | [m/s] | [-] | [-] | [-] |
| s2_004 | 4.14 | 0.36 | 4 | 0.481 | 0.500 | 0.504 | 2.28 | 2.29 | 2.4 |
| s2_006 | 4.14 | 0.36 | 4 | 0.535 | 0.563 | 0.568 | 2.99 | 3.18 | 3.99 |

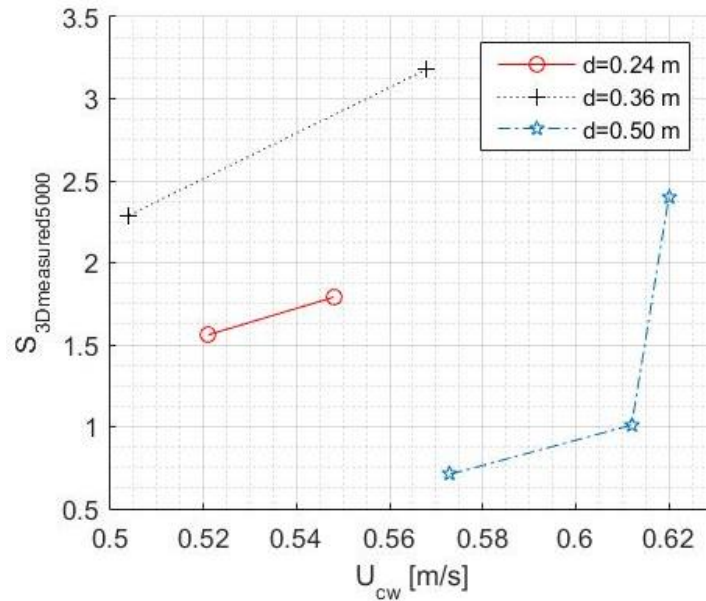


Figure 4.23 – Influence of U_{cw} on S_{3D5000} [-] for comparable scour protections ($D_{50}=4.135$ mm) in different series.

Another aspect that relates to the wave-current regime is the relationship with the KC and the Re_p numbers. As noted in section 4.2.3.4, [148] suggested that, for small pile diameters, the KC number determined the damage development, whilst for large pile diameters, the Re_p number was the dominant parameter. Due to the influence of KC and Re_p on the scour mechanisms, it is reasonable to expect that both numbers may have a relationship with the damage number of a scour protection under combined waves and current. The present dataset did not test different pile diameters, thus it is not possible to properly evaluate the previous remark. Future research should address this aspect, as little to no generalised knowledge is reported in the literature on the influence of KC and Re_p on the damage development of the scour protection.

4.2.6.3.7 Influence of the number of waves

The number of waves has a cumulative effect on the damage number of the scour protection, as it was noted in previous sections. Generally, if the armour layer fails, then the damage progresses between sub-areas, causing the generalized failure of the scour protection. However, when a dynamic scour protection is successfully designed, such progression is intended to stabilize due to reshaping of the armour layer. Eventually, stones that were displaced in a previous wave train may refill the sub-areas that were exposed. In fact, according to [1] and [26], dynamic scour protections may accept larger damage numbers. Of main importance is that damage does not progress over time. The cumulative loading effect of different wave trains on the scour protection is, therefore, much associated to the number of waves in a storm (N) and also to the sequence of magnitude of the several waves. The physical model studies regarding the stability and failure of scour protections are typically based on the definition of a storm event (duration and magnitude), e.g. [100, 101] or [151]. The model of the scour protection is commonly subjected to modelled storm conditions, for which failure may occur. Such hydrodynamic conditions are usually defined as an extreme sea state, which depends on the location intended for the prototype. In this sense, when considering the number of waves, two key aspects should be addressed: firstly, the value of N that corresponds to the design storm; secondly, the fact that the protection may also collapse for hydrodynamic conditions, which albeit not being as extreme as the design condition, are experienced for a considerably longer period of time. For

example, it may be assumed that a scour protection is designed for a storm duration of 12 hours, for which $H_s=7$ m and $T_p=12$ s. This does not mean that the scour protection will not fail under several storms of $H_s=5$ m, $T_p=12$ s and 16 hours duration that occur frequently throughout the same month. Regarding these two aspects, the present experimental research addressed the scour protection design under specific storms (design storms as defined in section 4.2.3.1). However, it did not address the aspect of the smaller magnitude storms, which may present a larger N value (storm duration) and/or may occur in a consecutive manner through a longer time window. This second situation is somehow comparable to the one that causes scour-induced failure at bridge piers for consecutively high floods (but not extreme), as the case registered, for example, in Hintze Ribeiro bridge [83]. The consecutive effects of minor storms is still a gap in scour research literature, which is hereby pointed as an important topic for future research. Regarding the present model, it can be argued that 1000, 3000 and 5000 waves may be considered as a sequence of extreme storms. However, it must be noted that this sequence does not include periods of modelled normal conditions between the storm wave trains, which could contribute to a better re-shaping of the dynamic armour layer. Nevertheless, the sequence is defined to understand if a dynamic profile, i.e. equilibrium of the armour layer, is obtained. The required number of waves to reach the equilibrium profile, i.e. the one associated to non-significant damage progression, was already discussed in section 3.5.3. It was concluded that there is no consensus on the minimum number of waves that leads to the dynamic profile, as seen in [26, 31] and [102].

The influence of the number of waves in the MARINET data was also addressed in [26], also summarized in [11]. The conclusions obtained are hereby revisited. The analysis performed by [26] concluded that in dynamically stable tests, stone movement is mostly observed after 1000 waves. In deep water conditions (s3), failure mostly occurred after 5000 waves, whereas in intermediate and shallow waters, failure often occurred after 1000 waves only. In the former case, scour depths often developed after 3000 and 5000 waves and new scour holes appeared. Figure 4.24, taken from [26], compares a dynamic scour protection and a failure occurrence, where it is possible to note that between 1000 and 5000 waves no damage progression occurs in the profiles of the dynamic configuration, while on the failure case there is a considerable variation and the filter is exposed. Moreover, [26] also analysed the variation of global damage numbers of the scour protections (ΔS_{3D}) tested per number of stone layers applied in each scour protection (n_a). The evolution of damage is depicted by the damage increase $\Delta S_{3D}/n_a$ between 0 and 1000 waves, 1000 and 3000 waves, and 3000 and 5000 waves (Figure 4.25).

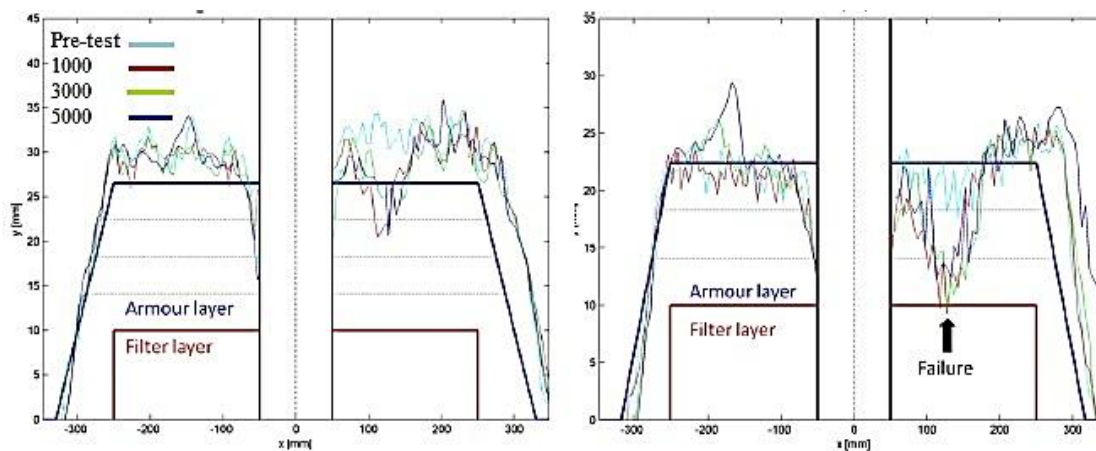


Figure 4.24 – Comparison of profile evolution for a dynamically stable test (left) and failure (right) for 1000, 3000 and 5000 waves [26].

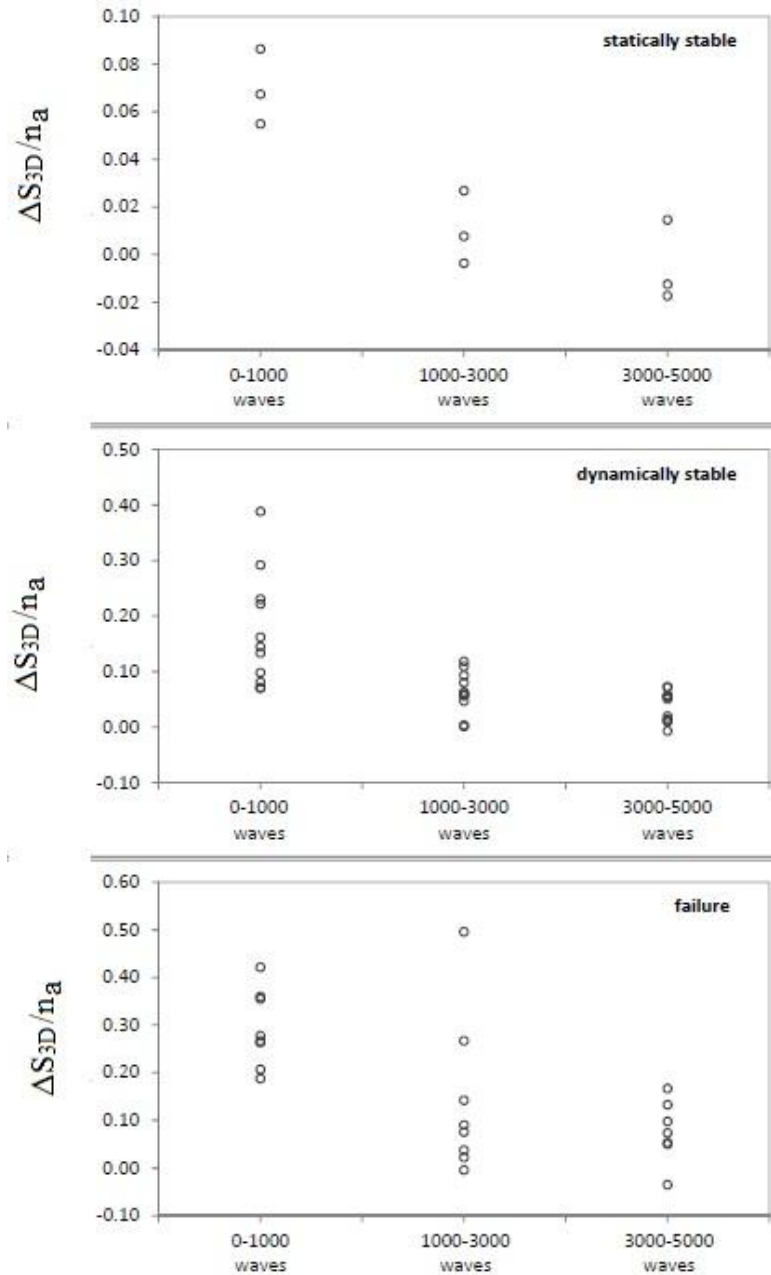


Figure 4.25 - Damage increase $\Delta S_{3D}/n_a$, for statically stable (top), dynamically stable (middle) and failure (bottom) tests [26].

For the statically stable tests, a very small damage development rate is observed during the first 1000 waves ($\Delta S_{3D}/n_a = 0.05 - 0.09$). The damage development rate reduces between 1000 and 3000 waves ($\Delta S_{3D}/n_a = 0.00 - 0.03$), and slightly further reduces or becomes negative (indicating a net accretion) between 3000 and 5000 waves ($\Delta S_{3D}/n_a = -0.02 - 0.01$).

For dynamically stable tests, a much higher damage development rate is observed during the first 1000 waves ($\Delta S_{3D}/n_a = 0.07 - 0.39$). The damage development rate strongly reduces between 1000 and 3000 waves ($\Delta S_{3D}/n_a = 0.00 - 0.12$), and slightly further reduces between 3000 and 5000 waves ($\Delta S_{3D}/n_a = -0.01 - 0.07$). According to [26], these results indicate that an equilibrium state is reached after 3000 to 5000 waves, thus confirming the feasibility of a dynamic design approach. For the failure tests, a high damage development rate is observed during the first 1000 waves ($\Delta S_{3D}/n_a = 0.19 -$

0.42). For most tests, the damage development rate reduces between 1000 and 3000 waves, but some large rates still occur ($\Delta S_{3D}/n_a = 0.00 - 0.50$). The higher damage development rates further reduce between 3000 and 5000 waves ($\Delta S_{3D}/n_a = -0.04 - 0.17$). No equilibrium is reached after 5000 waves for the failure tests. As an overall idea, it can be said that increasing number of waves increases the damage number. However, the following behaviour is noted per type of stability (see Figure 4. 26):

- Static stability – Number of waves initially leads to an increase in the damage number, which tends to decrease as N increases, eventually due to deposition of sand on top of the armour layer;
- Dynamic stability - Number of waves initially leads to an increase in the damage number, which is fast in a first stage but that tends to decrease towards an equilibrium variation of damage;
- Failure - Number of waves leads to an increase in the damage number, which quickly progresses, leading to generalise collapse of the protection.

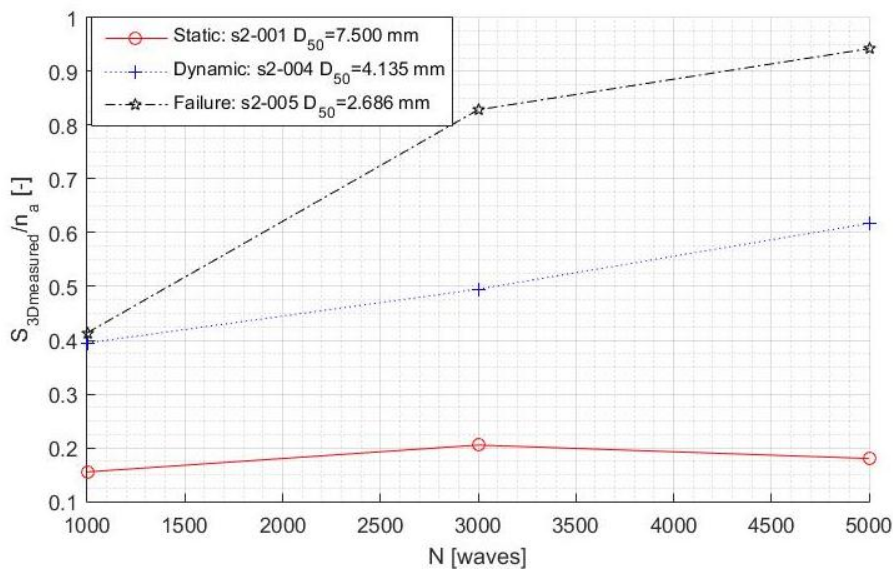


Figure 4. 26 – Measured damage number after each wave train for statically stable, dynamically stable and failure tests taken from series s2 ($d=0.36$ m).

4.2.6.3.8 Influence of the stone size and the armour layer thickness

The stone size and armour thickness were identified as structural parameters of the scour protection that are key variables when defining the configuration of the scour protection. As it was discussed throughout sections 3.6.2 and 3.7.1 (and sub-sections), the stone size is a common object of optimization when attempting to improve the design of scour protections. However, the size reduction comes at the cost of stability problems, caused by the drag shear-stress and uplifting forces. The MARINET data analysed the possible reductions in the stone size towards a dynamic stability, eventually obtained with a suitable combination between a reduced D_{50} and an increased armour layer thickness ($t_a=n_a D_{50}$).

Table 4.23 shows that dynamic stability is obtained by means of a reduction in the mean stone diameter, for which the armour layer thickness must be increased in order to enable reshaping of the armour layer. These results are in agreement with the main findings presented in [1, 32] and [148], however covering a wider range of thicknesses. Table 4.23 shows that large diameters (7.500 mm and 6.015 mm) led to static stability, whilst the small diameters (4.135 mm and 2.686 mm) enabled dynamically stable configurations. Particular configurations, which have failed, could be re-designed

for dynamic stability with the same mean stone diameter but increased armour layer thickness, e.g. test s1_004 ($2D_{50}$) failed but, for the same D_{50} , adding an extra layer of stones ($3D_{50}$) led to dynamic stability in test s1_003.

For the smallest stone diameter, $D_{50}=2.686$ mm, dynamic stability was only achieved for test series s3 and for a considerable thickness of $8D_{50}$. As discussed in Chapter 3, the results seem to show that the mean stone size can only be reduced until a certain extent, because either the required thickness becomes too costly or the mean stone diameter may not be sufficient to endure the storm conditions (regardless of the thickness used). For the same environmental conditions, the reduction of D_{50} makes the armour layer more prone to damage, because the stones have a smaller threshold of motion than the ones with larger diameters.

This can be perceived from Figure 4.27, which shows that for scour protections with the same number of layers but with different stone sizes, the damage number increases with decreasing D_{50} .

Table 4.23 – Classification of tests results: failure (red), statically stable (blue) and dynamically stable (green) tests [26]

| d [m] | D_{50} | | | |
|-------|-----------|-----------|--------------------------|------------------|
| | 7.500 mm | 6.015 mm | 4.135 mm | 2.686 mm |
| 0.24 | | | $2D_{50}$ | |
| | $4D_{50}$ | $2D_{50}$ | (s1_004) | $8D_{50}$ |
| | (s1_001) | (s1_002) | $3D_{50}$ | (s1_005) |
| | | | (s1_003; s1_006) | |
| 0.36 | | | $3D_{50}$ | |
| | $2D_{50}$ | $2D_{50}$ | (s2_003) | $8D_{50}$ |
| | (s2_001) | (s2_002) | $4D_{50}$ | (s2_005) |
| | | | (s2_004; s2_006) | |
| 0.50 | | | $2D_{50}$ | $4D_{50}$ |
| | | | (s3_002; s3_010) | (s3_006) |
| | | $2D_{50}$ | $3D_{50}$ | $6D_{50}$ |
| | - | (s3_001) | (s3_004; s3_008; s3_009) | (s3_007) |
| | | | $4D_{50}$ (s3_003) | $8D_{50}$ |
| | | | | (s3_005; s3_011) |

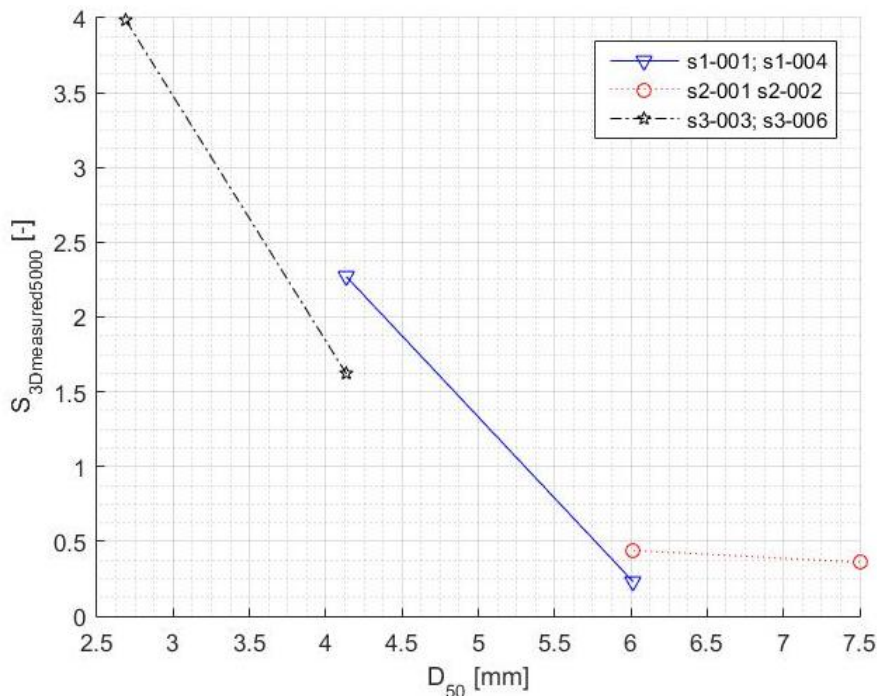


Figure 4.27 – Influence of the stone size on the measured damage number after 5000 waves.

The research presented by [1] and [32] tested a very narrow range of thicknesses. Nevertheless, it was observed that for small damage numbers the protection thickness did not have a considerable effect on the measured damage number. The authors state that this is due to the fact that for static stability no movement of the stones occurs, thus meaning that damage will not significantly progress over time, i.e. no reshaping of the armour occurs regardless of its thickness. The present dataset did not enable one to address this aspect in a detailed manner, since only three configurations led to static stability. From those three, only two were performed within the same water depth (i.e. tests s1_001 and s1_002), and while the first one is performed with $4D_{50}$, the second is performed with $2D_{50}$.

However, the mean stone diameter is different in both cases, thus a bias is expected due to this difference. Moreover, both tests present slight differences in H_{m0} and U_c (Table 4.7), which may also contribute to possible differences in the measured damage numbers. Table 4.16 shows that the difference is more noticeable for damage measured after 5000 waves. However, damage seems rather small and very similar for 1000 and 3000 waves. Furthermore, the obtained damage is also comparable in magnitude to the one obtained in test s2_001 (also statically stable), which was performed with a larger water depth ($d=0.36$ m). Note that test s2_001 has the same armour thickness as test s1_001 but a different one from test s1_002. Despite the short number of statically stable protections, it can be confirmed that the damage numbers are similar to each other, ranging from 0.23 to 0.41, with a decreasing damage registered between 3000 and 5000 waves, thus being indicative that damage occurrence is not much dependent on the armour thickness, since no displacements occur.

However, when considering dynamically stable scour protections, the protection thickness can indeed make a difference between stability and failure occurrence, as seen in Table 4.23, e.g. tests s1_004 (failure with $2D_{50}$) and s1_003 or s1_006 (dynamically stable with $3D_{50}$), for $D_{50}=4.135$ mm. This is also the case for tests performed with $D_{50}=2.868$ mm, i.e. s3_006 ($4D_{50}$) and s3_007 ($6D_{50}$) that have also failed, whilst tests s3_005 and s3_011, performed with $8D_{50}$, were dynamically stable. Future research should also address this topic due to its importance in the reshaping process of the armour layer, noting, however, that some of the remarks presented may not be valid for wide-graded

layers in which the division between filter and armour does not exist. The visual observations performed during testing showed that a thicker armour layer contributes with a larger volume of stones, which may cover the scour holes caused by displacement of other stones. Hence, it seems reasonable that damage progression can somehow be related with the armour layer thickness. Nonetheless, the formulation given by [32], in Eq. (3.57), does not consider this variable when predicting damage on the scour protection. For small damage numbers, this is not problematic, because one is in the domain of static stability. However, for dynamic scour protections that are designed with large damage numbers, this may contribute to departures from the actual measured numbers, which may lead one to ignore possible failure situations. Note that the physical model study performed in [101], also discussed in [100], have used buried or partially buried dynamic scour protections, as shown in Figure 3.16. Therefore, the discussion on the protection thickness regarding those scour tests is not exactly comparable to the one performed here for scour protections with an armour layer that is not levelled with the sand bed.

4.2.6.3.9 Notes on the influence of unstudied parameters

The scour phenomenon at an unprotected or protected pile encompasses complex processes that ultimately depend on several variables. The previous section has addressed the influences of variables that were covered by the MARINET data. Some of them could be analysed, *ceteris paribus*, whilst others were studied within predictable scenarios of multiple variation, e.g. significant wave height and current increase simultaneously. However, other variables, as the filter type, the density and grading of the armour layer stones, were not varied within the same hydrodynamic conditions or protection configuration. This section elaborates on these variables in order to understand their expected influence on the damage number:

- Density of the armour layer stones – varied between each grading used, i.e. D_{50} . However it also depended on the available material and need to account for the difference in water density between the model and the prototype. In a similar way to the mean stone diameter, the damage number decreases with increasing stone density (for the same D_{50}). In flat sand beds, as the ones applied in this study, as the stone density increases the stabilising force (weight) also increases, hence making the armour layer less prone to stone displacements, resulting in smaller damage in the protection. The influence of stone density on the damage of the protection is analogous to the influence of the density of the sand-bed sediments on the scour phenomenon and sediment transport. If the density of the sediments decreases the transport rate increases, thus scour depth also increases [52]. In [1, 32] and [148], the armour stone density was varied between 2650 kg/m^3 and 3200 kg/m^3 . These works confirmed that the damage number decreases for an increasing mass stone density. In the present study, one has analysed the damage number decrease obtained in tests 4, 16, 17, 20, 49, 51, 72, 74, 75, 76, 82 and 85, reported in [32], and concluded that an increase of 17% in the mass density led to a mean damage number decrease of 39%. This is an important aspect, as smaller diameters combined with high mass density stones may be adopted to obtain considerable cost reductions in the scour protection. Of course such cost reduction will always dependent on the price and availability of rock material. Moreover, the reduction in the D_{50} is only usefull if the volume of rocks needed for a thicker armour layer is not unreasonable increased.
- Armour layer grading – varied between tests, similarly to the mass density, but no comparable tests were performed because the uniformity parameter ($\sigma_U = D_{85}/D_{15}$) changes if the mean stone diameter is also changed, thus creating a bias in possible comparisons. In the literature, a lack of consensus is found regarding the influence of armour stone grading on the scour

protection behaviour. In [1], it is stated that, unlike the threshold of motion, damage of the protection is practically not influenced by the armour layer grading. As mentioned before, when addressing statically stable scour protections, [30] states that the stability, based on the threshold of motion, increases for an increasing $\sigma_U = D_{85}/D_{15}$, which is also in agreement with the results obtained for wide-graded scour protections in [31] and [103]. At the present state-of-the-art, it is not possible to ensure the extent of the influence of the armour layer grading on the damage number. It is a fact that the predictive formula from Eq. (3.57) does not consider this variable in the predictions of S_{3D} and still provides satisfactory results. However, in order to assess the formula's accuracy for large gradings, further research is required. The majority of the tests in [1, 32, 148] and also in [100, 175, 151] were performed for rather uniform sediments ($\sigma_U \approx 1.50$). However, some tests were performed for σ_U ranging from 2.48 to 5.17, which is short for generalised conclusions. The dynamic scour protections studied in the OPTI-PILE project, which imply the calculation of the stability parameter, are also based on the threshold of motion, for which the grading is of great importance. The armour layer grading plays a role on the smaller stone sheltering and on the pore pressure, which influences the behaviour of the scour protection [181]. Therefore, it may seem counter-intuitive that the damage number is independent from the armour stone grading, as identified in [1]. Although the influence of this variable on S_{3D} was not systematically studied in the present research, it should be recognised that this as an important aspect for future research.

- Filter type – as discussed in section 4.2.3.4, only a granular filter type was used, which compares to the geotextile filter used in the majority of the tests presented in [1, 32] and [148]. This choice was made to account for a more realistic representation of common prototype conditions. The results reported in [1, 32] show that the granular filter leads to larger damage numbers than geotextile filters. An interesting aspect is the fact that the tests performed without filter layer, in the previously mentioned research, led to damage numbers between the ones obtained with the geotextile and the granular filter. According to [32], a possible reason for larger damage numbers in tests with the granular filter might be related to the higher location of the bed material due to the larger thickness of the granular filter compared with the remaining options. Furthermore, the use of a geotextile filter does not allow the sand-bed sediments to be washed out through the armour layer, as seen in one of the failure modes addressed in section 3.3 (see also Figure 3.6). Therefore, damage induced by armour layer sinking is neglected when using a geotextile filter. Further details on the armour layer sinking are provided in [111]. In [32], despite the rather short number of tests, the results also indicated that the influence of the filter type was more noticeable for smaller mean stone diameters, which seems reasonable since the damage development rates are larger for smaller values of D_{50} (section 4.2.6.3.8). For larger diameters, i.e. configurations moving towards static stability, the volume of stones displaced is not expected to be large, thus meaning that there is no exposure of the filter layer. Hence, for small damage numbers, the filter layer is not expected to affect the evaluation of damage at the protection. However, it seems reasonable to assume that the geotextile filter may lead to underestimation of damage when considering scour protections that are within the transition between dynamic stability and failure. It should also be considered the potential effect of the filter layer in the pore pressure “inside” the scour protection, as discussed in section 3.9. The pressure gradient is affected by the filter layer, which may also affect the damage number results.
- Pile diameter – did not vary between tests (0.1 in the model, 5 m in the prototype), as previously addressed during the discussion of the test range conditions. In the original

research that led to the predictive formula of the damage number, it is recommended that its use is restricted to the same pile diameter. However, the pile diameter varied in [148] and, as seen in section 3.9, it was concluded that for small pile diameters, the KC number determines the damage development, whilst for large pile diameters, the Re_p number is the dominant parameter. As recognised in the literature, the pile diameter contributes to an amplification of the bed shear stress, which influences a design based on the threshold of motion, e.g. [52] or [57]. The dynamic scour protection designed according to [32] does not consider the amplification factor, thus it does not account for the pile influence either. Future research should address this aspect, as typically, it is known that the pile diameter influences scour severity.

- Type of foundation – the type of foundation (and also the shape of the monopile) influences the flow pattern, thus leading to possible changes in the damage number behaviour. So far, not many studies are reported for the damage number at dynamic scour protections with different shapes, or completely different from a monopile, e.g. jacket structure, tripod or GBF. Nevertheless, the majority of the foundations for offshore wind turbines consist on slender cylindrical piles, as seen in section 1.3, thus the present study still has a broad range of applicability. In [144], an empirical optimisation of the GBF foundation of offshore wind platform Dolwin Beta is presented for a foundation with 6 squared columns and 2 pontoons. Despite the successful configurations obtained in the physical model, the damage number was not measured throughout the tests. Instead, only the bathymetry, i.e. scour depths at the armour layer, was measured based on the stereophotographic technique reported in [182]. Therefore, the study showed the applicability of dynamic scour protections for other types of structures, but no comparisons were reported for the damage number.
- Configuration and construction of the scour protection – the final configuration of the scour protection, i.e. the method of construction, may also affect the damage number. As seen before, the dynamic scour protections tested in the OPTI-PILE project were levelled with the sand bed [100]. A reason for this particular configuration is that, when the scour protection is levelled with the bed, less perturbations in the bed boundary layer are expected, due to the sudden bathymetry change at the sand bed and the armour layer interface. This may also contribute for smaller damage numbers at the edge scour zone (the outer rings of the protection) than in the MARINET data. When assessing damage with different filter types, [32] noted that damage increased due to the increase of the height at which the stones are placed in the armour layer. Therefore, one expects that the damage number is larger in non-levelled scour protections, e.g. [1, 26, 32] or [102, 151], than in levelled ones, i.e. [100] and [101]. Another aspect that may influence the damage number is the radial extension of the scour protection, which remained as $5D_p$ for all tests presented. The test results showed that the damage numbers were higher at rings R1 and R2, which are closer to the monopile, thus being less influenced by the radial extension (provided that it is large enough), and at the outer rings, e.g. R5 and R6. Although the extension of the scour protection was not varied, the damage number near the foundation is expected to be less influenced by this variable. On the other hand, the damage number at the outer rings is probably more influenced by the extension. It is expected that, as the extension increases, the damage number at the outer rings decreases, because the edge scour is less affected by the foundation's presence (amplification of bed shear stress) and solely results from the differences in the bed roughness.

4.2.6.4 Damage location

The present section provides a brief summary on the damage location, regarding the MARINET data. A more detailed analysis of damage location was carried by [183] and also analysed in [26], as already introduced in section 4.2.6.3.7 when discussing the damage development due to the influence of the number of waves. The analysis hereby presented refers to the sub-areas division presented in Figure 4.14, with the wave-current direction from the bottom to the top in each figure.

4.2.6.4.1 Scour

The research carried out by [183] has concluded that the sub-areas more prone to scour occurrence were the leeside of the pile, more specifically, rings R1 and R2, in sectors S3, S4 and S5. The analysis also showed that the upstream side of the scour protection, in the outer ring R6, presented considerable edge scour in sectors S8, S9, S10, S11 and S12. The critical sub-areas regarding the edge scour phenomenon are analysed in the following sections, due to the different origin of this particular phenomenon, which is more related to the sudden change in the bed roughness than to the amplified bed shear stress. Using the same colour code outlined in Figure 4.15, [183] defined the general scour pattern after 5000 waves presented in Figure 4.28, which also shows that ring R2, although being similar to ring R1, presented a slightly higher damage rate. This analysis did not use test s3_007, which was stopped after 3000 waves. The results showed that scour occurrence was more severe between $0.5D_p$ and $1D_p$, which is in agreement with the observations made in [1], which concluded that damage for waves in a following current was typically located up to a distance of $0.5D_p$ and sometimes extended after $1D_p$. Such pattern changes for waves alone or waves in an opposing current, which were not analysed in the MARINET data. In [1] and [148], for waves in a following current, the damage was frequently not located immediately at the downstream face of the pile, but was a bit spaced from it. This confirms the observation of a slightly higher damage rate in ring R2 than R1, previously mentioned. In front of the pile (upstream) and at the inner sub-areas, still in ring R1, it is seen that scour occurs within the sub-areas where the amplification factor is typically larger (see the amplification factor patterns in [49] or [61]). Sometimes, damage was also noted to increase at both 90° locations, as noted in the 3D-profile analysis performed by [26].

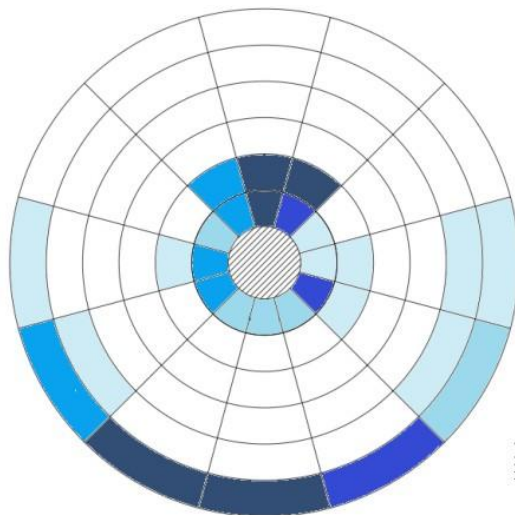


Figure 4.28 – General scour pattern after 5000 waves [183].

Typically, the outer and intermediate rings downstream of the pile presented no scour because they consisted in the deposition zone of displaced stones and sediments transported from the upstream side. The scour location shown in Figure 4.28 also agrees with the location of the common scour

mechanisms, namely the horseshoe vortex in front of the pile and lee-wake vortices behind, as discussed in section 2.5. The results also indicate that, apparently, the vortex shedding led to a more severe scour process than the horseshoe vortex, which is also in agreement with the scour pattern for combined waves and current, commonly described in the literature [61]. When analyzing the damage evolution between each wave train, it was observed that some of the sub-areas were able to recover from previous damage, whilst others showed a lack of backfilling occurrences [183]. However, the analysis performed by [183] did not comment on the fact that uni-directional wave-current tests in live-bed regime may enable sediment deposition on the scour protection, but that does not occur with the armour stones that are dragged downstream. Hence, the backfilling capacity might be underestimated in the model, compared to the prototype situation, thus leading to possible damage overestimations in the model. A typical marine environment is affected by tidal currents and the variability in the direction of oceanic currents, which under non-extreme conditions can contribute to a damage reduction by means of local backfilling of upstream sub-areas. Despite the lower backfill time-scale compared to the scour hole, this process is found to reduce the scour depth under combined waves and current, namely in scour occurrence with small KC numbers [184].

The scour pattern was also analysed by [26], which has considered the DTMs obtained from the 3D profiles. The research noted that failure was mostly observed at the backside of the monopile at angles of $\pm 30^\circ$ or at the front sides of the monopile. In some shallow water conditions, failure was initiated at 0° and 90° angles. A very clear scour pattern was found in failed tests. A first scour hole was found surrounding the updrift side of the pile, due to horseshoe vortices. This hole was initiated by two scour holes at a 30° to 40° angle with respect to the current direction, which developed during the test, and eventually merged together at the front side. This merging was often already observed after 1000 waves. At the backside, a triangular scour hole close to the downstream side of the pile was caused by vortex shedding. Both scour holes in front and behind the monopile developed simultaneously. Rocks were accumulated between and behind the scour holes, and formed two “wings”, which were designated by [26] as the V-shape that typically increased with increasing damage in the scour holes. The plots of the dynamic tests show a comparable pattern, albeit much less pronounced for the same number of waves. A comparison between static, dynamic and failure configurations is plotted in Figure 4.29.

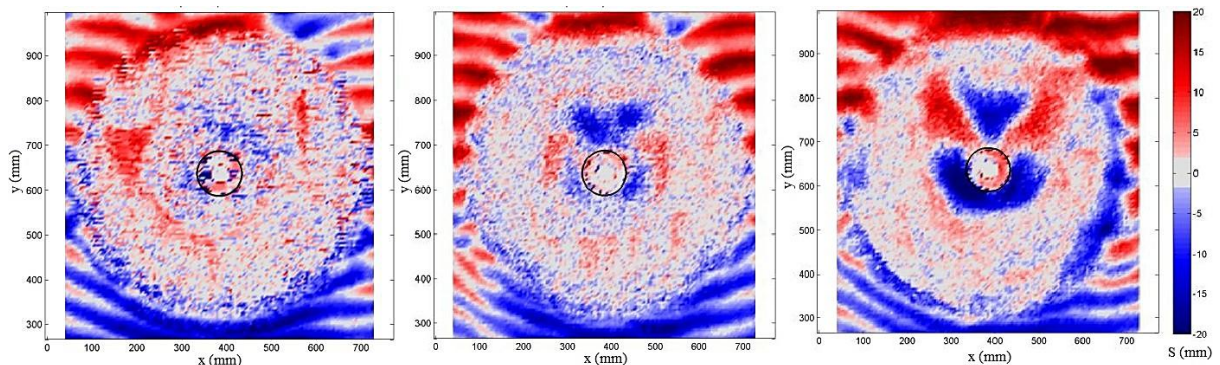


Figure 4.29 – Examples of Digital Terrain Models – Left: Statically stable scour protection (s2_001). Middle: Dynamically stable scour protection (s2_004). Right: Failure at the scour protection (and developed V-shape). Flow direction from bottom to top [26].

Moreover, based on the analysis of 2D cross profiles after 5000 waves of each test, [26] provided the smoothed average profiles after 5000 waves at 0° , 30° , 60° and 90° . These smoothed average profiles are shown in Figure 4.30, which shows that the surface elevation in the average dynamic profile, after 5000 waves, is generally closer to the statically stable one. It is possible to see that the

profiles at 0° and 30° lie between the static and the failure profile, with some deposition occurring at the peak zones. At 60° profile the occurrence of deposition is more evident, whilst the 90° profile seems similar for the three cases. Finally, the analysis of Figure 4.28, Figure 4.29 and Figure 4.30 shows a lack of a perfect symmetry in the damage occurrence, typically found in monopile foundations, e.g. as noted in [83]. This fact is justified by three possible uncertainties:

- Existence of local asymmetries in the current flow, which were identified during the calibration procedure (see [175]). The calibration performed and the monitoring of the depth-average current velocity showed that these asymmetries were not significant, however it may contribute for the scour pattern asymmetry;
- The manual construction of the scour protection, which was performed as similar as possible in all tests. However, the fact that it is being manually placed may contribute for slight differences in the stones placement (and sometimes the degree of compaction) at the armour layer. A mitigation measure to this problem is reported in [163] and consists in using always the same person when building the model, so that the error might be less random in nature.
- The wave-current flume filling process. The models of the scour protection were built with the flume drained, thus when filling it with water some of the armour material could be washed out from certain sub-areas, making them more prone to damage occurrence. This aspect was also noted in [1, 32].

Nevertheless, the asymmetries noted in the patterns were not found to be large enough to invalidate the obtained conclusions, also comparable to the findings reported in the aforementioned works.

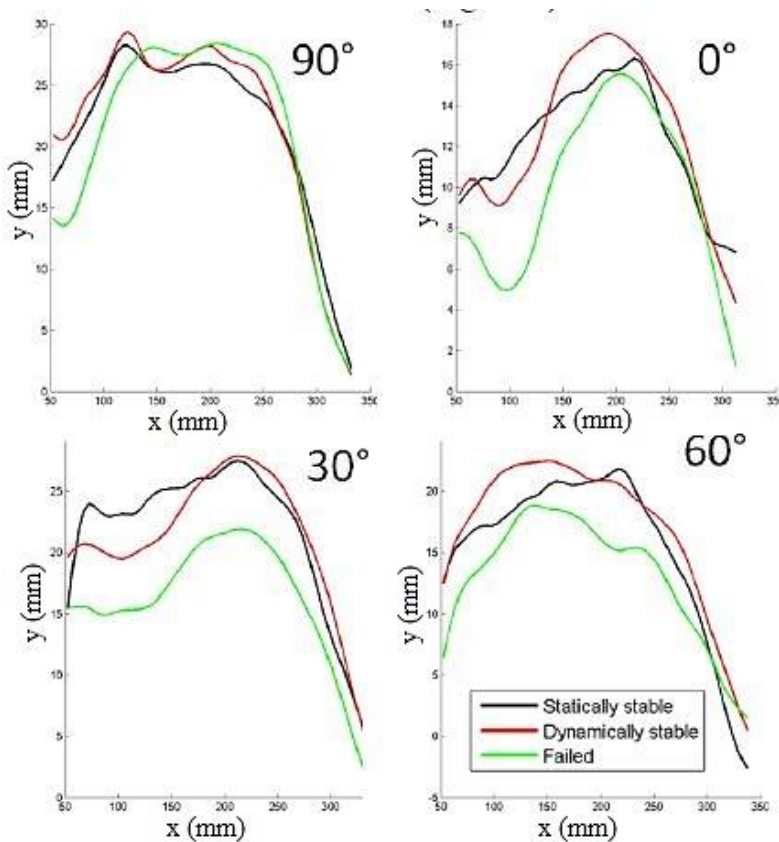


Figure 4.30 – Smoothed average 2D cross profiles after 5000 waves [26].

4.2.6.4.2 Deposition zones

A similar analysis was performed to understand the deposition process, namely regarding the sub-areas that registered a considerable surface elevation. It was already noted that a deposition zone with a V-shape started to appear for dynamic profiles and then becoming even more evident for failed scour protections. A problem related to the deposition analysis is the fact that, sometimes, neither the 3D profiles, neither the photographic records, enable one to clearly see if the armour stones are beneath some of the sediments that were dragged from the upstream side and deposited on top of the armour layer. Nevertheless, for the present tests, [183] has concluded that the accretion process was more dynamic than the erosion one. It is also mentioned that the stones displaced and the sand-bed sediments dragged to certain sub-areas of the armour layer led to an increase of the bed roughness (due to the increase in elevation). These bathymetric changes contributed to the erosion of the sub-areas where the accretion process had previously occurred [183]. Regarding the deposition location, it was also possible to observe a slight asymmetry, which could also be justified by the reasons discussed before.

The deposition pattern is provided in Figure 4.31, which shows that deposition typically occurred on the downstream side of the pile. It is interesting to note that in certain sub-areas where the scour commonly occurred, e.g. R1 and R2, S3 and S5 were also the ones that showed a considerable accretion rate. This is important, since this accretion can compensate the loss of rock material during the scour phenomenon, thus reshaping the armour layer. The V-shape previously identified by [26] seems evident in Figure 4.31, namely in sectors S2, S3, S5 and S6 in all rings. The evolution of the V-shape form for a failure occurrence is presented in Figure 4.32 concerning test s1_005. The considerably large rate at the downstream side of the outer ring R6 is rather alarming. The stones displaced from upstream to these sub-areas will probably not be able to return to the armour layer if they are dragged to the areas that lie outside the foundation's influence area. However, one must note that these tests did not consider a current inversion, e.g. tidal environmental. Therefore, in case of such inversion, it is expected that under normal sea-state conditions, some of the deposited material downstream may be dragged back to the upstream side of the scour protection, thus contributing to a dynamic equilibrium profile. An important observation is the fact that sector S4 only registered accretion in the outer rings R5 and R6. Therefore, when considering the scour sub-areas (Figure 4.28), one sees that R1S4 and R2S4 are critical zones of the protection for which the loss of rock material may not be compensated by the deposition process. Note that such compensation may exist, for example, in sectors S3 and S5.

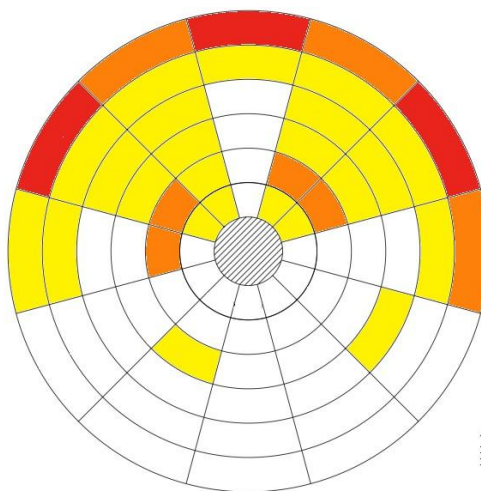


Figure 4.31 – General deposition pattern [183].



Figure 4.32 – Evolution of the V-shape form registered during s1_005: left – after 1000 waves, middle – after 3000 waves, right – after 5000 waves. Flow direction from the bottom to the top.

The deposition of sand-bed sediments on top of the armour layer was sometimes more evident in some tests than in others. Figure 4.33 shows two statically stable scour protections where sediment depositions differ. After 5000 waves, the deposition on the downstream side is more evident for test s1_002 than for s1_001. Such occurrences are commonly related to the hydrodynamic conditions of each test. However, this must be taken into consideration when analyzing scour occurrences, because as mentioned previously, the sediment deposition may complicate a clear vision of stone displacements.

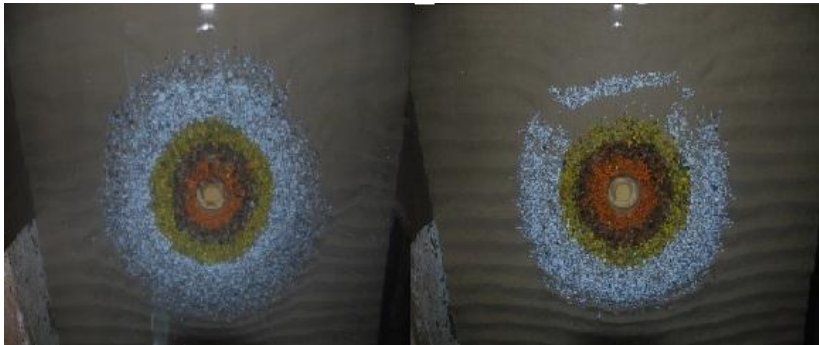


Figure 4.33 – Left: test s1_001 statically stable with less deposition at the downstream side. Right: test s1_002 with downstream deposition at the white ring. Flow direction from the bottom to the top.

4.2.6.4.3 Edge scour

This section addresses the damage number and damage development obtained in each test for rings R5 and R6, which correspond to the edge scour results. The damage inherent to these two rings is different in nature to the one obtained in the monopile's vicinity, because it results from the differences in the bed roughness that may eventually be added to the amplification of the bed shear stress.

A failure occurrence in the outer rings may not have a direct impact on the foundation's stability as in the inner rings. However, scour research shows that the edge scour phenomenon may lead to damage progression from the outer to the inner rings, thus leading to failure of the protection, e.g. [34, 144] or [185]. Edge scour holes in the outer parts of the system may induce losses of the filter material, particularly, if the current velocities are large enough and if the protection layer system has a considerable porosity [11]. The edge scour failure in the outer rings may also hamper the reshaping capacity of the armour layer of a dynamic scour protection. The edge scour and edge accretion are given in Figure 4.34.

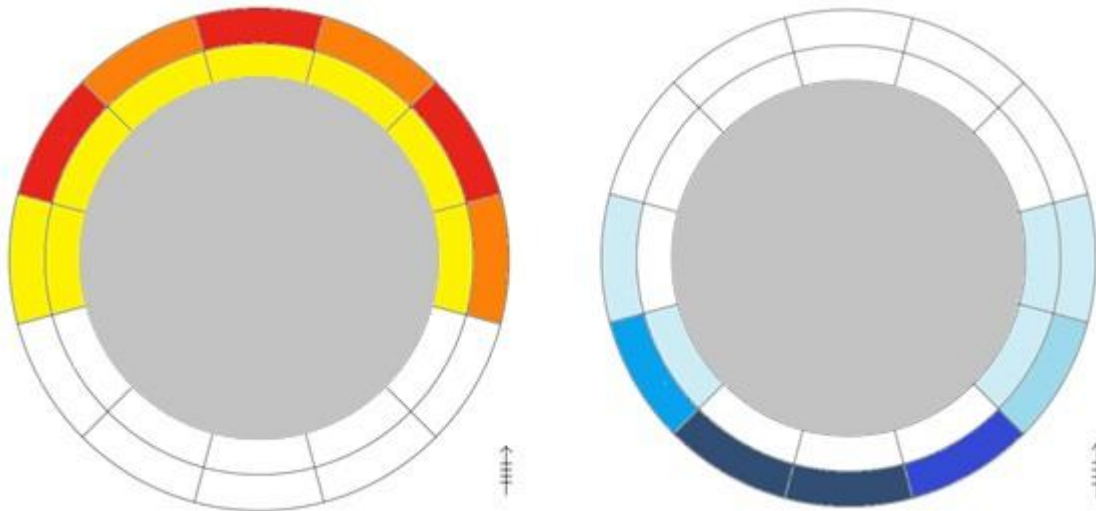


Figure 4.34 – General edge accretion and scour pattern for the MARINET tests.

The edge scour phenomenon may be responsible for a major quantity of cases where $S_{3Dsub} < -1$. Note that negative values for S_{3Dsub} represent erosion, whilst for overall measured S_{3D} , one only refers to positive values, which also correspond to erosion. In [175], it was noted that 34.1% of the total cases for which $S_{3Dsub} < -1$ had occurred in ring R6, with particular emphasis on sectors S9, S10 and S11, which are the ones more exposed to the first contact with the bed boundary layer on the upstream side. It was also noted that after the aforementioned sectors were eroded, a propagation of damage could be seen in the adjacent sectors, namely in S7, S8 and S12. Table 4.24 shows the values of S_{3Dsub} for ring R6 (in the upstream front sectors) for tests performed with equal or very similar hydrodynamic conditions. The aim is to analyse if the thickness of the armour layer leads to an increase of the edge scour in R6, for the same D_{50} . The following tests can be compared:

- s1_003 and s1_006;
- s2_003 and s2_004;
- s3_005, s3_006 and s3_007.

Since the edge scour depends on the bed roughness, it is expected that thicker scour protections are more prone to edge scour. This was discussed previously and also identified by [1] and [32] when addressing the influence of the filter type on the damage number.

Regarding tests s1_003 and s1_006, both are dynamically stable. However, the one with larger armour thickness, i.e. test s1_003 ($n_a=3$), only registered more edge scour in sectors S8 and S9. Despite the larger roughness introduced by a thicker armour layer, these tests do not enable the conclusion that the armour thickness may induce larger damage numbers in the upstream sectors of ring R6. It must be noted that a bias may occur, since after 5000 waves, test s1_006 has a slightly larger value of U_c than test s1_003 and a smaller value of H_{m0} (see Table 4.7).

In series s2, the tests show a different behaviour: s2_003 failed and s2_004 was dynamically stable. The edge scour is consistently smaller in s2_004 than in s2_003, with the exception of sector S8. Since Table 4.7 shows that the hydrodynamic conditions between tests are equal (after 5000 waves), it may be stated that the increased armour layer thickness in test s2_004 has not contributed to generate edge scour values that can overcome the ones registered in test s2_003. However, it is crucial to note that test s2_003 failed. Therefore, the results obtained for S_{3Dsub} in R6 may also be a result of the considerable progression of damage that results from a generalized failure of the scour protection and not only from the edge scour induced by the bed roughness differences.

The tests within series s3 are compared for $N=3000$ waves, because test s3_007 was stopped after that wave train (failure had occurred). Test s3_005, which corresponds to a thickness of $8D_{50}$ ($n_a=8$), presented accretion in all sectors. On the other hand, between tests s3_007 ($4D_{50}$) and s3_006 ($6D_{50}$), it seems that the edge scour reduced in the configuration with lower thickness (s3_007).

Table 4.24 – S_{3Dsub} in the upstream sectors of ring R6 for scour protections with different number of stone layers (n_a). Negative values – erosion, Positive values – accretion.

| Test | n_a | D50 | N | Type of Stability | R6 - upstream sectors | | | | |
|--------|-------|-------|---------|-------------------|-----------------------|--------|--------|--------|--------|
| | | [mm] | [waves] | [-] | S8 | S9 | S10 | S11 | S12 |
| s1_003 | 3 | 4.14 | 5000 | Dynamic | -2.190 | -2.210 | -1.290 | -2.310 | -1.630 |
| s1_006 | 2 | 4.135 | 5000 | Dynamic | -1.640 | -2.000 | -1.950 | -2.670 | -1.980 |
| s2_003 | 3 | 4.135 | 5000 | Failure | -0.344 | -1.730 | -2.015 | -2.059 | -0.864 |
| s2_004 | 4 | 4.135 | 5000 | Dynamic | -0.570 | -1.210 | -1.230 | -1.720 | -0.080 |
| s3_005 | 8 | 2.69 | 3000 | Dynamic | 0.012 | 0.234 | 0.115 | 0.170 | 0.198 |
| s3_006 | 4 | 2.69 | 3000 | Failure | 0.667 | -0.042 | -0.124 | -0.700 | -0.365 |
| s3_007 | 6 | 2.69 | 3000 | Failure | -0.581 | -1.607 | -2.466 | -2.987 | -5.571 |

The analysis of Table 4.24 shows inconclusive results regarding the effect of the armour layer thickness in the damage numbers of the edge scour sub-areas. As seen before, it is known that the difference in the bed roughness and the thickness of the protection may contribute to the enhancement of the edge scour phenomenon. However, since ripples are formed, it is important to note that the bed-roughness is also influenced by the ripples' height and not only by the mean stone diameter of the armour layer [52]. Nevertheless, the following observations can be summarised:

- In dynamically stable scour protections, e.g. s1_003 and s1_006, the increase of the armour layer thickness did not seem to contribute to the increase in the edge scour. However, a bias caused by the hydrodynamic difference in U_c may have been the reason for this. Note that these two tests were very slightly current-dominated (see also Table 4.21);
- When comparing s2_003 and s2_004, the increasing armour layer thickness did not lead to larger values of S_{3Dsub} in R6, which might be explained by the fact that failure occurred in s2_003, while s2_004 was dynamically stable. The result suggests that the increase in the armour layer thickness for dynamic scour protections may lead to an increased stability of the protection without enhancing the edge scour;
- By comparing the tests within series s3, it is possible to see that the edge scour only increased for an increasing armour layer thickness in the configurations that corresponded to failure.

Further research should be performed to properly address the observations made regarding the edge scour.

4.2.6.5 Acceptable damage of a scour protection

Before addressing the reliability of scour protections, it is necessary to evaluate the performance of the design methodology presented in [32], which is based on the damage number prediction introduced by

Eq. (3.57). Moreover, it is also required to determine the acceptable damage that might be endured by the scour protection without actually causing failure. The following paragraphs mainly address the performance of the predictive formula for $N=3000$ waves, in order to include the damage number analysis of all tests, since test s3_007 was not performed for $N=5000$. Moreover, $N=3000$ waves was also the reference number used for the reliability case study introduced in following chapters.

4.2.6.5.1 Application of the damage number formula

Figure 4.35 compares the values of the measured damage number (S_{3D}) with the predicted ones from Eq. (3.57). The red and black lines correspond to $S_{3D\text{measured}}=2S_{3D\text{predicted}}$ and $S_{3D\text{measured}}=0.5S_{3D\text{predicted}}$, respectively. The formula was originally developed for the data range used in [32]. The predictions are quite accurate for this particular dataset, with a root-mean-square-error (RMSE) of 0.114.

If the tests performed in [148] and in the MARINET proposal 61 are added to the original dataset, the RMSE increases to 0.756. As expected, the RMSE shows that for an extended range of H_{m0} , T_p , U_c , d , ρ_s and D_{n50} the predictive formula performs less well. Note that, although [148] and the MARINET data have similar H_{m0} values, the new range of test conditions of d , ρ_s and D_{n50} contribute to an increased damage in the tests, despite the similar combinations of H_{m0} and T_p .

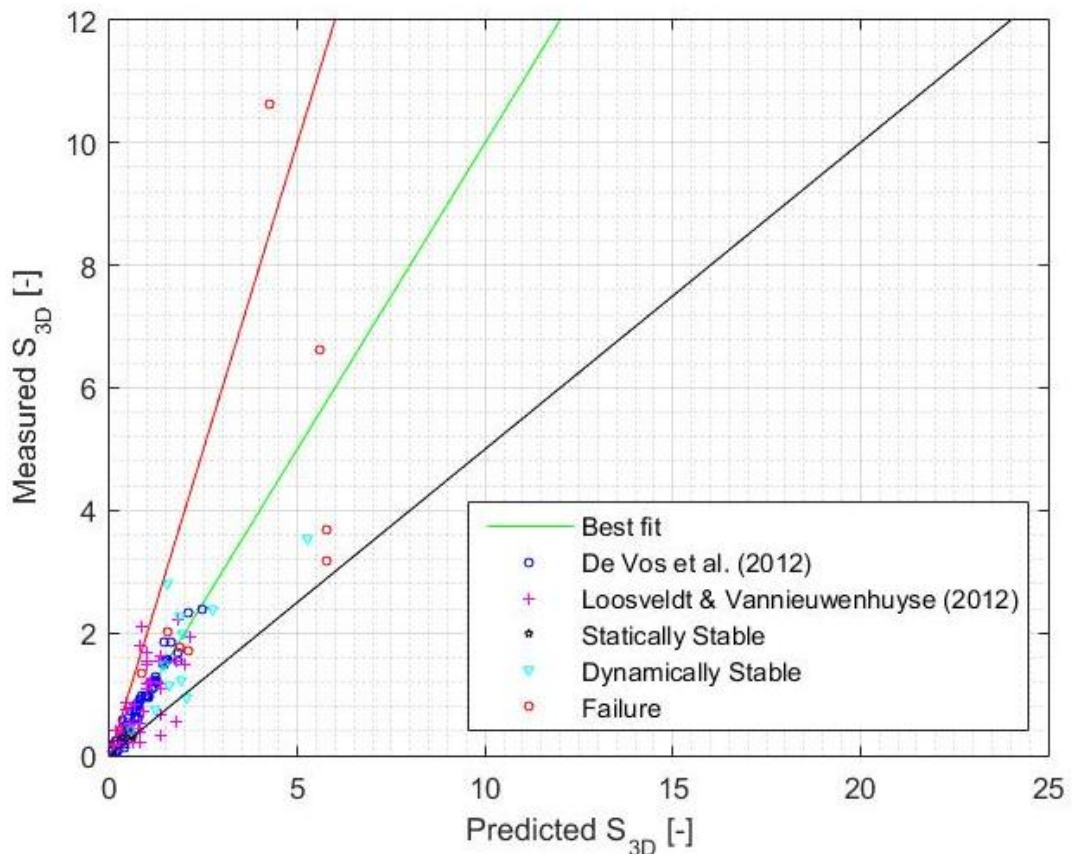


Figure 4.35 – Comparison between the measured and the predicted values of S_{3D} (after 3000 waves) [151].

The predicted and measured values of S_{3D} in the interval $[0;3]$ are close to the best-fit line, i.e. the line where the predicted S_{3D} values equal the measured ones. However, once the values approach the upper part of the interval, the deviation from the best-fit line tends to increase. One is led to think that the error in the prediction tends to increase with increasing damage.

Although such a fact may seem fairly reasonable, there are not sufficient data available in the range of predicted S_{3D} over the interval [3;5] to substantiate this conclusion. In order to confirm this tendency, it is important to extend the present database to analyse the dominant variables leading to this effect. However, the tests which deviated more from the line of best fit are placed above the measured $S_{3D}=3$ and after the predicted $S_{3D}=5$. For these tests, only test s3_005 displayed a dynamically stable behaviour. The others correspond to configurations with an exposure of the filter layer larger than $4D_{50}^2$, i.e. failure of the armour layer.

In Figure 4.35, Eq. (3.57) seems to underestimate S_{3D} for large water depths, i.e. series s3 with $d=0.5$ m. In series s2, with $d=0.36$ m, the prediction is closer to the best-fit line, while for series s1, with $d=0.24$ m, the equation seems to overestimate the measured damage number. In Figure 4.36, Figure 4.37 and Figure 4.38 the tests were separated according to their water depth. In series s1, it is possible to see that the predictive formula underestimated the damage number, while in series s3 the opposite happened in the majority of the cases. In series s2, the formula provided more accurate predictions than in series s1 and s3.

The data suggest that outside the original range, the equation overestimates the measured values of S_{3D} for deeper water conditions and underestimates in shallower water depths. For intermediate water depths, the predictions are more satisfactory, which makes sense since $d=0.36$ m is within the original range studied by [1, 30] and [32]. In these works, despite the water depth was either 0.20 or 0.40 m, only 6 tests, out of 85, were performed with $d=0.20$ m. Therefore, there are also departures noted for series s1, where $d=0.24$ m. Further physical modelling should be performed to fully assess the equation's applicability to the new range presented in the MARINET proposal 61. Moreover, the tests performed only included uni-directional waves and current. Future work should also include waves in opposing currents, which according to [32] might lead to more severe damage in the protection.

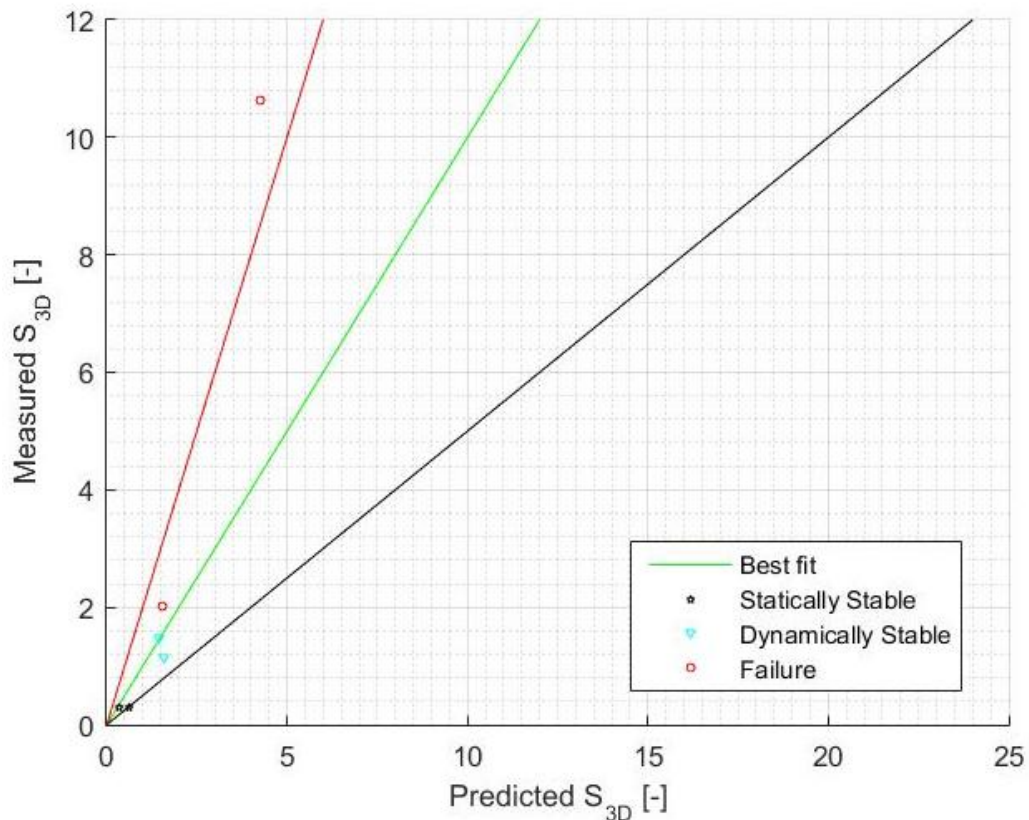


Figure 4.36 – Comparison between measured and predicted values of S_{3D} for test series s1 ($d=0.24$ m) [151].

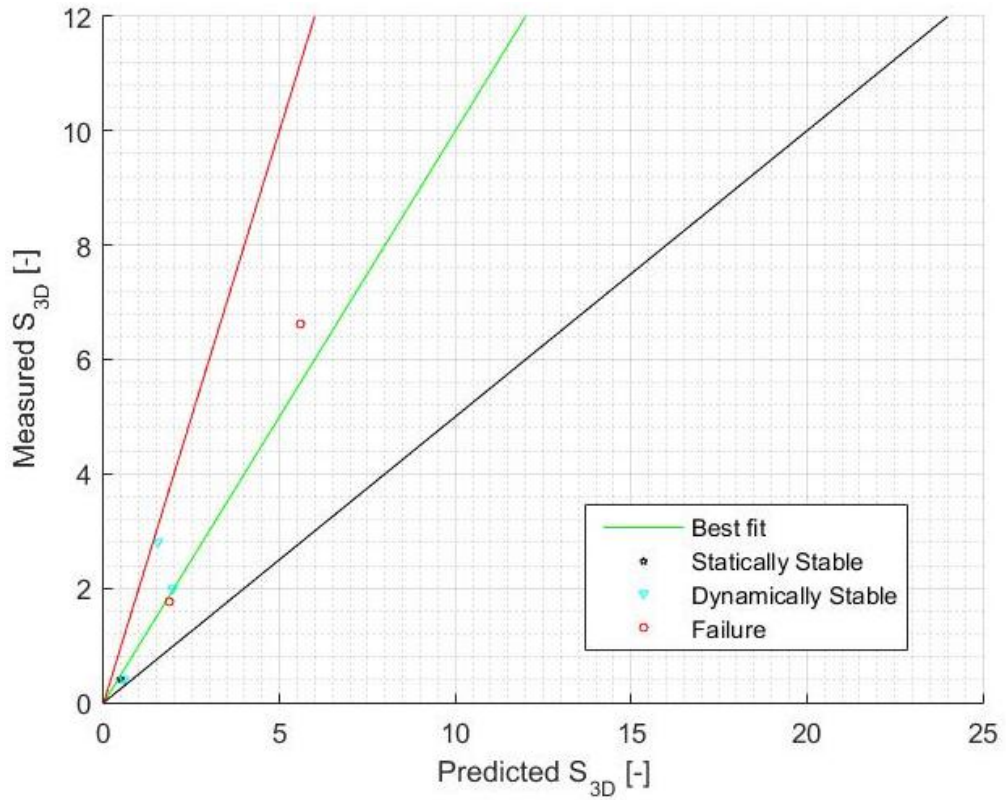


Figure 4.37 – Comparison between measured and predicted values of S_{3D} for test series s2 (d=0.36m) [151].

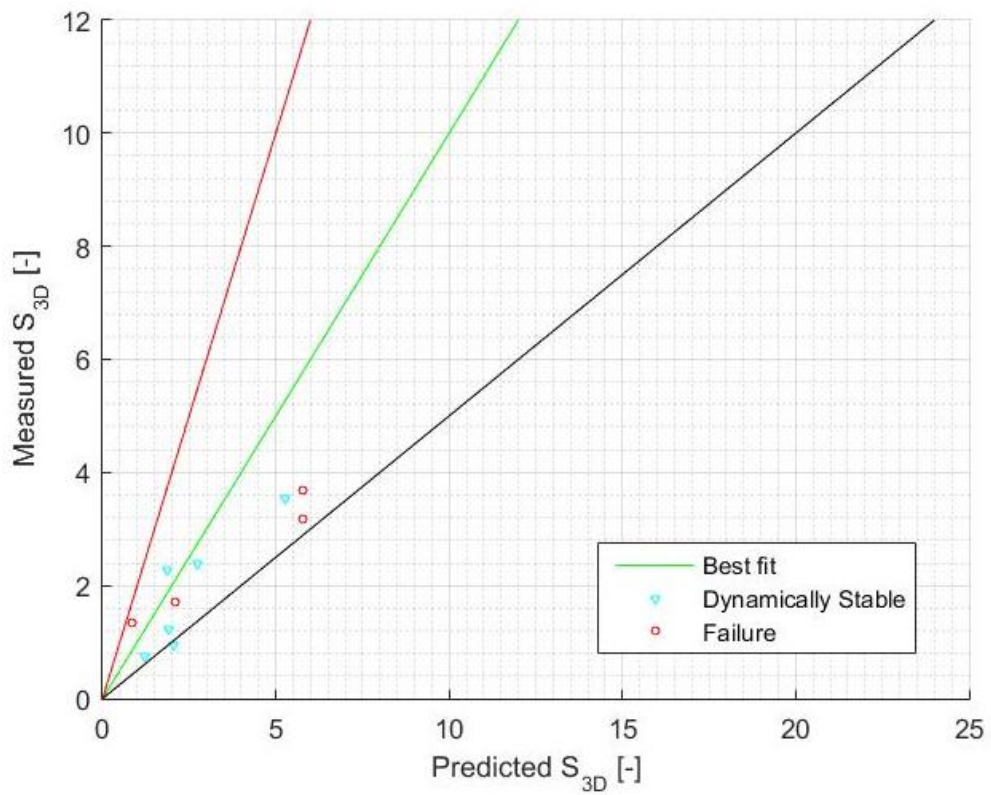


Figure 4.38 - Comparison between measured and predicted values of S_{3D} for test series s3 (d=0.50m) [151].

Nevertheless, for dynamic scour protections, the equation provides reasonable estimations of the damage number. The majority of them are encompassed between the lines given by 2 and 0.5 times the measured values. Moreover, the deviations from the best-fit line reduce in the interval [0;3] for both predicted and measured damage numbers, compared to the values outside that range. Figure 4.39 shows a zoom in the interval [0;3]. This suggests that a conservative approach should restrict the formula's use to these bounds, which are discussed further on.

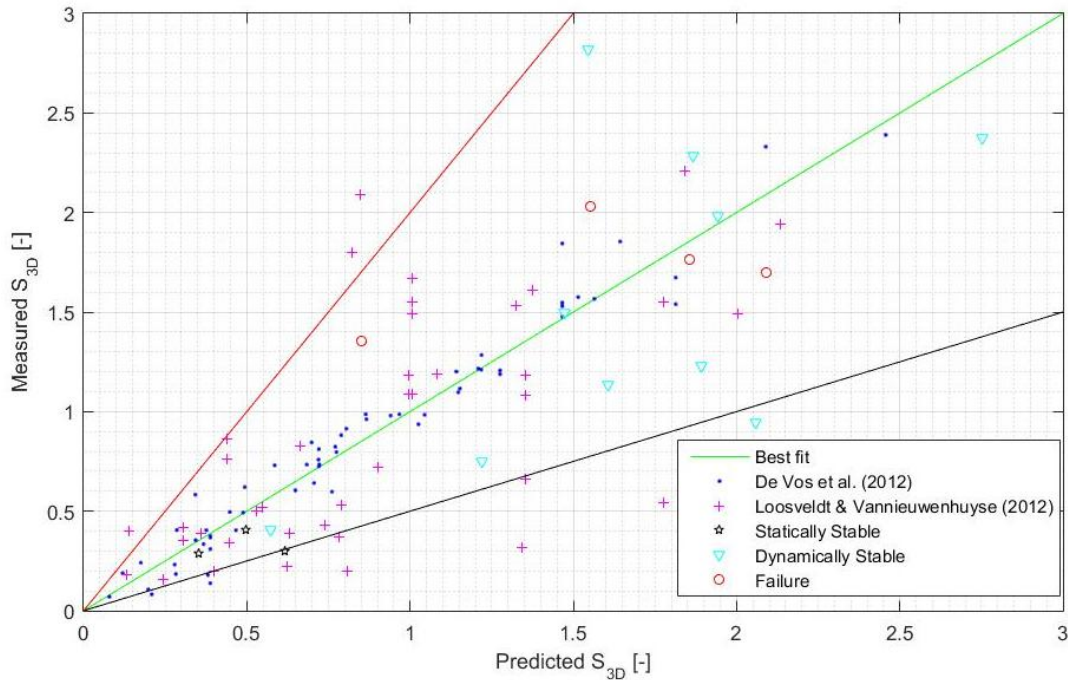


Figure 4.39 – Zoom in the interval of $S_{3D} = [0;3]$, [151].

Figure 4.40 shows similar tests performed with different water depths and the same nominal stone diameter (D_{n50}) and number of layers of armour stones (n_a). As seen in the previous figures, the accuracy of the equation is sensitive to the water depth. This supports the conclusions obtained from Figure 4.36 to Figure 4.38. For similar values of H_{m0} , T_p and U_c , the equation underestimates the values measured for series s1, as well as for series s2 when $D_{n50}=2.3$ mm. A cross-over occurs for series s2 with $D_{n50}=3.5$ mm. In series s3, the measured values are overestimated, as seen before. Figure 4.40 also shows that the differences between predicted and measured S_{3D} are higher for tests performed with $D_{n50}=2.3$ mm than the ones with $D_{n50}=3.5$ mm.

Although this happens in this particular case, it is not possible to generalise this conclusion, due to the lack of data for tests performed with $D_{n50}=6.3$ mm and 5.1 mm. Nevertheless, the highest departures from the best-fit line occurred for large damage numbers, which were obtained mainly for tests performed with low thickness of the armour layer combined with small stone diameters.

Therefore, it seems reasonable that Figure 4.40 shows larger differences for $D_{n50}=2.3$ mm than for $D_{n50}=3.5$ mm. In the original range of the formula, only two water depths were tested (0.2 m and 0.4 m), while in the MARINET data three new series were added (0.24 m, 0.36 m, 0.50 m). Thus, it is reasonable to expect deviations between the new predicted and measured damage numbers.

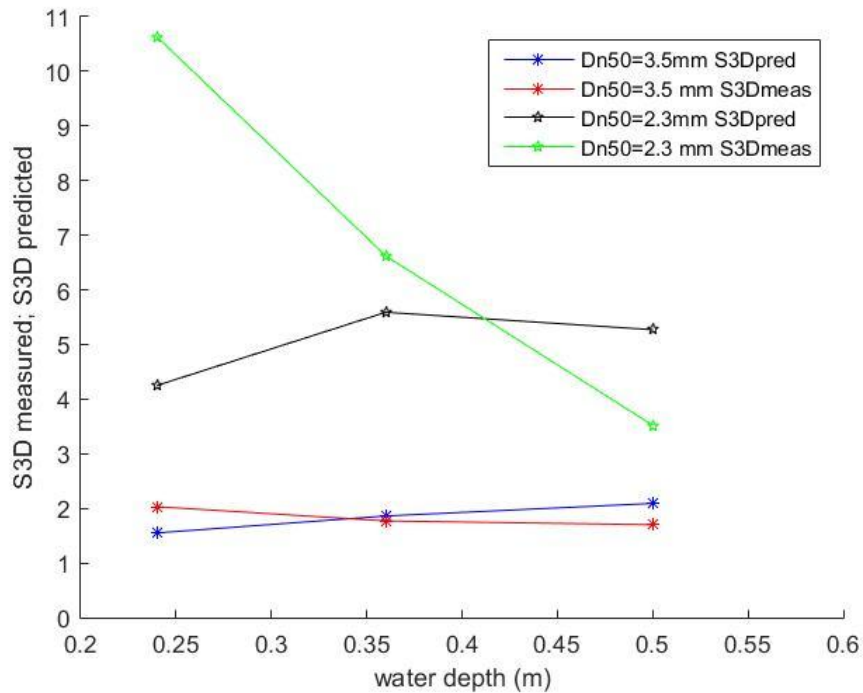


Figure 4.40 – Influence of the water depth on measurements and predictions of S_{3D} [151].

4.2.6.5.2 Influence of the scour protection thickness on the damage number

Based on the original data, [32] stated that the dynamically stable profiles did not develop to large damage numbers. Furthermore, the authors suggested that the dynamic design should only be performed for a limited accepted damage level, up to $S_{3D}=1$, when applying a scour protection with limited thickness (e.g. $2.5D_{50}$). The new tests performed seem to indicate that dynamic profiles might be feasible for values above this limit and with small armour thicknesses. Figure 4.41 shows that dynamic profiles were obtained for a measured S_{3D} in the interval [0.40; 3.53]. These profiles were obtained for a very broad spectrum of armour thicknesses between $2D_{50}$ and $8D_{50}$.

The tests showed that dynamic profiles could be achieved even for small values of the armour thickness. In all test series, the thicknesses of $2D_{50}$, $3D_{50}$ and $4D_{50}$ enabled a dynamic profile even after 5000 waves. A small number of tests was conducted by [148], with waves in both an opposing and a following current, until 9000 waves, which indicated that the damage rate decreased with increasing number of waves, with the equilibrium profile being achieved after 5000 waves. Further experimental work, considering large durations, namely for 7000 and 9000 waves, as in [103], will help to assess if this dynamic behaviour is maintained in long-term situations, as indicated in the previous research. Nevertheless, this work indicates that the dynamic design concept might be feasible for a minimum thickness of the amour layer of $2D_{50}$, depending on D_{50} , with a damage number that slightly exceeds the value of $S_{3D}=1$. Despite that, a conservative design approach would recommend that the suggestions made in [32] are followed. This becomes evident in Figure 4.41, where the overlap between failure and dynamic stability clearly occurs for S_{3D} between 1.30 and 3.50, approximately. There is also, at $S_{3D}=0.25$, an overlap between static stability and “movement without failure”, which emphasises the gradational transition between limits. However, at $S_{3D}=0.25$, the scour protection is expected to be safe, thus this seems a conservative limit to the static stability.

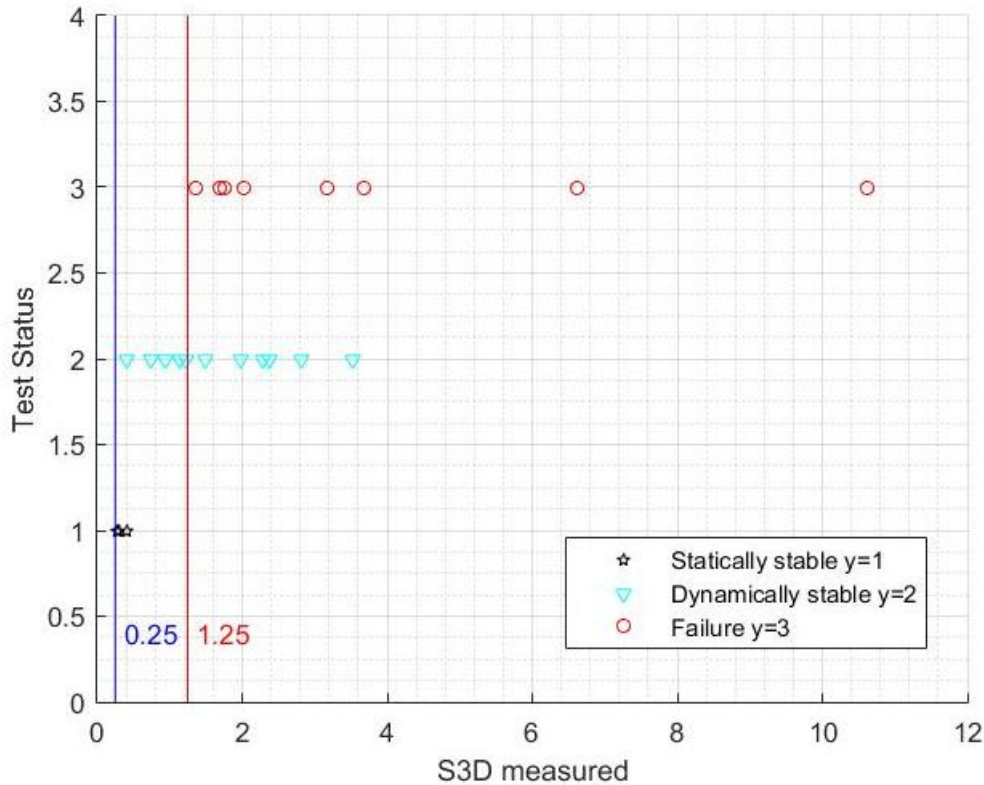


Figure 4.41 – Test classification and measured S_{3D} with the limits for static and dynamic stability [151].

According to [1], the original data showed that the values of S_{3D} between 0.25 and 1 were the limits for dynamic scour protections, i.e. movement occurred but without failure. Moreover, the same data did not present any dynamic profile above $S_{3D}=1.5$. Although the present data set supports the limits suggested, it is found that the upper limit moved to 1.25 and the dynamic profiles were achieved for a maximum value of $S_{3D}=3.53$, which corresponded to test s3_005 ($D_{n50}=2.23$ mm; $n_a=8D_{50}$). Another example of a successful dynamic scour protection is the one from test s2_006 with a measured $S_{3D}=2.82$ ($D_{n50}=3.5$ mm; $n_a=4D_{50}$). The present study extends the range of armour thicknesses as a function of the stone size and concludes that, depending on the combination of these two variables, the dynamic profiles can be obtained for a damage number above 1.

4.2.6.5.3 Comparison with the stability parameter – OPTI-PILE project

As seen in 3.7.1.4, according to [100], the initiation of movement is given by $stab=0.416$, while the transition between “movement without failure” and failure is made when $stab=0.460$. Note that these transitions are gradational, thus meaning that values of $stab$ that are close to a boundary might, in practice, fall into an adjacent category of damage.

In [1], it is stated that the stability parameter is not suitable to predict if a scour protection is statically stable, dynamically stable or if it fails. In fact, this is also confirmed by the present research. Figure 4.42 provides the stability parameter for each test and the corresponding movement classification. In a similar way to the results presented by [1] and [32], the spread in the stability parameter is too large for a specific limit to be identified for dynamic profiles. The limits proposed before are not suitable for the new dataset. Figure 4.42 was obtained considering $\theta_{cr} = 0.056$ and the value of θ_{max} computed with D_{50} of the stones in the armour layer. An alternative approach to account

for wide graded armour layers, which tend to be more stable since the smaller stones find shelter in the larger ones, is discussed in [30]. In this case, the authors account for this effect by using the $D_{67.5}$ instead of D_{50} to compute θ_{max} and a reference value of $\theta_{cr}=0.035$. This procedure was not adopted in this case since the focus was a direct comparison with the OPTI-PILE motion limits. Moreover, this change only causes a positive horizontal translation of the stability parameters by a constant factor and does not bring significant differences for the conclusions taken from Figure 4.41 and Figure 4.42.

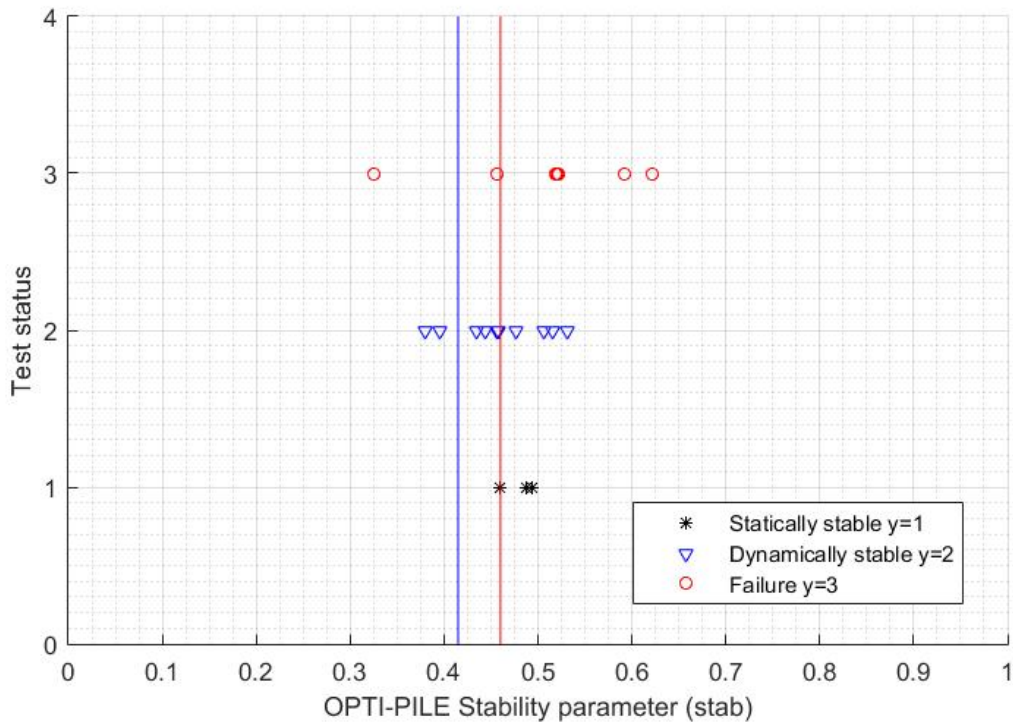


Figure 4.42 – Test classification versus stability parameter (bue left line – $stab=0.416$, red right line – $stab=0.460$), [151].

On one hand, the protections identified as statically stable overcame the line $stab=0.416$ (initiation of motion). On the other hand, both failed and dynamically stable protections were spread far beyond the limits for the initiation of motion and failure. This also occurred in the original data and a possible reason is the fact that the influence of the thickness of the armour layer is not included in the stability parameter. It should be noted that two tests with the same stone size and hydrodynamic conditions may fail, or not, according to this thickness, and the consequent exposure of the filter. Also in agreement with the original data, the stability parameter seems to underestimate the damage, in several failed tests and dynamically stable ones. In Figure 4.41 the trend between the damage number and the rock movement is clear, i.e. if the degree of motion increases the damage also increases. In the case of the stability parameter this trend is not evident, as it can be seen in Figure 4.42. Another interesting aspect is the fact that the stability parameter from OPTI-PILE is dependent on the theories used to obtain the combined maximum shear stress, e.g. [52] or [57]. This should be taken into account when defining possible limits for the classification of the scour protection, based on the stability parameter. When this parameter is plotted against the ratio of damage number to armour thickness, no clear trend is noted, as seen in Figure 4.43, although it seems that for $stab=[0.4; 0.6]$, the damage number increases with increasing values of the stability parameter.

For the tested stone sizes, the variation around the limits previously defined for the stability parameter is considerable, hence leading to the conclusion that, for this particular dataset, the stability

parameter is not suitable to distinguish the dynamically stable protections from the static and failed ones. Moreover, due to the overlap between the tests (e.g. statically stable ones that exceeded the $stab=0.416$ or failed tests on the left of the $stab=0.460$), an adjustment to these limits does not seem straightforward. Caution is advised when extrapolating beyond the limits of the original OPTI-PILE work. It is noted by [100] that for other structures or conditions outside the range tested, the $stab$ parameter only provides indicative responses and will require calibration with physical model testing to refine the values. Moreover, the OPTI-PILE project only focused on armour layers with a thickness that is limited to $2.5D_{50}$. These aspects should also be addressed in further research to clarify the required adjustments to the limits obtained from the OPTI-PILE project.

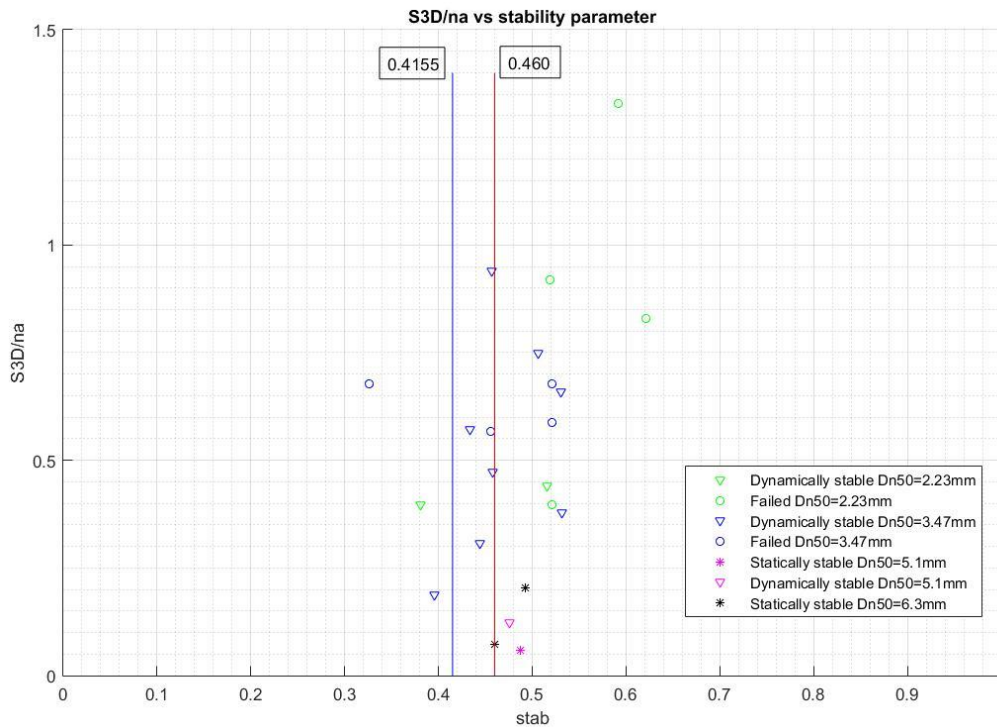


Figure 4.43 – Ratio of the damage number divided by the number of rock layers used in the protection versus the stability parameter, [151].

4.2.6.5.4 Summary on the damage number formula

The damage number formula tends to underestimate the damage number in series s1 (performed with $d=0.24$ m) and to overestimate this parameter in series s3 ($d=0.5$ m). The results in series s2 were closer to the line of best fit than the other series. This behaviour shows that the water depth has a major importance in the accuracy of the predictions. Future work should include a broader spectrum of water depths, in order to fully understand the corrections needed for test series s1 and s3.

The results obtained are in agreement with what was found between the S_{3D} measured in MARINET and [32] for statically stable protections. The limit proposed by [32] of $S_{3D}=0.25$ appears reasonable, although in this dataset the static configurations were obtained for slightly larger values. This was expected since the tests were designed to be within the transition between the static and the dynamic profiles. The dynamic profiles were mainly obtained between $S_{3D}=0.25$ and $S_{3D}=1.25$, which slightly exceeds the upper value proposed in [32]. After this limit, the tests were either dynamic ones or failed ones, which indicates that in design situations a careful use of the formula is advised.

Nevertheless, the physical modelling proved that, depending on D_{50} of the armour layer, it is possible to obtain dynamically stable protections with values of S_{3D} ranging from 0.40 to 3.53, with the protection thickness varying from $2D_{50}$ to $8D_{50}$. It is clear that depending on the combination of armour thickness and mean stone diameter, dynamic profiles can be obtained for a damage number above 1, which extends the range proposed in the original data. The effects under waves in opposing currents remain to be studied and fully understood. The OPTI-PILE stability parameter was not able to accurately describe the dynamic or static stability of the tested protections. The limits proposed by [100] were not suitable to differentiate the protections' ability to develop a dynamic profile. The statically stable protections presented stability parameters higher than 0.416 (initiation of movement) and several failures occurred below 0.460 (the transition between dynamic profiles and failure). When the ratio of damage number to armour thickness was plotted against the stability parameter, no clear trend was noted. It was pointed out that the influence of the theories used to compute the maximum shear stress should be considered when attempting to adjust the limits of the stability parameter. In this case, no clear adjustment of the limits was found. Moreover, the variability of the stability parameter showed that failure can occur for a very broad spectrum of stab values. A possible reason for this might be the fact that the armour thickness is not included in this parameter. Moreover, the inclusion of such influence on the stability parameter is not straightforward. While the ratio of damage number to armour thickness might be interpreted as the damage per metre of protection layer, it seems rather difficult to find a physical meaning for this ratio. Despite the conclusions of the present research, in design situations it seems wise to maintain the limits proposed by [32] and to compare them with other traditional approaches used for statically stable scour protections.

4.3 Experimental research programme at FEUP

The experimental research also included the analysis of a small set of tests performed at the Hydraulics Laboratory at the Faculty of Engineering of the University of Porto. This dataset mainly focuses on the analysis of the damage number on a scour protection under wave loading alone. The experimental research aimed to develop a deeper understanding of the influence of the scour protection thickness on the damage number, caused by equal (or as similar as possible) hydrodynamic conditions. This aspect was somehow less deepened in the previous datasets [1, 32, 148] or [175]. Despite the fact that this dataset also concerned the analysis of S_{3D} , it is not directly comparable to the one obtained in the MARINET proposal 61 for the following particular reasons:

- Hydrodynamic conditions – attempts were made to build a setup that enabled a combined regime of waves and current. This was proven to be unfeasible with the material available. Therefore, the experiments solely concern waves alone.
- Measurements of S_{3D} – measurements of the bathymetry at the scour protection were obtained with a 2D bed profiler, which is an intrusive equipment compared to the 3D laser profiler used before. This may lead to a somehow less accurate measurement procedure. In the longitudinal direction, the profiler was moved within a metallic rail, for which the movement step is controlled automatically. However, in the cross-sectional direction, the rail had to be placed manually across the desired grid, which also contributes to a less accurate evaluation of the profiles. Nevertheless, the use of the 2D bed profiler did not require the flume to be drained. This aspect is important since the wave tank at FEUP is considerably larger than the wave flume at Aalborg University [175].

Nevertheless, the following paragraphs elaborate on the main findings obtained throughout these experiments, which also contributed to the experimental work reported in [157] and [186]. Those

works concern the preliminary analysis of the influence of dynamic scour protections on the natural frequency of monopile foundations and the probability of failure of scour protections under a marine environment. The scour protection tests at FEUP were performed at a 1/50 scale, respecting the Froude similitude.

4.3.1 Prototype conditions

The prototype considered for the present setup does not include a wide range of hydrodynamic conditions as the studies discussed in section 4.2.2. Instead, a wider range of armour layer thicknesses were covered for the same storm conditions. Taking this into consideration, the prototype conditions presented in Table 4.25 were studied. In this case, only one series of tests was performed, i.e. series F1, which is very similar to series s1 in the MARINET proposal 61 (Table 4.1). The target conditions were slightly changed based on the experience of the previous setup: the target wave height was slightly increased to 5 m and the effects of currents were discarded ($U_c=0$).

Table 4.25 – Hydrodynamic prototype target conditions at FEUP.

| Target prototype values | | | | | | |
|-------------------------|-------|-------------|--------------|-----------|-----------|----------|
| Series | d [m] | U_c [m/s] | H_{m0} [m] | T_p [s] | D_p [m] | d/ D_p |
| F1 | 12 | 0 | 5 | 10.7 | 5 | 2.4 |

The aim of the present series was to understand the behaviour of the damage number according to different thicknesses of the scour protection, for which the filter layer thickness was kept constant, whilst the number of layers of the armour stones varied within $2D_{50}$ and $8D_{50}$. A problem with the MARINET data that reduced the number of comparable tests was the fact that the hydrodynamic conditions varied (although only slightly, sometimes) for tests performed with the same protection's configuration and the same water depth. In the present series, an effort was made to keep the wave height and period as similar as possible to avoid bias in the comparisons between configurations. Nevertheless, the tests are performed with irregular waves and minor changes are always expected in the spectral wave parameters. Table 4.26 presents the characteristics of the prototype of the scour protection. It was intended to use a mean stone diameter suitable to obtain dynamically stable configurations. Therefore, regarding the previous tests from the MARINET proposal 61, it was considered that the former armours 3 and 4 would be the most suitable to be studied under the new setup (see also Table 4.2). As it will be seen further, it was not possible to obtain exactly the same mean stone diameters in the model due to the available material. However, the model introduced further ahead is reasonably close to armour 3.

Table 4.26 – Prototype characteristics of the armour layer stones and granular filter for series F1.

| Material | $D_{50,prototype}$ [m] | $D_{n50,prototype}$ [m] | ρ_s [kg/m ³] | Prototype grading | Installation |
|----------|---------------------------|----------------------------|----------------------------------|-------------------|-----------------------------------|
| Armour 3 | 0.207 | 0.174 | 2597 | 10-60kg | Can be installed with a fall pipe |
| Armour 4 | 0.134 | 0.113 | 2564 | 40-200kg | Can be installed with a fall pipe |
| Filter | 0.05 | 0.042 | 2632 | - | Can be installed with a fall pipe |
| Sand | 0.009 | 0.008 | 2564 | - | Not applicable |

4.3.2 Facilities at the laboratory, scour protection test setup and model conditions

The scour protection tests were performed at the wave tank from the Hydraulics Laboratory at FEUP. The wave tank is 28 m long, 12 m wide and 1.2 m deep, with a gravel absorbing beach (5% slope, ≈ 8 m long) to minimize reflection effects at the model's section. The wave tank is equipped with the wave generation system HR WaveMaker with 16 paddles, which is managed by the software HR WaveMaker Wave generation control program. For detailed specifications on both the HR WaveMaker and the controlling software, the reference of [187] is recommended. A scheme of the overall wave tank and a photographic record are provided in Figure 4.44 and Figure 4.45, respectively.

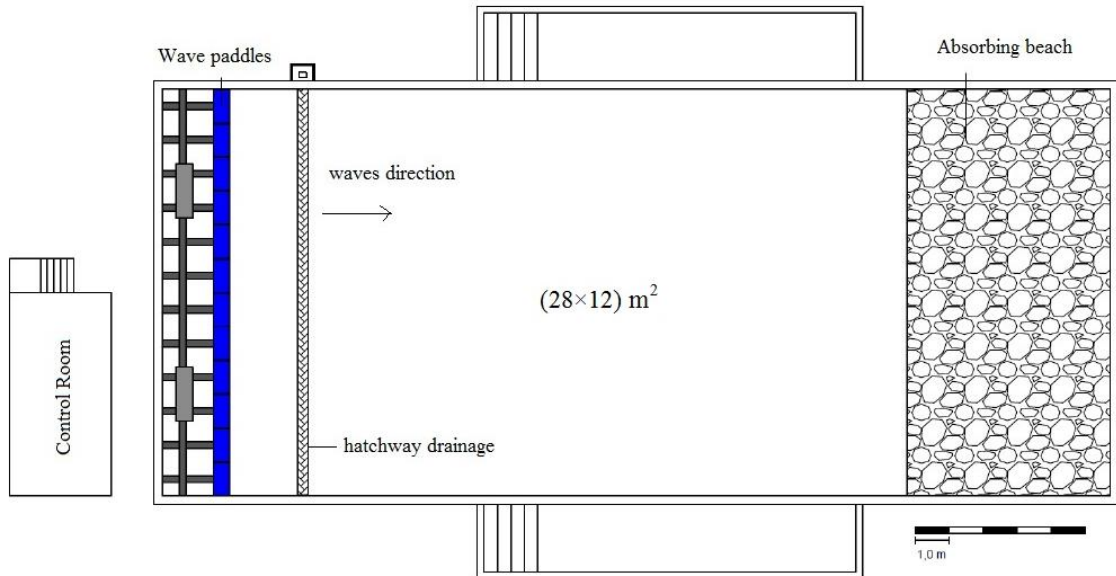


Figure 4.44 – Scheme of the overall wave tank at FEUP (adapted from [157]).



Figure 4.45 – Wave tank view from the downstream side, at the absorbing beach, towards the multi-element wave paddles.

The scour protection tests were performed at the aforementioned geometric scale of 1/50, thus meaning that only a channel within the wave tank was used in the experiments. The corridor was set at

the left side of the wave tank, from the downstream view, with a width correspondent to one wave paddle, i.e. 0.80 m. The corridor had a Perspex wall on the right side and a concrete wall on the left side. Therefore, possible interference in the wave field could be expected due to the differences in the wall's roughness. The corridor is hereby referred to as the wave flume and is provided in Figure 4.46.



Figure 4.46 – Downstream view of the wave flume (wave tank corridor) with the model of the monopile placed at the center [157].

Before initiating the tests programme there was an attempt to implement a similar setup to the one reported in [175] so that the tests could be performed with combined uni-directional waves and current. Similarly to the tests performed under the MARINET proposal 61, there was also a try to install a pump system at the downstream end of the flume linked to an outlet box on the upstream side in front of the wave paddles.

The pumps available at the facilities were a LOVARA DOC 7 and a DOMO 20t, which only enabled a maximum flow of 11 m³/h each. For a target water depth of 0.24 m (12 m in the prototype) and a flume's width of 0.80 m, the maximum flow velocity at the monopile section was about 0.032 m/s (0.23 m/s in prototype), which is far from the target current velocity of series s1 (see Table 4.2). During the preparatory work and before the monopile installation, the pump system was installed and the current velocity measured without waves. The wave tank was filled at 24 cm above the sand bed and the ADV was installed at the centre of the sediment box. The current was run for 20 min in each test and two velocity profiles were taken (one profile per test). The depth velocity profiles consisted in measuring the flow velocity in intervals of 2 cm for 1 min each. The profiles were measured from the sand-bed position, i.e. d=0 cm, to 6 cm below the water surface, i.e. d=18 cm. This occurs because the ADV needs to be submerged to perform the velocity reading. Moreover, a minimum distance of 4.5 cm from the probe is required to obtain a velocity measurement at a certain point, which corresponds to about 6 cm from the water free surface. The velocity profiles are given in Figure 4.47. As expected, the profiles indicated that the velocities obtained with the available pumps were not sufficiently large to reach the 0.18 m/s from series s1. Furthermore, it was also noted that the velocity depth distribution seemed rather distant from the logarithmic velocity profile, commonly recognized in the literature, e.g. [54]. Such fact is particularly evident in Profile 1. Due to the lack of confidence in the obtained results and the very low values of the current velocity, it was decided that the scour protection tests would be

performed with waves alone. Similar problems were encountered when developing the experimental work reported in [157] and [186]. However, neither of these works has provided the velocity profiles for the tested setups. For the waves alone setup, the pumps, the outlet box and the submerged pipes were removed.

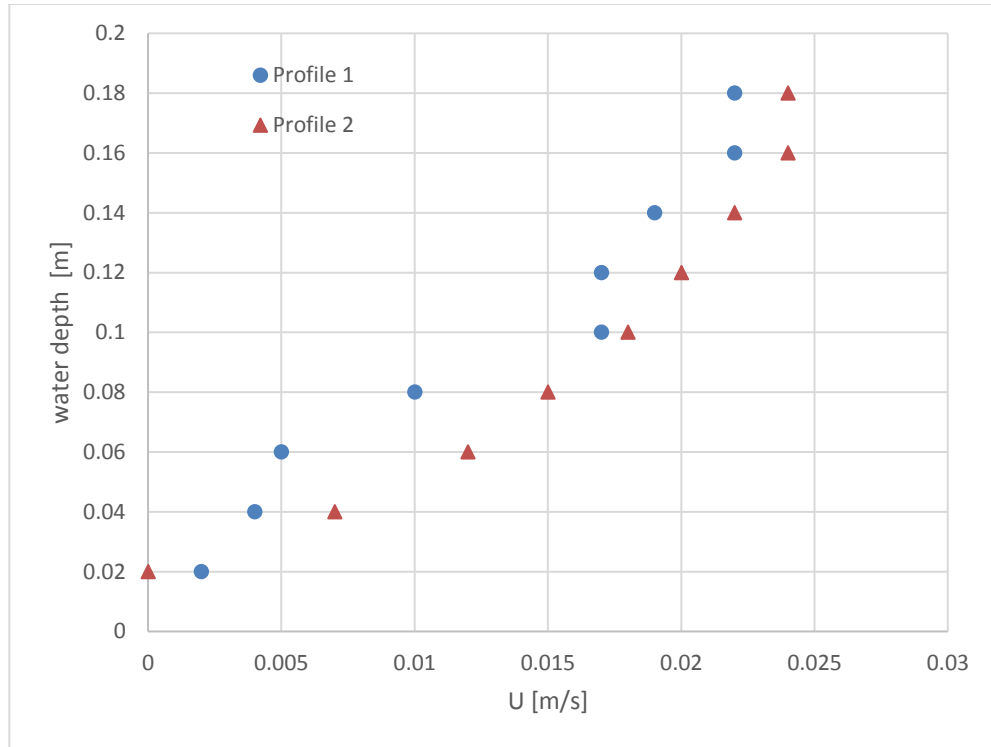


Figure 4.47 – Velocity profiles obtained after the pumps installation, without the monopile present and at the monopile section ($d=0.24$ m).

Despite the bypass section and pump system, the final setup was similar to the one presented in the MARINET proposal 61. Between the wave paddle and the absorbing beach an approaching upward slope and a downward slope were implemented to perform the transition between the flat bottom of the wave tank and the sediment box. The upward and downward slopes were 1/10, both consistently larger than the ones typically employed, as seen in section 4.2.5. However, this was necessary since the available length of the flume was rather small. The wave tank has 28 m length, which was reduced by the 8.10 m length of the absorbing beach and the maximum distance occupied by the HR WaveMaker (approximately 3.70 m). Moreover, one also wanted to include the sediment box (2 m length) and to ensure that any object was at least 2.5 m way from the wave maker, in order to avoid any wave disturbance. According to [163], the objects must be distanced from the wave paddles a minimum value of 2 times the wave length. In this case, L is about 2.16 m, for $d=0.24$ m and $T_p=1.51$ s. The first slope was placed at a shorter distance, to avoid possible effects from the rear end of the setup. Nevertheless, the waves were monitored at the monopile section and the registered values of H_{m0} were close to the target ones. Also, no breaking waves were registered at the upward and downward slopes. Since no combined waves and current regime was tested, a smaller degree of turbulence was expected at the boundary layer. Nevertheless, the slopes were covered with sand-bed material with a mean sediment diameter $d_s=0.23$ mm, which is the same material used in the foundation soil of the monopile. Similarly to the previous set of described tests, this was performed to minimize the effects of the bottom roughness in the bed boundary layer at the transition between the flume's bottom and the monopile section. The sediment box was 2 m long, 0.80 m wide and 0.40 m

deep. In each test, the sediment box was filled with the sand-bed material and flattened to avoid non-scaled ripples. The approaching slopes and the sediment box are presented in Figure 4.48.



Figure 4.48 – Upstream view (left) and downstream view (right) of the approaching slopes and the sediment box, before the sand bed installation.

The model of the monopile consisted in a perspex tube with 1.20 m height and an external diameter of 0.10 m. A transition piece was created at the same height of the sand-bed bottom (i.e. 0.40 m) so that the top part of the pile could be removed before flattening the sand bed. The monopile model was fixed to the bottom by a perspex base. The transition piece is provided in Figure 4.49. The ratio of monopile diameter to flume's width was set to $1/8$, i.e. smaller than $1/6$, which is enough to avoid the blockage effect, as mentioned in [49] and also discussed in section 4.2.5.



Figure 4.49 – Monopile base and transition piece at 40 cm height.

A set of 3 wave gauges (WG) was used to monitor the wave field along the flume. The first wave gauge was placed at the beginning of the approaching slope, the second one placed near the monopile section (1 m in front of the monopile). The third wave gauge was placed at the end of the downward slope. The active absorption system of the HR WaveMaker was used to minimize wave reflection. According to [188], the absorbing beach reduces reflection to values smaller than 12%. Although no reflection analysis was performed, the total wave measured at the monopile section was used for the calculations of the damage number. Moreover, the wave gauge placed at the downstream position did not register significant wave height differences compared to the previous two wave gauges. In addition to the wave gauges, a 2D bed profiler was used in order to measure the scour depths at the protection, which were used afterwards to estimate the eroded volume of stones at the protection. The overall setup is presented in Figure 4.50, while the monopile model is presented in Figure 4.51.

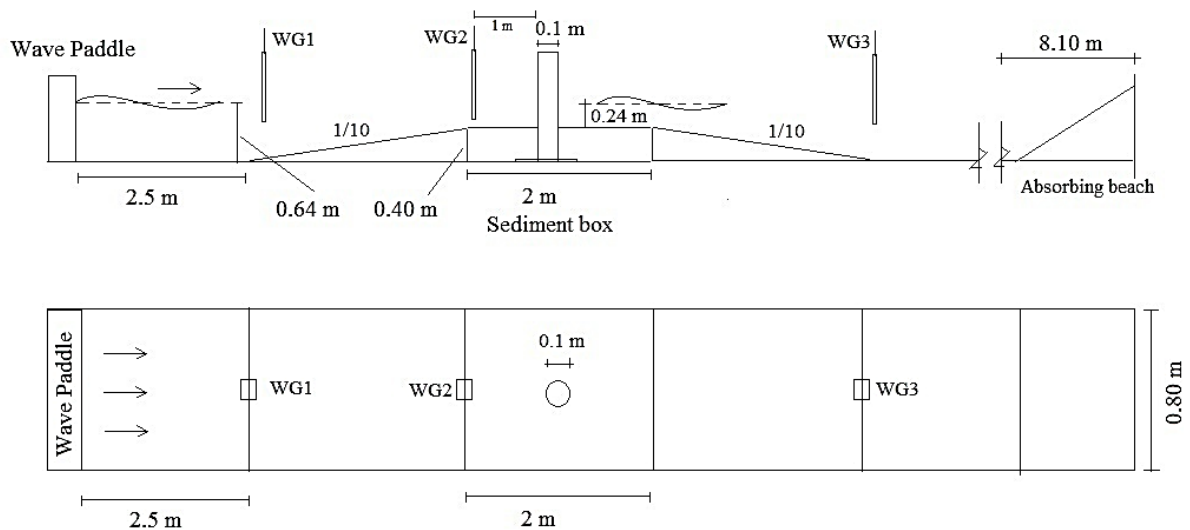


Figure 4.50 – Scheme of the setup used for test series F1.



Figure 4.51 – Model of the monopile foundation: during testing without protection (left), before testing with protection (center), during testing with protection (right).

4.3.2.1 Model hydrodynamic conditions

The tests were performed with freshwater temperatures ranging from 15°C to 18°C, which is higher than the temperatures registered in the previous dataset. The water mass density was $\rho_w=1000 \text{ kg/m}^3$. Therefore, as in the previous dataset, the armour stones of the scour protection were scaled according to the water mass density difference between the laboratory and the sea water. The scour protection tests did not consider the existence of current, as previously mentioned. The experiments were performed with irregular waves, following a JONSWAP spectrum with a peak enhancement factor

$\gamma=3.3$. Before testing, the wave height was defined and calibrated at the monopile section without the presence of the foundation model. During the tests, the waves were monitored at the monopile section to ensure that the tested values corresponded to the target conditions. Each test was performed for 5000 waves and the overall spectral significant wave height was calculated according to Eq. (3.54). The sequence of wave trains described in section 4.2.3.1 was also used for the present experiments. However, no 3D laser profiler was used. Instead, the profiles were obtained with the 2D bed profiler [189], between each wave train. The sequence of wave trains used also corresponds to the target storm durations presented in section 4.2.3.1. Taking into consideration the scale used, the final target hydrodynamic conditions in the model were obtained (Table 4.27). These conditions are indeed very similar to the ones used for s1, albeit no current was present.

Table 4.27 – Target prototype and model hydrodynamic conditions.

| Target prototype values | | | | | | |
|---|--------------|-------------------------------|--------------------------------|-----------------------------|-----------------------------|---------------------------|
| Series | d [m] | U_c [m/s] | H_{m0} [m] | T_p [s] | D_p [m] | d/D_p |
| F1 | 12 | 0 | 5 | 10.7 | 5 | 2.4 |
| Target model values (1/50 scale – Froude similitude) | | | | | | |
| Series | d [m] | U_c [m/s] | H_{m0} [m] | T_p [s] | D_p [m] | d/D_p |
| F1 | 0.24 | 0 | 0.1 | 1.51 | 0.1 | 2.4 |

4.3.2.2 Scour protection model

The scour protection model was also very similar to the one adopted in the MARINET proposal 61 (see section 4.2.3.2). The scour protections tested had a minimum of two layers. The first layer consisted in a granular filter and the top layer was made out of the armour stones material. The thickness of the filter layer remained the same throughout the tests, whilst the armour layer thickness varied between $2D_{50}$ and $8D_{50}$.

In the present case, the stones were not coloured in concentric rings. Although this was a shortcoming of the present setup, it was concluded that the time taken to colour and dry the stone material for each test would lead to a considerable reduction in the number of tests performed, due to the limited time window available to perform the experimental work. Instead, the attention was focused on the measurements obtained with the bed profiler, which would lead to the values of the damage number of the scour protections. Also, the coloured stones were useful when draining the flume to take the photographic records between the wave trains [175], which were not taken systematically during series F1.

As in the MARINET proposal 61, the scour protection had a total width of $5D_p$ and an extra radial extension extension corresponding to a slope of 1/3 used to cover the filter layer, as formerly shown in Figure 4.11. The method used to build the filter layer is equal to the one previously presented in Figure 4.10. The filter layer was made of sand material (non-cohesive) with $D_{50}=0.991$ mm (see also

Table 4.4). An example of the scour protection in the model is provided in Figure 4.52.



Figure 4.52 – Monopile and scour protection models after a test.

Considering the material available for the armour stones and the smaller water mass difference in the model, the model, quarry stone material was used with $D_{50}=4.1$ mm and a slightly smaller mass density of 2585 kg/m^3 . 2585 kg/m^3 . This value is not exactly the same as the initially proposed material (Armour 3 from

Table 4.4 and Table 4.26), due to unavailability at the time. Nevertheless, both materials are rather similar and both belong to the same prototype grading class. The Armour 4 material previously used in the MARINET data was disregarded due also to lack of availability. The armour and the filter layer materials of the present setup were designated as armour F1 and filter F1 (Table 4.28) for the purpose of distinction from the previous dataset. The filter layer material was slightly smaller than the one used in [175], although this difference was not very significant compared to other uncertainties inherent to the various setups used. The model and correspondent prototype values used in the final setup are provided in Table 4.28.

Table 4.28 – Model and prototype values used for the armour layer in series F1.

| Material | $D_{50,model}$ [mm] | $D_{n50,model}$ [mm] | $D_{50,prototype}$ [m] | $D_{n50,prototype}$ [m] | ρ_s [kg/m ³] |
|-----------|------------------------|-------------------------|---------------------------|----------------------------|-------------------------------|
| Armour F1 | 4.100 | 3.460 | 0.205 | 0.172 | 2585 |
| Filter F1 | 0.900 | 0.756 | 0.045 | 0.038 | 2600 |

4.3.2.3 Measurements and equipment

The wave gauges used to monitor the wave characteristics had the same features as the ones presented in section 4.2.3.3, with an error of ± 0.4 mm. Since no ADV was used during the scour protection tests, the wave gauges frequency was set to 100 Hz, enabling a higher sampling frequency rate than the one used in the MARINET proposal 61. The distribution of the wave gauges along the flume was set as in Figure 4.50, in order to monitor possible wave distortions at the slopes and the transition to the sediment box. The wave gauge placed nearest to the monopile (WG2) was 1 m way from the foundation to avoid the interference in the flow pattern and the scour mechanisms on top of the scour protection. The ADV used for the preliminary assessment of the current velocity profiles was a Nortek Vectrinoplus, with an accuracy of ± 1 mm/s.

The damage number was determined based on the profiles taken with the 2D bed profiler, which has an accuracy of ± 0.5 mm (in horizontal and vertical resolutions) and an intrusive touch-sensitive probe. The profiler was set to measure the vertical distances over an horizontal measurement grid of 10 by 10 mm, which provides a considerably lower resolution than the one given in [175], thus leading to a less accurate measurement of the damage numbers (Figure 4.53). The eroded volume was evaluated over the scour protection without including the extra-material used in the outer slope that covered the filter layer. The sub-areas considered were the same ones presented in Figure 4.14, with all profiles being centred at the monopile base for further comparison. The monopile top section was removed before the profiles were taken.



Figure 4.53 – 2D bed profiler mounted on the longitudinal rail (left) and ruled cross-sectional rail used to guide the profiler in the measurement grid.

4.3.2.4 Note on the range of test conditions

The range of test conditions of the experimental work developed at FEUP is rather limited compared to the ones analysed in Table 4.5. However, one must recognize that this is a result of the specific intention of testing the effect of the armour layer thickness in the damage number of the scour protection. One may compare the test conditions of Table 4.5 with the ones in Table 4.29. It is possible to confirm that the variables tested lie within the overall range of the previous datasets, with the exception of the armour thickness, which is extended to 32.8 mm, corresponding to $8D_{50}$ when using Armour F1.

The majority of the notes previously given in section 4.2.3.4 remain valid for the present dataset, since the variables are encompassed within the overall test range. Therefore, one does not extend the present analysis for the sake of clarity and to avoid unnecessary repetitions. Regarding the absence of current loading, this fact needs to be taken into account when analyzing the damage number of the scour protection.

Typically, damage on the scour protection is larger for combined waves and current, even when small currents are superimposed to waves [1]. Therefore, one expects that the present dataset leads to smaller damage numbers than the ones obtained in the MARINET proposal 61, provided that the wave height and the water depth are similar.

Table 4.29 – Range of target test conditions at FEUP.

| Variable | Symbol | Unit | Overall | FEUP |
|----------------------------------|---|----------------------|---------------------|---------------|
| Significant Wave Height | H_{m0} | [m] | 0.050-0.168 | 0.100 |
| Peak Period | T_p | [s] | 1.13-1.55 | 1.51 |
| Current Velocity | U_c | [m/s] | 0-0.31 | 0 |
| Currents Direction | α | [-] | Following; Opposing | - |
| Water Depth | d | [m] | 0.2-0.5 | 0.24 |
| Pile Diameter | D_p | [m] | 0.05-0.125 | 0.10 |
| Mean Stone Diameter | D_{50} | [mm] | 2.7-11.9 | 4.1 |
| Mass Density | ρ_s | [kg/m ³] | 2564-3200 | 2585 |
| Armour Thickness | n_a | [m] | 0.007-0.0252 | 0.0082-0.0328 |
| Keulegan-Carpenter Number | KC | [-] | 0.8-7.6 | 1.3 |
| Pile Reynolds Number | Re_p | [-] | 11220-43000 | - |
| Scale | Geometric scale of 1/50 - Froude similitude | | | |

4.3.2.5 Scour protection tests and configurations

The configuration of each scour protection is presented in Table 4.30. The hydrodynamic conditions are very similar, for both the spectral significant wave height and the peak period. Since no currents were applied, the minor changes may be assumed to be a result of possible model effects or equipment uncertainty. All scour protections are performed with a filter layer thickness of 1 cm in the model, i.e. 0.5 m in the prototype. The number of tests performed is rather short. However, it must be noted that 4 tests, out of 12, were disregarded due to problems either related with the 2D bed profiler or with the wave generation system. Unlike the tests performed in the MARINET proposal 61, each test was not performed as a function of the result obtained in the previous experiment, i.e. if a test failed, the next one was performed with a larger thickness. In this case, the armour layer thickness was simply increased from test to test in order to analyse the influence of the thickness on the damage development.

4.3.3 Methodology of analysis

The methodology of analysis implemented for the present set of tests is identical to the one described in section 4.2.4. However, since during the present setup photographic records were not taken between wave trains, the damage level was identified visually through direct observation. The minimum armour layer thickness corresponded to at least 2 layers of stones, i.e. $n_a=2D_{50}$, and no single layer scour protections were tested. Therefore, the failure criterion implemented for the MARINET dataset and also used in [1, 32, 100, 101] has been applied. The scour protection is considered to have failed when the area of exposed filter layer exceeds the value of $4(D_{50})^2$. The remaining remarks made in section 4.2.4, regarding the evaluation of the measured damage number and the colour code used for erosion and accretion (sediment accretion), are also valid for the present dataset. Since no current loading was applied in the present tests, it is expected that the measured damage numbers are smaller

than the ones in the MARINET tests. However, caution is advised when comparing these datasets, due to the larger uncertainty associated to the measurements performed with the 2D bed profiler compared to the digital terrain models obtained with the 3D laser profiler.

Table 4.30 – Scour protection tests and configuration with overall hydrodynamic conditions at FEUP.

| Test-series | D_{50} [mm] | n_a [mm] | n_a [times D_{50}] | H_{m0} [m] | T_p [s] | d [m] | N [-] |
|---------------|------------------|---------------|-------------------------------|--------------|-----------|---------|---------|
| 001 | 4.1 | 8.2 | 2 | 0.107 | 1.51 | 0.24 | 3000 |
| 002 | 4.1 | 8.2 | 2 | 0.104 | 1.53 | 0.24 | 3000 |
| 003 | 4.1 | 12.3 | 3 | 0.096 | 1.51 | 0.24 | 5000 |
| 003* | 4.1 | 12.3 | 3 | - | 1.51 | 0.24 | 937 |
| 004 | 4.1 | 16.4 | 4 | 0.100 | 1.51 | 0.24 | 5000 |
| 004* | 4.1 | 16.4 | 4 | 0.101 | 1.51 | 0.24 | 3000 |
| F1 005 | 4.1 | 20.5 | 5 | 0.102 | 1.52 | 0.24 | 5000 |
| 006 | 4.1 | 24.6 | 6 | 0.112 | 1.53 | 0.24 | 5000 |
| 006* | 4.1 | 24.6 | 6 | 0.110 | 1.51 | 0.24 | 1000 |
| 006** | 4.1 | 24.6 | 6 | 0.099 | 1.51 | 0.24 | 1000 |
| 007 | 4.1 | 28.7 | 7 | 0.103 | 1.51 | 0.24 | 5000 |
| 008 | 4.1 | 32.8 | 8 | 0.110 | 1.51 | 0.24 | 5000 |

003* - Wave paddles stopped before 1000 waves.
 004*, 006*, 006** - The bed profiler damaged the protection by entering through the armour layer.

4.3.4 Discussion of scale and model effects of the experimental work at FEUP

As previously discussed in sections 3.9 and 4.2.5, the scour protection tests at FEUP are also subject to model and scale effects, which need to be accounted for. In this case, no scale or model effects are expected from the wave-current interaction, because no current loading is applied. However, the possible existence of standing waves potentially generated through reflection phenomena remains as a problem. As pointed out before, little to no solutions exist to avoid this problem. Nevertheless, the incident wave characteristics were monitored at the entrance of the sediment box and no abnormal values were registered. Moreover, the absorbing beach and the active absorption system are expected to minimize this problem.

Also, the upward approaching slope was placed at a smaller distance from the wave paddles than the one recommended in the literature (2L), e.g. [163]. However, this was required to avoid possible interferences from the downstream sections in the monopile section. At the rear end of the corridor, waves are dissipated at the absorbing beach, which generates higher turbulence levels than the ones obtained in the upstream sections of the setup. Nevertheless, the upward slope is placed 2.5 m way from the position of the wave paddle at the maximum extension. This means that the upward slope is roughly 3 m way from the paddle's mean position, which may slightly vary depending on the stroke required to obtain H_{m0} . Moreover, the upward slope was designed to be a smooth transition between

the bottom of the tank and the sediment box. Once again, the incident wave characteristics at WG2 indicate that no abnormal values were registered at the entrance of the sediment box, where the foundation was being tested. WG2 was used as a reference for the hydrodynamic conditions at the scour protection, whilst WG1 and WG3 were used to control possible outliers at the entrance and the rear end of the setup. The reflection associated to the absorbing beach, according to [188], is lower than the 18% and the 15% reflection levels reported for the MARINET data [102] and the data from [1] and [32], respectively. Nevertheless, the wave reflection was accounted for by using the total incident wave height, as recommended in [32].

There is an asymmetry in the side walls, since one of them is made of removable perspex sections and the other is a concrete wall with glass windows at the sediment box section. In order to disregard the wall effects and as mentioned before, [1] recommends that the wave heights are monitored as near as possible to the monopile section (without affecting the flow pattern), as done with WG2. Regarding the sediment transport, the walls may also affect the scour pattern at the edge of the protection. In the present case the scour protection was performed with a radial extension of $5D_p$, thus leaving 15 cm between the wall and the beginning of the scour protection (without including the extra-slope). This is expected to have a greater effect on the edge of the scour protection than the effects concerning the MARINET setup, potentially contributing to a damage overestimation at the outer slopes due to local constrictions. However, it must be noted that this effect is somehow reduced by the fact that no current is present. Also, the profiles did not include the analysis of the extra-slope, which is the region that is most likely affected by the interaction between the walls and the wave field. In order to minimize the blockage effect, the ratio of pile diameter to flume's width was kept as $1/8$, which is below the recommendation of $1/6$ given by [49] and [163].

The present setup did not have any type of artificial sediment feeding. However, as discussed in section 4.2.5, the present sediment box was also made large enough to ensure that this effect was minimized in a similar way to the MARINET experiments. No significant scour holes were noted at the transition section between the upward slope and the sediment box. This effect is expected to be less significant than in the previous setup, because no current was present, which reduces the sediment transport rates. Regarding the model construction, the present setup also presents the same problems identified in section 4.2.5, namely, the initial displacement of stones when filling the wave tank and the manual installation compared to the fall-pipe vessel installation performed in prototype situations. As performed in the MARINET tests, the initial profiles were taken after the flume was filled to minimize possible overestimation of the damage number.

The effects on the bed boundary layer are once again present, because the sand-bed sediments were not scaled to avoid the interference caused by cohesive properties typical from very fine material. Moreover, Eqs. (3.73), (3.76) and (3.77) were used to calculate the minimum mean stone diameter that ensures a rough boundary layer on top of the scour protection. By using the hydrodynamic target conditions of series F1, it is possible to conclude that the minimum mean stone diameter according to Eq. (3.73) is 0.042 mm and according to Eqs. (3.76) and (3.77) is 1.2 mm, which are below the 4.1 mm used as D_{50} for all tests. Regarding the ripples formation at the sand bed, $d_s=0.23$ mm, which is smaller than $D_p/25$, which enables neglecting the ripples effect according to [63]. Regarding this aspect, the considerations made in section 4.2.5 also remain valid.

In this case, the Reynolds number is not directly comparable to the one presented in the MARINET data, Table 4.5, which was calculated considering the depth-averaged current velocity. However, if the Reynolds number is calculated with respect to the pile diameter (D_p) and the orbital bottom velocity (U_m), a target $Re_p=2.1 \times 10^5$ is obtained, which enables the neglectation of the viscous effects according to [190]. Nevertheless, it does not comply with the limits referred in section 3.9,

which states that the differences (between the model and the prototype) in the vortex shedding can be disregarded if $Re_p > 2.5 \times 10^5$. This problem is also common to the datasets analysed in section 4.2.5 and may imply a scale effect on the vortex shedding regime, which must be accepted in order to respect the Froude similitude defined for the model. Moreover, $KC=1.3$ is framed within the boundaries set by the studies analysed in Table 4.5 and Table 4.29. Thus, it might be considered small according to [75], which states that for small KC numbers, the influence of Re_p on the vortex shedding is small. The KC number scales geometrically, since it depends on the orbital velocity, the water depth and the peak wave period. Consequently, no scale effects are expected to arise from KC , which is accurately scaled with the Froude similitude.

The pile roughness remains a possible model effect, due to the reduced roughness presented by the perspex material. Also, no fouling occurs in the model. The considerations made in section 4.2.5 regarding this aspect also remain valid for the present setup.

4.3.5 Analysis and discussion of results from the experimental work at FEUP

4.3.5.1 Measured conditions

The measured hydrodynamic conditions for each wave train, considering the application of Eqs. (3.53) and (3.54) for the second and the third wave trains with 2000 waves, are presented in Table 4.31. Some variations in the spectral significant wave height and peak period were recorded, but no abnormal values were observed. As mentioned in Table 4.30, tests F1_003*, F1_004*, F1_006* and F1_006** were excluded from further analysis due to equipment malfunctions. The measured conditions are close to the target values in Table 4.29, although slight variations can be noted. The majority of the tests were performed up to 3000 waves, because some of the configurations had failed or the 2D bed profiler had damaged the protection's profile.

Table 4.31 – Measured hydrodynamic conditions of series F1.

| Series | Test | 1000 waves | | | 3000 waves | | | 5000 waves | | | | | | | |
|--------|----------|------------|-----------------|------|--------------------------|----------------------------------|------|-----------------|----------------|------|-----------------|----------------|------|-----------------|----------------|
| | | d | D ₅₀ | na | na | D ₈₅ /D ₁₅ | N | H _{m0} | T _p | N | H _{m0} | T _p | N | H _{m0} | T _p |
| | | [m] | [mm] | [mm] | [times D ₅₀] | [-] | [-] | [m] | [s] | [-] | [m] | [s] | [-] | [m] | [s] |
| F1 | F1_001 | 0.24 | 4.10 | 8.2 | 2 | 1.56 | 1000 | 0.102 | 1.51 | 3000 | 0.106 | 1.52 | - | . | |
| | F1_002 | 0.24 | 4.10 | 8.2 | 2 | 1.56 | 1000 | 0.104 | 1.51 | 3000 | 0.104 | 1.51 | - | . | |
| | F1_003 | 0.24 | 4.10 | 12.3 | 3 | 1.56 | 1000 | 0.094 | 1.51 | 3000 | 0.096 | 1.51 | 5000 | 0.096 | 1.51 |
| | F1_003* | 0.24 | 4.10 | 12.3 | 3 | 1.56 | 937 | . | . | - | . | . | - | . | |
| | F1_004 | 0.24 | 4.10 | 16.4 | 4 | 1.56 | 1000 | 0.099 | 1.52 | 3000 | 0.100 | 1.51 | 5000 | 0.100 | 1.52 |
| | F1_004* | 0.24 | 4.10 | 16.4 | 4 | 1.56 | 1000 | 0.100 | 1.51 | 3000 | 0.101 | 1.51 | - | . | |
| | F1_005 | 0.24 | 4.10 | 20.5 | 5 | 1.56 | 1000 | 0.103 | 1.52 | 3000 | 0.102 | 1.52 | 5000 | 0.102 | 1.5 |
| | F1_006 | 0.24 | 4.10 | 24.6 | 6 | 1.56 | 1000 | 0.118 | 1.51 | 3000 | 0.112 | 1.51 | 5000 | 0.112 | 1.51 |
| | F1_006* | 0.24 | 4.10 | 24.6 | 6 | 1.56 | 1000 | 0.110 | 1.51 | - | . | . | - | . | |
| | F1_006** | 0.24 | 4.10 | 24.6 | 6 | 1.56 | 1000 | 0.099 | 1.51 | - | . | . | - | . | |
| | F1_007 | 0.24 | 4.10 | 28.7 | 7 | 1.56 | 1000 | 0.106 | 1.51 | 3000 | 0.105 | 1.51 | 5000 | 0.103 | 1.51 |
| | F1_008 | 0.24 | 4.10 | 32.8 | 8 | 1.56 | 1000 | 0.110 | 1.53 | 3000 | 0.112 | 1.51 | 5000 | 0.111 | 1.51 |

4.3.5.2 Test repeatability

In the present setup, some repetitions of tests F1_001, F1_003, F1_004 and F1_006 were planned. However, the treatable data were only available for test F1_001 and its repetition, i.e. test F1_002. The profiles of both tests were analysed, to understand if the damage number development was consistent for the same scour protection design under similar hydrodynamic conditions. Based on Table 4.32 and Table 4.33, it is possible to confirm that test F1_002 provides similar damage numbers per sub-area compared to test F1_001. Although the number of repeated tests is indeed very limited compared to the planned experiments from Table 4.30, the repeatability of the test conditions was well captured in these tests.

In Figure A2.3 (APPENDIX 2), the linear relationship between the S_{3Dsub} , after 3000 waves, of tests F1_001 and F1_002, shows that both tests yield an $R^2=0.87$, which can be considered satisfactory if the uncertainties of the model and the variations of the hydrodynamic conditions is considered. The profiles from 0 to 1000 waves and from 1000 to 3000 waves show an even closer agreement than the ones analysed in section 4.2.6.2, regarding the MARINET data. It is important to note that the tests performed at FEUP had much similar hydrodynamic conditions than the ones from MARINET. Moreover, at FEUP no current flow was applied and the measurement technique of S_{3Dsub} is also different from the one used at UAalborg. Therefore, this also contributes for different results in the repeatability between both datasets, thus a comparison of the damage number per sub-area between the MARINET data and FEUP data was avoided.

Table 4.32 – Damage number (S_{3Dsub}) per sub-area, i.e. ring and sector for test F1_001, after each wave train.

| {0;1000} waves | S1 | S2 | S3 | S4 | S5 | S6 | S7 | S8 | S9 | S10 | S11 | S12 |
|---------------------------|-----------|-----------|-----------|-----------|-----------|-----------|-----------|-----------|-----------|------------|------------|------------|
| R1 | -0.93 | -0.85 | -0.25 | 0.03 | -0.32 | -0.75 | -0.68 | -0.92 | -0.42 | -0.36 | -0.33 | -0.97 |
| R2 | -0.33 | -0.59 | -0.15 | -0.07 | -0.08 | -0.24 | -0.53 | -0.35 | -0.21 | -0.18 | -0.26 | -0.23 |
| R3 | -0.26 | -0.09 | -0.01 | 0 | 0 | -0.12 | -0.36 | -0.07 | -0.09 | 0.01 | 0 | -0.16 |
| R4 | -0.21 | 0.03 | 0.01 | 0 | 0.12 | -0.01 | -0.21 | 0 | 0.1 | 0.17 | 0 | 0.02 |
| R5 | 0.06 | 0.06 | 0.21 | 0.43 | 0.29 | 0.06 | 0.03 | -0.11 | -0.1 | -0.02 | -0.26 | -0.12 |
| R6 | -0.17 | 0.11 | 0.4 | 0.33 | 0.46 | 0.1 | -0.1 | -0.16 | -0.4 | -0.27 | 0.42 | -0.13 |

| {1000; 3000} waves | S1 | S2 | S3 | S4 | S5 | S6 | S7 | S8 | S9 | S10 | S11 | S12 |
|-----------------------------------|-----------|-----------|-----------|-----------|-----------|-----------|-----------|-----------|-----------|------------|------------|------------|
| R1 | -1.27 | -1.09 | -0.49 | -0.1 | -0.43 | -0.95 | -1.19 | -1.13 | -0.79 | -0.36 | -0.33 | -1.02 |
| R2 | -0.63 | -0.98 | -1.32 | -0.18 | -0.57 | -0.78 | -0.94 | -0.65 | -0.51 | -0.36 | -0.56 | -0.69 |
| R3 | -0.26 | -0.22 | -0.18 | 0.59 | -0.74 | -0.26 | -0.52 | -0.33 | -0.22 | -0.08 | -0.29 | -0.26 |
| R4 | -0.23 | -0.13 | -0.12 | 0.23 | 0.25 | -0.32 | -0.42 | -0.09 | -0.03 | 0.1 | -0.06 | -0.09 |
| R5 | 0.03 | 0.26 | 0.28 | 0.62 | 0.31 | 0.16 | 0.15 | -0.31 | -0.35 | -0.19 | -0.53 | -0.21 |
| R6 | -0.42 | 0.3 | 1.08 | 1.02 | 1.19 | 0.32 | -0.46 | -0.48 | -0.76 | -0.44 | -0.78 | -0.35 |

Both tests were visually classified as failure, with rings R1 and R2 in sectors S1, S2, S3, S5, S6 and S7 being the most critical ones in terms of the occurrence of erosion. Both tests show similar edge scour in the front sectors of the protection at the edge, ring R6. Comparing the erosion and accretion patterns, it is possible to see that the most severe scour occurs in the inner rings R1 and R2 in both sides of the pile, i.e. sectors S1 and S7. In the MARINET data, these rings showed larger damage numbers in sectors S3, S4 and S5. This difference is a result of the absence of currents.

The pattern obtained in Table 4.32 and Table 4.33 is consistent with the one obtained for waves alone in the research presented by [1, 32] and [148]. The scour protection tests at FEUP showed that for waves alone the damage number tends to be maximum at the sides of the pile, typically occurring at a distance of $0.5D_p$, as it was also stated in [1, 32]. These tests show that the maximum damage of all sub-areas is -1.32 for F1_001 and -1.35 for F1_002. These values are also within the range of the ones that led to failure of the protection for waves alone, reported in [32]. For those cases, [32] shows that the maximum damage number varied between -1.19 and -1.54. However, one should note that the mentioned research used larger significant wave heights and a larger water depth, i.e. $d=0.40$ m.

Table 4.33 - Damage number (S_{3Dsub}) per sub-area, i.e. ring and sector for test F1_002, after each wave train.

| {1000; 3000} waves | S1 | S2 | S3 | S4 | S5 | S6 | S7 | S8 | S9 | S10 | S11 | S12 |
|--------------------------|-------|-------|-------|-------|-------|-------|-------|-------|-------|-------|-------|-------|
| R1 | -1.13 | -1.08 | -0.95 | -0.12 | -0.38 | -0.95 | -1.1 | -0.98 | -0.53 | -0.35 | -0.33 | -0.75 |
| R2 | -0.36 | -0.62 | -0.25 | 0.13 | 0.05 | -0.32 | -0.35 | -0.37 | -0.23 | -0.12 | -0.21 | -0.23 |
| R3 | -0.31 | -0.19 | -0.08 | 0.02 | -0.1 | -0.25 | -0.24 | -0.13 | -0.06 | -0.1 | -0.03 | -0.16 |
| R4 | -0.26 | 0.12 | 0.15 | 0.08 | 0.12 | 0 | -0.27 | 0.12 | 0.09 | 0.26 | 0.06 | 0.05 |
| R5 | 0.22 | 0.09 | 0.19 | 0.38 | 0.22 | 0.1 | 0.19 | -0.07 | -0.11 | -0.23 | -0.07 | -0.12 |
| R6 | -0.05 | 0.13 | 0.32 | 0.41 | 0.33 | 0.1 | -0.08 | -0.26 | -0.65 | -0.27 | -0.55 | -0.26 |

| {1000; 3000} waves | S1 | S2 | S3 | S4 | S5 | S6 | S7 | S8 | S9 | S10 | S11 | S12 |
|--------------------------|-------|-------|-------|-------|-------|-------|-------|-------|-------|-------|-------|-------|
| R1 | -1.34 | -1.26 | -1.13 | -0.22 | -0.46 | -1.17 | -1.35 | -1.21 | -0.75 | -0.56 | -0.68 | -0.97 |
| R2 | -0.63 | -0.75 | -1.02 | -0.11 | -0.02 | -0.42 | -0.58 | -0.72 | -0.31 | -0.26 | -0.56 | -0.77 |
| R3 | -0.41 | -0.34 | -0.13 | 0.13 | -0.52 | -0.34 | -0.45 | -0.23 | -0.17 | -0.19 | 0.02 | -0.16 |
| R4 | -0.33 | -0.02 | -0.07 | 0.37 | 0.22 | -0.12 | -0.59 | -0.28 | -0.19 | 0.42 | -0.13 | 0.25 |
| R5 | 0.09 | 0.23 | 0.29 | 0.51 | 0.33 | 0.26 | 0.12 | -0.24 | -0.43 | -0.32 | -0.41 | -0.27 |
| R6 | -0.49 | 0.46 | 0.91 | 1.03 | 0.87 | 0.29 | -0.47 | -0.4 | -0.75 | -0.41 | -0.69 | -0.39 |

4.3.5.3 Overall measured damage numbers

As discussed in section 4.2.6.3, the tests might be classified into statically stable, dynamically stable and failure of the scour protection. This stability status can also be related to the overall damage number, which corresponds to the maximum value of all sub-areas as in Eq. (4.4). The overall measured damage number of each test is provided in Table 4.34. When comparing Table 4.34 with the MARINET data (Table 4.16), it is possible to see that the values of $S_{3Dmeasured}$ are generally smaller than the ones presented for series s1 (with $D_{50}=4.135$ mm). This results from the fact these tests only include wave loading. Tests F1_001, F1_002 and F1_003 were identified as failure.

However, the increase in the armour layer thickness from $2D_{50}$ to $3D_{50}$ seemed to be enough to delay the failure occurrence of the scour protection. Tests F1_001 and F1_002 were identified as failure after 3000 waves, whilst F1_003 has only failed after 5000 waves. Nevertheless, a repetition of test F1_003 would be important to confirm the stability status obtained after 5000 waves. As noted in the previous datasets, the damage number tends to increase with the increasing number of waves. However, the damage development in dynamically stable and statically stable scour protections seems to be larger from 0 to 1000 waves than in the following wave trains. This is somehow consistent with the conclusions obtained by [26], which stated that the rate of damage development tends to decrease with N. Tests F1_007 and F1_008, both statically stable, registered very similar damage numbers,

which remains practically unaltered from 1000 waves to 5000 waves. In this case, the increase of the armour layer thickness did not present any significant influence on the damage number. This makes sense since no movements of the stones occurred, thus meaning that the damage does not increase over time. In test F1_006, also statically stable, the damage number is slightly larger than in F1_007 and F1_008. This could be due to the reduction of the armour layer thickness, but further tests should be performed in order to validate such hypothesis.

An interesting aspect to be noted is that the successive increase in the armour thickness seemed to contribute more to the stability of the scour protection than to the increase of the damage number caused by a higher placement of the armour layer stones. As discussed during the analysis of the MARINET data, [32] noted that when changing the geotextile filter by the granular one, a damage increase was observed due to the higher placement of the armour layer stones. However, it is important to note that when addressing this matter, [32] compares scour protections that have the same armour thickness, which is not the case in the present research. The set of tests performed represents an increase of the armour thickness from 0.82 cm to 3.28 cm, which is considerable, particularly, since the water depth (d) is only 24 cm. Nevertheless, the results show that the corresponding decrease of the water distance to the armour layer did not lead to an increase in the damage number. Despite the limited number of tests performed, the results indicate that an increase in the armour layer thickness leads to a decrease in the damage number, for the same wave characteristics and mean stone diameter. This was expected, because the available volume of stones for the armour layer reshaping is larger with increasing armour layer thickness. It is important to note that this behaviour is not captured by the damage predictions given by Eq. (3.57), which does not consider the armour layer thickness nor the number of layers of stones applied to the protection.

Table 4.34 - Measured damage numbers ($S_{3D_{measured}}$) after 1000, 3000 and 5000 waves representative overall value of the scour protection, positive values representing erosion.

| Test series | Test | $S_{3D_{measured}}$ | | | | Type of Stability |
|-------------|----------|---------------------|------|------|------|-------------------|
| | | n_a | 1000 | 3000 | 5000 | |
| | | [times D_{50}] | [-] | [-] | [-] | |
| F1 | F1_001 | 2 | 0.97 | 1.32 | - | Failure |
| | F1_002 | 2 | 1.13 | 1.35 | - | Failure |
| | F1_003 | 3 | 0.96 | 1.20 | 1.54 | Failure |
| | F1_003* | 3 | - | - | - | - |
| | F1_004 | 4 | 0.86 | 0.98 | 1.10 | Dynamically |
| | F1_004* | 4 | 0.96 | 1.03 | - | - |
| | F1_005 | 5 | 0.79 | 0.94 | 1.20 | Dynamically |
| | F1_006 | 6 | 0.43 | 0.48 | 0.52 | Statically |
| | F1_006* | 6 | - | - | - | - |
| | F1_006** | 6 | - | - | - | - |
| | F1_007 | 7 | 0.24 | 0.33 | 0.33 | Statically |
| | F1_008 | 8 | 0.21 | 0.30 | 0.29 | Statically |

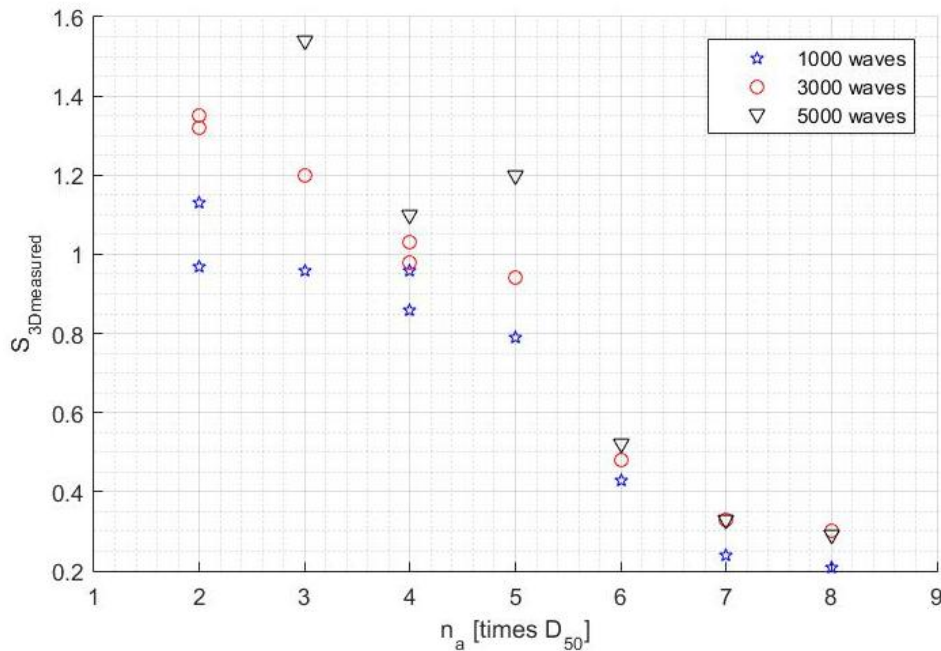


Figure 4.54 – Variation of $S_{3Dmeasured}$ with increasing armour layer thickness.

Conversely, from the practical point of view, the increase of the armour layer thickness implies a raised cost of the scour protection, due to the increased volume of rock material needed. Moreover, the stability improvement has a limit, as shown in Figure 4.54. As one moves from a failed configuration to a dynamically stable one, the benefits of the armour layer increase are evident, but the reduction in damage number tends to decrease as one moves to a statically stable configuration. After static stability is reached, there is no benefit in increasing the armour layer thickness. As noted by [102], the overall configuration of the scour protection has to consider the economical and practical aspects of the construction and installation of the protection, thus meaning that the thickness increase may not always be the best solution. This becomes even more evident if other configurations of the protection are considered, e.g. the seabed levelled scour protections studied in [100] may imply a smaller volume of stones compared to the non-levelled configurations with increased $n_a D_{50}$, as the ones analysed here (see also Figure 3.16).

4.3.5.4 Measured damage numbers and type of stability

Figure 4.55 shows the type of stability of each configuration according to the measured damage number in each wave train. The black vertical lines provide the acceptable damage number suggested by [32], for each type of stability. One sees that the measured damage numbers of statically stable protections, after 3000 and 5000 waves, overcome the suggested limit for the corresponding acceptable damage, i.e. $S_{3D}=0.25$. Hence, for this set of tests, the suggested limit provides a conservative assessment of the acceptable damage for statically stable scour protections, thus meaning that more damage might be endured by such protections. However, one must also note that similarly to the 3D laser profiler used in the MARINET data, the 2D bed profiler may also tend to overestimate small damage numbers, for which no movement is expected to occur. Further research is required to address this aspect. Nevertheless, it is important to note that a conservative assessment of $S_{3Dacceptable}$ may also contribute to a conservative reliability assessment of a statically stable scour protection.

When considering the dynamically stable scour protections, Figure 4.55 shows that for $N=5000$ waves, the limit suggested by [32], i.e. $S_{3D_{\text{acceptable}}}=1$, underestimates the damage that a dynamic scour protection may endure. Note that both dynamic scour protections reported measured damage numbers of 1.10 and 1.20 after 5000 waves. Despite the short number of dynamic configurations tested, the values of $S_{3D_{\text{measured}}5000}$ are in agreement with the remarks made in section 4.2.6.5. In that section, it was noted that dynamic scour protections under combined waves and current were obtained for a maximum $S_{3D_{\text{measured}}}$ of 3.53. Moreover, it was concluded that the limit suggested by the original data [32] could be further extended to $S_{3D_{\text{acceptable}}}=1.25$. The data from series F1 validate this extended limit for $N=3000$ and 5000 waves, since no overlaps are found between dynamic scour protections and failed ones. Note that there are two failures occurring below the $S_{3D_{\text{acceptable}}}$ for dynamic scour protections. However, such failures correspond to tests F1_001 and F1_002, which report considerably large values of $S_{3D_{\text{measured}}}$ (but still below 1) right after the first wave train. This emphasises the fact that the type of stability should not be defined for such a small number of waves, because the rate of damage development might still be considerably high. Nevertheless, when proposing the acceptable damage for each type of stability, [32] only addressed damage numbers that were measured either after 3000 or 5000 waves. The overall measured damage numbers seem to indicate that the acceptable damage provided by the original data might be used for reliability analysis, as it provides rather conservative design limits. Still, as noted throughout section 4.2.6.5, the transitions between the static stability, dynamic stability and failure might vary around the vertical lines showed in Figure 4.55, thus meaning that the transitional behaviour is not a sharp one. As in the stability parameter from the OPTI-PILE project (see section 3.7.1.4), the transitional behaviour of the stability is gradational. Therefore, caution is advised when using the aforementioned limits for design situations. Typically, for specific situations, these limits should be validated and eventually calibrated by a physical model study, as suggested in [100] and [151].

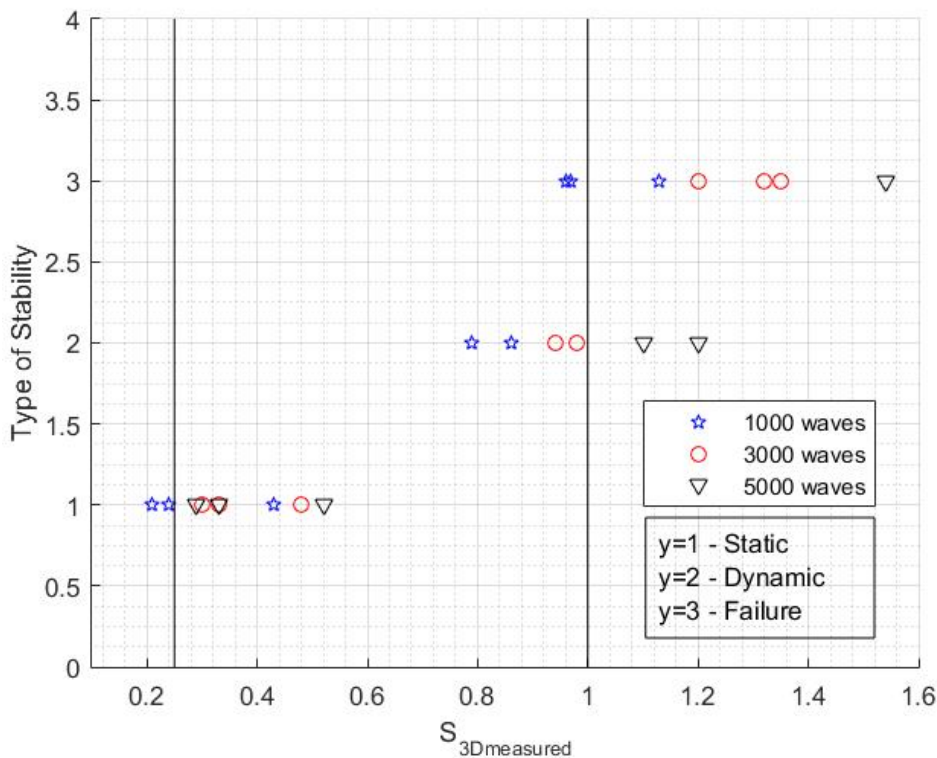


Figure 4.55 – Type of stability versus the evolution of $S_{3D_{\text{measured}}}$. Vertical lines $S_{3D_{\text{measured}}}=0.25$ and $S_{3D_{\text{measured}}}=1$.

4.3.5.5 Comparison with the stability parameter from OPTI-PILE

For the present set of tests, the stability parameter was calculated according to Eq. (3.43), assuming $\theta_{cr}=0.056$ and a θ_{max} from Eq. (3.44) that is a result of the wave-induced bed shear stress alone, i.e. Eq. (2.9). In these calculations, the orbital bottom velocity for irregular waves was obtained according to [113], with the wave friction factor based on the formulation presented in [52] and [54]. The stability parameter per wave train and the type of stability are presented in Table 4.35.

Table 4.35 – Stability parameter (stab) per test and per wave train.

| Test | stab₁₀₀₀ | stab₃₀₀₀ | stab₅₀₀₀ | Type of Stability |
|-----------------|----------------------------|----------------------------|----------------------------|--------------------------|
| F1_001 | 0.506 | 0.536 | - | Failure |
| F1_002 | 0.521 | 0.521 | - | Failure |
| F1_003 | 0.449 | 0.463 | 0.463 | Failure |
| F1_003* | - | - | - | - |
| F1_004 | 0.485 | 0.492 | 0.492 | Dynamic |
| F1_004* | 0.492 | 0.499 | - | - |
| F1_005 | 0.514 | 0.507 | 0.506 | Dynamic |
| F1_006 | 0.628 | 0.581 | 0.581 | Static |
| F1_006* | - | - | - | - |
| F1_006** | - | - | - | - |
| F1_007 | 0.536 | 0.507 | 0.514 | Static |
| F1_008 | 0.567 | 0.581 | 0.574 | Static |

The minor variations noted in the stab values are related to the variations in the hydrodynamic conditions (see Table 4.31). Nevertheless, the results show that all values are above $stab=0.460$ (with the exception of $stab_{1000}$ for test F1_003), identified by [100] as the transition between “movement without failure” (dynamic stability) and “failure”.

Table 4.35 shows that the stability parameter was not able to differentiate the type of stability of each scour protection. This becomes even more evident than in the MARINET data, because all tests were performed for very similar hydrodynamic conditions, albeit the different type of stability obtained. This is consistent with the results obtained in section 4.2.6.5.3 and reported by [32] and [151]. Furthermore, as shown in Figure 4.56, when plotting the measured damage number ($S_{3Dmeasured}$) divided by the number of layers of armour stones (n_a) versus $stab$, no clear trend is noted.

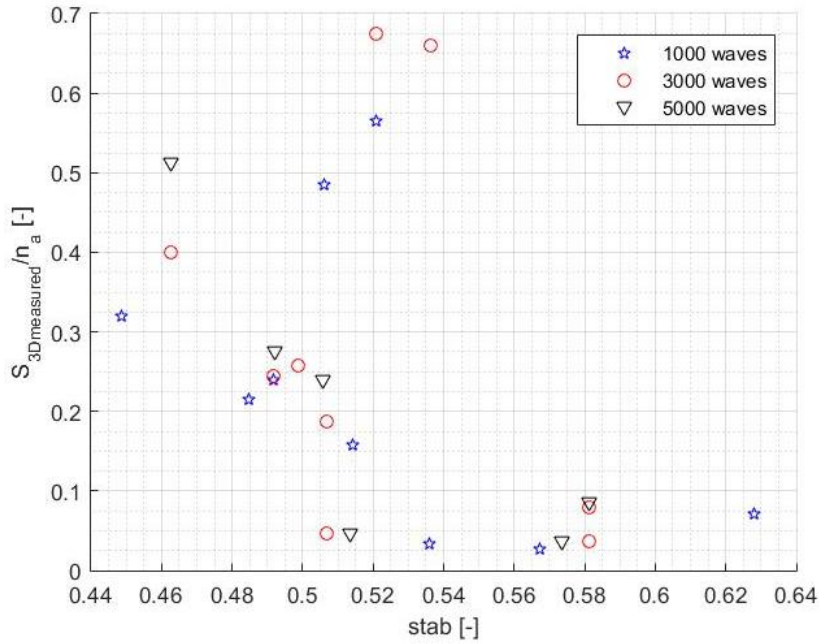


Figure 4.56 – Measured damage number ($S_{3D\text{measured}}$) versus stability parameter (stab) per wave train.

4.3.5.6 Predicted damage numbers

The prediction of the damage numbers by means of Eq. (3.57) only makes use of the first term, i.e. the one associated to coefficient a_0 . This occurs because the depth-averaged current velocity is null, thus meaning that $a_1=0$, because $U_c/(gD_{n50})^2 < 0.92$, Eq. (3.48). The predicted damage numbers of each test are given in Table 4.36. A comparison between Table 4.36 and Table 4.34 shows that Eq. (3.57) is unaffected by the armour layer thickness. Since the hydrodynamic conditions are similar in all tests, the predicted damage does not vary as much as the measured one. This was already expected, since the original data did not include a broad range of scour protection thicknesses [1, 32]. However, an interesting aspect that must be noted is that, for series F1, the majority of the predicted damage numbers were overestimated compared to the measured ones. This is perceivable from Figure 4.57, which shows most of the damage numbers below the line of best fit, i.e. $S_{3D\text{predicted}}=S_{3D\text{measured}}$. Note that Figure 4.57 provides the comparison of the damage number non-dimensionalized by the number of layers of armour stones times the number of waves, i.e. $S_{3D}/(n_a N^{b_0})$.

It is also possible to note that for a water depth of 0.24 m the equation overpredicted the damage numbers in waves alone (series F1), while it tended to underestimate some of them in the MARINET data for combined waves and current (see Figure 4.40). When comparing series F1 with the tests performed with waves alone in [32] and [148], it is possible to see that Eq. (3.57) provides conservative estimates of the damage number for all datasets. Therefore, the use of Eq. (3.57) in reliability analysis of scour protections under waves alone is expected to provide a conservative assessment of the protection's safety. A comparison between F1, [32] and [148] is provided in Figure 4.58, which uses the damage number after 3000 waves for series F1 to allow the inclusion of tests F1_001, F2_002 and F1_004*. Regarding series F1, the largest departures from the best-fit line in Figure 4.58 occur for the statically stable scour tests. This happens due to the fact that these tests were performed with larger armour thicknesses ($6D_{50}$ to $8D_{50}$), which are not accounted for by Eq. (3.57) but have been shown to influence the measured damage numbers, as seen in Figure 4.54.

Table 4.36 – Predicted damage numbers for test series F1.

| | n_a | $S_{3Dpredicted}$ | $S_{3Dpredicted}$ | $S_{3Dpredicted}$ | $S_{3Dpredicted}/n_a$ | $S_{3Dpredicted}/n_a$ | $S_{3Dpredicted}/n_a$ |
|----------|-------------------|-------------------|-------------------|-------------------|-----------------------|-----------------------|-----------------------|
| Waves | | 1000 | 3000 | 5000 | 1000 | 3000 | 5000 |
| Test | [times D_{50}] | [-] | [-] | [-] | [-] | [-] | [-] |
| F1_001 | 2 | 1.20 | 1.76 | - | 0.60 | 0.88 | - |
| F1_002 | 2 | 1.27 | 1.66 | - | 0.64 | 0.83 | - |
| F1_003 | 3 | 0.93 | 1.30 | 1.47 | 0.31 | 0.43 | 0.49 |
| F1_003* | 3 | - | - | - | - | - | - |
| F1_004 | 4 | 1.12 | 1.48 | 1.71 | 0.28 | 0.37 | 0.43 |
| F1_004* | 4 | 1.12 | 1.52 | - | 0.28 | 0.38 | - |
| F1_005 | 5 | 1.27 | 1.60 | 1.74 | 0.25 | 0.32 | 0.35 |
| F1_006 | 6 | 1.87 | 2.09 | 2.36 | 0.31 | 0.35 | 0.39 |
| F1_006* | 6 | 1.51 | - | - | - | - | - |
| F1_006** | 6 | 1.10 | - | - | - | - | - |
| F1_007 | 7 | 1.35 | 1.71 | 1.83 | 0.19 | 0.24 | 0.26 |
| F1_008 | 8 | 1.51 | 2.09 | 2.29 | 0.19 | 0.26 | 0.29 |

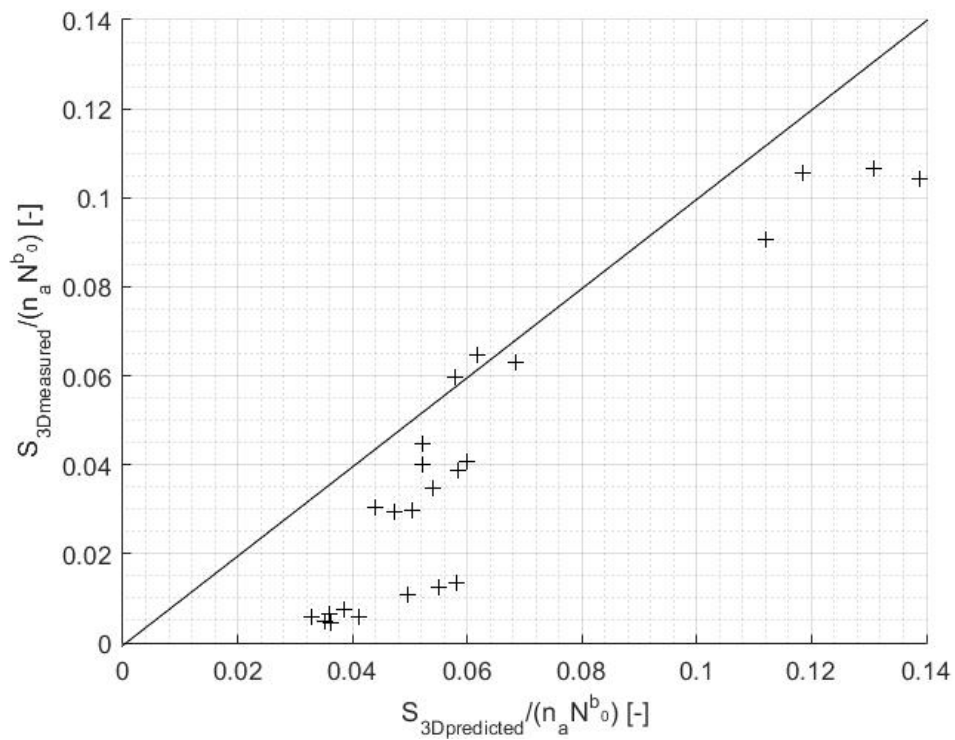


Figure 4.57 – Comparison between measured and predicted damage numbers for test series F1 (includes 1000, 3000 and 5000 wave trains).

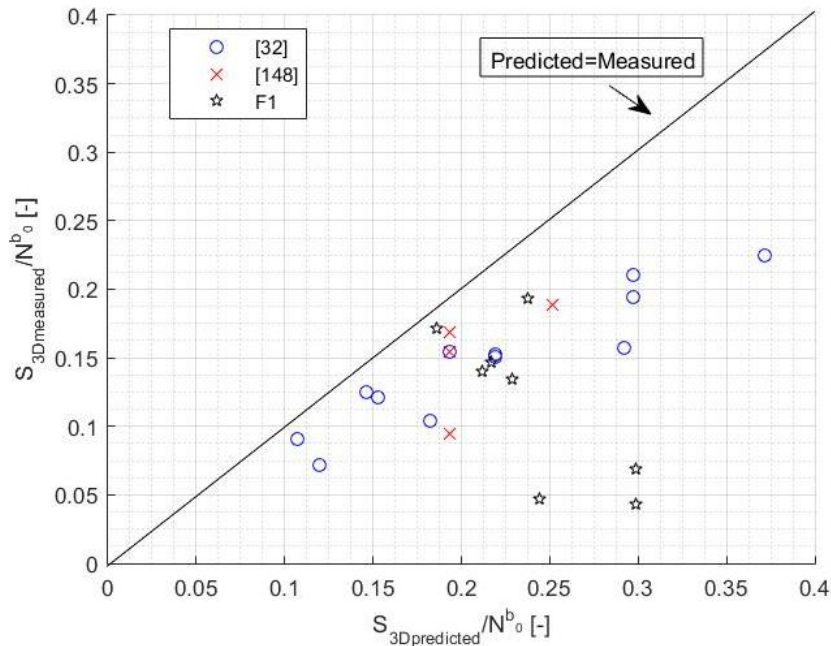


Figure 4.58 – Comparison between predicted and measured damage numbers for series F1, [32] and [148].

4.4 Conclusions

In this chapter, the concepts of statically and dynamically stable scour protections were discussed and analysed by means of two physical model studies: one developed at Aalborg University, for combined waves and current; and one developed at FEUP, for waves alone. Both models have proven their primary objective, which was to extend and confirm the feasibility of dynamic scour protections outside the range of the test conditions introduced in [1] and [32]. Moreover, both datasets were used to assess the suitability of the damage number and its predictive formula as input for the reliability assessment of dynamic scour protections. The studied physical models enabled some answers to the questions presented in section 4.2, which are revisited and summarized in the following paragraphs.

- Is there a dynamically stable scour protection for a given combination of waves and current loading and a stone size smaller than the one for a static scour protection system for these design conditions? The MARINET dataset showed that for similar hydrodynamic conditions it was possible to optimise the design of the scour protection by reducing the mean stone diameter (D_{50}) and increasing the armour layer thickness. The comparison between predicted and measured damage numbers under combined waves and current indicates that for design situations the best configuration should be validated by means of a physical model, as performed, for example, in [144]. Both the MARINET data and the tests performed at FEUP show that the damage number is suitable to define the type of stability of a certain configuration provided that this number is determined by means of a physical model, as in [1, 32] or [151]. The importance of the physical model is mainly related to the possible departures between the predictions given by Eq. (3.57) and the actual measured values. Moreover, as shown through series F1, the predictive formula does not fully account for the armour layer thickness, which is an important aspect regarding the type of stability obtained. Nevertheless, the overall results show that reducing the mean stone diameter and increasing the armour layer

thickness may provide an optimisation of a statically stable protection towards a dynamically stable one.

- *How thick should this armour layer be to allow for reshaping but to maintain full coverage of the filter layer?* The MARINET data left this aspect to be fully covered. However, the increase in the armour layer thickness enabled the reduction of the mean stone diameter, whilst obtaining configurations that were able to maintain a stable coverage of the filter layer. Albeit not including the wave-current loading, the tests performed at FEUP showed that, for the same mean stone diameter, increasing the armour layer thickness progressively leads from failure occurrence to static stability. Dynamically stable scour protections were obtained for series F1, with an armour layer thickness ranging from $4D_{50}$ to $5D_{50}$. For both datasets it was not possible to define a minimum thickness that automatically results in dynamically stable configurations. This occurs because the dynamic stability results as a combination of the armour thickness with the mean stone diameter applied. As initially expected, the results showed that reducing the armour layer thickness increases the damage number of the protection, whilst increasing the armour layer thickness reduces this damage, towards static stability. Once the static stability is obtained, the variations of the damage number with the armour layer thickness are much less significant, eventually, not justifying the additional volume of rock material associated to the thickness increase. Further research should be carried in order to define the relationship between the armour layer thickness and the reshaping ability of this layer. Nevertheless, the results indicate that both of these characteristics are related. The way to quantify the reshaping capacity of a scour protection configuration remains unknown and it is identified as a crucial aspect to obtain the dynamic profile.
- *Where is failure initiated? Is it always at the same place or is it dependent on the storm conditions?* The tests performed in series s1, s2, s3 and F1 showed that the damage development and pattern are indeed dependent on the storm conditions and the hydrodynamic characteristics of such storm events. As an overall conclusion, the damage patterns described by [1, 26, 32] and [183] were confirmed for combined waves and current. The damage development and pattern for waves alone were also consistent with the description made in [1] and [32], which is different from the one found for combined waves and current. Moreover, it was possible to note that the water depth plays an important role in the magnitude of the damage number. The MARINET dataset led to the conclusion that decreasing the water depth increased the damage number, under combined waves and current. Also, other influences were addressed, namely, regarding the wave height, the orbital bottom velocity or the current velocity. It is hereby noted that the reduced number of comparable tests did not allow a generalisation of some of the remarks made on these influences. Nevertheless, the results showed an agreement with the main findings reported on the previous datasets, i.e. [1, 32] and [148]. For combined waves and current and for waves alone, it was noted that the edge scour in the upstream sectors of the outer ring (R6) was one of the most critical areas regarding damage severity. However, in combined waves and current, the damage number tended to be larger in the inner rings (R1 and R2), at a distance ranging from $0.5D_p$ to $1D_p$. In this case, the most critical sectors were S3, S4 and S5, located at the downstream face of the pile. For waves alone, the damage tended to be larger at the left and right sides of the pile, approximately at 90° with the wave direction. The most scoured sub-areas were sectors S1 and S7 of the inner ring (R1). It was also noted that the highest damage typically occurred at a distance of $0.5D_p$. Significant scour could occur in sectors S12, S2, S3 and S6, S8 and S9. The damage number

increased for current-dominated regimes, i.e. for larger values of U_{cw} . However, further research should extend the comparable data to validate this conclusion. An important aspect which was not addressed in this study was the damage development under waves in an opposing current and other combinations of waves-current direction. This should also be addressed in future research, since the marine environment often presents a broad spectrum of directions between waves and currents, which may lead to different damage patterns than the ones identified in the present research.

- *How does the profile evolve once the filter is exposed over a certain area?* It was noted that the damage development can be associated to the type of stability showed by a certain configuration. If a scour protection fails, then the damage progresses between sub-areas at a considerable rate. Often the uncontrolled damage development occurs after 3000 waves with a considerable development rate evidenced during the first wave train (1000 waves). Once the protection fails, i.e. the area of exposed filter layer exceeds $4(D_{50})^2$, the adjacent sub-areas register a considerable damage progression, as the protection stones are dragged to the downstream side. Conversely, for statically stable scour protections, the profile remains practically unchanged, because no movements occur at the armour layer. In this case, the damage numbers might be a result of the profiler's over estimations and they do not tend to change during the tested wave trains. In the dynamic profiles, the filter layer does not exceed the exposure of $4(D_{50})^2$ and the damage progression rate decreases considerably between 3000 and 5000 waves. Nevertheless, dynamic scour protections may endure higher damage numbers than the ones obtained in statically stable scour protections. However, such damage is smaller than that of a failed scour protection for the same hydrodynamic conditions. It was seen that dynamic scour protections tended to develop an equilibrium profile, for which damage increased between 0 and 3000 waves. After 3000 waves, the damage rate decreased considerably. Further research is needed for a proper generalization of these findings. However, it must be noted that the inversion of the current component was not tested and this could contribute to the backfill process when performed after waves in a following current situation.
- *Where did the stones move to? Do they stay inside the original area of the scour protection or do they disappear? Do the stones accumulate in a specific area or is it the influence of the waves/current important in the profile response?* The combined waves and current were not tested in series F1. However, the MARINET data showed that the current played an important role in the stones' movement, which were consistently dragged to the outer rings R5 and R6, more specifically, to the downstream sectors S2 to S6. The majority of the stones' accretion was observed in these sub-areas and it was not possible to conclude if the stones could be dragged away from the protection or not. However, it is important to note that if the currents were inverted, these stones were expected to refill the scoured sub-areas at the upstream side of the monopile. Moreover, in future tests, it would be interesting to perform long-duration tests, which are scarcely reported in the literature and do not provide information on the final location of the dragged stones at the end of the tests, e.g. [103] and [148]. The present experimental research was not able to address the effects of long-duration tests, e.g. 9000 waves or more, in the profile evolution. The tests performed within the scope of the MARINET project and FEUP's experimental research confirm that the presence or absence of a current superimposed on irregular waves plays an important role in the profile response, namely in the damage location.

- *Does the profile still change a lot between 3000 and 5000 waves or is it already more or less stable?* The present chapter indicated that discussion on the effects of the number of waves in the damage progression still requires further research. While series s1, s2, s3 and F1 showed that the damage rate considerably decreases between 3000 and 5000 waves, it was not possible to confirm beyond doubt that damage stops to progress after 5000 waves. Nevertheless, test s3_004 performed until 7000 waves registered a damage number decrease and the analysis performed in [26] indicates that for $N=3000$ waves, if a scour protection is dynamically stable, the damage number is not expected to considerably increase. It was noted for both physical models that failure typically occurred for the first two wave trains, i.e. until 3000 waves. Further research should clarify this aspect. However, taking into consideration the prototype storm conditions, it seems reasonable to assume that the stability of scour protections should be assessed at least after $N=3000$ waves, because for lower values of N , the damage number might still experience a considerable development.

As mentioned at the beginning of this chapter, the experimental research hereby presented aimed at a physical model based validation of the concept of dynamic scour protections for offshore wind monopile foundations. The answers provided to the previous questions helped to validate this concept, whilst identifying key aspects that should be focused in future research related to this topic. The work performed accomplished with the first objective outlined in Chapter 1, section 1.4, which was to “Provide a contribution to the novel concept of Dynamic Scour Protections, by means of a physical model study”. Besides the contributions directly related to the research questions previously mentioned, the influence of the water depth, the armour layer thickness (under waves alone) and the discussion on the acceptable damage number, could be highlighted as important contributions that help to build-up the confidence on feasibility of dynamic scour protections, which represent an optimization of the statically stable design, typically employed.

Finally, an important analysis was performed concerning the acceptable damage number and its relationship with the type of stability shown by the configuration of the scour protection. The following underlying question was inherent to the present experimental work:

Is the predictive formula proposed by [32] suitable for further reliability analysis of scour protections? Which limitations can be found regarding Eq. (3.57) that must be considered during the reliability assessment and risk analysis of dynamic scour protections? The comparison between predicted and measured damage numbers enabled the following conclusions:

- Some departures between predicted and measured damage numbers were noted for combined waves and current. However, the new data showed that the limits for the acceptable damage proposed by [32] could be considered as conservative ones, thus suitable for a preliminary design of optimised dynamic scour protections. It was confirmed that statically stable scour protections could be obtained for S_{3D} smaller than 0.25, whilst dynamic scour protections registered an S_{3D} between 0.25 and 1. After $S_{3D}=1$, the MARINET data and series F1 showed that dynamically stable scour protections could be obtained. However, possible overlaps could occur between dynamic stability and failure occurrences. Moreover, it was also found that the acceptable limits proposed by [32] were still valid for scour protection models performed with granular filter, instead of geotextile.
- In series F1, Eq. (3.57) tended to provide a conservative assessment of the damage number caused by waves alone, which is aligned with the behaviour noted for the original dataset presented by [1, 32] and the extended range from [148], for similar hydrodynamic conditions.

- The experimental research did not address waves in an opposing current or other combinations concerning the angle between these flow components. This is an important limitation for further reliability analysis, because one is not able to address the damage number evolution for such situations. The predictive formula accounts for waves in opposing currents and the acceptable damage limits, proposed by [32], include such tests. However, a reliability assessment based on the predicted damage number according to Eq. (3.57) is not directly applicable to other situations, where waves and currents present oblique directions.
- The effect of the armour layer thickness on the armour reshaping is also not included in the predictive formula. Therefore, the reliability assessment based on Eq. (3.57) will not be able to account for this effect when addressing scour protections with the same mean stone diameter but different armour thicknesses.
- Despite the formula's limitations, it must be noted that the reliability and safety assessment of scour protections based on the damage number seems rather reasonable, due to its ability to describe the type of stability in a conservative manner, whilst still representing an optimisation of the mean stone diameter compared to the statically stable design, e.g. proposed in [30, 52] or [57].

As a result from the experimental research performed in the first part of this thesis, it is possible to conclude that dynamic scour protections are a viable alternative to the traditional statically stable design. Therefore, the following chapters proceed to the reliability assessment of scour protections based on the case study concerning the Horns Rev 3 offshore windfarm. The analysis will be performed with a particular focus on the design methodologies presented by [30, 52] for statically stable scour protections and [32] for dynamic ones.

Fundamentals of Reliability Analysis and Statistical Modelling

5.1 Introduction

The previous chapters were dedicated to the theoretical background of scour phenomena and scour protections and also to the experimental work that contributed to validate and to better understand the design methodology proposed by [1, 32] concerning dynamic scour protections, for offshore wind turbines founded in monopiles. Chapter 5 addresses the theoretical fundamentals that are used in the reliability analysis of dynamic scour protections. In this chapter one aims at providing to the reader a compendium of basic knowledge and references that can be used in further research related to the reliability analysis of scour protections. Moreover, in this chapter, the fundamentals regarding the statistical models, used to describe the interaction of the scour protection with the random environmental loading conditions, are provided.

The reliability analysis is an important part of the overall risk analysis that can typically be performed on a system, in this case the scour protection. Typically, the risk analysis implies the quantification of both the probabilities of failure and the associated consequences of such failure [11]. While the quantification of the consequences might be of remarked subjective nature, the quantification of the probabilities of failure should preferably correspond to an objective evaluation, affected by uncertainty, surely, but still objective, i.e. with a clearly defined process of assessment and numerically quantified.

Quantifying the consequences of a scour protection failure might be dependent on the possible collapse of the foundation and the cost of re-filling the protection or other technical aspects, which can be more or less quantified in an objective manner. However, if the collapse of the foundation leads, for example, to life losses or a degradation of a company's public image, the consequences might be harder to quantify, e.g. in monetary units. *How much does it cost when the public image of a company is lost due to an infrastructure collapse? How is it quantified this cost in the following years of activity? How much does one life cost? Is it the same value in every part of the World?* These are some of the important questions that add subjectivity to the risk analysis process. These questions are indeed of great importance for both the risk assessment and the risk communication that is made to the general public. However, a reduction of the overall subjectivity, encompassed in risk analysis, might be achieved by means of a proper implementation of the reliability techniques to the design of scour protections. The present research is dedicated to such implementation, which has yet to be fully developed in the scour research field. The reliability analysis of scour protections mainly implies two key components:

- The multivariate modelling of the correlated variables involved in the failure mode of the protection, i.e. the influencing variables discussed in sections 3.5, 3.6 and 4.2.6.3, as the wave characteristics, current velocity, water depth, mean stone diameter and others. The multivariate correlated modelling intends to predict the possible loading conditions that may lead, or not, to the failure of the protection.
- The safety measure of the system, i.e. the probability of failure according to a specific design criterion of the scour protection, under the design structural parameters and the environmental loading ones. The probability of failure intends to provide a quantified notion on how reliable a certain scour protection is. Throughout the present research, the probability of failure is interpreted as the chance of a design criterion, e.g. [30, 32, 52], not being met by the scour protection under the expected loading conditions. Note that if the design criterion is not met, the protection may enter into collapse, thus meaning that further remedial actions might be required.

Chapter 5 is dedicated to the introduction of the theoretical concepts required for both the aforementioned aspects. However, a joint model for sea-state characteristics is often difficult to find due to the complex nature of the wave climate and the physical constraints of sea-state phenomena. Therefore, the practical application of the multivariate modelling will mainly focus on the correlation between the wave height and the wave period.

5.2 Background and introduction to reliability analysis

Reliability analysis of technical components and systems became a central issue for scientific community during the Second World War, namely approaching several problems of performance in electrical systems [191]. In the XX century the 40's decade presented high failure rates of electronic equipment (e.g. radios, bulbs, radars). At the time modern battle ships were reported non-operable in up to 40% of the time [191], also 50% of the airborne electronics equipment in storage was unable to meet the requirements of the Air Core and Navy [192], [193] stated that 60% of the failures of one Army missile system was due to components. The lack of reliability in such important technical components led to the need of developing efforts in order to improve the performance of electrical systems. Such point in History is assumed as the beginning of reliability analysis and reliability engineering [191, 192] and [194].

Reliability analysis was further developed and applied to a wide range of industries and scientific fields, such as aeronautics, nuclear and chemical industry and also in building industry and civil engineering. In a wider perspective, reliability analysis is considered a part of decision theory, which is commonly referred to as risk assessment. Reliability analysis mainly concerns to the quantification of probabilities, which are usually linked to a certain state of a component. Those states normally regard to the components failure, partial function or a level of damage. Nevertheless, these probabilities can be interpreted for states with positive consequences, e.g. the probability of success. When risk and reliability analysis is performed, the adverse consequences are the ones which are typically the focus of study. If an event with positive consequences is being studied, the process of analysis remains the same, but instead of looking for the decrease of risk and fewer adverse consequences, the objective is to maximize the consequences, which can be called gains in opposition to losses. The initial purpose of reliability techniques was to estimate the useful life cycle of a component and to ensure that an adequate level of safety was used, in order to guarantee a satisfactory performance of the component or system [194].

Later on, such techniques were applied to structural analysis, which are problems of different nature when compared to the ones frequently faced in electronic engineering for example. Reliability analysis of structures becomes difficult due to the very number of experiences needed for the calculations of the probabilities of collapse (or structural failure) and the high costs associated to them. Through the 50's decade, applied structural reliability gained a new drive with its basic principles being presented by [195] and [196]. Consistent research was then developed in the 60's with the publications of [197] and [198] (as cited in [194]).

The following years were crucial for the development of reliability analysis in Civil Engineering. The First Order Second Moment Reliability Method was introduced by [199], followed by [200] which allowed the calculation of failure probabilities that did not vary according to the resistance criterion used. The concept of basic variables (non-Gaussian) and their statistic distributions were implemented in the First Order Reliability Methods (FORM) by [201]. The next decade brought the Second Order Reliability Methods (SORM), which allowed second order modelling of the resistance function [202, 203] or [204] (as cited in [194]).

During the latter 80's and the 90's, more advanced techniques started to be developed such as the perturbation methods [205] and response surface methods [206]. Furthermore the development of simulation techniques to account for numerical integrations, e.g. [207], as Monte Carlo and others led to the possibility of determining failure probabilities for non-linear systems. Nowadays, the techniques of reliability and risk analysis are well implemented and have continuously been the focus of new research, extended and well documented for several applications, to different fields of Civil Engineering, for example, in geotechnics [208, 209, 210], in structural safety [211] and [212], or in hydraulics [37, 39] or [41] amongst numerous others. However, the random complex nature of sea state phenomena, as well as the random properties of the scour protection's material led to challenging difficulties when trying to implement the reliability techniques in the design methodologies discussed throughout Chapters 3 and 4. Often these difficulties arise from the statistical modelling of correlated variables involved [123] and the statistically unknown properties of the scour protection [43]. More recently, research works have been presented concerning scour phenomena, but only concerning the fluvial environment and typically not referring to the protection itself, e.g. [41] or [213]. The implementation of reliability techniques as a crucial part of the risk analysis of scour protections in offshore environment has only been addressed in the very recent past, namely, as a result of the present research, e.g. [11, 12, 43, 44] or [214]. Therefore, the present work is also developed as a continuation of the research mentioned above, aiming for an extension of reliability and risk analysis to scour protection systems, often used in offshore wind foundations.

5.3 Probabilistic reliability measure and reliability problems

5.3.1 Probabilistic measure of reliability

When designing any structure, the loads considered to obtain the final dimensions of the structural elements are commonly associated to a certain return period (T_r). The return period can be defined as the statistical measurement, typically based on historic records, denoting the average recurrence interval of an event over an extended period of time. For example, if it is said that the return period of a seismic event is 500 years, it is assumed that the particular earthquake occurs on average 1 time per each 500 years interval. However, the return period doesn't account for the fact that a certain variable has its variability in a certain point in time [194].

Offshore structures, as several others, present loads (S) and resistances (R) which are functions of time and space. Usually resistances tend to decrease with the structures' life cycle, while loads tend to

increase. Both variables present a wider range of variability as time advances. Therefore the probability density functions f_R and f_S become wider and flat (i.e. with platikurtic shape). Increasing the variability means that situations where the loads exceed the design resistance can become more common. Figure 5.1 presents a summary of the previous consideration

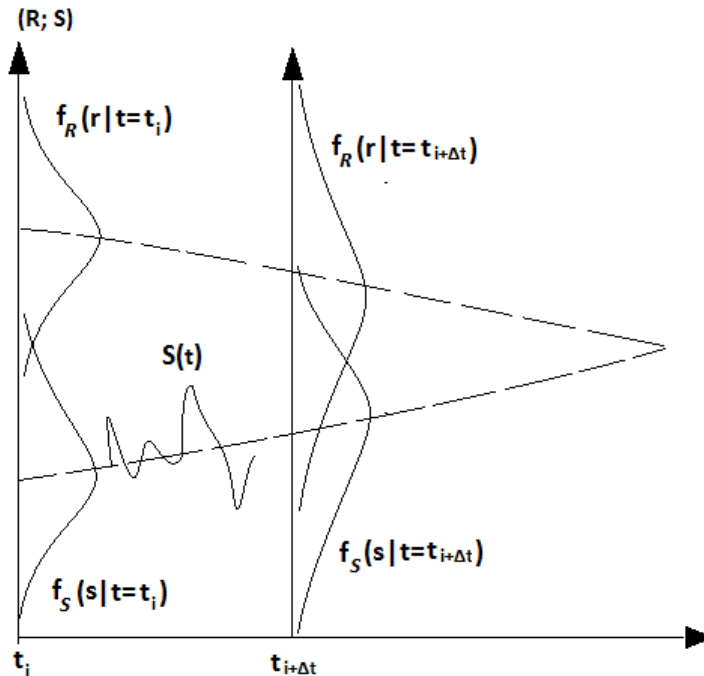


Figure 5.1 – General reliability problem (adapted from [194]).

Whenever the loads exceed the structure’s resistance, the so-called limit states can also be exceeded as well. If this happen the collapse becomes a possibility. Such situation is usually defined by Eq. (5.1) or Eq. (5.2).

$$R(t)-S(t) \leq 0 \tag{5.1}$$

$$\frac{R(t)}{S(t)} \leq 1 \tag{5.2}$$

The probability of occurrence of the above mentioned conditions is commonly referred to as the probability of failure, P_f , which can be a function of time as well. The variability with time is a complex problem to be analysed. In design situations it may be convenient to assume that R and S aren’t time dependent [194]. In design, the simplified cases must be faced carefully, especially due to the fact that resistances and loads, can decrease and increase respectively, during the structure’s life cycle, as mentioned. Typically, if the mechanical properties of materials are assumed to be constant and equal in the short and long term duration values, and also if the loads are considered equal to the maximum associated to the time period considered for design, it means that time dependency is being neglected.

Although time dependency may present a major role in structural failures promoted, for instance, by corrosion or fatigue, the major cause for structural components’ failure is the occurrence of extreme events such as extreme series of waves or winds, service loads, earthquakes, or combinations thereof [191]. In scour protection’s design, one may often simplify the problem by assuming that certain

properties, e.g. the rock mass density (ρ_s) or the mean stone diameter of the armour layer (D_{50}) remain constant throughout time. However, other variables, such as the wave heights and periods or the current velocity may present a considerable random behaviour through the scour protection's life cycle, which can not be ignored.

In order to consider the worst case scenario, for a certain system, it is important to understand the correlations between resistances and loads. The definition of a return period, the maximum loads associated to it and the resistance of the structure will have a major influence on the assessment of the probability of failure.

5.3.2 Fundamental reliability problem

Due to the uncertainty, generated by the lack of knowledge about properties of loads and resistances (i.e. the environmental and structural parameters), the probabilities of failure given by reliability theory are typically interpreted as nominal values. This means that the probability of failure achieved is not the actual true value of the probability of failure. Instead, it is a measure of reliability that also includes the lack of knowledge about a system's performance [215].

The fundamental problem of reliability theory considers the resistance R and the load S , both characterized by the probability density functions f_R and f_S , respectively. For this particular case, R and S are assumed as statistically independent, which simplifies the calculus of P_f . Then the probability of failure might be calculated according to Eqs. (5.3), (5.4), (5.5), which can be generalised into Eq. (5.6)

$$P_f = P(R \leq S) \quad (5.3)$$

$$P_f = P(R - S \leq 0) \quad (5.4)$$

$$P_f = P(R/S \leq 1) \quad (5.5)$$

$$P_f = P(g(R, S) \leq 0) \quad (5.6)$$

The above mentioned g function is also known as the performance function or the limit state function (LSF) and defines the state that once violated corresponds to failure of the structure, or in the case of the scour protection means that the design criterion is not being met. Such failure can be relative to a non-operative state or to the actual collapse. Note that in section 3.3, four failure mechanisms of the scour protection were distinguished. Each mechanism may have its own limit state function, which means that different probabilities of failure must be studied. The reliability analysis performed in the present research concerns to the failure mode caused by the erosion of the top layer, which was also focused in the experimental research presented in Chapter 4.

The most suitable function to describe the limit state function of the protection's failure modes is not a consensual issue, in scour research [43]. For example, only depending on the hydrodynamic conditions several semi-empiric expressions may exist to design the protection (see section 3.7) and thus to describe its failure (or limit state).

If D is the failure domain, i.e. the domain where $g < 0$, and f_{RS} is the joint probability function of R and S , the probability of failure can be calculated according to Eq. (5.7).

$$P_f = P(g(R,S) \leq 0) = \iint_D f_{RS}(r,s) dr ds \tag{5.7}$$

Since the fundamental reliability problem assumes that R and S are statistically independent, the previous equation can be simplified into Eq. (5.8), [194].

$$P_f = P(g(R,S) \leq 0) = \int_{-\infty}^{+\infty} \int_{-\infty}^{s>r} f_R(r) \cdot f_S(s) dr ds \tag{5.8}$$

Considering that the marginal function for a generic random variable X, $F(X)$, also known as the cumulative distribution function of X, is given by Eq. (5.9), the integral that gives P_f is provided by a much simpler expression, usually known as the convolution integral, which corresponds to the sum of all cases where the loads exceed the resistance, Eq. (5.10).

$$F_X(x) = P[X \leq x] = \int_{-\infty}^x f_X(y) dy \tag{5.9}$$

$$P_f = P(g(R,S) \leq 0) = \int_{-\infty}^{+\infty} F_R(x) \cdot f_S(x) dx \tag{5.10}$$

The previous equations can be graphically seen in Figure 5.2, where the marginal and joint distributions are represented and the geometric plan, defined by $g=0$, separates the safety domain and the failure one. In terms of the distributions of each variable a similar representation is provided in Figure 5.3.

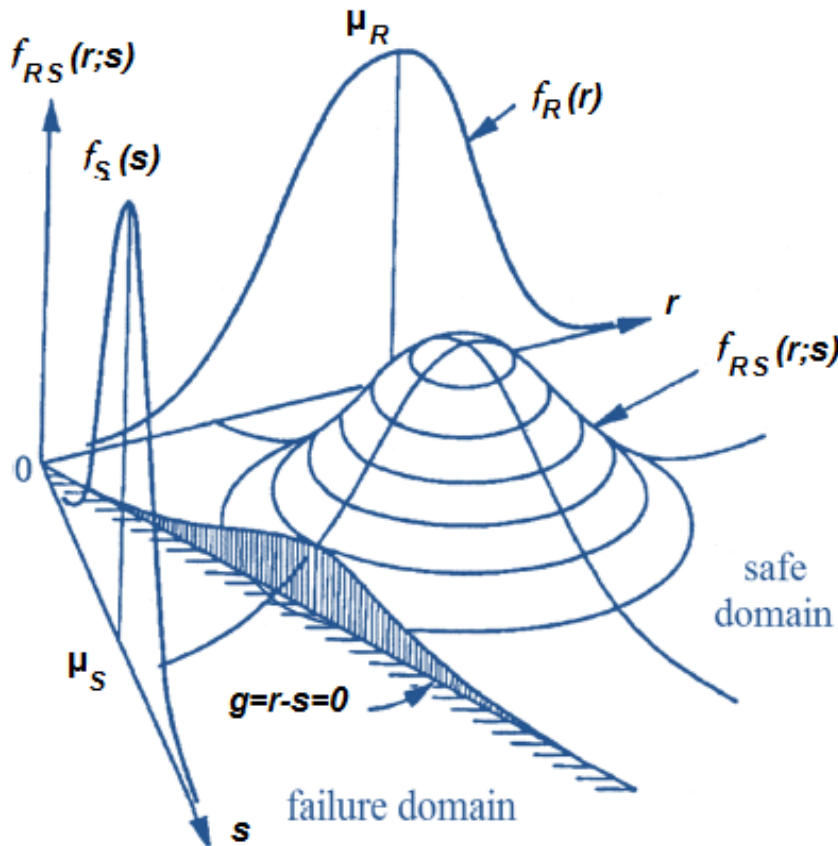


Figure 5.2 - Graphic representation of the failure domain and the associated probability of failure, [216].

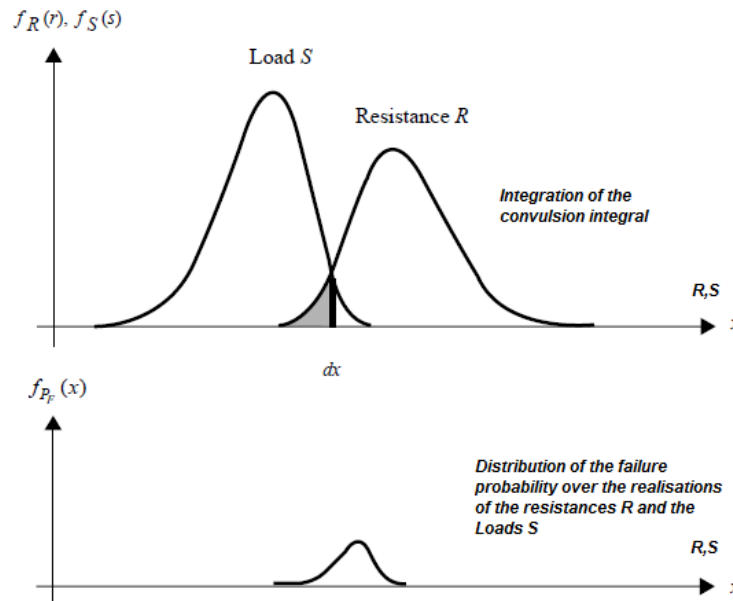


Figure 5.3 – Representation of the probability of failure as a solution for Eqs. (5.8) and (5.10).

5.3.3 Probability of failure for normally distributed variables alone

The solution of the integral to obtain P_f , is not by any means trivial and there is no general closed form to do it in practical situations, for which scour protections are no exception [11]. However in some particular cases, a simple solution can be derived. One of the most known cases, in civil engineering, is the one where both resistances and loads are Gaussian variables, i.e. with Normal distributed loads and resistances. Considering the so called safety margin (M) as the difference between the resistance (R) and the load (S), $M=R-S$, the probability of failure can be directly computed. Since R and S are Gaussian variables, M is also a Normal distribution with the mean and standard deviation provided by Eqs. (5.11) and (5.12), respectively [217]. Note, however, that R and S are assumed as independent, e.g. with null correlation.

Based on the normality assumption, the probability of failure can be further simplified into Eqs. (5.13) and (5.14), where ϕ is the standard normal distribution of the so-called reliability index ($\beta=\mu_M/\sigma_M$) [217]. The reliability index geometrically corresponds to the multiplying factor of the standard deviation of M , that separates the mean value of M from the failure domain $M<0$. The variables μ and σ stand for the mean and standard deviation, respectively. As shown in Figure 5.4. β is the distance from the mean value of the safety margin and the most likely failure point.

$$\mu_M = \mu_R - \mu_S \tag{5.11}$$

$$\sigma_M^2 = \sigma_R^2 + \sigma_S^2 \tag{5.12}$$

$$P_f = P(R-S \leq 0) = P(M \leq 0) \tag{5.13}$$

$$P_f = \phi\left(\frac{0 - \mu_M}{\sigma_M}\right) = \phi(-\beta) \quad (5.14)$$

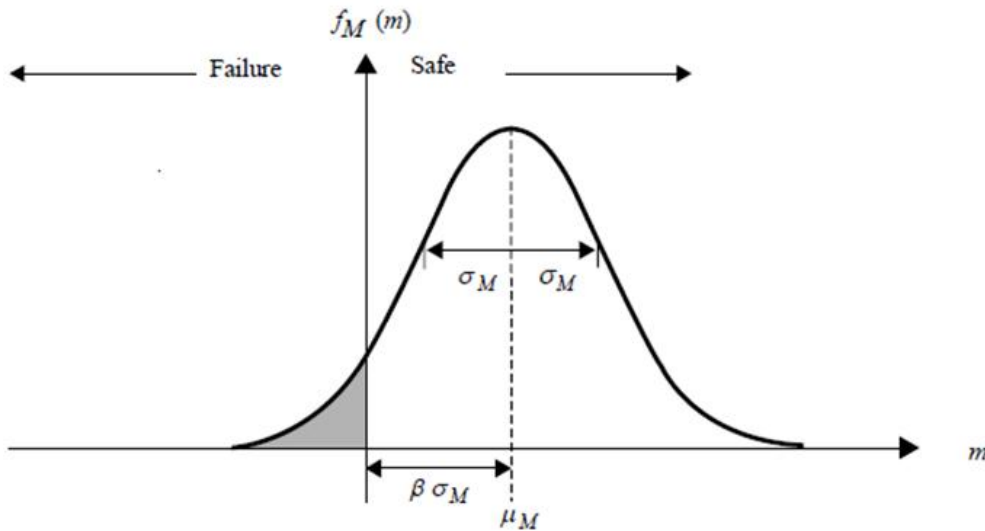


Figure 5.4 – Graphic representation of the probability density function for the Normal distributed safety margin M and the reliability index β [191].

5.3.4 General case of a reliability problem

However in scour protection design, similarly to several other coastal and maritime engineering situations, as the design of breakwaters or floating foundations [125], the analysed variables may not follow Normal distributions. For example, [37] and [39] reported that variables as the flow’s Froude number (Fr) and the soil’s uniformity parameter (σ_U) may present lognormal distributions, whilst the significant wave height often follows Rayleigh distribution for short-term conditions [121], with many other distributions presented for long-term records, e.g. [218, 219]. Therefore, the simplifications presented in section 5.3.3 might not be valid.

Usually the resistance and the loads are described by the different probability density functions of random variables $f(X)$. As discussed in section 3.5 and 3.6, X might be composed of several environmental and structural parameters (variables) that must be included in the design of the scour protection. Therefore, the reliability analysis of scour protection, should typically address the probability density function of the resistance, i.e. $R=f_1(X)$, and the probability density function of the loads, i.e. $S=f_2(X)$.

In this case, the safety margin or the limit state function, $M=g(X)=f_1(X)-f_2(X)$, may not be Normal distributed, thus $g(X)=0$ defines a $(n-1)$ dimensional hyper surface in the space spanned by the n basic random variables, which separates the realizations of X , for which failure occurs, i.e. $g(X)\leq 0$, from the ones where the protection is safe, i.e. $g(X)> 0$. In general terms, being $g(X)\leq 0$ the failure domain, the probability of failure can be determined through the n dimensional integral provided by Eq. (5.15), [217].

$$P_f = \int_{g(x)\leq 0} f_x(X)dX \quad (5.15)$$

The vector of basic random variables, concerning to loads and resistances is considered in the joint probability distribution, f_X , integrated over the failure domain. In scour protection systems, the failure criterion depends on the design methodology applied. For example, a reliability analysis of static scour protections should be preferably addressed by means of the threshold of motion, e.g. f_X can be defined according to [30, 52] or [57], as explained in section 3.7.1.2 and 3.7.1.3. Conversely, a dynamic scour protection should preferably use an f_X defined according to the acceptable damage number (see section 3.7.1.5). The number of variables, and the possible statistical distributions associated to each one of them, makes the reliability assessment of scour protections a general case, for which the probability of failure can only be obtained by somehow solving Eq. (5.15).

In complex engineering problems Eq. (5.15) can be solved by numerical integration techniques [217]. However, such techniques may require a considerable numerical effort to solve the integral with adequate accuracy, particularly for very low values of the probability of failure. In civil engineering, it is often common to work with probabilities of failure lower than 10^{-4} , e.g. [21] or [220], which may imply thousands of simulations of the limit state function to obtain a statistically meaningful value of P_f [215]. Furthermore, another difficulty that may affect the numerical calculation of the probability of failure is the representation of the failure domain (integration domain) for computational algorithms [191]. This difficulty typically increases with the number of basic random variables included in limit state function.

Scour protection problems deal with very complex phenomena, often approached by semi-empirical methodologies, as seen in Chapter 3. Therefore, challenging equations are faced when attempting to define a limit state function. Besides that, the difficulty in designing static and dynamic protections exponentially increases if one takes into consideration that the definition of certain variables is not straightforward, namely, when dealing with waves spectral analysis.

Moreover, the assessment of the probability distribution function of each variable, possibly correlated with others, increases the difficulty of solving the integral of the limit state function over the failure domain. In order to deal with the nature of the scour problem, the so-called methods of structural reliability can be used to solve the integral of the probability of failure. Some of them will be further presented in section 5.4.

5.4 Methods of reliability analysis

Typically, the methods used to perform the reliability analysis can be classified according to their “Level”, “Moment” and “Order”, Table 5.1. According to [221], the level of each method might be divided into:

- Level I – deterministic reliability methods that use only one “characteristic” value to describe each random variable. Such methods usually correspond to standard deterministic design codes;
- Level II – methods which use two values to describe each uncertain variable. The most common values used are the mean and the variance. These methods complement the variables’ information by considering the correlation between them (e.g. covariance). For instance the so-called first –order second-moment is an example of a level II reliability method;
- Level III – reliability methods that use the joint probability distribution, $f_X(\mathbf{X})$, of the several random variables to describe each one of them. This level includes the numerical integration, the approximate analytical methods, as the first-order and second-order reliability methods, and the simulation methods (e.g. the ones based on Monte Carlo simulations [222]) and

- Level IV – combine and compare structural scenarios and a reference prospect based on principles of engineering economic analysis under uncertainty. Such methods usually result in analysis of minimum cost and maximum benefit type.

Table 5.1 – Classification of reliability methods [221]

| Level | Calculation methods | Probability distributions | Limit State functions | Uncertainty Data | Result |
|----------------------------------|--|---|----------------------------------|--------------------------------|--|
| I. Code level methods | (calibration to existing code rules using level II or III) | Not used; only a characteristic value is used | Linear Functions (usually) | Arbitrary Factors | Global or Partial safety factors |
| II. Second moment methods | Second moment algebra | Normal Dist. only | Linear or approximated as linear | Included as second moment data | Nominal Probability of failure P_{fN} or Nominal Reliability index β_N |
| III. Exact methods | Transformations | Equivalent Normal Distributions | Linear or approximated as linear | Included as random variables | Probability of failure P_f or Reliability index β |
| | Numerical integration and Simulations | Fully used | Any form | | |
| IV. Decision methods | Combination of economic data and any of the other 3 levels | | | | Minimum cost or Maximum Benefit |

Reliability methods can also be classified in terms of moment and order into approximate methods, as it is the example of the first-order second-moment. Generally, if the limit state function is linear, a first order reliability method (FORM) can be applied. However if the limit state function is nonlinear but approximated by a second order representation, then a second order reliability method (SORM) is used [222]. The reliability methods may also be classified by the exactness of the calculation of the probability of failure [217]:

- Approximate methods;
- Simulation methods;
- Direct integration methods.

The following sections provide a brief overview of some of the basic reliability methods, an extensive review of such methods can be seen in [217] and [222]. The reliability analysis performed throughout the practical Chapters 6 and 7, might be classified into a Level III method, as it addresses the joint probability of the most important random basic variables. By using a Level III method one sets the basis for future research on Level IV methods, which may combine the procedure implemented to calculate P_f with a cost-benefit analysis. Also the present research will mainly address

the use of the Monte Carlo Simulation method, which falls into the exactness category of the Simulation methods.

5.4.1 Approximate methods

Since the probability of failure (P_f) and the probability of reliability (P_r) of a certain system are contrary events, P_r is obtained as $P_r=1-P_f$. If the problem is reduced to two Gaussian and independent variables, R and S, then the correspondent reliability index is then given by Eq. (5.16):

$$\beta = -\phi^{-1}(P_f) \tag{5.16}$$

The cumulative distribution function ϕ is denoted as the standard normal distribution. However, the vector X may present several distributions for different basic variables and this needs to be considered in each problem approached. Another important fact is the existence of several limit states that can influence the serviceability/operability or collapse conditions. Marine structures often consider several limit states, thus meaning that the reliability analysis should be performed for operating conditions and possible collapse situations. However, in scour protection systems and as a first approach to their performance, the most important limit state concerns to the failure of the protection. Typically, as referred in [223], after a storm occurrence the potential failure of the scour protection at an offshore wind foundation might not be immediately perceived. Firstly, because a time lapse may occur between the protection's failure and the structural instability caused by scour phenomena at the monopile. Secondly, because the scour protection is a non-visible element of the foundation, which means that failures are often noted during Operation and Maintenance (O&M) campaigns [223]. Therefore, when performing the reliability analysis of a scour protection, one refers to the probability of failure as the chance of the design criterion being exceeded under the simulated loading and resistance conditions. The approximate methods, or analytical ones, present some advantages. The computation time is not as large as in other techniques and the calculations involved are usually simple. However, this may come at the cost of a less accurate assessment of the reliability measure. These methods include first- and second-order reliability methods, as FORM and SORM for instance. Nevertheless, disadvantages become more evident when exact results are expected, particularly for types of structures with very low probabilities of failure.

5.4.1.1 Mean-Value First-Order Second-Moment (MVFOSM) method

Considering the limit state function g as non-linear, where the linearization is performed at the mean values of each variable x_i of the vector X, errors may be introduced at increasing distance from the linearization points, which corresponds to neglecting higher order terms. The limit state is achieved when $M=g(x_i) \leq 0$. The lack of information to determine the joint probability density function of the design variables and the difficulties in the evaluation of the multiple integrals for complex limit state functions can conduct to difficulties in practical applications, when the integration of Eq. (5.15) is performed. In order to solve such problem, the approximate methods, which are level II reliability methods, were developed and the reliability index concept was introduced [199]. The limit state function can be expanded by means of Taylor series, which leads to Eq. (5.17) if the first order terms are retained:

$$g(x_1, x_2, \dots, x_n) \approx g(x_1^*, x_2^*, \dots, x_n^*) + \sum_{i=1}^n (x_i - x_i^*) \left(\frac{\partial g}{\partial x_i} \right)_{x^*} \tag{5.17}$$

The so-called linearization point is denoted as x_i^* and the partial derivatives of g , i.e. $\partial g/\partial x_i$ are evaluated at that same point. In MVFOSM the linearization is performed around the mean value, i.e. $x_i^*=(\mu_{x1}; \mu_{x2}; \dots; \mu_{xn})$. The linearization point corresponds to the vector of expected values for each basic random variable. In a Taylor series the mean and variance can be obtained according to Eqs. (5.18) and (5.19), [217].

$$\mu_m = g(\mu_{x_1}, \mu_{x_2}, \dots, \mu_{x_n}) \quad (5.18)$$

$$\sigma_m^2 \approx \sum_i \sum_j (x_i - x_i^*) \left(\frac{\partial g}{\partial x_i} \right)_{\mu_{x_i}} \left(\frac{\partial g}{\partial x_j} \right)_{\mu_{x_j}} \rho_{x_i x_j} \sigma_{x_i} \sigma_{x_j} \quad (5.19)$$

Eqs. (5.18) and (5.19) are also applicable to correlated variables, if one is able to evaluate the correlation coefficients between each pair of variables, i.e. $\rho_{x_i x_j}$. Further details on the formulation for correlated variables are given in [217]. Eq. (5.19) requires the evaluation of the partial derivatives of g at the mean point of each variable μ_{x_i}, μ_{x_j} . If the variables are statistically independent, the variance is simplified into Eq. (5.20).

$$\sigma_m^2 = \sum_i \left(\frac{\partial g}{\partial x_i} \right)_{\mu_{x_i}}^2 \sigma_{x_i}^2 \quad (5.20)$$

The linearization tends to present a higher amount of error depending on the effect of neglecting the higher order terms of the Taylor series. For particularly complex limit state functions, with very high-order terms, using the linear terms of the series may imply a considerable loss of information, meaning lower exactness of results. The safety margin, M , can be standardized to zero mean and unit standard deviation, i.e. G_M , according to Eq. (5.21). As seen before, if the safety margin is smaller than zero, the limit state is achieved. This allows the calculation of P_f in similar manner to the one presented in the fundamental problem of reliability, section 5.3.2, as shown in Eq. (5.22), where F_{GM} is the cumulative distribution function of the standardized safety margin [217].

$$G_M = \left(\frac{M - \mu_m}{\sigma_m} \right) \quad (5.21)$$

$$P_f = P[M \leq 0] = F_{G_M}(0) = F_{G_M} \left(\frac{-\mu_m}{\sigma_m} \right) = F_{G_M}(-\beta) \quad (5.22)$$

If the distribution F_{GM} is known the probability of failure can be obtained. Even for the cases where the distribution is unknown, there will be a corresponding though unspecified probability of failure for each value of β , thus β can be seen as the safety measure or reliability index also applicable to the MVFOSM [217]. This interpretation for β is applicable to several other methods as it will be seen further on. Remember that β geometrically corresponds to the shortest distance from the origin to the failure hyper-surface (Figure 5.2), meaning that the point of intersection between the limit state function, $M=0$, and the line defined through β and the origin is the most likely failure point. The point where it is most likely for the system to fail is often called the design point. Similarly to Figure 5.4, Figure 5.5 provides the geometrical interpretation for the reliability index. The information to be retained is the fact that MVFOSM uses the first-order terms of the Taylor series of the limit state

function, calculated around the mean value of each basic random variable, i.e. the mean of value of $g(X)$, to obtain an approximate value of P_f .

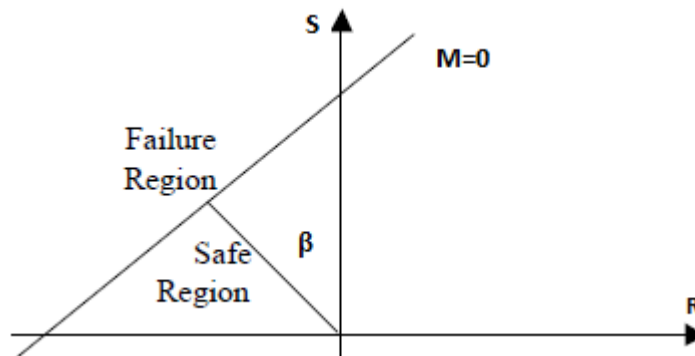


Figure 5.5 – Geometric representation of the limit state function ($M=g(x)=0$) and the reliability index (β) in the standardized space of loads (S) and resistances (R).

5.4.1.2 Advanced First-Order Second-Moment (MVFORM) method

The linearization presented in MVFOSM has some drawbacks. The linearization of $g(x)$ takes place at the mean values of x_i . Due to this fact, an error is introduced at increasing distance from the chosen point. Because only the first term of Taylor series is considered at μ_{x_i} . In addition, there is the fact that the method fails to be invariant to different equivalent formations of the same problem. This means that the reliability index may vary considerably depending on the formulation of the limit state g . This problem is also described as the lack of invariance [221] and refers to situations where small differences in β tend to be associated to large variations of g . For example, if the safety margin is given as a non-linear function of S and R , e.g. $M=R^2-S^2$, then the probability of failure could be calculated according to the previous Eq. (5.22). However, if μ_M and σ_M are computed from Eqs. (5.18) and (5.20) and substituted in Eq. (5.23), the reliability index from Eq. (5.24), which is very different from the one obtained when $M=R-S$, even though the probability of failure is still given by Eq. (5.22).

$$\beta = \frac{\mu_M}{\sigma_M} \quad (5.23)$$

$$\beta = \frac{\mu_R^2 - \mu_S^2}{2\sqrt{\mu_R^2\sigma_R^2 + \mu_S^2\sigma_S^2}} \quad (5.24)$$

5.4.1.2.1 Hasofer-Lind Index

Both the invariance problem and the linearization error around the μ_x can be avoided by using the so called Hasofer-Lind method [200]. The procedure is similar to the previous one. However, instead of performing the linearization, i.e. the Taylor series expansion, around the mean value point, such procedure is performed at a point on the failure surface ($g=0$). This method takes advantage of the fact, that on the failure surface, the limit state function g and its partial derivatives are independent of how the formulation is performed. Such procedure eliminates the invariance problem. In order to apply this method, the original variables, loads and resistance ones, x_i , are transformed into the standard variables with mean zero and unit variance (y_i), according to Eq. (5.25),

$$y_i = \left(\frac{x_i - \mu_i}{\sigma_{x_i}} \right) \quad (5.25)$$

The Hasofer-Lind index is defined as the shortest distance from the origin to the failure surface in the reduced standardized space. Such point is found iteratively by solving the Eqs. (5.26), (5.27) and (5.28). The function G is the limit state function in the standardized space, i.e. evaluated at y_i , and $\partial g / \partial y_i$ are the partial derivatives of G evaluated at the design point with coordinates μ_i .

$$G(y_1^*, y_2^*, \dots, y_n^*) = 0 \quad (5.26)$$

$$y_i^* = -\alpha_i^* \beta \quad (5.27)$$

$$\alpha_i^* = \frac{\left(\frac{\partial G}{\partial y_j} \right)_{y_i^*}}{\left(\sqrt{\sum_i \left(\frac{\partial G}{\partial y_j} \right)_{y_i^*}^2} \right)} \quad (5.28)$$

In comparison to MVFOSM, the Hasofer-Lind method corresponds to a linearization of the limit state function in the reduced variables space, at the checking point and the correspondent computation of β . After applying the Hasofer-Lind method the original coordinates must be obtained, in order to know the loads and resistance variables in the original space. The design point is obtained by means of Eq. (5.29).

$$x_i^* = \bar{x}_i + \sigma_{x_i} \alpha_i^* \beta \quad (5.29)$$

This method provides the same value of the reliability index, β , for linear limit state functions, as the one given in MVFOSM [221]. But for non-linear functions the result obtained through Hasofer-Lind method is a value of β , which is invariant regardless the formulation of the limit state function.

5.4.1.2.2 Incorporation of the distribution function

The advanced method allows the inclusion of the distribution's information in the computation of the reliability index and the associated probability of failure. In the MVFOSM the index β was related to the probability of failure for cases where the variables were following a Normal distribution, and the performance function was linear in x_i . Such relation was given by the standard normal distribution function as seen before through $P_f = 1 - \Phi(\beta)$. If the limit state function encompasses non-normal variables, a transformation can be performed so that equivalent normal ones are obtained, before each iteration is performed to find the solution of Eqs. (5.26) and (5.28). In structural engineering problems, it is often the tail of the distribution that represents the higher contribution for the probability of failure. For this reason, several authors prefer to fit the normal distribution to the tail of the non-normal one at the linearization of x_i^* , which is where the failure is most likely to occur, i.e. minimum distance β . The method provided by [201] (also see [224]) is based on this concept of tail fitting [217]. Considering the equality at the linearization point for the cumulative distributions and the probability density functions of both the actual distribution (non-normal) and the normal one, it is possible to

determine the mean μ_x' and the standard deviation σ_x' of the equivalent normal variable according to Eqs. (5.30) and (5.31), as in [217].

$$F_x(x^*) = \Phi\left(\frac{x^* - \mu_x'}{\sigma_x'}\right) \quad (5.30)$$

$$f_x(x^*) = \frac{1}{\sqrt{2\pi}\sigma_x'} \exp\left[-0.5\left(\frac{x^* - \mu_x'}{\sigma_x'}\right)^2\right] = \frac{1}{\sigma_x'} \varphi\left(\Phi^{-1}\left[F_x(x^*)\right]\right) \quad (5.31)$$

Note that φ stands for the standard normal probability density function. By solving the expressions above, at the linearization point, in terms of the desired parameters, the following solutions are obtained in Eq. (5.32) and Eq. (5.33).

$$\sigma_x' = \frac{\varphi\left(\Phi^{-1}\left[F_x(x^*)\right]\right)}{f_x(x^*)} \quad (5.32)$$

$$\mu_x' = x^* - \left(\Phi^{-1}\left[F_x(x^*)\right]\right)\sigma_x' \quad (5.33)$$

The linearization point changes with each iteration. Therefore the parameters of the equivalent normal distribution (μ_x' ; σ_x') must be re-calculated. Those values are then inputted in previous Eqs. (5.26) and (5.28). If the iteration is performed in the reduced space, then the distribution transformation into reduced space must be performed in each iteration. A detailed algorithm to implement the iterative procedure of the Hasofer-Lind method is provided in [11]. For the purposes of scour analysis and its respective protection, the basic variables can be faced as statistically independent in the less complex cases. However, if the random basic variables, i.e. vector X , present statistical correlation between them a more complicated approach must be performed, since the previous one was assuming independency. In marine structures, the dependence between variables can be of great importance. Therefore, the application of normalization techniques may lead to inaccurate representations of the correlation between some of the variables included in the calculation of the performance function associated to the scour protection. A preliminary correlation analysis must be performed when experimental scour tests are being conducted. Particularly, the correlation between bed-shear stress on the armouring layer and the hydrodynamic conditions has to be analysed, in order to avoid errors due to a misleading independency assumption. The case of correlated variables can be seen in detail in structural reliability literature, e.g. [36]. The representation of the correlation between variables is one of the aspects that may lead to a preferable use of the simulation methods, as the Monte-Carlo simulations, [11].

5.4.1.3 Second-order methods

The second-order methods were created in order to account for the non-linearity of the limit state functions [217]. The existence of such methods become very important since the linear approximation to the limit state surface, $g=0$, presents considerable errors for limit surfaces with significant curvature, i.e. highly non-linear g functions.

In the second order methods, the main idea is to fit a parabolic, quadratic or higher order surface to the actual limit state surface, centred on the design point. Such fitting requires a decision about the extent to which the approximation is valid away from the design point, y^* . One of the most known methods included in the second order classification is the so called SORM - Second-Order Reliability Method. In SORM the limit state surface, defined by $g=0$, is approximated by a second order quadratic surface in the design point [36]. The calculation of the probability of failure through the quadratic approximation can be done through several ways. Nevertheless, two of the most common approaches can be found in [217]:

- The first one relies on sampling the space between the linear approximation and the quadratic one, to estimate the probability content between these two approximations to the limit state surface.
- As an alternative, the FORM result for a linear limit state can be taken as the starting point for simulation around the design point to estimate the error in the probability of failure between the one given by the linear limit state approximation and the actual limit state.

The use of asymptotic concepts, provided by [225] and [226], also allow the evaluation of the probability content for the second order approach. Considering the independent standard normal random variables (y space) and the limit state function, the probability of failure can be estimated from a determination of the limit state surface curvatures K_i , at the design point y^* , and using the asymptotic expression as in Eq. (5.34):

$$P_f \approx \phi(-\beta) \sum_{j=1}^k \left[\prod_{i=1}^{n-1} (1-\beta \cdot k_i) \right]^{-0.5} \tag{5.34}$$

where $k_i = -\left(\frac{\partial^2 y_n}{\partial y_n^2}\right)$ and corresponds to the negative partial second derivative, which is the i^{th} principal curvature of the limit state surface ($g(y^*)=0$) at the design point y^* . In civil engineering FORM method is widely applied. However SORM can be also useful in cases were the non-linearity generates considerable approximation errors (Figure 5.6). Despite the utility of SORM it is important to note that, if the X vector has too many basic random variables, it can be a demanding method for large problems and very complex limit state functions, which might be the case of scour protections design.

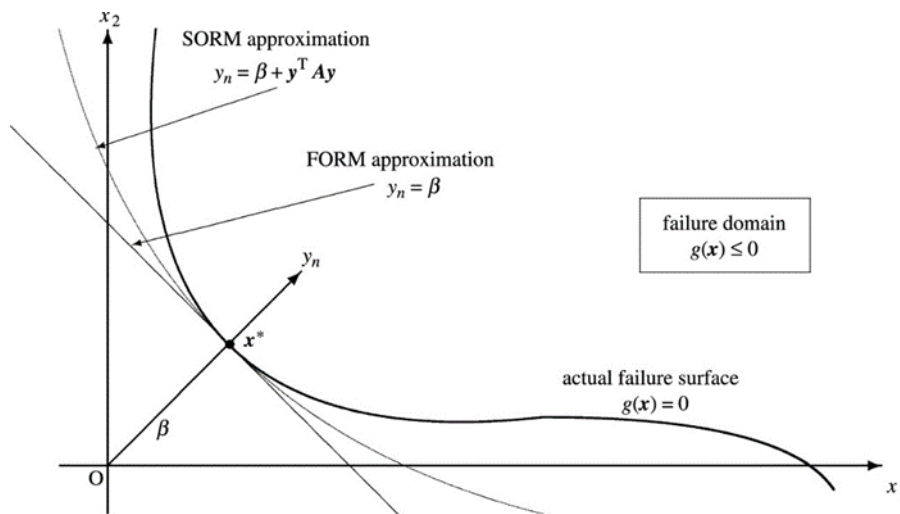


Figure 5.6 – FORM and SORM approximations to the limit state surface at the design point [227].

Figure 5.6 provides a graphic scheme of both approaches to the design point. As it can be perceived, both methods are approximated but SORM provides a closer fitting to the limit state surface than FORM. The quality of the fit decreases for increasing non-linearity in g .

5.4.2 Direct integration methods

The direct integration method is the name given to the technique that actually approaches the direct integral of P_f defined by Eq. (5.15). This method intends to integrate the joint probability density function $f_x(X)$, over the failure domain, i.e where the performance function is smaller than zero. The equation of P_f can be simplified as seen before. Eq. (5.15) is a multivariable integration, which in practical cases it might not be easy to estimate. A detailed review on the direct integration methods is provided in [36] and [217].

5.4.2.1 Standardised integral region

According to [217], the P_f integral can be rewritten as in Eq. (5.35), by means of the so-called indicator function $I[g(X)]$, where $F_x(X)$ is the cumulative distribution function of (X) . The indicator function provides unitary or null values if the limit state function is in the safety region or in the failure region, respectively, as shown in Eq. (5.36).

$$\begin{aligned}
 P_f &= \int \dots \int_{g(X) \leq 0} f_x(X) dX = \int \dots \int_{\Omega} I[g(X)] f_x(X) dX \\
 &= \int \dots \int_{\Omega} F_x(X) dX = \int_{a_1}^{b_1} \dots \int_{a_n}^{b_n} F_x(X) dX
 \end{aligned}
 \tag{5.35}$$

$$I[g(X)] = \begin{cases} 1 \rightarrow g(X) \leq 0 \\ 0 \rightarrow g(X) > 0 \end{cases}
 \tag{5.36}$$

Each the integration limits of each basic random variable are given by a_i and b_i . These limits can be determined by the variable's distribution and the integral precision, usually noted as α , obtained by means of Eq. (5.37).

$$\int_{b_i}^{a_i} f_x(x) dx \geq 1 - \alpha
 \tag{5.37}$$

5.4.2.2 Joint probability density function

Often, in engineering problems, the joint probability function is unknown. However it is possible to obtain its marginal probability density function and the correlation between the random basic variables, e.g. wave characteristics, currents, sediments and rock material. If the variables are dependent the necessity of going for more complex approaches is inevitable. Nevertheless, in offshore engineering and structures it is common to assume them as statistically independent to each other. If variables are independent, then the joint probability density function is equal to the product of the marginal density functions, of the basic variables involved in the vector $X(x_i)$, i.e. $f_x(X) = f(x_1) \cdot f(x_2) \dots f(x_n)$, [215]. This is for example the case of Gaussian independent variables, seen before in the fundamental problem of reliability. However, as it will be addressed in the reliability analysis of the

scour protection at Horns Rev 3 offshore windfarm, the independency assumption does not hold for some of the variables. Moreover, the exact separation between the resistance and load parcel is not straightforward, particularly for the damage number formula and the combined wave-current shear stress. Therefore, the joint probability density function of X , is not only very complex, but also practically impossible to address in a generalized manner. Such drawbacks require one to make partial independency assumptions, which can then be combined with partial joint distribution functions that are used for the most important correlations, e.g. the one between wave heights and periods addressed in Chapter 6. Some of the works concerning the reliability analysis of scour phenomena have concluded that for scour depths at bridge piers the independency assumption leads to overestimated, and thus conservative, probabilities of failure, e.g. [37, 39]. However, this may not be the case of scour protections in offshore environment, as discussed in [223]. The difficulty in obtaining the joint probability density function of X , also leads to an increasing difficulty of the use of direct integration methods for limit state functions based on the formulations discussed in section 3.7.

5.4.2.3 Multivariate integration

The multivariate integration aims to solve the multivariate integral from Eq. (5.38). The integration domain can be divided into small portions, where $[a_i; b_i]$ are divided into $k_1, k_2 \dots k_n$ regions. Considering the notion of the integral as an infinite sum and that a_{ji} is a value in the integral's domain $[a_j; b_j]$, the previous equation can be transformed into Eq. (5.39).

$$I = \int_{b_1}^{a_1} dx_1 \dots \int_{b_n}^{a_n} F(x_1, \dots, x_n) dx_n \quad (5.38)$$

$$I \approx \sum_{j_1=1}^{k_1} \dots \sum_{j_n=1}^{k_n} F(a_{1j_1}, \dots, a_{nj_1}) \Delta a_{1j_1} \dots \Delta a_{nj_1} \quad (5.39)$$

Note that Δa_{ji} corresponds to the length of $[a_j; b_j]$ given by $\Delta a_{ji} = b_j - a_j$. Once again it must be pointed out that such integral may be hard to solve for a large amount of variables, due to the excessive amount of computation time needed. There are several approaches developed to solve such problem, namely the ones considering numerical integration through the definition of limited regions for the integration domain, or the importance sampling method, which for example can be used for multi-normal integrations. Details on these integration techniques are provided in [11] and [217].

5.4.3 Simulation methods

According to [217] the analytical methods are usually applied for probabilities of failure smaller than 0.05 and they are able to provide approximate results, which are often satisfactory in practical engineering problems. If the probabilities become larger the direct integral method can provide better results. However, the direct integration has its drawbacks in the complexity of the integral for large numbers of basic random variables. Besides that, if the joint probability density function is unknown, it is impossible to know the integral's equation and/or the approximation to be performed at the design point. As discussed in sections 5.4.1 and 5.4.2, the errors associated to the approximate methods for non-linear limit functions and the difficulties associated to the direct integration methods, namely, concerning the joint distribution function of X and its integral, may pose difficulties to the reliability assessment of scour protection systems, which are designed with several variables and highly non-

linear equations. These problems can somehow be mitigated with the application of the simulation methods, e.g. the Monte Carlo Simulation Method or the Importance Sampling Simulation method further detailed in [222].

Depending on the simulated phenomena, if the joint probability density function is not known, the use of simulation methods also enables the use of experimental data or in situ data that can be statistically interpreted to describe or predict the phenomena's behaviour. This is often the case for scour research and scour protection design, which is mainly dependent on physical model validations and field data acquired during monitoring campaigns (see section 3.9).

By definition, simulation is a technique for conducting experiments in a laboratory or in a software aiming to model the behaviour of a system [217]. In this sense, such models result in simulated data, often used as a predictive tool. The study of scour protections and scour phenomena on sand-beds is usually coupled with experimental data, which is obtained from physical modelling as seen throughout Chapters 2, 3 and 4. Therefore simulation methods can take advantage of this fact by using the experiments performed, with physical modelling of scour tests on offshore foundations, to collect calibration and validation data. There is also the possibility of coupling numerical and experimental studies to construct a robust simulation model, which offers endless possibilities for future developments in this scientific matter. The close relationship between the simulation models and the input data from numerical and experimental models, make it easier one to test limit state functions that present a more or less remarked semi-empiric nature, but that were already validated experimentally, numerically or in the actual field. Therefore, the simulation methods are a rather appealing technique to perform reliability analysis of scour protections.

5.4.3.1 Monte Carlo Simulation method

Monte Carlo simulations are usually used for problems which encompass random variables of known or assumed probability distributions, which may be obtained through field records for example. Based on these distributions the values of the random variables are generated by means of statistical sampling techniques. The values generated through Monte Carlo simulations are treated as being similar to a sample of experimental observations and are used to obtain the so-called sample solution [217]. For example, if a set of experimental data is available in sufficient number, which allows the assumption of a certain probability distribution, within a certain confidence interval, the Monte Carlo method can be used to increase the sample's size (experimental data + simulated data). By repeating the process and generating several sets of sample data, many sample solutions can be determined and submitted to statistical analysis. The simulated data of the random basic variables, might then be used to assess the limit state function.

Once the main variables of the scour protection design are modelled, i.e. the marginal distributions are defined, and that the spectral parameters are jointly modelled taking into consideration their dependence structure, one is able to simulate the limit state function as many times as needed to obtain a meaningful probability of failure. The simulation of the limit state function based on the Monte Carlo simulation can be performed as in the following example (for 2 variables). Consider two continuous random variables x_1 and x_2 . The variable x_1 follows $F(x_1)$, which is a standard normal distribution $N(0,1)$ and x_2 follows $F(x_2)$, which is a uniform distribution $[0;1]$. Assume that the failure criterion is defined by: the system fails if the resistance $|x_1|$ is exceeded by the load x_2 . Thus leading to the limit state function $M = |x_1| - x_2$. If $M \leq 0$ the system fails. One can simulate the limit state function with the following steps:

- Consider the transformed variables given by $u=F(x_1)$ and $v=G(x_2)$, which follow uniform distributions between 0 and 1, $u\sim U(0,1)$ and $v\sim U(0,1)$;
- Generate n random values between 0 and 1 for u and v ;
- According to the probability density functions of x_1 and x_2 obtain the resistance and the load as $X=F^{-1}(u)$ and $Y=G^{-1}(v)$ (see Figure 5.7);
- Simulate $M=|X|-Y$ for all the n pairs $(x_{1i}; x_{2i})$;
- Obtain P_f according to Eq. (5.40).

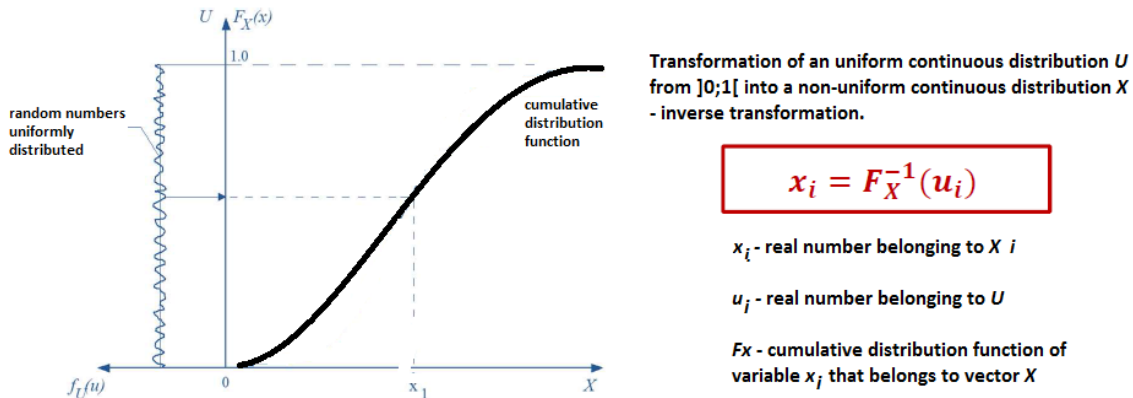


Figure 5.7 - Scheme of random generation of the random basic variables (Adapted from [216]).

As shown in the aforementioned example, after the generation of random values for each variable x_i the vector X is complete. After that it is possible calculate probability of failure, based on the Monte Carlo simulations. The number of simulations to be performed depends on the magnitude, i.e. the order, of the probability of failure and also on the structural problem itself, i.e. the limit state function. If the probabilities of failure are very low, the number of simulations required increases considerably. The probability of failure is obtained by Eq. (5.40), where the function $g(X)$ is calculated for each simulation. Then according to the classical definition of probability, the value of P_f is obtained as the number of times that $g(X)$ corresponds to failure, i.e. $\#[g(X)\leq 0]$, divided by the number of simulations performed.

$$P_f = P[g(X) \leq 0] = \lim_{n \rightarrow \infty} \frac{\#[g(X) \leq 0]}{n} \tag{5.40}$$

If N tends to infinity, the estimated probability of failure, tends to its true value. If $M=g(X)$ is simulated for $n=10$, each time $M\leq 0$ it means that P_f will increase at least 10%. While if $n=100$, each failure leads to an increase of 1%. Therefore, one should perform a number of simulations that leads to a stabilized probability of failure. However, the limited computation capacity brings a boundary to the number of simulations that can be performed, especially if $g(X)$ is so complex that makes each iteration last for significant time. Several techniques as the Latin Hypercube sampling or the variance reduction techniques might be applied in order to reduce the number of simulations required for a meaningful estimate of the probability of failure. An extensive review on the optimisation of the Monte Carlo method for reliability purposes is provided in [222]. Often, these methods imply an optimisation of the combination of the random values of each basic variable, x_i , included in the limit state function. Therefore, this may lead to problems for systems that are dependent on strongly correlated variables. Note that this is the case of scour protections and scour phenomena, for which at least the correlation between wave heights and wave periods must be respected. Recent works

concerning the reliability assessment of scour protections have tried to implement the optimised sampling techniques, e.g. the Latin Hypercube was applied in the reliability assessment of statically stable scour protections by [12] and [228]. However, such works assume the independency between the basic random variables included in the calculation of the bed shear stress, in a similar way to the one performed by [39] regarding the scour depth at bridge piers. As mentioned previously, such independency assumption may lead to combinations of the environmental parameters that contribute to the inaccurate evaluation of the probability of failure. At the present state-of-the-art the extent of such inaccuracy is yet to be fully understood and should be the aim of further research.

5.4.3.2 Required sample size

The data obtained with the Monte Carlo simulation method should be treated as a sample of experimental observation. Since its generation is based or has a correspondence with the information provided in samples of $X(x_i)$, it is subjected to sampling error. The probabilities of failure in structural engineering can be very small. Therefore, if they are assessed by means of simulated data, the underlying error becomes a relevant element to evaluate the obtained values of P_f . The error of the estimated probability of failure depends on the number of simulations (n), as stated before, and can be calculated as in [217] through Eq. (5.41):

$$\text{error} = 2 \sqrt{\frac{1 - P_f}{n \cdot P_f}} \quad (5.41)$$

The error decreases with increasing number of simulations, while on the other hand it increases for very small values of P_f [217]. The lower these values are, the higher should be the number of simulations to reduce the error obtained. Sampling theory can be a complex issue on simulation techniques. Some methods allow the estimation of the sample size needed, i.e. the number of simulations required for a certain confidence level. A detailed review on this matter is available in [222]. The limit state function is a random variable, which results from $X(x_i)$ and therefore the indicator function $I[g(X) \leq 0]$, which has 2 possible outcomes 0 and 1, is also a random variable. Consider the distribution J_1 given by the sum of independent sample functions. According to the central limit theorem it can be said that J_1 approaches the normal distribution as n tends to infinite, thus being applicable the Eq. (5.42), as in [217]:

$$P_f \approx J_1 = \frac{1}{n} \sum_{j=1}^n I[g(X_j) \leq 0] \quad (5.42)$$

The expected value of J_1 is provided by Eq. (5.43) and the variance is given by Eq. (5.44), [217]:

$$E(J_1) = \frac{1}{n} \sum_{j=1}^n E[I(g(X) \leq 0)] = E[I(g \leq 0)] \quad (5.43)$$

$$\sigma_{J_1}^2 = \sum_{i=1}^n \frac{1}{n^2} \text{var}[I(g \leq 0)] = \frac{\sigma_{I(g \leq 0)}^2}{n} \quad (5.44)$$

The previous equations demonstrate that J_1 and the Monte Carlo estimate varies directly with the standard deviation of the indicator function, $I[g(X) \leq 0]$. Besides that it is seen that the variation is

proportional to $n^{0.5}$. The variance of the indicator function and the sample variance are respectively given by Eqs. (5.45) and (5.46).

$$\text{var}[I(\cdot)] = \int \dots \int [I(g \leq 0)]^2 dX - J^2 \quad (5.45)$$

$$s_{I(G \leq 0)}^2 = \frac{1}{n-1} \left(\left\{ \sum_{j=1}^n I[g(\hat{X}_j) \geq 0] \right\} - n \left\{ \sum_{j=1}^n I[g(\hat{X}_j) \leq 0] \right\}^2 \right) \quad (5.46)$$

Assuming that the central limit theorem applies, the following confidence statement, Eq. (5.47), can be obtained for the number of trials in which failure occurs:

$$P(-k\sigma < J_1 - \mu < k\sigma) = C \quad (5.47)$$

where μ is the expected value of J_1 , given by $E(J_1)$ and σ is given by Eq. (5.45). The previous expression associates $k=1.96$ for a confidence level of $C=95\%$ [215]. The standard deviation σ is typically unknown and can be estimated as previously seen by Eq. (5.46). However, according to [217], the values of μ and σ can also be approximated by the binomial parameters, i.e. $\mu = (np)$ and $\sigma = (npq)^{0.5}$, provided that $q=1-p$ if $np \geq 5$ and $p \leq 0.5$. If the binomial parameters are substituted in the Eq. (5.47) the following expression is obtained for the confidence level, Eq. (5.48):

$$P_f \left[-k(npq)^{0.5} < J_1 - (\#g(X) \leq 0)p < k(npq)^{0.5} \right] = C \quad (5.48)$$

The error between the actual value of J_1 and the observed value is given by Eq. (5.49):

$$\varepsilon = \frac{J_1 - np}{np} \quad (5.49)$$

If ε is substituted in Eq. (5.49) the error is calculated according to Eq. (5.50):

$$\varepsilon = k \sqrt{\frac{1-p}{np}} \quad (5.50)$$

For a number of simulations of $n=100\,000$ and for a probability of failure $P_f=p=10^{-3}$, the error in J_1 and thus in P_f will be less than 20% for a confidence level of 95% [217]. A first idea of the number of simulations needed for a desired confidence level and probability of failure is provided by Eq. (5.51), according to [229].

$$n > \frac{-\ln(1-C)}{P_f} \quad (5.51)$$

A simpler alternative procedure to obtain a reliable value of P_f , which was also adopted in the present case study and e.g. in [37, 44] or [214], is to analyse the behaviour of the probability of failure with the increasing number of simulations. [37] studied the probability of failure in scour at bridge piers, coupling the Monte Carlo method with variance reduction techniques. In this research the stabilization of P_f was reached after $n=4000$ cycles for a pier depth equal to 0.8 and 1.4 times the scour depth. If the probability of failure is plotted versus the number of simulations another possible criterion for N is the correspondent value associated to the limit of P_f when n tends to ∞ . These plots

can also provide a measure of the variance of P_f . The variance tends to diminish with the increasing number of simulations (samples). Nevertheless, it is important to note that the rate of convergence and its stability can depend, to some extent, on the quality of the random number generator used. Therefore in some unfavourable circumstances, it is possible to obtain an apparent convergence, which is not real. For offshore engineering, [220] suggests that simulations by indicator-based Monte Carlo methods are carried with $n \geq 100/P_f$, whilst other methods must be carried for an estimate of P_f with a coefficient of variation lower than 10%. Instead of directly performing the Monte Carlo simulation, which implies the simulation of each variable (x_i) in all the possible domain, i.e. in safety and failure regions, it is also possible to simulate the data on the region of interest, i.e. where the failure is most likely to occur. Such procedure is often addressed to as the adaptive importance sampling [217], which requires the definition of the probability density function in the area of interest, $h(X)$, for the purposes of sampling, as shown in Figure 5.8. In this case, the probability of failure obtained must be then “corrected” for the fact that the limit state function is being simulated near the failure region only.

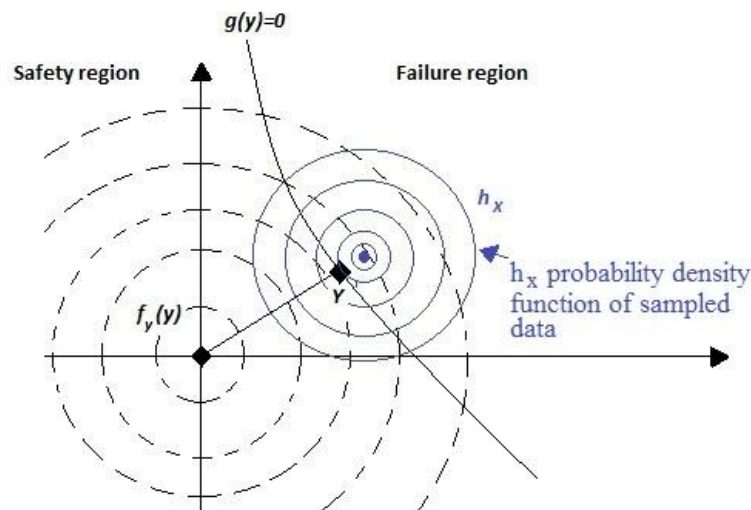


Figure 5.8 – Importance sampling in the most likely point of failure Y , in the normal reduced space of variables (adapted from [194]).

A review on the adaptive sampling is available in [230]. Although this procedure is commonly used in structural reliability, e.g. [36, 194], in order to minimise the number of simulations required by the Monte Carlo, as far as it concerns to scour protections' reliability no applications were found during the present review. However, it can be noted that the adaptive importance sampling is somehow an upgrade of the Monte Carlo simulation method that, as mentioned before, only recently has been applied to scour protections design, namely as a result of the research hereby presented e.g. [214] or [223]. Nevertheless, the works performed on risk and reliability analysis of pipelines under the sinking failure mode, e.g. by [231] or [232], also relatable to scour phenomena and the wave- and current-induced bed shear stress, apply the Monte Carlo method and the adaptive importance sampling method, thus providing a good prospect on future applications of these methodologies to scour phenomena and protection to other types of structures as the monopile foundations.

5.4.3.3 Response surface methods

Considering the research gap regarding the methodologies of risk and reliability analysis to scour phenomena and scour protections, the Monte Carlo simulation method seems a reasonable starting point, in order to obtain primary applications of such methodologies, namely, with the intent of

evaluating if the dynamic scour protection systems can be considered as reliable as the statically stable ones. Nevertheless, since the utility of more complicated approaches might be explored in future research, it is important to provide a brief overview on some of those methods that may be considered as a result of the development of the present investigation. In this sense the following presentation about response surface methods is made in this section.

In some cases the limit state function can only be computed in a non-continuous way, particularly in problems that require the use of finite elements' approach [36]. In such cases the limit state function can correspond to a discrete data set. The finite elements techniques became widely used in structural engineering problems, due to the simplicity of its application. Therefore the utility of response surface methods increased accordingly [194].

Assuming the basic random variables' vector $X=(x_1, x_2, \dots, x_n)$ and the structural response S as a function of X , i.e. $S=g(X)$, where $g(X)$ is unknown, the response surface consists in replacing the original relation between S and X by an analytical function, $\tilde{g}(X)$. This new function is usually a quadratic polynomial one, albeit higher order equations can also be considered. The algorithm to apply a response surface method is detailed in [215] and can be described as follows:

- Define a set of X vectors, with enough quantity to characterize the function $\tilde{g}(X)$ and evaluate the fitting to the real values;
- Identify the structural response for each set of X previously defined, by means of finite elements technique;
- Determine the fitting coefficients of $\tilde{g}(X)$ by means of the finite elements results;
- Assess the quality of fitting, if the quality is not satisfactory the previous steps must be repeated;
- Once the structural response function is defined, the structural reliability is obtained by means of the previously introduced methods, e.g. FORM, MVFOSM or simulation methods.

The choice of the response function is very important, since the description of the response surface depends on it and the determination of the coefficients depends on the order of $\tilde{g}(X)$ as well. Generally the order of $\tilde{g}(X)$ should be lower or equal to the one presented by $g(X)$, in order to obtain appropriate systems of linear equations to determine the coefficients. Besides that the higher order terms can present errors for certain regions of the domain, which were not approached by the values considered in the analysis [194]. Frequently, despite the fact that the higher order terms may provide a better fitting, the computational costs may not justify their application.

The reliability evaluation requires that the representation of $g(X)$ must give preference to the best possible fitting in the region of the design point, i.e. in the failure region. Therefore such zone must be well described by the fitting process. Sometimes this zone is unknown and reliability techniques can also be used as a first approach to determine a fitting procedure, which is oriented to the vicinity of the design point. Usually, in the absence of prior information on the choice of the sets of X , the mean values of the basic random variables can be used as a starting point [217]. The X_i points can be defined around the centred value X_{ci} (e.g. mean values of X) and the standard deviation coupled with a coefficient h that can be reduced between the first iteration of $\tilde{g}(X)$ and the following ones. In the definition of $X_i=X_{ci}+h.\sigma_{X_i}$, h can vary from 2 or 3 in the first iteration and 1 in the next ones [194]. The general matrix form of $\tilde{g}(X)$ is provided by Eq. (5.52), where A , B and C are the polynomial coefficients, also in the matrix form.

$$\tilde{g}(x) = A + X^T B + X^T C X \quad (5.52)$$

These coefficients can be determined through a series of “numerical experiments”, e.g. structural simulations with the input of variables selected according to the “experimental design” [217]. Such design takes into account the fact that the main purpose is to determine the probability of failure as accurately as possible. As mentioned before, this implies that the most important region is the one within the failure domain around the maximum likelihood point. Figure 5.9 provides an example of the “experimental design” for two variables ($X_1; X_2$), which uses the mean values as a first approach, in the case where the region of interest (with the design point) is unknown. Figure 5.10 plots the representation with three variables. For more than three it becomes hard to obtain a graphic visualization.

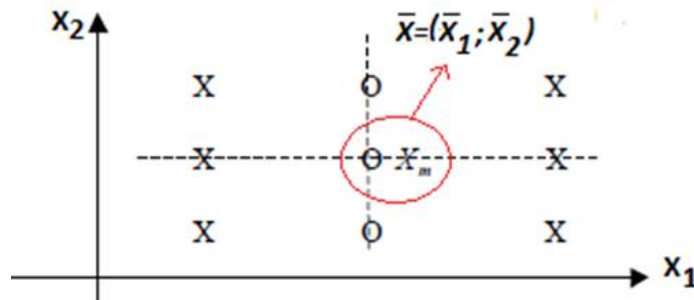


Figure 5.9 – Experimental design for a two variable problem with X_m as the mean point, [217].

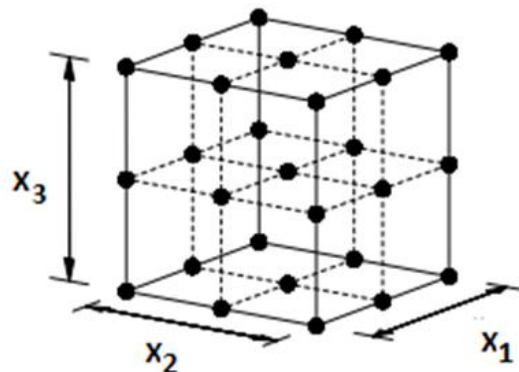


Figure 5.10 – Generic example of an experimental design for three variables, [217].

The design’s complexity increases with the increasing number of variables. Note that in scour problems the difficulty in the application of the response surface methods may easily increase, due to the number of basic variables that can be involved in the phenomena’s description. Besides that the response surface function needs to deal with the fact that the evaluation of the measure reliability of a scour protection system strongly depends on the failure criteria as shown by [43].

The response surface methods pose an interesting option to build an approximated limit state function, which still needs to be simulated in order to obtain the probability of failure from Eq. (5.40), where the number of failures is counted as the number of times that $\tilde{g}(X) \leq 0$, instead of using the actual function $g(X)$. Due to the fact that in scour research and design the limit state function is typically well defined according to a design methodology, as seen in Chapter 3, the response surface method is not commonly found in the literature concerning scour protections, unlike the Monte Carlo simulation method [11].

5.5 Notes on the choice of reliability methods for scour protection design

Throughout section 5.4 it was possible to perceive that the appropriateness of each reliability method is often dependent on the complexity and the nature of the system to be addressed. Often, since there is a state of complementarity between the aforementioned reliability techniques, it is possible to verify results between different techniques in order to fully assess the reliability of a certain system. However, some of the shortcomings associated to each method may lead to a preferential choice, which in the present research lies on the Monte Carlo simulation method.

If the limit state function is linear, the FORM and SORM methods are often preferred. However, as seen in section 3.7, the design methodologies of static and dynamic scour protections, namely [30, 32, 52, 57] or [100], are based on highly non-linear dependencies. For example, the predictive damage number formula, Eq. (3.57), shows dependences on $(U_m)^2$, $(T_{m-1,0})^3$, $(D_{n50})^{3/2}$ and others. On the other hand, the bed shear stress according to Eqs. (2.3) and (2.9), depend on $(U_c)^2$ and $(U_m)^2$, respectively. Moreover, they also depend on f_c and f_w , which are also highly non-linear with respect to the water depth (d), the bottom roughness (k_s), the mean stone diameter (D_{50}) or the roughness length, as shown in section 2.2. Therefore, the application of approximate methods as the FORM or SORM, even when combined with an approximated limit state function obtained through the Response Surface method, may lead to considerable errors in the evaluation of the probability of failure. Moreover, due to the lack of works performed on this matter it is hard to have an estimate on the magnitude of such errors, thus meaning that potentially more accurate methods should be preferred as a first approach. If the dimension of X is smaller than 5, [217] recommends the use of the direct integration methods. However, as noted in sections 3.4, 3.5 and 3.6, the number of basic random variables, i.e. structural and environmental design parameters, is considerably large depending on the design methodology employed. Moreover, the dependencies between these variables increase the complexity of Eq. (5.15), which may require costly efforts on the assessment of the probability of failure, particularly, if the simulation methods correspond to a reasonably short computation time.

As mentioned in section 5.4.3.3, the Response surface methods are typically applied when the limit state function is an implicit one, or eventually too complicated to integrate. However, as clearly stated in section 5.1, the present research is focused on the probability of failure interpreted as the probability of a specific design criterion not being met, under certain design and loading conditions. Therefore, the use of a fitted alternative limit state function might not be suitable for the reliability assessment of the scour protections designed under the methodologies addressed in Chapter 3 and further experimentally studied in Chapter 4.

The reliability methods must be chosen in conjunction with the available information about the environmental and structural parameters of the scour protection, i.e. depending on the information available for the case study. In light of the experimental and field data, it might be possible to statistically model the variables, which can then be used for the purposes of simulation. As it will be seen in section 6.2.3, the data regarding the case study of Horns Rev 3 mainly consists in wave data with sufficient quantity so that it might be treated statistically. In this sense, due to the available data and the shortcomings of the remaining methods, the Monte Carlo simulation method was chosen to perform the reliability assessment of scour protections, in the second part of this research. The application of this method, at least, requires the statistical modelling of the most important variables is included in the design of the protection. The following sections address the theoretical concepts used for that purpose. An effort was made to avoid the basic notions, regarding the univariate modelling of random variables, so that a focus could be given to the multivariate modelling techniques and the correlation between variables. An extensive review regarding the basic notions of probability and univariate statistical modelling is provided in [233].

Finally, as an overall idea it should be kept in mind the reliability models presented so far might be seen as instruments to answer the following research questions:

- How reliable is a scour protection designed according to a specific criterion?
- Is a dynamic scour protection as reliable, i.e. as safe, as a statically stable one?

The reliability methods presented can be coupled with innovative design of scour protections, e.g. [1, 30, 32], or with the empiric knowledge already existent, e.g. [52] and [57], to provide a design that answers to these questions by means of the probability of failure. This measure provides a notion of safety, which relies on statistical knowledge regarding the uncertainty of the basic random variables. A reliability-based design might be associated to predictions about the rate of maintenance needed during the foundation's life cycle, namely, concerning backfilling needs or assessment of armour layer conditions. Ultimately, the goal of measuring scour risk in such protections is only possible if the reliability analysis is developed for scour problems around offshore foundations with the same extent as in other research fields of structural engineering. The second part of this thesis aims to contribute to this goal.

5.6 Limit state functions and the need to model correlated variables and statistical model framework

As seen in section 5.4.3.1, the Monte Carlo simulations require that a limit state function is defined for the scour protection system. Theoretically, as discussed in section 3.3 one limit state function per failure mode should be addressed, thus implying the calculation of the probability of failure associated to each mode, which can then be combined into the overall probability of failure of the system. However, the present research only addresses the failure caused by the erosion of the armour layer, since this was the focus of the design methodologies addressed in Chapter 3 and studied by means of physical models throughout Chapter 4 (also see Figure 3.6). Therefore, it is important to clearly state that the possible conclusions – obtained from the reliability analysis of Chapters 6 and 7 – concern to this failure mode alone and should not be generalised to the remaining failure modes, which are governed by different limit state functions.

The limit state functions proposed to perform the reliability analysis of the scour protections at Horns Rev 3, are introduced and discussed with further detail during the presentation of the case study. This is performed for the sake of clarity, as the limit state functions will depend on specific considerations and eventual simplifications that might be the direct result of the environmental conditions at Horns Rev 3 location or the result of the type and quality of the data available for the random variables. Nevertheless, at the present stage it is important to provide a brief introduction on the possible limit state functions to be used, so that the most important variables of the scour phenomena are properly identified for further statistical modelling.

From a general point of view, the limit state function can be based on a failure criterion. For example, if a static scour protection is being designed, the failure criterion can be defined based on a comparison of the threshold of motion of the armour layer material, i.e. the critical bed shear stress (τ_{cr}) associated to D_{50} , with the maximum combined wave- and current-induced bed shear stress (τ_{cw}). For a random sea state, i.e. wave loading given by H_s and T_p , a specific location and water depth (d) and depth-averaged current velocity (U_c) the protection will fail if τ_{cr} is smaller than τ_{cw} , because movement of the armour stones will occur. This is valid, regardless on the methodology by which the critical and the bed shear stress are being evaluated and compared. This failure criterion might be expressed according to the limit state function state in Eq. (5.53), where X is the vector composed by the environmental and structural parameters addressed in sections 3.5 and 3.6. Moreover, note that if

$g(X)$ is equal to or smaller than zero, the scour protection has failed, i.e. it is no longer statically stable under the simulated values of X , thus meaning that the original design criterion is not being met.

$$g(X) = \tau_{cr} - \tau_{cw} \quad (5.53)$$

A similar thinking might be applied to a dynamically stable scour protection. As it will be seen throughout the following chapters the limit state of dynamic protections can not be defined by means of the threshold of motion. However, as concluded in Chapter 4, one may propose that its failure is defined according to an acceptable damage number ($S_{3D\text{acceptable}}$), which might be compared with the expected damage number under the random sea state and current conditions (S_{3D}). If the damage associated to those conditions exceeds the acceptable limit for which the protection was designed, thus correspondent to a certain value of D_{50} , then the protection may have its filter exposed and eventually collapse. In this case, the limit state function might be defined according to Eq. (5.54). Again, it can be noted that if $g(X)$ is equal to or smaller than zero, the scour protection might be entering into collapse, since the design criterion was violated for the simulated load conditions.

$$g(X) = S_{3D\text{acceptable}} - S_{3D} \quad (5.54)$$

Despite the methodology used to obtain the shear stresses or the acceptable limits of the damage number and if one recalls Eqs. (2.3), (2.9), (2.26) and (3.57), one obvious conclusion arises from the previous limit state functions: the vector of basic random variables, X , will include three key environmental parameters:

- The current velocity (U_c);
- The significant wave height (H_s);
- The wave peak period (T_p).

Other variables, as the water depth (d) or the stone size are also important. The simulations performed with the Monte Carlo method will be mainly focused on these three variables, with further justifications provided during the case study analysis. The evaluation of the limit state functions provided in Eq. (5.53) and Eq. (5.54) requires that the probability density functions of each variable are modelled, in order to generate the random values that will be used to simulate $g(X)$. Moreover, the generated values of the wave heights and periods must be generated through their joint probability density function, because they are correlated.

A reliability design of a dynamic scour protection is at least a problem with 9 dimensions, depending on the vector $X = \{T_{m-1,0}; U_m; d; D_{n50}; U_c; g; s; T_p; H_s\}$. If other physical dependencies are considered the dimensions of the problem increase. For example, note that the coefficient a_4 depends on the Ursell number (U_r), which depends on the wave length (L), hence meaning that an additional dimension is added to the problem.

In case of static stability, the problem does not imply so many variables. However, if the design is performed by means of the threshold of motion, the influence of waves and currents in the induced bed shear stress can also be accounted in a probabilistic manner.

Extensive research has been dedicated to model the statistical properties of the hydrodynamic conditions in offshore locations, e.g. [234, 235] or [236]. Some of them applied to floating foundations and mooring lines, e.g. [237]. However, regarding scour protections in monopile foundations, the state-of-the-art shows a lack of multivariate models used to assess their reliability. Moreover, a full probabilistic model is always difficult to obtain, because for some industrial applications, namely, in the offshore wind sector, there is an evident lack of field data publicly available. Typically, an

offshore wind structure is designed for a life time of 25 years and sometimes with considered lifetime extensions of 50 years [27]. However in common cases, the data concerning the wave heights and peak periods is limited to rather short periods, e.g. 10 years. If the design wave height is the one obtained for a return period of 100 years [106], it is likely that the statistical model, based on a 10 years record, presents a considerable degree of uncertainty. This also happens to other variables, hence limiting the chances of having a detailed full probabilistic model. In addition to that, the extended deployment of a wave buoy to directly measure wave conditions and the application of wave transformation models, including public domain models such as Wavewatch and SWAN, are both expensive [238] and time consuming.

In order to adopt the reliability techniques, some design standards for offshore wind turbines require a minimum record of 10 years of wave heights and periods [21, 220]. However, the uncertainty is considerable, when an attempt is made to estimate return periods that far exceed the available record, e.g. use 10 years record to predict the wave height design associated to a return period of 50 years.

Either because of the complexity of scour phenomena or the lack of data, when performing a reliability design of a scour protection one should clearly define a statistical model framework that is focused on:

- Considering the governing parameters of the scour protection – defining the main variables of the problem;
- Performing an accurate univariate analysis of each variable previously defined;
- Describing the most important and evident correlations;
- Performing a multivariate analysis of the variables – whose correlation may strongly influence the failure of the system.

As referred before the lack of data concerning the main variables can also influence the reliability assessment. A “rule of thumb” is to assume that “more data available is always better”. However, a wise practice recommends that the influence of the duration of the data records is analysed. This enables one to understand if the probabilities obtained are sensitive to the records used for predictive purposes. Finally, the framework should state *a priori* all the simplifications and assumptions of the statistical model that will be used to perform the reliability assessment. The present work dedicates Chapter 6 to the study of the joint probability distribution of the wave heights and periods at Horns Rev 3. The following sections will detail the methods used for this purpose, as well as the techniques used to evaluate the marginal distributions and possible dependences between wave heights and periods at the case study location.

5.7 Goodness-of-fit of the Marginal Distributions

Once the dimensions of the problem are defined the marginal distribution of each variable must be studied. The marginal distribution can be chosen regardless the existent correlations between variables, mainly, because one is only interested in describing the univariate behaviour of the variable. In the absence of detailed information or mandatory regulations, the designer should test several distributions and then evaluate the goodness-of-fit measures. Depending on the problem’s nature, one may test different distributions. For instance, if one is interested in analysing the extremes’ distribution of a specific variable, a probability density function associated to extremes can be chosen, e.g. Gumbel or GEV. In order to assess the goodness-of-fit regarding the marginal distributions, the Kolmogorov-Smirnov distance and the Wasserstein distance, can be used and are further detailed in [239]. Both distances can be used as a comparative measure to analyse which distribution fits the sample more

accurately among a set of tested distributions. The fundamental theory and detailed explanation of these concepts is respectively given in [240] and [241].

Consider a continuous random variable $x = \{a_1, a_2, \dots, a_i\}$, for $i = [1; n]$, with $n = \text{number of values in } x$. The empirical cumulative distribution function of x , $J(x \leq a_i)$ can be expressed according to Eq. (5.55).

$$J(x) = \sum_{i=1}^n \frac{\text{number of elements in the sample } \leq x}{n} = \frac{1}{n} \sum_{i=1}^n 1_{\{a_i \leq x\}} \quad (5.55)$$

Now, consider that an attempt was made to fit a theoretical cumulative distribution function to x . The Wasserstein distance between the empiric and the theoretical cumulative distribution function (WS_{JF}) is obtained as in Eq. (5.56), [239]:

$$WS_{JF} = \int_{-\infty}^{\infty} |J(x) - F(x)| dx \quad (5.56)$$

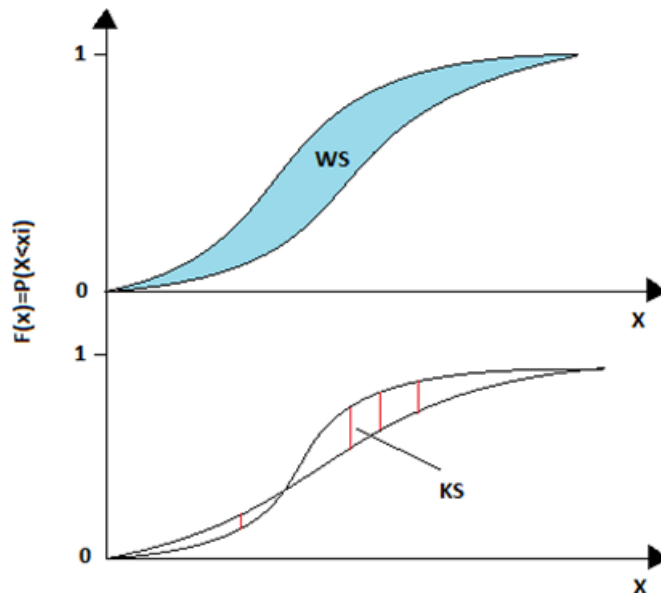


Figure 5.11 – Scheme of the Kolmogorov-Smirnov distance and the Wasserstein distance between two distributions.

In a simple way the Wasserstein distance, between two distributions, graphically corresponds to the difference between the areas encompassed by each cumulative distribution function (Figure 5.11). If one assumes that the best theoretical distribution is the closest to the empiric $J(x)$, then the metric WS_{JF} can be used to compare different theoretical distributions. The one with the lowest value of WS_{JF} is the distribution that presents the best comparative goodness-of-fit.

For illustration purposes, a continuous random variable x , with $n = 10\,000$ values, was generated according to a Gaussian distribution function $G(x)$ with mean $\mu = 2$ and standard deviation $\sigma = 0.2$. Then an attempt was made to fit a Normal distribution, $N(x)$, and a Rayleigh distribution $Rp(x)$. The empiric cumulative distribution function was also calculated. One expects that the Normal distribution presents a lower value of WS_{JF} than the Rayleigh distribution, because x was generated to have the Gaussian distribution indeed.

The generated sample of x had the following Gaussian parameters, $\mu^* = 1.9978$ and $\sigma^* = 0.1993$. The correspondent Rayleigh parameter was $Rp = 1.4198$. The lowest Wasserstein distance was

obtained for $G(x \leq a_i)$, i.e. $WS_{JG}=0.0018$, which compares to $WS_{JRp}=0.4223$. Thus indicating that Gaussian distribution seems to be a better marginal for x than the Rayleigh (Figure 5.12). It can be graphically confirmed in Figure 5.12 that the $G(x)$ is indeed closer to $J(x)$ than $Rp(x)$. Note that if n tends to infinity then $G(x)$ and $J(x)$ tend to the real distribution $N(x)$.

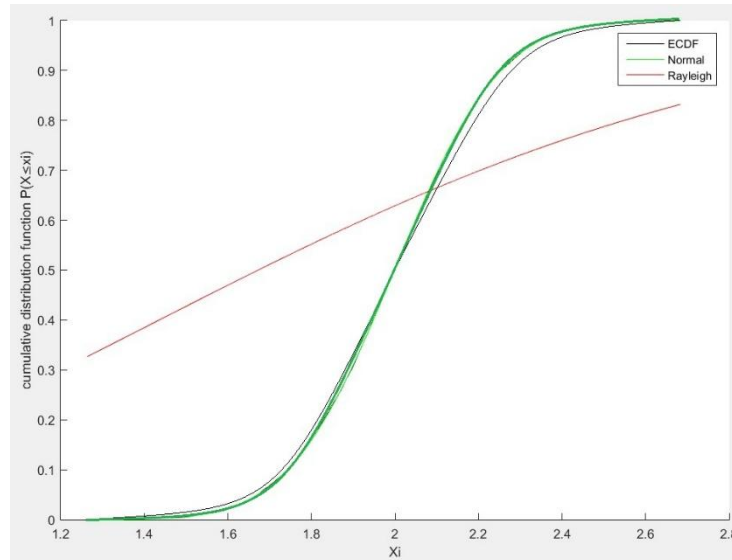


Figure 5.12 – Comparison between the fit of a Normal and a Rayleigh distribution to the empirical distribution of x .

The Rayleigh distribution provides a very poor fit to the CDF of x . This was expected, since x was generated as Gaussian variable. Although in this case the poor fit is evident (Figure 5.12), usually when testing more “flexible” distributions the graphical differences are not so evident, thus the Wasserstein distance provides a simple and somehow elegant way of comparing different marginal distributions.

The Kolmogorov-Smirnov distance also has a graphical interpretation. When used to compare two distributions, e.g. $J(x)$ and $G(x)$ or $J(x)$ and $Rp(x)$, the KS metric represents the maximum absolute vertical distance between the evaluated curves (Figure 5.11). The best marginal is the one that minimizes the maximum vertical distance to $J(x)$. The Kolmogorov-Smirnov distance between a theoretical marginal (F) and the empiric cumulative distribution function (J) is obtained as in Eq. (5.57):

$$KS_{JF} = \sup(|J(x) - F(x)|) \tag{5.57}$$

For the example previously introduced, one obtains the following KS metrics, $KS_{JG}=0.0052$ and $KS_{JRp}=0.4528$, thus indicating that $G(x)$ is closer to the empiric cumulative distribution than $Rp(x)$. Note that if a theoretical distribution $F(x)$ is indeed the cumulative distribution function of x , both metrics tend to 0 as n tends to ∞ . It is not the aim of this work to discuss the significance level (p) and the convergence of the present metrics. In this research both metrics were used to compare the selected theoretical distributions only, thus selecting the best marginal among the candidates. For further details on these aspects and on the associated hypothesis tests, it is recommended the consultation of [242]. In the present research both the KS and WS metrics are applied to select the marginal distributions of the significant wave heights and peak periods, as it will be seen in the case study analysis.

5.8 Correlated variables and measures of dependence

5.8.1 Measures of dependence

As mentioned in 5.6 a proper reliability assessment of dynamic and statically stable scour protections, by means of the Monte Carlo simulation method, requires the joint (and correlated) modelling of the spectral parameters included in the design methodologies. Therefore, the analysis of the correlation and the dependence between these parameters is crucial for realistic random number generation of the wave heights and peak periods, which will be used to simulate the limit state function of the scour protection. The measures of dependence are particularly important in the copula-based models used for the referred joint modelling during the case study.

In order to apply a copula based model, the Pearson linear correlation does not always meet the desired properties of the dependence measures [243]. Therefore, it is common to use the Kendall's tau (τ_k) or the Spearman's rho (ρ_{spear}) to represent the dependence between variables [243]. Often other measures, such as the tail dependence coefficients might be used. However, they are not the primary focus of this research. Both τ_k and ρ_{spear} can be used in order to estimate the copulas' parameters, eventually leading to differences in models. Details on how to estimate τ_k and ρ_{spear} and how to estimate the copulas parameters can be found in [125] and [243].

Considering two independent and identically distributed random vectors $(X_1; Y_2)$ and $(X_2; Y_2)$, each with the same joint modelling distribution function (CDF), Kendall's tau (τ_k) can be defined as the difference of the probabilities of concordance and discordance Eq. (5.58), [125]:

$$\tau_k = P[(X_1 - X_2)(Y_1 - Y_2) > 0] - P[(X_1 - X_2)(Y_1 - Y_2) < 0] \quad (5.58)$$

If there is a random sample of size n from a vector $(X; Y) = \{(x_1, y_1), \dots, (x_n, y_n)\}$ then the Kendall's tau estimate for the sample is given by Eq. (5.59). Note that $(n-2)$ is the number of different pairs in the sample, while c' and d' are the number of concordant and discordant pairs respectively.

$$\tau_k = \frac{c' - d'}{c' + d'} = (c' - d') / \binom{n}{2} \quad (5.59)$$

The Spearman's rho is defined as the Pearson coefficient (Ω) of the transformed variables $F(X)$ and $G(Y)$, which correspond to the CDF of X and Y , as in Eq. (5.60) according to [125]:

$$\rho_{\text{spear}} = \Omega(F(X), G(Y)) \quad (5.60)$$

Consider r_x and r_y as the ranks of the sample for X and Y , respectively ($k=1 \dots n$). The sample version of Spearman's rho is given from Eq. (5.61) where $d_k^2 = r_{xk} - r_{yk}$.

$$\rho_{\text{spear}} = 1 - \frac{6 \sum_{k=1}^n d_k^2}{n(n^2 - 1)} \quad (5.61)$$

5.8.2 Assessing dependence with graphical tools

As complement to the dependence measures introduced above, one can assess the dependence between the spectral parameters with graphical tools. In this section, as a brief introduction, the basic concepts

of the graphical tools are introduced to help the reader in the discussion of results provided in Chapter 6. Two of the most well known graphical tools are the Chi-plot and Kendall plot. In [244] a summary of their application is provided. This section is mainly based on the original explanations provided in [245]. Motivated by the need for a graphical method in which independence manifests itself in a more evident way than the scatterplots, [246] and [247] introduced the Chi-plots. For a given pair $(X_i; Y_i)$ with $1 \leq i \leq n$ let H_i be the joint cumulative distribution function of X and Y , and F_i and G_i be the cumulative distribution function of X and Y , respectively [245] i.e.:

$$H_i = \frac{1}{n-1} \# \{j \neq i : X_j \leq X_i, Y_j \leq Y_i\} \quad (5.62)$$

$$F_i = \frac{1}{n-1} \# \{j \neq i : X_j \leq X_i\} \quad (5.63)$$

$$G_i = \frac{1}{n-1} \# \{j \neq i : Y_j \leq Y_i\} \quad (5.64)$$

If X and Y are independent, it would be expected that $H_i = F_i \times G_i$, up to sampling variation. In the Chi-plots the pairs $(\lambda_i; \chi_i)$ are plotted according to Eqs. (5.65) and (5.66), [244]:

$$\chi_i = \frac{H_i - F_i G_i}{\sqrt{F_i(1-F_i)G_i(1-G_i)}} \quad (5.65)$$

$$\lambda_i = 4 \text{sign} \left[\left(F_i - \frac{1}{2} \right) \left(G_i - \frac{1}{2} \right) \right] \max \left[\left(F_i - \frac{1}{2} \right)^2, \left(G_i - \frac{1}{2} \right)^2 \right] \quad (5.66)$$

The variable $\lambda_i \in [-1; 1]$ is a measure of the distance of the pair $(X_i; Y_i)$ from the centre of the dataset [245]. [247] recommend that only the pairs for which $|\lambda_i| \leq 4 \{1/(n-1) - 1/2\}^2$ are plotted to avoid spurious observations. The χ_i is the signed square root of the traditional chi-square test statistic for independence, in the two way table generated by counting the points in the four regions delineated by the lines $x=x_i$ and $y=y_i$ [244]. In a simple interpretation, it can be said that the values of the pairs $(\lambda_i; \chi_i)$ that fall too far from zero are indicative departures of the hypothesis of X and Y being independent.

Moreover the horizontal lines introduced by [246, 247] correspond to the confidence intervals of the chi-plot, also known as ‘‘control limits’’. They are given by $(-c_p/n^{0.5}; c_p/n^{0.5})$ where c_p is 1.54, 1.78 and 2.18, for $p=0.90, 0.95$ and 0.99 of confidence, which is roughly the proportion of the observations falling within the horizontal bounds, as might be expected under independence [244]. These limits are accounted for n equal to the number of analysed observations. If both variables are independent, then χ_i is randomly distributed around 0. Figure 5.13 provides an example for $n=100$ of two independently generated variables. X follows a uniform distribution between 0 and 1, while Y follows a Gaussian distribution with mean 0 and standard deviation 1. It is possible to see that the majority of pairs $(\lambda_i; \chi_i)$ are within the control limits, thus indicating that X and Y are independent. Also the χ_i seems uniformly distributed around 0.

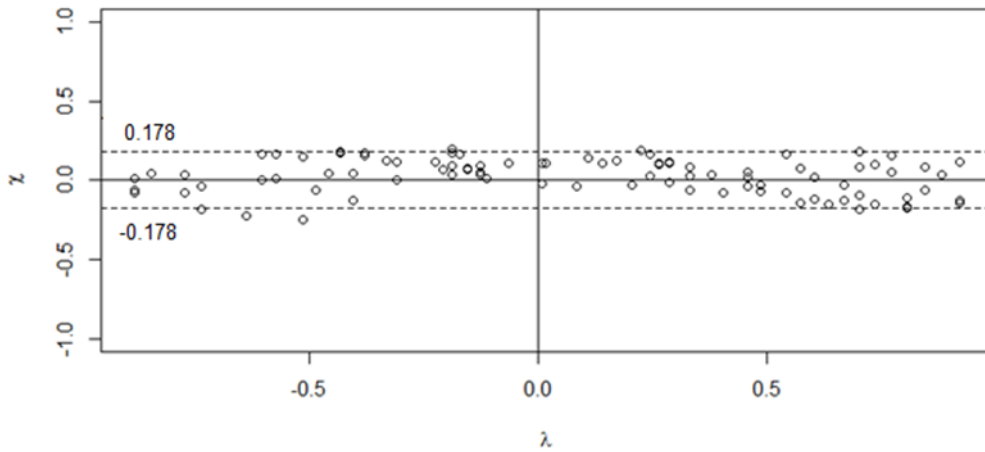


Figure 5.13 – Example of a Chi-plot for X and Y (independent variables).

Regarding the Kendall plot or the K-plot, consider the distribution $H_i(X;Y)$, previously defined, for $1 \leq i \leq n$. Also consider that H_i is sorted in the following ascending order $H(1) \leq \dots \leq H(n)$, where equalities are possible. The Kendall plot consists in building a graph with the pairs $(W_{i:n}; H(i))$, where $W_{i:n}$ represents the expectation of the i^{th} order statistic in a random sample of size n from the distribution K_0 of H_i under the null hypothesis of independence (see [245]). The values of $W_{i:n}$ are obtained from Eq. (5.67).

$$W_{i:n} = n \binom{n-1}{n-1} \int_0^1 w \{K_0(w)\}^{i-1} \times \{1-K_0(w)\}^{n-i} dK_0(w) \tag{5.67}$$

According to [248] under mild regularity conditions, the empirical distribution of K_n of the pseudo-observations H_1, \dots, H_n is an asymptotically Gaussian, $n^{0.5}$ – consistent estimator of $K(w) = P\{H(X,Y) \leq w\}$, for $0 \leq w \leq 1$. [245] point that this conclusion that is intuited from the fact that $H_i = H^* \cdot n(X_i, Y_i)$, i.e. the empirical distribution function based on (X_j, Y_j) , converges to H as n tends to ∞ . If X and Y are independent then $H(X,Y) = F(X) \cdot G(Y)$, which leads to Eq. (5.68):

$$K(w) = K_0(w) = P(uv \leq w) = w - w \log(w) \quad \text{for } 0 \leq w \leq 1 \tag{5.68}$$

where u and v are independent uniform random variables on the interval $[0,1]$. If both variables are independent the pairs $(W_{i:n}; H_i)$ are placed across $W_{i:n} = H_i$ (main diagonal). Any deviance from the main diagonal is a sign of dependence [244], in fact the further the distance the greater the dependence. Positive dependence corresponds to pairs above the main diagonal. Conversely, negative dependence is expressed by pairs below the line $W_{i:n} = H_i$. If two variables are perfectly negative dependent, the pairs are aligned with the ordinates axis ($H_i = 0$). If the variables X and Y display a perfectly positive dependence, then the points are aligned on the upper curve $K_0(w)$.

As an example, assume that X and Y follow a uniform distribution between 0 and 1. Both variables are independent, thus leading to situation A from Figure 5.14. Note that the pairs tend to be aligned with the main diagonal. In situation B, one considers that X follows a uniform distribution between 0 and 1 and that $Y = 2X$. This example of perfectly positive dependence is expressed with the pairs plotted above the $K_0(w)$ curve. Finally, if Y is considered as $Y = 1 - X$ the situation C occurs. Since both variables display a perfect negative dependence, i.e. the pairs are aligned in $H_i = 0$ (the ordinate axis).

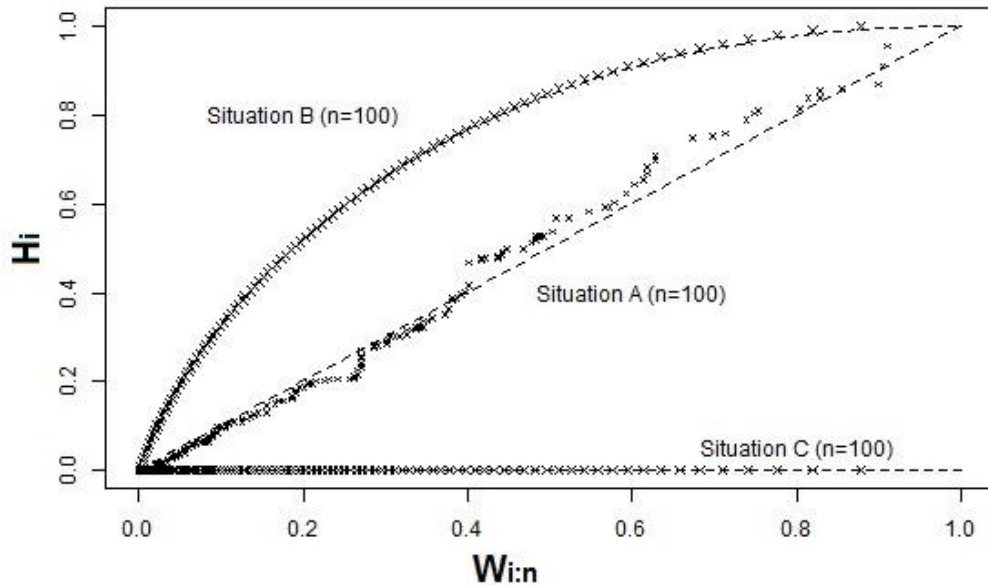


Figure 5.14 – Example of Kendall plots for situation A - Independent X and Y; situation B - Perfect positive dependence of X and Y; situation C - Perfect negative dependence of X and Y.

5.9 Introduction and review of joint models applied to correlated wave heights and wave periods

The design of offshore wind structures, scour protections included, is a complex task, which requires a detailed knowledge on the environmental conditions during their construction and lifetime. Moreover, the reliability and safety assessment of these structures is very much dependent on the ability to account for the uncertainties related to the environmental loads. When dealing with met-ocean data, the wave climate, i.e. wave height and wave period, is a crucial component for a safe design. Therefore, several standards for the offshore wind and marine industry require a proper modelling of these random variables and the inherent uncertainties, e.g. [21, 27, 106, 249] or [250].

Also when attempting to estimate extreme events associated with a specific return period, e.g. 100-year significant wave height, one often has to deal with the statistical modelling and inference techniques applied to the long-term sea-state characteristics. However, the complex nature of ocean environment, the physical constraints of wave propagation and steepness and other uncontrolled climate effects, make it practically impossible to perfectly model the wave climate at the desired location. Therefore, a full probabilistic model is not commonly viable in scour related problems. Nevertheless, the statistical description of relevant ocean parameters is a requirement for risk and reliability analysis [123].

Despite the extensive use of numerical models to describe the wave climate and the deployment of monitoring buoys, cost-related problems have contributed to the development of statistical models. Often the time series provided by buoy systems have considerable missing data created by a damage or vagrant buoy or because the observations at a temporary site are not enough to build an accurate model for extreme events. Sometimes, during extreme events, which are very energetic, buoys present malfunctions due to the harsh oceanic environment [238], thus leading to the lack of information during these occurrences. On the other hand, the deployment of buoys and the use of numerical models such as WAVE Modelling (WAM) or the Simulating WAVes Nearshore (SWAN) are considerably expensive, both in man and simulation hours and computational requirements [238]. In

fact, the common project of an offshore foundation or a marine structure often implies a balanced mix between buoy observations, numerical and statistical models, which are further used for design, construction and maintenance operations. Scour protections are no exception to this reality.

In the majority of structures placed at sea the significant wave height is the parameter adopted to express the severity of sea state [251]. However, the joint modelling of the significant wave height and the mean up-crossing period, or eventually the peak period, enables a more precise description of the sea-state and it is fundamental for several aspects of design, e.g. in the fatigue limit state assessment [252], the scour phenomena at the foundation [102] or the reliability of structural elements as the mooring lines [125].

Joint modelling of long-term sea state has been attempted by means of several statistical approaches, for example: the earlier Peak Over Threshold method and the Annual Block Maxima (e.g. see [114]), the conditional modelling approach, Conditional Extremes models, the bi-variate Maximum Entropy Method, the bi-variate lognormal model and the normality transformation-based models (e.g. see [253] and [254]), among others. The number of statistical approaches to model wave characteristics has increased considerably, not only in quantity but also in complexity. Comprehensive reviews on these and other models are given in [255] and also in [256].

An alternative that has been used for this purpose is the Copula approach. The use of copula-based models to build the joint distribution function of the significant wave height and mean up-crossing period, or the spectral peak period, has been recently applied in [123] or [219]. The use of copulas is mainly due to their simplicity of calculation and due to their ability to describe the dependence structure between random variables, regardless of the assumptions made for the marginal distributions [180]. Moreover, copula-based models present a straightforward and computationally fast method to simulate the random variables [257]. Despite the former applications of copula theory to the analysis of met-ocean data several works have been recently performed as an attempt to improve their applicability to model wave characteristics. Therefore, the present thesis is also dedicated to the use of copula-based models, which will be further used for the simulation of the proposed limit state functions for reliability analysis.

There are numerous families of copulas (see [21]). Furthermore, if one attends to the techniques used to combine different copulas, this number is practically infinite [123]. The most used families are the elliptical copulas, which are radially symmetric, the Archimedean copulas, which are only able to capture either lower or upper tail dependences, and the extreme value copulas, which according to [123] arise in the limit of component-wise maxima, but are also used to model general dependence structures. However, one of the major problems with these families is the fact that they are not able to account for asymmetry in the data. Asymmetry is often due to physical limitations related to e.g. wave breaking and maximum wave steepness. As it will be seen during the analysis of the case study, the significant wave height and peak periods are very asymmetric, thus implying that new models and more accurate models must be proposed for a proper joint modelling of these variables.

Still the above mentioned copula families have been applied with a reasonable degree of success in other studies, namely, when modelling single storms with multivariate Archimedean copulas [258]. Also, [238] successfully used the Gaussian and t-copula, from the elliptical family, to estimate the wave height records through spatial correlation at the south coast of England. Still using the same Elliptical and Archimedean copulas (Clayton, Frank and Gumbel), [259] found that the Gaussian and the Gumbel copulas could accurately fit the empirical densities of the individual wave steepness and height. However, as stated by [123] and re-confirmed in the present study, it is far from

straightforward to find a good copula-based model for non-symmetric met-ocean data, such as the significant wave height and the up-crossing mean wave period (or the peak period).

A possible way to solve the asymmetry problem is to use more complex copula-based models. For instance, one can use non-symmetric copulas as the Marshall-Olkin family [243], the dependence trees association [218] or the C- and D-vine copulas [260], which are usually applicable for higher dimensional problems. In the bi-variate cases, a simpler way of combining different copulas is to use the extra-parametrization technique, originally proposed by [261] and later on extended by [262]. This technique was then applied by [263] to develop multivariate extreme models. More recently, by using the same copula construction, [123] concluded that extra-parametrization with an independent or a pairwise copula could be used to model significant wave heights and mean up-crossing periods. Using the root-mean-square error (RMSE), the author concluded that this technique provided a better fit than the bivariate lognormal model, widely used in practice and introduced by [264]. Moreover, this work concluded that extra-parametrization of copulas provided a similar goodness-of-fit when compared with the conditional modelling used in current practice [122] and introduced by [265]. However, in these works no extra-parametrization was performed with different copulas, e.g. Frank-Clayton or Gumbel-Clayton.

Finally, another important aspect is the fact that the literature does not present many works comparing the copulas' performance and their possible parametrizations to the separated components of wind-sea and swell. The majority of the works performed so far are dedicated to modelling the total sea-state, e.g. [123, 266] or [267]. The separated performance of copula-based models for the total sea and the wind-sea and swell components has not been extensively addressed in the literature. This aspect is of great importance, since sea components may present less asymmetry than the one showed by the combined sea. This may lead to an improvement of certain copulas' performance, i.e. the ones that are constructed to deal with symmetric cases only, as the Archimedean copulas. Furthermore, the study of wind-sea and swell components may be of importance when dealing with bi-modal sea states or in certain fields of application, e.g. the dynamic analysis of FPSO units or the floating foundations for offshore wind structures [268]. Typically, in scour protections design one is expecting to design the structure based on the total wave height.

The present thesis also provides inputs to these literature gaps, i.e. the use of copulas to deal with data asymmetry and the wind-sea and swell components. A particular focus will be given to the extra-parametrization of these models, during the analysis of the case study. Along with the copula-based models the conditional model proposed by [126] and further extended in [265], will be used due to its wide applicability within the common standards used in the design of offshore and marine structures, e.g. [122] and [220]. Moreover, the Bi-variate Kernel Density Estimation method is also addressed due to its non-parametric nature [269], which enables to fit a smoothed model to the available data for further statistical treatment. The following sections will provide the basis for the applications made of these models in the case study analysis.

Extra-parametrization of copulas will be applied with an independent copula and pairwise copulas to the total sea (also referred here as the combined sea) and the wind-sea (referred to as the wind component) and the swell (swell component). Going one step further, an attempt is made to combine copulas from different families and with different tail dependences, to understand if any improvements are obtained when fitting the available hindcast data. The case study corresponds to a record of 124 months of significant wave heights and mean up-crossing and peak periods at the Horns Rev 3 offshore wind farm, located in the North Sea.

5.10 Copula-based models

5.10.1 Introduction to copulas

Comprehensive insights on copula's theory and a large spectrum of copula's families is provided by [124] and [243]. In this section only the fundamentals of copula's theory and extra-parametrization are described. The families of copulas used throughout Chapter 6 are well described in the literature and will not be addressed in detail, an exception is made to the Archimedian and the Elliptical families presented in section 5.10.2, which were used as the main families to extra-parameterize existent copulas families. The work of [243] is recommended for this puporse.

A copula is a function that couples multivariate distributions to their marginal distributions [125]. These functions have uniform one-dimensional margins on the interval $[0; 1]$ and are invariant under monotone increasing transformations of the marginal distributions [243]. The main advantage of copulas is that they enable the separation of the marginal behaviour and the dependence structure of the variables from their joint distribution function [270]. Copulas present a simple way to build the joint distribution function in multivariate problems, taking into consideration the dependence structure between the considered random variables. The representation of the dependence structure is vital when dealing with reliability problems that somehow imply a random variable generation process. For instance, in maritime and offshore engineering problems one often needs to simulate pairs of wave heights and periods, which must be in agreement with the location's characteristics. If one considers X as a vector of random variables (x_i) with the marginal distribution functions defined by $F_i(x_i)$, with $i=1\dots d$. The transformation $U_i=F(x_i)$ is a dependent uniformly distributed vector of random variables, with $U=(u_1,\dots,u_d)$ on the space $[0,1]^d$. If $F(x_i)$ are continuous, the joint distribution function of X can be expressed as in Eq. (5.69).

$$F(X)=C(F_1(x_1),\dots,F_d(x_d))=C(u_1,\dots,u_d) \quad (5.69)$$

where $C(u)$ is the copula of the distribution, $C:[0,1]^d \rightarrow [0,1]$ and $U=(u_1,\dots,u_d)$. Eq. (5.69) was originally introduced as the Sklar's theorem [243]. The copula $C(U)$ and the correspondent copula density $c(U)$ can also be defined as in Eqs. (5.70) and (5.71), thus leading to the joint density of X given by Eq. (5.72):

$$C(U)=F(F_1^{-1}(u_1),\dots,F_d^{-1}(u_d)) \quad (5.70)$$

$$c(U)=\frac{\partial(C(u_1,\dots,u_d))}{\partial u_1\dots\partial u_d} \quad (5.71)$$

$$f(X)=f(x_1,\dots,x_2)=c\{F_1(x_1),\dots,F_d(x_d)\}\prod_{i=1}^d f_i(x_i) \quad (5.72)$$

Note that $f_i(x_i)$ is the probability density function of each variable x_i , e.g. of the wave height and period for example. Therefore, the joint distribution function of X corresponds to the combination of each marginal in X and the information on the dependence structure, which is retained by the copula function [123].

Copulas are built on parametric estimations, usually based on ρ_{spear} and τ_K (introduced in section 5.8.1). Information on the parameter estimation for several copulas can be seen in [243]. Nevertheless, the following Eqs. (5.73) and (5.74) can be applied for both measures, in the bi-variate case, where φ is

the so-called generator function of the copula [271] and X is composed of the uniform transformed variables $u=F_1(x_1)$ and $v=F_2(x_2)$.

$$\tau_K=4\int_0^1\int_0^1C(u,v)dC(u,v)-1 \quad (5.73)$$

$$\rho_{\text{spearr}}=12\int_0^1\int_0^1C(u,v)dudv-3 \quad (5.74)$$

5.10.2 Basic copula families

5.10.2.1 Empirical and Independent copulas

As reference to the parametric models one can use the non-parametric empirical copula (C_n), which is built on the empirical distribution function $F_n(x_i)$ of each random variable (x_i). Regarding the possible formulations of the empirical distribution functions of a variable, it is recommended the consultation of [233]. The empirical copula can be defined as in Eq. (5.75), according to [272]:

$$C_n(\mathbf{U})=F_n\left(F_{n1}^{-1}(u_1),\dots,F_{nd}^{-1}(u_d)\right) \quad (5.75)$$

where F_n and F_n^{-1} denote the p -th empirical cumulative distribution function and its generalized inverse, for $p=1,\dots,d$ and u is in the interval $[0;1]^d$.

Perhaps the simplest case of a copula model is the independent one. For independent variables, the joint distribution function of X is expressed as the product of their marginal distribution functions. Hence, considering two random independent variables x_1 and x_2 with $u=F(x_1)$ and $v=G(x_2)$, the independent copula can be defined according to Eq. (5.76).

$$C(u,v)=\prod(u,v)=uv \quad (5.76)$$

5.10.2.2 Elliptical copulas

Although the class of elliptical distributions provide a wide range of multivariate distributions [271] the present research only used the Gaussian copula and the t-copula, which are perhaps the most well-known copulas from this family. If $\Phi_R^{-1}(u)$ and $\Phi_R^{-1}(v)$ define the quantile functions associated with the normal standard distribution function Φ_R , where R is the correlation matrix, then the Gaussian copula is defined by Eq. (5.77):

$$C(u,v)=\Phi_R\left(\Phi^{-1}(u),\Phi^{-1}(v)\right) \quad (5.77)$$

The correlation matrix R is obtained with the Pearson coefficient between u and v . Similarly, the t-copula (5.78) can also be obtained from the multivariate version of the student-t distribution:

$$C_t(\mathbf{u})=t_{R,v}\left(t_v^{-1}(u),t_v^{-1}(v)\right) \quad (5.78)$$

where v is the degrees-of-freedom parameter and t_v^{-1} is the inverse of the univariate standard student-t distribution function. Also the $t_{R,v}$ is the multivariate standard-t distribution parametrized by the correlation matrix and the degrees-of-freedom as shown in [273].

5.10.2.3 Archimedean copulas

The Archimedean copulas are commonly used due to their straightforward application and many useful properties [125]. An Archimedean copula $C(u,v)$ exists if there is a convex, decreasing generator function $\varphi:[0,1]\rightarrow[0, \infty[$ such as $\varphi(1)=0$. Moreover this family presents the generic formulation, Eq. (5.79):

$$C(u,v)=\varphi^{-1}\{\varphi(u)+\varphi(v)\} \quad (5.79)$$

In the Archimedean copulas the relationship between the generator function and the Spearman's rho is sometimes not explicit. However, the association with Kendall's tau is often much simpler. According to [243] it can be obtained as in Eq. (5.80):

$$\tau_K=1+4\int_0^1\frac{\varphi(t)}{\varphi(t)}dt \quad (5.80)$$

Frank, Gumbel and Clayton copulas are usually identified as the most common copulas from the Archimedean family [125]. Like the Gaussian copula, these three are uniparametric. While Gumbel is a copula with upper tail dependence, the Clayton one has lower tail dependence. Frank copula has radial symmetry, i.e. neither lower nor upper tail dependence. Further details on copulas tail dependence are provided in [243]. These copulas are constructed as functions of the so-called copula parameter (θ), often estimated by means of the measure of dependence. The Gumbel copula has a parameter θ restricted on $[1, \infty[$ and is defined as in Eq. (5.81):

$$C(u,v)=\exp\left(-\left[(-\log(u))^\theta+(-\log(v))^\theta\right]^{1/\theta}\right) \quad (5.81)$$

Clayton copula has the parameter θ within the range of $] -1; \infty[\setminus 0$ and is defined by Eq. (5.82):

$$C(u,v)=\left[\max\{u^{-\theta}+v^{-\theta}-1\};0\right]^{-1/\theta} \quad (5.82)$$

Finally the Frank copula is obtained from Eq. (5.83) for any parameter θ belonging to $] -\infty;\infty[\setminus 0$.

$$C(u,v)=\left[\max\{u^{-\theta}+v^{-\theta}-1\};0\right]^{-1/\theta} \quad (5.83)$$

Table 5.2 provides the association between the parameter and the Kendall's tau. Moreover the upper and lower tail dependence coefficients (λ_U and λ_L , respectively) for each Archimedean copula are included [270].

All copula copula families used throughout the present work were implemented either with 'copula' and 'VineCopula' R packages software, detailed in [274, 275], and software MATLAB® software version R2016a (see [276] for software manual and specifications).

Table 5.2 – Relation between measures of dependence and the tail dependence coefficients for Archimedean copulas [270].

| Copula | τ_k | ρ_{spear} | λ_U | λ_L |
|---------|-----------------------------------|--|------------------------|-----------------|
| Gumbel | $\theta/(\theta + 2)$ | Complicated | 0 | $2^{-1/\theta}$ |
| Clayton | $1 - \theta^{-1}$ | No closed form | $2 \cdot 2^{1/\theta}$ | 0 |
| Frank | $1 + 4[D_1(\theta) - 1] / \theta$ | $\rho_{\text{spear}} = 1 - 12[D_2(-\theta) - D_1(-\theta)] / \theta$ | 0 | 0 |

$$D_k(\theta) = \frac{k}{\theta^k} \int_0^\theta \frac{t^k}{\exp(t) - 1} dt \quad \text{for } k = \{1, 2\}$$

5.10.3 Extra-parametrization of copulas

In order to build asymmetric copula-based models the extra-parametrization technique [261] can be applied to combine different copulas. This algorithm results in a new copula, with extra-parameters α and β , which retain the information regarding the asymmetry present in the (u, v) -space. If one considers the symmetric copulas $C_1(u, v)$ and $C_2(u, v)$, the new asymmetric copula $C(u, v)$ is obtained as in Eq. (5.84), according to [123]:

$$C(u, v) = C_1(u^\alpha; v^\beta) \times C_2(u^{1-\alpha}; v^{1-\beta}) \tag{5.84}$$

Note that if C_1 and C_2 have the parameters θ_1 and θ_2 , the new copula C will have four parameters, the ones that come from each parametric copula plus the pair $(\alpha; \beta)$. The parameters α and β may vary between 0 and 1. If α is different from β , $C(u, v)$ corresponds to an asymmetric copula [123]. Note that the resulting new copula can be combined with another one, say $A(u, v)$, which leads to a new set of parameters, thus the number of copula combinations is almost infinite [123]. However, there is no guaranty that the goodness-of-fit is improved with the number of copulas combined. Therefore, using the Crámer-von Mises distance, the Akaike Information criterion (AIC) [277], the Bayesian Information Criterion (BIC) [278] or other goodness-of-fit criteria should always be performed to understand if the complexity of the combinations is actually leading to better copula-based models.

In the present research, the estimation of the copula parameter (θ) is either made based on Kendall’s tau (τ_k) for cases where only one parameter is being addressed. For cases of copulas that are extra-parametrized or eventually compared with extra-parametrized copulas, the estimation of α , β and θ is performed as in [123] and [219], which seek for the minimum value of the Crámer-von Mises distance (s). The Crámer-von Mises distance is defined as the sum of the distances between the empirical copula and the parametric copula distribution function, over a grid of $[0; 1] \times [0; 1]$ as in Eq. (5.85), where u_i^* and v_i^* are the observations of the transformed variables $F_1(x_1)$ and $F_2(x_2)$, respectively. All calculations of s were performed for the referred grid with $100 \times 100 = 10\,000$ points, where the empirical and the tested copulas are evaluated.

$$s = \sum_{i=1}^N \left[C_n(u_i^*; v_i^*) - C_{\alpha, \beta, \theta}(u_i^*; v_i^*) \right]^2 \tag{5.85}$$

5.10.3.1 Extra-parametrization with an independent copula

Assume that C_1 is one of the copulas proposed in previous sections and that C_2 is an independent copula, referred to as $I(u^{1-\alpha}, v^{1-\beta})$. The independent copula yields $I(u^{1-\alpha}, v^{1-\beta}) = u^{1-\alpha} v^{1-\beta}$, which leads from Eq. (5.84) to Eq. (5.86):

$$C(u,v)=C_1(u^\alpha;v^\beta) \cdot I(u^{1-\alpha};v^{1-\beta})=C_1(u^\alpha;v^\beta) \times u^{1-\alpha} \times v^{1-\beta} \quad (5.86)$$

This procedure corresponds to the definition of a new asymmetric copula, which is extra-parametrized with an independent copula. For the tested copula-based models, one obtains a set of 3 parameters and the associated Crámer-von Mises distance.

5.10.3.2 Extra-parametrization with a pairwise copula

If one recalls Eq. (5.84) and assumes that $C_1(u,v)$ is coupled with a copula $C_2(u,v)$ of the same family, the Khoudraji algorithm can be applied to perform an extra-parametrization with pairwise copulas, e.g. Gumbel-Gumbel, Clayton-Clayton or Plackett-Plackett. In this case, the procedure is similar, but one needs to estimate the parameters of the first and the second copulas, respectively θ_1 and θ_2 . This leads to Eq. (5.87).

$$C(u,v)=C_{101}(u^\alpha;v^\beta) \times C_{102}(u^{1-\alpha};v^{1-\beta}) \quad (5.87)$$

5.10.4 AIC and BIC criterion

Besides the estimation of the copula parameters by means of the minimization of the Crámer-von Mises distance, the relative performance of the copula-based models may also be compared with the AIC and BIC criteria. Regarding the AIC and BIC criteria, the best model is the one that presents the lowest score [244]. This is also applicable to the negative loglikelihood evaluation. Although there is no consensus about the criterion that should be followed, both AIC and BIC are widely used in the literature, e.g. [258] or [279]. According to [280], BIC tends to perform better for large samples, while AIC is superior in small samples. The common formulation for the AIC and BIC criteria is presented in Eq. (5.88) and Eq. (5.89), where k is the number of parameters and n is the sample's size:

$$AIC=-2\loglikelihood + 2k \quad (5.88)$$

$$BIC=-2\loglikelihood + \ln(n) \times k \quad (5.89)$$

5.11 Conditional modelling approach

The conditional model used to estimate the joint distributions of wave heights and periods is a widely used model, particularly, due to its implementation in some of the most used offshore standards, namely, in [122] to account for environmental conditions and loads and in [220] for the reliability analysis of maritime structures. The conditional modelling approach estimates the joint density function as the product of a marginal distribution for the first parameter and a conditional distribution of the other parameter, given the first, as in Eq. (5.90), for $H_{si} > \gamma$.

Typically, the significant wave height is considered as the first parameter, due to its dominance in the loads calculation. Then the wave period (T) is modelled conditionally to the given value of H_s [123], Eq. (5.91), for $T_{wi} \geq 0$. The parameters $\mu_{T_{wi}(H_{si})}$ and $\sigma_{T_{wi}(H_{si})}$ are given by the mean and standard deviation values of T for a given value of H_s , respectively. Both parameters are estimated according to [122] (see [123] for further detail).

$$f_{H_s}(H_{s_i}) = \frac{\beta}{\alpha} \left(\frac{H_{s_i} - \gamma}{\alpha} \right)^{\beta-1} e^{-\left[\frac{H_{s_i} - \gamma}{\alpha} \right]^\beta} \quad (5.90)$$

$$f_{T_{wi}|H_s}(T_{wi}|H_{s_i}) = \frac{1}{T_{wi} \sqrt{2\pi} \sigma_{T_{wi}(H_{s_i})}} e^{-\left[\frac{(\ln(T_{wi}) - \mu_{T_{wi}(H_{s_i})})^2}{2(\sigma_{T_{wi}(H_{s_i})})^2} \right]} \quad (5.91)$$

For the purpose of this research, a 3-parameter Weibull distribution (with the parameters: scale - α , shape - β , location - γ) is assumed as the marginal distribution for significant wave height and a conditional log-normal distribution is assumed for the wave period (mean up-crossing or peak) with parameters conditional on the value of H_s . The implementation of the conditional modelling approach made in the present research follows the procedure given by [123].

The conditional model for the wave period is estimated by dividing the support of H_s into several shorter intervals and calculating the expected value and the standard deviation of the corresponding T (logarithm) within each interval. In this way one will obtain several pairs of wave heights and periods, which can then be used to perform the Monte Carlo simulations of the limit state function of a scour protection. The outcome might be sensitive to the size of the intervals of H_{s_i} . In the absence of further information bins of 0.5 m H_s are to be assumed by the reader. In order to avoid the possible generation of negative values of wave heights and periods the procedure described in [123] was adopted.

5.12 Kernel density estimation method

In sections 5.10 and 5.11 two parametric models have been addressed. However, non-parametric models are often used for further comparison with the parametric ones. This is due to the fact that the non-parametric models do not need a parameter estimation and they tend to be more flexible, thus more able to capture the sample's joint behaviour. However, they often do not present an explicit function of the modelled variables, which difficults the inference procedures. Also depending on the model and formulation used their predictive capacity outside the sample's range is limited. In the present thesis, when adequate, the kernel density estimation method was used to build a non-parametric model of the wave heights and periods.

Originally introduced by [281] and [282] the kernel density estimation method is one of the most used non-parametric models for multivariate analysis. The kernel density estimation has been consistently applied to describe statistical properties of oceanic waves, e.g. [251], [283] applied it to extreme significant heights, [284] applied this method to model the wave energy flux and power. Kernel density estimation does not assume any particular distribution, which is an advantage if the distribution is indeed not known a priori. Due to its flexibility the Bivariate Kernel Density Estimation method (BKDE) is expected to be as close as possible to the original dataset. However, this model also presents some disadvantages. For instance, one should bear in mind that the Kernel density estimation method strongly relies on the quality and quantity of the data available for the location of the scour protection. Therefore, it leads to an evaluation of the probabilities that may lose their actual meaning outside the sample's range. In the present study non-parametric estimation of the probability density function was performed using a bivariate kernel density estimation approach implemented in the MASS R package [285]. A detailed review on this method is provided in [269].

5.13 Conclusions

The present chapter provided the fundamental concepts related to the topic of reliability analysis. Moreover, the aspects related to the joint statistical modelling of correlated variables and their importance to simulate the limit state function of scour protections were also addressed. Throughout the present chapter, it was possible to note that the reliability methods are a crucial part of risk analysis of a system, as they enable the quantification of a measure of safety, i.e. in this case the probability of failure associated to a scour protection designed under a specific criterion. The methods and theory exposed in Chapter 5 provide the required theoretical knowledge to address the following questions (see section 5.1), which will be addressed for the case study of Horns Rev 3 offshore windfarm:

- How reliable is a scour protection?
- Are dynamic scour protections as reliable as the statically stable ones?

Scour protection design, particularly in marine environment, is not commonly addressed by means of risk and reliability analysis. Therefore, besides the lack of knowledge regarding the design of scour protections under waves and current combined, typically, no measure of safety is associated to the design of this crucial part of the foundation. The probability of failure of a scour protection provides a notion of how reliable the protection is, whilst enabling the comparison of scour protections designed according to different methodologies. Eventually, the optimization of a scour protection might be obtained if it is found that the novel design, e.g. [30] or [32], has a similar reliability level as a protection designed according to the traditional methodologies, e.g. [52] or [57]. Based on the fundamentals provided in Chapter 5 the following conclusions might be outlined:

- State-of-the-art of scour protection design does not provide methodologies that aim at a long-term probabilistic design of the protection, thus they do not provide a measure of safety associated to the protection;
- The design of a scour protection can be interpreted as a reliability problem, where the system is subjected to resistances and loads that may lead to its failure;
- The reliability of scour protections aims at quantifying the probability of failure associated to a certain design. The present research defines this as the chance of a certain design criterion not being met under random environmental conditions and only concerns to the failure mode “erosion of the top layer”;
- The limit state function associated to this failure mode might be based on the threshold of motion for statically stable scour protections, i.e. Eq. (5.53). For dynamic scour protections the limit state function might be associated to an acceptable damage number, as in Eq. (5.54);
- Several methods might be used to obtain the probability of failure. However, due to the high non-linearity in the formulations the shear stresses and the damage number, the use of approximate methods may lead to considerable errors in the assessment of the probability of failure. Also the direct integration methods may be difficult to apply, not only because of the complexity of the limit state functions, but also due to the number of basic random variables and their dependencies;
- The Monte Carlo simulation method was identified as a good starting point for a first application of reliability methods to scour protections. However, as a simulation method it requires that the basic random variables are statistically described, e.g. according to their probability density functions or cumulative distribution functions;
- At the present state-of-the-art, a full probabilistic model for scour protections is difficult to obtain. However, the correlation between the most important variables must be respected in order to properly simulate the limit state functions;

- In the present work, the joint models to account for correlated variables will be dedicated to the study of the significant wave height and the corresponding mean up-crossing or peak periods. This choice is related to their importance for both the calculation of the wave- and current-induced shear stresses and the damage number;
- The copula-based models were introduced, as they provide a fairly novel modelling technique, with a considerable potential to model asymmetric data, as the wave's characteristics;
- Also the Conditional Modelling Approach and the Kernel density estimation method were used for further analysis of the case study, due to their widely spread use in offshore engineering standards.

The fundamentals of reliability analysis and statistical modelling, presented throughout Chapter 5, correspond to a crucial part of risk quantification, which is yet to reach its mature state in terms of scour phenomena and scour protections design. The following Chapter 6 will provide the reliability analysis of dynamic scour protections, which includes the statistical modelling of the variables included in the limit state functions.

Reliability Analysis of Dynamic Scour Protections

6.1 Introduction

The reliability analysis of dynamic scour protections was performed for the met-ocean data available for Horns Rev 3 offshore windfarm. The present chapter addresses the reliability of scour protections based on the optimisation of the mean stone diameter of the armour layer, implemented through the methodology discussed in section 3.7.1.5 and experimentally studied in Chapter 4.

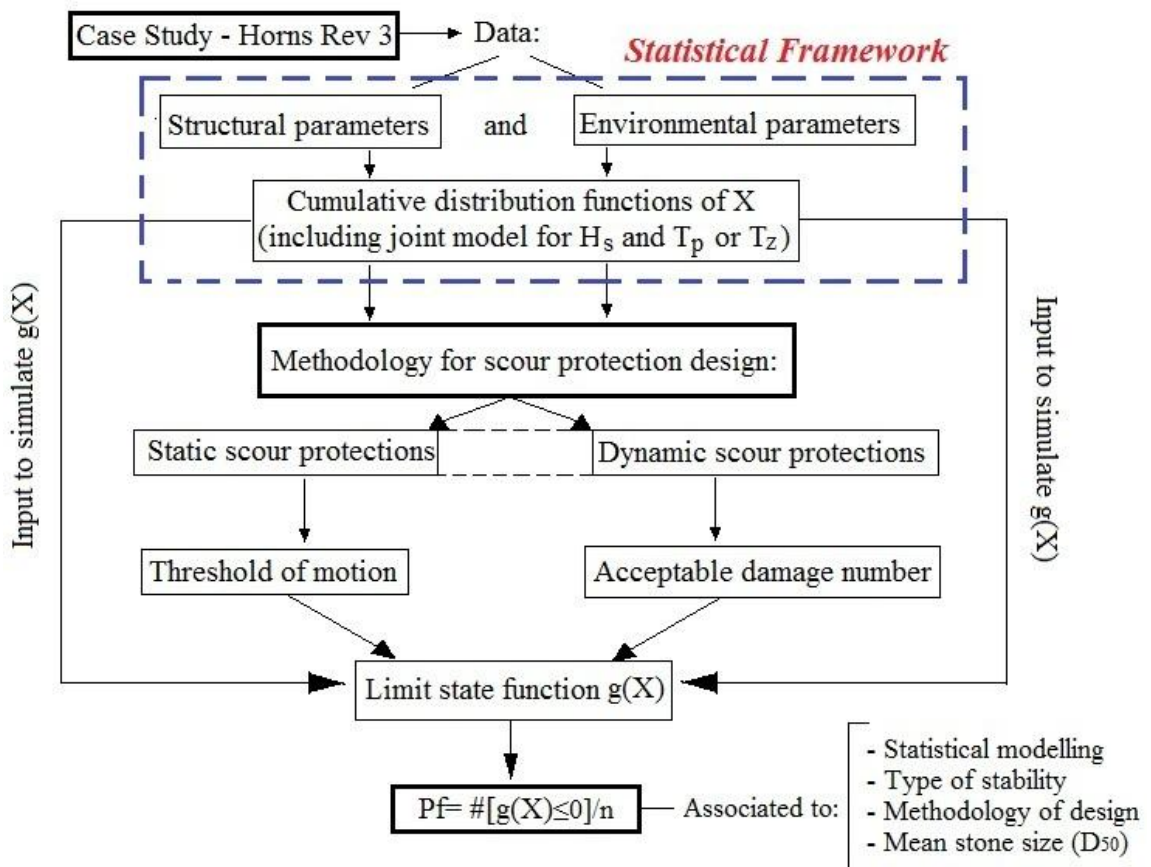


Figure 6.1 – Flow chart of the reliability analysis of scour protections and statistical framework.

The statistical framework and the statistical modelling of the basic random variables used for the reliability analysis is also presented, with a particular focus to the joint modelling of the significant wave height, the mean up-crossing period (T_z) and peak period (T_p). The data treated throughout the

present research is fully available in [286]. The flow chart regarding the reliability analysis presented in this chapter is provided in Figure 6.1, which also includes the static scour protections that will be further compared with the dynamic ones, in terms of their measure of safety (in Chapter 7).

In the previous Chapter 5 the introduction to reliability analysis was focused on two main goals (also see section 5.1):

- The multivariate modelling of the correlated variables;
- The safety measure of the system, i.e. the probability of failure.

The present chapter, in section 6.2, uses the Monte Carlo Simulation method to obtain and study the probabilities of failure of dynamic scour protections, based on the multivariate modelling of H_s and T_p , with simple and symmetric copula-based models. After this application, it was concluded that such models could be improved for future research purposes. Therefore, in section 6.3, some of the knowledge gaps concerning these models for met-ocean data are covered by means of the extra-parametrized copulas.

6.2 Reliability assessment of dynamic scour protections at Horns Rev 3 with copula models

During the course of the present research, an attempt was made to use simple copula-based models to assess the reliability of dynamic scour protections. This assessment is presented and discussed in the sub-sections of section 6.2. The main goal of this part of the study was to assess the following key aspects:

- Quantification and discussion of the probability of failure associated to the design methodology proposed by [32] for dynamic scour protections;
- Address the copula-based modelling of the correlation between the significant wave height (H_s) and the peak period (T_p) and the model effect on the probability of failure and;
- Determine the influence of the size of the records' length in the safety analysis of the scour protection.

6.2.1 Failure criterion of dynamic scour protections

The reliability analysis of dynamic scour protections was based on the limit state function from Eq. (5.54), which also relies on the application of Eq. (3.57) to predict the damage number of the scour protection under the simulated conditions. As discussed in Chapter 3 and 4, when developing the damage number formula the protection was considered to have failed when the filter was exposed over a minimum area of four armour units, i.e. equal to $4D_{50}^2$. This was the same criteria adopted for statically stable scour protections in [100]. [32] found that for $S_{3D} > 1$ the scour protections had failed. Still, the original results showed that the acceptable damage level was not immediately clear. This was addressed in Chapter 4, namely, in section 4.2.6.5, where the limits were validated and considered as being slightly conservative, thus being suitable for a rather conservative reliability assessment.

In order to have a meaningful estimate of the probabilities of failure, one would have to perform literally thousands of scour tests. This is unfeasible when dealing with physical models of marine scour protections, due to the cost and the number of hours needed per test, until the equilibrium profile is reached. Therefore, the failure criterion adopted in the present reliability study consisted on the comparison of the predictive formula Eq. (3.57) with the suggested limit $S_{3D\text{acceptable}}=1$, which leads to Eq. (6.1). The predictive formula combines several variables related to the loads acting on the protection, e.g. U_m , U_c or $T_{m-1,0}$, or to the structural resistance of the protection, e.g. D_{n50} or ρ_s .

Therefore, and despite the fact that it is being compared with a somehow deterministic limit ($S_{3D_{\text{accept}}}=1$), the formula does account for the variability in the loads and the resistance parameters of the protection, hence, being a suitable starting candidate to assess the reliability of a dynamically designed scour protection.

$$N^{b_0} \left(a_0 \frac{U_m^3 T_{m-1,0}^2}{\sqrt{gd} (s-1)^{\frac{3}{2}} D_{n50}^2} + a_1 \left(a_2 + a_3 \frac{\left(\frac{U_c}{w_s} \right)^2 (U_c + a_4 U_m)^2 \sqrt{d}}{g D_{n50}^{\frac{3}{2}}} \right) \right) < 1 \quad (6.1)$$

The lack of data regarding the scour and other phenomena related to the design of offshore wind turbines and their foundations always affects the choice regarding the $S_{3D_{\text{acceptable}}}$ used to define the failure criterion, thus influencing the outcome of the probabilities of failure. Likely due to confidential policies followed by the offshore wind industry, [32] points out that not many results are reported in the literature regarding the methods and the validation models.

Therefore, only a very restrict group of people has the knowledge and experience to design these protections. In this sense, this research also contributes for the discussion of a common ground to build a framework for reliability assessment of riprap systems, namely regarding the failure criterion and the associated limit state function.

6.2.2 Reliability assessment of dynamic scour protections

A dynamic scour protection placed around an offshore wind turbine foundation must be designed to be stable under combined waves and currents loading that may include extreme conditions. The failure mode due to the erosion of the top layer can be described by the limit state function in Eq. (6.2).

$$g(U_m; U_c; T_{m-1,0}; D_{n50}; \rho_s; \rho_w; d; g; w_s) = S_{3D_{\text{acceptable}}} - S_{3D_{\text{predicted}}} \quad (6.2)$$

The limit defined for the acceptable damage number can be interpreted as the maximum damage that can occur in the armour layer, without causing failure to the protection. On the other hand, the predicted damage is the expected damage caused by the environmental conditions acting on the top layer. This damage depends on the sea state characteristics, i.e. H_s and T_p , and also on the current's velocity, the water depth and other variables, which are random in nature.

Although not knowing the actual damage occurring in the top layer, one can assume that if the predicted damage exceeds acceptable damage, then safety measures must be taken to avoid the system failure. If the acceptable damage is defined as $S_{3D_{\text{acceptable}}}=1$, then the limit state function can be expressed as shown in Eq. (6.3).

$$g(U_m; U_c; T_{m-1,0}; D_{n50}; \rho_s; \rho_w; d; g; w_s) = 1 - S_{3D_{\text{predicted}}} \quad (6.3)$$

Each time the limit state function is negative ($g(X) \leq 0$) it means that the predicted damage is higher than the acceptable one, thus the protection may fail, since the design criterion is not being met. Conversely, if $g > 0$ the damage occurring is still complying the bearing capacity of the protection and the same is considered to be safe. In other words, considering X as the vector of variables stated in Eq. (6.3), the failure of the scour protection can be stated by Eq. (6.4).

$$g(\mathbf{X}) = \begin{cases} 1 - S_{3D\text{predicted}} \leq 0 & \text{system fails} \\ 1 - S_{3D\text{predicted}} > 0 & \text{system survives} \end{cases} \quad (6.4)$$

The probability of failure can be presented as the number of times that failure occurs over the number of times that the protection is subjected to the environmental conditions that may or may not lead to failure. If one could evaluate the limit state function repeatedly the probability of failure (P_f) would be expressed as in Eq. (5.40). When the number of simulations (n) tends to infinity the estimated probability of failure tends to its true value. This procedure was used to perform the reliability assessment for dynamic scour protection at Horns Rev 3 offshore windfarm.

6.2.3 Horns Rev 3 offshore windfarm

The data used to build the statistical model for the environmental variables, more specifically concerning the wave heights, the periods and the currents' velocity, was defined according to the environmental impact study regarding the Horns Rev 3 offshore wind farm [286]. This windfarm is located in the Danish sector of the North Sea, 20-35 km north-west of Blåvands Huk and 45-60 km from the city of Esbjerg [286] (Figure 6.2).

Horns Rev 3 is yet to be fully operational, it is planned to enter into full operational mode in 2019 [287]. This offshore windfarm has a total of 49 turbines of the type Vestas 164-8MW, with a capacity of 8.3 MW per turbine and a total installed capacity of 406.7 MW and estimated annual production of 1 700 000 MWh. The maximum height of the turbines is 187.1 m with a rotor blade length of 80 m and a rotor diameter of 187.1 m. The nacelle is 20.7 m long, 9.3 m high and 8.7 m wide. The rotor blade, the nacelle and the tower weights are equal to 33 t, 381 t and 350 t, respectively.

The foundation varies between 420 and 706 t. The cut-in speed is 4 m/s and the cut-out speed is 25 m/s. The distance between turbines varies between 1.1 and 1.5 km, thus no contraction scour between foundations is expected. According to [287] the total investment overcomes the amount of 7.5 billion DKK (Denmark Krone), at the present currency rates, roughly 1.01 billion €.

This area is relatively shallow and the water depth ranges closely from 10 m to 20 m. The local seabed is dominated by non-cohesive sands [288]. The position for met-ocean data sampling and modelling is reported in [286] and corresponds to the following coordinates: Latitude of 55.725°N and Longitude of 7.750°E. The hindcast modelling and validation of the met-ocean data was performed in [286] and [288], which are referred to for further detail. The present research is mainly focused on the correlated statistical modelling of the spectral parameters H_s and T_p . The available database resulted in a total of 90 553 pairs of significant spectral wave height and peak period. Moreover, the data available also included the values of mean up-crossing period (T_z), for the combined, the wind and the swell components.

This corresponds to an hourly output resolution within the period of 01-01-2003 to 01-05-2013, hereby designated as the 124 months dataset. Table 6.1 provides the data descriptive statistics for the referred coordinates. This information refers to the overall data, without any processing concerning seasonality, short-term dependence and wave direction. Seasonality and short-term dependence will be addressed during the discussion of the asymmetric copula models, whilst the wave direction was not analysed under the present research.

Table 6.1 – Descriptive statistics of the significant wave height and peak period at Horns Rev 3 offshore wind farm.

| | H_s (m) | T_p (s) | | H_s (m) | T_p (s) |
|---------------------------|-----------|-----------|-------------------------|-----------|-----------|
| Mean | 1.46 | 7.24 | Percentile 50% | 1.22 | 6.67 |
| Median | 1.22 | 6.67 | Percentile 75% | 1.85 | 8.59 |
| Standard deviation | 0.93 | 2.98 | Percentile 90% | 2.69 | 11.45 |
| Max | 6.11 | 21.61 | Percentile 99% | 4.78 | 16.28 |
| Min | 0.14 | 1.68 | Percentile 99.5% | 5.32 | 17.57 |
| Percentile 25% | 0.8 | 5.09 | Percentile 99.9% | 5.89 | 19.23 |

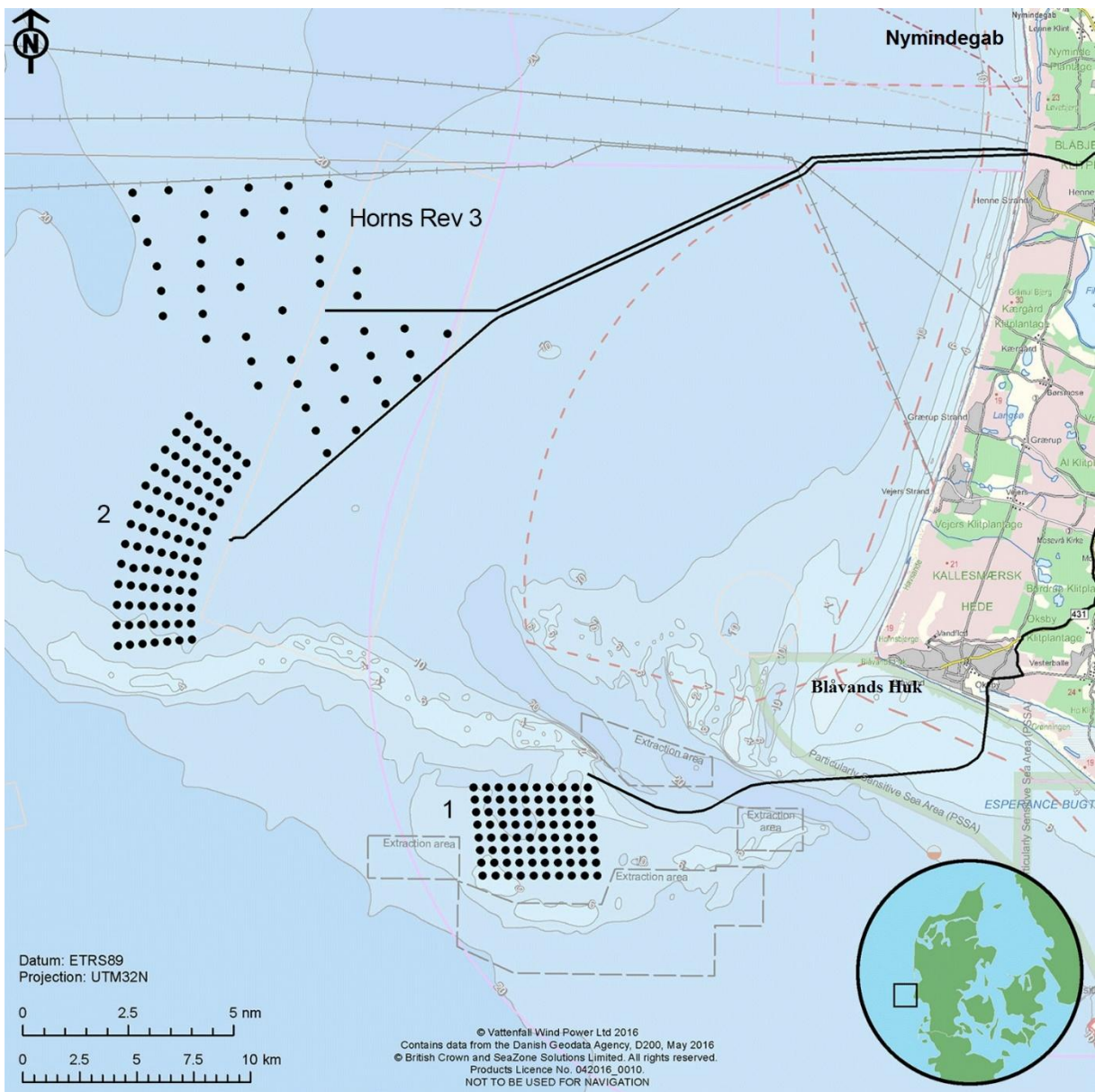


Figure 6.2 – Location of Horns Rev 3 at the Danish Sector of the North Sea [287].

Table 6.2 summarizes the information concerning the field data hindcast and validation used to the reliability assessment hereby presented. According to [286], the hindcast framework consisted in three models: DMI-HIRLAM (meteorological model), DMI-WAM (wave model) and DMI-HBM (3D hydrodynamic model). The characteristic values used for the statistical models are discussed in further sections.

Table 6.2 – Summary of the hindcast data characteristics and validation.

| Variable | Hindcast model; spatial and time resolution | Record duration | Hindcast validation | Output for the statistical modelling |
|----------------|---|-----------------|--|---|
| H_s T_p | DMI-WAM; 2 km; 1 hour | 124 months | 1 year of observations (2012) available from Nymindégab and Horns Rev 2 met mast. | Time series of (H_s ; T_p) |
| U_c | DMI-HBM; 5 km; 1 hour | 124 months | Currents verified by water level verification at coastal tide gauges (Esbjerg Havn and Hvide Sande Havn) | Current bottom velocity (m/s) |
| D_{50} | Non-applicable | Non-applicable | Non-applicable | Energinet Technical project description $D_{50}=[0.3m;0.5m]$ |
| Source | | [286] | | [286]; [289]; [290] |

6.2.4 Statistical model and Marginal distributions

As discussed in section 5.6, the development of a full probabilistic model is often difficult to obtain. Therefore, this statistical model considers 4 dimensions (T_p ; H_s ; D_{50} ; U_c). The other variables are simplified as deterministic ones or obtained through empirical approaches that mainly rely on these four dimensions. The present statistical framework is based on the following simplifications: U_c is an independent random variable and its statistical analysis is purely univariate; H_s and T_p are correlated and modelled by means of copula-based models. Table 6.3 provides a summary of the analysis performed and the correlations considered. In order to evaluate the sensitivity of the probabilities of failure to the lack of data, the reliability assessment was performed for the 124 months dataset and six other sub sets. The data were chronologically divided into periods of 62 months and 31 months, excluding the ending date (see

Table 6.4).

Table 6.3 – Summary of the statistical analysis and correlations.

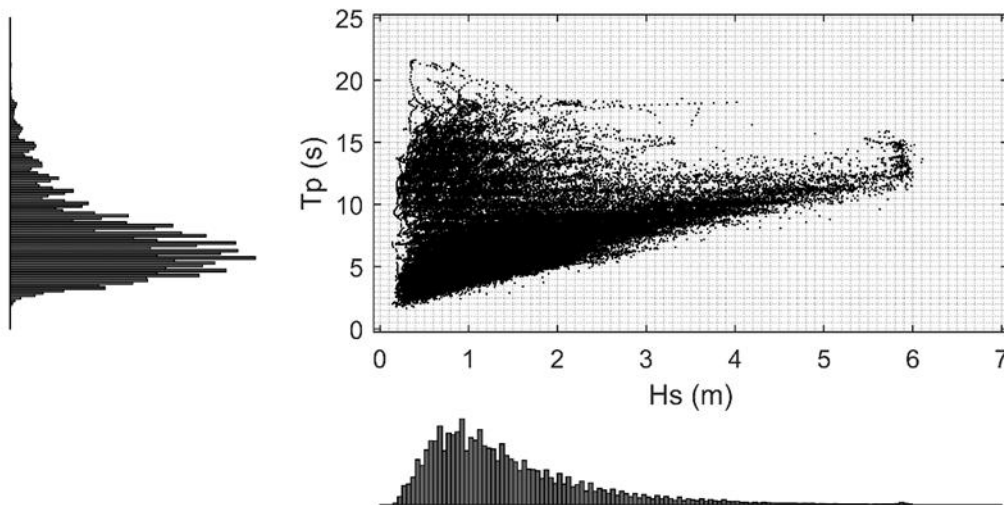
| Variable | Correlation | Type of statistical analysis | Dependence measure |
|----------------|--------------------------------|------------------------------|-----------------------------------|
| H_s T_p | H_s and T_p are correlated | Univariate and Multivariate | Kendall's tau ($\tau_K=0.3452$) |
| U_c | Independent | Univariate | Not applicable |
| D_{50} | Independent | Univariate | Not applicable |

Table 6.4 – Chronological division of the hindcast data into datasets of 62 and 31 months.

| Dataset | 124 | 62a | 62b | 31a | 31b | 31c | 31d |
|---------|------------|------------|------------|------------|------------|------------|------------|
| From | 01/01/2003 | 01/01/2003 | 01/03/2008 | 01/01/2003 | 01/08/2005 | 01/03/2008 | 01/10/2010 |
| To | 01/05/2013 | 01/03/2008 | 01/05/2013 | 01/08/2005 | 01/03/2008 | 01/10/2010 | 01/05/2013 |

6.2.4.1 Significant wave heights and peak period

Figure 6.3 provides the scatter diagram of the 124 months dataset (H_s ; T_p). A first look to the diagram shows that a lognormal behaviour could be expected, particularly regarding the wave heights. When dealing with wave heights, as H_s increases, the number of occurrences tends to decrease, since the variable is moving towards an extreme value. However, in the present case near $H_s=6$ m a concentration of occurrences seems to exist. The majority of the values are placed between 0.14 m and 3 m for significant wave heights and between 2 s and 15 s for the peak periods. Figure 6.3 indicates that smaller wave heights are correlated to smaller peak periods. The wave height increases with the period until a certain extent. The concentration of occurrences near 6 m, with peak periods ranging from 10 s to 15 s, leads to a small peak in the histogram's upper tail of H_s . Such behaviour may contribute to a worse goodness-of-fit, when attempting to fit the theoretical distributions. Nevertheless these values were included in the analysis of the marginal distributions.

Figure 6.3 – Scatter diagram and histograms of the 124 months dataset (H_s ; T_p) [223].

Several distributions were tested both for the significant wave height and the peak period, whose parameters are given in Table 6.5. In addition, the Kolmogorov-Smirnov and the Wasserstein distances were used to assess the goodness-of-fit associated to each marginal. Table 6.6 provides the Kolmogorov-Smirnov and the Wasserstein distances referred to the theoretical distribution assumed and the empirical cumulative distribution function. The lognormal distribution is the one providing the minimum distances for H_s and T_p , therefore, indicating this is the most reasonable distribution among the tested ones. Regarding the lognormal distribution, it was found that the best fit for the present dataset was obtained for the following parameters: $\log(\mu)$ of H_s equal to 0.193; $\log(\sigma)$ of H_s equal to 0.612; $\log(\mu)$ of T_p equal to 1.902; $\log(\sigma)$ of T_p equal to 0.393.

A final note on this matter concerns the limitations of the distributions' ability to accurately describe the physics of waves at the location of the scour protection. When fitting a theoretical statistical model to describe the wave's behaviour, it must be noted that the distribution chosen for the wave heights must be limited on the upper side. This is important because the random variables generated must still respect the physical constraints of the natural phenomena. One of the important aspects of ocean waves is the fact that their height might be limited by the water depth and bathymetry. In the present case, a simplified limit of $H/d \leq 0.78$ was adopted, in order to avoid unreasonable wave heights, randomly generated in the upper tail of the log-lognormal distribution. The factor of 0.78 is in fact considerably conservative, since [119] recommends this value for regular waves. The same source applies a factor of 0.6 for irregular waves. Moreover, this limit is applicable to the maximum wave height at a certain depth d (m). Here the analysis is focused on the significant wave height. Therefore considering the 0.78 limit is expected to contribute to a conservative assessment of the probabilities of failure. The reliability assessment presented in section 6.2.6, considers a damage number calculation assuming a JONSWAP spectrum ($\gamma=3.3$).

Table 6.5 – Parameters of the tested distributions for the 124 months data set of H_s and T_p .

| Marginal Distribution | H_s | | T_p | |
|-----------------------|-------------------|----------------------|-------------------|----------------------|
| | | | | |
| Exponential | $\nu=1.458$ | | $\nu =0.138$ | |
| Rayleigh | $R_p=1.223$ | | $R_p=5.535$ | |
| Normal | $\mu=1.460$ | $\sigma=0.932$ | $\mu=7.24$ | $\sigma=8.98$ |
| GEV | $\gamma=1.982$ | $\beta=-1.276$ | $\gamma=8.864$ | $\beta=3.680$ |
| Lognormal | $\log(\mu)=0.193$ | $\log(\sigma)=0.612$ | $\log(\mu)=1.902$ | $\log(\sigma)=0.393$ |
| GP | $\alpha=1.821$ | $\beta=-0.283$ | $\alpha =9.500$ | $\beta =-0.437$ |
| Weibull 2p | $\alpha=1.6452$ | $\beta=1.6951$ | $\alpha =8.1671$ | $\beta=2.5567$ |
| Weibull 3p | $\alpha=1.645$ | $\beta =1.695$ | $\alpha =8.167$ | $\beta =2.557$ |
| | | $\gamma=0.139$ | | $\gamma=1.673$ |

Table 6.6 – Kolmogorov-Smirnov and Wasserstein distances for the tested distributions.

| | KS | | WS | |
|-------------|-------|-------|-------|-------|
| | H_s | T_p | H_s | T_p |
| Normal | 0.117 | 0.095 | 0.217 | 0.598 |
| Exponential | 0.213 | 0.340 | 0.346 | 2.505 |
| Rayleigh | 0.113 | 0.139 | 0.182 | 0.634 |
| GEV | 0.222 | 0.171 | 0.371 | 1.115 |
| GP | 0.172 | 0.289 | 0.229 | 1.668 |
| Lognormal | 0.007 | 0.018 | 0.016 | 0.129 |
| Weibull 2p | 0.059 | 0.078 | 0.115 | 0.493 |
| Weibull 3p | 0.059 | 0.060 | 0.125 | 0.438 |

6.2.4.2 Current velocity

The Horns Rev 3 area is dominated by the tidal currents, which present a bimodal north-south directional distribution and large coherence between surface and bottom currents with the lack of annual variations [286]. In normal conditions the surface currents range from 0.2m/s to 0.4 m/s [286]. According to [286], the wind-induced currents in connection with surges are responsible for the extreme events. It was not possible to study the correlation or dependence measures between the waves and the current velocity, due to the lack of treatable data available. It was assumed that the currents were independent from waves, which is indeed a simplification of the probabilistic model.

Further studies should be performed to assess the influence of such correlation in the probabilities of failure. Moreover, the interaction between the wave direction and the current direction or even their seasonality should be the aim of further research. Note that this could also contribute to a more accurate description of the wave parameters, because the interaction between strong currents and waves leads to changes in wave heights and wave periods [122]. This is also discussed in Chapter 7.

[286] reports that often the waves and currents are orthogonal to each other. This is an important aspect, because, in the damage number calculated from Eq. (3.57), the waves and the currents are either following or opposing ones. Orthogonal directions are not considered in the present failure criterion. Here a simplified assumption was made considering only a positive (following) or negative (opposing) U_c . The analysis could be further improved to consider the different directions associated to both variables.

A Weibull distribution was applied to model the variable U_c . In the existence of historical or hindcast records, one should study the possible marginal distributions as previously done for the wave parameters. Taking into consideration the values reported in [286], one could say that the annual mean would be between 0.2 m/s and 0.6 m/s. The division between both classes was assumed as a suitable choice for the mean current velocity ($\mu_{U_c}=0.4\text{m/s}$). Since some values occur above the 0.6 m/s threshold, the standard deviation was assumed as $\sigma_{U_c}=0.2$ m/s. Note that more values occur between 0-0.2 m/s than above 0.6 m/s, so, assuming these values, one can derive the correspondent parameters of the Weibull distribution. Here the scale parameter is $\alpha= 0.453$ and the shape parameter is $\beta= 2.123$. For dynamic scour protections, once the random current velocities are generated, the following or opposing situation is defined by attributing a random factor of 1 or -1, respectively.

6.2.4.3 Water depth

In this case, a reference level of 18 m was adopted based on Figure 6.4. In normal conditions, depending on the tide and the wind, the sea level may vary from -1 m to 1m. Nevertheless, [286] records showed that a maximum variation of 2.40 m has occurred during the 2003-2013 period, with several other occurrences exceeding 1.5 m. This includes the effects of the astronomical tides, which present a maximum range 0.62 m, above and below the mean surface level relative to Geodetic Reference System 1980.

The water depth influences the scour severity but also the hydrodynamic parameters used in the failure criterion. A detailed study on this variable should be performed in real design situations. However, in benefit of a more parsimonious model, a deterministic value of 18 m is used for the case study presented in section 6.2.3. Future research should address this aspect to improve the generation of random variables to include the variation of the water depth for each pair of H_s and T_p .

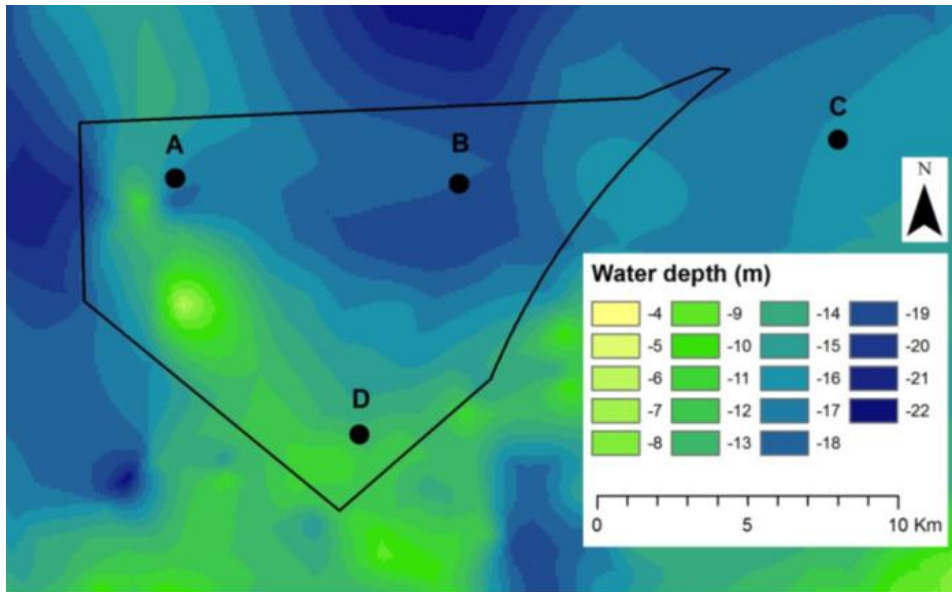


Figure 6.4 – Water depth at Horns Rev 3 [286].

6.2.4.4 Nominal mean stone diameter of the armour layer

Often the size of the rock material not only depends on the nearby availability or the transport costs, but it may also depend on technical aspects, such as the size of the available pipe vessels [26]. Therefore, the optimum solution is a result of multiple factors, which do not concern solely the size obtained according to a design criterion. As mentioned before, typically, the criterion establishes the minimum D_{n50} or D_{50} that ensures the stability of the armour layer (static or dynamic), associated to a particular specific weight of the rubble mound material. In this case, this variable is modelled with a certain degree of variability since the rock material will not present the same size for all units. On the other hand, the rock material is ordered for a specified grading curve, which means that very large deviations are unlikely to occur.

This research assumes that the diameter of the stones used in the armour layer ranges from 0.3 to 0.5 m, as indicated in [289]. Another important aspect is the uniformity parameter of the material, here obtained as $\sigma_U = D_{85}/D_{15}$, which also influences the results of the design criterion [1].

One can assume that the scour protection is designed for a target D_{50} and that the rock material should be as close as possible to this target value. In this perspective, the natural choice relies on using a uniformity parameter equal to 1, implying a perfectly uniform material.

However, note that if one assumes that the range [0.3; 0.5] m can correspond to the D_{15} and D_{85} limits, this would imply that $\sigma_U = 1.67$, which can still be considered close enough to assume that the material is uniform [83]. In the present case, σ_U is defined as 1.67. The D_{50} is modelled for a $\mu_{D50} = 0.4$ m. In order to ensure that the uniformity parameter is respected, a triangular distribution was adopted so that $[D_{15}; D_{85}] = [0.3; 0.5]$ (m). This leads to a triangular distribution centered at 0.4, which has a lower limit of 0.179 m and an upper limit of 0.621 m.

6.2.5 Joint models for significant wave heights and peak periods

6.2.5.1 Measures of dependence

Considering the 124 months dataset of H_s and T_p , the correlation between variables is given by $\tau_k=0.345$, i.e. there is a positive correlation, i.e. large significant wave heights are generally associated to large wave peak periods. Note that small wave heights (say up to 2 m) present a larger range of peak periods when compared with the large wave heights (say above 4 m), as shown in Figure 6.3. As the significant wave increases the variability of peak periods decreases. In terms of the scour protection, one expects that the small wave heights contribute less to failure situations, because they lead to smaller values of the orbital bottom velocity (U_m). On the other hand, the effect of peak periods might be harder to assess, because their influence is reflected in the numerator of the damage number and simultaneously in the denominator of U_m .

Despite the positive correlation showed by both dependence measures, the correlation at the upper tail (large wave heights and periods) may influence the probabilities of failure in a way that is not reflected by τ_k . Usually when dealing with the tails' behaviour, the tail dependence coefficients are a more reliable measure [243], as it will be discussed in further sections. The failure of the scour protection is usually associated to the occurrence of extreme wave heights. However, the occurrence of smaller wave heights with shorter or longer peak periods still influences the probability of failure. This occurs because the probability is dependent on the proportion of the extreme events and the so-called "normal sea-state conditions". The first main idea to withdraw from the value of τ_k is that the magnitude of this correlation is being affected by the dispersion associated to T_p and H_s , shown in Figure 6.3. No Peak Over Threshold was defined to limit the copulas' application to the extreme waves occurrences, because at this stage one aims at quantifying the probabilities of failure of the scour protection for the 124 months scenario, without excluding any data. Note that the approximately 10 years of data available, in a typical approach as the annual block maxima, leads to a dataset of 10 pairs, which is an irrelevant quantity for reliability purposes. When looking for extreme wave heights associated to a specific return period, say $H_{s100years}$, one could indeed filter the dataset to extreme data alone. This is not the case when looking for the probability of failure for a scour protection based on the 124 months. Note that the probability of failure computed from Monte-Carlo simulations performed only near the failure region, corresponds to the use of the adaptive sampling techniques discussed in section 5.4.3.2, which was not addressed within the practical scope of the present research.

The value obtained for τ_k is similar to the ones presented in other works, e.g. [123, 125, 238] and [254] that [254] that reported values of τ_k for several locations, ranging from 0.21 to 0.8. Ultimately, the measures of dependence may vary depending on the site characteristics and also on the data available. For further analysis, the measures of dependence were chronologically calculated for blocks of 62 months and 31 months and 31 months (referred to as datasets), the values are summarized in Table 6.7 (also see

Table 6.4). One can see that the first chronological half (62a) of the hindcast data presents higher dependence measures than the second one (62b). As expected the overall sample (124 months) captures the influence of the data's first and second half, meaning that τ_k is placed between the ones presented by the several blocks.

Table 6.7 – Measure of dependence, τ_k , per dataset.

| N° of months | 124 | 62a | 62b | 31a | 31b | 31c | 31d |
|--------------|--------|--------|--------|--------|--------|--------|--------|
| τ_k | 0.3452 | 0.3642 | 0.3231 | 0.3625 | 0.3659 | 0.3174 | 0.3289 |

6.2.5.2 Assessing dependence with graphical tools

In the present study, the Chi-plots were computed for random periods of 1, 6 and 12 months (Figure 6.5). The plots indicate a clear region where departures of independence occur. Therefore, the periods selected indicate that the independence between H_s and T_p is not a reasonable assumption, or else several points would be placed very close to the origin ($\lambda_i=0; \chi_i=0$). This is not the case for the periods analysed. Most of the points are placed in the positive region of χ_i , i.e. $\chi_i>0$. This fact is in agreement with the positive dependence noted in section 6.2.5.1.

Although the plots concern shorter periods than in the hindcast time series, they indicate that both variables should not be interpreted as independent. To the author knowledge, no works have been presented regarding the reliability assessment of marine scour protections, namely, focusing on the differences between considering these two variables as independent or correlated. This is an important aspect of reliability assessment, because the assumption of independence may lead to a considerable reduction of computation efforts when computing the probability of failure. However, these simplifications may come at a cost in terms of the accuracy of the probabilities of failure. The Kendall's plots (K-plots) were obtained for periods of 1, 6, 12 and 31 months.

The K-plots (Figure 6.6) clearly indicate departures from the 45° line, with the data located above the line. This fact confirms that there is a positive dependence between H_s and T_p . This fact agrees with the information given by the Chi-plots. The 1 month and 6 months plots present fewer values on the right side of the charts. This was expected since the shorter periods are less likely to “catch” the extreme values of wave heights. Moreover, at the same region of the charts occasional occurrences seem to appear below the independence line. However, it seems reasonable to assume that the positive dependence exists and its effect should be accounted for when performing the reliability assessment.

Regarding the dependence of the wave parameters, another aspect that should be mentioned is the difference between reliability design and the traditional design approaches that tend to consider extreme wave events as independent from each other. Traditional maritime design approaches, e.g. [42] or [122], account for the design wave height associated to a specific return period. Typical design of scour protections is no exception, e.g. [30] or [100]. The concept of return period (T_r) is usually associated to the definition of an extreme event that occurs in a periodical manner. For example, one could use the 100 years significant wave height (H_{s100}), which is associated to $T_r=100$ years. In this case, assuming that two of these events are not dependent is reasonable. It is very unlikely that they might occur in a very short period (say 1 day or even 1 month). Even if they occur in the same chronological year, the short-term dependence is reduced if they are not occurring in consecutive days or within the same storm event.

When performing reliability design this is not the case. One is designing the protection in association with a specific probability of failure, which is estimated for the overall population of significant wave heights, regardless of the periodical occurrence of each one of them. In this sense, not only the temporal dependence between the waves is important, but it is also crucial the analysis of the dependence between the wave height and wave period, because it is their combined effect that may lead to a failure or not.

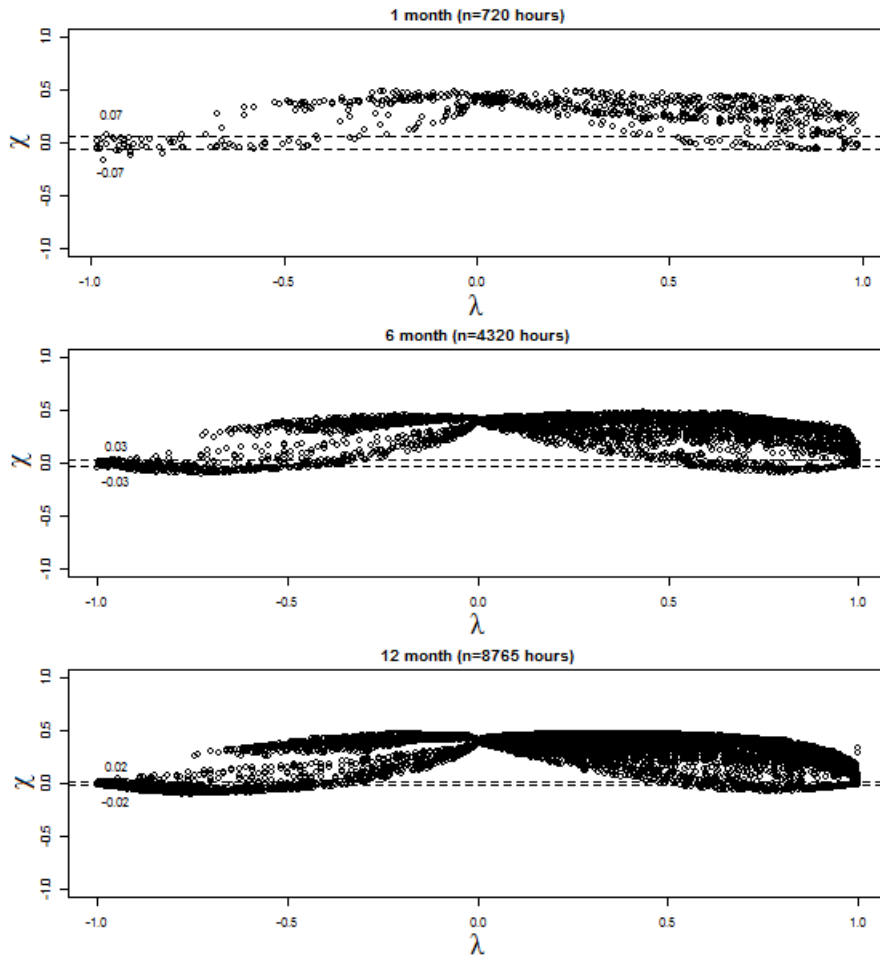


Figure 6.5 – Chi-plots ($\lambda_i; \chi_i$) for 1, 6 and 12 months randomly selected from the 124 months dataset.

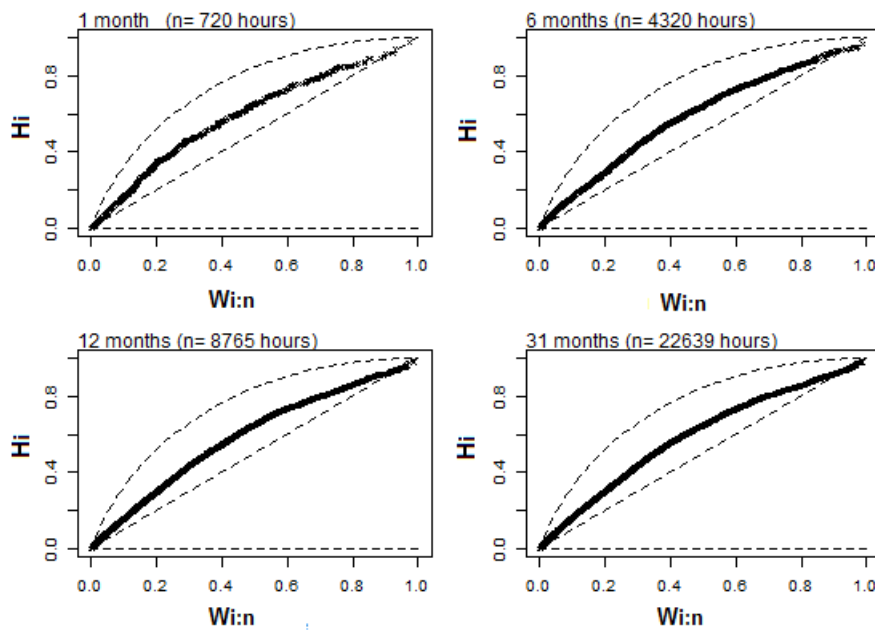


Figure 6.6 – Kendall plots for 1, 6, 12 and 31 months randomly selected from the 124 months dataset.

6.2.5.3 Independent copula and Bivariate Kernel density estimation method (BKDE)

As reference models, the Independent copula and the bivariate Kernel Density Estimation method (BKDE) were applied. The independent copula assumes that H_s and T_p follow a lognormal distribution with the previously mentioned parameters (section 6.2.4.1), but without any correlation. This will be crucial to assess the probabilities of failure under the independence assumption. It is expected that this simplification provides different probabilities of failure, when compared to the other models that account for the correlation between the spectral parameters.

This research identified a literature gap in the reliability assessment and design of scour protections, namely the ones designed for marine environment with a dynamic criterion. However, the independence of other environmental variables and parameters has been studied in several works related to current induced scour. For instance, [37] and [39] performed a reliability assessment of scour phenomena at bridge piers. Both works concluded that considering the environmental variables as independent ones led to an over-estimation of the probabilities of failure. Nevertheless, scour at bridge piers is current induced, while scour at marine structures can be either wave or current dominated. Therefore, it is important to assess the effects of correlation in the probabilities of failure to analyse if the remarks made by [37] and [39] still hold for scour protections at offshore monopile foundations. Although in theory the independent copula is not a true model to represent the joint distribution T_p and H_s , it may lead to conservative values of P_f , when compared to other copulas, hence providing a simpler and quicker evaluation of the protection's reliability. The BKDE model does not assume any theoretical distribution of H_s or T_p . However, it provides a model as close as possible to the hindcast data sample.

Figure 6.7 provides a random sample of 10 000 pairs (H_s ; T_p) from the independent copula, imposed over the 124 months dataset. The comparison does not correspond a perfect match, because the correlation between both spectral parameters is not being considered. Moreover, the copula generation is "blind" in terms of the maximum significant wave height and the associated peak period. To account for the fact that wave heights can be depth limited, the present generation algorithm accounts for a maximum wave height of 0.78 times the water depth (18 m). This is applied to all models. Nevertheless, the main idea to retain is that the models fitted may provide wave heights that are overestimated but, from the practical point of view, this leads to a conservative assessment of the reliability, i.e. an over-estimation of the probability of failure. The independent copula presented a significantly different upper tail when compared to the 124 months dataset. Above H_s equal to 3 m, this copula provided larger values for the significant wave height and lower values for the peak period, when compared with the dataset. The direct effect of overestimated significant wave heights and under-estimated peak periods on the damage number of the scour protection is not simple to analyse. Note that the damage number formula, Eq. (3.57) is related to the orbital bottom velocity, which indirectly depends on H_s and T_p . Intuitively, one could think that large wave heights with short periods tend to increase the shear stress on the armour layer, hence, producing a high damage rate and eventually failure, i.e. the possible exceedance of the acceptable damage number.

The wave-induced shear stress depends on U_m^2 . However, the influence of the wave period on the wave friction factor (f_w) depends on a power law with respect to $A=(U_m.T_p)/(2\pi)$. Several authors studied and proposed an equation of the type $f_w=C.(A/k_s)B$, where C is a constant and k_s is the bottom roughness as computed in [30]. The B constant also assumes different values depending on the ratio A/k_s . For example, [52] uses $B=0.52$, [57] suggest -0.25 for $A/k_s>50$, while [58] suggest -0.8 for $0.2<A/k_s<10$. This leads to the conclusion that the influence of T_p in the wave induced shear stress is very much dependent on the formulation applied to calculate the friction factor.

Due to these physical dependencies it is harder to predict the influence of the wave parameters in the reliability of the scour protection. Moreover, several pairs appear outside the original data near the upper tail, where the failure domain is more likely to be. In Figure 6.8, a sample of 10 000 pairs (H_s ; T_p) from the BKDE was plotted over the original hindcast data (124 months dataset). One can see that the kernel density estimation provides close values to the 124 months dataset. Due to its empiric nature, the BKDE method is not able to provide values much higher than 6 m for the significant wave height and 22 s for the wave period. This method is important as it can be related to an empiric probability of failure, i.e. estimated from the available data.

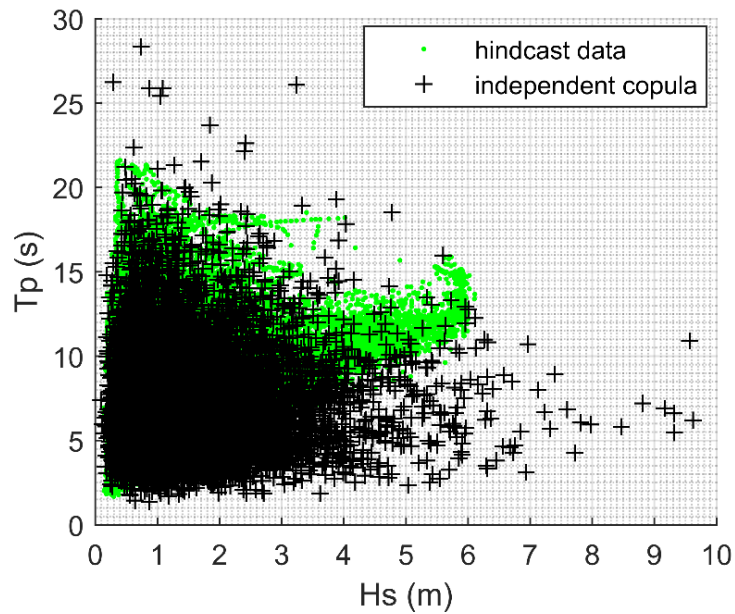


Figure 6.7 – Random sample of 10 000 pairs of H_s and T_p from the independent copula over the 124 months of hindcast data.

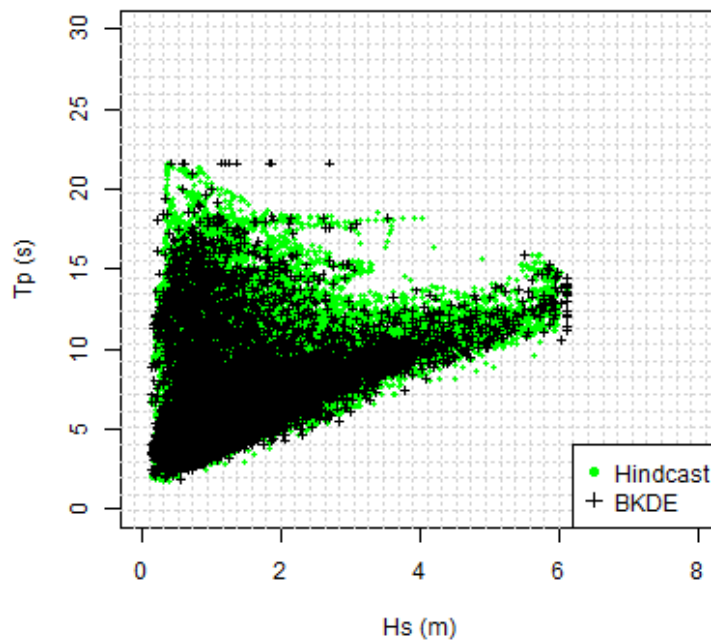


Figure 6.8 – Random sample of 10 000 pairs of H_s and T_p from the independent copula over the 124 months of hindcast data.

6.2.5.4 Copula-based models

For this first assessment of the reliability of scour protections, and in addition to the reference models, two copulas from the elliptical family were applied: the Gaussian (Normal) and the t-copula. Three widely used Archimedean copulas were implemented, namely the Frank, Gumbel and Clayton copulas. Due to their straightforward application these copulas were chosen with the purpose of describing the joint probability of significant wave heights and peak periods. Moreover, the Tawn type 2 copula was applied due to its flexibility and non-symmetry when compared with the previously mentioned ones. This has proven to be an important factor to achieve a better goodness-of-fit with the datasets. It was observed that the symmetric tested copulas did not capture the asymmetry present in the hindcast data.

One should note that more complex copulas could be used, e.g. [123] or [219]. However, the present research sets the first steps to perform a reliability assessment of scour protections, with a copula-based model applied to the sea-state parameters. Note that copula-based models have not been extended to the reliability analysis of scour protections. Therefore, it seems reasonable to start by using these examples, which rely on their simplicity and low number of estimated parameters.

The aforementioned copulas were applied for the several datasets defined in Table 6.7, ultimately leading to different values of the probability of failure, because the copula parameters are estimated with different quantities of data. In this application, the copula parameters were estimated according to its relationship with τ_K by means of the maximum likelihood estimation [244], with R software, using the “Icopula” package [291]. The parameters of each copula, by dataset, are presented in Table 6.8. Figure 6.9 and Figure 6.10 provide a random sample of 10 000 pairs of significant wave heights and peak periods (H_s ; T_p) from the Gaussian and t-copula compared with the original data (124 months).

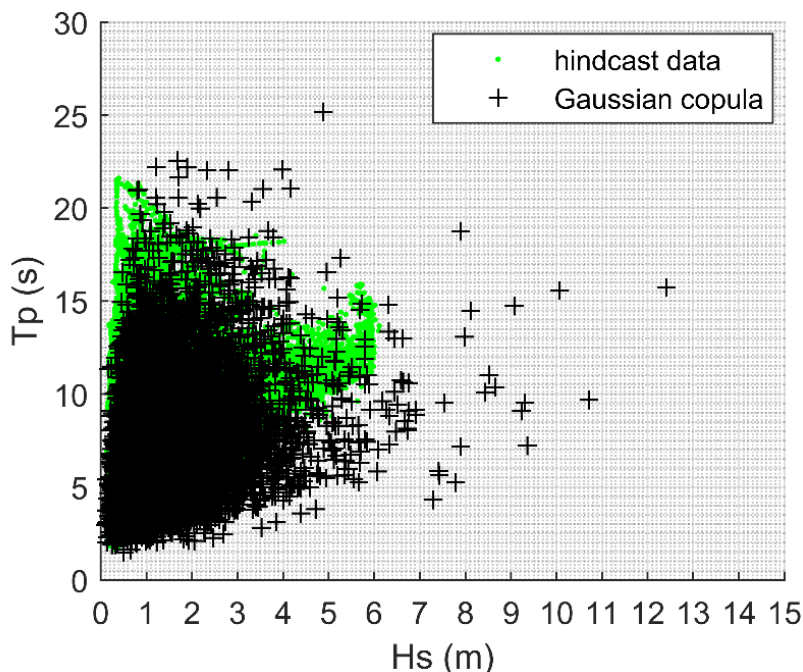


Figure 6.9 – Random sample of 10 000 pairs of H_s and T_p from the Gaussian copula over the 124 months of hindcast data.

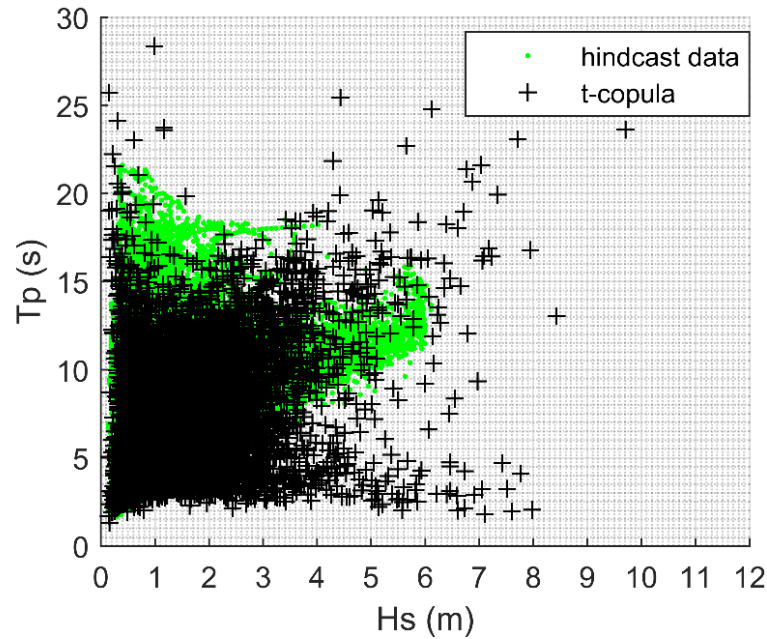


Figure 6.10 – Random sample of 10 000 pairs of H_s and T_p from the t-copula over the 124 months of hindcast data.

In a similar way to the independent copula, the elliptical copulas predict significant wave heights above 6 m and peak periods that exceed the 25 s. It seems reasonable to assume that these cases may contribute for the failure of the scour protection, thus increasing the probability of failure when compared to the empiric estimation performed based on the BKDE.

On the other hand, it is possible to note that several waves above 3 m are occurring with lower peak periods, than the ones presented by the hindcast data. As mentioned previously, it is hard to assess the combined effect of T_p and H_s in the damage number of the protection. Nevertheless, both copulas seem to provide several pairs that correspond to waves in the range of $H_s=[0;4]$ (m) and $T_p=[0;25]$ (s).

These waves alone are not expected to contribute to the protection's failure, although, the cumulative effects of long sequences of waves are yet to be deeply understood. For example, a long duration storm of waves with 4 m, may lead to the failure of the protection due to damage accumulation, even without the occurrence of a major wave, e.g. 6 m or higher

Although this is not the focus of the present research, the author notes that the present concept of probability of failure concerns the general occurrence of extreme events within the overall population of waves. Still the probability of failure within the occurrence of a sequence of intermediate wave heights should be the aim of further research. The failure due to sequences of waves opposed to the one caused by extreme events is still closely related to the technical and scientific knowledge gaps regarding the long-term evolution of damage, discussed in Chapter 4, namely in, section 4.2.6.3.7.

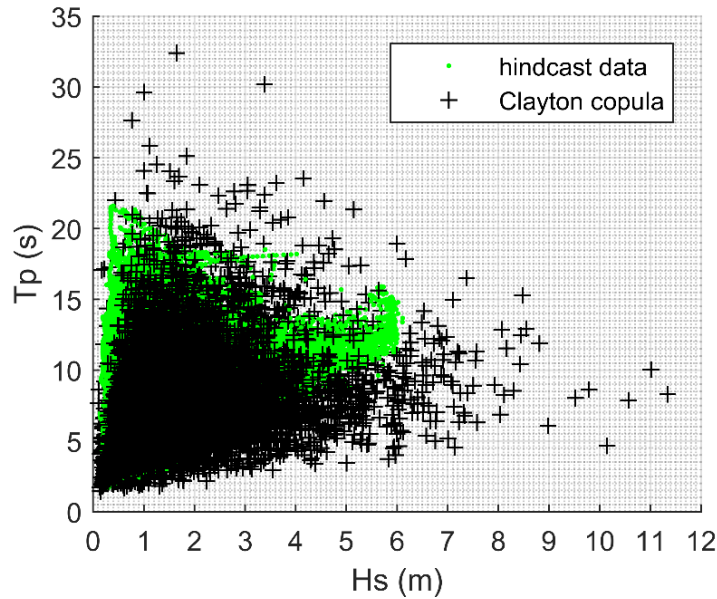


Figure 6.11 – Random sample of 10 000 pairs of H_s and T_p from the Clayton copula over the 124 months of hindcast data.

The visual assessment of Figure 6.10 and Figure 6.11 indicates a poor fitting when the peak periods and the significant wave heights increase. The fit improves when the peak periods and the significant wave heights are small. For $H_s > 4$ m the tendency to provide larger waves with shorter periods than the ones provided by the original data seems clear. This is evident for the Gaussian (Figure 6.9), the Clayton (Figure 6.11) and the Frank copula (Figure 6.12). This fact is not so evident in the t-copula (Figure 6.10) and the Gumbel copula (Figure 6.13), which present several points above and below the right tail of the original data. These models provided a considerable dispersion when compared with the original hindcast data (124 months dataset). This dispersion is also extended to the other datasets, i.e. the datasets of 62 and 31 months.

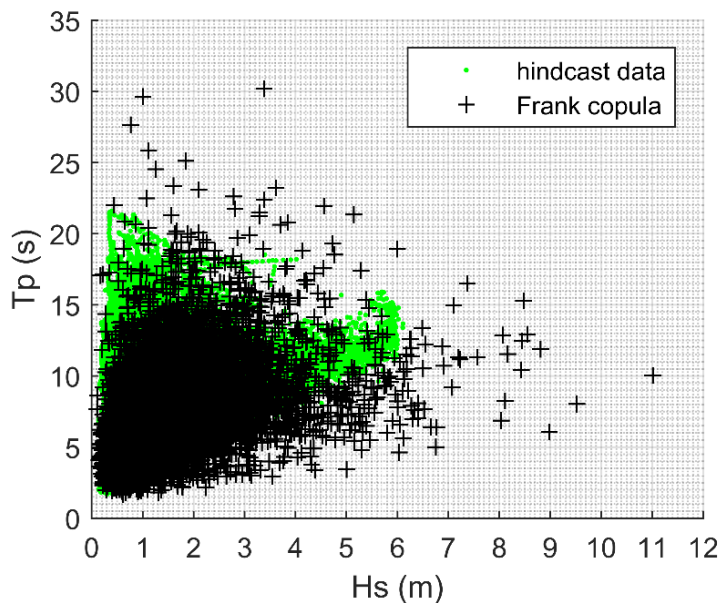


Figure 6.12 – Random sample of 10 000 pairs of H_s and T_p from the Frank copula over the 124 months of hindcast data.

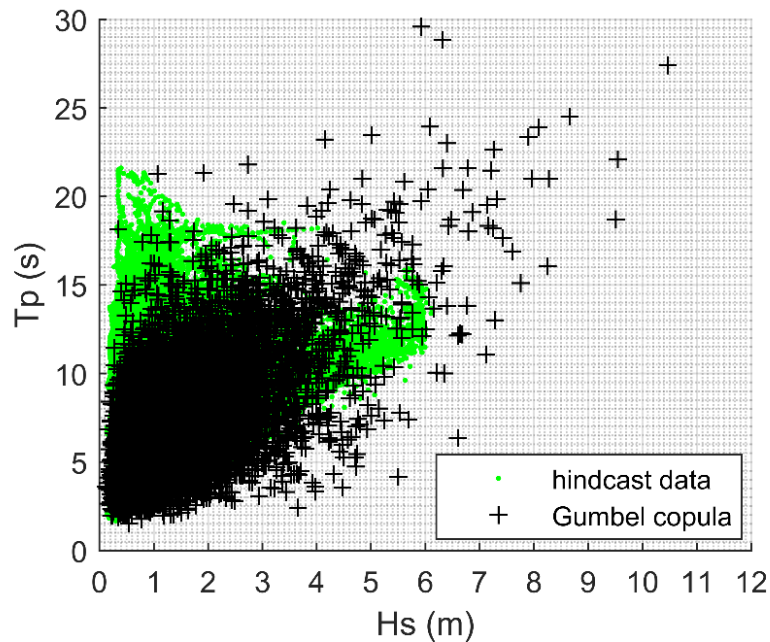


Figure 6.13 – Random sample of 10 000 pairs of H_s and T_p from the Gumbel copula over the 124 months of hindcast data.

The use of more complex models could lead to a better fit between the datasets and the simulated data, e.g. [123]. Still, the copulas presented so far have been applied with a reasonable degree of success in other studies, namely when modelling single storms with multivariate Archimedean copulas [258].

Also [238] successfully used the Gaussian and t-copula to estimate the wave height records through spatial correlation at the south coast of England. Still using the same Elliptical and Archimedean copulas (Clayton, Frank and Gumbel), [259] found that Gaussian and Gumbel copulas could accurately fit the empirical densities of the individual wave steepness and height.

However, as stated by [123] and re-confirmed in the present study and very recently addressed by [292], it is far from straightforward to find a good copula-based model for non-symmetric data, such as significant wave height and wave period. The graphical assessment of these two families of copulas indicate that they are closer to the independent copula than they are to the BKDE model. This was already expected because these copulas do not perform well under non-symmetric data.

Since the Archimedean and Elliptical copulas did not seem to fit the datasets in a satisfactory way, the non-symmetric copula Tawn type 2 was used in this first assessment of the reliability of dynamic scour protections (Figure 6.14). Full details on the formulation of this 3-parameter copula are provided in [293] and it was implemented as in [275].

Due to its higher “flexibility”, when compared with the previous models, this copula seemed to be a reasonable candidate for fitting purposes. As it will be addressed in further sections, this model showed significant improvements in the AIC and BIC criteria. As it is perceivable from Figure 6.14, the fit between this copula and the 124 months dataset appears to be considerably better than the previous ones.

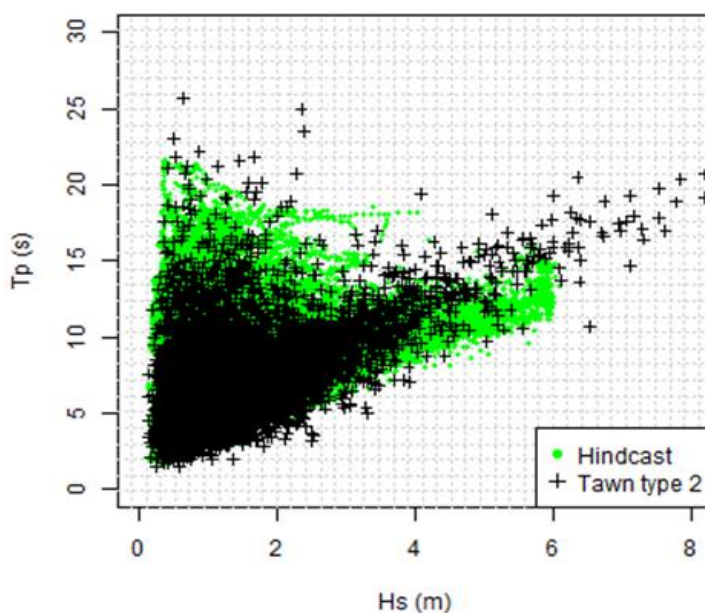


Figure 6.14 – Random sample of 10 000 pairs of H_s and T_p from the Tawn type 2 copula over the 124 months of hindcast data.

The analysis performed with the Tawn type 2 copula showed that the asymmetry of the datasets with 31 and 62 months was also captured. On the upper tail, the generated data showed a tendency to present higher significant wave heights and periods than the original data (Figure 6.14). This behaviour opposes the one showed by the Clayton, the Frank and the Gaussian copulas. In the lower tail the generated values appear to be in a relatively good agreement with the original data, when compared with the remaining copulas.

The main idea to retain is that for each specific case one should study several possible models and then make an informed decision. State-of-the-art indicates that modelling significant wave heights and peak spectral periods strongly depends on the copula and the dependence measures used. Therefore, a case-by-case approach should be adopted. [125] pointed the relevance of selecting an appropriate model that best represents the dependence structure of the significant wave heights and peak periods. The visual analysis gave clues on the fact the Tawn type 2 copula seems to be a good candidate to model the wave parameters for reliability analysis. Moreover, it is perceived that the asymmetry of the data is a key aspect when addressing the joint models for met-ocean data.

6.2.5.5 AIC and BIC criteria

Table 6.8 provides the values obtained for the whole datasets, by means of the maximum likelihood estimation method. The AIC and BIC results pointed the Tawn type 2 as the copula with the lowest AIC and BIC values for all the datasets. This fact confirms the visual analysis of the copulas performed previously. The Frank copula provided the best scores for dataset 31b when compared with the other Archimedean and Elliptical copulas. However, the t-copula was the second best model for the datasets 62a, 62b, 31a, 31c and 31d, both with AIC and BIC criteria.

In the present case, there is a consistency in the fact that the Tawn type 2 copula provided the best results. However, one should keep in mind that this may not hold for other samples from different locations than the one studied in this thesis. Regarding other applications of copula-based models and due to the lack of a “rule of thumb” to choose the better one, a reasonable approach is to apply more

than one criterion and to select the model that provides the overall best scores, as performed in this study.

Table 6.8 – Copula parameters and AIC and BIC criteria used to select the best model for each dataset.

| Copula | | Dataset (by months) | | | | | | |
|------------------|------------------|---------------------|--------|--------|-------|--------|-------|-------|
| | | 124 | 62a | 62b | 31a | 31b | 31c | 31d |
| Gaussian copula | θ | 0.42 | 0.44 | 0.4 | 0.44 | 0.43 | 0.39 | 0.42 |
| | AIC | -17593 | -10190 | -7439 | -5315 | -4873 | -3593 | -3858 |
| | BIC | -17584 | -10181 | -7430 | -5306 | -4864 | -3584 | -3848 |
| Student t copula | θ | 0.46 | 0.47 | 0.44 | 0.47 | 0.47 | 0.45 | 0.44 |
| | ν | 5.75 | 6.05 | 5.45 | 6.02 | 6.07 | 4.84 | 6.42 |
| | AIC | -21933 | -12324 | -9636 | -6414 | -5906 | -5079 | -4583 |
| | BIC | -21914 | -12305 | -9617 | -6395 | -5888 | -5060 | -4564 |
| Clayton copula | θ | 0.68 | 0.71 | 0.64 | 0.67 | 0.76 | 0.6 | 0.69 |
| | AIC | -19306 | -10839 | -8501 | -5438 | -5433 | -4299 | -4235 |
| | BIC | -19296 | -10830 | -8491 | -5429 | -5423 | -4290 | -4225 |
| Frank copula | θ | 3.23 | 3.39 | 3.07 | 3.35 | 3.43 | 3.13 | 3.01 |
| | AIC | -21606 | -12279 | -9375 | -6233 | -6046 | -4808 | -4569 |
| | BIC | -21597 | -12270 | -9365 | -6224 | -6037 | -4798 | -4559 |
| Gumbel copula | θ | 1.35 | 1.36 | 1.34 | 1.38 | 1.34 | 1.36 | 1.33 |
| | AIC | -14740 | -8341 | -6404 | -4535 | -3821 | -3271 | -3138 |
| | BIC | -14731 | -8332 | -6394 | -4526 | -3811 | -3262 | -3128 |
| Tawn type 2 | θ | 3.03 | 3.15 | 2.90 | 3.01 | 3.28 | 2.74 | 3.03 |
| | $\hat{\epsilon}$ | 0.37 | 0.38 | 0.35 | 0.38 | 0.39 | 0.34 | 0.36 |
| | ξ | 1 | 1 | 1 | 1 | 1 | 1 | 1 |
| | AIC | -40312 | -22068 | -17959 | -9989 | -11955 | -8189 | -9757 |
| | BIC | -40294 | -22051 | -17942 | -9973 | -11939 | -8173 | -9741 |

6.2.6 Probability of failure of dynamic scour protections

6.2.6.1 Validation and comparison of results

The values obtained from the hindcast data show that the maximum values for H_s and T_p were respectively 6.11 m and 21.61 s (Figure 6.3). However, the copula models may lead to considerably larger values than these ones. The following underlying question seems to be reasonable: are the copula-based models wrong? One cannot simply provide a straight answer to this question. Therefore, hoping to understand the accuracy of the copula-based models, an application was performed by means of three theoretical examples. The first one considering a situation A where the probabilities of failure are expected to be “low” (say in the order of 10^{-3}), the second one related to “high” probabilities of failure (in order of 10^{-1}), i.e. situation B. Then a third example was designed to obtain an intermediate P_f (in the order of 10^{-2}), i.e. situation C. The aim of these examples is to assess if the copulas-based models are at least providing probabilities of failure, which are in the same order of the one presented by the non-parametric model (BKDE). Moreover, these examples enable one to analyse how the probability of failure is varying depending on the model used. The situations considered in order to force the low, the high and the intermediate probabilities of failure are summarized in Table 6.9.

If the models are at least roughly accurate, the probabilities should have the same order of magnitude, after a considerable number of simulations of the function $g(X)$. In situation A, the values of H_s and T_p are reduced and the acceptable limit for the damage number is 1. In addition, the mean value of D_{50} (0.6 m) is increased to ensure that harshest hydrodynamic conditions are needed in order to cause high values of the damage number. The current velocity is also dropped to 0.1 m/s with a standard deviation of 0.05 m/s. In situation B, the failure rate is increased by considering a high current velocity (2 m/s) with a standard deviation of 0.2 m/s. The adopted D_{50} corresponds to 0.4 m. While the maximum wave peak period is maintained as 22 s the significant wave height is increased to a maximum of 6 m, which is roughly the maximum value expected from the hindcast data and the BKDE model. Figure 6.15, Figure 6.16 and Figure 6.17 give the failure probabilities according to the number of Monte-Carlo simulations (n) for the 124 months dataset, calculated from Eq. (5.40).

Table 6.9 – Simulation conditions for situation A, B and C.

| Situation | A – Low P_f | B – High P_f | C – Intermediate P_f |
|----------------------------|------------------------------------|---------------------------------|-----------------------------------|
| H_{smax} (m) | 4 | 6 | 6 |
| T_{pmax} (s) | 22 | 22 | 22 |
| d (m) | 10 | 10 | 10 |
| U_c (m/s) | $\mu_{U_c}=0.1; \sigma_{U_c}=0.05$ | $\mu_{U_c}=2; \sigma_{U_c}=0.2$ | $\mu_{U_c}=0.4; \sigma_{U_c}=0.2$ |
| D_{50} (m) | 0.6 | 0.4 | 0.4 |
| p_s (kg/m ³) | 2650 | 2650 | 2650 |
| p_w (kg/m ³) | 1025 | 1025 | 1025 |
| N (number of waves) | 3000 | 3000 | 3000 |
| g (m/s ²) | 9.81 | 9.81 | 9.81 |
| $S_{3Dacceptable}$ (-) | 1 | 0.25 | 1 |
| $g(x)$ (-) | $1 - S_{3Dpredicted}$ | $0.25 - S_{3Dpredicted}$ | $1 - S_{3Dpredicted}$ |

The three situations indicate that the obtained probabilities of failure seem to be stable after a number of simulations $n=200\ 000$. Although some variations may occur within each model, the P_f does not change in its order of magnitude. These variations seem to be more noticeable for situation B. However, one must note that this is not the usual domain of failure when dealing with engineering problems. Although situation B may serve as a theoretical case, having probabilities near 20% is an absurd value when dealing with reliability of offshore and marine structures. Still, it seems fair to admit that the probabilities of failure are indeed stabilized for situations A, B and C. In these situations, the Tawn type 2 copula provides the highest values of P_f , somehow closer to the Gumbel copula. It makes sense that both copulas provide similar values, since the first is a non-symmetric version of the second. In the previous sections it was noted that the Tawn type 2 copula presented a better fit to the original data (see section 6.2.5.5). The fact that the Tawn type 2 copula is able to capture the upper tail behaviour of the hindcast data, better than the Gumbel copula, might be related

to the higher values of P_f . Note that the Gumbel copula has upper tail dependence and zero lower tail dependence.

While the Tawn type 2 copula sets the higher limit of the obtained probabilities, the Independent copula seems to set the lower one. Taking into consideration the discussion regarding the independence assumption of the spectral parameters, one can suspect that the independent copula might be providing unreasonable values of the probabilities of failure. However, it is interesting to note that this copula is systematically providing the lowest values in situations A, B and C. The Clayton copula, which has lower tail dependence and zero upper tail dependence, is the closest one to the independent copula. The results indicate that the lack of ability to capture the upper tail behaviour of the hindcast data might be leading to smaller values of the probability of failure. Another interesting aspect is that the non-parametric BKDE and the Frank copula have a similar behaviour between situations. When the order of the probability of failure is 10^{-3} (situation A) they are closer to the independent copula, while for P_f in the order of 10^{-1} these models get close to the upper limit provided by the Tawn type 2 copula. For the intermediate case, the BKDE and the Frank copula get closer to the Gaussian copula, which is somehow in the middle of the limits set by the Independent and the Tawn type 2 copulas.

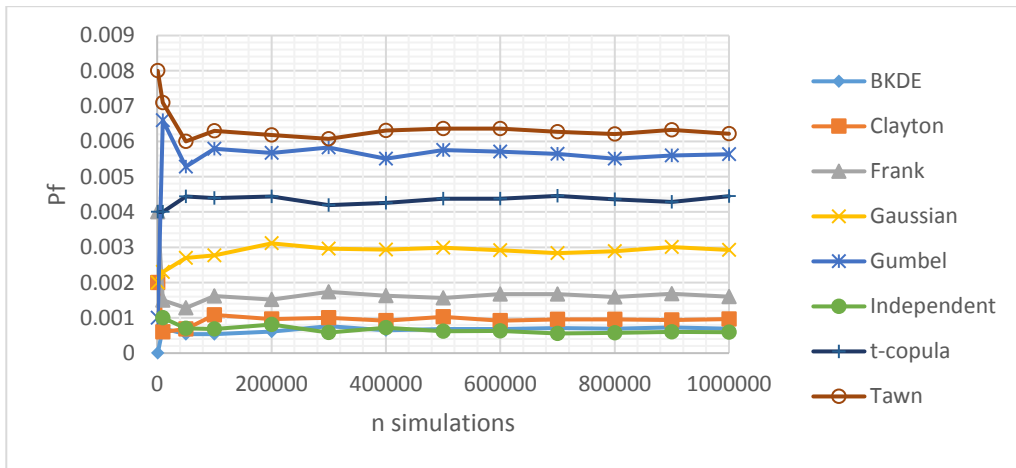


Figure 6.15 – Situation A for low probabilities of failure ($H_{smax}=4$ m; $T_{pmax}=22s$).

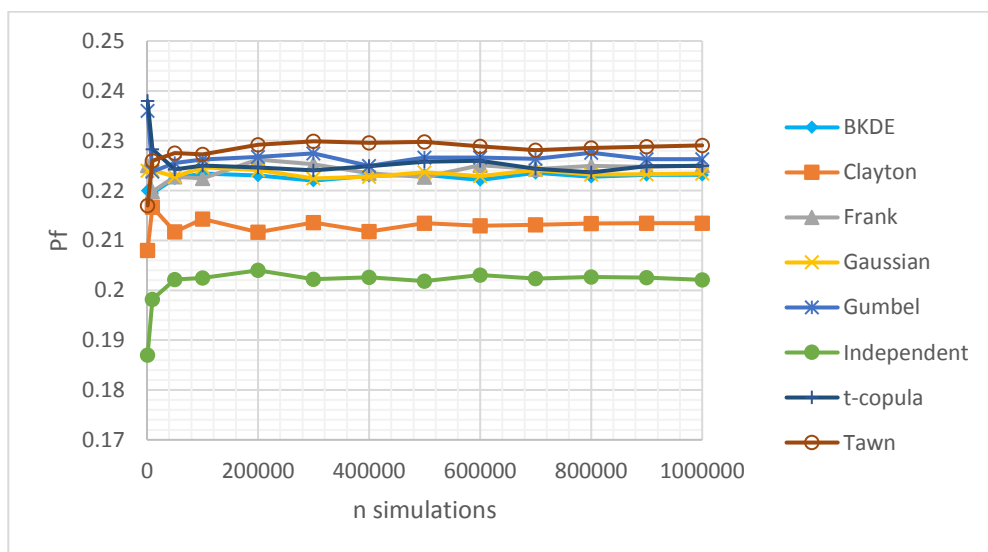


Figure 6.16 – Situation B for high probabilities of failure ($H_{smax}=6$ m; $T_{pmax}=22s$).

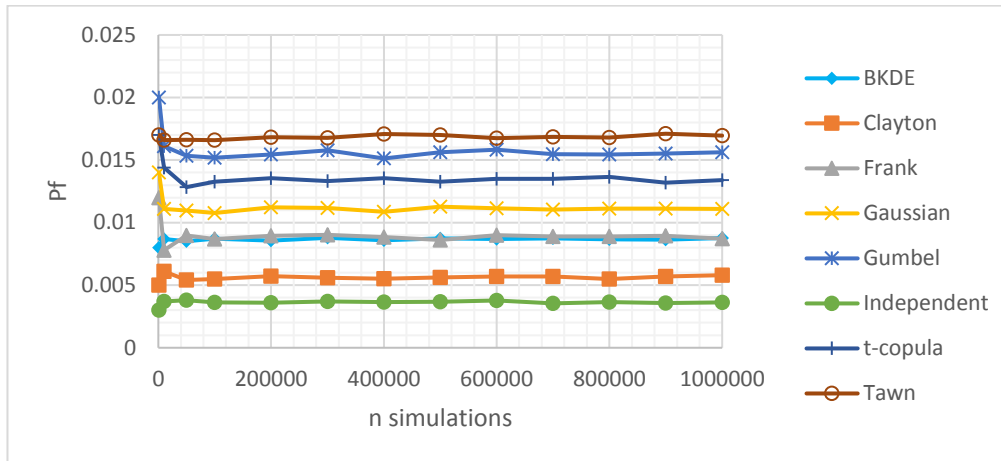


Figure 6.17 – Situation C for intermediate probabilities of failure ($H_{smax}=6$ m; $T_{pmax}=22s$).

Table 6.10 provides the probabilities of failure for the Independent and the Tawn type 2 copulas after 1 000 000 simulations and the ratio between them. One can see that the gap between these copulas increases when the order of magnitude of P_f decreases.

Table 6.10 – Probabilities of failure for the Tawn type 2 and the Independent copula for situations A, B and C.

| Situation | Tawn type 2 | Independent | Ratio $P_{fTawn}/P_{fIndependent}$ |
|-----------|---------------------------|---------------------------|------------------------------------|
| A | $P_f=6.21 \times 10^{-3}$ | $P_f=5.88 \times 10^{-4}$ | 10.57 |
| B | $P_f=2.29 \times 10^{-1}$ | $P_f=2.02 \times 10^{-1}$ | 4.66 |
| C | $P_f=1.69 \times 10^{-2}$ | $P_f=3.64 \times 10^{-3}$ | 1.13 |

Since in typical engineering problems one is looking for very low probabilities of failure, say in the order of 10^{-4} or 10^{-5} , the increasing gap between these models poses a source of uncertainty when dealing with the models choice. The present results are not conclusive regarding the best model to be adopted. There is no direct relation between the scores obtained in the AIC and BIC criterion and the outcome of the probabilities between the models. The probabilities given by Tawn type 2 copula, the t-copula and the Frank copula vary from situation to situation. Although the Tawn type 2 copula presents the best AIC and BIC scores, this model is not providing similar probabilities of failure when compared with the BKDE. On the other hand the independent copula gets closer to the BKDE for situation A ($P_f \approx 10^{-3}$). This is not so evident when the order of the probability of failure gradually increases, as in situation B and C.

However, due to the scores obtained in the BIC and AIC criteria and from a conservative perspective, it seems reasonable to use the model that provided the best fit to the hindcast data and that simultaneously gave the highest values of P_f , which in this case is the Tawn type 2 copula. Due to the inconclusive data, it is recommended that in practical situations the designer uses several models before making a decision purely based on the information criteria. A conservative approach recommends that the models choice relies on the one that provides the highest probabilities of failure. Moreover it can be noted that considering the wave parameters as independent may result in the underestimation of the probabilities, eventually leading to an unsafe scour protection design. Note that this contradicts the results provided by [37] and [40], regarding the reliability analysis of scour phenomena at bridge piers (current alone).

Finally, the uncertainty of these predictions associated to the choice of the marginal distributions, i.e. the lognormal for H_s and T_p , was not focused in this research and may also contribute to deviations from the BKDE result. Details on the marginal's uncertainties are presented by [123] and were not focused in this research, since the marginal distribution of H_s and T_p was defined by comparing the Kolmogorov-Smirnov and the Wasserstein distances among the tested candidates (see section 6.2.4). The conservative limit chosen of $H/d < 0.78$ is also contributing for differences between the models probability of failure and the non-parametric estimation given by the BKDE.

6.2.6.2 Application to Horns Rev 3

In this section a somehow more real situation based on Horns Rev 3 offshore windfarm is considered. No limits are imposed on the peak period and the significant wave height, with the exception of the depth limitation already mentioned. The new simulation values are provided in Table 6.11. This case study is similar to situations A and C previously defined. Nevertheless, the water depth is increased to 18 m and the values of the wave parameters (H_s ; T_p) are now able to achieve considerably higher values than the ones obtained from the hindcast data. In Table 6.12 the probabilities of failure based on the 124 months scenario are obtained for $n = 300\ 000$ simulations, which is above $n = 200\ 000$ simulations previously identified as a stabilization point for P_f .

Table 6.11 – Reference values used to calculate the probabilities of failure for a dynamic scour protection at Horns Rev 3 offshore windfarm.

| Situation - Case study | | | |
|----------------------------|-------------------------------|-------------------------------------|--------------------|
| H_{smax} (m) | No limit imposed | ρ_w (kg/m ³) | 1025 |
| T_{pmax} (s) | No limit imposed | N (number of waves) | 3000 |
| d (m) | 18 | g (m/s ²) | 9.81 |
| U_c (m/s) | $\mu=0.4$; $\sigma_{Uc}=0.2$ | S_{3D}acceptable (-) | 1 |
| D₅₀ (m) | 0.4 | g(x) (-) | 1- S _{3D} |
| p_s (kg/m ³) | 2650 | | - |

Table 6.12 – Probabilities of failure for the scour protection considered in the case study ($D_{50}=0.4$ m).

| Model (124 months) | $P_f(n=300\ 000)$ | $P_{f0}(n=300\ 000)$ |
|---------------------|-----------------------|-----------------------|
| Independent | 4.30×10^{-4} | 4.16×10^{-5} |
| BKDE | 4.97×10^{-4} | 4.81×10^{-5} |
| Clayton | 5.8×10^{-4} | 5.62×10^{-5} |
| Frank | 1.02×10^{-3} | 9.88×10^{-5} |
| Gaussian | 2.16×10^{-3} | 2.10×10^{-4} |
| t-copula | 3.16×10^{-3} | 3.06×10^{-4} |
| Gumbel | 4.45×10^{-3} | 4.32×10^{-4} |
| Tawn type 2 | 4.69×10^{-3} | 4.55×10^{-4} |

The Independent and the Tawn type 2 copula set the lower and upper limit for the probabilities of failure, respectively. In the present case, the increasing water depth contributed to reduce the values of the probability of failure, when compared with situation C. This is in agreement with the expected behaviour of scour phenomena, for which the severity tends to decrease with the increasing water depth [49]. From the Independent copula to the Tawn type 2 copula, the magnitude of the probability of failure increases from 10^{-3} to 10^{-2} . Moreover, the BKDE is closer to the Independent copula, as it occurred in situation A. The case study and the previous situations indicate that the probability of failure is very much dependent on the copula proposed for the wave parameters. This fact is similarly reported in other elements of offshore foundations, e.g. [125] state that for mooring lines the probability of failure may vary one or two orders of magnitude, depending on the copula model.

To the author knowledge, no studies are reported regarding the probabilities of failure in dynamic scour protections. This leads to an increased difficulty when it comes to assess if the values obtained in Table 6.12 are acceptable or not. In fact, these values are based on a 124 months dataset, which approximately corresponds to a scenario of 10.33 years. However, for a proper comparison with the common standards, one is more interested in the annual probability of failure (P_{10}). As a simplification, if it is assumed that the failures of the scour protection are continuous-time stochastic process, with the failure events being independent from each other, i.e. a Poisson process, then the probability of failure can be converted to the annual values by means of the continuous exponential distribution $F(t)=1-e^{-vt}$, where t is the time associated to the probability desired, in this case 1 year, and v is the rate of the events occurring in the time interval associated to the reference scenario. Considering a constant rate over the 10.33 years, one obtains the rate as $v=-\ln(1-P_{f_{10.33\text{years}}})/t$, where t corresponds to the 10.33 years.

This conversion leads to the third column of Table 6.12, which provides the annual probability of failure associated to each model, based on the 124 months dataset as the reference scenario. In offshore wind structures the IEC standards [294] and [295] indicate a design lifetime of 20 years, for both the turbine generator and the foundation. [27] recommends a value of 10^{-4} as nominal annual probability of failure for the foundation design (in unmanned structures). On the other hand, if these values are used in the approach proposed by [42] the correspondent return period exceeds by far the standard return period used in current practice [23], i.e. T_r is approximately 199 990 years.

If the failure probability considered is 10^{-5} (manned structures) the return period increases even more. Such values are extremely above the typical ones considered in common design standards. They are not in line with the statements from the offshore wind recommendations regarding the return periods. Scour protections are not typically designed by means of failure probabilities, as they would on a reliability based methodology. Due to the lack of studies performed on the present subject it is hard to evaluate what is an acceptable probability of failure for a specific scour protection. In [23] the comparison between reliability design techniques and the return periods typically used in offshore wind industry is discussed with further detail. According to [27], which for reliability purposes recommends the use of [220], one is able to gain a sense on the annual probabilities of failure acceptable for marine structures (Table 6.13).

For a consequence of failure to be described as “less serious” the risk of life upon failure must be considered as being relatively negligible. If one considers a scour protection at an offshore wind turbine, this is likely the case, since the structure is typically unmanned. Moreover, during extreme weather events it is not expected that any maintenance or inspection operation be performed, which limits the consequence of failure in terms of life losses, thus being reasonable to admit that the consequence of failure can be considered less serious.

Table 6.13 – Annual probability of failure (P_{f0}) for marine structures [220].

| Class of failure | Consequence of failure | |
|---|------------------------|------------------|
| | Less serious | Serious |
| I – Redundant Structure | $P_{f0}=10^{-3}$ | $P_{f0}=10^{-4}$ |
| II – Significant warning before the occurrence of failure in a non-redundant structure | $P_{f0}=10^{-4}$ | $P_{f0}=10^{-5}$ |
| III – No warning before the occurrence of failure in a non-redundant structure | $P_{f0}=10^{-5}$ | $P_{f0}=10^{-6}$ |

Note, however, that this does not mean that the failure of the protection may not lead to considerable consequences, as the wind turbine can collapse due to scour occurrence, even though the present probability of failure is only addressing the chance of the design criterion not being met. Moreover the consequences scale up in terms of economic losses if the importance of the foundation in the capital expenditures (CAPEX) and the operating expenses (OPEX) parcels are considered [14].

The acceptable annual probability of failure is within the range of 10^{-3} and 10^{-5} (Table 6.13). The annual probabilities of failure obtained with the Tawn type 2 and the Independent copulas range from 10^{-4} to 10^{-5} . The failure of a scour protection is often noted long after the occurrence, due to the periodicity of maintenance and inspection operations. Since this is a submerged element of the offshore wind turbine, it is reasonable to admit that there is no warning before failure occurrence. Therefore, a probability of failure in agreement with the standards should be in the order of 10^{-5} . However, it is important to note that these standards are used for reference, but at the present state-of-the-art no standards provide guideline values for the reliability assessment of scour protections for offshore wind turbines. A comparison between the standard values and the case study shows that depending on the model, the probability outcome may or may not be in agreement with the standards. This emphasises the importance of the model used to correlate the wave parameters and further assess the safety of the protection.

Often re-filling operations can be planned for scour protections after storm events. Furthermore, the fact that the time-scale of scour phenomena may not lead to the immediate instability of the structure, as the backfilling process occurs, may somehow contribute to accept probabilities of failure, which are in the order of 10^{-4} .

Although offshore wind farms frequently require maintenance operations [296], designing a scour protection for high values of P_f may undermine the cost-benefit of having a scour protection, as it will lead to very large OPEX costs for a lifetime of 20-25 years, which is considerably short in comparison to traditional structures. When dealing with other offshore structures and their elements, e.g. floating foundations [297], mooring lines [237], or structural elements of offshore wind turbines [298], higher orders of the probability of failure can be found. Often the probabilities of failure are close to 10^{-6} and sometimes higher. Therefore, a balance between the acceptable consequences of failure and their influence on the cost of the scour protection must be achieved. Furthermore, the correlation between failure modes of the wind turbine can play a major role in the structural behaviour and must be analysed in the safety assessment. For instance, scour phenomena is often related to fatigue problems. The influence of the scour protection failure in the probability of failure related to the fatigue limit

state is unknown for the present case. Such facts may lead the designer to assume that the protection's reliability is not compatible with measures of safety, i.e. probabilities of failure, in the order of 10^{-4} .

6.2.7 Tail dependence analysis

The model with lowest AIC and BIC criteria (Tawn type 2 copula) did not present the closest probability of failure to the non-parametric model (BKDE). This interesting aspect can be pointed, as one may tend to exclude certain models based on these criteria, even before performing the probability calculations. The AIC and BIC criteria provide an assessment of the overall fit of the model. However, when dealing with probabilities of failure, the domain of interest is typically related to the tails' behaviour. The extremes of the joint distribution are the ones that may contribute to increase the failure rates. Therefore, the tail dependence is important to understand which model might be better when estimating the probability of failure.

In situations A, B and C, as the probabilities become smaller and smaller, the Tawn type 2 copula deviated more and more from the BKDE. Table 6.14 provides the upper (λ_U) and lower (λ_L) tail dependence coefficients for each copula model, as calculated in [243]. Furthermore, this non-parametric estimation of the tail dependence coefficients was performed according to [299] considering the upper and lower quantiles of 10%, 5%, 2.5% and 1%.

H_s and T_p are considered to be upper (or lower) asymptotically dependent if λ_U (or λ_L) belongs to the interval $]0;1]$. If λ_U (or λ_L)=0 the variables are considered to be asymptotically independent [243]. Note that if the tails are asymptotically independent, that does not mean that the variables are actually independent. It solely means that as one moves to the upper or lower tail, the probability that T_p exceeds a certain quantile is independent from the probability that H_s exceeds the same quantile. In Table 6.14, the non-parametric estimation of the upper tail for the 10% quantile is already very low (0.0256). For even smaller quantiles one is able to see that the spectral parameters are showing an asymptotically independent behaviour. Given this upper tail behaviour it is understandable that the Tawn type 2 copula was providing probabilities of failure which are not in the range of the ones provided by the BKDE. By definition, the Tawn type 2 copula imposes an upper tail dependence, which in this case is about $\lambda_U=0.3504$. In order to obtain the same tail dependence with the non-parametric estimation, one would define the tail as starting in the 45.4% quantile, which is far from being the actual tail of the data.

One is able to conclude that the Tawn type 2 copula did not catch the asymptotic independence of the spectral parameters, as other models did, e.g. Frank or Clayton copula. Note that the Gumbel copula, with λ_U close to 0.33, is also providing probabilities near those of the Tawn type 2 copula.

The fact that the lower tail for the quantile of 1% has a positive dependence (in the non-parametric estimation), which in this case is closer to the t-copula model, also causes perturbations in models' ability to provide closer values of the probability of failure to the BKDE. Note that the lower tail coefficient is not stabilized in Table 6.14. Further iterations should be made to access the value for which λ_L stabilizes. The present study emphasises the dependence of the probabilities on the tails' modelling provided by each copula. An important conclusion arises from the tail dependence analysis: "when calculating a probability of failure one should select a model that is not only based on the information criteria (AIC or BIC) but also on the tail dependence behaviour". Future research should address the quality of these models in the tail fitting. For such purpose it is common to study the variation of λ_L and λ_U along the sample's quantiles (as in [123]), which was not performed at the present state of this research. However, the author recognises that, doing it, could provide a better

assessment of the model’s behaviour at the tails region, namely in the upper tail, which is expected to contribute more to the occurrence of failures.

Table 6.14 – Theoretical and non-parametric estimation tail dependence coefficients for the 124 months dataset.

| Tail dependence coefficients | | | | |
|-------------------------------------|------|-------------|------|-------------|
| 124 months | | λ_L | | λ_U |
| Independent | | 0 | | 0 |
| Gaussian | | 0 | | 0 |
| t-copula | | 0.1591 | | 0.1591 |
| Clayton | | 0.3586 | | 0 |
| Gumbel | | 0 | | 0.3316 |
| Frank | | 0 | | 0 |
| Tawn type 2 | | 0 | | 0.3503 |
| Non-Parametric | 10% | 0.2887 | 10% | 0.0256 |
| | 5% | 0.2373 | 5% | 0 |
| | 2.5% | 0.1919 | 2.5% | 0 |
| | 1% | 0.1509 | 1% | 0 |

6.2.8 Influence of Kendall’s τ (τ_K)

Another important aspect of the present research concerns to the influence of the records’ duration, i.e. the dataset, in the probabilities of failure. The same case of Table 6.11 was analysed for each dataset and the probabilities were obtained for the BKDE and three models with lowest AIC or BIC. The results are provided in Figure 6.18. Although for a small range of τ_K , one is able to see that the probability of failure increases for an increasing dependence measure. Since the dependence measure is affected by the datasets’ properties, one can conclude that the dataset is of great importance when aiming to assess the safety of the scour protection. This points out an important limitation of these models, which relates to the quality of the hindcast or the observed data available. Nevertheless, this limitation is common to the majority of the statistical models available. Further investigation should be performed to analyse the influence of the dependence measure in the probabilities of failure.

Despite the short range of tested datasets and respective values of τ_K , it is evident that both the copula and the measure of dependence influence the assessment of the probabilities of failure. The order of magnitude may vary between different models, which is in agreement with other works performed for other offshore foundations, e.g. [125]. The present research emphasizes that modelling the dependence structure of met-ocean data with copula-based models is very much dependent on the models’ selection. These results also agree with works performed for other locations and records, e.g. [123], [238] or [267].

The present research only deals with a very short range of τ_K . Still, the values of P_f are clearly influenced. One should also note that despite the large variation in the duration of the datasets, e.g. 50% from 124 to 62 months and 75% from 124 to 31 months, the maximum and minimum values of τ_K are only varying 12.3%.

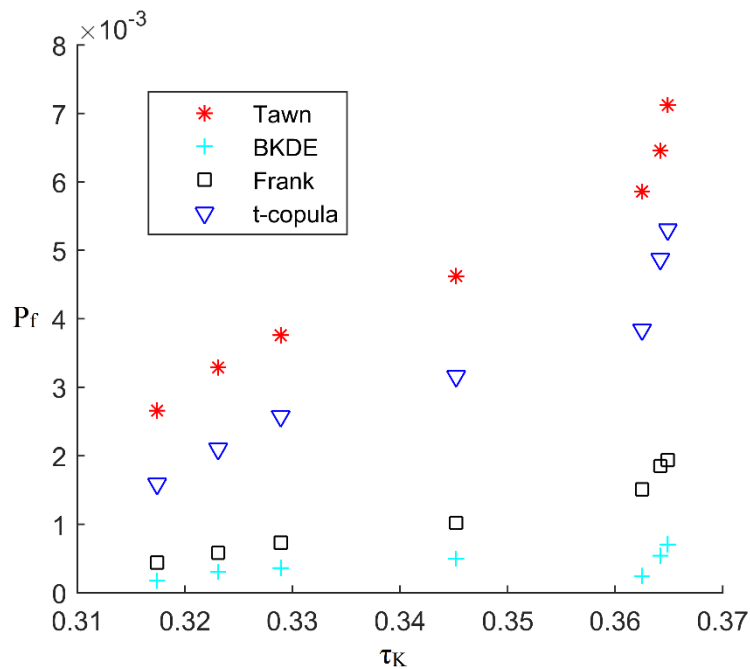


Figure 6.18 – Probability of failure versus τ_k per dataset for the Frank, the Tawn type 2, the t-copula and the BKDE, $n=300\,000$.

6.2.9 Sensitivity analysis

6.2.9.1 Sensitivity to the mean stone diameter (D_{50})

The literature has demonstrated by physical model studies that dynamic scour protections tend to be more stable for large armour stones (see sections 3.6.2, 3.7.1 and 4.2.6.3.8). For non-cohesive sediments and wave and currents combined, scour phenomena increases for finer sediments. In dynamic scour protections one is aiming at a mean stone diameter that simultaneously gives the required stability to the armour layer, but does not exceed the equivalent value of a statically stable design. Several known offshore windfarms use values of D_{50} , that may vary from $D_{50}=0.3$ m to $D_{50}=0.50$ m, e.g. North Hoyle, Egmond aan zee, Arklow bank [59] are in this range. Other offshore windfarms may present slightly lower values, e.g. Scroby sands has a $D_{50}=0.15$ m. However, in offshore structures literature, the reports on such technical details of scour protections are often limited. The present sensitivity analysis was performed for an interval between 0.2 m, which is likely to be a small size for the armour stones in common cases, and 1 m. Note that 1 m is indeed a theoretical value for the sake of analysis, as the fall-pipe vessel installation of the protection rarely deals with values above 0.5 m, as mentioned throughout Chapter 4.

Figure 6.19 shows the variation of the probabilities of failure with the mean stone diameter of the armour material. After $D_{50}=0.50$ m the differences are small. One is able to state that all models are sensitive to changes in this variable, which was already expected, as the diameter is an important resistance variable of the protection. The main effects on the probability of failure are registered between 0.2 m and 0.5 m, which are the common sizes found in the industry.

Although the order of P_f may change with the D_{50} value, it should be noted that the reduction of P_f for D_{50} above 0.5 m may not compensate from the economical point of view. Moreover, using such large values for the armour units does not comply with the dynamic stability of the protection, as the

static stability is achieved with large diameters and weights of the rock material. For the simulated conditions, with constant water depth, provided that the distribution of U_c and the copula model for H_s and T_p remain the same, it was noted that P_f follows an hyperbolic function of D_{50} of the type $P_f=A \times D_{50}^\lambda$ where A and λ are constants that depend on the copula model. Considering the Tawn type 2 and Independent copulas, which set the highest and lowest values of P_f , the constants obtained were respectively: $A=0.0006$; $\lambda=-2.083$; for a squared correlation coefficient of $R^2=0.9976$ and $A=8 \times 10^{-6}$; $\lambda=-3.285$; $R^2=0.9807$. One can also note that if the mean diameter increases, the differences between the models decrease.

An important aspect, which is not the focus of the present reliability assessment, is the influence of the armour layer thickness in the probability of failure. Further research should be performed to adapt the failure criterion to include this variable and its effects in the probability of failure. Nevertheless, the main idea that seems useful to retain is the fact that the probability of failure tends to decrease with increasing D_{50} and that D_{50} values of interest are lying between 0.2 m and 0.5 m. This idea is in agreement with other works performed on the stability of dynamic scour protections, e.g. [43].

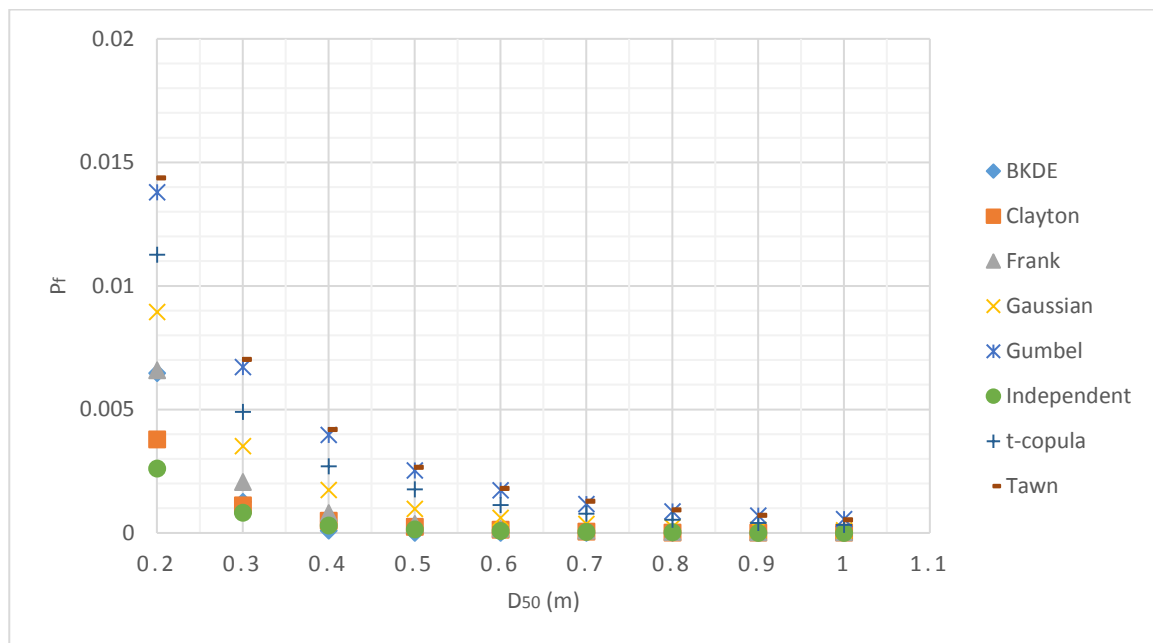


Figure 6.19 – Probabilities' sensitivity to the mean stone diameter of the armour layer modelled with triangular distribution with lower and upper limits of $\mu_{D50} \pm 0.1$ m, e.g. for $\mu_{D50}=0.4$ m $D_{50}=[0.3;0.5]$ m.

6.2.9.2 Sensitivity to current velocity (U_c)

To analyse the effect of the current velocity, the simulations were performed for U_c ranging from 0.1 m/s and 1 m/s. The standard deviation used was maintained at 0.2 m/s. The range of variation is based on the minimum bottom velocity reported in [286]. The value associated to the bottom velocity at Horns Rev 3 location is 0.9 m/s, for a return period of 50 years. However, surface values were reported to be above 1 m/s [286]. Although one is interested in the depth-averaged velocity, the upper limit of 1m/s was defined in order to be slightly above the reported bottom value for $T_r=50$ years. Often the design values for currents velocity deal with a return period of 10 years [122].

Figure 6.20 shows that for the tested models the probability of failure increases with increasing current velocity. The results are in agreement with expected behaviour of the scour protection.

Increasing current velocity tends to increase the bed shear stress, thus increasing the instability on the armour layer. Moreover, the increase in the probability of failure approximately follows a linear function, for which a vertical translation is obtained depending on the model used for the spectral parameters. As in the previous case, the Independent and the Tawn type 2 copulas tend to set the lowest and highest limits for the probabilities domain. When the current velocity increases, the differences in the model's probabilities also increase. For a linear approximation, one obtains for the Tawn type 2 copula $P_f=0.0017U_c+0.004$ and $R^2=0.9928$, while in the Independent copula the approximation is given by $P_f=0.0002U_c+0.0003$ and $R^2=0.946$. The present failure criterion only considers following and opposing wave-current environment. Further research is needed to improve the failure criterion for multi-directions between waves and current. For example, in [32] it is pointed that the damage number increases under waves opposing currents, although no other information is found for other angles between flow components. However, it is expected that the probability of failure not only depends on the magnitude of the current velocity but also on the relative direction between current and waves.

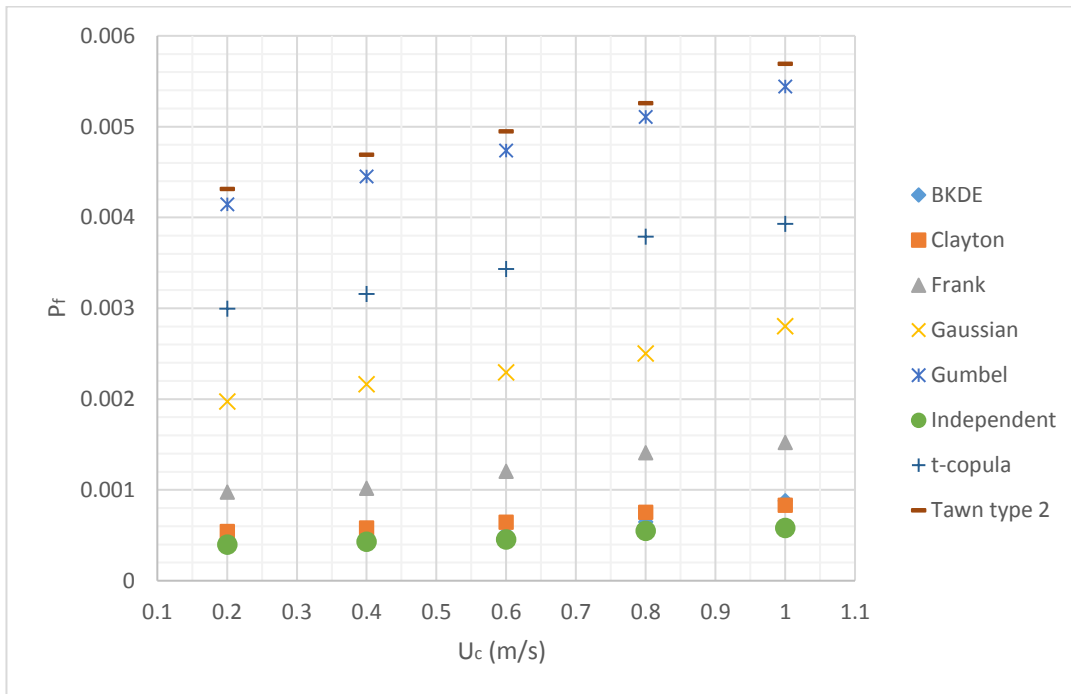


Figure 6.20 – Probabilities' sensitivity to the currents mean velocity ($\sigma_{U_c}=0.2$ m/s).

6.2.9.3 Sensitivity to the acceptable damage number ($S_{3D_{\text{acceptable}}}$)

The acceptable damage number can be interpreted as a resistance variable of the scour protection. If one considers that the acceptable limit can be increased, then the probability of failure should be reduced, given that the other variables remain the same. As discussed in section 3.7.1.5, the statically stable scour protections were obtained for $S_{3D_{\text{acceptable}}}=0.25$, whilst dynamic ones were obtained for a limit of $S_{3D_{\text{acceptable}}}=1$. The criterion stated in Eq. (6.1) and Eq. (6.4) is based on Eq. (3.57), thus developed for dynamic scour protections. Therefore, the probabilities of failure obtained for $S_{3D_{\text{acceptable}}}$ equal to 0.25 (statically stable protections) may not be in agreement with the ones evaluated for example using a failure criterion based on the static design proposed by [30]. The comparison between static and dynamic failure criterion is analysed in Chapter 7. Nevertheless, studying the probabilities' sensitivity in the interval [0.25; 1.25] is important to understand if the methodology proposed for the

reliability assessment is matching the expected behaviour of P_f for a conservative limit ($S_{3D_{\text{acceptable}}}=0.25$) or a less conservative one ($S_{3D_{\text{acceptable}}}=1.25$).

Figure 6.21 provides the probability of failure as a function of the acceptable damage number. When the acceptable damage number increases the probability of failure decreases, because increasing the acceptable damage number means that the designer assumes that the protection is able to endure large damage quantities. Thus meaning that failure is only considered to occur for larger displacements at the armour layer. On the other hand, assuming that the acceptable limit is 0.25 means that the scour protection must present an equivalent static stability. This leads to larger probabilities of failure, since the protection is designed to be dynamically stable, which implies that the actual S_{3D} is likely to be higher than 0.25. If the acceptable limit decreases, the differences between the models increase (Figure 6.21). This emphasises the need to properly define the joint model of H_s and T_p , particularly, when the acceptable damage is smaller. For an acceptable damage number of 1.0 the differences between models can still be significant.

The analysis showed that the sensitivity to the acceptable damage number is similar to the one showed for the mean stone diameter of the armour layer. An approximation to the hyperbolic function of the type $P_f=A \times S_{3D_{\text{acceptable}}}^\lambda$ can also be adopted here. For the Tawn and the Independent copula one respectively obtains: $A=0.004$; $\lambda=-0.744$; $R^2=0.9996$; $A=0.0004$; $\lambda=-1.206$; $R^2=0.9975$. The probabilities of failure obtained for $S_{3D_{\text{acceptable}}} = 0.25$ should be further compared with a statically stable criterion, in order to clarify the consistency of the values obtained.

From Figure 6.21 it seems that the potential gains obtained from adopting a value of 1.25 might be somehow risky and does not lead to a considerable reduction in the probabilities. Conversely, values near to 0.25 seem to express a very conservative approach that seems more suitable for a static stability than for a dynamic one. Considering $S_{3D_{\text{acceptable}}}=0.25$ may require a reformulation of the failure criterion inspired in threshold of motion.

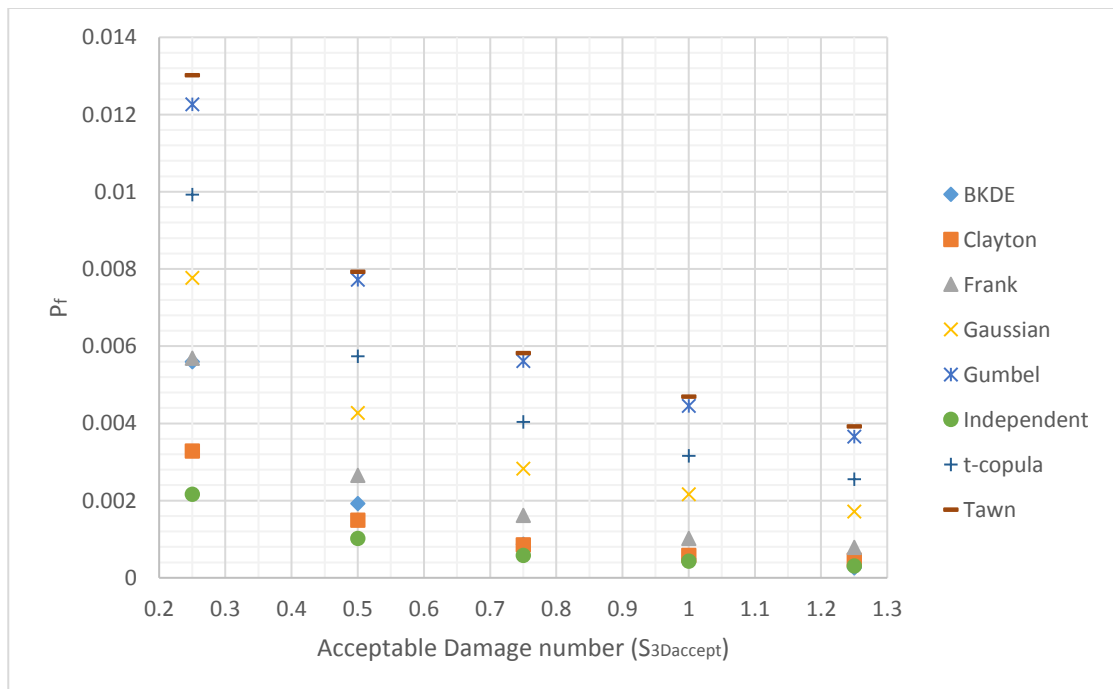


Figure 6.21 – Probabilities' sensitivity to different limits of acceptable damage number.

6.2.9.4 Sensitivity to the water depth (d)

Taking into consideration the depth limited wave heights and the bathymetry at Horns Rev 3 a new series of H_s and T_p were generated. Then the probability of failure based on a 124 months scenario was calculated for a water depth ranging from 10 to 22 m. This is roughly the minimum and maximum values expected at Horns Rev 3. For large water depth to pile diameter ratio, the local scour effect tends to decrease [49]. Here the pile diameter is not considered in the damage number calculation. Still one can fairly assume that if the other variables are kept constant, then increasing the water depth is expected to generate smaller damage numbers, thus leading to smaller probabilities of failure.

Figure 6.22 shows that the models were able to capture the expected relation. As the water depth increases, the influence on the probability of failure decreases. In the tested range of water depths the order of magnitude of P_f can change. This emphasizes the influence of the water depth for locations where the bathymetry is shallower and shallower. A decrease in the water depth limits the possible wave heights at the scour protection. However, this also affects the orbital bottom velocity and increases the wave's related term in Eq. (3.57). Therefore, the damage number increases for the remaining conditions. Similarly to D_{50} and $S_{3Dacceptable}$, an approximation between the water depth and the probability of failure can be obtained by means of a hyperbolic function of the type $P_f=A \times d^\lambda$. For the Tawn and the Independent copula, one respectively obtains: $A=3.5526$; $\lambda=-2.288$; $R^2=0.9979$; $A=24.481$; $\lambda=-3.842$; $R^2=0.9946$.

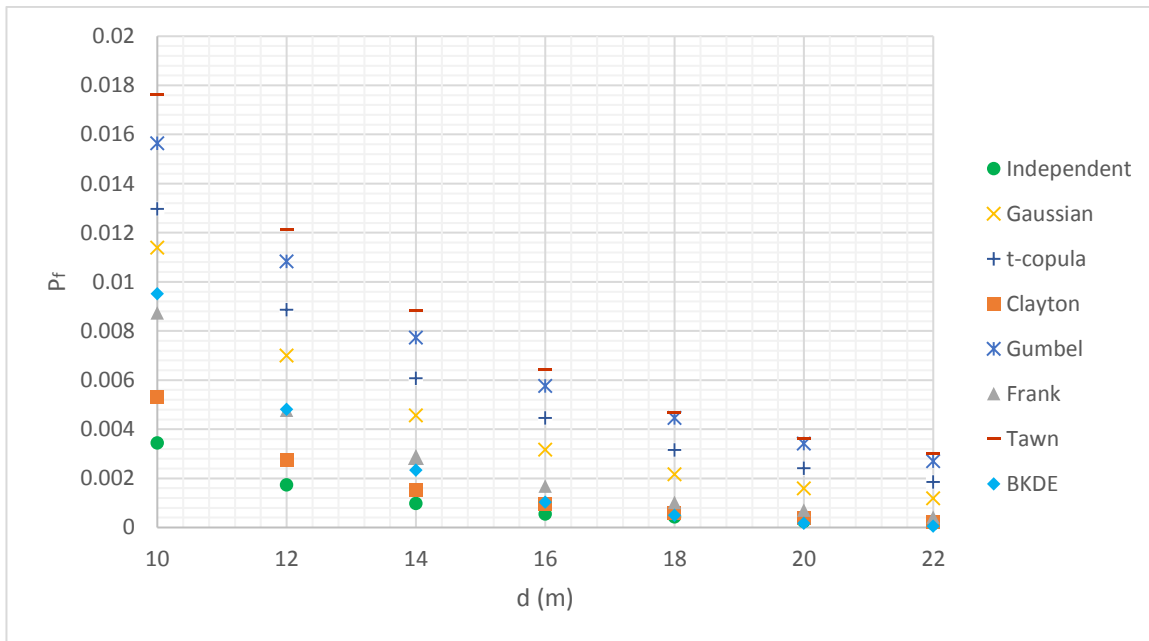


Figure 6.22 – Probabilities' sensitivity to the water depth.

6.2.10 Final remarks on the reliability of dynamic scour protections with copulas

Throughout section 6.2, the reliability assessment of dynamic scour protections around offshore wind monopile foundations was addressed (also see Figure 6.1). The methodology is focused on copula-based models used to describe the joint distribution function of the significant wave heights and the peak periods. The reliability assessment of the scour protection is based on the failure criterion introduced by [32] and further studied by means of a physical modelling approach in Chapter 4.

The probabilities of failure of a scour protection are calculated based on met-ocean data at Horns Rev 3 offshore wind farm (North Sea), where the reference mean stone diameter was assumed to be 0.4 m. The following remarks can be drawn from section 6.2:

- The probability of failure is considerably influenced by the copula used to model the dependence of the considered wave parameters. The sensitivity to τ_K was also evident despite the short range tested. Based on the 124 months dataset, the annual probability of failure could vary from 10^{-4} to 10^{-5} , depending on the copula model.
- The probability of failure is also much dependent on the duration of the dataset. When considering datasets of 31 and 62 months the probability of failure is mainly influenced by the fact that the measure of dependence τ_K changes between datasets.
- When dealing with copula-based models, one should be careful when choosing a model purely based on the AIC and BIC criteria. The case study showed that the copula with the best scores on the information criteria may not lead to the closest probabilities of failure, when compared with the non-parametric estimation. This was verified for the Tawn type 2 copula and the BKDE method. Therefore, a wise approach recommends that several models are applied and the sensitivity of the probability of failure is analysed per each model.
- The symmetric copulas were not able to capture the asymmetry of the hindcast data. Other models should be tested in order to improve this aspect.
- The asymptotic behaviour of the spectral parameters may influence the probability of failure. Therefore, assessing the tail dependence coefficients enables one to understand, which copula displays the most similar tail behaviour when compared with the non-parametric estimation.
- The sensitivity analysis showed that the proposed copula-based models were able to capture the physical effects of the mean stone diameter of the armour units, the current velocity, the acceptable limit for the damage number and the water depth.
- The statistical framework applied is a simplified one, which does not consider all the random variables included in the failure mode of the top layer. Therefore, further research should also aim at a better representation of the remaining basic random variables and their correlations.

The reliability assessment as proposed herein is a straightforward way to assess the scour protection's safety based on a simple Monte-Carlo simulation method. However, this research outlined aspects that should be further investigated to make a generalisation of the method. Considering asymmetric copulas or adapt the failure criterion, to include a wider range of directions between waves and currents, may improve the accuracy of the probabilities obtained. For the safety assessment of dynamic scour protections at offshore wind farms the author recommends that several models are tested and compared.

6.3 Asymmetric copula-based distribution models for met-ocean data

As introduced in section 5.9 and discussed in section 6.2 the asymmetry in the met-ocean data is one of the key aspects regarding the use of copula-based models. Due to the recent application of copulas to obtain the joint model of the sea climate, the majority of the works found in the literature are based on symmetric copulas, whose parameter is commonly estimated through the value of τ_K , e.g. [125] or [238]. Moreover, the data pre-processing regarding the serial (short-term) dependence or the seasonality effects is not always deeply studied and might be important to provide a copula model that accurately fits the joint behaviour of the met-ocean variables. Only recently, the application of asymmetric copula models starts to be consistently applied to met-ocean data, such as the joint modelling of significant wave heights and periods, e.g. [123, 219] and [292]. However, the application

of such models remains to be fully developed for the referred purposes. Aiming at contributing to fill the present knowledge gap, the present research developed an extensive work on the application of asymmetric copula models to the data available for Horns Rev 3. Throughout the course of the present research it was not possible to implement the reliability analysis for these models. The main reason for this is the fact that, for the time schedule available, a preference was given to the comparison of the reliability analysis between the static and dynamic stability design according to the conditional modelling approach used in current practice (see Chapter 7). Nevertheless, the models hereby presented provide a starting point for future research concerning the reliability analysis of dynamic scour protections. Furthermore, the potential of these models for other problems of the offshore wind engineering domain also benefit from this research and are addressed in the following sections.

6.3.1 Wave data

The present models were developed for the same case study described in section 6.2.3. However, the mean up-crossing period (T_z) was analysed instead of the peak period. This was performed since no peak period data was available for the wind-sea and swell components. [286] provides the hindcast data of the significant wave height and mean up-crossing period, for the same coordinates and time window also referred in section 6.2.3. As mentioned in section 5.9, the data available is referred to as the wind component, for wind-sea, swell component and the combined sea state. Table 6.15 shows that the wind significant wave height tends to be higher than the swell one, whilst the swell component tends to present larger mean periods. Positive kurtosis and skewness values indicate, respectively, that fat and long upper tails are expected. This is important, as the upper tail is the region of interest in the failure of marine systems and structures, because it is related with the largest wave heights.

Table 6.15 – Descriptive statistics for the combined sea state, the wind-sea and swell components (hindcast data of 124 months – $n = 90\,553$).

| Descriptive | Combined | | Wind | | Swell | |
|-------------------------|-----------|-----------|-----------|-----------|-----------|-----------|
| | H_s (m) | T_z (s) | H_s (m) | T_z (s) | H_s (m) | T_z (s) |
| Mean | 1.46 | 5.9 | 1.03 | 3.9 | 0.88 | 7.2 |
| Median | 1.22 | 5.6 | 0.79 | 3.6 | 0.76 | 6.9 |
| Std.deviation | 0.93 | 1.7 | 0.94 | 1.9 | 0.52 | 2.0 |
| Max | 6.11 | 14.0 | 6.04 | 13.8 | 5.12 | 17.8 |
| Min | 0.14 | 2.2 | 0.00 | 1.0 | 0.11 | 2.6 |
| Skewness | 1.58 | 0.8 | 1.64 | 0.9 | 1.56 | 0.7 |
| Kurtosis | 6.16 | 3.6 | 6.43 | 4.0 | 6.59 | 3.6 |
| Percentile 25% | 0.80 | 4.6 | 0.36 | 2.5 | 0.51 | 5.8 |
| Percentile 50% | 1.22 | 5.6 | 0.79 | 3.6 | 0.76 | 6.9 |
| Percentile 75% | 1.85 | 6.9 | 1.42 | 4.9 | 1.12 | 8.4 |
| Percentile 90% | 2.69 | 8.2 | 2.27 | 6.4 | 1.56 | 9.8 |
| Percentile 95% | 3.35 | 9.0 | 2.94 | 7.5 | 1.90 | 10.8 |
| Percentile 99% | 4.78 | 10.7 | 4.40 | 9.5 | 2.64 | 12.7 |
| Percentile 99.5% | 5.32 | 11.3 | 4.95 | 10.2 | 2.96 | 13.4 |
| Percentile 99.9% | 5.89 | 12.7 | 5.70 | 11.7 | 3.64 | 15.3 |

When dealing with the combined results from wind and swell components the asymmetry between H_s and T_z is considerable. This may lead to difficulties when attempting to fit a statistical model to the overall data. [123] points out that fitting a model to the separate components may contribute to better fittings and to reduce the asymmetries in the data. The present research presents several copula-based models and analyses their comparative performance to understand if treating wind and swell components separately leads to a better goodness-of-fit compared to the overall models.

6.3.2 Wave data pre-processing

Copula-based models built on measures of dependence, which are rank-based, e.g. the Kendall's tau (τ_K) or the Spearman's rho (ρ_{spear}). Therefore, the data had to be treated for the existence of ties. Moreover, albeit the fact some works tend to simplify this aspect (as performed in the previous section 6.2 or [125] and [300]), serial dependence should be removed for an accurate joint model ([33], [6]).

The R package RANKS was used to randomly break ties present in the data, when constructing the pseudo-observations used to fit the copulas. Similarly, to the data presented by [123], it was found that this did not affect the marginal distributions of the significant wave height and mean period, nor their parameters, which were estimated as discussed in section 6.2.4.

The serial dependence was reduced by subsampling the data. The underlying question is “which time interval should be used to subsample the data?” The auto-correlation function (ACF) was computed for several intervals, namely 1 hour, 3 hours, 1 day, 2 days, 3 days and 1 week. For each interval the maximum value of the significant wave height and the respective mean up-crossing period was selected as the subsample object. In the present study, the maxima are selected instead of the means in order to preserve the extremes information. It was concluded that, for both the significant wave height and mean up-crossing period no substantial reductions of short-term (serial) dependence were obtained from considering intervals larger than 2 days, e.g. 3 days or 1 week, as shown in Figure 6.23.

Moreover, this interval complies with the value used in [286] to define a storm event for the Peak Over Threshold application. One should note that the definition of storm duration and storm threshold of H_s is always questionable. [301] provides further details on storm characterization for different climate conditions, which is not the focus of this work. However, according to the auto-correlation analysis (Figure 6.23), subsampling the maximum significant wave height and the associated mean up-crossing period for a two-day interval still shows some serial dependence. This can be due to the fact that the maximum significant wave height of a block of 2 days can be chronologically close to the maximum of the next block of 2 days. Nevertheless, in the present case, it was considered that the two-day maxima was a suitable subsampling.

This subsampling led to samples of 1887 pairs of H_s and T_z for the combined sea state, the wind and the swell components. Figure 6.24 provides the subsampling before seasonality is removed from the data.

According to [123], seasonal effects can be removed by calculating the seasonal mean and the standard deviation for each annual cycle. The weekly data is then normalized by subtracting the seasonal mean and then dividing by the standard deviation for each week of the annual cycle. Then the overall mean is added. This procedure may lead to pre-processed data that may have negative values. This may pose a problem when dealing with the domain of certain distributions, e.g. the lognormal or the Weibull distributions. A possible way to deal with negative values is to work with the log of the

data. If the data are indeed lognormal, their log should lead to new variables that follow a Gaussian (Normal) marginal distribution.

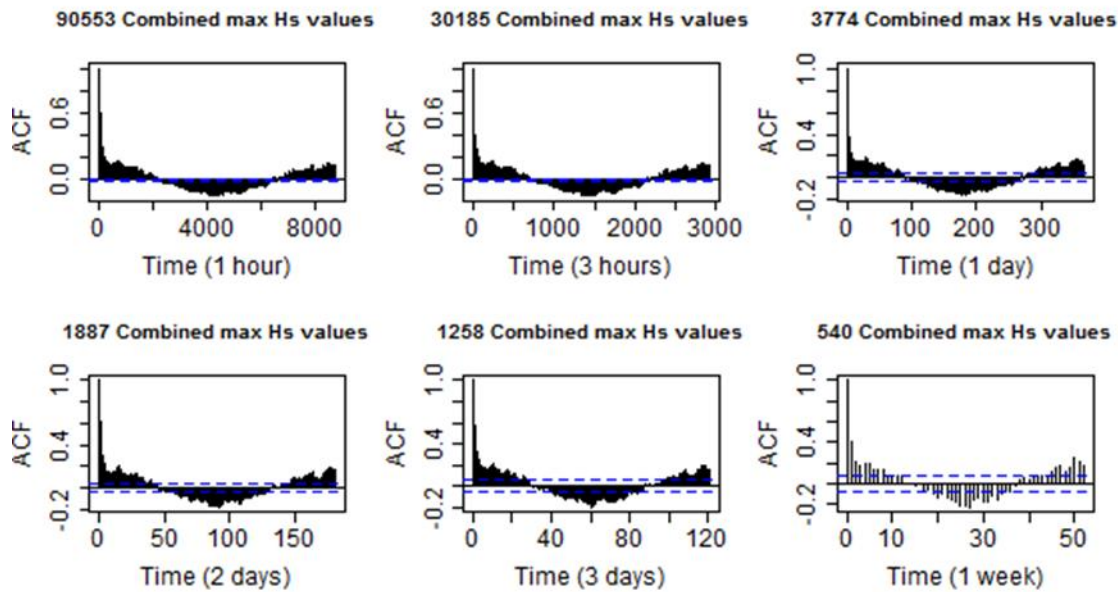


Figure 6.23 - Autocorrelation function for the maximum value selected for different time intervals.

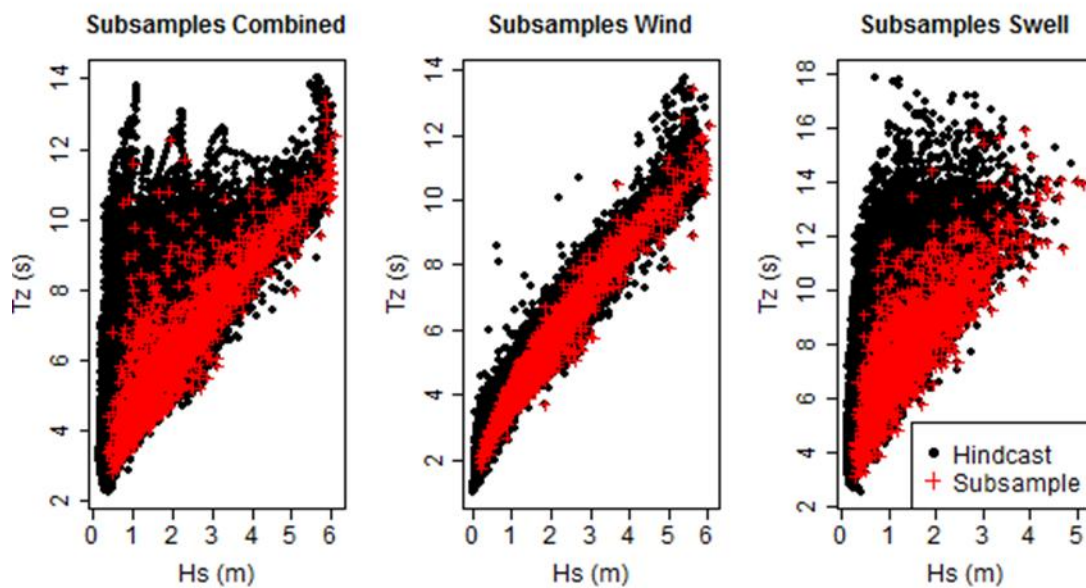


Figure 6.24 – Subsamples obtained from choosing the maximum H_s and the coexisting T_z for intervals of 2 days.

However, for the present case, the Shapiro-Wilk test for normality showed that neither the logarithmic transformation of the significant wave height or the mean up-crossing period followed a Gaussian distribution, as shown in Table 6.16. One should also note that for such large samples as these ones ($n=1887$ pairs), the Shapiro-Wilk test tends to be very sensitive to any departures from normality. An ad hoc solution was adopted by adding to the sum of the overall mean (as explained before) the minimum integer number of standard deviations necessary to turn negative values into positive ones. This does not affect the dependence structure of the pre-processed data, since it

corresponds to a location shift solely. Moreover, after the copula-based models are fitted to the data the seasonality is added back again. Therefore, adding the overall mean alone or adding this value plus the necessary standard deviations, does not lead to differences in the models' outcome.

Table 6.16 – Shapiro-Wilk test for normality of the $\log(H_s)$ and $\log(T_z)$ applied to each subsample. Confidence interval of 90%. Rejection of null hypothesis H_0 for $p < 0.1$.

| H_0: X follows normal distribution; X is either $\log(H_s)$ or $\log(T_z)$ | | | | | | |
|--|-----------------------|-----------------------|-----------------------|-----------------------|----------------------|-----------------------|
| Subsample | Combined | | Wind | | Swell | |
| C=90% | H_s | T_z | H_s | T_z | H_s | T_z |
| Shapiro-Wilk | 0.9933 | 0.9931 | 0.9911 | 0.9948 | 0.9962 | 0.9988 |
| p value | 1.36×10^{-7} | 9.66×10^{-8} | 2.55×10^{-9} | 3.64×10^{-6} | 1.1×10^{-4} | 2.44×10^{-2} |
| Evaluation | Reject | Reject | Reject | Reject | Reject | Reject |

The seasonality is removed according to Eq. (6.5), where y_i is the pre-processed data, x_i is the subsampled value of H_s or T_z , and the μ_j and σ_j are respectively the mean and standard deviation of the significant wave height or the mean period of the week j , with $j=[1;52]$. M stands for the overall mean of the subsampled data and w represents the minimum integer number of overall standard deviations of the subsampled data (S_d) necessary to make all y_i positive.

$$y_i = \frac{x_i - \mu_j}{\sigma_j} + M + w \cdot S_d \quad (6.5)$$

For the present dataset all values of T_z in the pre-processed data were already positive. However, for the significant wave height, it was found that the required w was equal to 0 for the combined sea and 1 for the wind and swell components. Note that the S_d of the subsampled wind and swell components is different, respectively, equal to 1.221 m and 0.78 m. Note that with such transformation, the pre-processed data of the combined sea does not necessarily have the highest H_s , when compared with the wind and swell components. The same is valid for the percentiles of H_s , as mentioned when the seasonality effects are added back to the pre-processed data and this somehow counter-intuitive aspect gets dissipated.

Figure 6.25 shows that the subsampling and seasonality treatment led to a considerable reduction in the autocorrelation functions for the significant wave heights in the wind-sea, the swell and the combined sea. The same was concluded for the mean up-crossing period, thus leading to pre-processed data that can be used to obtain the pseudo-observations for copula fitting. The left-most images of Figure 6.25 concern the original hindcast data, while the right-most ones concern the pre-processed data, i.e. two-day maximum H_s and respective T_z with seasonal effects removed. Figure 6.25 also shows that the seasonality effect is more evident in the swell component than in the wind-sea component.

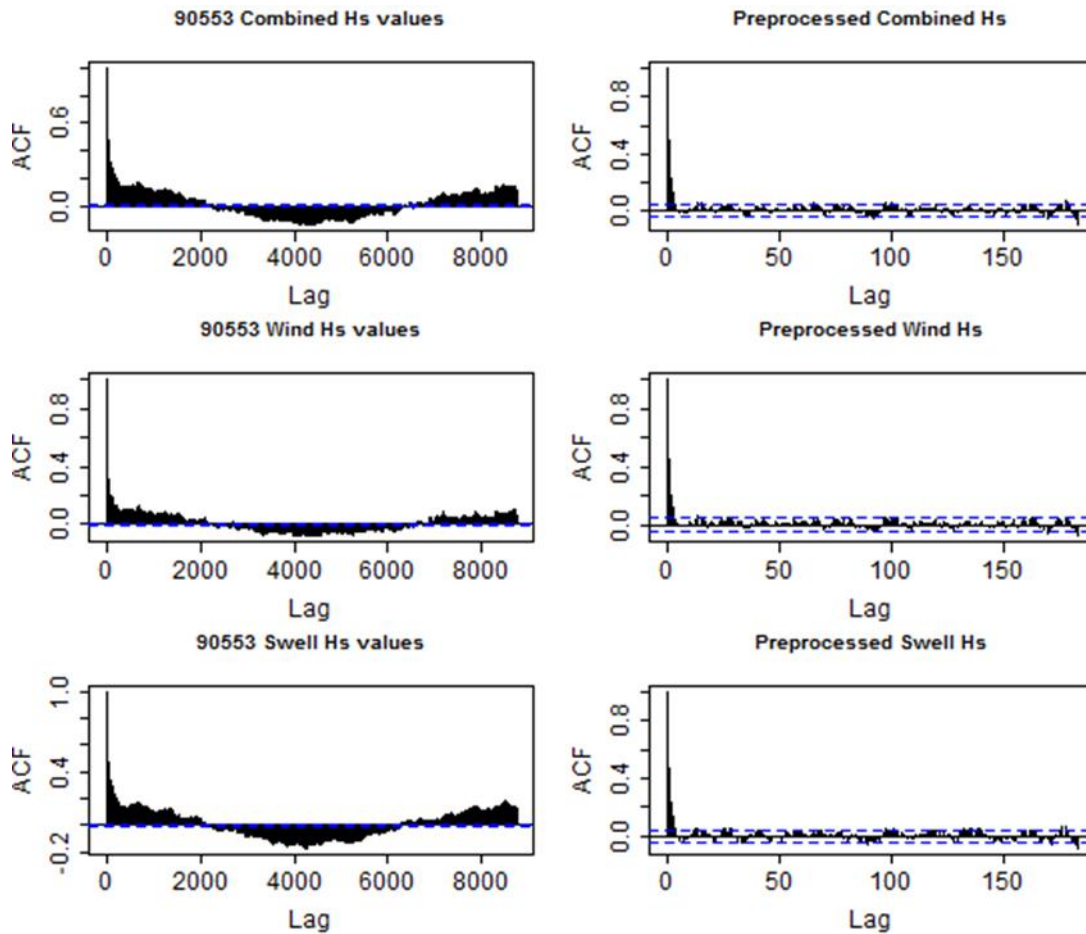


Figure 6.25 - Autocorrelation functions for the original hindcast data (left) and the pre-processed data (right). Values presented for H_s .

Figure 6.26 presents the scatterplots for the original data (hindcast data), the subsampled and the pre-processed data. When performing the subsampling procedure, one is able to see that the dependence between H_s and T_z changes considerably. This occurs because only the maximum data for the wave heights is being selected along with the coexisting up-crossing mean periods. Once again, since the season effect will be added back again, one expects that this change is dissipated after the final generation process. In the present case, the generated data will of course correspond to a model that expresses the 2 days maxima for the significant wave heights and the associated values of the mean wave up-crossing periods. The straight comparison between the original hindcast data and the pre-processed data becomes less relevant, because the first concerns to an hourly output, while the latter concerns the two-day maxima. Therefore, further comparisons are to be performed between the subsample and the pre-processed data.

The models output will correspond to maximum values per each two days, which are useful for offshore wind engineering design, namely in loads calculation. However, for reliability assessment purposes, the fact that the models refer to local maxima of H_s and T_z may lead to an overestimation of a system's probability of failure. Although this may result in a conservative assessment of an offshore system's safety, this option should be the aim of further detailed research. It should be noted that the dependence measures have changed. In this work the measure of dependence, τ_K , was corrected for ties existence and obtained for all datasets. These values are summarized in Table 6.17.

From Table 6.17 it is also possible to understand that for the wind-sea component the positive dependence between H_s and T_z is more evident than the one showed by the swell component. This is maintained after the subsampling and the removal of seasonality.

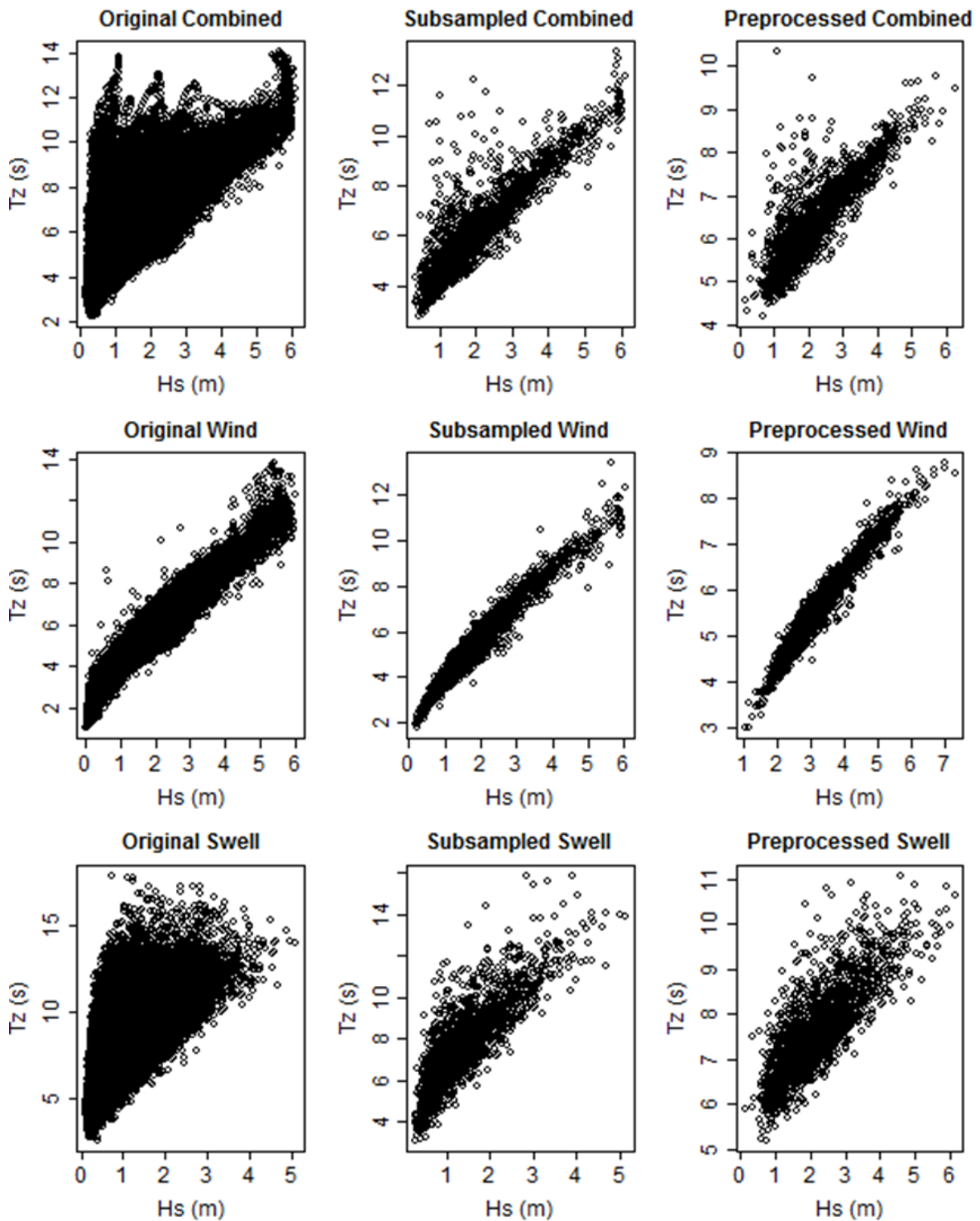


Figure 6.26 – Comparison of H_s and T_z before and after the subsampling and the pre-processing.

Table 6.17 – Measure of dependence (τ_K) for the original data, the subsamples and the pre-processed data.

| τ_K | Original | Subsample | Pre-processed |
|-----------------|----------|-----------|---------------|
| Combined | 0.534 | 0.719 | 0.688 |
| Wind | 0.893 | 0.875 | 0.864 |
| Swell | 0.539 | 0.648 | 0.621 |

At a first glance one should expect that the best fit is not provided by the same copula for the wind-sea, swell and the combined data, not only because the asymmetry shown by the data varies (Figure 6.24 and Figure 6.26), but also because the measure of dependence τ_K is different (Table 6.17). Also note that for the same copula, the estimation of the copula parameter depends on τ_K . An important aspect to be noted is that τ_K may not be a suitable analysis parameter when the behaviour of the tails is being analysed. For this matter the asymptotic dependence should be looked into in further detail.

The dependence in the tails region considerably affects the choices on the possible models to be tested, because different copulas display different dependences at the lower or upper tails. At this stage it should be kept in mind that the values obtained for the overall dependence measure τ_K seem to be reasonable, in the sense that due to the wave steepness it is physically impossible to have very large wave heights with very short periods. In general, as the significant wave height increases the mean up-crossing period is also expected to increase.

6.3.3 Marginal distributions

Before applying the copula-based models to the pre-processed data, an assessment of the goodness-of-fit of several marginal distributions was performed. The Kolmogorov-Smirnov distance (KS) and the Wasserstein (WS) distance were calculated between each tested marginal and the empirical cumulative distribution function of the pre-processed data.

Table 6.18 provides these distances. One is able to conclude that for both measures the lognormal distribution function (Table 6.18 in *italic*) was the one that provided a closer fit to the significant wave heights and the mean up-crossing periods. In fact, this distribution was also the best candidate for the hindcast and the subsampled data.

The Maximum Likelihood Estimation method (MLE) was then used to estimate the lognormal distribution parameters associated with the pre-processed data. In Table 6.19, these parameters and the 95% confidence interval are shown. Table 6.20 gives the descriptive statistics of the pre-processed data.

Table 6.18 – Kolmogorov-Smirnov (KS) and Wasserstein (WS) distances between theoretical marginal distribution and the empirical cumulative distribution function of the Pre-processed data.

| Distribution | Combined | | Wind | | Swell | |
|--------------|----------|----------|----------|----------|----------|----------|
| | KS H_s | KS T_z | KS H_s | KS T_z | KS H_s | KS T_z |
| Normal | 0.097 | 0.063 | 0.100 | 0.077 | 0.068 | 0.061 |
| Exponential | 0.313 | 0.513 | 0.416 | 0.496 | 0.286 | 0.527 |
| Rayleigh | 0.107 | 0.409 | 0.246 | 0.382 | 0.079 | 0.434 |
| GEV | 0.152 | 0.117 | 0.155 | 0.120 | 0.151 | 0.110 |
| GP | 0.254 | 0.445 | 0.354 | 0.420 | 0.226 | 0.454 |
| Lognormal | 0.024 | 0.042 | 0.051 | 0.046 | 0.035 | 0.035 |
| Weibull | 0.071 | 0.080 | 0.092 | 0.085 | 0.041 | 0.088 |
| Weibull 3p | 0.071 | 0.047 | 0.092 | 0.076 | 0.041 | 0.046 |

| Distribution | Combined | | Wind | | Swell | |
|--------------|----------|----------|----------|----------|----------|----------|
| | WS H_s | WS T_z | WS H_s | WS T_z | WS H_s | WS T_z |
| Normal | 0.186 | 0.115 | 0.191 | 0.134 | 0.142 | 0.114 |
| Exponential | 0.709 | 1.528 | 1.096 | 1.476 | 0.715 | 1.621 |
| Rayleigh | 0.124 | 1.073 | 0.455 | 1.003 | 0.113 | 1.246 |
| GEV | 0.341 | 0.252 | 0.358 | 0.298 | 0.317 | 0.291 |
| GP | 0.441 | 1.086 | 0.742 | 1.047 | 0.445 | 1.182 |
| Lognormal | 0.059 | 0.076 | 0.081 | 0.075 | 0.069 | 0.061 |
| Weibull | 0.125 | 0.173 | 0.196 | 0.195 | 0.081 | 0.211 |
| Weib 3p | 0.162 | 0.100 | 0.176 | 0.147 | 0.118 | 0.098 |

Table 6.19 – Parameters and 95% Confidence interval of the lognormal distribution fitted to the pre-processed data. C is the respective 95% confidence interval.

| | Combined | | Wind | | Swell | |
|------------------|-------------------|-------------------|-------------------|-------------------|-------------------|-------------------|
| | H_s | T_z | H_s | T_z | H_s | T_z |
| $\log(\mu)$ | 0.691 | 1.840 | 1.119 | 1.693 | 0.679 | 2.018 |
| C_{μ} 95% | [0.669; 0.711] | [1.833; 1.847] | [1.106; 1.133] | [1.685; 1.701] | [0.657; 0.700] | [2.013; 2.024] |
| $\log(\sigma)$ | 0.454 | 0.152 | 0.296 | 0.175 | 0.467 | 0.128 |
| C_{σ} 95% | [0.440; 0.469] | [0.147; 0.157] | [0.286; 0.305] | [0.170; 0.181] | [0.454; 0.484] | [0.123; 0.132] |

Table 6.20 – Descriptive statistics of the pre-processed data.

| Descriptive stats | Combined | | Wind | | Swell | |
|-------------------|--------------------|--------------------|--------------------|--------------------|--------------------|--------------------|
| | H _s (m) | T _z (s) | H _s (m) | T _z (s) | H _s (m) | T _z (s) |
| Mean | 2.20 | 6.4 | 3.20 | 5.5 | 2.19 | 7.6 |
| Median | 1.98 | 6.2 | 2.96 | 5.4 | 2.03 | 7.5 |
| Std. Deviation | 0.99 | 1.0 | 0.99 | 1.0 | 0.98 | 1.0 |
| Max | 6.26 | 10.3 | 7.29 | 8.8 | 6.14 | 11.1 |
| Min | 0.14 | 4.2 | 1.04 | 3.0 | 0.11 | 5.2 |
| Percentile 25% | 1.46 | 5.6 | 2.48 | 4.8 | 1.43 | 6.9 |
| Percentile 50% | 1.98 | 6.2 | 2.96 | 5.4 | 2.03 | 7.5 |
| Percentile 75% | 2.77 | 7.1 | 3.75 | 6.2 | 2.80 | 8.2 |
| Percentile 90% | 3.69 | 7.7 | 4.65 | 6.9 | 3.54 | 9.0 |
| Percentile 99% | 4.99 | 8.8 | 5.97 | 8.1 | 5.04 | 10.3 |
| Percentile 99.5% | 5.30 | 9.0 | 6.29 | 8.4 | 5.58 | 10.5 |
| Percentile 99.9% | 5.87 | 9.7 | 6.98 | 8.7 | 5.96 | 10.9 |

6.3.4 Copula-based models for the significant wave height and up-crossing mean period

In this section several copula-based models are fitted to the pre-processed data. The goodness-of-fit is comparatively assessed by means of the Crámer-von Mises distance (s) which, according to [244], corresponds to a more formal goodness-of-fit test for copulas. The present analysis is mainly focused on the Crámer-von Mises distance, as it enables a straightforward comparison of each model with the empirical copula of the pre-processed data. In this section, an attempt to fit the data is made with a set of symmetric copulas. This trial will be followed by the application of the extra-parametrization procedure with an independent copula and pairwise copulas. Going one step further and based on the best scores of the Crámer-von Mises distance, pairs of different copulas will be tested.

6.3.4.1 Empirical copula

Figure 6.27 gives the empirical copula of the pre-processed data in the (u,v) -space, $(F^{-1}(H_s); F^{-1}(T_p))$. From the left to the right, one has the combined sea, the wind-sea and swell components. One can confirm that the data has an asymmetric behaviour in the (u,v) -space, i.e. generated pseudo-observations (u,v) , thus $C(u,v) \neq C(v,u)$. As in other works and datasets, e.g. [123], [218] and [238], the asymmetry in the data was already expected. This can be explained by the physical limitations of the wave steepness, i.e. due to wave breaking after a certain limit, it is not possible to have very high waves with very short periods. The evident asymmetry indicates that symmetric copulas will struggle when fitting with quality the present data (as seen for the peak period in section 6.2.5). One expects that a straightforward application of such copulas does not perform well under the Crámer-von Mises evaluation. A solution for this is proposed further on with the extra-parametrization technique based on the Khoudraji algorithm. As it will be demonstrated, the fits will be improved in the copula constructions with extra parameters. Figure 6.27 also indicates that the wind-sea component is the

dataset with the least degree of asymmetry, whilst the combined sea seems to be the most asymmetric one. With the available dataset from [286] it was not possible to assess why the wind component was less asymmetric than the swell. Due to the Horns Rev 3 location, it is possible that this fact might be related to shallow water depth effects. The improvements obtained in the Crámer-von Mises distance are expected to be more pronounced in the swell component and the combined sea, because symmetric models may fit the wind component better than they do for the combined sea and the swell.

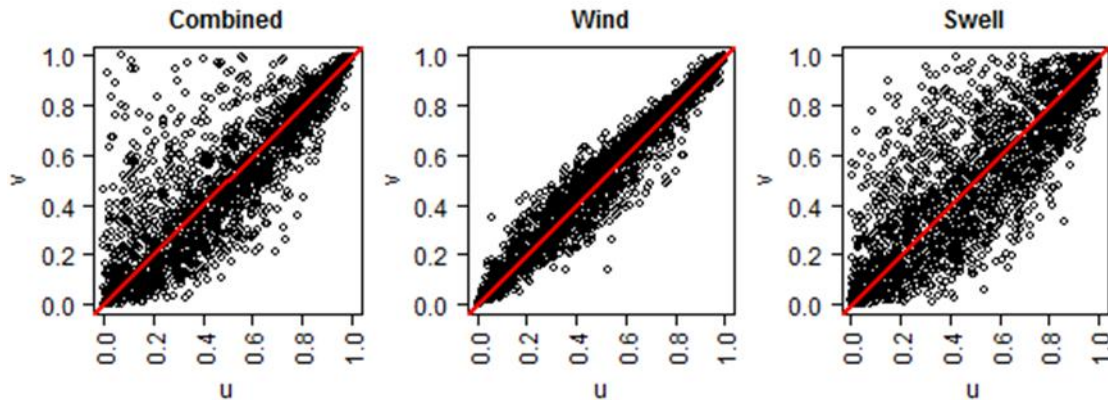


Figure 6.27 – Empirical copulas of the pre-processed data in the (u,v) -space.

6.3.4.2 Symmetric copula-based models

To confirm the suspicion based on the asymmetry shown by the empirical copulas, a first attempt was performed with the following list of copulas: the Gumbel, the Frank, the Clayton, the Galambos, the Hüssler-Reiss (HR), the Joe, the Normal (Gaussian), the Tawn the Plackett, the Ali-Mikhail-Haq (AMH) and the Farlie-Gumbel-Morgenstern (FGM). Further details on these copulas are provided in [243].

As expected the tested copulas failed at capturing the data's asymmetry. In Table 6.21 the estimated parameter and the Crámer-von Mises distance of the tested copulas are presented. The mentioned distance is quite large when compared with the extra-parametrized copulas. The copulas with the lowest score in the Crámer-von Mises distances were the Gumbel copula for the combined sea, the Hüssler-Reiss for the wind-sea component and the Normal copula for the swell. These values are presented in italic format in Table 6.21. When comparing Figure 6.28 with Figure 6.27 (empirical copulas) it becomes obvious that the best option among the proposed copulas is not able to accurately reproduce the asymmetry shown by the empirical copulas. However, as referred before, the wind-sea component, which was the less asymmetric one seems to be the case where the proposed copulas are able to provide the lowest value of the Crámer-von Mises distance. In the combined dataset, the distances are evidently larger (Table 6.21) when compared with the components' distances (wind-sea and swell). The asymmetry of the swell component is not as evident as in the combined dataset but it is still present (see Figure 6.26). Still, the copulas shown in Figure 6.28 reproduced symmetric data which, do not comply with the knowledge obtained by the empirical copulas in Figure 6.27. This is the case where extra-parametrization could be applied to improve the goodness-of-fit.

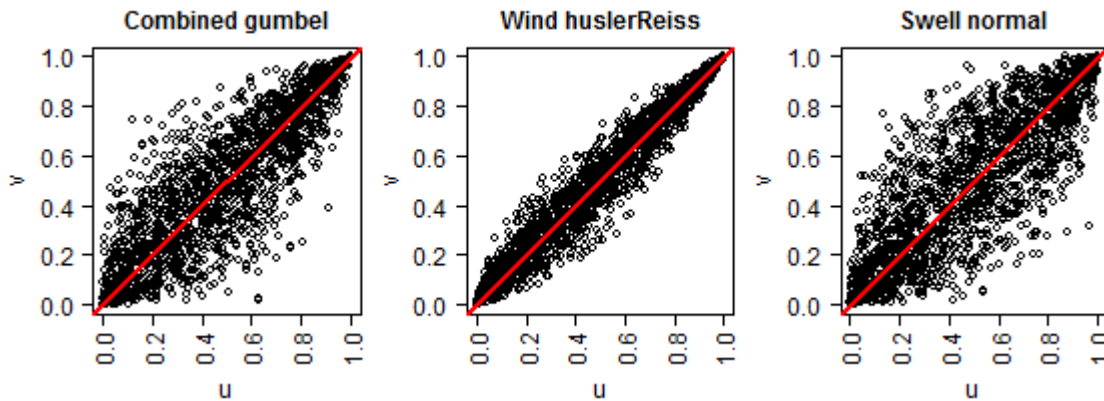


Figure 6.28 – Symmetric copulas without extra-parametrization with the lowest Crámer-von Mises distances, (u,v)-space per dataset.

An aspect worth mention in the present analysis is the fact that separating the total sea into its swell and wind-sea components does not necessarily lead to an improvement of a certain copula's performance. For example, in Joe copula one obtains $s=0.5857$, a lower Crámer-von Mises distance than the same copula applied to the swell component, which yields $s=0.9948$. On the other hand, in the wind-sea component, the Joe copula presents an $s=0.1250$, which reflects the fact that the copula's goodness-of fit is very much dependent on the symmetry/asymmetry present in the data.

As a result, when fitting copula models the separation of the combined sea into its components only results in a better goodness-of-fit, if the actual components yield a degree of symmetry that is retained by the symmetric copulas.

According to Table 6.21, the AMH, the FGM and the Tawn copula (with one parameter, i.e. symmetric version) provided the worst (i.e. highest) values of the Crámer-von Mises distance. The parameter estimation leading to the minimization of s yields $\theta=1$, which is in the limit of the parameters' interval for the three cases [243]. This enables one to conclude that these families of copulas are not suitable for the present case study. The extra-parametrization of these copulas is not expected to present any benefit for the present analysis, as it will be confirmed. This is related with the specific nature of these copulas, for example, FGM copula is designed to hold a quadratic section in the (u,v)-space. The quadratic section, say in u , implies that $C(u,v)=a(v)^2+b(v)u+c(v)^2$. The pre-processed data do not hold a quadratic section within FGM's θ limit and therefore this copula is not suitable for these data. The Tawn copula tested in this case only has one parameter (unlike the previous one used in section 6.2.5.4).

In the other copulas presented in Table 6.21, only the wind-sea component presents Crámer-von Mises distances that are in the order of 10^{-2} . Since these copulas imply different tail dependences, this is also a reason that contributes to the disparity in the goodness-of-fit of the tested copulas. As an overall remark, it should be noted that the asymmetry in the data is a key factor when using copulas to model the significant wave heights and the mean up-crossing periods. Therefore, the statistical modelling of the sea components *per se* may not contribute to a better goodness-of-fit of given copulas. Nevertheless, it should be recognised that if the components have a noticeable symmetry, simple copulas could indeed be used to model the data. This can be perceived by the low values of s obtained for some copulas applied to the wind-sea component, e.g. the Galambos, the Gumbel or the HR copulas.

In terms of the Crámer-von Mises distance, some of the copulas seem to compare well with the values obtained with extra-parametrization for the combined sea analysed by [123]. This could be due to the characteristics of the present dataset and also due to the accuracy of the estimation of the parameters and the Crámer-von Mises distance. Although not specified in [123], in this study, the estimation of the copulas' parameters and the values of s were performed with an iterative procedure, until the Crámer-von Mises distance is stabilized at the fourth decimal place. These distances can be improved with the extra-parametrization technique. Therefore, wave parameters modelling and reliability problems studied under the use of simple Archimedean or elliptical copulas, e.g. [125, 237, 259] or [300], can improve their accuracy with the use of the same copula with extra-parameters. In the next section, the extra-parametrization is introduced and compared with the results obtained in the symmetric models (Table 6.21).

Table 6.21 – Estimated symmetric copulas, without extra-parametrization and their Crámer-von Mises distances (lowest in italics).

| Copula | Combined | | Wind | | Swell | |
|-----------------|----------|---------------|----------|---------------|----------|---------------|
| | θ | s | θ | s | θ | s |
| AMH | 1 | 19.733 | 1 | 32.7288 | 1 | 14.4045 |
| Clayton | 5.105 | 2.2590 | 17.655 | 0.2697 | 3.517 | 1.7917 |
| FGM | 1 | 30.9645 | 1 | 48.5962 | 1 | 24.7091 |
| Frank | 9.779 | 0.6682 | 24.909 | 0.0944 | 7.910 | 0.3478 |
| Galambos | 2.451 | 0.3913 | 6.438 | 0.0171 | 1.965 | 0.2364 |
| Gumbel | 3.161 | <i>0.3840</i> | 7.151 | 0.0172 | 2.675 | 0.2347 |
| HR | 3.149 | 0.4159 | 7.661 | <i>0.0169</i> | 2.592 | 0.2451 |
| Joe | 5.252 | 0.5857 | 14.682 | 0.1250 | 4.267 | 0.9948 |
| Normal | 0.879 | 0.6536 | 0.976 | 0.0376 | 0.829 | <i>0.2258</i> |
| Plackett | 36.288 | 0.5463 | 259.693 | 0.0615 | 23.181 | 0.2845 |
| Tawn | 1 | 9.8314 | 1 | 20.8852 | 1 | 6.4406 |

6.3.4.3 Extra-parametrization with an independent copula

Using the procedure described in section 5.10.3.1, new asymmetric copulas can be extra-parametrized with an independent copula. For the tested copula-based models, one obtains a set of 3 parameters and the associated Crámer-von Mises distance. These values are summarized in Table 6.22. It is possible to see that the AMH, the FGM and the Tawn copulas, were not able to catch the asymmetry of the data. Note that these copulas yield $\alpha=\beta=1$. This was already expected, since in the application without extra-parametrization, the copula's parameter θ had reach its limit and still the values of s were very high when compared with the other models.

Without reaching its θ limit, the Plackett model also led to $\alpha=\beta=1$ for the wind-sea component. Hence, this model did not catch the asymmetry of this dataset, which was the one closest to symmetry. One is also able to note that the estimation of θ and the Crámer-von Mises distance obtained in Table 6.22 is the same as in Table 6.21 ($s= 0.0615$). However, note that the symmetric Plackett copula applied to the wind-sea component still provided a lower distance than the asymmetric models obtained with the Frank, the Joe and the Clayton copulas. This interesting result is justified by the fact that the present data do not have a much remarked asymmetry for this sea component, as it is

presented for the combined sea and the swell component. This emphasises again the fact that copula's performance is very much dependent on the asymmetry of the data. Also, the tested models account for different tail dependences, which may also contribute for the disparity of the Crámer-von Mises distance between models.

From Table 6.22 one can also conclude that the pre-processed data for the combined sea was best fitted by the extra-parametrized Gumbel copula, which was closely followed by the extra-parametrized Galambos and the extra-parametrized HR copulas. The swell component was best fitted by extra-parametrizing the Normal copula, which was followed by extra-parametrizing the Gumbel and the HR ones. The HR copula provided the lowest Crámer-von Mises distance for the wind-sea component, which also presented very similar values of s , when modelled with the Galambos and the Gumbel copulas. The lowest Crámer-von Mises distances appear in italics in Table 6.22.

In general, the Gumbel and the HR copulas, with extra-parametrization with an independent copula, were the models that tended to provide the lowest Crámer-von Mises distances. If one compares the distances obtained between the models with the same copula, with and without extra-parametrization with an independent copula, i.e. Table 6.21 and Table 6.22, it is possible to conclude that the construction proposed by Eq. (5.86) leads to reductions in the s values, thus, approximating the proposed models to the empirical copulas of the pre-processed data. The exception occurs for the AMH, the FGM and the Tawn copulas, which remain the same as the symmetric versions explained before. For the other models, the improvements obtained with the extra-parametrization are more noticeable for the combined and the swell pre-processed datasets. This occurs because the asymmetry in these datasets contributed to worse estimations with the symmetric set of copulas. This emphasizes the notion that the added complexity of the extra-parametrization procedure is more valuable if the asymmetry in the data is more evident. The improvement of the Crámer-von Mises distances agrees with the results reported in [123] and [263].

Figure 6.29 provides the extra-parametrized copulas that led to the lowest Crámer-von Mises distances. One can visually confirm that these copulas provide asymmetric results, which are closer to the empirical copulas shown in Figure 6.27 than the results provided by the set of symmetric copulas from Figure 6.28. One may also want to look at the original $(H_s; T_z)$ -space. A series of 1887 points generated in this original space are presented in Figure 6.30. In order to obtain the values in the original $(H_s; T_z)$ -space the seasonality is added back to the pre-processed data, by inverting Eq. (6.5). Once the seasonality is added, the autocorrelation function becomes similar to the subsampled data. The autocorrelation function for H_s in the generated series of 1887 pairs of $(H_s [m]; T_z [s])$ is shown in Figure 6.31. The analysis also showed that the autocorrelation of the mean up-crossing period agreed with the subsampled data.

In Figure 6.30 the generated series include values that can exceed the maximum of the hindcast significant wave heights. Sometimes the exceedances may be up to 2 m, which is quite striking. Despite the reasonable agreement between the generated pairs of $(H_s; T_z)$, the models tended to provide a worse fit when dealing with the upper tail of the distributions. At a first look, it seems that the marginal distributions previously defined are too heavy tailed for the present data. It should be noted that this might be a problem of the marginal modelling and not necessarily due to the employed copula models. This also occurred with the extra-parametrization with pairwise and the Gumbel copulas. This emphasizes the importance of a good marginal definition, regardless of the copula model employed for the joint distribution of H_s and T_z . There are also large uncertainties in the fitting of the marginal models and this would particularly affect the tails of the distributions. The author recognizes that this aspect should be investigated in further research. However, the same marginal distributions applied to the pre-processed data are used when converting the data to the original $(H_s; T_z)$ -space.

Therefore, relative comparisons between models are still valid. The overestimation of significant wave heights may lead to a conservative safety/reliability assessment of offshore wind or marine structures, including scour protections, because the large significant wave heights are the most energetic phenomena and the most likely to lead to the failure of a structure. However, one should note that such models may provide an overestimation of the probabilities of failure, which does not contribute to the optimization of the structures' design.

Table 6.22 – Estimated asymmetric copulas, with extra-parametrization with an independent copula and their Crámer-von Mises distances (lowest in italics).

| Extra-parametrization with an Independent copula | | | | | | |
|--|----------------------------|---------------|----------------------------|---------------|-------------------------|---------------|
| Copula | Combined | | Wind | | Swell | |
| | $\alpha; \beta; \theta$ | s | $\alpha; \beta; \theta$ | s | $\alpha; \beta; \theta$ | s |
| AMH | 1; 1; 1 | 19.7326 | 1; 1; 1 | 32.7288 | 1; 1; 1 | 14.4045 |
| Clayton | 0.936; 0.812; 26.776 | 0.4084 | 0.971; 0.978; 28.699 | 0.1707 | 0.912; 0.804; 10.759 | 0.5466 |
| FGM | 1; 1; 1 | 30.9645 | 1; 1; 1 | 48.5963 | 1; 1; 1 | 24.7091 |
| Frank | 0.977; 0.846; 18.203 | 0.2207 | 0.986; 0.992; 28.867 | 0.0836 | 0.985; 0.869; 10.838 | 0.1923 |
| Galambos | 1; 0.868; 3.729 | 0.0667 | 0.997; 1; 6.572 | 0.0165 | 0.965; 0.845; 3.048 | 0.1649 |
| Gumbel | 1; 0.868; 4.445 | <i>0.0665</i> | 0.997; 1; 7.293 | 0.0166 | 1; 0.911; 3.067 | 0.1171 |
| HR | 0.992; 0.864; 4.785 | 0.0696 | 0.995; 1; 7.887 | <i>0.0159</i> | 0.985; 0.865; 3.462 | 0.1200 |
| Joe | 0.985; 0.856; 8.147 | 0.0869 | 0.982; 0.989; 17.809 | 0.1022 | 0.943; 0.827; 6.983 | 0.4705 |
| Normal | 0.983; 0.849; 0.956 | 0.1674 | 0.992; 0.997; 0.979 | 0.0348 | 1; 0.888; 0.882 | <i>0.0728</i> |
| Plackett | 1; 0.868; 93.048 | 0.2055 | 1; 1; 261.051 | 0.0615 | 1; 0.905; 35.11 | 0.1799 |
| Tawn | 1; 1; 1 | 9.8314 | 1; 1; 1 | 20.8852 | 1; 1; 1 | 6.4406 |

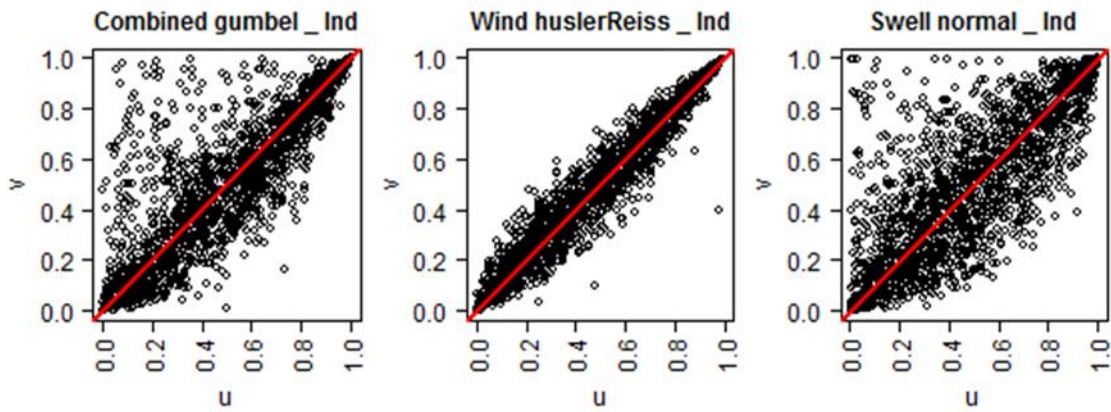


Figure 6.29 – Asymmetric copulas, with extra-parametrization with an independent copula, with the lowest Crámer-von Mises distance, (u,v)-space per dataset.

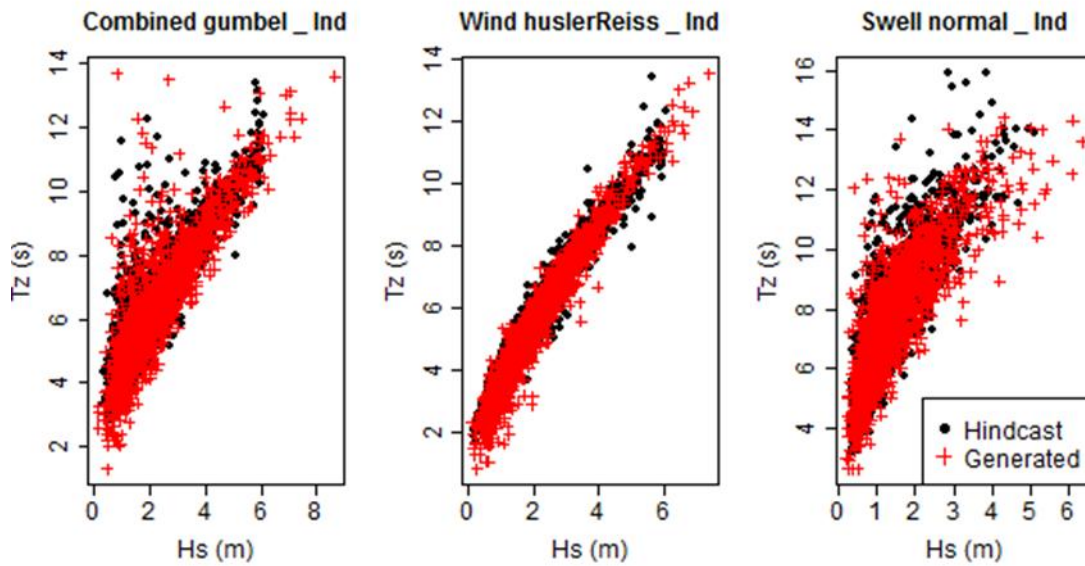


Figure 6.30 – Generated series (+) of 1887 pairs of $(H_s; T_z)$ over the subsampled data (o) based on the best copulas extra-parametrized with an independent copula.

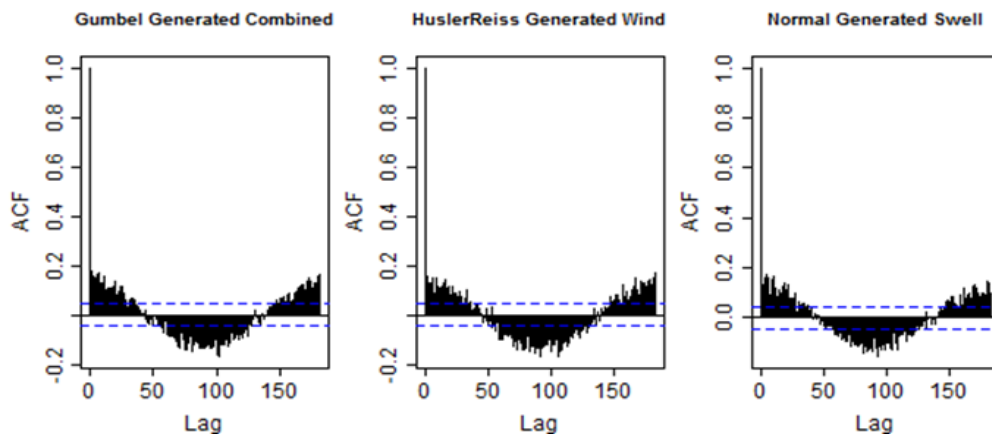


Figure 6.31 - Autocorrelation function for H_s in the generated series of 1887 pairs of $(H_s; T_z)$ based on the best copulas extra-parametrized with an independent copula.

6.3.4.4 Extra-parametrization with a pairwise copula

In this section, only a set of the copulas with the lowest Crámer-von Mises distances obtained in the previous section will be tested. Therefore, the models based on the Tawn copula, the FGM and the AMH copulas are excluded from the analysis. The estimated parameters for the pairwise copulas, Eq. (5.87), and the Crámer-von Mises distances are provided in Table 6.23. Comparing Table 6.23 with Table 6.21 and Table 6.22, the extra-parametrization with a pairwise copula leads to improvements in the Crámer-von Mises distances. The improvements are more noticeable in some copulas than in others. Generally, the models that had already presented low values of s are the ones where the improvement is less noted, e.g. the Gumbel-Gumbel or the HR-HR copulas in the wind component. However, the improvements are quite remarkable in some other models, for example in the swell component, the Plackett model extra-parametrized with an independent copula (Table 6.22) has $s=0.1799$, while the Plackett-Plackett model is improved to $s=0.0455$.

Table 6.23 shows that the pairwise models with lowest Crámer-von Mises distances were the Joe-Joe copula for the combined sea, the Gumbel-Gumbel copula for the wind-sea component and the Plackett-Plackett copula for the swell component. One should also note that for the three datasets, the Galambos-Galambos and the HR-HR copulas still present low Crámer-von Mises distances. Although their distances are not the lowest ones, the differences for the best models are not so large. Due to the existence of several models with similar Crámer-von Mises distances, it is important to understand if these models are actually very different when dealing with generated series. Note that the Crámer-von Mises distance provides a measure on the overall goodness-of-fit.

Therefore, two copulas with the same Crámer-von Mises distance, may fit the extreme events, i.e. upper tail, with different accuracy. Hence the tail behaviour of the models should be analysed depending on the final objective or intended use of the proposed model. For instance, if one wants to predict the extreme significant wave height and the mean up-crossing period for a specific return period, one may chose the model that fits the upper tail the best, although not being the best model in terms of the Crámer-von Mises distance.

On the other hand, if one wishes to deal with probabilities of failure of a marine structure, it is important to reach a balance between the overall goodness-of-fit and the upper-tail fit, mainly, because the probability of failure depends on the proportion between the extreme events that can cause failure and the common events that are not expected to lead to the collapse of the system (unless adaptive sampling methods are used).

Before addressing the tail dependence analysis, Figure 6.32 provides the data for the pairwise copulas that provided the lowest Crámer-von Mises distances. It is possible to see that the asymmetry present in the data is also captured with the pairwise copulas. The generated series of 1887 points in the original $(H_s; T_z)$ -space is provided in Figure 6.33, which compares with Figure 6.30. One is able to see that the extra-parametrization with a pairwise copula enables one to generate the values which are within the range of the subsampled data. Once again the effect of subsampling the maximum values in each block of 2 days from the original hindcast data should be the aim of further research, as well as the effect of the selected marginal distributions.

In Figure 6.34 it is presented the autocorrelation function of the significant wave heights for the generated series with the pairwise copulas. The autocorrelation compares well with the one presented by the subsampled data. Also in this case, the analysis showed that the autocorrelation of the mean up-crossing period also agreed with the subsampled data.

Table 6.23 – Estimated asymmetric copulas, with pairwise extra-parametrization, and their Crámer-von Mises distances (lowest s in italics).

| Copula | Combined | | Wind | | Swell | |
|--------------------------|--------------------------------------|---------------|---------------------------------------|---------------|-------------------------------------|---------------|
| | $\alpha; \beta; \theta_1; \theta_2$ | s | $\alpha; \beta; \theta_1; \theta_2$ | s | $\alpha; \beta; \theta_1; \theta_2$ | s |
| Clayton-Clayton | 0.124; 0.373; 31.824; 31.824 | 0.2937 | 0.491; 0.605; 82.324; 100 | 0.0380 | 0.252; 0.558; 24.872; 14.832 | 0.1586 |
| Frank-Frank | 0.047; 0.248; 20.992; 64.998 | 0.1984 | 0.481; 0.370; 84.998; 99.978 | 0.0344 | 0.147; 0.422; 17.492; 28.602 | 0.0984 |
| Galambos-Galambos | 0.029; 0.181; 4.077; 0.934 | 0.0622 | 0.581; 0.515; 9.592; 6.579 | 0.0152 | 0.243; 0.455; 3.568; 1.564 | 0.0901 |
| Gumbel-Gumbel | 0.041; 0.195; 4.926; 1.651 | 0.0624 | 0.382; 0.447; 7.317; 10.770 | <i>0.0151</i> | 0.241; 0.475; 4.467; 2.452 | 0.0926 |
| HR-HR | 0.119; 0.275; 6.065; 1.503 | 0.0653 | 0.435; 0.476; 6.849; 10.710 | 0.0152 | 0.181; 0.377; 4.030; 1.923 | 0.0883 |
| Joe-Joe | 0.105; 0.260; 9.056; 1.806 | <i>0.0529</i> | 0.472; 0.369; 18.906; 15.475 | 0.0233 | 0.212; 0.502; 7.795; 3.944 | 0.2059 |
| Normal-Normal | 0.922; 0.745; 0.852; 0.951 | 0.1583 | 0.115; 0.173; 0.984; 1 | 0.0280 | 0.115; 0.346; 0.934; 0.934 | 0.0492 |
| Plackett-Plackett | 0.064; 0.255; 162.688; 209.984 | 0.1634 | 0.463; 0.563; 998.976; 2474.976 | 0.0238 | 0.289; 0.543; 185.984; 46.413 | <i>0.0455</i> |

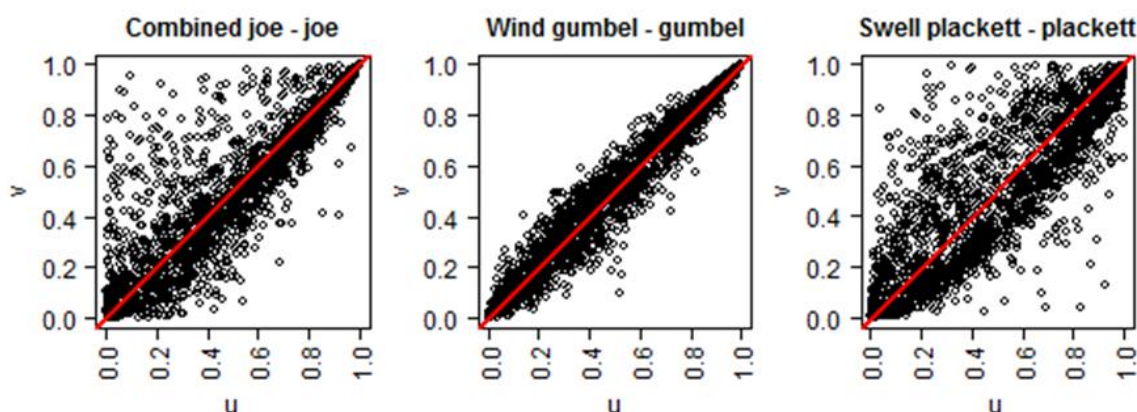


Figure 6.32 – Asymmetric copulas, with extra-parametrization with a pairwise copula, with the lowest Crámer-von Mises distance, (u,v)-space per dataset.

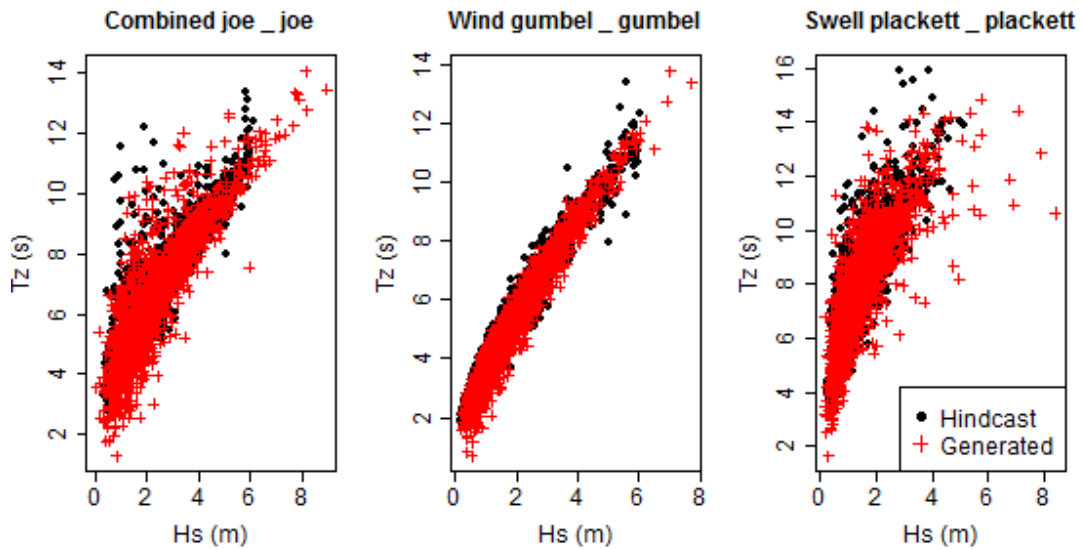


Figure 6.33 – Generated series (+) of 1887 pairs of $(H_s; T_z)$ over the original hindcast data (o) based on the best copulas extra-parametrized with a pairwise copula.

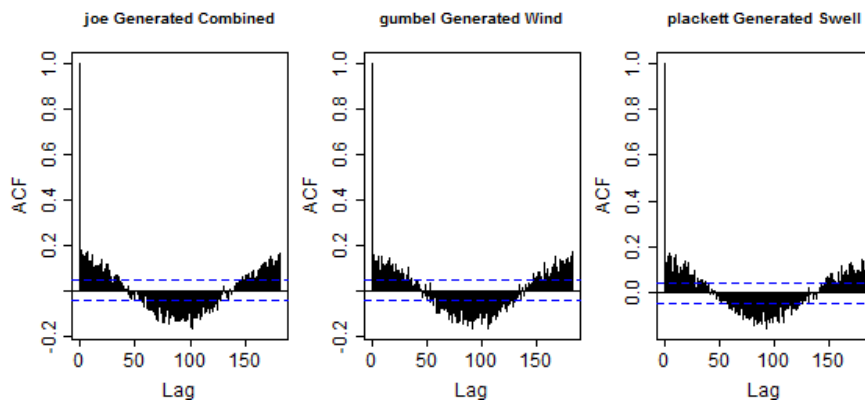


Figure 6.34 – Autocorrelation function for H_s in the generated series of 1887 pairs of $(H_s; T_z)$ based on the best copulas extra-parametrized with a pairwise copula.

6.3.4.5 Extra-parametrization with a Gumbel copula

In this section, an attempt was made to extra-parametrize the remaining copulas with a Gumbel copula. The same procedure presented in section 5.10.3 is applied, where the second copula is the Gumbel one. Note, however, that other combinations could have been tested. The parameters obtained and the optimised Crámer-von Mises distance are provided in Table 6.24. The Gumbel copula is not tested because it corresponds to the pairwise model obtained from the Gumbel-Gumbel model. Table 6.24 shows that extra-parametrization enabled one to build copula-based models based on the AHM, the FGM and the Tawn copulas. One is also able to note that the Crámer-von Mises distances did not improve for all models. Comparing Table 6.24 with Table 6.23, in the combined dataset the Joe-Joe model provides a slightly lower Crámer-von Mises distance than the Joe-Gumbel model.

All the Crámer-von Mises distances obtained in Table 6.24 are improved when compared with the symmetric models from Table 6.21. These improvements also occur in the wind-sea and swell components. The wind-sea component, which was the most symmetric dataset, provided low values of the Crámer-von Mises distance for models which only had an upper-tail dependence in the symmetric

version. Note that the Hüssler-Reiss and the Galambos copulas extra-parametrized with a Gumbel copula give similar distances when compared with their pairwise extra-parametrization. In the swell component, the Plackett copula (extra-parametrized with a Gumbel copula) remained as the model with the lowest Crámer-von Mises distance. In this case, the distance is slightly above the one obtained with the pairwise extra-parametrized Plackett copula. For some copulas, e.g. the Frank or the Clayton copulas in the combined dataset, the extra-parametrization with a Gumbel copula gave smaller Crámer-von Mises distances when compared with the extra-parametrization made with an independent copula. However, in other models this did not occur, e.g. the Galambos-Gumbel copula did not provide a smaller distance than the Galambos-Independent copula. From the tested extra-parametrizations, the pairwise copulas were the ones that provided the best goodness-of-fit in terms of the Crámer-von Mises distances. Nevertheless, it is concluded that testing the Khoudraji algorithm with different copulas may lead to fit improvements.

Table 6.24 – Estimated asymmetric copulas, with extra-parametrization with a Gumbel copula and their Crámer-von Mises distances.

| Extra-parametrization with a Gumbel copula | | | | | | |
|--|-------------------------------------|--------|-------------------------------------|--------|-------------------------------------|--------|
| | Combined | | Wind | | Swell | |
| | $\alpha; \beta; \theta_1; \theta_2$ | s | $\alpha; \beta; \theta_1; \theta_2$ | s | $\alpha; \beta; \theta_1; \theta_2$ | s |
| AMH | 0.046; 0.156; 6.049; -0.933 | 0.1387 | 0.018; 0.013; 8.694; -0.704 | 0.0350 | 0.117; 0.226; 5.112; 1.000 | 0.3141 |
| Clayton | 0.115; 0.343; 6.483; 27.833 | 0.1381 | 0.456 ;0.351; 12.843; 79.998 | 0.0242 | 0.264; 0.548; 5.365; 11.573 | 0.0731 |
| FGM | 0.046; 0.143; 6.055; -0.90 | 0.1386 | 0.018; 0.011; 8.654; -0.704 | 0.0356 | 0.112; 0.217; 4.985; 1.000 | 0.2976 |
| Frank | 0.887; 0.691; 2.010; 25.004 | 0.1660 | 0.433; 0.535; 10.016; 109.648 | 0.0243 | 0.804; 0.532; 3.030; 17.960 | 0.0883 |
| Galambos | 0.902; 0.696; 2.464; 5.306 | 0.0859 | 0.547; 0.465; 10.937; 7.445 | 0.0154 | 0.199; 0.480; 4.926; 2.469 | 0.1143 |
| HR | 0.861; 0.657; 2.315; 6.803 | 0.0849 | 0.448; 0.529; 8.002; 12.145 | 0.0153 | 0.792; 0.509; 3.128; 5.268 | 0.1129 |
| Joe | 0.155; 0.360; 6.704; 2.578 | 0.0799 | 0.473; 0.564; 8.771; 16.468 | 0.0175 | 0.234; 0.520; 5.203; 3.841 | 0.1563 |
| Normal | 0.967; 0.770; 50.333; 0.967 | 0.1561 | 0.679; 0.609 ;33.889; 0.984 | 0.0263 | 0.712; 0.835; 33.889; 0.835 | 0.0744 |
| Plackett | 0.898; 0.693; 2.260; 333.342 | 0.1619 | 0.517; 0.610; 10.459;995.73 0 | 0.0222 | 0.900; 0.685; 3.576; 60.302 | 0.0698 |
| Tawn | 0.189; 0.327; 7.310; 1.000 | 0.0814 | 0.042; 0.035; 8.840; 1.000 | 0.0280 | 0.334; 0.452; 6.206; 1.000 | 0.1558 |

The Crámer-von Mises distances obtained in the present study seem to compare well with the ones presented for different datasets by [123] and [292]. The results from Table 6.24 also show that the separation between wind-sea and primary swell components does not necessarily lead to a better goodness-of-fit when compared with the combined dataset. For instance, the Hüssler-Reiss (HR) copula extra-parametrized with a Gumbel copula presents a lower Crámer-von Mises for the combined

sea than for the swell component. In Figure 6.35, simulated data from the copulas extra-parametrized with a Gumbel copula also show an asymmetry, which is in agreement with the one obtained for the empirical copula of the pre-processed data. In Figure 6.36, the generated values show a visually good agreement with the subsampled data, as it occurred for the copulas extra-parametrized with independent or pairwise copula.

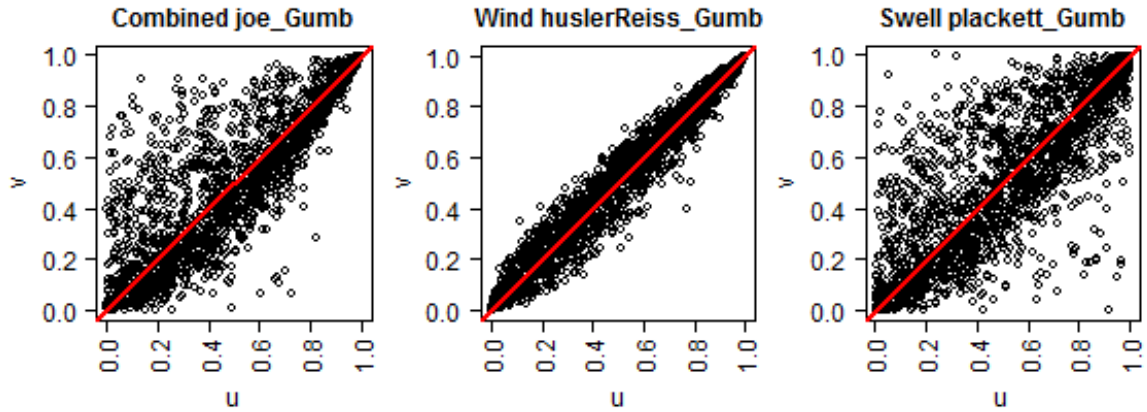


Figure 6.35 – Asymmetric copulas, with extra-parametrization with a Gumbel copula, with the lowest Crámer-von Mises distance, (u,v)-space per dataset.

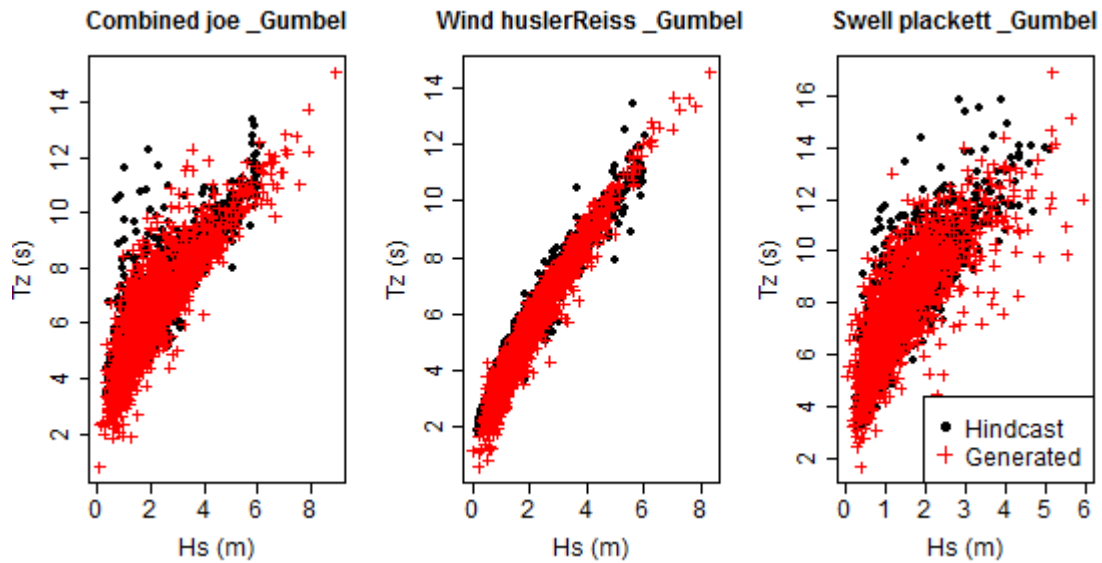


Figure 6.36 – Generated series (+) of 1887 pairs of $(H_s; T_z)$ over the original hindcast data (o) based on the best copulas extra-parametrized with a Gumbel copula.

6.3.5 Tail dependence analysis

Similarly to section 6.2.7, the non-parametric estimation originally introduced by [299] is implemented. Some of the symmetric copulas do not have tail dependence, e.g. the Clayton copula does not have upper tail dependence, the Gumbel copula does not have lower one and the Frank copula has both upper and lower zero tail dependency. As it turns out, the non-parametric estimation method proposed, [299], converges very slowly to these dependences. Therefore, in limited samples, the obtained values of the tail coefficients may not correspond to the most realistic evaluation. Still,

this non-parametric estimation of finite tail dependence is widely referred to and used in the copula's literature, e.g. [302] or [303]. Moreover, it is a straightforward method that can easily be implemented for the more complex copulas built with the Khoudraji algorithm, as the ones implemented in this research. Since the same method is used for all the copula-based models presented in this work, the use of [299] estimator introduces a systematic bias, which is not relevant for the relative comparison of the tested copulas. However, one should keep in mind that the estimator is useful for relative comparison but it might not lead to the most accurate assessment of the tail dependence coefficients.

In order to have a better perception of the differences in the tail dependences, the lower and upper tail coefficients were computed, respectively at the 5% and the 95% quantiles, i.e. $\lambda_L(u=5\%)$ and $\lambda_U(u=95\%)$. These values are summarized in Table 6.25 and they were computed for 10 random samples of 10 000 pairs (u,v) , which lead to the mean values presented. One is able to note that the models that provided the best Crámer-von Mises distance may not be the ones that provided the closest non-parametric estimation of $\lambda_L(u=5\%)$ and $\lambda_U(u=95\%)$. For example, in the extra-parametrization with a pairwise copula, the combined sea fitted with a Joe-Joe copula had provided the best Crámer-von Mises distance (see Table 6.23).

However, the values of $\lambda_L(u=5\%)$ and $\lambda_U(u=95\%)$ in this case are better approximated by the Galambos and the Normal copula respectively. Despite these occurrences, it is fair to note that the best models in terms of the Crámer-von Mises distance were not the worse models in terms of the non-parametric estimation of $\lambda_L(u=5\%)$ and $\lambda_U(u=95\%)$. This could somehow be expected because, as mentioned before, the Crámer-von Mises distance provides a measure of the overall goodness-of-fit, thus not ensuring the best fit on the tails, but still including them in the estimation process of α , β and θ .

An interesting aspect from Table 6.25 is that the pairwise models Gumbel-Gumbel, the HR-HR, Joe-Joe and Galambos-Galambos, assume a perfect asymptotic dependence at the 95% quantile in the wind-sea component. The same occurs for the Gumbel model extra-parametrized with an Independent copula. Although for the pre-processed data this does not occur, it seems reasonable to admit that the data has a strong upper-tail dependence for the wind-sea component. This occurs more frequently in the extra-parametrization with the Gumbel copula, which is expected since the Gumbel copula introduces a strong upper-tail dependence.

Table 6.25 shows that for the combined dataset, in the models extra-parametrized with an independent copula, λ_L was better approximated by the Gumbel-Independent copula, whereas λ_U was better approximated by the Frank-Independent Copula. In pairwise models, these coefficients were better approximated by the Galambos-Galambos and the Normal-Normal copulas, respectively. In the models extra-parametrized with a Gumbel copula, it can be seen that the best approximation for λ_L is given by the Tawn-Gumbel copula and for λ_U is provided by the Clayton-Gumbel copula.

Regarding the wind component, the best approximations to λ_L are given by the Clayton-Independent, the Gumbel-Gumbel and the Normal-Gumbel copulas. Still in the wind-sea λ_U is better approximated by the Plackett-Independent model, the Normal-Normal model and the Frank-Gumbel model. For the swell component the best approximations to λ_L are given by the Galambos-Independent, the Clayton-Clayton and the Plackett-Gumbel copulas, whereas for λ_U , one has the Frank-Independent, the Plackett-Plackett and the Clayton-Gumbel copulas.

Table 6.25 – Non-parametric estimation of the tail dependence at the 5% and the 95% quantiles for extra-parametrized copulas (closest values to empirical estimation in italics- bold).

| Empirical copula of the pre-processed data | | | | | | |
|---|--------------------|---------------------|--------------------|---------------------|--------------------|---------------------|
| | Combined | | Wind | | Swell | |
| | $\lambda(u=5\%)$ | $\lambda(u=95\%)$ | $\lambda(u=5\%)$ | $\lambda(u=95\%)$ | $\lambda(u=5\%)$ | $\lambda(u=95\%)$ |
| Pre-processed | 0.450 | 0.775 | 0.887 | 0.890 | 0.393 | 0.509 |
| Extra-parametrization with an independent copula | | | | | | |
| Copula | Combined | | Wind | | Swell | |
| | $\lambda_L(u=5\%)$ | $\lambda_U(u=95\%)$ | $\lambda_L(u=5\%)$ | $\lambda_U(u=95\%)$ | $\lambda_L(u=5\%)$ | $\lambda_U(u=95\%)$ |
| Clayton | 0.740 | 0.782 | 0.886 | 0.568 | 0.553 | 0.562 |
| Frank | 0.509 | 0.773 | 0.620 | 0.484 | 0.399 | 0.518 |
| Galambos | 0.525 | 0.954 | 0.800 | 0.989 | 0.395 | 0.854 |
| Gumbel | 0.451 | 0.961 | 0.880 | 1.000 | 0.397 | 0.879 |
| HR | 0.561 | 0.794 | 0.680 | 0.947 | 0.430 | 0.888 |
| Joe | 0.498 | 0.846 | 0.432 | 0.959 | 0.602 | 0.830 |
| Normal | 0.647 | 0.758 | 0.939 | 0.946 | 0.561 | 0.578 |
| Plackett | 0.565 | 0.798 | 0.856 | 0.890 | 0.390 | 0.463 |
| Extra-parametrization with a Pairwise copula | | | | | | |
| | Combined | | Wind | | Swell | |
| | $\lambda_L(u=5\%)$ | $\lambda_U(u=95\%)$ | $\lambda_L(u=5\%)$ | $\lambda_U(u=95\%)$ | $\lambda_L(u=5\%)$ | $\lambda_U(u=95\%)$ |
| Clayton | 0.512 | 0.717 | 0.798 | 0.729 | 0.394 | 0.602 |
| Frank | 0.446 | 0.733 | 0.762 | 0.674 | 0.398 | 0.629 |
| Galambos | 0.450 | 0.920 | 0.757 | 1.000 | 0.433 | 0.912 |
| Gumbel | 0.532 | 0.604 | 0.897 | 1.000 | 0.386 | 0.888 |
| HR | 0.538 | 0.866 | 0.707 | 1.000 | 0.389 | 0.818 |
| Joe | 0.452 | 0.860 | 0.802 | 1.000 | 0.420 | 0.809 |
| Normal | 0.594 | 0.734 | 0.863 | 0.873 | 0.448 | 0.675 |
| Plackett | 0.509 | 0.644 | 0.865 | 0.940 | 0.441 | 0.590 |
| Extra-parametrization with a Gumbel copula | | | | | | |
| | Combined | | Wind | | Swell | |
| | $\lambda_L(u=5\%)$ | $\lambda_U(u=95\%)$ | $\lambda_L(u=5\%)$ | $\lambda_U(u=95\%)$ | $\lambda_L(u=5\%)$ | $\lambda_U(u=95\%)$ |
| Clayton | 0.344 | 0.746 | 0.812 | 0.766 | 0.290 | 0.613 |
| Frank | 0.413 | 0.423 | 0.842 | 0.812 | 0.341 | 0.383 |
| Galambos | 0.479 | 0.381 | 0.823 | 1.000 | 0.437 | 0.751 |
| HR | 0.504 | 1.000 | 0.696 | 1.000 | 0.353 | 0.799 |
| Joe | 0.500 | 0.840 | 0.826 | 1.000 | 0.324 | 0.787 |
| Normal | 0.588 | 0.709 | 0.882 | 0.711 | 0.510 | 0.704 |
| Plackett | 0.579 | 0.727 | 0.587 | 0.755 | 0.368 | 0.321 |
| Tawn | 0.467 | 0.865 | 0.750 | 1.000 | 0.364 | 0.800 |
| FGM | 0.474 | 0.840 | 0.799 | 1.000 | 0.501 | 0.759 |
| AMH | 0.494 | 0.897 | 0.844 | 0.997 | 0.464 | 0.794 |

The flexibility introduced with the extra-parametrization enables one to obtain the optimized model parameters. Nevertheless, the results from Table 6.25 emphasize the need for specific models when dealing with the tails' region. From the analysis of Table 6.25 it is not clear which model might be the best to fit the asymmetric data. Nevertheless, one can conclude that the choice of the extra-parametrization with a Gumbel copula is a valid attempt to deal with the present data. However, it is important to note that often the reliability and risk analysis imply the simulation of the overall population of random variables, as mentioned before. In this sense, the present technique seems to achieve an interesting balance for the overall goodness-of-fit.

Therefore, a corollary from this observation is that when using copula models applied to the significant wave height and a characteristic wave period, the extra-parametrization is a reasonable way to try to improve the results obtained from symmetric copulas, which are still the main copulas applied in the ocean modelling literature.

Of course, when simulating random sea-state parameters for reliability analysis, one may adopt optimised sampling techniques based solely on the tail behaviour. These are not approached in the present research as mentioned before. As noted in [123] and confirmed in the present study, it is often difficult to visually assess which copula-based model provides the best fit, particularly in (u,v) -space but also in the original $(H_s;T_z)$ -space.

Moreover, the results obtained from the Crámer-von Mises distance and the non-parametric estimations of tail dependence are sometimes very close between models. Nevertheless, some of the copula models can be disregarded based on the Crámer-von Mises distance and the tail dependences criteria, which is the case of several symmetric copulas and some of the extra-parametrized ones. In the next section, one introduces the weighted version of the Root-Mean-Square Error (WRMSE), adapted to account for the departures at the upper tail of the significant wave heights and their joint mean up-crossing wave periods.

6.3.6 WRMSE analysis

6.3.6.1 Extra-parametrized copulas (independent and pairwise copula)

A discussion on the advantages and pitfalls of the evaluation of significant wave height models based on the root-mean-square error can be seen in [304]. If one assumes that the significant wave height is the dominant variable, in terms of reliability interest, one can also assume that the errors performed on the upper tail of H_s should have a stronger penalty when compared with the errors related to the central part of the joint distribution of H_s and T_z .

In this research, a similar procedure to the one adopted in [123] is implemented. First, a set of $N=100\,000$ pairs $(H_s; T_z)$ is obtained from each copula model, with the seasonality effects added back in. Then the original space is divided into bins of size $0.1\text{ m} \times 0.1\text{ s}$ and the points falling in each bin are computed for both the empirical subsampled data and the simulated ones. The sum of the squared difference between fractions is calculated, thus providing a measure on the goodness-of-fit of the models.

Consider B_{ij} as the i -th bin in the H_s direction and the j -th in the T_z direction. Also consider that x_{ij} is the fraction of points from the empirical dataset that fall into B_{ij} and that y_{ij} is the fraction of simulated points that fall into the same bin (B_{ij}). Then x_{ij} and y_{ij} are obtained as in Eqs. (6.6) and (6.7), while the WRSME is obtained from Eq. (6.8), where w_{ij} are the weights attributed to the errors. Note that w_{ij} varies between 0 and 1.

$$x_{ij} = \frac{1}{N_x} \sum_{k=1}^{N_x} I((H_s; T_z) \in B_{ij}) \quad (6.6)$$

$$y_{ij} = \frac{1}{N_y} \sum_{k=1}^{N_y} I((H_s; T_z) \in B_{ij}) \quad (6.7)$$

$$\text{WRMSE} = \sqrt{\sum_{ij} w_{ij} (x_{ij} - y_{ij})^2} \quad (6.8)$$

As mentioned in this case one is interested in penalizing the errors made on the upper tail of the joint distribution. The present dataset comes from a location for which the water depth ranges from 10 m to 20 m, at the Horns Rev 3 offshore windfarm. In [286] it is assumed that the maximum wave height at the location is two times the significant one.

According to CEM, [119], for the breaker index, i.e. H/d , a value of 0.6 is applied for irregular sea states. Therefore the maximum expected non-breaking wave height for $d=18$ m should roughly be $H=0.6 \times 18=10.8$ m. In the present case, one is concerned with the significant wave height, which means that wave heights over $H_s=10.8$ m will be breaking.

However, assuming that the maximum H_s is equal to 10.8 m is indeed a conservative limit when modelling the significant wave height for reliability assessment purposes at the case study location. The limits proposed for the breaker index can be seen as reference levels and for practical situations one could definitely use a lower value than the one proposed for the maximum significant wave height. Note that several works have been performed on the discussion of the breaker index variations. Here, the limit of $H/d=0.6$ is assumed as a simplistic approach. For further details on this matter the reference [118] is recommended.

A possible way to account for these physical limitations, which are not perceived in the probabilistic models, is to truncate the marginal distribution used to obtain the random values of H_s . This was performed in the present case, i.e. wave height is limited by $H/d=0.6$. Taking into consideration the maximum values of the subsamples, which are slightly above 6 m, the scale of weights applied to the WRMSE is defined as in Eq. (6.9).

Table 6.26 provides the WRMSE values for the extra-parametrized copulas with an independent or a pairwise copula. The AMH, the Tawn and the FGM copulas are not presented, because they were already excluded based on the parameter's values and the respective Crámer-von Mises distance obtained for the extra-parametrized models with independent or pairwise copulas.

$$w_{ij} = \begin{cases} 0 & 0 \text{ m} < H_s \leq 2 \text{ m} \\ 1/3 & 2 \text{ m} < H_s \leq 4 \text{ m} \\ 2/3 & 4 \text{ m} < H_s \leq 6 \text{ m} \\ 1 & 6 \text{ m} > H_s \end{cases} \quad (6.9)$$

Table 6.26 – WRMSE for the extra-parametrization with Independent and Pairwise copulas. Lowest WRMSE in bold italics.

| Copula | Extra-parametrization with an Independent copula | | |
|----------|--|-----------------|-----------------|
| | Combined | Wind | Swell |
| Clayton | 0.000253 | 0.000327 | 0.000246 |
| Frank | 0.000233 | 0.000275 | 0.000226 |
| Galambos | 0.000236 | 0.000276 | 0.000221 |
| Gumbel | 0.000226 | 0.000272 | 0.000228 |
| HR | 0.000239 | 0.000273 | 0.000228 |
| Joe | 0.000238 | 0.000306 | 0.000235 |
| Normal | 0.000227 | 0.000283 | 0.000227 |
| Plackett | 0.000228 | 0.000288 | 0.000235 |
| Copula | Extra-parametrization with Pairwise copula | | |
| | Combined | Wind | Swell |
| Clayton | 0.000241 | 0.000273 | 0.000219 |
| Frank | 0.000225 | 0.000262 | 0.000218 |
| Galambos | 0.000228 | 0.000272 | 0.000224 |
| Gumbel | 0.000227 | 0.000266 | 0.000224 |
| HR | 0.000231 | 0.000274 | 0.000223 |
| Joe | 0.000231 | 0.000268 | 0.000221 |
| Normal | 0.000231 | 0.000275 | 0.000229 |
| Plackett | 0.000228 | 0.000271 | 0.000216 |

Since

Table 6.26 refers to the original $(H_s; T_z)$ -space, one is able to see which models hold the highest and the lowest weighted errors, with higher penalties directly given to departures on the upper tail. The models that provided the lowest errors in the extra-parametrization with an independent copula, are not the same as the ones that gave the lowest Crámer-von Mises distance. In this case, the combined sea is best approximated by the Gumbel-Independent copula, while the wind-sea and swell components are approximated the best by the Gumbel-Independent and the Galambos-Independent copulas, respectively. Regarding the models extra-parametrized with pairwise copulas, one is able to see that the models that provide the lowest errors are the Frank-Frank copula for the combined sea and for the wind-sea and the Plackett-Plackett copula for the swell component.

The different results in terms of the Crámer-von Mises and the WRSME were already expected, because the first measure concerns the overall fit and the second one deals with the upper-tail fit considering increased penalties with the increasing wave height. The differences between criteria were

already noted for a different dataset in [267]. This emphasizes the need of analysing several goodness-of-fit criteria when dealing with copula-based models.

Table 6.26 also shows that, unlike in the Crámer-von Mises distance, the extra-parametrization with a pairwise copula did not lead to a generalized reduction of the WRMSE, when compared with the extra-parametrization with an Independent copula. In some models, e.g. in the Joe copula-based ones the error is reduced, in the combined sea, while for others, e.g. the Normal-Normal model for the combined sea, the error increases when compared with the Normal-Independent model. Such observations confirm that the minimization process of the Crámer-von Mises distance does not necessarily lead to a minimization of the weighted root-mean-square error, for the same copula-based model. Also the separation in the wind-sea and the swell components did not hold an improvement of the WRMSE when compared with the combined sea. This can be noted for example in the Plackett model extra-parametrized with an Independent copula and a pairwise copula. This occurs due to the fact that a model that presents a certain tail dependence may not be suitable for a specific dataset that does not yield a similar tail dependence. The dependence structures of the combined sea and its components are different, therefore the performance of a specific copula-based model does not remain the same.

6.3.6.2 Extra-parametrized copulas with a Gumbel copula

Table 6.27 provides the WRSME values for the copulas extra-parametrized with a Gumbel copula. One can see that the Galambos-Gumbel copula provided the lowest errors for the combined sea, while the HR-Gumbel copula provided the lowest ones for both the wind-sea and the swell components. No systematic improvements are registered in these models' WRMSE when compared with the extra-parametrization technique with an Independent or a pairwise copula (

Table 6.26). However, one cannot guarantee that models based on other copulas could not result in smaller values of WRMSE than the ones presented in Table 6.27. The WRMSE presented in both

Table 6.26 and Table 6.27 are considerably small when compared with the ones obtained by [123]. This could be due to the dataset used, which is different, but also due to the number of simulations performed to obtain the model's parameters. Further research should be carried out to clarify this aspect. When dealing with new datasets and based on the lack of improvements in both the Crámer-von Mises distance and the WRMSE, it seems reasonable to implement the extra-parametrized copulas with an Independent or a pairwise copula, before moving on to models with different copulas, which automatically increase the number of possible combinations to be tested.

Table 6.27 – WRMSE for the extra-parametrization with a Gumbel copula (lowest WRMSE in bold italics).

| Extra-parametrization with a Gumbel copula | | | |
|---|-----------------|-------------|--------------|
| | Combined | Wind | Swell |
| AMH | 0.000231 | 0.000275 | 0.000238 |
| Clayton | 0.000231 | 0.000269 | 0.000223 |
| FGM | 0.000231 | 0.000288 | 0.000240 |

| | | | |
|-----------------|-----------------|-----------------|-----------------|
| Frank | 0.000236 | 0.000277 | 0.000217 |
| Galambos | 0.000226 | 0.000272 | 0.000225 |
| HR | 0.000228 | 0.000260 | 0.000210 |
| Joe | 0.000233 | 0.000263 | 0.000220 |
| Normal | 0.000228 | 0.000276 | 0.000221 |
| Plackett | 0.000235 | 0.000281 | 0.000226 |
| Tawn | 0.000240 | 0.000282 | 0.000227 |

6.3.7 Discussion and applications to wind engineering

Section Table 6.3 outlined and discussed the results obtained and the pitfalls encountered in the asymmetric copula based models proposed. Although not being possible to apply these models to the probability of failure of scour protections, as explained previously, some insights on possible applications to offshore wind engineering are hereby provided for future research. The results showed that further research should be performed to improve the univariate modelling of the marginal distributions. The main reason for this is the fact that using the log-normal distribution revealed itself as a very heavy tail distribution, which contributed for a worse fit in the upper tail region of the datasets. However, this distribution provided the lowest Kolmogorov-Smirnov and Wasserstein distances, thus being the best choice among the tested marginal distributions (Table 6.18). Nevertheless, this work covered a wide range of distributions, often used in the offshore wind engineering and met-ocean data modelling, e.g. [21, 122] or [265].

Other aspects, such as the choices made on the breaker-index, the truncation of the marginal distributions, the selection of subsampled data based on the 2 day maximum significant wave height and the associated mean up-crossing period or the weights defined for the WRMSE, affect the model's choice and model's output. Although further research should be carried out to quantify the influence of these choices, at the end of the day, it is recommended that the designer tests several possibilities, before making a decision. Since each dataset may present its own particularities, the experience of the designer is also a key aspect to assess the quality of the joint model proposed to deal with met-ocean data. Furthermore, the quality of the data itself is a crucial factor for an accurate model, particularly regarding the number of extreme events caught on the available record.

Other procedures can be used to remove the data's seasonality, e.g. see [305] and [306]. The method used, based on [123], proved to be suitable. Although these copula models are built to add back in the seasonality effects to the generated values of $(H_s; T_z)$, some practical issues may appear when dealing with the pre-processed data, namely the occurrence of negative pre-processed values. Negative values of pre-processed data may pose some difficulties when trying to fit marginal distributions that only have a positive domain, e.g. lognormal or Weibul distributions. Although this problem can be solved by performing a shift location, either on H_s or T_z direction, this contributes to obtain a set of pre-processed data that is not directly comparable with the original data. The application of the proposed models remains valid, but the designer should pay attention to the possibility of having some counter-intuitive information, as it occurred in Table 6.20, which presented a maximum pre-processed H_s that was higher than the maximum presented for the total sea.

Also, another aspect that can be further improved is the non-parametric estimation of tail dependence. In this study the estimation based on [299] was applied. However, this estimation does not really enable one to understand the actual asymptotic behaviour of the data. A somehow ad hoc solution consisted in the application of the non-parametric estimation of the finite quantile dependence

at the 5% and the 95% quantiles. Tail dependence analysis can be crucial to rule out some of the initially proposed models. Therefore, other tail and asymptotic dependence analysis, e.g. [244], should be further implemented to improve the present research.

Moreover, in order to obtain a better assessment of these copula-based models, one can complement the analysis made with the tail dependence, the Crámer-von Mises distance or the WRMSE, with a response-based analysis, as mentioned in [307]. Several models can be employed to model the met-ocean data and then used e.g. for load estimations at an offshore wind turbine or for dragging forces acting on the soil-structure interaction, and then the behaviour of the response, say the loads in the first case, is further analysed. For example, when dealing with scour protections for offshore wind turbines, the bed shear stress response for several distributions of the environmental variables might be studied. By performing this analysis one is able to compare the responses obtained from different modelling assumptions. One is also able to statistically study the response variables along with the environmental ones. In this matter, obtaining an non-parametric estimation of the response is also useful to validate the statistical models.

This research also showed that opting for a joint modelling (based on copulas) of the combined sea, might be a good option, because the asymmetry of combined data is not necessarily reduced for the separated wind-sea and primary swell components. Additionally, in current practice, the separation of the components might be problematic, namely, if one is dealing with real observations instead of the hindcast data. However, being able to statistically describe the sea components might be of great importance when dealing with specific matters of wind engineering design. For example, in offshore wind turbines, the failure caused by waves from the wind-sea component, which is related with the wind speed, can also be related to the operation mode of the turbine, which depends on the cut out and cut in wind speed, e.g. [308]. On the other hand, the swell component can also be important, for example, when dealing with the dynamic behaviour of offshore wind floating foundations, e.g. [309] or [310].

The results obtained from the extra-parametrization technique led to lower values than the ones presented in [123] for both the Crámer-von Mises distances and the WRMSE. Also the estimated copula parameters are not only within the theoretical copula's range (see [243]) but seem to compare reasonably well with the ones used in copulas application to met-ocean data, e.g. [125, 237, 292]. However, these works only include symmetric models, which leaves space for the present technique to be tested, possibly leading to fitting improvements in the datasets related to the mentioned works.

In this case the significant wave height and the mean up-crossing period are analyzed. Nevertheless, these asymmetric copula-based distribution models can also be extended to the analysis of peak periods and extreme wave heights [254, 292], hydrodynamic loads [254], wind speed analysis [311] among other environmental variables needed for design. Note that wind speed is often very asymmetric in terms of directional distribution and spatial correlation. Copula applications as the ones presented here, and for instance in [238], can be used to model this variable. This type of modelling is not only useful for design purposes but it also yields potential applicability to broader aspects of wind engineering, e.g. to weather prediction for offshore maintenance operations [312], to the estimation of seasonal energy production [313], to the lifetime extension of wind turbines [122] or to scour protections design [12].

The majority of the works performed with copulas for met-ocean data is typically applied to a bi-variate case. However, it should be recognized that the proposed models can be applied to problems with several dimensions. This means that one is able to create joint models, for example, for wave heights, peak periods and incident directions, wind speed and ocean current velocity, among several

other variables of interest. In this sense, the extra-parametrization technique poses a straightforward alternative to nested copulas and C,D-Vine copulas, applied for example in wind resource estimation by [218] or by [314] to perform spatiotemporal modeling of wind generation power for storage sizing.

A final remark should be made to the fact that the popularity of asymmetric copula models is increasing. This occurs not only due to the models flexibility but also due to their ability to tackle the complexity and computational burden of modeling high-dimensional data. This advantage coupled with its simple application and the promising results, which often confirm that these models compare reasonably well with current practice methods, e.g. see [253], make them an interesting alternative for several wind engineering applications, with a special emphasis on the ones related to the offshore wind industry, including scour protection design.

6.3.8 Final remarks on asymmetric copula-based distribution models for met-ocean data

As seen throughout section 6.2, copula-based models are useful but their implementation in marine and offshore structures remains to be fully developed, particularly in scour protection design. Therefore, section 6.3 proposed several extra-parametrized copula-based models, which were applied to a dataset of hindcast significant wave height and up-crossing mean wave period referring to Horns Rev 3 offshore wind farm. An extensive application was performed for the combined sea and its respective components of wind-sea and primary swell. With this research it was possible to conclude that the separate modelling of the wind-sea and primary swell components does not always lead to a better fit of the copula models. Therefore, for scour protections design it seems reasonable to model the total sea, without separation of its components. Moreover, using the extra-parametrization technique it becomes easier to catch the asymmetry of the total sea.

It was noted that the copula's performance is very much dependent on the asymmetry of the data itself, which is in agreement with the recent findings of [123] and [292]. Therefore, if primary swell and wind-sea, are asymmetric in the (u,v) -space, it is recommended to use asymmetric copulas to improve the goodness-of-fit. It is concluded that problems caused by asymmetries in the data, can be reduced by the flexibility introduced with the extra-parametrization of copulas.

The extra-parametrization led to significant improvements of the Crámer-von Mises distance, between the models and the empirical copula. The improvements were noticed for the extra-parametrization with both an independent copula and with the pairwise copulas. The flexibility introduced enables one to easily build joint models for the significant wave height and the up-crossing mean period, based on simple symmetric copulas, such as the Archimedean or the Elliptical ones. Using this technique to combine different copulas is also possible. In this section, an example was shown for the extra-parametrization with a Gumbel copula. These copula constructions also improved the goodness-of-fit when compared with the symmetric copulas. However, they still presented higher Crámer-von Mises distances when compared with the pairwise construction and some of the independent copula based models.

It was also confirmed that a model that gives the lowest Crámer-von Mises distance, may not always provide the lowest WRMSE adapted to penalize more the departures on the upper tail of the significant wave heights. Therefore, the Crámer-von Mises distance must be seen as an overall goodness-of-fit measure, while the proposed loss function based on WRMSE is more suitable to deal with errors on the tails of the distributions. Although the present models were not applied to the reliability analysis of scour protections, future research should test these asymmetric copulas and their effects on the calculation of the probability of failure. These models are expected to provide a more accurate assessment of P_f than the one performed in section 6.2.6.

6.4 Conclusions

Throughout Chapter 6 the reliability analysis of dynamic scour protections was introduced, whilst existent limitations of the copula-based models, mostly used in marine engineering were addressed. The improvement of such models also poses a contribution to the reliability analysis, since they are crucial to provide the random data used to simulate the limit state function. The main findings of the present chapter are addressed in previous sections 6.2.10 and 6.3.8. However, in this section a brief summary of these finds is provided:

- When proposing a specific design for a scour protection, the measure of safety associated to the system is not typically addressed in the literature;
- The probability of failure is crucial to understand if the optimised design, e.g. the dynamic scour protection concept from [32], is holding an acceptable level of safety;
- The definition of a standard probability of failure for scour protections is yet to be defined in offshore engineering guidelines and recommended practices;
- Moreover, probability of failure depends on the statistical framework considered, i.e. the variables that are defined as random and the models used to randomly generate them;
- It was also perceived that the assumptions made regarding the failure criterion also affect the probability of failure, as it will be discussed in Chapter 7;
- Section 6.2, performed a reliability assessment for a scour protection design with a D_{50} equal to 0.4 m and considering a failure criterion and a limit state function based on [32];
- The results showed that the probability of failure could be compared to the common values adopted for other offshore engineering applications;
- Noting that the probability of failure was obtained for a simplified probabilistic model, dependent on U_c , H_s and T_p , a sensitivity analysis to the remaining variables was performed. The results showed that the methodology used was able to capture the expected behaviour of the scour protection's safety;
- Albeit not focused on the present research, the accurate modelling of the marginal distributions was also pointed as a key aspect for an accurate statistical framework;
- It was also concluded that the quality of the data and the records' length does influence the outcome of the probability of failure. This is particularly evident in models that rely on the measure of dependence of the environmental data, as the copula-based ones;
- The reliability assessment was performed for the set of Elliptical and Archimedean copulas that are most commonly found in the literature of met-ocean data modelling;
- The Tawn type 2 copula showed that asymmetric models provided a better fit to the wave parameters used to simulate the limit state function. Therefore, section 6.3 was dedicated to the extra-parametrization of symmetric copulas. These models might be seen as a contribution for future reliability research of scour protections at Horns Rev 3. They may also be used for several other offshore wind engineering applications as discussed in section 6.3.7;
- The analysis of asymmetric copula models was performed for the significant wave height and mean up-crossing period, in order to show that the separated modelling of the sea components may not lead to a better quality of fitting;
- It was perceived that the extra-parametrization technique provides a straightforward procedure to build flexible joint models for the wave parameters, eventually leading to a more accurate assessment of the protection's safety;

- It was concluded that the use of copulas in offshore maritime engineering is yet to be fully developed, thus meaning that the reliability analysis of scour protections should also be performed for models that are already recognised in offshore engineering standards, e.g. the Conditional Modelling Approach, which is used in Chapter 7 to compare statically and dynamically stable scour protections.

Based on the concepts presented in Chapter 5, throughout Chapter 6 the flow chart from Figure 6.1 was followed as a methodology to perform the reliability assessment of dynamic scour protection for offshore wind foundations. As discussed in section 5.5, the reliability analysis of scour protections should provide an answer to the following research questions:

- How reliable is a scour protection designed according to a specific criterion?
- Is a dynamic scour protection as reliable, i.e. as safe, as a statically stable one?

Regardless of the statistical framework, the simplifications and the reliability techniques used, the first question is somehow answered with the methodology applied and discussed in Chapter 6. However, the second question remains unanswered. The optimisation of dynamic scour protections is only effective if one is able to reduce the mean stone diameter (D_{50}) and still associate it to an equivalent level of safety as the one showed by a statically stable protection. In Chapter 7, the second question is addressed.

Safety of Static and Dynamic Scour Protections

7.1 Introduction

As noted in section 3.7.1, a key aspect of scour protection design is the definition of the mean diameter of the stones (D_{50}) of the armour layer placed above the granular filter [107]. However, the safety level of the optimisation of this diameter is not commonly compared with the traditional design methodologies [44].

However, such comparison is crucial to understand if two scour protections, designed under different stability concepts, yield similar safety levels. Moreover, performing the reliability analysis of scour protections not only enables the quantification of the safety level, but it also enables one to perform a probabilistic design, which contributes to reduce the uncertainty and eventually overestimated mean diameters that come from deterministic methodologies. In this chapter, the met-ocean data from the Horns Rev 3 is used to perform the reliability assessment of a scour protection designed according to deterministic methodologies. Furthermore, a novel probabilistic design method is proposed for static and dynamic scour protections. The new methodology is based on Monte-Carlo simulations combined with the limit state function proposed in Eqs. (5.53) and (5.54), and provides the mean stone diameter of the scour protection for a pre-defined probability of failure. In section 6.2, the reliability analysis was performed for D_{50} equal to 0.4 m. In this chapter, the reliability analysis is performed for several values of D_{50} , in order to associate them to the correspondent P_f . The data from Horns Rev 3 will be used to deterministically obtain the D_{50} according to the widely used methodology [52] and the optimisations proposed by [30, 32]. The safety level associated to the obtained solutions will be compared by analysing the probabilities of failure. After that, a probabilistic approach which associates P_f to D_{50} will be implemented. The establishment of this relationship enables the designer to adopt a certain value of D_{50} depending on the desired safety level, where P_f defines the probability of the design criterion not being met under the simulated environmental random conditions. In summary, this chapter uses the deterministic methodologies to obtain the design of the scour protection at Horns Rev 3. Then the probability of failure of each design is obtained and compared. Finally, the relationship between this safety measure and the mean stone diameter is obtained to enable the probabilistic design of the protection. This allows for the comparison of safety between static and dynamic scour protections for the same met-ocean situation.

This chapter is a contribution to the very few existent studies concerning the maritime environment and the failure of the protection. Hence, it aims to provide a measure of safety to the proposed optimisation of the protection, under waves and currents combined.

7.2 Revisiting the deterministic design and failure of scour protections

7.2.1 Static scour protections

The design of statically stable scour protections generally involves the assessment of the bed shear stress induced by the combined effect of waves and currents (τ_{cw}). If the protection is intended for static stability, the armour stones are not allowed to move. Hence, the stones placed in the armour layer must be large enough to ensure that their critical shear stress (τ_{cr}) is higher than the bed shear stress acting on the protection [50], including the effect of the monopile's presence [52].

In order to account for the monopile's presence, the amplification factor (α) is typically employed. The amplification factor is defined as the ratio of the undisturbed bed shear stress to the increased shear stress in the presence of a structure, in this case the monopile foundation (see section 2.3). The amplification factor may vary depending on the hydrodynamic conditions. According to [30], physical model studies show that for waves alone α varies between 2.2 and 2.5, but when the effect of currents is included one commonly uses α equal to 4. Note, however, that the amplification factor may be larger depending on the case, e.g. [49] and [61] report other situations where α is larger than 4, e.g. for monopiles under waves and current combined.

One of the problems of dealing with waves and currents combined lies in obtaining the maximum bed shear stress caused by their simultaneous action (τ_{cwmax}), as discussed in section 2.2.2. In current practice, one of the most widely used methodologies used to obtain τ_{cwmax} , due to its simplicity and accuracy, is the one presented by [52], which is also discussed in [54] and adapted to account for non-linear effects in [55]. In order to perform the deterministic design of a scour protection according to [52], the critical shear stress can be defined by re-arranging Eq. (2.26) in order to τ_{cr} as in Eq. (7.1).

$$\tau_{cr} = g(\rho_s - \rho_w) D_{50} \theta_{cr} \quad (7.1)$$

where g is the gravitational acceleration, ρ_w is the water density, ρ_s is the density of the rock material and θ_{cr} is the non-dimensional critical Shields parameter as introduced in [50]. As showed in [30] for sufficiently large non-cohesive sediments, one can use $\theta_{cr}=0.056$. Then the maximum shear stress, under waves and currents combined, can be assessed according to Eq. (2.22), where τ_m is the mean combined bed shear stress, i.e. Eq. (2.23), τ_w is the wave-induced bed shear stress from Eq. (2.9), τ_c is the current-induced bed shear stress, from Eq. (2.3), and ϕ is the angle between the waves and currents [52]. Combining both Eqs. (2.22) and (2.23) the Eq. (7.2) is obtained.

$$\tau_{cwmax} = \left[\left(\tau_c \left[1 + 1.2 \left(\frac{\tau_w}{\tau_c + \tau_w} \right)^{3.2} \right] + \tau_w \cos \phi \right)^2 + (\tau_w \sin \phi)^2 \right]^{1/2} \quad (7.2)$$

As described in section 3.7.1.2, D_{50} is the minimum value that complies with Eq. (7.3), which depends on the selected amplification factor (α). Note that in former Eq. (3.31), α is considered equal to 4, but both equations are the same.

$$\tau_{cr} > \alpha \cdot \tau_{cwmax} \quad (7.3)$$

Still regarding statically stable scour protections, the same design procedure is applicable to the optimisation proposed by [30], which considers the modifications of τ_{cr} and τ_{cwmax} discussed in section 3.7.1.3. Briefly revisiting those modifications, it is possible to mention that [30] proposes the calculation of τ_{cwmax} (N/m^2) according to Eq. (3.48), whereas τ_{cr} is computed from Eq. (3.49).

According to the deterministic design implemented in [30], the critical shear stress is computed for θ_{cr} equal to 0.035 and using a stone diameter for which 67.5% of the stones (by weight) are retained in the sieving process ($D_{67.5}$). These changes are made to account for the fact that stones in a scour protection with smaller grading tend to move faster than those in a scour protection with a wide grading [30]. The mean stone diameter D_{50} is related with $D_{67.5}$ by means of Eqs. (3.50) or (3.51). Then the minimum value of D_{50} is the one that complies with Eq. (7.4), noting that D_{50} depends on $D_{67.5}$, which is included in Eq. (7.1). Moreover, it must be noted that the wave- (τ_w) and current-induced bed shear stresses (τ_c) are dependent on the diameter D_{50} , which is used to calculate the bed roughness (k_s), assumed as $2.5D_{50}$ in the absence of ripples formation [30, 32]. In the methodology presented by [30] no amplification factor is employed. Research showed that the design proposed by [30] led to smaller stone sizes when compared with the one proposed by [52].

$$\tau_{cr}(D_{67.5}; \theta_{cr}=0.035) > \tau_{c_{wmax}} \quad (7.4)$$

7.2.2 Dynamic scour protections

The design of dynamic scour protections is performed as described in section 3.7.1.5, which implies the definition of an acceptable damage number as discussed in sections 4.2.6.5 and 6.2.1. Therefore, in the present case, the dynamic design is performed with Eq. (3.57), assuming that the acceptable damage number of the protection is equal to 1. The deterministic value of D_{50} that leads to a dynamically stable scour protection is the one that complies with Eq. (7.5). Note that D_{50} is considered to be equal to $D_{n50}/0.84$.

$$N^{b0} \left[a_0 \frac{U_m^3 T_{m-1,0}^2}{\sqrt{gd} (s-1)^3 D_{n50}^2} + a_1 \left(a_2 + a_3 \frac{\left(\frac{U_c}{w_s} \right)^2 (U_c + a_4 U_m)^2 \sqrt{d}}{g D_{n50}^3} \right) \right] < 1 \quad (7.5)$$

As it can be noted, this methodology does not imply the definition of the amplification factor. However, the study of the final design of the scour protection by means of physical modelling is still required by [32], for a proper validation. This matter is also addressed in [214], which concludes that physical modelling validation is required for both dynamic and statically stable protections, even if the reliability analysis of the proposed designs is performed. As discussed throughout Chapter 4, and also considered in the present chapter, the application of the damage number as introduced in [32] should be restricted to scour protections implemented with a filter and an armour layer, which invalidates its application to single layer wide-graded scour protections. Moreover, the present analysis also considers N equal to 3000 waves as a suitable number of waves for damage stabilisation. However, this matter is yet to be fully defined by the literature, as also noted in [214] and further discussed in Chapters 3 and 4.

7.2.3 Notes on the design methodologies

In section 3.8, notes were given regarding the fact the deterministic design of scour protections, namely regarding the absence of the long-term predictions and long-term correlations on the wave height and period or the different values used for the design wave height. Regarding the methodologies applied in this chapter, i.e. [30, 32] and [52], it should be remembered that those notes are important, as they may contribute for possible differences in the outcome of mean stone diameter applied in the armour layer.

The use of methodologies [30, 32] is rather logic, since they represent the optimisation of the mean stone diameter aiming at avoiding the erosion of the top layer. However, despite being widely used and eventually one of the most recognised design methods, the methodology [52] could be, perhaps, substituted by other methodologies, e.g. [53] or [57], which consider, for example, different wave friction factors. Furthermore, such friction factors influence the evaluation of the wave-induced bed shear stress (remember Figure 2.1), which will affect the results of methodology [30]. Firstly, it is important to be aware that the comparisons made between [30] and any other static design approach should consider the same assumptions regarding friction factors, bed roughness calculations and the remaining aspects that influence the design [214].

Secondly, and as perceived by [44], the present wave data include wave stroke to bed roughness ratios (A/k_s) that lie outside the interval [0.2;10]. Therefore, as noted in [30], the application of [58] to obtain the wave friction factor and the bed boundary layer is no longer valid. In addition, when developing the Eq. (3.48), [1] and [30] noted that the wave friction factor obtained from [53] gave abnormally large values of τ_w for considerably small values of the wave period, thus this methodology was excluded from the present application. The effect of the wave friction factor, with a particular focus on the comparison between [52] and [57], was studied by [44]. The authors concluded that the probability of failure could differ depending on the methodology used to obtain f_w . It was noted that the probabilities of failure obtained from those methodologies presented larger departures between them, then the difference presented by the methodology [30] with f_w calculated from [52] and [57]. The amplification factor considered under each methodology also leads to differences in the mean stone diameter. This aspect is addressed in further sections for [30] and [52].

Note that [30] considers U_m , according to the linear wave theory. The calculation of the orbital bottom velocity also influences the D_{50} (or D_{n50}) output, thus also having an effect on the probabilities of failure associated to each design criterion. Furthermore, as discussed in section 3.8, the considered design wave height also has influence. At the present state-of-the-art it is clear that further research should address the influence of these methodologies in the reliability assessment of the scour protection.

As performed in the copula-based reliability assessment, the present section considers a JONSWAP spectrum, with a peak enhancement factor of 3.3. Moreover, it does not consider the correlation between waves and current or the variability in the rock mass density (ρ_s), among other aspects that may affect the failure of the protection. In addition, the reliability analysis and probabilistic design performed in this chapter, considers the Conditional Modelling Approach, as it is the one implemented in offshore wind engineering standards (see section 6.3).

These assumptions might be improved in future research, but it is important to note that probabilistic analysis should be performed within the limits of applicability of the design methodologies used to predict damage occurrence in scour protection. Nevertheless, due to the aforementioned reasons the selection of methodologies [30, 32] and [52] seems to provide a reasonable starting point to establish a reliability comparison and probabilistic design procedure for both static and dynamic scour protections. In future work, the MATLAB® scripts developed during this research might be adapted to consider other formulations in the limit state functions of the scour protection.

7.3 Reliability analysis and probabilistic design of scour protection

In section 6.2, the reliability assessment was performed for a reference value of D_{50} , i.e. 0.4 m, which was associated to a triangular probability distribution function, for a uniformity parameter (σ_U) equal

to 1.67. In the present case, one will consider that the value of D_{50} does not follow any particular statistical distribution, because one is interested in obtaining the probability of failure associated to each value of D_{50} . The uniformity parameter considered for statically stable scour protections was considered to be equal to 2.5, as this was the value considered in the majority of the scour tests performed by [1, 30].

In order to perform the reliability assessment of the deterministic solutions and establish the relationship between P_f and D_{50} , the limit state functions described in section 5.6 might be used. Those functions, i.e. Eqs. (5.53) and (5.54), can be adapted according to the design methodology and the failure criterion defined in the previous section 7.2, i.e. Eqs. (7.3) and (7.5). The procedure for dynamic scour protections was already explained in section 6.2.2, namely in Eqs. (6.3) and (6.4). For static scour protections it is important to note that the combined wave and current induced shear stress, may imply the aforementioned amplification factor when using the methodology [52]. Besides the amplification factor, the combined bed shear stress is obtained from Eq. (7.2), whereas Eq. (3.48) is used for methodology [30]. With the Monte Carlo simulation procedure the random basic variables are obtained from their statistical distributions and then the limit state functions are simulated to obtain the probability of failure from Eq. (5.40).

The results obtained from Eq. (5.40) provide the probability of failure for a certain mean diameter of the armour stones. Furthermore, one can derive the probability associated to a range of mean diameters, for specific design conditions, and then design the protection in a probabilistic manner by choosing the value of D_{50} that corresponds to a certain admissible probability of failure. In the following section the Horns Rev 3 case study is addressed for which the deterministic and probabilistic design is performed and discussed. In the absence of a full probabilistic model, the variables H_s , T_p (and consequently U_m) and U_c where statistically modelled. This reliability analysis procedure is summarised in Figure 7.1. The limit state functions used for methodology [30, 52] and [32] are provided by Eqs. (7.6), (7.7) and (7.8), respectively.

$$g(\mathbf{X}) = \tau_{cr}(D_{67.5}; \theta_{cr} = 0.035) - \tau_{cwmax} \quad (7.6)$$

$$g(\mathbf{X}) = \tau_{cr}(D_{50}; \theta_{cr} = 0.056) - \alpha \cdot \tau_{cwmax} \quad (7.7)$$

$$g(\mathbf{X}) = 1 - S_{3Dpredicted} \quad (7.8)$$

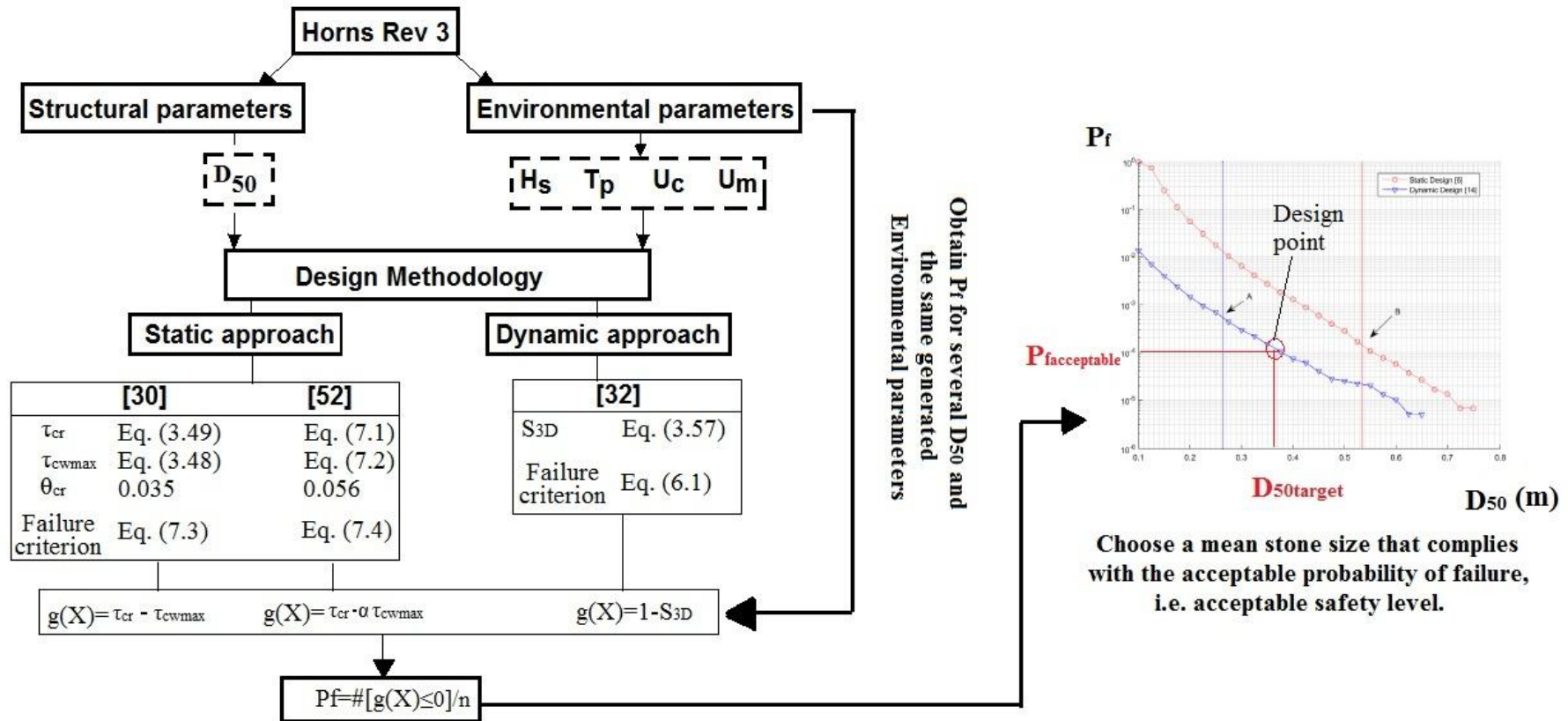


Figure 7.1 – Reliability analysis and procedure to associate each mean stone diameter to a certain safety level.

As already mentioned, the present analysis is performed for the same met-ocean data introduced in section 6.2.3. The Conditional model was applied in order to simulate the significant wave height (H_s) and the peak period (T_p), which are further used to compute the remaining variables, e.g. included in Eqs. (3.48), (3.57) or (7.2), e.g. U_m or $T_{m-1,0}$. The conditional modelling approach is important as it enables one to obtain a model that allows for the variables extrapolation. One only has 10 years and 4 months of data. The hindcast data concerning H_s and T_p is provided in Figure 7.2, as well as an example of a random sample of 50 000 pairs of (H_s ; T_p) obtained from the Conditional Model, as implemented in [123]. A visually good agreement is obtained between the sample and the generated data (Figure 7.2). The same generated samples of size n are used to simulate the limit state functions, when determining the probability of failure for the static and dynamic scour protections. It is important to note that when applying the conditional model, some of the generated values may fall outside the original range for which the damage number formula, Eq. (3.57), was derived by [32]. For example, Figure 7.2 shows that some of the smaller wave heights may present very large peak periods, e.g. 22 to 30 s. However, it is unlikely that such pairs of H_s and T_p contribute to damage numbers that exceed S_{3D} equal to 1. This occurs because, although the peak periods might be overestimated, the significant wave height is not large enough to produce damage numbers above 1, according to Eq. (3.57). Nevertheless, the future research should also be focused on the effects of the generation model in the predicted damage numbers given according to [32], i.e. Eq. (3.57).

The statistical model, used to generate the random values of significant wave height and peak period, will also affect the reliability assessment of the scour protection. For example, if extreme wave heights (or periods) are underestimated, one may underestimate the probability of failure associated to each criterion. Conversely, if the extreme wave heights (or periods) are overestimated, the estimated probabilities of failure might be too conservative when compared to the truthful (and unknown) value. Since the same model is used for all methodologies this does not pose a problem in terms of the criteria comparison. However, it does influence the assessment of each probability *per se*.

Nevertheless, this remains as a problem of the model fitting more than the methodology of reliability assessment discussed in the following sections. Regarding this matter one must also note that the accuracy of the probabilities is also dependent on the quality of the hindcast data, which in this case only has 10 years and 4 months (as discussed throughout Chapter 6). However, for offshore locations the available data is often scarce and one has to fit the statistical model to the records available, in spite of them being rather short.

As a model simplification, the current velocity is considered independent from the wave height and the peak period. No time series were available for the current velocity (U_c), as mentioned before. This assessment considered that the current velocity followed a Weibull distribution, with an equivalent mean of 0.4 m/s and a standard deviation of 0.2 m/s. While the methodology presented in [52] considers different angles between U_c and the wave's direction, the methodology presented in [32] only considers unidirectional or opposing waves and currents. Therefore, a random angle of 0° and 180° was assigned to each simulation of the limit state functions (as done in section 6.2.6). This is also a simplification of the present model and future research should be adapted to consider a wider range of this angle.

Nevertheless, this must be seen as a limitation of the criteria studied previously, more than a limitation of the reliability assessment proposed here. If concurrent directional wave and current data are available, it is possible to establish a probability distribution for the angle and simulate this accordingly. Remember that the failure criteria influences the probability of failure, as shown in [43].

The water depth is also an important varying parameter that may influence the damage number and the acting bed shear stress at the armour layer. However, in the present model and as a simplification, this parameter was assumed to be deterministic variable in the process. At the present stage of the research, a preference was given to the accurate model of the significant wave height and the correlated values of the wave peak period, as performed in section 6.2. Nevertheless, it must be noted that reductions in the water depth may lead to an increasing severity of the scour process on the armour layer of the scour protection, eventually, contributing to reduce the reliability of a scour protection, with the same thickness and the same mean stone diameter.

On the other hand, the water depth decrease may lead to limitations on the non-breaking wave heights at the protection's location. Therefore, if the water depth is reduced one also has to account for the effects on the wave's characteristics, which may difficult the straightforward identification on the immediate effect on the damage number and the combined bed shear stress. To avoid a possible bias on the interpretation of such effects from the water depth and the wave height, the model was simplified to assume a constant water depth.

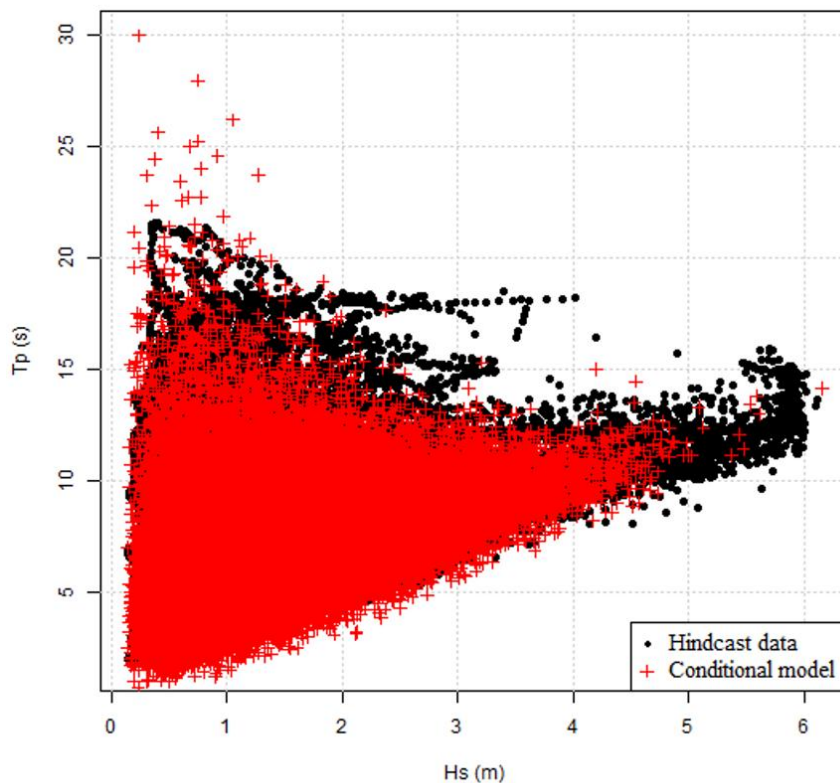


Figure 7.2 – Hindcast data concerning the significant wave height and peak period at Horns Rev 3 and random generated sample with $n=50\,000$ pairs of $(H_s; T_p)$.

As previously discussed in section 6.2.3, Horns Rev 3 windfarm is under development at the present date. However, D_{50} equal to 0.4 m or 0.35 m is suggested as possible mean stone diameters for the protection by [288] and [290], respectively. Moreover, in the present case the following variables are analysed as deterministic, according to the methodologies previously mentioned: the mass density of the rock material was considered as $\rho_s=2650\text{ kg/m}^3$, $N=3000$ waves, $\rho_w=1025\text{ kg/m}^3$, $g=9.81\text{ m/s}^2$. The uniformity parameter ($\sigma_U=D_{85}/D_{15}$) was defined as 2.5 as in [30]. In the following section the results concerning the deterministic and the probabilistic design are presented and discussed.

7.4 Design Results

7.4.1 Deterministic design results

The deterministic design of scour protections typically uses the design wave height as the significant wave height associated to a return period (T_r) of 50 years. In [286], the Peak Over Threshold based on the Generalised Pareto distribution determined that, for this location, H_d was equal to $H_{s50\text{year}}=6.7$ m. The concurrent wave peak period was calculated as for a JONSWAP spectrum with a wave enhancement factor of $\gamma=3.3$, i.e. $T_p=4.4(H_s)^{0.5}=11.4$ s. However, the hindcast data available concerns to 10 years and 4 months only. Therefore, one should keep in mind that a considerable uncertainty is inherent to the estimated values for $T_r=50$ years.

The design performed with [30] uses the mean wave height of the 10% highest waves in order to calculate the orbital bottom velocity, thus, U_m is calculated for $H_{1/10}=1.27H_{s50\text{year}}=8.5$ m, assuming Rayleigh distribution for the waves. The methodology [32] was applied with the significant wave height associated to $T_r=50$ years as in [52]. Both of these methodologies use the peak period associated to the selected H_s . The orbital bottom velocity for [30] is obtained with the linear wave theory, whereas in [32] is directly obtained from the wave spectrum (see section 3.7.1.5).

Table 7.1 provides the results for the deterministic design, which depends on the characteristic values used to calculate the shear stress on the protection. Moreover, for the methodology presented in [52], the mean diameter of the armour stones is calculated for several amplification factors (α). A similar application is shown in [32]. One can see that the values obtained in this case are similar to the ones reported for the referred deterministic design.

Table 7.1 shows that the innovative methodologies proposed by [30] and [32] lead to smaller diameters when compared with the one obtained by the methodology from [52], which is more conservative. This is a result of the different failure criteria that were selected and of the different design values that were used. It is also possible to confirm that the dynamic scour protection corresponds to the smallest stone size. In dynamic scour protections the difference between the design for opposing waves and currents is not very noticeable, due to the small mean current velocity ($U_c=0.4$ m/s). For large values of U_c , say 1-1.5 m/s, the differences in D_{50} are larger, as shown in [1]. Nevertheless, the largest stone size given by [32] is associated to waves opposing current. This is consistent with the fact that the damage number tends to be larger for waves opposing currents than for waves following currents, as shown in [1] and [32].

For a typical rip-rap scour protection, commonly placed with fall-pipe vessels [12], the diameters given by the methodology [52] for an amplification factor of 3 and 4 are rather large. Moreover, the diameters obtained ($D_{50}=1.41$ m and $D_{50}=2.56$ m) are also very large when compared with the size of rock material commonly used. Table 7.1 provides acceptable diameters when compared to existent scour protections for waves and currents combined, e.g. the offshore windfarms of Horns Rev 1 ($H_s=5.2$) and Egmond aan Zee ($H_s=3.6$) use $D_{50}=0.40$ m. An extensive review of some design examples can be found in [13] and [59]. The designs obtained by the methodologies from [30] and [32] seem more appealing since the corresponding diameter of the stones is considerably smaller. Furthermore, the dynamic design of the scour protection enables one to use $D_{50}=0.26$ m, which is less than half of the size obtained by the methodology from [52] with $\alpha=2$.

A question arises from Table 7.1: “Are the reduced diameters proposed by [30] and [32] as safe as those proposed by [52]?” In order to answer this question, the reliability of the proposed solutions is assessed. One considers that the wave height and the peak period are randomly generated from the Conditional model [126, 265], while the mean current velocity follows the previously mentioned distribution. Random series of these variables were used to simulate the limit state functions, i.e. Eqs.

(7.6), (7.7) and (7.8). The probability of failure of each diameter was then calculated according to Eq. (5.40). The results are summarized in Figure 7.3 which presents the probability of failure as a function of the number of simulations performed.

Table 7.1 – Deterministic design of the scour protection at Horns Rev 3.

| [52] | | | [30] | | | [32] | | |
|-------------------------|--|----------------------|-------------------------|---|----------------------|--------------------------|--|----------------------|
| Static Scour Protection | | | Static Scour Protection | | | Dynamic Scour Protection | | |
| θ | 0.056 | [-] | θ | 0.035 | [-] | Direction | 0;180 | ° |
| σ_U | 2.5 | [-] | σ_U | 2.5 | [-] | N | 3000 | waves |
| ρ_s | 2650 | [kg/m ³] | ρ_s | 2650 | [kg/m ³] | ρ_s | 2650 | [kg/m ³] |
| ρ_w | 1025 | [kg/m ³] | ρ_w | 1025 | [kg/m ³] | ρ_w | 1025 | [kg/m ³] |
| d | 18 | m | d | 18 | m | d | 18 | m |
| D_p | 6.5 | m | D_p | 6.5 | m | D_p | 6.5 | m |
| γ | 3.3 | [-] | γ | 3.3 | [-] | γ | 3.3 | [-] |
| H_s | 6.7 | m | H_s | 6.7 | m | H_s | 6.7 | m |
| T_p | 11.4 | s | T_p | 11.4 | s | T_p | 11.4 | s |
| U_c | 0.4 | m/s | U_c | 0.4 | m/s | U_c | 0.4 | m/s |
| U_m | U _m (H _s ;T _p) | m/s | U_m | U _m (H _{1/10} ;T _p) | m/s | U_m | U _m (H _s ;T _p) | m/s |
| g | 9.81 | m/s ² | g | 9.81 | m/s ² | g | 9.81 | m/s ² |
| Result | | | Result | | | Result | | |
| D ₅₀ (α=2) | 0.610 | | | | | D ₅₀ (0°) | 0.250 | |
| D ₅₀ (α=3) | 1.410 | [m] | D ₅₀ | 0.540 | [m] | | | [m] |
| D ₅₀ (α=4) | 2.560 | | | | | D ₅₀ (180°) | 0.260 | |

Figure 7.3 shows that the methodology from [30] leads to the lowest probabilities of failure. The values of the probability seem rather stabilised after n=300 000. The probabilities are plotted in the logarithmic scale. It is somehow counterintuitive that D₅₀=0.54 m yields a lower probability of failure (P_f=1.7×10⁻⁴) than D₅₀=0.61 m (P_f=2.2×10⁻⁴). However, the failure criteria that leads to those probabilities is different, and as also noted by [43], the failure criteria does influence the probability of failure. Therefore, the probability of failure must be understood as the chance of a design criterion is not being met, under the random loading conditions given by H_s, T_p and U_c. This means that D₅₀=0.54 m has a smaller probability of not meeting the design criterion given by [30], than the D₅₀=0.61 has of not meeting the design criterion given by [52]. Nevertheless, Figure 7.3 seems to indicate that both methodologies for static design lead to diameters that have very similar probability of failure, i.e. the same probability that each design criterion is not being respected. This suggests that the optimised solution provided by [30] not only gave a smaller D₅₀ than [52], but it seems to be within the same level of safety, i.e. P_f in the order of 10⁻⁴.

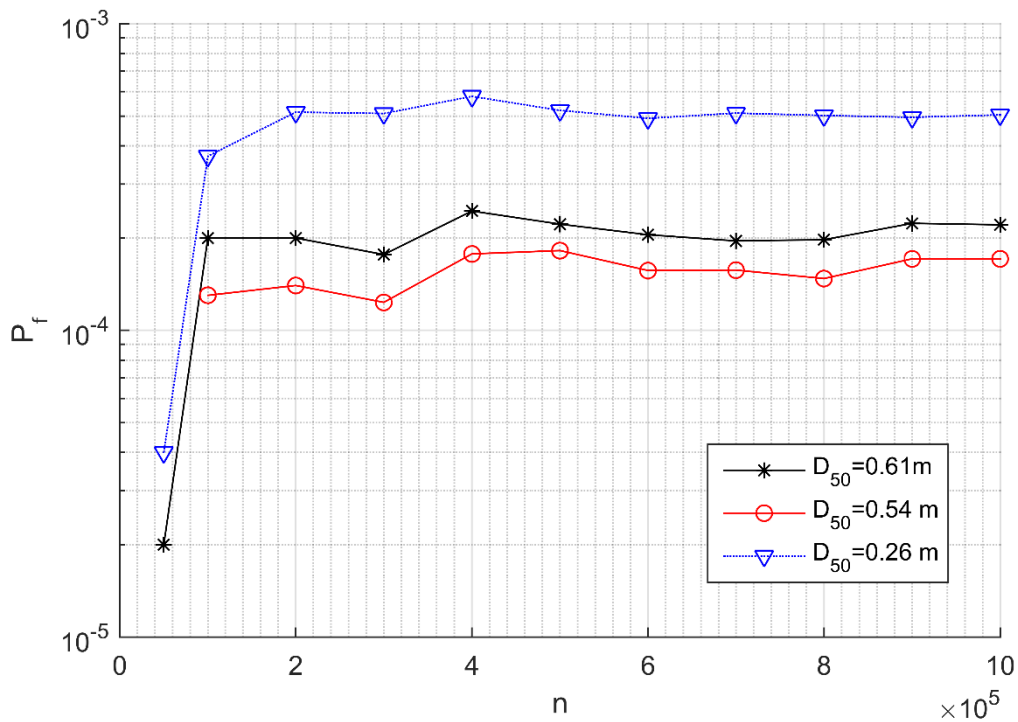


Figure 7.3 – Probability of failure for each design methodology versus number of simulated values of H_s , T_p and U_c .

However, the reliability assessment was performed for an amplification factor of 2. Note that several authors typically apply $\alpha=4$ in several design situations, which means that those solutions tend to be more conservative than $D_{50}=0.61$ m. One can argue that the curve given by [52] with $\alpha=2$ is not directly comparable to the curve given by [30]. As it will be discussed further, this argument is reasonable due to several differences between the static design criteria.

The probabilities associated to the methodology [32] are slightly larger than those obtained with the statically stable solutions from [30] and [52]. The $D_{50}=0.26$ m has $P_f=5 \times 10^{-4}$. However, if one takes into consideration the variability and the uncertainty of the met-ocean environment, the values obtained might be considered acceptable in light of the substantial reduction of the mean stone diameter. An important aspect that can be noted is the consistency in the criteria provided by [30] and [32]. The design of a dynamic scour protection with a reduced diameter ($D_{50}=0.26$ m) gives a slightly larger probability of failure ($P_f=5 \times 10^{-4}$) than the static scour protection ($P_f=1.7 \times 10^{-4}$) with a larger mean diameter ($D_{50}=0.54$ m). Once again, note that the failure of both protections is analysed under different failure criteria. In the present case, it seems that a dynamic scour protection has a reliability level, which is in the same order as the static one designed according to [30], i.e. both of them in the order of 10^{-4} . This is of great importance, because not only the size reduction may lead to lower costs of the scour protection, but it also minimizes the occurrence of other problems, e.g. the edge scour phenomenon, which increases for large stone diameters due to the sudden increase of the bed-roughness [185].

The results from Table 7.2 are somehow difficult to compare with other cases in the literature, because there is an evident lack of research performed on the reliability and safety assessment of scour protections analysed by means of the probabilities of failure, as noted in section 6.2.6. A reliability assessment of statically stable scour protections, designed according to [30], is presented by [12]. However, the authors did not consider the correlation effects between the significant wave height and

the peak period. Moreover, H_p , T_p and U_c were assumed to follow Gaussian distributions. The minimum probability of failure obtained by [12] was in the range of 10^{-3} for a global safety factor of 1.5, defined as the ratio of the acting bed shear stress to the critical shear stress. These values seem to indicate that the model chosen for the random variables considerably affects the probability of failure. Such evidence was also confirmed in studies related to other offshore components, e.g. in mooring lines by [125].

Table 7.2 – Stabilized probability of failure calculated with the Conditional model approach (124 months).

| Design Methodology | D_{50} [m] | P_f (n=1 000 000) |
|--------------------------------------|--------------------------------|---------------------------------------|
| Static Scour Protection [52] | 0.61 | 2.2×10^{-4} |
| Static Scour Protection [30] | 0.54 | 1.7×10^{-4} |
| Dynamic Scour Protection [32] | 0.26 | 5×10^{-4} |

As discussed in section 6.2.6.2, the scour protection at a monopile foundation consists of a system designed to mitigate scour related failures. However, if the scour protection fails, the monopile is not expected to fail immediately nor results in loss of human life (offshore wind turbines are unmanned structures). In this sense, one could argue that probabilities of failure in the order of 10^{-4} might be acceptable for the scour protection.

The probabilities of failure presented in Table 7.2 are computed based on a 124 months record. As mentioned, regarding the probability of failure in scour protections there is no guidance or obligatory offshore standards to be followed, typically, in marine structures the annual probability of failure may range from 10^{-3} to 10^{-6} , depending on the systems redundancy, the warning prior to failure and the possibility of loss of life, e.g. see [220]. The values obtained for the present design might be difficult to convert to equivalent annual values for a proper comparison with the mentioned references. This is due to the fact that there is a dependence between the sea-state conditions for each simulation, because hourly data is used. Since the event from hour (t_i) might be dependent from the event of hour (t_{i-1}), one is not able to assume a constant rate of failure. Therefore, the annual probability of failure will not be equal to the number of hours in a year multiplied by the probabilities obtained in Table 7.2. Of course the peak period bins used to fit the joint model of H_s and T_p also leads to an influence in P_f . Regarding the comparative analysis between criteria this does not pose a problem, because the same hourly data is used for the three design situations. However, when trying to analyse the probability of failure associated to extreme values, e.g. H_s associated to $T_r=100$ years or similar, the values of P_f are not directly comparable with the ones being focused in the present chapter.

The effects of the temporal resolution used to compute the probability of failure in offshore engineering applications are analysed in [315]. Although favouring models, which are fitted to annual maxima or clustered data, may lead to a better assessment of the extreme events, it must be recognised that this may also lead to uncertainties when the records are rather short, as this one. Nevertheless and as stated before, the main idea from the comparison presented in Figure 7.3 and Table 7.2 is that the deterministic solutions seem to present similar reliability measures. The authors recognise that further research considering other data records and other sampling resolutions of H_s and T_p (than the hourly data) should be carried in order to properly compare these probabilities of failure with the annual values currently employed in structural design of offshore foundations.

7.4.2 Probabilistic design of scour protections

Instead of solely assessing the probability of failure of the scour protection, it might be relevant to analyse the values of the mean stone diameter associated to a specific probability. This can be performed by determining the relationship between D_{50} and P_f according to each methodology. In Figure 7.4, this relationship is established for the design of a static scour protection according to the methodologies presented by [30] and [52], with an amplification factor of 2 applied to the latter. Results are obtained for a number of simulations set to 300 000, which is large enough to ensure a stabilised value of the probability of failure (see Figure 7.3).

Figure 7.4 indicates that there is a decrease of the probability of failure for increasing values of the mean stone diameter, which is expected since larger diameters exhibit higher critical bed shear stresses, therefore, being less likely to be dragged away from the armour layer. This behaviour is in agreement with the results obtained by [12].

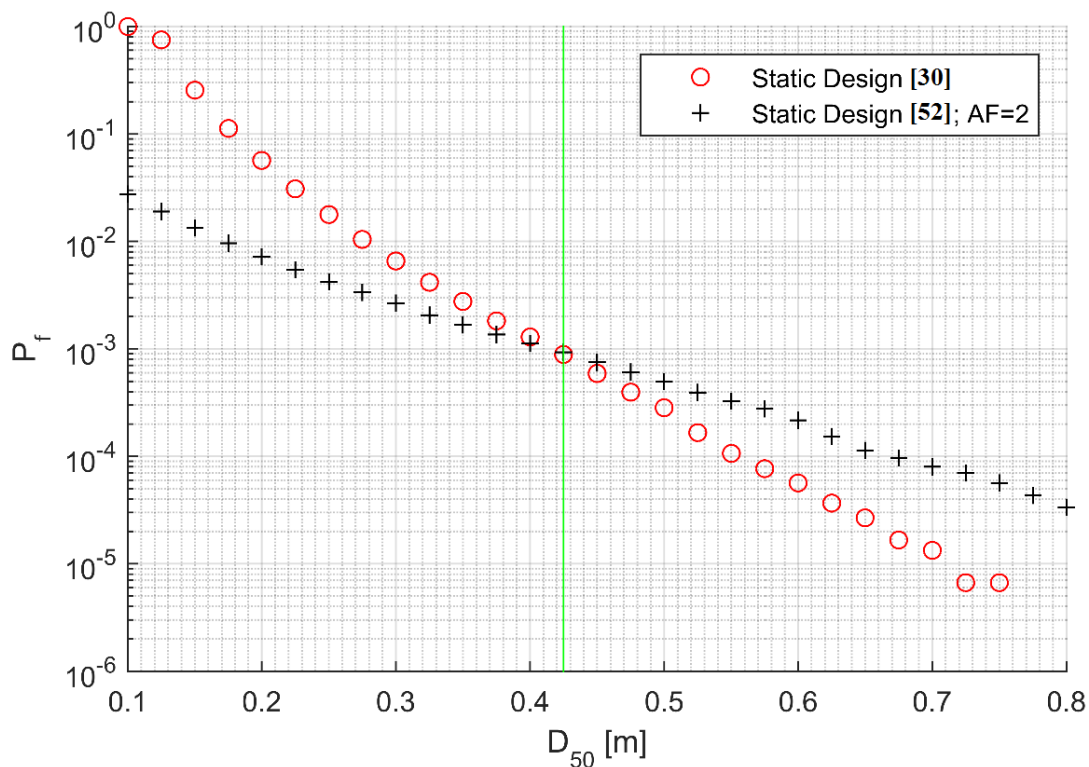


Figure 7.4 – Safety comparison between static design criteria ($n=300\,000$). AF – amplification factor.

The deterministic design, previously presented, indicated that the methodology [52] yielded more conservative sizes of the mean diameter. However, Figure 7.4 indicates that this methodology seems to be more conservative only for mean diameters larger than 0.42 m (vertical line in Figure 7.4). Conversely, as D_{50} decreases, the methodology in [52] yields smaller probabilities of failure than the methodology in [30]. Moreover, the methodology in [30] leads to a probability of failure of 1 for a mean diameter of 0.1 m, while according to the methodology in [52] the probability is much smaller, roughly 0.03. Such difference should be the aim of further research and might also be caused by an invariance problem of the limit state function based on methodology [52]. Given these results, one may ask “are these two curves comparable?” i.e. can they be used to assess the same design situation? It is possible to argue that they are not, since several different factors influence both criteria and may contribute for this somehow peculiar behaviour. Firstly, the results in Figure 7.4 consider an amplification factor of 2, which may not be the most reasonable choice for the waves and currents

combined. As can be shown in Figure 7.5, the probability of failure for the same mean stone diameter is highly dependent on the amplification factor, which is often determined by physical models adapted for a specific construction site.

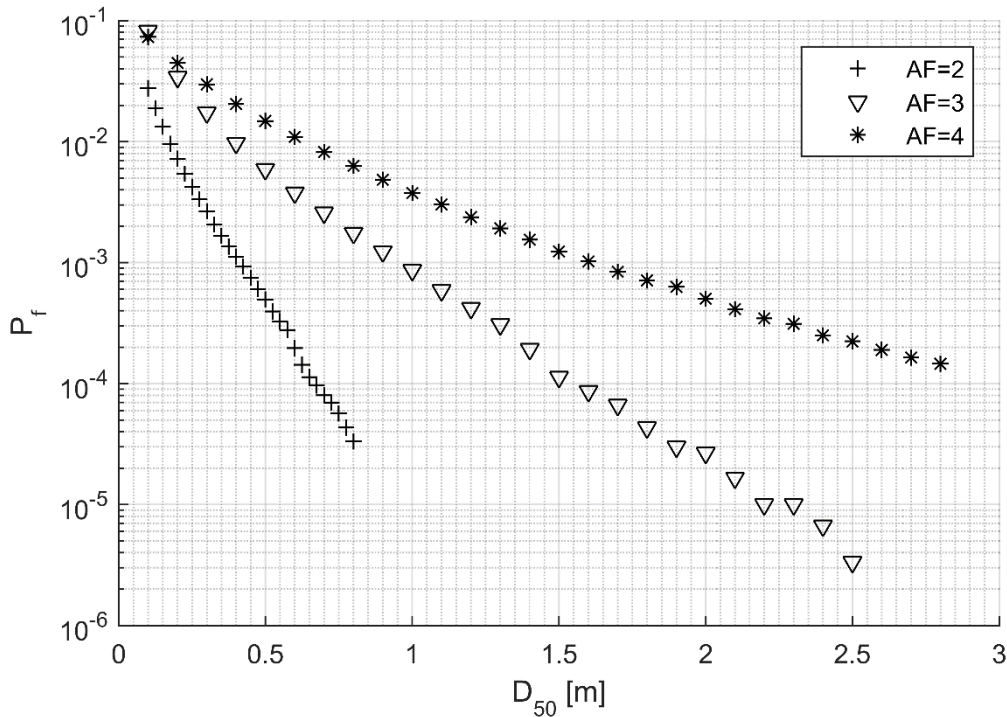


Figure 7.5 – Influence of the amplification factor in the probability of failure for methodology [52] (n=300 000).

Figure 7.5 shows that when the amplification factor increases, a larger mean diameter must be chosen to obtain the same probability of failure. This emphasises the fact that the methodology proposed by [52] tends to be more conservative when the amplification factor is increased. Nevertheless, it can be noted that the definition of the amplification factor may represent a drawback to the probabilistic design of static scour protections according to the methodology in [52]. Although, several authors use $\alpha=4$, this value can be larger or smaller, depending on the hydrodynamic conditions [61]. The fact that its evaluation is still assessed based on the empirical knowledge of the designer, makes it harder to define standard values of α that should be used to obtain the curve showed in Figure 7.4, which is intended to be comparable with the methodology in [30]. The effect of the amplification factor on the probability of failure increases for an increasing D_{50} .

In agreement with the deterministic design previously performed, Figure 7.5 shows that amplification factors of 3 or 4 leads to very large mean stone diameters, which for a rip-rap scour protection may not be a feasible material to be placed with the fall-pipe vessels, as mentioned in [11].

Another aspect that may contribute to the behaviour shown in Figure 7.4 is the calculation of the critical bed shear stress. Figure 7.6 shows the critical bed shear stress as a function of the diameter of the stones. Note that, according to [30], the critical bed shear stress is calculated with θ_{cr} equal to 0.035 and using the diameter $D_{67.5}$. On the other hand, the methodology in [52] uses θ_{cr} equal to 0.056 and the mean stone diameter D_{50} . One can think about the critical bed shear stress as being the resistance component of the limit state functions in Eqs. (7.6) and (7.7). Figure 7.6 shows that, for smaller diameters, the difference between the resistance values obtained by both methodologies is less significant. This difference becomes more relevant as D_{50} increases. When the mean stone diameter

increases, the resistance given by the methodology in [30] can be seen to increase less than the resistance obtained by the methodology in [52] (Figure 7.6). This should lead to larger probabilities given by the design according to [30] than according to in [52]. However, this effect may be opposed by the different calculation of the acting bed shear stress which varies non-linearly with the increasing D_{50} .

Moreover, the non-linearity of the combined wave- and current-induced bed shear stress with the variation of the mean stone diameter may also contribute for the different behaviour between the curves shown in Figure 7.4. Further research should be carried to fully address the influence of this aspect. Note that the non-linear effects are mainly due to the influence of D_{50} on the wave and current friction factors, as shown by [147] and [316].

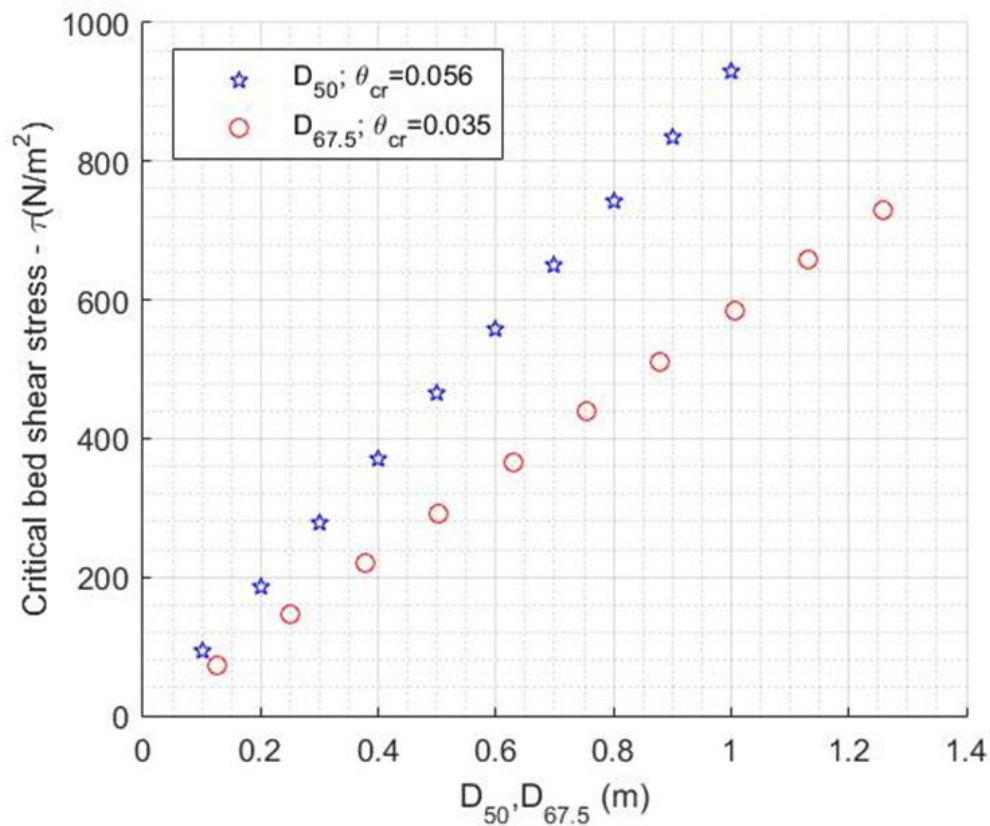


Figure 7.6 – Comparison of the critical bed shear stress calculated by the methods in [30] and [52].

Finally, one must also note that the wave orbital bottom velocity (U_m) is calculated for the significant wave height (H_s) in the methodology in [52], while in the methodology in [30] it is calculated for the mean wave height of the top 10% of the waves ($H_{1/10}$). Therefore, the orbital bottom velocity used in [30] is more conservative than the one used in [52]. In non-cohesive sediments, as the ones studied in this case, research shows that the combined bed shear stress increases faster for smaller stone diameters, e.g. [1] and [30]. Therefore, when the diameter decreases, the effect caused by the different calculation of U_m may also contribute to the larger values of the probability of failure given by the methodology in [30]. When the mean diameter increases, the effects associated to U_m dissipate and the methodology in [30] yields larger values of the probability of failure.

Figure 7.7 shows the probabilities of failure obtained with the methodology in [30] compared to those obtained with the methodology in [52] calculated with an amplification factor equal to 4 and U_m

calculated with $H_{1/10}$. As expected, the probabilities of failure for the methodology in [52] increase considerably since $U_m(H_s) < U_m(H_{1/10})$. For the sake of comparison, Figure 7.7 is limited to $D_{50}=0.9$ m, because the methodology in [52] only yields smaller probabilities of failure than [30] for very small diameters (also see Figure 7.5). In the case of Figure 7.7, it is possible to see that the intersection point between both methodologies occurs sooner than shown in Figure 7.4, close to $D_{50}=0.16$ m (green line Figure 7.7).

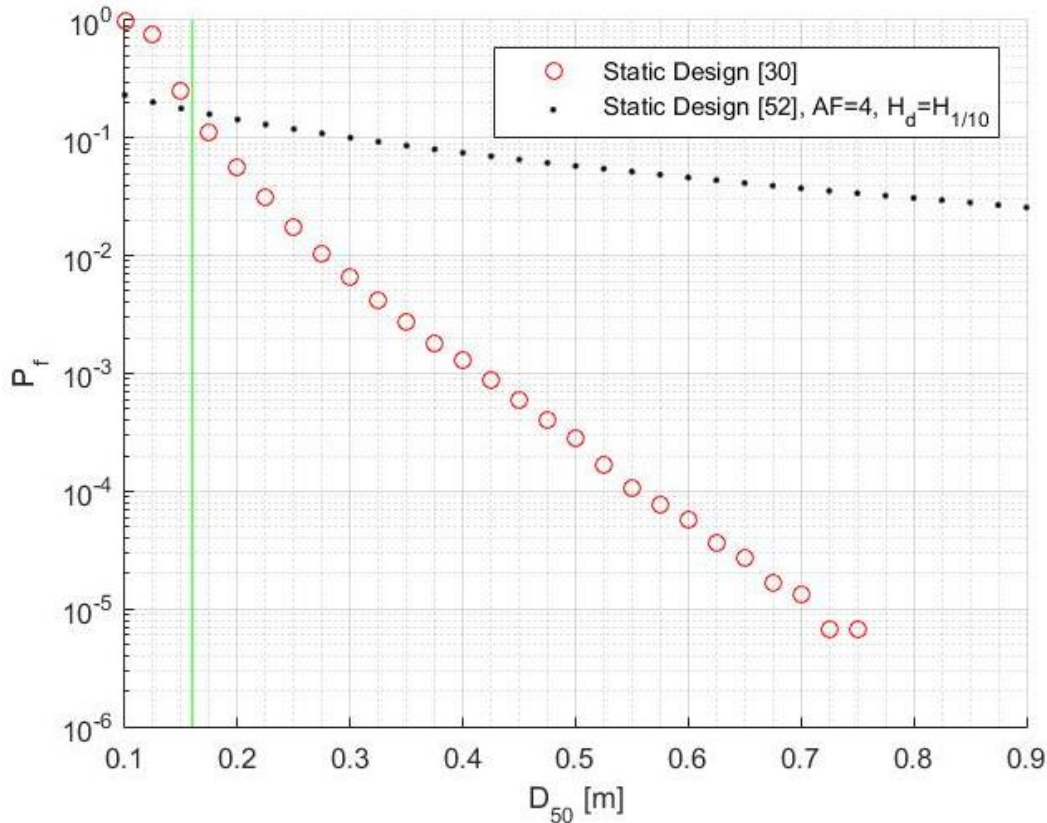


Figure 7.7 – Influence of U_m in the probability of failure for the methodology in [52], compared with the application of the methodology in [30] ($n=300\ 000$).

These results show that, for static scour protections, it might be difficult to select a D_{50} for a pre-defined probability of failure. Nevertheless, in the present case study, for probabilities of failure smaller than 10^{-3} , the methodology in [30] consistently leads to smaller mean stone diameters (see Figure 7.4 and Figure 7.5).

In practical situations, it is recommended that both curves are established and analysed before selecting the design value of D_{50} . Moreover, it is also noted that selecting D_{50} may also depend on factors such as the available material, the transportation cost and the construction technique (e.g. fall-pipe vessels, cranes, lifters), which may lead the designer into avoiding the use of very large diameters, e.g. above 0.8 m.

When designing a dynamic scour protection, it is important to establish the relation between the stone diameter and the probability of failure for the criterion presented in [32]. Moreover, since the methodology presented in [32] is an improvement of the method for static scour protections proposed in [30], it is also important to understand if both criteria provide an equivalent safety level, i.e. if there is a relation between a static scour protection designed with a certain D_{50} and a dynamic scour protection designed with a reduced D_{50}^* , for any $D_{50}^* < D_{50}$.

Figure 7.8 presents the comparison of both methodologies for the case study introduced in the previous section. For the tested range of mean stone diameters, it can be seen that the criterion proposed by the static design consistently leads to larger probabilities of failure for the same mean stone diameter. This is expected since the dynamic design allows for the movement of the stones, which means that smaller diameters can be used in the design without considering that failure occurs. However, a fair comparison between criteria must be performed for different diameters, i.e. the one used for a static design and the reduced one used in the dynamic design.

Point A (0.26 m; 5×10^{-4}) and Point B (0.54 m; 1.7×10^{-4}) in Figure 7.8 correspond to the deterministic design values previously presented for the dynamic and static scour protections, respectively. As seen before, these two points show that the probability of failure is larger for the reduced diameter D_{50}^* . However, one is able to see that other values of D_{50} could be used, smaller than $D_{50}=0.54$ m but larger than 0.26 m, still yielding probabilities of failure which are in the order of 10^{-4} .

For example, if the designer is not comfortable with using a $D_{50}^*=0.26$ m, he may still use, for instance, a $D_{50}=0.45$ m, which yields a value of P_f in the order of 10^{-5} for the dynamic criteria and 10^{-4} in the static one, but still represents a smaller mean diameter when compared with the one required for static stability, i.e. $D_{50}=0.54$ m. In this sense, and for design purposes, one is now able to select the mean stone diameter for a pre-defined probability of failure from the curves showed in Figure 7.8.

Figure 7.8 shows that, depending on the level of safety, i.e. for the same probability of failure, the “static mean stone diameter” can be approximately reduced by 10 to 15 cm if one uses a “dynamic mean stone diameter”. This is of great importance as, for the present case study, it helps to validate that a solution based on a dynamic scour protection yields a similar level of reliability as the one based on the static design.

Furthermore, it enables the designer to understand how the proposed reduction in the diameter is influencing the safety level according to the statically stable or dynamically stable criteria. Eventually, the designer may adopt an intermediate solution between both diameters and he is still optimising the dimension of the protection when compared with the traditional static design.

As seen when dealing with the reliability assessment of the deterministic design approach, the author notes that further research should be performed in order to generalize this procedure for other case studies. The lack of research addressing the probabilistic design of scour protections for offshore wind turbines leaves space to improve these results and to compare them with different design conditions.

However, the confidential policies concerning data sharing, design procedures and the occurrence of failures in the offshore wind industry do not facilitate the increase in the number of case studies to be analysed. Therefore, only a confined group of people has experience and knowledge to design scour protections [30].

Nevertheless, the successful development of physical model studies concerning dynamic scour protections, e.g. [26, 32, 101] and [102], as well as the consistent levels of safety that were identified for the present case study justify the need for further research on the matter as a possible way to optimise the design of scour protections.

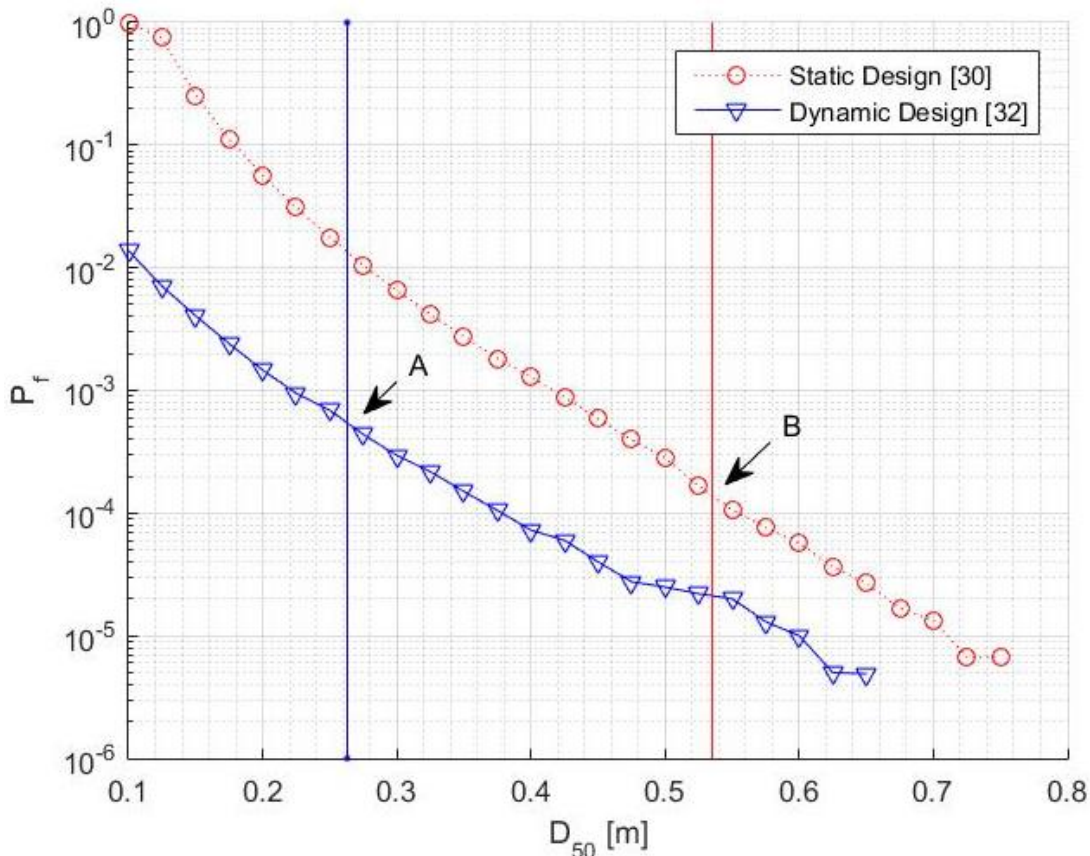


Figure 7.8 – Probabilities of failure as a function of the mean stone diameter. Comparison between static [30] and dynamic design [32].

7.5 Conclusions

The present chapter was dedicated to the need of understanding if a dynamic scour protection might be considered as equally safe as a static protection, provided that the estimated environmental conditions remain the same. In Chapter 6, an answer to this problem was identified as being crucial, in order to build up the confidence in the use of dynamic scour protections. Chapter 7 addressed this aspect for the available data at Horns Rev 3. Moreover, the relationship between the safety measure (probability of failure) and the mean stone diameter of the armour layer was obtained. This relationship has been proven to be useful for design purposes enabling the designer to define a zone of possible diameters that lie between the static and the dynamic design, with a safety level that might be considered acceptable by the designer.

The research developed in this chapter represents a novel way to look at scour protection design, which does not provide a specific diameter. Instead, this probabilistic and reliability-based design defines the safety level associated to each possible solution, which the designer can use to optimise the solution proposed according to the static stability from [30], eventually, moving towards the dynamic stability as defined in [32]. The work hereby presented allowed for the following conclusions:

- For the considered case study, it was concluded that it is possible to design a dynamic scour protection, according to [32], with a similar reliability of a static scour protection designed according to [30];

- Both design methodologies showed that the reduction of the mean diameter, from a static stability towards a dynamic stability, may be used for practical purposes;
- It is possible to use a mean diameter between the statically and the dynamically stable ones within the same order of the probability of exceeding the design criterion;
- Due to uncertainty associated to several design variables, e.g. the amplification factor and others, further research should be carried in order to properly address the comparison between the probabilistic design made with the methodology [30] and [52];
- The probability of failure was influenced by the amplification factor, the Shields critical parameter, the diameter used to compute the critical bed shear stress and the calculation of the orbital bottom velocity;
- Therefore, design options made regarding these aspects may difficult a straight comparison between the criteria adopted by [30] and [52]. Nevertheless, for probabilities smaller than 10^{-3} , regardless of the amplification factor the methodology [52] tended to provide larger mean diameters than the methodology [30];
- It is advisable to perform the reliability assessment for several values of the amplification factor and several design methodologies, so that the design decisions are better informed.
- It is also concluded that the physical modelling activities that help the designer to define these somehow empirical values, remain as indispensable for a proper reliability comparison between solutions. Moreover, the proposed design should always be validated by means of physical model studies, as it is common in scour protection studies, e.g. [12] or [26].
- The analysis of the influence of the sampling rate of H_s and T_p on the probability of failure remains to be fully understood;
- As mentioned in section 6.4, the influence of the statistical model used to generate correlated wave heights and periods, as well as the correlation between the sea-state and the current velocity, are key aspects to improve the accuracy of reliability analysis applied to scour protections.

Finally, it should also be noted that the reliability analysis based on different design criteria and the possible probabilistic design require a clear definition on the general rules that define the required protection's safety level, which are yet not found in the literature and should be the aim of future research. The present research addresses the reliability of dynamic scour protections and provides the means to obtain a measure of safety associated to a specific design solution. However, at the present state-of-the-art, typical offshore wind standards as [21] or [106] do not suggest any common ground for the required safety level of a scour protection, which is crucial for a meaningful implementation of this research in the current design practices.

Conclusions and Future Developments

8.1 Conclusions

The present thesis was dedicated to the study of dynamic scour protections for offshore monopile foundations. Two key aspects related to this topic were extensively addressed. The first one concerned the suitability of the damage number to describe the failure caused by the erosion of the armour layer. The second aspect concerned the reliability of dynamic scour protections and the potential to optimise the mean stone diameter for a suitable safety level, i.e. probability of failure.

At the beginning of this research two main objectives were established:

- Provide a contribution to the novel concept of Dynamic Scour Protections, by means of a physical model study;
- Propose a Reliability Assessment Methodology for Scour Protections, by developing a statistical framework to perform the safety analysis of scour protections.

The first objective was approached in Chapter 4, whereas the second one was addressed in Chapters 6 and 7. The specific main findings and concluding remarks of each chapter were already provided throughout this thesis. However, in this section, the broader conclusions and achievements of the present research are summarised. After the present research the following main conclusions were obtained:

- Scour phenomena and the methodologies currently applied to quantify the bed shear stresses acting on the sand bed, or on the scour protection, present a considerable empirical nature. Therefore, the reliability analysis and the probability of failure of the protection will be considerably affected by the designer's choice regarding the empirical aspects mentioned in Chapter 2, namely the wave friction factor and the amplification factor;
- Other variables as the current friction factor, the Shields parameter also affect the probability of failure. It is important to make consistent decisions through the reliability analysis of the protection, namely when comparing the critical bed shear stress with the maximum acting shear stress, i.e. using the Shields parameter and the friction factors according to the recommendation of each methodology, e.g. [30, 52];
- In Chapter 3 it was concluded that the design methodologies of scour protections for offshore environment are far less developed than the ones used in other cases, e.g. bridge piers. Several factors contribute to this aspect, e.g. the lower amount of data available for offshore locations, the fact that offshore structures design is more recent and in a less mature state of development, when compared to fluvial ones, or the difficulty in account for the complex

combination of environmental factors (waves and currents). Therefore, a considerable uncertainty surrounds these methodologies;

- For both static and dynamic scour protections, the options made regarding the empirical aspects of the methodologies presented may result in different mean stone diameters, which again contributes to differences in the assessment of the reliability of the protection. This becomes evident for example when computing the critical shear stress according to [30] or [52]. It also occurs if the stability parameter is used instead of damage number to design the dynamic scour protection;
- The studies performed on dynamic scour protections, namely [32] and [101], show that the transition between static stability, dynamic stability and failure is gradational. This makes it harder to define of a generalised damage number to be used in the quantification of the probability of failure. Therefore, the limits concerning the acceptable damage number should be calibrated through physical model studies for each case study;
- The design methodologies addressed in Chapter 3 can be considered deterministic, at least regarding the long-term behaviour and correlation of the design variables. Therefore, the reliability analysis might be considered as an important supplement to the traditional design of scour protections, as it enables to associate a measure of safety to the mean stone diameter, thus quantifying the design uncertainty;
- Nevertheless, these methodologies are crucial to build the failure criteria to be adopted in the reliability analysis;
- It was concluded that there is a lack of extensive research regarding the design of dynamic scour protections. Only in recently new studies started to emerge on a consistent basis. However, the problem caused by the lack of publically available field data is also important to obtain a notion on the failure occurrence of scour protections and the feasibility of the dynamic stability concept at a prototype scale;
- Chapter 4 presented two physical model studies concerning a monopile foundation in typical North Sea storm conditions, which validated the feasibility of dynamic scour protections for the model conditions. Some of the aspects concerning the predictive formula for the damage number were studied with further detail, whereas the formula's limitations were also discussed, namely regarding the effect of the armour layer thickness;
- Dynamically stable profiles were obtained in each physical model considered. However, the effect of large duration tests and opposing waves and current were left to be deeply studied. Moreover, the isolated effect of the armour layer was only studied for waves alone situation. At the present stage of research, it is recommended that the dynamic mean stone diameter is calibrated through physical model for each practical situation, preferably within the original limits of the predictive formula proposed by [32];
- It was concluded that the design based on the acceptable damage number consistently led to optimised, i.e. reduced, mean stone diameters of the scour protection, thus creating the possibility to minimise the OPEX and CAPEX parcels of a commercial scale project, as explained in Chapter 1;
- It was found that despite the gradational transition between static stability, dynamic stability and failure, the acceptable damage numbers originally proposed by [32] are rather conservative. Therefore, they could be used for the reliability analysis, since they are not contributing for an underestimation of the probability failure;
- Although further research should be carried for a proper generalisation of the methodology in [32], it was concluded that dynamic scour protections represent an optimisation of the

traditional statically stable ones. However, the commercial aspects concerning the construction and installation of the protection or the maintenance operations may impose practical restrictions to the final solution obtained from [32];

- Several reliability techniques were described in Chapter 5, which concluded that the Monte-Carlo simulation method was a reasonable choice as a starting candidate to implement the reliability analysis of scour protections;
- The fundamental notions on reliability analysis were introduced and identified as a crucial part of risk analysis applied to the design of offshore foundations. It was noted that, typically, the design of scour protections does not associate a measure of safety to the minimum required stone size of the protection, thus being difficult to understand the risk associated to optimised solutions;
- Based on the methodologies addressed in Chapter 4, Chapter 5 discusses the possible limit state functions of the protection, concluding that different functions can be associated to the damage number and the threshold of motion;
- It was concluded that the reliability assessment of scour protections by means of a full probabilistic model, which accounts for all random variables, is almost impractical. Therefore, the designer should restrict the assessment to the most important variables and the most important long-term correlations;
- This research focused the correlation between the wave heights and the wave periods. In Chapter 5, it was concluded that copula-based models could be an interesting alternative to the conditional modelling approach, already included in offshore wind engineering standards;
- Chapter 6 showed how to perform a reliability assessment of a dynamic scour protection for a previously defined mean stone diameter, considering Horns Rev 3 met-ocean data. It was concluded that the probability of failure is a useful measure of safety, which is crucial to understand how reliable a scour protection is under random environmental conditions;
- The study performed, concluded that the statistical framework, i.e. the random variables, the dependence measures and the statistical model influence the probability of failure. Therefore, comparisons of reliability should always be performed for the same statistical framework;
- The probabilities of failure obtained in Chapter 6 are comparable, in their order of magnitude, to the ones currently used for other marine structures. However, this matter should be further studied in detail, since the lack of reliability studies of scour protections is yet a very recent topic of research. Moreover, the procedure to obtain the annual values of the probability of failure might be questionable, since a constant rate and independence between failure events is being assumed. At the present stage this aspect remains to be fully clarified;
- It was noted that symmetric models were unable to account for the asymmetry present in the met-ocean data. Therefore, Chapter 6 proposed the extra-parametrized copula models as possible alternative for future research regarding reliability of scour protections. The performance of the extra-parametrized copulas provided promising results, which may lead to a more accurate quantification of the protection's reliability;
- In order to understand if the dynamic scour protections provide a safe optimisation of the traditional statically stable ones, Chapter 7 provided a reliability comparison of scour protections designed according to [30, 32] and [52]. Moreover, it was concluded that it is possible to obtain a relationship between the mean stone diameter and the probability of failure according to different design criteria, which can then be used to design the scour protection;

- For the case study considered, it was concluded that it is possible to design a dynamic scour protection with a similar reliability of a statically stable protection, thus meaning that the mean stone diameter can be optimised without compromising the safety level. However, the reliability analysis and the associated probabilistic design do not exclude the need to evaluate the protection's performance by means of a physical model study. This occurs due to the empirical nature of the methodologies early mentioned;
- If the designer is not truly confident on the optimisation associated to the dynamic stability based on the damage number, the methodology presented in Chapter 7 concludes that it is possible to perform a probabilistic and reliability-based design that defines the safety level associated to different solutions between the statically stable and the dynamically stable design. Therefore present research contributes with a reliability assessment methodology that enables the designer to optimise the solution proposed according to the static stability from [30], eventually, moving towards the dynamic stability as defined in [32];
- This thesis also showed that, so far, no guidance exists on the acceptable level of safety for scour protections applied to the foundation of offshore wind turbines. Therefore, the scientific community and the stakeholders of the offshore wind energy sector should orient their efforts towards the definition of a common ground for the required safety level of scour protections.

Besides the conclusions obtained with the present research and their associated limitations, the main idea of this research is that reliability analysis can and should be implemented as a tool to improve the optimization of scour protections, namely regarding their safety and their cost. Moreover, coupling this analysis with innovative design concepts, as the dynamic stability, unlocks new doors that contribute to the competitiveness of the offshore wind energy sector and other marine renewable energy sources.

8.2 Future research

During the present research, several aspects were identified as future research topics. This section provides guidance for future works, aiming at the improvement of the research hereby developed. Notwithstanding the interest of the conclusions previously obtained, the following topics could be addressed to increase potential applicability of this work to the offshore wind industry:

- Performing the reliability analysis for an extended range of amplification factors, friction factors and other empirical design methodologies, will help to validate the conclusions obtained. Moreover, it will be essential to define a common safety level that is suitable regardless of the methodology applied;
- Extend (and validate) the range of applicability of the methodology [32], namely regarding the waves and current direction, the wave characteristics, the KC and the Re numbers, will help to clarify the acceptable damage number for different situations;
- Extend the physical model studies to other optimisation concepts, as the wide-graded single layer scour protections. This will enable the reliability comparison with other optimisations proposed in the literature.
- Improve the statistical framework to consider more complex models, as the extra-parametrized copulas and the correlation between waves and current or the variation of the water depth in order to improve the accuracy of the reliability assessment performed;
- Compare the probabilities obtained in the present study with the ones obtained from other models available in the literature. Moreover, assess the confidence level and the error of the probabilities obtained in Chapters 6 and 7, to analyse if the differences between the tested

models are statistically meaningful or not. This could be performed by bootstrapping the values of the probability of failure, for several random series of the variables considered in statistical framework;

- A detailed study should be performed regarding the comparison of the failure analysis performed with extreme value analysis (and the adaptive importance sampling techniques) and the one performed in this work, which uses the 10 years and 4 months of met-ocean data. This contributes to clarify the proper relationship between the return period of the environmental variables and the return period of the actual failure of the protection;
- The influence of the number of waves, in a single-storm, on the probability of failure and its relation with the long-term record of the data is also a matter to be fully clarified. Moreover, the conversion of the probabilities of failure into annual values should be addressed with further detail, so that a realistic comparison can be made with the safety levels employed in other maritime and offshore structures, as mooring lines or breakwaters.

Finally, for a proper implementation of reliability analysis techniques in the design of scour protections, a considerable effort should be made to gather field data and to perform monitoring campaigns, which provide useful information on the failure occurrence of these protections and a true notion of the accuracy of the results obtained with this research.

Bibliography

- [1] L. De Vos, “Optimisation of Scour Protection Design for Monopiles and Quantification of Wave Run-Up - Engineering the Influence of an Offshore Wind Turbine on Local Flow Conditions”, PhD Thesis, University of Ghent, Ghent, 2008.
- [2] C. Matutano, “Caracterización de los sistemas de protección basados en materiales naturales destinados al control de la socavación en obras marítimas presentes en instalaciones eólicas marinas”, PhD Thesis, Universidade Politécnica de Madrid, Madrid, 2013.
- [3] United Nations, “Kyoto Protocol”, 11 December 1998. [Online]. Available: <http://unfccc.int/resource/docs/convkp/kpeng.pdf>. [Accessed 25 January 2018].
- [4] United Nations, “Adoption of the Paris Agreement”, 12 December 2015. [Online]. Available: <https://unfccc.int/resource/docs/2015/cop21/eng/l09r01.pdf>. [Accessed 25 January 2018].
- [5] WindEurope, “The European Offshore Wind Industry: key trends and statistics 2016”, WindEurope, Brussels, 2017.
- [6] WindEurope, “Wind Energy Scenarios for 2030”, WindEurope, Brussels, 2017.
- [7] Offshore Wind, “<https://www.offshorewind.biz>”, Offshore Wind, 3 October 2017. [Online]. Available: <https://www.offshorewind.biz/2017/10/03/offshore-wind-breaks-record-in-europe/>. [Accessed 25 January 2018].
- [8] WindEurope, “Financing and Investment trends, the European Wind Industry in 2016”, WindEurope, Brussels, Belgium, 2017.
- [9] A. G. A Athanasia, “European Wind Energy Association Report - Deep Water: The Next Step for Offshore Wind Energy”, July 2013. [Online]. Available: http://www.ewea.org/fileadmin/files/library/publications/reports/Deep_Water.pdf. [Accessed 11 May 2017].
- [10] R. McKenna, P. O. v. Leye and W. Fichtner, “Key challenges and prospects for large wind turbines”, *Renewable and Sustainable Energy Reviews. Volume 53*, pp. 1212-1221, 2016.
- [11] T. Fazeres-Ferradosa, “Risk Analysis Applied to Scour Dynamical Protection Systems for Offshore Foundations Optimisation”, Department of Civil Engineering, Faculty of Engineering of University of Porto, Porto, 2016.

- [12] T. Fazerer-Ferradosa, F. Taveira-Pinto, L. d. Neves and M. T. Reis, "Design of scour protections and structural reliability techniques", in *Sustainable Hydraulics in the Era of Global Change*, London, Taylor & Francis Group, 2016, pp. 527-531.
- [13] R. Whitehouse, J. Harris, J. Sutherland and J. Rees, "The nature of scour development and scour protection at offshore windfarm foundations", *Marine Pollution Bulletin. Volume 62. Issue 1*, pp. 73-88, 2011.
- [14] A. Gonzalez-Rodriguez, "Review of offshore wind farm cost components", *Energy for Sustainable Development*, vol. 37, pp. 10-19, 2017.
- [15] EY, "Ernst & Young Global Limited Offshore wind in Europe - Walking the tightrope to success", Ernst & Young et Associés, London, 2015.
- [16] Crown Estate, "<http://www.thecrownestate.co.uk/>", 22 May 2015. [Online]. Available: <http://www.thecrownestate.co.uk/>. [Accessed 2018 January 26].
- [17] BVG Associates, "Unleashing Europe's offshore wind potential - A new resource assessment", WindEurope, Brussels, Belgium, 2017.
- [18] S. Bhattacharya, "Challenges in Design of Foundations for Offshore Wind Turbines", *Engineering and Technology Reference*, pp. 1-9, 2014.
- [19] O. Adedipe, F. Brennan and A. Kolios, "Review of corrosion fatigue in offshore structures: Present status and challenges in the offshore wind sector", *Renewable and Sustainable Energy Reviews.*, vol. 61, pp. 141-154, 2016.
- [20] NREL, "Offshore Wind Market and Economic Analysis", Navigant Consulting Inc., Burlington, 2014.
- [21] DNVGL, "DNV OS J101 - Design of Offshore Wind Turbine Structures", Det Norsk Veritas AS, Høvik, 2017.
- [22] S. Rodrigues, C. Restrepob, E. Kontos, R. T. Pinto and P. Bauer, "Trends of offshore wind projects", *Renewable and Sustainable Energy Reviews*, vol. 49, p. 1114–1135, 2015.
- [23] V. Negro, J.-S. López-Gutiérrez, M. D. Esteban and C. Matutano, "Uncertainties in the design of support structures and foundations for offshore wind turbines", *Renewable Energy*, vol. 63, pp. 125-132, 2014.
- [24] W.-G. Qi and F.-P. Gao, "Physical modeling of local scour development around a large-diameter monopile in combined waves and current", *Coastal Engineering*, vol. 83, pp. 72-81, 2014.
- [25] T. Fazerer-Ferradosa, F. Taveira-Pinto, R. Simons, M. T. Reis and L. D. Neves, "Probability of Failure of Monopile Foundations Based on Laboratory Measurements", in *Proceedings of the 6th International Conference on the Application of Physical Modelling in Coastal and Port Engineering and Science*, Ottawa, 2016.
- [26] P. Schoesitter, S. Audenart, L. Baelus, A. Bolle, A. Brown, L. d. Neves, T. Fazerer-Ferradosa, P. Harens, F. Taveira-Pinto, P. Troch and R. Whitehouse, "Feasibility of a dynamically stable rock armour layer scour protection for offshore wind farms", in *International Conference on*

- Ocean, Offshore and Artic Engineering*, San Francisco, California, 2014.
- [27] DNVGL, “DNVGL - ST- 0262 - Lifetime extension of wind turbines”, Det Norske Veritas AS, Høvik, 2017.
- [28] P. Hou, P. Enevoldsen, W. Hu, C. Chen and Z. Chen, “Offshore wind farm repowering optimization”, *Applied Energy*, vol. 208, pp. 834-844, 2017.
- [29] E. Topham and D. McMillan, “Sustainable decommissioning of an offshore wind farm”, *Renewable Energy*, vol. 102, pp. 470-480, 2017.
- [30] L. De Vos, J. De Rouck, P. Troch and P. Frigaard, “Empirical design of scour protections around monopile foundations. Part 1: Static approach”, *Coastal Engineering*, vol. 58, pp. 540-553, 2011.
- [31] A. Schendel, N. Goseberg and T. Schlurmann, “Erosion Stability of Wide-Graded Quarry-Stone Material Under Unidirectional Current”, *Journal of Waterway, Port, Coastal and Ocean Engineering*, vol. 142, no. 3, pp. 1-19, 2016.
- [32] L. De Vos, J. De Rouck, P. Troch and P. Frigaard, “Empirical design of scour protections around monopile foundations - Part 2 - Dynamic approach”, *Coastal Engineering*, vol. 60, pp. 286-298, 2012.
- [33] G. Hoffmans and H. Verheij, *Scour Manual*, Rotterdam: CRC Press, 1997.
- [34] T. Petersen, M. Sumer, J. Fredsøe and J. Schouten, “Edge scour at scour protections around piles in marine environment - Laboratory and field investigation”, *Coastal Engineering*, vol. 106, pp. 42-72, 2015.
- [35] U. Zanke, T. H. A. Roland and R. Diab, “Equilibrium scour depths around piles in noncohesive sediments under currents and waves”, *Coastal Engineering*, vol. 58, no. 10, pp. 986-991, 2011.
- [36] C. Cremona, "Structural performance – Probability-based assessment", Hoboken, John Wiley & Sons Inc., 2011.
- [37] P. Johnson, “Reliability-Based Pier Scour Engineering”, *Journal of Hydraulic Engineering*, vol. 118, no. 10, pp. 1344-1358, 1992.
- [38] L. Bolduc, "Probabilistic models and reliability analysis of scour depth around bridge piers", MSc. Thesis, Texas: Texas A&M University, 2006.
- [39] M. Muzzammil and N. Siddiqui, “A reliability-based assessment of bridge pier scour in non-uniform sediments”, *Journal of Hydraulic Research*, vol. 47, no. 3, pp. 372-380, 2009.
- [40] M. Muzzammil, N. Siddiqui and A. Siddiqui, “Reliability considerations in bridge pier scouring”, *Structural Engineering and Mechanics*, vol. 28, no. 1, pp. 372-380, 2008.
- [41] J. Briaud, P. Gardoni and C. Yao, “Statistical, risk, and reliability analyses of bridge scour”, *Journal of Geotechnical and Geoenvironmental Engineering*, vol. 140, no. 2, pp. 1-10, 2014.
- [42] Puertos Del Estado, “Recomendaciones para Obras Marítimas - Procedimiento General y Bases de Cálculo en el proyecto de Obras Marítimas y Portuarias - Parte I”, Puertos del Estado

- Ministerio de Fomento, Granada (Spain), 2001.

- [43] T. Fazeres-Ferradosa and F. Taveira-Pinto, “Pre-assessing the feasibility of a design performance function for scour protection systems in offshore foundations”, in *Conference Proceedings of the 36th IAHR World Congress*, The Hague, 2015.
- [44] T. Fazeres-Ferradosa and F. T. Pinto, “Reliability study of scour protections: a comparison between the static and the dynamic failure criteria”, in *Proceedings of the 37th International Conference on Ocean, Offshore & Arctic Engineering*, Madrid, 2018.
- [45] P. Rosa-Santos, F. Taveira-Pinto, L. Teixeira and J. Ribeiro, “CECO wave energy converter: experimental proof of concept”, *Journal of Renewable and Sustainable Energy*, vol. 7, no. 6, 2015.
- [46] M. López, F. Taveira-Pinto and P. Rosa-Santos, “Influence of the power take-off characteristics on the performance of CECO wave energy converter”, *Energy*, vol. 120, pp. 686-697, 2017.
- [47] M. Karimirad, *Offshore Energy Structures, for Wind Power, Wave Energy and Hybrid Marine Platforms*, Trondheim: Springer, 2014.
- [48] F. Taveira Pinto, G. Iglesias, P. Rosa-Santos and Z. Deng, “Preface to Special Topic: Marine Renewable Energy”, *Journal of Renewable and Sustainable Energy*, vol. 7, no. 6, pp. 1-5, 2015.
- [49] R. Whitehouse, *Scour at marine structures: A manual for practical applications*, London: Institution of Civil Engineers, 1998.
- [50] A. F. Shields, “Application of similarity principles and turbulence research to bed-load movement”, *Mitteilungen der Preussischen Versuchsanstalt fuer Wasserbau und Schiffbau*, vol. 26, pp. 5-24, 1936.
- [51] B. M. Sumer and J. Fredsøe, *Hydrodynamics around Cylindrical Structures*, Singapore: World Scientific, 1997.
- [52] R. Soulsby, *Dynamics of marine sands: a manual for practical applications*, London, Thomas Telford, 1997.
- [53] P. Nielsen, *Coastal Bottom Boundary Layers and Sediment Transport - Advanced Series on Ocean Engineering. Vol. 4*, Singapore, World Scientific, 1992.
- [54] R. Soulsby and S. Clarke, “Bed Shear-Stresses Under Combined Waves and Currents on Smooth and Rough Beds. Report TR 137”, HR Wallingford, UK, 2005.
- [55] J. Malarkey and A. Davies, “A simple procedure for calculating the mean and maximum bed stress under wave and current conditions for rough turbulent flow based on Soulsby and Clarke’s (2005) method”, *Computers & Geosciences*, vol. 43, pp. 101-107, 2011.
- [56] Z. Liu, *Sediment Transport (2 ed.)*, Aalborg: University of Aalborg, 2001.
- [57] J. Fredsøe and R. Deigaard, *Mechanics of Coastal Sediment Transport - Advanced Series on Ocean Engineering, vol 3*, Singapore, World Scientific, 1992.

- [58] M. Dixen, F. Hatipoglu, M. Sumer and J. Fredsøe, "Wave boundary layer over a stone-covered bed", *Coastal Engineering*, vol. 55, no. 1, pp. 1-20, 2008.
- [59] C. Matutano, V. Negro, J.-S. López-Gutiérrez and M. D. Esteban, "Scour prediction and scour protections in offshore wind farms", *Renewable Energy*, vol. 57, pp. 358-365, 2013.
- [60] A. Saruwatari, Y. Yoneko and Y. Tajima, "Effects of wave, tidal current and ocean current coexistence on the wave and current predictions in the Tsugaru Strait", in *Coastal Engineering Proceedings*, Seoul, Korea, 2014.
- [61] B. M. Sumer and J. Fredsøe, *The Mechanics of Scour in the Marine Environment*, Singapore: World Scientific, 2002.
- [62] P. E. Steven Hughes, "Review of The Mechanics of Scour in the Marine Environment", *Journal of Waterway Port Coastal and Ocean Engineering*, vol. 129, no. 6, p. 297, 2003.
- [63] H. Breusers and A. Raudkivi, *Scouring-hydraulic Structures Design Manual*, Madrid: International Association of Hydro-Environment and Research, 1991.
- [64] P. Hjorth, *Studies on the nature of local scour*, Institute of Technology, Department of Water Resources Engineering, Lund, 1975.
- [65] B. Melville and S. Coleman, *Bridge Scour*, Colorado, Water Resources Publications, 2000.
- [66] A. Roulund, M. Sumer, J. Fredsøe and J. Michelsen, "Numerical and experimental investigation of flow and scour around a circular pile", *Journal of Fluid Mechanics*, vol. 534, pp. 351-401, 2005.
- [67] A. Nielsen, X. Liu, M. Sumer and J. Fredsøe, "Flow and bed-shear stresses in scour protections around a pile", *Coastal Engineering*, vol. 72, pp. 20-38, 2013.
- [68] Z. Lin, D. Pokrajac, Y. Guo, D. Jeng, T. Tang, N. Rey, J. Zheng and J. Zhang, "Investigation of nonlinear wave induced seabed response around monopile-foundation", *Coastal Engineering*, vol. 212, pp. 197-211, 2017.
- [69] H. Zhao, D. S. Jeng, C. Lio and J. Zhu, "Three-dimensional modeling of wave-induced residual seabed response around a mono-pile foundation", *Coastal Engineering*, vol. 128, pp. 1-21, 2017.
- [70] M. Sumer and J. Fredsøe, "The horseshoe vortex shedding around a vertical wall-mounted cylinder exposed to waves", *Journal of Fluid Mechanics*, vol. 332, pp. 41-70, 1997.
- [71] S. Umeda, M. Yuhi and H. Ishida, "Numerical study of three-dimensional flow fields around the base of a vertical cylinder in oscillatory plus mean flow", in *Proceedings of the Conference Coastal Structures 2003*. pp. 751-763, Reston, 2003.
- [72] J. Miles, T. Martin and L. Goddard, "Current and wave effects around windfarm monopile foundations", *Coastal Engineering*, vol. 121, pp. 167-178, 2017.
- [73] C. Baker, "The laminar horseshoe vortex", *Journal of Fluid Mechanics*, vol. 95, pp. 347-367, 1979.
- [74] O. Link, F. Pflieger and U. Zanke, "Characteristics of developing Scour-holes at a sand-

- embedded cylinder”, *International Journal of Sediment Research*, vol. 23, no. 3, pp. 258-266, 2005.
- [75] M. Sumer, J. Fredsøe and N. Christiansen, “Scour around a vertical pile in waves”, *Journal of Waterway, Port, Coastal and Ocean Engineering*, vol. 118, no. 1, pp. 15-31, 1992.
- [76] N. Hansen and K. Gislason, “Movable scour protection on highly erodable sea bottom”, in *International Coastal Symposium*, Hornafjörður, 2005.
- [77] M. Sumer, N. Christiansen and J. Fredsøe, “Time scale of scour around a vertical pile”, in *International Offshore and Polar Engineering*, San Francisco, 1992.
- [78] B. Melville and Y. Chiew, “Time scale for Local Scour at Bridge Piers”, *Journal of Hydraulic Engineering*, vol. 125, no. 1, pp. 59-65, 1999.
- [79] S. Lee, T. Sturm, A. Gotvald and M. Landers, “Comparison of laboratory and field measurements of bridge pier scour”, in *International Conference on Scour and Erosion*, Nanyang, Singapore, 2004.
- [80] Federal Highway Administration Research and Technology, “Field Observations and Evaluations of Scour at Bridges”, U.S. Department of Transportation, U.S.A., 2005.
- [81] J. Harris, W. Herman and B. Cooper, “Offshore Windfarms - an approach to scour assessment”, in *International Conference on Scour and Erosion*, Nanyang, Singapore, 2004.
- [82] LIC Engineering A. S., “Scroby Sands Wind Farm - Offshore Foundation series”, Esberg, 2004.
- [83] T. Fazerer-Ferradosa, “Scour around marine foundations in mixed and layered sediments. MSc. Thesis”, Faculdade de Engenharia da Universidade do Porto, Porto, 2012.
- [84] Federal Highway Administration, “Scour in cohesive soils”, U.S. Department of Transportation, Georgetown, 2015.
- [85] L. Deng and C. S. Cai, “Bridge Scour: Prediction, Modeling, Monitoring, and Countermeasures—Review”, *Practice Periodical on Structural Design and Construction*, vol. 15, no. 2, pp. 125-134, 2010.
- [86] Y. M. Chiew, “Mechanics of Riprap Failure at bridge Piers”, *Journal of Hydraulic Engineering*, vol. 121, no. 9, pp. 635-643, 1995.
- [87] E. Richardson and S. Davis, "Evaluating scour at bridges", 4th Ed. - Hydraulic Engineering Circular no. 18 (HEC-18), Washington DC: Federal Highway Administration, 2001.
- [88] P. Julien, J. Ruff and U. Ji, Alternative designs of pier-scour protection for the Gupo and Subway Bridge on the Lower Nakdong River, “www.engr.colostate.edu”, 2006. [Online]. Available: https://www.engr.colostate.edu/~pierre/ce_old/Projects/linkfiles/Gupo%20report%204-19-06.pdf. [Accessed 6 January 2018].
- [89] D. M. Sheppard and J. W. Miller, “Live-bed Local Pier Scour Experiments”, *Journal of Hydraulic Engineering*, vol. 132, pp. 635-642, 2006.
- [90] U. Zanke, “Scour at piles in steady flow and under the influence of waves. Technical

- Communication 54”, University of Hannover, Hannover, Germany, 1982.
- [91] M. Sumer and J. Fredsøe, “Scour around pile in combined waves and current”, *Journal of Hydraulic Engineering*, vol. 127, no. 5, pp. 403-411, 2001.
- [92] L. Chen and W.-H. Lam, “Methods for predicting seabed scour around marine current turbine”, *Renewable and Sustainable Energy Reviews*, vol. 29, pp. 638-692, 2014.
- [93] J. Harris, R. Whitehouse and R. J. Sutherland, “The time evolution of scour around offshore structures”, *Proceedings of the Institution of Civil Engineers, Maritime Engineering*, vol. 163, no. MA1, pp. 3-17, 2010.
- [94] D. Rudolph and J. K. Bos, “Scour around monopile under combined wave-current conditions and low KC numbers”, in *Proceedings of the 3th International Conference on Scour and Erosion*, Amsterdam, The Netherlands, 2006.
- [95] T. C. Raaijmajmakers and D. Rudolph, “Time-dependent scour development under combined current and wave conditions- laboratory experiments with online monitoring technique”, in *Proceedings of the 4th International Conference on Scour and Erosion*, Tokyo, Japan, 2008.
- [96] U. Zanke, T. Hsu, A. Roland, O. Link and R. Diab, “Equilibrium scour depths around piles in noncohesive sediments under currents and waves”, *Coastal Engineering*, vol. 58, pp. 986-991, 2011.
- [97] R. W. P. May, J. C. Ackers and A. M. Kirby, "Manual on Scour at Bridges and Other Hydraulic Structures", London: CIRIA, 2002.
- [98] A. Agrawal, M. Khan and Z. Yi, “Handbook of Countermeasures Designs - report No FHWA-NJ-2005-027”, New Jersey Department of Transportation & Federal Highway Administration US Department of Transportation Washington D.C., Washington D.C., 2007.
- [99] M. Beg and S. Beg, “Scour Reduction around Bridge Piers: A review”, *International Journal of Engineering Inventions*, vol. 2, no. 7, pp. 7-15, 2013.
- [100] J. H. den Boon, J. Sutherland, R. Whitehouse, R. Soulsby, C. J. M. Stam, K. Verhoeven, M. Høgedal and T. Hald, “Scour behaviour and scour protection for monopile foundations of offshore wind turbines”, in *European Wind Energy Conference & Exhibition*, London, UK, 2004.
- [101] E-Connection; Vestas Wind Systems; D.K. Germanischer; Lloyd Windenergie, “OPTI-PILE, Fifth Research and Technological Development Framework”, 2002-2004.
- [102] R. Whitehouse, A. Brown, S. Audenaert, A. Bolle, P. Schoesitter, P. Haerens, L. Baelus, P. Troch, L. d. Neves, T. Fazeres-Ferradosa and F. Taveira-Pinto, “Optimising scour protection stability at offshore foundations”, in *Proceedings of the 7th International Conference on Scour and Erosion*, Perth, Australia, 2014.
- [103] A. Schendel, N. Goseberg and T. Schlurmann, “Experimental study on the performance of coarse grain materials as scour protection”, in *Coastal Engineering Proceedings - 34th International Conference on Coastal Engineering*, Seoul, 2014.
- [104] J. van der Tempel, “Design of support structures for offshore wind turbines - PhD Thesis”, TU

Delft, Delft, The Netherlands, 2006.

- [105] L. Prendergast, K. Gavin and P. Doherty, "An investigation into the effect of scour on the natural frequency of an offshore wind turbine", *Ocean Engineering*, vol. 101, no. 1, pp. 1-11, 2015.
- [106] DNVGL, "DNVGL - ST 0126 - Support structures for wind turbines", Det Norske Veritas, Høvik, 2016.
- [107] M. B. Zaaijer and J. Tempel, "Scour Protection: A Necessity or a Waste of Money?", in *Proceedings of the 43th IEA Topical Expert Meeting*, Stockholm, 2004.
- [108] B. Nedam and J. C. Oud, "Foundation Design Monopile - Comparison extra steel consumption versus scour protection - 3.6 & 6.0 MW wind turbines", DOWEC, Amstelveen, 2002.
- [109] S. A. Herman, H. J. T. Kooijman, H. B. Hendricks, E. v. d. Brug, B. Nedam, W. o. d. Velde, A. C. Z. V. Oord, R. v. d. Berg and L. M. G. Holland, "Variations on a 500 MW offshore wind farm design", *Offshore Wind Energy in the Mediterranean and other European Seas*, Naples, Italy, 2003.
- [110] K. Peters and K. Werth, "Offshore Wind Energy Foundations - Geotextile Sand-Filled Containers as Effective Scour Protection Systems", in *6th International Conference on Scour and Erosion*, Paris, 2012.
- [111] M. Sumer and A. Nielsen, "Sinking failure of scour protection at wind turbine foundation", *Energy - Proceedings of the Institution of Civil Engineers*, vol. 166, no. EN4, pp. 170-188, 2013.
- [112] CIRIA, CUR and CETMEF, "The Rock Manual. The Use of Rock in Hydraulic Engineering" (2nd Edition). C683, London: CIRIA, 2007.
- [113] P. Wiberg and C. Sherwood, "Calculating wave-generated bottom orbital velocities from surface-wave parameters", *Computers & Geosciences*, vol. 34, no. 10, pp. 1243-1262, 2008.
- [114] L. H. Holthuijsen, "Waves in Oceanic and Coastal Waters", Cambridge, UK: Cambridge University Press, 2007.
- [115] G. B. Airy, "Tides and Waves", *Encycl. Metropolitana*, pp. 241-396, 1845.
- [116] J. D. Fenton, "The numerical solution of steady water wave problems", *Computers & Geosciences*, vol. 14, no. 3, pp. 357-368, 1988.
- [117] J. H. Michell, "The highest waves in water", *Phil Mag*, vol. 36, no. 5, pp. 430-437, 1893.
- [118] T. Shand, W. Peirson and R. Cox, "Engineering Design in the Presence of Wave Groups", in *Proceedings of 32nd Conference on Coastal Engineering*, Shanghai, China, 2010.
- [119] US Army Corps Engineers, "Coastal Engineering Manual", USACE - Army Publications, USA, 2012.
- [120] J. D. Fenton and W. D. Mckee, "On calculating the length of water waves", *Coastal Engineering*, vol. 14, pp. 499-513, 1990.

- [121] Y. Goda, "Random Seas and Design of Marine Structures" - Advanced series on Ocean Engineering, Singapore: World Scientific, 2000.
- [122] DNVGL, "DNV Recommended Practice C205 - Environmental Loads and Conditions", Det Norsk Veritas AS, Høvik, 2017.
- [123] E. Vanem, "Joint statistical models for significant wave height and wave period in a changing climate", *Marine Structures*, vol. 49, pp. 180-205, 2016.
- [124] F. Durante and C. Sempi, "Principles of Copula Theory", London: CRC Press, Taylor & Francis Group, 2015.
- [125] R. Montes-Iturrizaga and E. Heredia-Zavoni, "Reliability analysis of mooring lines using copulas to model statistical dependence of environmental variables", *Applied Ocean Research*, vol. 59, pp. 564-576, 2016.
- [126] E. M. Bitner-Gregersen and S. Haver, "Joint Environmental Model for Reliability Calculations", in *Proceedings of the 1st International Offshore and Polar Engineering Conference*, Edinburgh, United Kingdom, 1991.
- [127] P. Troch, "Offshore Constructions, lecture notes", Department of Civil Engineering, Ghent, Belgium, 2007.
- [128] J. W. Van der Meer, "Rock slopes and Gravel Beaches under Wave Attack", Delft Hydraulics, Delft, The Netherlands, 1988.
- [129] K. Bruserud and S. Haver, "Waves and associated currents—experiences from 5 years metocean measurements in the northern North Sea", *Marine Structures*, p. In Press, 2017.
- [130] K. Bruserud, S. Haver and D. Myrhaug, "Joint description of waves and currents applied in a simplified load case", *Marine Structures*, vol. 58, pp. 416-433, 2018.
- [131] S. K. Chakrabarti, "Handbook of Offshore Engineering", Volume I, Illinois, USA: Elsevier, ISBN-13: 978-0-08-044568-7, 2005.
- [132] M. Matos Fernandes, "Mecânica dos Solos, Conceitos e Princípios Fundamentais", Edições FEUP, Porto, Portugal, 2006.
- [133] L. C. van Rijn, "Principles of Sediment Transport in Rivers, Estuarines and Coastal Seas", Acqua Publications, Amsterdam, 1993.
- [134] S. G. Boekhout, "The relation between particle settling velocity and shape: A critical review", TU Delft, Delft, 2012.
- [135] Public Safety Section and Water Management Branch, "Riprap Design and Construction Guide", Province of British Columbia - Ministry of Environment, Lands and Parks, British Columbia, 2000.
- [136] W. S. Nicolaas, "Grading control on Quarried Rock", TU Delft, Delft, The Netherlands, 1997.
- [137] A. Schendel, N. Goseberg and T. Schulmann, "Processes and effects of reversing currents on the erosion stability of wide-graded grain material", in *Proceedings of the 13th International Symposium on River Sedimentation*, Stuttgart, Germany, 2016.

- [138] A.C.Z., Van Oord, "Scour Protection for 6 MW OWEC with Monopile Foundation in North Sea", A. C. Z. Van Oord, Gorinchem, 2003.
- [139] K. W. Pilarczyk, "Stability criteria for revetments", in *Proceedings of the 1990 National Conference on Hydraulic Engineering, American Society of Civil Engineers*, San Diego, USA, 1990.
- [140] M. Escarameia and R. W. P. May, "Channel protection - turbulence downstream of structures - HR Report SR 313", Wallingford: HR Wallingford, 1992.
- [141] S. T. Maynard, "Gabion-matress channel-protection design", *Journal of Hydraulic Engineering*, vol. 121, pp. 1035-1039, 1995.
- [142] C. Wang, X. Yu and F. Liang, "A review of bridge scour: mechanism, estimation, monitoring and countermeasures", *Natural Hazards*, vol. 87, pp. 1881-1906, 2017.
- [143] R. Whitehouse, "Scour at Offshore Structures (invited lecture)", in *Proceedings of the 3rd International Conference on Scour and Erosion - ICSE*, Tokyo, Japan, 2006.
- [144] B. d. Sonnevile, G. v. Velzen and J. Wigaard, "Design and optimization of scour protection for offshore wind platform Dolwin Beta", in *Proceedings of the ASME 33rd International Conference on Ocean, Offshore and Arctic Engineering*, San Francisco, USA, 2014.
- [145] R. Whitehouse, J. Sutherland and D. O'Brien, "Seabed scour assessment for offshore windfarm", in *International Conference on Scour and Erosion*, Nanyang, Singapore, 2006.
- [146] Cefas Lowestoft Laboratory, "Scroby Sands Offshore Wind Farm - Coastal Processes Monitoring", Department of Trade and Industry, Lowestoft, UK, 2006.
- [147] A. Roulund, J. Sutherland, D. Todd and J. Sterner, "Parametric equations for Shields parameter and wave orbital velocity in combined current and irregular waves", in *International Conference on Scour and Erosion*, Oxford, UK, 2016.
- [148] N. Loosveldt and K. Vannieuwenhuysse, "Experimental validation of empirical design of a scour protection around monopiles under combined wave and current loading", M.Sc. Thesis, Ghent University, Ghent, 2012.
- [149] M. Høgedal and T. Hald, in *Proceedings of the Conference Copenhagen Offshore Wind*, Copenhagen, Denmark, 2005.
- [150] T. C. Raaijmakers, M. C. v. Oeveren, D. Rudolph, V. Leenders and W. C. P. Sinjou, "Field performance of Scour Protection Around Offshore Monopiles", in *5th International Conference on Scour and Erosion*, San Francisco, California, 2010.
- [151] T. Fazeris-Ferradosa, F. Taveira-Pinto, M. T. Reis and L. das Neves, "Physical modelling of dynamic scour protections: Analysis of the Damage Number", *Proceeding of the Institution of Civil Engineers - Maritime Engineering*, vol. In Press, pp. 1-48, 2018.
- [152] Bureau Waardenburg, "Eco-friendly design of scour protection: potential enhancement of ecological functioning in offshore wind farms - towards an implementation guide and experimental set-up", Ministry of Economic Affairs, The Netherlands, 2017.

- [153] M. Bonasoundas, “Stromungsvorgang und kolkproblem - Oscar von Miller Institute”, Technical University of Munich, Munich, Germany, 1973.
- [154] T. Carstens, “Sea bed scour by currents near platforms”, in *3rd Conference on port and ocean engineering under arctic conditions*, University of Alasca, USA, 1976.
- [155] A. Löffler and A. Kortenhaus, “Non breaking waves and pressures on berms - Chapter 4.6”, in *Probabilistic design tools for vertical breakwater - Mast III/PROVERBS. MAS CT95-0041*, Steenwijk, The Netherlands, A. A. Balkema Publishers, 1999, p. vol. Ila.
- [156] L. Prendergast and K. Gavin, “A review of bridge scour monitoring techniques”, *Journal of Rock Mechanics and Geotechnical Engineering*, vol. 6, no. 2, pp. 138-149, 2014.
- [157] J. Ferreira, “Avaliação do efeito do fenómeno de erosões localizadas no comportamento dinâmico de estruturas de torres eólicas offshore - MSc. Thesis”, University of Porto, Faculty of Engineering, Department of Civil Engineering, Porto, Portugal, 2017.
- [158] Renewable Energy Marine Structures , “<http://www.rems-cdt.ac.uk/>”, 4 October 2017. [Online]. Available: <http://www.rems-cdt.ac.uk/download/dac7d7f3-7b59-11e7-8011-5df3e44771ad/>. [Accessed 21 February 2018].
- [159] HR Wallingford, “www.hrwallingford.com”, 10 October 2017. [Online]. Available: <http://www.hrwallingford.com/news/working-with-e-on-and-oxford-university-to-minimise-the-effects-of-scour-on-wind-turbine-foundations>. [Accessed 21 February 2018].
- [160] M. Sumer, “Mathematical modelling of scour: A review”, *Journal of Hydraulic Research*, vol. 45, no. 6, pp. 723-735, 2007.
- [161] D. Rudolph, T. C. Raaijmakers and B. d. Sonnevile, “Challenges and recent advances in offshore scour modelling”, in *12th International Conference The JACK-UP PLATFORM Design, Construction & Operations*, London, UK, 2009.
- [162] M. Sumer, “A review of recent advances in numerical modelling of local scour problems”, in *7th International Conference on Scour and Erosion*, Perth, Australia, 2014.
- [163] L. Frostick, S. McLelland and T. Mercer, (eds) "Users Guide to Physical Modelling and Experimentation: Experience of the HYDRALAB Network", Leiden, International Association for Hydro-Environment Engineering and Research. CRC Press, Taylor & Francis Group, 2011.
- [164] P. Troch, V. Stratigaki, C. Arboleda, W. M. P. Rosa-Santos, T. Fazerer-Ferradosa, F. Taveira-Pinto, A. Bolle, L. Baelus, L. d. Neves, P. Haerens, L. D. Vos, A. Schendel, M. Welzel, T. Schulmann and R. Whitehouse, “Large scale experiments to improve monopole scour protection design adapted to climate change – methodology and first results”, in *5th IAHR Europe Congress*, Trento, Italy, 2018.
- [165] A. Kortenhaus, J. V. d. Meer, H. Burcharth, J. Geeraerts, T. Pullen, D. Ingram and P. Troch, “Report on conclusion of scale effects - Report D40 - CLASH project”, Aalborg University, Aalborg, Denmark, 2005.
- [166] J. Sutherland and R. Whitehouse, “Scale effects in the physical modelling of seabed scour”, HR Wallingford, Wallingford, UK, 1998.

- [167] L. C. van Rijn, “Local scour near structures”, 27 January 2018. [Online]. Available: <http://www.leovanrijn-sediment.com/papers/Localscour2013.pdf>. [Accessed 21 February 2018].
- [168] D. Baghbadorani, B. Ataie-Ashtiania, A. Beheshti and M. Hadjzaman, “Prediction of current-induced local scour around complex piers: Review, revisit, and integration”, *Coastal Engineering*, vol. 133, pp. 43-58, 2018.
- [169] B. Larsen and P. Frigaard, “Scour and Scour Protection of Windturbine Foundations for the London Array”, Aalborg University, Aalborg, Denmark, 2005.
- [170] T. Raaijmakers and D. Rudolph, “Offshore windpark Egmond ann Zee – Performance of scour protection and edge scour development”, in *Proceedings European Offshore Wind Conference*, Berlin, Germany, 2007.
- [171] A. Bolle, P. Haerens, K. Trouw, J. Smits and G. Deqaele, “Scour around gravity-based wind turbine foundations - prototype measurements”, in *Coasts, Marine Structures and Breakwaters. Adapting to Change (Allsop W. (ed))*, London, Thomas Telford, 2009, pp. 103-118.
- [172] L. Baelus, P. Troch, N. Loosveldt and K. Vannieuwnhuyse, “Extended Validation of Dynamic Design Formula for Scour Protection Around Monopiles”, in *4th International Conference on the Application of Physical Modelling to Port and Coastal Protection, Coastlab12*, Ghent, Belgium, 2012.
- [173] T. Raaijmakers, “Evaluation of performance of scour protection and edge scour development - Technical Project for Deltares”, Deltares, Delft, The Netherlands, 2009.
- [174] J. W. B. Schumann, U. Smolka and P. W. Cheng, “Detecting critical scour developments at monopile foundations under operating conditions”, in *Proceedings of the European Wind Energy Association Annual Event, EWEA 2015*, Paris, France, 2015.
- [175] International Marine & Dredging Consultants, “MARINET proposal 61 - Optimising the design of dynamic scour protection around offshore foundations”, IMDC, Antwerp, Belgium, 2013.
- [176] E. Mansard and B. Funke, “The measurement of incident and reflected spectra using a least square method”, in *Coastal Engineering Proceedings 1, 17*, 1980.
- [177] Aalborg University, “Aalborg University Software for laboratories”, Aalborg University, 2013. [Online]. Available: <http://www.hydrosoft.civil.aau.dk/>. [Accessed 13 December 2014].
- [178] P. Meinart, “EPro Non-contact erosion profiling, hardware overview”, *Hydraulics and Coastal Engineering*, vol. 40, 2006.
- [179] M. Afzal, L. Homedal and D. Myrhaug, “Effect of bottom roughness on sediment transport due to streaming beneath linear propagating waves with an angle of attack on current”, in *Proceedings of the 8th International Conference on Scour and Erosion*, London, 2016.
- [180] A. Nielsen and E. Hansen, “Time-varying wave and current -induced scour around offshore wind turbines”, in *International Conference on Offshore and Arctic Engineering - OMAE*, San Diego, California, 2007.

- [181] W. Qi, F. Gao, X. Han and Q. Gong, "Local Scour And Pore-water Pressure Around a Monopile Foundation Under Combined Waves And Currents", in *The Twenty-second International Offshore and Polar Engineering Conference*, Rhodes, Greece, 2012.
- [182] T. C. Raaijmakers, F. Liefhebber and B. H. a. P. Meys, "Mappind of 3D-Bathymetries and structures using stereophotography throug an air-water-interface", in *Coastlab 12*, Ghent, Belgium, 2012.
- [183] T. Sousa, "Avaliação e Verificação dos Níveis de Segurança da Proteção de Fundações de Estruturas Offshore do tipo Monopilar. MSc. Thesis", Faculty of Engineering, University of Porto, Porto, Portugal, 2013.
- [184] M. Sumer, T. Petersen and L. Locatelli, "Backfilling of a Scour Hole around a Pile in Waves and Current", *Journal of Waterway Port Coastal and Ocean Engineering*, vol. 139, no. 1, pp. 9-23, 2013.
- [185] T. Petersen, M. Sumer, K. Meyer, J. Fredsøe and E. Christensen, "Edge scour in current adjacent to stone covers", in *6th International Conference on Scour and Erosion*, Paris, France, 2012.
- [186] I. Leão, "Reliability-based assessment of scour protections in offshore fixed foundations. MSc. Thesis", Faculty of Engineering, University of Porto, Porto, Portugal, 2016.
- [187] HR Wallingford Ltd, "www.hrwallingford.com", 2017. [Online]. Available: <http://www.hrwallingford.com/expertise/wavemakers>. [Accessed 22 March 2018].
- [188] Hydraulics, Water Resources and Environment Division (SHRHA), "https://paginas.fe.up.pt/~shrha/laboratorios", FEUP, 2007. [Online]. Available: https://paginas.fe.up.pt/~shrha/laboratorios/desc_func.html. [Accessed 24 March 2018].
- [189] HR Wallingford Ltd., "www.hrwallingford.com", 2007. [Online]. Available: http://equipit.hrwallingford.com/brochures/EQ-001-Bed_profiling_system.pdf. [Accessed 2018 March 26].
- [190] S. Hughes, "Physical Models and Laboratory Techniques in Coastal Engineering", in *Advanced Series on Ocean Engineering*, 7, Singapore, World Scientific, 1993, p. 568.
- [191] M. Faber, "Statistics and Probability Theory - In Pursuit of Engineering Decision support", London: Springer, 2009.
- [192] J. McLinn, "A short history of reliability", North American Space Agency (NASA), 2010. [Online]. Available: <http://kscsma.ksc.nasa.gov/Reliability>. [Accessed 15 February 2015].
- [193] D. Loyd and M. Lipow, "Reliability: Management, Methods and Mathematics", Englewood Cliffs: Prentice Hall, 1962.
- [194] A. Henriques, "Aplicação de novos conceitos de segurança no dimensionamento do betão estrutural", *PhD Thesis*, Porto: Faculdade de Engenharia da Universidade do Porto, 1998.
- [195] A. Freudenthal, "The safety of structures", *Transaction - American Society of Civil Engineers (ASCE)*, vol. 112, pp. 1125-1180, 1947.

- [196] A Freudenthal, "Safety and probability of structural failure", *Transaction - American Society of Civil Engineers (ASCE)*, vol. 121, pp. 1137-1197, 1956.
- [197] V. Bolotin, *Statistical methods in structural mechanics*, Holden-Day Inc., London, 1965.
- [198] J. Ferry-Borges and M. Castanheda, *Structural safety*, Lisboa: Laboratório Nacional de Engenharia Civil, 1968.
- [199] C. Cornell, "A probability based structural code", *Journal of the American Concrete Institute*, vol. 66, no. 12, pp. 974-985, 1969.
- [200] A. Hasofer and N. Lind, "An exact and invariant first order reliability format", *Journal of Engineering Mechanics Division*, vol. 100, no. EM1, pp. 111-121, 1974.
- [201] R. Rackwitz and B. Fiessler, "Structural reliability under combined random load sequences", *Computers and Structures*, vol. 9, no. 5, pp. 489-494, 1978.
- [202] P. Thoft-Christensen and M. Baker, *Application of structural systems reliability theory*, vol. 147, Berlin: Springer Verlag, 1986.
- [203] R. Melchers, *Structural reliability analysis and prediction*, London: Ellis Horwood Series in Civil Engineering, 1987.
- [204] H. L. A Kiureghian and S. Hwang, "Second order reliability approximations", *Journal of Engineering Mechanics Division*, vol. 113, no. 8, pp. 1208-1225, 1987.
- [205] W. Liu, G. Besterfield, M. Manhartdt and U. Zanke, "Variational approach to probabilistic finite elements", *Journal of Engineering Mechanics Division*, vol. 114, no. 12, pp. 2115-2133, 1988.
- [206] S. Lo, "*Stochastic finite element analysis*", *PhD Thesis*, Cambridge: Massachusetts Institute of Technology, 1989.
- [207] National Cooperative Highway Research Program - NCHRP, "Reference guide for applying risk and reliability-based approaches for bridge scour prediction - Report 761", Transportation Research Board of the National Academies, Washington D.C., 2003.
- [208] C. Cornell, "Reliability-based earthquake-resistant design: the future", in *11th World Conference on Earthquake Engineering*, Acapulco, Mexico, 1996.
- [209] G. Baecher and J. Christian, *Reliability and Statistics in Geotechnical Engineering*, London, England: Ed. John Wiley & Sons Ltd., 2003.
- [210] M. Ettouney and M. Alampali, *Infrastructures Health in Civil Engineering. Applications and Management*, Florida: CRC Press, 2011.
- [211] Joint Committee on Structural Safety (JCSS), "Risk Assessment in Civil Engineering, Principles, System Representation and Risk Criteria", Technical University of Denmark, Copenhagen, Denmark, 2008.
- [212] I. Chaves and R. Melchers, "Extreme value analysis for assessing structural reliability of welded offshore steel structures", *Structural Safety*, vol. 50, pp. 9-15, 2014.

- [213] P. Johnson, P. Clopper, L. Zevenbergen and P. Lagasse, “Quantifying Uncertainty and Reliability in Bridge Scour Estimations”, *Journal of Hydraulic Engineering*, vol. 141, no. 7, pp. 1-9, 2015.
- [214] T. Fazeres-Ferradosa, F. Taveira-Pinto, X. Romão, E. Vanem, M. T. Reis and L. das Neves, “Probabilistic Design and Reliability Analysis of Scour Protections for Offshore Windfarms”, *Engineering Failure Analysis*, vol. 91, p. 291–305, 2018.
- [215] X. Romão, *Uncertainty analysis and Sensitivity analysis - Lecture notes on Uncertainty Modelling and Risk Analysis - INFRARISK PhD Program*, Porto, Portugal: Faculdade de Engenharia da Universidade do Porto, 2015.
- [216] A. Henriques, *First order second-moment propagation of uncertainty - Lecture notes on Uncertainty Modelling and Risk Analysis - INFRARISK PhD Program*, Porto, Portugal: Faculdade de Engenharia da Universidade do Porto, 2015.
- [217] P. Das and W. Zhang, “Theoretical methods of structural reliability”, in *Guidance on structural reliability analysis of marine structures*, Glasgow, United Kingdom, Department of Naval Architecture and Marine Engineering, University of Glasgow, 2003, pp. 22-51.
- [218] W. Jäger and O. M. Napoles, “Sampling joint time series of significant wave heights and periods in the North Sea”, in *Safety and Reliability of Complex Engineered Systems*, London, United Kingdom, CRC Press, 2015, pp. 4287-4294.
- [219] T. Fazeres-Ferradosa, F. Taveira-Pinto, E. Vanem, M. T. Reis and L. das Neves, “Asymmetric copula-based distribution models for met-ocean data in offshore wind engineering applications”, *Wind Engineering*, p. In Press, 2018.
- [220] DNV, “Classification Notes 30.6 - Structural Reliability Analysis of Marine Structures”, Det Norske Veritas AS, Norway, 1992.
- [221] J. Matos, *Reliability according to design codes - Lecture notes on Reliability and Risk Analysis - INFRARISK PhD Program*, Braga, Portugal: Faculdade de Engenharia da Universidade do Minho, 2015.
- [222] F. Fajardo, J. Perez, M. Alsina and J. R. Marques, *Simulation Methods for Reliability and Availability of Complex Systems*, New York: Springer, 2010.
- [223] T. Fazeres-Ferradosa, F. Taveira-Pinto, X. Romão, M. T. Reis and L. d. Neves, “Reliability Assessment of Offshore Dynamic Scour Protections using Copulas”, *Wind Engineering*, p. In Press, 2018.
- [224] R. Rackwitz, “Reliability analysis - a review and some perspectives”, *Structural Safety*, vol. 23, issue 4, pp. 365-395, 2001.
- [225] K. Breitung, “Asymptotic Approximations for Multinormal Integrals”, *Journal of Engineering Mechanics*, vol. 110, no. 5, pp. 357-366, 1984.
- [226] K. Breitung and M. Hohenbichler, “Asymptotic approximations for multivariate integrals with an application to multinormal probabilities”, *Journal of Multivariate Analysis*, vol. 30, pp. 80-97, 1989.

- [227] S. Adhikari, “Asymptotic distribution method for structural reliability analysis in high dimensions”, *Proceedings of the Royal Society A*, vol. 461, pp. 3141-3158, 2005.
- [228] T. Fazerer-Ferradosa, F. Taveira-Pinto, R. Simons, M. T. Reis and L. D. Neves, “Probability of Failure of Monopile Foundations Based on Laboratory Measurements”, in *6th International Conference on the Application of Physical Modelling in Coastal and Port Engineering and Science - CoastLab*, Ottawa, 2016.
- [229] W. Broding, F. Dierderich and P. Parker, “Structural optimization and design based on a reliability design criterion”, *Journal of Spacecraft and Rocket*, vol. 1, no. 1, pp. 56-61, 1964.
- [230] R. Kawai, “Adaptive importance sampling Monte Carlo simulation for general multivariate probability laws”, *Journal of Computational and Applied Mathematics*, vol. 3119, no. 1, pp. 440-459, 2017.
- [231] X. Li, G. Chen, H. Zhu and T. Zhang, “Quantitative risk assessment of submarine pipeline instability”, *Journal of Loss Prevention in the Process Industries*, vol. 45, pp. 108-115, 2017.
- [232] Y. Li, Y. Zhang and D. Kennedy, “Reliability analysis of subsea pipelines under spatially varying ground motions by using subset simulation”, *Reliability Engineering & System Safety*, vol. 172, pp. 74-83, 2018.
- [233] S. Coles, *An Introduction to Statistical Modeling of Extreme Values - Springer series in Statistics*, London: Springer, 2001.
- [234] M. Siewert, C. Schlamkow and F. Saathoff, “Spatial analyses of 52 years of modelled sea state data for the Western Baltic Sea and their potential applicability for offshore and nearshore construction purposes”, *Ocean Engineering*, pp. 284-294, 2015.
- [235] A. Martinez-Asensio, M. Marcos, M. Tsimplis, G. Jordà, X. Feng and D. Gomis, “On the ability of statistical wind-wave models to capture the variability and long-term trends of the North Atlantic winter wave climate”, *Ocean Modelling. vol 103.*, pp. 177-189, 2016.
- [236] J. Lin-Ye, M. García-León, V. Gràcia, M. Ortego, P. Lionello and A. Sánchez-Arcilla, “Multivariate statistical modelling of future marine storms”, *Applied Ocean Research. vol. 65*, pp. 192-205, 2017.
- [237] C. Redón-Conde and E. Heredia-Zavoni, “Reliability assessment of mooring lines for floating structures considering statistical parameter uncertainties”, *Applied Ocean Research. vol. 52.*, pp. 295-308, 2015.
- [238] R. Jane, L. D. Valle, D. Simmonds and A. Rabya, “A copula-based approach for the estimation of wave height records through spatial correlation”, *Coastal Engineering. vol. 117*, pp. 1-18, 2016.
- [239] S. Vallender, “Calculation of the Wasserstein Distance Between Probability Distributions on the Line”, *Theory of Probability & Its Applications*, vol. 18, no. 4, pp. 784-786, 1974.
- [240] A. Basu, H. Shioya and C. Park, *Statistical Inference - Minimum distance approach*, London: CRC Press, Taylor & Francis Group, 2011.
- [241] C. Villani, “The Wasserstein distances”, in *Optimal Transport. Grundlehren der*

mathematischen Wissenschaften (A Series of Comprehensive Studies in Mathematics). vol. 338, Berlin, Springer, 2009.

- [242] D. Taeger and S. Kuhnt, *Statistical Hypothesis Testing with SAS and R*, John Wiley & Sons, Ltd., 2014.
- [243] R. Nelsen, *An Introduction to Copulas*, New York: Springer, 2006.
- [244] C. Genest and A. C. Favre, “Everything You Always Wanted to Know about Copula Modeling but Were Afraid to Ask”, *Journal of Hydrologic Engineering*. vol. 12 issue 4, pp. 347-368, 2007.
- [245] C. Genest and J.-C. Boies, “Detecting Dependence with Kendall Plots”, *The American Statistician*, vol. 57, no. 4, pp. 275-284, 2003.
- [246] N. Fisher and P. Switzer, “Chi-plots for assessing dependence”, *Biometrika*, vol. 72, no. 2, pp. 253-265, 1985.
- [247] N. Fisher and P. Switzer, “Graphical Assessment of Dependence: is a picture worth 100 tests?”, *American Statistician*, vol. 55, no. 3, pp. 233-239, 2001.
- [248] C. Genest and L. Rivest, “Statistical Inference Procedures for Bivariate Archimedean Copulas”, *Journal of American Statistical Association*, pp. 1034-1043, 1993.
- [249] API, “API - RP 2FPS Planning, Designing and Constructing Floating Production Systems”, American Petroleum Institute, USA, 2011.
- [250] API, “API Recommended Practice 2A-WSD - Planning, Designing, and Constructing Fixed Offshore - Working Stress Design”, American Petroleum Institute, United States of America, 2014.
- [251] J. Ferreira and C. Guedes-Soares, “Modelling bivariate distributions of significant wave height and mean wave period”, *Applied Ocean Research*, vol. 24, no. 1, pp. 31-45, 2002.
- [252] L. Ziegler, S. Voormeeren, S. Schafhirt and M. Muskulus, “Sensitivity of Wave Fatigue Loads on Offshore Wind Turbines under Varying Site Conditions”, *Energy Procedia*, vol. 80, pp. 193-200, 2015.
- [253] P. Jonathan and K. Ewans, “Statistical modelling of extreme ocean environments for marine design”, *Ocean Engineering*, vol. 62, pp. 91-109, 2013.
- [254] S. Dong, N. Wang, H. Lu and L. Tang, “Bivariate distributions of group height and length for ocean waves using Copula methods”, *Coastal Engineering*, vol. 96, pp. 49-61, 2015.
- [255] C. Guedes-Soares and M. Scotto, “Long term and extreme value models of wave data”, in *Marine Technology and Engineering*, London, Taylor & Francis Group, 2011, pp. 97-108.
- [256] K. Ewans and P. Jonathan, “Evaluating environmental joint extremes for the offshore industry using conditional extremes model”, *Journal of Marine Systems*, vol. 130, pp. 124-130, 2014.
- [257] Y. Zhang, S. Quack and M. Beer, “Long-term reliability assessment of offshore structures in a complex environment”, in *Safety, Reliability, Risk and Lyfe-Cycle Performance of Structures & Infrastructures*, London, Taylor & Francis Group, 2013, p. 2209.

- [258] S. Corbella and D. Stretch, "Simulating a multivariate sea storm using Archimedean copulas", *Coastal Engineering*, vol. 76, pp. 68-78, 2013.
- [259] E. Antão and C. Guedes-Soares, "Approximation of the joint probability density of wave steepness and height with a bivariate gamma distribution", *Ocean Engineering*, vol. 126, no. 1, pp. 402-410, 2016.
- [260] E. Brechmann and U. Schepsmeier, "Modeling Dependence with C- and D-Vine Copulas: The R Package CD Vine", *Journal of Statistical Software*, vol. 52, no. 3, pp. 1-27, 2013.
- [261] A. Khoudraji, "Contributions à l'étude des copules et à la modélisation des valeurs extrêmes bivariées - PhD thesis", Université Laval, Québec, Canada, 1995.
- [262] E. Liebscher, "Construction of asymmetric multivariate copulas", *Journal of Multivariate Analysis*, vol. 99, pp. 2234-2250, 2008.
- [263] F. Durante and G. Salvadori, "On the construction of multivariate extreme models via copulas", *Environmetrics*, vol. 21, pp. 143-161, 2010.
- [264] M. Ochi, "Wave statistics for the design of ships and ocean structures", *SNAME Transactions*, vol. 86, pp. 47-76, 1978.
- [265] E. Bitner-Gregersen, "Joint met-ocean description for design and operation of marine structures", *Applied Ocean Research*, vol. 51, pp. 279-292, 2015.
- [266] C. Lucas and C. Guedes-Soares, "Bivariate distributions of significant wave height and mean wave period of combined sea states", *Ocean Engineering*, vol. 106, pp. 341-353, 2015.
- [267] E. Vanem, "A regional extreme value analysis of ocean waves in a changing climate", *Ocean Engineering*, pp. 277-295, 2017.
- [268] E. Bitner-Gregersen and A. Toffoli, "Uncertainties of Wind Sea and Swell Prediction From the Torsethaugen Spectrum", in *ASME 29th International Conference on Ocean, Offshore and Arctic Engineering*, Hawai - Honolulu, 2009.
- [269] M. Wand and M. Jones, *Kernel Smoothing*, London: CRC Press, Taylor & Francis Group, 1994.
- [270] M. Mahfoud, "Bivariate Archimedean copulas: an application to two stock market indices", 2012. [Online]. Available: https://beta.vu.nl/nl/Images/werkstuk-mahfoud_tcm235-277460.pdf.
- [271] P. Embrechts, F. Lindskog and A. McNeil, "Modelling Dependence with Copulas and Applications to Risk Management", in *Handbook of Heavy Tailed Distributions in Finance - Volume 1 of Handbooks in Finance*, Zurich, Department of Mathematics - ETHZ: Elsevier, 2001, pp. 329-384.
- [272] A. Bücher and S. Volgushev, "Empirical and sequential empirical copula processes under serial dependence", *Journal of Multivariate Analysis*, vol. 119, pp. 61-70, 2013.
- [273] Unknown Author, "*The Asymmetric t-Copula with Individual Degrees of Freedom*". MSc. Thesis, Oxford: University of Oxford, 2012.

- [274] CRAN, “cran.r-project.org”, 17 June 2017. [Online]. Available: <https://cran.r-project.org/web/packages/copula/copula.pdf>. [Accessed 16 September 2017].
- [275] U. Schepsmeier, J. Stoeber, E. C. Brechmann, B. Graeler, T. Nagler and T. Erhardt, “cran.r-project.org”, 17 June 2017. [Online]. Available: <https://cran.r-project.org/web/packages/VineCopula/VineCopula.pdf>. [Accessed 3 January 2018].
- [276] MathWorks, “<https://www.mathworks.com>”, 22 June 2016. [Online]. Available: <https://www.mathworks.com/help/doc-archives.html>. [Accessed 23 October 2017].
- [277] H. Akaike, “A new look at the statistical model identification”, *IEEE Transactions on Automatic Control*, vol. 19, pp. 716-723, 1974.
- [278] G. Schwarz, “Estimating the Dimension of a Model”, *The Annals of Statistics*, vol. 6, no. 2, pp. 461-464, 1978.
- [279] M. Masina, A. Lamberti and R. Archetti, “Coastal flooding: A copula based approach for estimating the joint probability of water levels and waves”, *Coastal Engineering*, vol. 97, pp. 37-52, 2015.
- [280] R. Shumway and D. Stoffer, *Time Series Analysis and its Applications with R examples*, London: Springer, 2011.
- [281] M. Rosenblatt, “Remarks on some nonparametric estimates of a density function”, *Annals of Mathematical Statistics*, vol. 27, no. 3, p. 832–837, 1956.
- [282] E. Parzen, “On estimation of a probability density function and mode”, *Annals of Mathematical Statistics*, vol. 33, no. 3, p. 1065–1076, 1962.
- [283] G. Muraleedharan, C. Lucas, D. Martins, C. Guedes-Soares and P. Kurup, “On the distribution of significant wave height and associated peak periods”, *Coastal Engineering*, vol. 103, pp. 42-51, 2015.
- [284] J. Jeon and J. Taylor, “Short-term density forecasting of wave energy using ARMA-GARCH models and kernel density estimation”, *International Journal of Forecasting*, vol. 32, no. 3, pp. 991-1004, 2016.
- [285] W. Venables and B. Ripley, *Modern Applied Statistics with S - Fourth Edition*, New York: Springer, 2002.
- [286] DMI, “Horns Rev 3 Offshore Wind Farm - Metaocean”, DMI - Danish Meteorological Institute & Orbicon A/S, Copenhagen, Denmark, 2013.
- [287] Vattenfall, “<https://corporate.vattenfall.com/>”, Vattenfall, 2017. [Online]. Available: <https://corporate.vattenfall.com/about-energy/renewable-energy-sources/wind-power/wind-power-at-vattenfall/horns-rev-3-offshore-wind-farm/>. [Accessed 17 04 2018].
- [288] H. Kristensen, H. L. B. Gurieff, J. Steer and N. Richard, “Horns Rev 3 Results Report - Geo investigation 2012”, Rambøll og Energinet, 2013.
- [289] Energinet, “Horns Rev 3 Offshore Wind Farm - marine mammals - technical report 043”, Energinet, Orbicon A/S, BioConsult SH GmbH & Co.KG, Denmark, 2014.

- [290] Vattenfall, “corporate.vattenfall.dk”, 2017. [Online]. Available: https://corporate.vattenfall.dk/globalassets/danmark/vores_vindmoller/horns_rev_3/hr3_nyhed_sbrev_01.pdf. [Accessed 11 01 2018].
- [291] L. Belzile, C. Genest, A. J. McNeil and J. G. Neslehova, “<https://cran.r-project.org>”, 23 January 2017. [Online]. Available: <https://cran.r-project.org/web/packages/lcopula/lcopula.pdf>. [Accessed 26 September 2017].
- [292] Y. Zhang, C.-W. Kim, M. Beer, H. Dai and C. Guedes-Soares, “Modelling multivariate ocean data using asymmetric copulas”, *Coastal Engineering*, vol. 135, pp. 91-111, 2018.
- [293] V.-N. Huynh, V. Kreinovich and S. Sriboonchitta, *Modeling Dependence in Econometrics*, New York: Springer, 2014.
- [294] IEC, “Wind turbines – part 1: design requirements (Technical Standard - IEC 61400 – 1)”, International Electrotechnical Commission, 2005.
- [295] IEC, “Wind turbines – part 3: design requirements for offshore wind turbines (Technical Standard - IEC 61400 – 3)”, International Electrotechnical Commission, 2009.
- [296] D. Chan and J. Mo, “Life Cycle Reliability and Maintenance Analyses of Wind Turbines”, *Energy Procedia*, pp. 328-333, 2017.
- [297] X. Zhang, L. Sun, H. Sun, Q. Guo and X. Bai, “Floating offshore wind turbine reliability analysis based on system grading and dynamic FTA”, *Journal of Wind Engineering and Industrial Aerodynamics*, vol. 154, pp. 21-33, 2016.
- [298] D. H. Kim and S. G. Lee, “Reliability analysis of offshore wind turbine support structures under extreme ocean environmental loads”, *Renewable Energy*, vol. 79, pp. 161-166, 2015.
- [299] F. Schmid and R. Schmidt, “Multivariate conditional versions of Spearman's rho and related measures of tail dependence”, *Journal of Multivariate Analysis*, vol. 98, no. 6, pp. 1123-1140, 2007.
- [300] R. Montes-Iturrizaga and E. Heredia-Zavoni, “Environmental contours using copulas”, *Applied Ocean Research*, vol. 52, pp. 125-139, 2015.
- [301] M. J. M. Soldevilla, M. Martín-Hidalgo, V. Negro, J. S. López-Gutiérrez and P. Aberturas, “Improvement of theoretical storm characterization for different climate conditions”, *Coastal Engineering*, vol. 96, pp. 71-80, 2015.
- [302] F. Durante, J. Fernández-Sánchez and R. Pappadá, “Copulas, diagonals and tail dependence”, *Fuzzy Sets and Systems*, vol. 264, pp. 22-41, 2015.
- [303] A. Pérez and M. Prieto-Alaiz, “A note on nonparametric estimation of copula-based multivariate extensions of Spearman's rho”, *Statistics & Probability Letters*, pp. 41-50, 2016.
- [304] L. Mentaschi, G. Besio, F. Cassola and A. Mazzino, “Problems in RMSE-based wave model validation”, *Ocean Modelling*, pp. 53-58, 2013.
- [305] M. Menéndez, F. J. Méndez, C. Izaguirre, Alberto Luceño and I. J. Losada, “The influence of seasonality on estimating return values of significant wave height”, *Coastal Engineering*, vol.

56, no. 3, pp. 211-219, 2009.

- [306] L. Sartini, Cassola and G. Besio, “Extreme waves seasonality analysis: An application in the Mediterranean Sea”, *Journal of Geophysical Research: Oceans*, pp. 6266-6288, 2015.
- [307] J. Su and L. Hua, “A general approach to full-range tail dependence copula”, *Insurance: Mathematics and Economics*, vol. 77, pp. 49-64, 2017.
- [308] J. Dowell, A. Zitrou, L. Walls, T. Bedford and D. Infield, “Analysis of Wind and Wave Data to Assess Maintenance Access to Offshore Wind Farms”, in *European Safety and Reliability Association Conference (ESREL)*, Amsterdam, 2013.
- [309] M. Brommundt, K. Ludwig, K. Merz and M. Muskulus, “Mooring System Optimisation for Floating Wind Turbines using Frequency Domain Analysis”, *Energy Procedia*, vol. 24, pp. 289-296, 2012.
- [310] A. Campanile, V. Piscopo and A. Scamardella, “Mooring design and selection for floating offshore wind turbines on intermediate and deep water depths”, *Ocean Engineering*, vol. 148, pp. 349-360, 2018.
- [311] Y. Wang, H. Ma, D. Wang, G. Wang, J. Wu, J. Bian and J. Liu, “A new method for wind speed forecasting based on copula theory”, *Environmental Research*, vol. 160, pp. 365-371, 2018.
- [312] J. Taylor and J. Jeon, “Probabilistic forecasting of wave heights for offshore wind turbines maintenance”, *European Journal of Operational Research*, vol. 267, no. 3, pp. 877-890, 2018.
- [313] N. Elginöz and B. Bas, “Life Cycle Assessment of a multi-use offshore platform: Combining wind and wave energy production”, *Ocean Engineering*, vol. 145, pp. 430-443, 2017.
- [314] H. Haghj and S. Lotifaard, “Spatiotemporal Modeling of Wind Generation for Optimal Energy Storage Sizing”, *IEEE Transaction on Sustainable Energy*, vol. 6, no. 1, pp. 113-121, 2015.
- [315] S. Winterstein, G. Kleiven and O. Hagen, “Comparing extreme wave estimates from hourly and annual data”, in *Proceedings of the International Offshore and Polar Engineering Conference*, Stavanger, Norway, 2001.
- [316] R. Simons, T. J. Grass, W. Saleh and M. M. Tehrani, “Bottom shear stresses under waves with a current superimposed”, in *24th International Conference on Coastal Engineering*, Kobe, Japan, 1994.

Bibliography

APPENDIX 1

Aiming at the repeatability of the present study, this appendix provides the information regarding the scour tests performed at FEUP. The following tables provide the damage number per sub-area, which led to the final measured damage numbers, Table 4.34. Tests F1_003*, F1_006* and F1_006** were excluded from this appendix, due to the problems reported in Table 4.30. The tests concerning MARINET data are also not included in this appendix since, as explained in section 4.2.6.4, the details on the S_{3Dsub} and the photographic records are reported in [183].

Table A1.1 - Measured damage numbers for test F1_001.

| {0;1000} waves | S1 | S2 | S3 | S4 | S5 | S6 | S7 | S8 | S9 | S10 | S11 | S12 |
|--------------------------|-------|-------|-------|-------|-------|-------|-------|-------|-------|-------|-------|-------|
| R1 | -0.93 | -0.85 | -0.25 | 0.03 | -0.32 | -0.75 | -0.68 | -0.92 | -0.42 | -0.36 | -0.33 | -0.97 |
| R2 | -0.33 | -0.59 | -0.15 | -0.07 | -0.08 | -0.24 | -0.53 | -0.35 | -0.21 | -0.18 | -0.26 | -0.23 |
| R3 | -0.26 | -0.09 | -0.01 | 0 | 0 | -0.12 | -0.36 | -0.07 | -0.09 | 0.01 | 0 | -0.16 |
| R4 | -0.21 | 0.03 | 0.01 | 0 | 0.12 | -0.01 | -0.21 | 0 | 0.1 | 0.17 | 0 | 0.02 |
| R5 | 0.06 | 0.06 | 0.21 | 0.43 | 0.29 | 0.06 | 0.03 | -0.11 | -0.1 | -0.02 | -0.26 | -0.12 |
| R6 | -0.17 | 0.11 | 0.4 | 0.33 | 0.46 | 0.1 | -0.1 | -0.16 | -0.4 | -0.27 | 0.42 | -0.13 |
| {1000; 3000} waves | S1 | S2 | S3 | S4 | S5 | S6 | S7 | S8 | S9 | S10 | S11 | S12 |
| R1 | -1.27 | -1.09 | -0.49 | -0.1 | -0.43 | -0.95 | -1.19 | -1.13 | -0.79 | -0.36 | -0.33 | -1.02 |
| R2 | -0.63 | -0.98 | -1.32 | -0.18 | -0.57 | -0.78 | -0.94 | -0.65 | -0.51 | -0.36 | -0.56 | -0.69 |
| R3 | -0.26 | -0.22 | -0.18 | 0.59 | -0.74 | -0.26 | -0.52 | -0.33 | -0.22 | -0.08 | -0.29 | -0.26 |
| R4 | -0.23 | -0.13 | -0.12 | 0.23 | 0.25 | -0.32 | -0.42 | -0.09 | -0.03 | 0.1 | -0.06 | -0.09 |
| R5 | 0.03 | 0.26 | 0.28 | 0.62 | 0.31 | 0.16 | 0.15 | -0.31 | -0.35 | -0.19 | -0.53 | -0.21 |
| R6 | -0.42 | 0.3 | 1.08 | 1.02 | 1.19 | 0.32 | -0.46 | -0.48 | -0.76 | -0.44 | -0.78 | -0.35 |

Table A1.2 - Measured damage numbers for test F1_002.

| {0;1000} waves | S1 | S2 | S3 | S4 | S5 | S6 | S7 | S8 | S9 | S10 | S11 | S12 |
|--------------------------|-------|-------|-------|-------|-------|-------|-------|-------|-------|-------|-------|-------|
| R1 | -1.13 | -1.08 | -0.95 | -0.12 | -0.38 | -0.95 | -1.10 | -0.98 | -0.53 | -0.35 | -0.33 | -0.75 |
| R2 | -0.36 | -0.62 | -0.25 | 0.13 | 0.05 | -0.32 | -0.35 | -0.37 | -0.23 | -0.12 | -0.21 | -0.23 |
| R3 | -0.31 | -0.19 | -0.08 | 0.02 | -0.1 | -0.25 | -0.24 | -0.13 | -0.06 | -0.1 | -0.03 | -0.16 |
| R4 | -0.26 | 0.12 | 0.15 | 0.08 | 0.12 | 0 | -0.27 | 0.12 | 0.09 | 0.26 | 0.06 | 0.05 |
| R5 | 0.22 | 0.09 | 0.19 | 0.38 | 0.22 | 0.1 | 0.19 | -0.07 | -0.11 | -0.23 | -0.07 | -0.12 |
| R6 | -0.05 | 0.13 | 0.32 | 0.41 | 0.33 | 0.1 | -0.08 | -0.26 | -0.65 | -0.27 | -0.55 | -0.26 |
| {1000; 3000} waves | S1 | S2 | S3 | S4 | S5 | S6 | S7 | S8 | S9 | S10 | S11 | S12 |
| R1 | -1.34 | -1.26 | -1.13 | -0.22 | -0.46 | -1.17 | -1.35 | -1.21 | -0.75 | -0.56 | -0.68 | -0.97 |
| R2 | -0.63 | -0.75 | -1.02 | -0.11 | -0.02 | -0.42 | -0.58 | -0.72 | -0.31 | -0.26 | -0.56 | -0.77 |
| R3 | -0.41 | -0.34 | -0.13 | 0.13 | -0.52 | -0.34 | -0.45 | -0.23 | -0.17 | -0.19 | 0.02 | -0.16 |
| R4 | -0.33 | -0.02 | -0.07 | 0.37 | 0.22 | -0.12 | -0.59 | -0.28 | -0.19 | 0.42 | -0.13 | 0.25 |
| R5 | 0.09 | 0.23 | 0.29 | 0.51 | 0.33 | 0.26 | 0.12 | -0.24 | -0.43 | -0.32 | -0.41 | -0.27 |
| R6 | -0.49 | 0.46 | 0.91 | 1.03 | 0.87 | 0.29 | -0.47 | -0.4 | -0.75 | -0.41 | -0.69 | -0.39 |

Table A1.3 – Measured damage numbers for test F1_003.

| {0;1000} waves | S1 | S2 | S3 | S4 | S5 | S6 | S7 | S8 | S9 | S10 | S11 | S12 |
|-----------------------------------|-----------|-----------|-----------|-----------|-----------|-----------|-----------|-----------|-----------|------------|------------|------------|
| R1 | -0.54 | -0.78 | -0.72 | -0.10 | -0.73 | -0.69 | -0.88 | -0.66 | -0.53 | -0.09 | -0.22 | -0.59 |
| R2 | -0.23 | -0.96 | -0.65 | 0.09 | 0.10 | -0.15 | -0.42 | -0.21 | -0.12 | -0.25 | -0.11 | -0.27 |
| R3 | -0.09 | -0.10 | 0.00 | 0.11 | -0.10 | -0.10 | -0.30 | -0.09 | -0.06 | -0.10 | 0.02 | -0.16 |
| R4 | 0.25 | 0.26 | 0.26 | 0.16 | 0.28 | 0.19 | -0.22 | 0.23 | 0.09 | 0.32 | 0.10 | 0.24 |
| R5 | 0.40 | 0.18 | 0.10 | 0.42 | 0.22 | 0.12 | 0.26 | 0.00 | -0.11 | -0.23 | -0.07 | 0.09 |
| R6 | -0.06 | 0.45 | 0.46 | 0.39 | 0.49 | 0.20 | -0.09 | -0.18 | -0.42 | -0.12 | -0.33 | -0.14 |
| {1000; 3000} waves | S1 | S2 | S3 | S4 | S5 | S6 | S7 | S8 | S9 | S10 | S11 | S12 |
| R1 | -0.92 | -0.99 | -0.86 | -0.15 | -0.82 | -0.75 | -0.93 | -0.75 | -0.53 | -0.12 | -0.31 | -0.66 |
| R2 | -0.52 | -1.20 | -1.12 | 0.07 | -0.91 | -0.23 | -0.60 | -0.32 | -0.12 | -0.32 | -0.19 | -0.36 |
| R3 | -0.29 | -0.19 | 0.13 | 0.26 | -0.26 | -0.12 | -0.35 | -0.16 | -0.06 | -0.31 | 0.02 | -0.28 |
| R4 | 0.16 | 0.10 | 0.31 | 0.19 | 0.21 | 0.17 | -0.09 | 0.10 | 0.09 | 0.12 | 0.03 | 0.15 |
| R5 | 0.35 | 0.26 | 0.10 | 0.59 | 0.26 | 0.21 | 0.31 | 0.16 | -0.11 | -0.39 | -0.35 | 0.11 |
| R6 | -0.45 | 0.63 | 1.02 | 1.09 | 0.99 | 0.27 | -0.53 | -0.36 | -0.42 | -0.21 | -0.52 | -0.24 |
| {1000; 5000} waves | S1 | S2 | S3 | S4 | S5 | S6 | S7 | S8 | S9 | S10 | S11 | S12 |
| R1 | -1.34 | -1.46 | -1.31 | -0.49 | -1.37 | -1.41 | -1.15 | -0.92 | -0.64 | -0.26 | -0.42 | -0.96 |
| R2 | -0.98 | -1.37 | -1.54 | -0.32 | -1.41 | -1.10 | -0.85 | -0.45 | -0.33 | -0.51 | -0.37 | -0.39 |
| R3 | -0.45 | -0.65 | -0.15 | 0.26 | -0.23 | -0.36 | -0.61 | -0.23 | 0.15 | -0.67 | 0.12 | -0.39 |
| R4 | 0.19 | 0.00 | 0.46 | 0.31 | 0.21 | 0.09 | 0.00 | 0.06 | 0.05 | 0.09 | 0.00 | 0.02 |
| R5 | 0.29 | 0.32 | 0.25 | 0.88 | 0.26 | 0.29 | 0.25 | 0.29 | -0.16 | -0.37 | -0.51 | 0.21 |
| R6 | -0.72 | 0.75 | 1.02 | 1.07 | 0.75 | 0.62 | -0.69 | -0.61 | -0.49 | -0.33 | -0.55 | -0.51 |

Table A1.4 – Measured damage numbers for test F1_004.

| {0;1000} waves | S1 | S2 | S3 | S4 | S5 | S6 | S7 | S8 | S9 | S10 | S11 | S12 |
|-----------------------------------|-----------|-----------|-----------|-----------|-----------|-----------|-----------|-----------|-----------|------------|------------|------------|
| R1 | -0.86 | -0.42 | -0.37 | -0.10 | -0.42 | -0.45 | -0.84 | -0.41 | -0.28 | 0.00 | -0.21 | -0.46 |
| R2 | -0.12 | -0.62 | -0.62 | 0.09 | -0.59 | -0.53 | -0.16 | -0.10 | -0.09 | -0.16 | -0.10 | -0.16 |
| R3 | -0.03 | -0.17 | 0.12 | 0.11 | 0.09 | -0.13 | -0.11 | 0.00 | 0.00 | -0.03 | 0.10 | 0.05 |
| R4 | 0.12 | 0.31 | 0.19 | 0.16 | 0.17 | 0.21 | 0.08 | 0.16 | 0.13 | 0.25 | 0.11 | 0.19 |
| R5 | 0.23 | 0.26 | 0.21 | 0.42 | 0.25 | 0.23 | 0.19 | 0.12 | -0.07 | -0.14 | -0.02 | 0.14 |
| R6 | -0.10 | 0.40 | 0.33 | 0.32 | 0.36 | 0.37 | -0.03 | -0.09 | -0.26 | -0.09 | -0.26 | -0.11 |
| {1000; 3000} waves | S1 | S2 | S3 | S4 | S5 | S6 | S7 | S8 | S9 | S10 | S11 | S12 |
| R1 | -0.98 | -0.56 | -0.49 | -0.07 | -0.61 | -0.57 | -0.92 | -0.57 | -0.32 | -0.12 | -0.30 | -0.53 |
| R2 | -0.21 | -0.77 | -0.53 | 0.21 | -0.61 | -0.73 | -0.30 | -0.23 | -0.16 | -0.16 | -0.22 | -0.26 |
| R3 | -0.11 | -0.33 | 0.23 | 0.09 | 0.17 | -0.26 | -0.16 | 0.11 | -0.11 | -0.11 | -0.08 | 0.03 |
| R4 | 0.21 | 0.41 | 0.12 | 0.21 | 0.09 | 0.33 | -0.19 | 0.22 | 0.03 | 0.12 | 0.07 | 0.26 |
| R5 | 0.19 | 0.29 | 0.31 | 0.56 | 0.33 | 0.26 | -0.25 | 0.31 | -0.13 | -0.27 | -0.15 | 0.29 |
| R6 | -0.16 | 0.51 | 0.62 | 0.54 | 0.59 | 0.52 | -0.21 | -0.26 | -0.32 | -0.16 | -0.34 | -0.31 |
| {3000; 5000} waves | S1 | S2 | S3 | S4 | S5 | S6 | S7 | S8 | S9 | S10 | S11 | S12 |
| R1 | -1.10 | -0.72 | -0.63 | -0.22 | -0.72 | -0.66 | -1.02 | -0.82 | -0.32 | -0.22 | -0.30 | -0.91 |
| R2 | -0.42 | -0.92 | -0.77 | 0.11 | -0.79 | -0.83 | -0.53 | -0.46 | -0.60 | -0.33 | -0.52 | -0.53 |
| R3 | -0.37 | -0.67 | 0.30 | 0.15 | 0.37 | -0.70 | -0.46 | 0.26 | -0.30 | -0.29 | -0.22 | 0.19 |
| R4 | 0.16 | 0.34 | 0.22 | 0.16 | 0.29 | 0.29 | 0.12 | 0.32 | 0.13 | 0.09 | 0.16 | 0.33 |
| R5 | 0.31 | 0.35 | 0.46 | 0.63 | 0.40 | 0.32 | 0.39 | 0.43 | -0.33 | -0.46 | -0.36 | 0.47 |
| R6 | -0.29 | 0.69 | 0.71 | 0.42 | 0.64 | 0.61 | -0.27 | -0.62 | -0.53 | -0.33 | -0.53 | -0.58 |

Table A1.5 – Measured damage numbers for test F1_004*.

| {0;1000} waves | S1 | S2 | S3 | S4 | S5 | S6 | S7 | S8 | S9 | S10 | S11 | S12 |
|--------------------------|-------|-------|-------|-------|-------|-------|-------|-------|-------|-------|-------|-------|
| R1 | -0.91 | -0.71 | -0.51 | -0.16 | -0.69 | -0.73 | -0.96 | -0.43 | -0.32 | 0.08 | -0.31 | -0.37 |
| R2 | -0.16 | -0.69 | -0.59 | 0.00 | -0.54 | -0.66 | -0.19 | -0.22 | -0.14 | -0.15 | -0.12 | -0.10 |
| R3 | -0.07 | -0.26 | 0.16 | 0.10 | 0.11 | -0.33 | -0.14 | 0.11 | 0.00 | -0.10 | 0.10 | 0.14 |
| R4 | 0.12 | 0.33 | 0.21 | 0.19 | 0.19 | 0.24 | 0.12 | 0.21 | 0.11 | 0.19 | 0.26 | 0.18 |
| R5 | 0.27 | 0.16 | 0.22 | 0.41 | 0.24 | 0.21 | 0.17 | 0.16 | 0.00 | -0.20 | 0.12 | 0.16 |
| R6 | -0.09 | 0.39 | 0.33 | 0.32 | 0.31 | 0.29 | -0.08 | -0.09 | -0.24 | -0.16 | -0.11 | -0.13 |
| {1000; 3000} waves | S1 | S2 | S3 | S4 | S5 | S6 | S7 | S8 | S9 | S10 | S11 | S12 |
| R1 | -1.01 | -0.89 | -0.51 | -0.11 | -0.62 | -0.61 | -1.03 | -0.61 | -0.30 | -0.12 | -0.29 | -0.63 |
| R2 | -0.27 | -0.82 | -0.54 | 0.26 | -0.59 | -0.74 | -0.32 | -0.25 | -0.17 | -0.16 | -0.19 | -0.21 |
| R3 | -0.19 | -0.34 | 0.26 | 0.05 | 0.16 | -0.31 | -0.18 | 0.16 | -0.02 | -0.11 | 0.00 | 0.11 |
| R4 | 0.27 | 0.42 | 0.17 | 0.37 | 0.12 | 0.32 | -0.16 | 0.22 | 0.09 | 0.12 | 0.12 | 0.21 |
| R5 | 0.26 | 0.31 | 0.33 | 0.59 | 0.30 | 0.26 | -0.27 | 0.33 | -0.16 | -0.27 | -0.16 | 0.31 |
| R6 | -0.26 | 0.64 | 0.65 | 0.61 | 0.51 | 0.51 | -0.22 | -0.22 | -0.35 | -0.16 | -0.34 | -0.36 |

Table A1.6 – Measured damage numbers for test F1_005.

| {0;1000} waves | S1 | S2 | S3 | S4 | S5 | S6 | S7 | S8 | S9 | S10 | S11 | S12 |
|--------------------------|-------|-------|-------|-------|-------|-------|-------|-------|-------|-------|-------|-------|
| R1 | -0.79 | -0.43 | -0.36 | -0.12 | -0.34 | -0.39 | -0.73 | -0.39 | -0.29 | 0.12 | -0.24 | -0.33 |
| R2 | -0.15 | -0.36 | -0.42 | 0.10 | -0.29 | -0.42 | -0.12 | -0.25 | -0.16 | -0.11 | -0.09 | -0.11 |
| R3 | -0.02 | -0.19 | 0.10 | 0.13 | 0.06 | -0.24 | -0.11 | 0.17 | 0.10 | -0.12 | 0.14 | 0.15 |
| R4 | 0.10 | 0.12 | 0.18 | 0.14 | 0.21 | 0.26 | 0.09 | 0.23 | 0.11 | 0.09 | 0.27 | 0.24 |
| R5 | 0.22 | 0.18 | 0.20 | 0.26 | 0.16 | 0.19 | 0.11 | 0.14 | 0.12 | -0.19 | 0.16 | 0.19 |
| R6 | -0.03 | 0.26 | 0.17 | 0.30 | 0.33 | 0.26 | -0.12 | 0.00 | -0.09 | -0.14 | -0.09 | -0.10 |
| {1000; 3000} waves | S1 | S2 | S3 | S4 | S5 | S6 | S7 | S8 | S9 | S10 | S11 | S12 |
| R1 | -0.88 | -0.91 | -0.59 | -0.32 | -0.52 | -0.90 | -0.94 | -0.41 | -0.33 | 0.09 | -0.21 | -0.39 |
| R2 | -0.26 | -0.63 | -0.66 | 0.19 | -0.48 | -0.72 | -0.26 | -0.38 | -0.21 | -0.29 | -0.12 | -0.21 |
| R3 | -0.12 | -0.28 | 0.21 | 0.21 | -0.14 | -0.37 | -0.19 | 0.41 | 0.16 | -0.10 | 0.22 | 0.28 |
| R4 | 0.06 | 0.28 | 0.29 | 0.22 | 0.33 | 0.42 | -0.07 | 0.31 | 0.27 | 0.18 | 0.35 | 0.25 |
| R5 | 0.31 | 0.26 | 0.16 | 0.37 | 0.18 | 0.26 | 0.21 | 0.21 | 0.25 | -0.21 | 0.32 | 0.14 |
| R6 | -0.14 | 0.34 | 0.33 | 0.43 | 0.30 | 0.37 | -0.19 | 0.12 | -0.16 | -0.23 | -0.16 | -0.22 |
| {3000; 5000} waves | S1 | S2 | S3 | S4 | S5 | S6 | S7 | S8 | S9 | S10 | S11 | S12 |
| R1 | -1.16 | -0.98 | -0.92 | -0.55 | -0.94 | -1.00 | -1.20 | -0.59 | -0.68 | 0.12 | -0.33 | -0.61 |
| R2 | -0.34 | -0.71 | -0.76 | 0.31 | -0.66 | -0.88 | -0.42 | -0.53 | -0.37 | -0.41 | -0.40 | -0.26 |
| R3 | -0.36 | -0.37 | 0.24 | 0.19 | -0.08 | -0.37 | -0.34 | 0.62 | 0.25 | -0.15 | 0.27 | 0.22 |
| R4 | 0.22 | 0.25 | 0.33 | 0.41 | 0.36 | 0.42 | 0.21 | 0.42 | 0.33 | 0.21 | 0.39 | 0.23 |
| R5 | 0.39 | 0.32 | 0.16 | 0.37 | 0.18 | 0.26 | 0.33 | 0.29 | 0.24 | -0.29 | 0.21 | 0.21 |
| R6 | -0.29 | 0.41 | 0.52 | 0.55 | 0.45 | 0.37 | -0.26 | 0.26 | -0.12 | -0.25 | -0.18 | 0.23 |

Table A1.7 – Measured damage numbers for test F1_006.

| {0;1000} waves | S1 | S2 | S3 | S4 | S5 | S6 | S7 | S8 | S9 | S10 | S11 | S12 |
|-----------------------------------|-----------|-----------|-----------|-----------|-----------|-----------|-----------|-----------|-----------|------------|------------|------------|
| R1 | -0.40 | -0.43 | -0.29 | -0.04 | -0.26 | -0.33 | -0.32 | -0.31 | -0.21 | 0.14 | -0.13 | -0.29 |
| R2 | -0.15 | -0.36 | -0.21 | 0.13 | -0.13 | -0.29 | -0.14 | -0.29 | -0.18 | -0.06 | -0.13 | -0.25 |
| R3 | -0.02 | -0.19 | 0.08 | 0.09 | 0.02 | -0.22 | -0.03 | -0.12 | 0.13 | -0.10 | 0.21 | -0.12 |
| R4 | 0.06 | -0.02 | 0.07 | 0.11 | 0.12 | 0.05 | 0.09 | 0.26 | 0.16 | 0.14 | 0.22 | 0.21 |
| R5 | 0.12 | 0.09 | 0.18 | 0.11 | 0.09 | 0.14 | 0.07 | 0.09 | 0.15 | 0.00 | 0.14 | 0.12 |
| R6 | 0.14 | 0.09 | 0.12 | 0.21 | 0.17 | 0.10 | 0.12 | 0.10 | 0.00 | -0.11 | -0.13 | 0.05 |
| {1000; 3000} waves | S1 | S2 | S3 | S4 | S5 | S6 | S7 | S8 | S9 | S10 | S11 | S12 |
| R1 | -0.43 | -0.48 | -0.32 | 0.00 | -0.38 | -0.34 | -0.40 | -0.33 | -0.25 | 0.09 | -0.21 | -0.32 |
| R2 | -0.17 | -0.42 | 0.17 | 0.09 | -0.41 | -0.41 | -0.33 | -0.19 | -0.16 | -0.12 | -0.13 | -0.17 |
| R3 | -0.08 | 0.05 | 0.13 | 0.24 | 0.12 | 0.08 | -0.06 | -0.09 | 0.15 | -0.21 | 0.21 | 0.01 |
| R4 | 0.02 | 0.09 | 0.21 | 0.25 | 0.23 | 0.12 | 0.11 | 0.32 | 0.24 | 0.17 | 0.22 | 0.29 |
| R5 | 0.09 | 0.15 | 0.26 | 0.37 | 0.24 | 0.19 | 0.13 | 0.22 | 0.26 | 0.12 | 0.14 | 0.26 |
| R6 | 0.23 | 0.21 | 0.36 | 0.42 | 0.40 | 0.20 | 0.25 | 0.21 | 0.11 | -0.09 | -0.13 | 0.30 |
| {3000; 5000} waves | S1 | S2 | S3 | S4 | S5 | S6 | S7 | S8 | S9 | S10 | S11 | S12 |
| R1 | -0.51 | -0.52 | -0.45 | -0.10 | -0.42 | -0.48 | -0.50 | -0.29 | -0.31 | 0.12 | -0.29 | -0.27 |
| R2 | -0.33 | -0.42 | 0.22 | 0.14 | -0.44 | -0.39 | -0.40 | -0.09 | -0.12 | -0.21 | -0.13 | -0.11 |
| R3 | -0.15 | 0.05 | 0.28 | 0.22 | 0.09 | 0.16 | -0.12 | 0.00 | 0.12 | -0.25 | 0.16 | -0.07 |
| R4 | 0.11 | 0.09 | 0.32 | 0.35 | 0.32 | 0.21 | 0.16 | 0.40 | 0.29 | 0.13 | 0.31 | 0.37 |
| R5 | 0.14 | 0.15 | 0.34 | 0.37 | 0.40 | 0.27 | 0.20 | 0.38 | 0.33 | 0.12 | 0.21 | 0.32 |
| R6 | 0.19 | 0.21 | 0.41 | 0.40 | 0.39 | 0.37 | 0.25 | 0.33 | 0.21 | 0.00 | 0.04 | 0.30 |

Table A1.8 – Measured damage numbers for test F1_008.

| {0;1000} waves | S1 | S2 | S3 | S4 | S5 | S6 | S7 | S8 | S9 | S10 | S11 | S12 |
|-----------------------------------|-----------|-----------|-----------|-----------|-----------|-----------|-----------|-----------|-----------|------------|------------|------------|
| R1 | -0.23 | -0.21 | -0.13 | 0.10 | -0.26 | -0.23 | -0.24 | -0.12 | -0.13 | 0.14 | -0.13 | -0.14 |
| R2 | -0.24 | -0.19 | -0.15 | 0.09 | -0.13 | -0.18 | -0.19 | -0.16 | -0.14 | -0.06 | -0.13 | -0.19 |
| R3 | 0.04 | -0.13 | 0.03 | 0.11 | 0.02 | -0.22 | 0.00 | -0.21 | -0.12 | -0.10 | 0.21 | -0.16 |
| R4 | 0.10 | -0.04 | 0.00 | 0.25 | 0.12 | 0.14 | 0.26 | 0.26 | 0.29 | 0.14 | 0.22 | 0.21 |
| R5 | 0.13 | 0.21 | 0.19 | 0.23 | 0.09 | 0.25 | 0.15 | 0.09 | 0.10 | 0.00 | 0.14 | 0.09 |
| R6 | 0.17 | 0.12 | 0.32 | 0.29 | 0.17 | 0.13 | 0.12 | 0.10 | 0.00 | -0.11 | -0.13 | 0.12 |
| {1000; 3000} waves | S1 | S2 | S3 | S4 | S5 | S6 | S7 | S8 | S9 | S10 | S11 | S12 |
| R1 | -0.19 | -0.33 | -0.22 | 0.09 | -0.23 | -0.31 | -0.14 | -0.29 | -0.13 | 0.06 | -0.13 | -0.29 |
| R2 | -0.18 | -0.33 | -0.04 | 0.03 | -0.11 | -0.26 | -0.21 | -0.25 | -0.18 | -0.16 | -0.19 | -0.15 |
| R3 | 0.10 | -0.13 | 0.09 | 0.15 | 0.19 | -0.24 | 0.12 | -0.14 | -0.18 | -0.26 | 0.21 | -0.10 |
| R4 | 0.09 | -0.12 | 0.09 | 0.31 | 0.14 | 0.09 | 0.12 | 0.22 | 0.37 | 0.20 | 0.33 | 0.32 |
| R5 | 0.11 | 0.28 | 0.31 | 0.43 | 0.28 | 0.23 | 0.15 | 0.03 | 0.00 | 0.00 | 0.14 | 0.07 |
| R6 | 0.21 | 0.33 | 0.38 | 0.52 | 0.40 | 0.22 | 0.26 | 0.27 | 0.00 | 0.12 | -0.13 | 0.34 |
| {3000; 5000} waves | S1 | S2 | S3 | S4 | S5 | S6 | S7 | S8 | S9 | S10 | S11 | S12 |
| R1 | -0.17 | -0.33 | -0.31 | 0.19 | -0.26 | -0.33 | -0.19 | -0.23 | -0.21 | 0.12 | -0.21 | -0.22 |
| R2 | -0.14 | -0.29 | -0.19 | 0.18 | -0.09 | -0.31 | -0.26 | -0.19 | -0.03 | -0.09 | -0.09 | -0.13 |
| R3 | 0.09 | -0.14 | 0.25 | 0.23 | 0.26 | -0.19 | 0.09 | -0.21 | -0.16 | -0.10 | -0.14 | -0.19 |
| R4 | 0.22 | -0.09 | 0.43 | 0.42 | 0.33 | 0.10 | 0.15 | 0.40 | 0.47 | 0.38 | 0.39 | 0.44 |
| R5 | 0.31 | 0.37 | 0.50 | 0.48 | 0.45 | 0.33 | 0.31 | 0.21 | 0.15 | 0.40 | 0.12 | 0.19 |
| R6 | 0.34 | 0.49 | 0.49 | 0.60 | 0.41 | 0.43 | 0.41 | 0.43 | 0.16 | 0.33 | 0.10 | 0.45 |

APPENDIX 1

Table A1.9 – Measured damage numbers for test F1_008.

| {0;1000} waves | S1 | S2 | S3 | S4 | S5 | S6 | S7 | S8 | S9 | S10 | S11 | S12 |
|-----------------------------------|-----------|-----------|-----------|-----------|-----------|-----------|-----------|-----------|-----------|------------|------------|------------|
| R1 | -0.21 | -0.21 | -0.13 | 0.16 | -0.10 | -0.18 | -0.23 | -0.09 | -0.10 | 0.14 | -0.11 | -0.14 |
| R2 | -0.16 | -0.14 | -0.09 | 0.13 | -0.10 | -0.11 | -0.12 | -0.14 | -0.19 | -0.06 | -0.16 | -0.19 |
| R3 | 0.20 | -0.07 | 0.14 | 0.19 | 0.12 | -0.12 | 0.17 | -0.17 | 0.00 | -0.10 | 0.01 | -0.16 |
| R4 | 0.03 | 0.12 | 0.11 | 0.32 | 0.09 | 0.09 | 0.11 | 0.21 | 0.31 | 0.14 | 0.28 | 0.21 |
| R5 | 0.16 | 0.25 | 0.21 | 0.21 | 0.19 | 0.23 | 0.14 | 0.14 | 0.14 | 0.00 | 0.10 | 0.09 |
| R6 | 0.21 | 0.14 | 0.23 | 0.22 | 0.21 | 0.29 | 0.24 | 0.03 | 0.02 | -0.11 | -0.13 | 0.12 |
| {1000; 3000} waves | S1 | S2 | S3 | S4 | S5 | S6 | S7 | S8 | S9 | S10 | S11 | S12 |
| R1 | -0.30 | -0.29 | -0.20 | 0.08 | -0.18 | -0.16 | -0.29 | 0.01 | -0.19 | 0.14 | -0.22 | -0.07 |
| R2 | -0.29 | -0.14 | -0.15 | 0.21 | -0.12 | -0.14 | -0.28 | -0.11 | -0.25 | -0.06 | -0.21 | -0.19 |
| R3 | 0.14 | 0.13 | 0.23 | 0.14 | 0.19 | -0.04 | 0.12 | 0.03 | 0.16 | -0.10 | 0.11 | 0.10 |
| R4 | 0.12 | 0.09 | 0.31 | 0.29 | 0.23 | 0.16 | 0.19 | 0.32 | 0.37 | 0.14 | 0.33 | 0.29 |
| R5 | 0.26 | 0.38 | 0.41 | 0.37 | 0.38 | 0.31 | 0.14 | 0.28 | 0.22 | 0.00 | 0.20 | 0.24 |
| R6 | 0.33 | 0.23 | 0.43 | 0.29 | 0.37 | 0.40 | 0.30 | 0.14 | 0.12 | -0.11 | -0.16 | 0.16 |
| {3000; 5000} waves | S1 | S2 | S3 | S4 | S5 | S6 | S7 | S8 | S9 | S10 | S11 | S12 |
| R1 | -0.27 | -0.29 | -0.14 | 0.02 | -0.11 | -0.23 | -0.24 | 0.12 | -0.14 | 0.26 | -0.13 | -0.16 |
| R2 | -0.28 | -0.09 | -0.16 | 0.16 | -0.13 | -0.13 | -0.29 | -0.09 | -0.21 | -0.02 | -0.22 | -0.18 |
| R3 | 0.20 | 0.25 | 0.23 | 0.26 | 0.23 | 0.12 | 0.19 | 0.16 | 0.31 | 0.10 | 0.36 | 0.23 |
| R4 | 0.22 | 0.19 | 0.31 | 0.32 | 0.29 | 0.23 | 0.28 | 0.40 | 0.47 | 0.26 | 0.46 | 0.37 |
| R5 | 0.14 | 0.42 | 0.39 | 0.48 | 0.42 | 0.39 | 0.19 | 0.34 | 0.35 | 0.12 | 0.29 | 0.37 |
| R6 | 0.42 | 0.23 | 0.50 | 0.49 | 0.48 | 0.29 | 0.38 | 0.28 | 0.30 | -0.03 | -0.07 | 0.22 |

APPENDIX 2

In order to clarify the discussion of sections 4.2.6.2 and 4.3.5.2 regarding the tests repeatability, the present appendix provides the plots concerning the S_{3Dsub} for the tests compared in the previous sections.

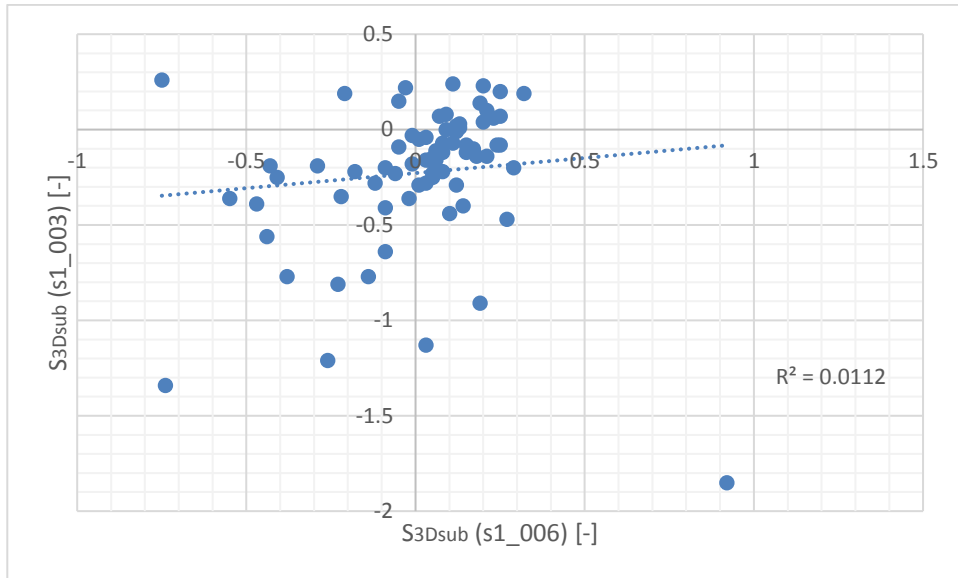


Figure A2.1 – Comparison of the S_{3Dsub} after 5000 waves for tests s1_003 and s1_006.

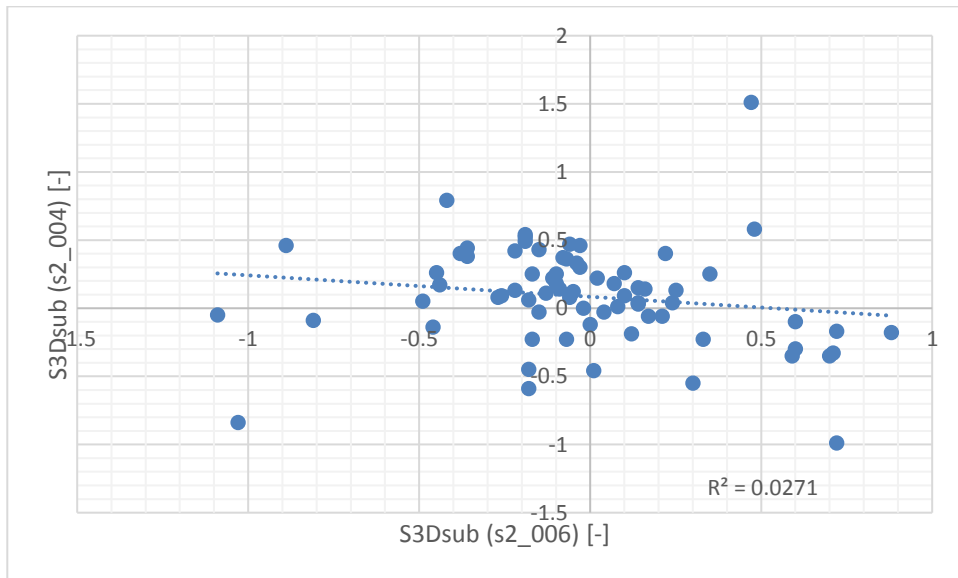


Figure A2.2 – Comparison of the S_{3Dsub} after 5000 waves for tests s2_004 and s2_006.

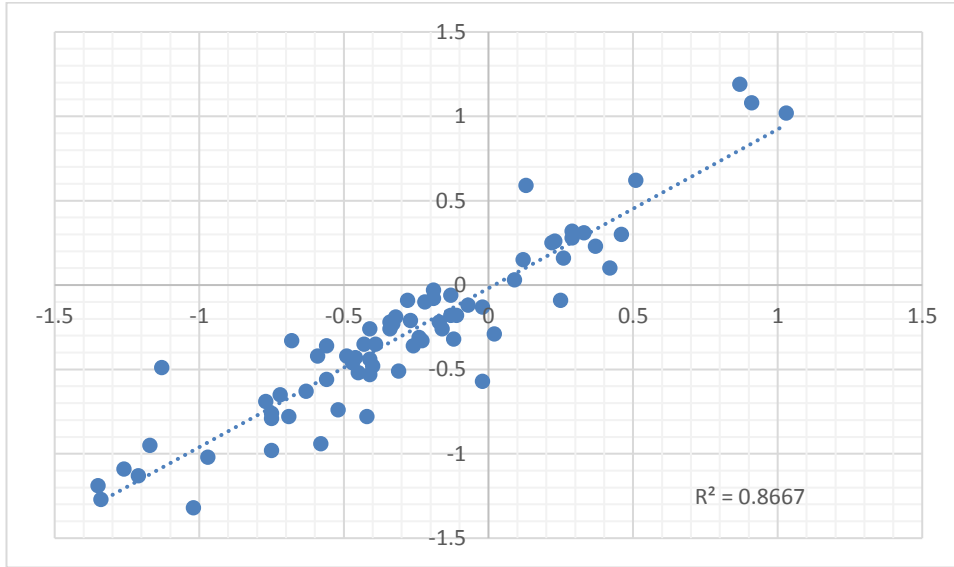


Figure A2.3 – Comparison of the S_{3Dsub} after 3000 waves for tests F1_001 and F1_002.